THE HONG KONG
POLYTECHNIC UNIVERSITY
香港理工大學
Pao Yue-kong Library
包玉剛圖書館

Copyright Undertaking

This thesis is protected by copyright, with all rights reserved.

By reading and using the thesis, the reader understands and agrees to the following terms:

1. The reader will abide by the rules and legal ordinances governing copyright regarding the use of the thesis.
2. The reader will use the thesis for the purpose of research or private study only and not for distribution or further reproduction or any other purpose.
3. The reader agrees to indemnify and hold the University harmless from and against any loss, damage, cost, liability or expenses arising from copyright infringement or unauthorized usage.

If you have reasons to believe that any materials in this thesis are deemed not suitable to be distributed in this form, or a copyright owner having difficulty with the material being included in our database, please contact lbsys@polyu.edu.hk providing details. The Library will look into your claim and consider taking remedial action upon receipt of the written requests.

Pao Yue-kong Library, The Hong Kong Polytechnic University, Hung Hom, Kowloon, Hong Kong

http://www.lib.polyu.edu.hk

BUCKLING OF EXTENSIVELY WELDED STEEL CYLINDRICAL SHELLS UNDER AXIAL COMPRESSION

By

Xiang LIN

BEng, MSc

A Thesis Submitted
in Partial Fulfillment of the Requirements for the Degree of
Doctor of Philosophy

Department of Civil and Structural Engineering
The Hong Kong Polytechnic University

March, 2004

Pao Yue-kong Library
PolyU • Hong Kong

DECLARATION

I hereby declare that this thesis entitled "**Buckling of Extensively Welded Steel Cylindrical Shells under Axial Compression**" has not been, either in whole or in part, previously submitted for a degree in this or other institutions, and the work presented in this thesis is original unless otherwise acknowledged in the text.

SIGNED

_____

Xiang LIN

ABSTRACT

Thin cylindrical shells in large civil engineering steel shell structures such as steel silos and tanks are subject to both axial compression and internal pressure. Buckling under axial compression often governs their design. These shells are commonly constructed by joining a large number of rolled panels using many short vertical welds and continuous circumferential welds. This fabrication method leads to unique geometric imperfections which have been argued to be severely detrimental to the shell axial buckling strength. In addition, welding-induced residual stresses in these shells may also have a significant effect on this buckling strength. A review of the existing literature reveals that few previous studies have examined the buckling behavior of these shells with a rigorous treatment of the geometric imperfections and residual stresses in these shells. This thesis presents both theoretical and experimental studies aimed at correcting this important deficiency in existing knowledge.

The first part of the thesis, consisting of Chapters 3-5, presents the results of theoretical studies into the characteristics of geometric imperfections measured in three large steel silos at Port Kembla, Australia, and their effect on buckling strength. In order to accurately represent these imperfections measured at non-uniformly spaced sampling points, a new iterative Fourier decomposition method was proposed. The traditional Fourier decomposition method cannot produce accurate Fourier representations, and the reasons for this difficulty are clarified in the thesis. This new iterative method was then employed in deducing accurate Fourier series representing the measured imperfections. It is explained in the thesis that these real imperfections, due to their non-zero values at the boundaries, can only be accurately represented using half-wave cosine series in the meridional direction, an important phenomenon overlooked by all previous researchers. The characteristics of the imperfections are next examined by studying the spectra of the deduced Fourier series, including both 1D and 2D Fourier series. It is shown that the dominant components of the imperfections in each shell are in the lower Fourier terms, with some of these components being closely associated

with the weld pattern. Finite element analyses of the three silo shells (referred to as Shells A, B, and C) showed that these shells have buckling strengths which are much lower than those of shells with many known forms of imperfections. A systematic parametric study revealed that the buckling strength of Shell A is dominated by significant axisymmetric imperfections, while those of Shells B and C are governed by highly non-symmetric imperfections. Based on the specification of Eurocode 3, an automated computer procedure was developed to numerically 'measure' the local dimples and out-of-roundness of these shells. This was undertaken to determine the quality classes of the three shells so that their buckling strengths as predicted by Eurocode 3 could be found. A comparison between the predictions of the code and finite element results from nonlinear analyses reveals that the existing rule in Eurocode 3 is too optimistic about shells of Class A but too pessimistic about shells of Classes B and C.

While detailed measurements of imperfections are available for the three large silos, the residual stresses in these shells due to welding are unknown. As residual stresses may have a significant effect on the buckling strength, an experimental study aimed at an indirect evaluation of this effect is presented in Chapters 6-8. In this experimental study, an innovative two-stage model fabrication technique was proposed and implemented with a sophisticated experimental set up for the fabrication of small models simulating large cylindrical shells with many welds. Three model shells were fabricated and tested under axial compression, each of which had a different weld pattern. The initial geometric imperfections in these model shells were precisely measured and decomposed into Fourier series. The imperfections were also found to be dominated by lower Fourier terms and closely associated with the weld patterns. The buckling loads of the model shells are very low compared to the value of a corresponding perfect shell, demonstrating the serious deleterious effect of the imperfections in these shells. Finite element buckling loads obtained from non-linear analyses with the measured imperfections accurately modeled are also presented. These buckling loads are close but slightly lower than the experimental buckling loads, indicating that the effect of residual stresses and other factors in these shells is small but beneficial, and may be safely ignored.

Finally, a parametric study is presented in Chapter 9, in which the buckling behavior and strength of the three real silo shells under the combined action of axial compression and

internal pressure were explored. Nonlinear finite element analyses revealed that the strengths of Shell A are considerably lower than those of Shells B and C, as the dominant imperfection components are significantly axisymmetric in Shell A, but are highly non-symmetric in Shells B and C. Comparisons between the finite element results and the predictions of Eurocode 3 indicate that the code overestimates the failure strengths of Shell A considerably. Modifications to the existing design rule are thus presented to achieve safe predictions.

ACKNOWLEDGEMENTS

The author is especially indebted to his supervisor, Professor Jin-Guang Teng, for his enthusiastic approach, continued inspiration, enlightening guidance, constant encouragement, and for his friendship. The author hopes that the work presented in this thesis could reflect to certain extent many of his creative ideas.

The author is grateful to Professor Shi-Lin Dong of Zhejiang University for his encouragement and support throughout the course of this work.

Professor J.M. Rotter of the University of Edinburgh and Dr X.L. Ding of The Hong Kong Polytechnic University provided me with data of imperfection measurements made on three large steel silos in service which were extensively exploited in the work presented in this thesis. In addition, Professor Rotter offered the author valuable help with the work presented in Chapter 4 and pictures of silo failures for use in this thesis, while Dr Ding spent much of his precious time discussing with the author various issues in the interpretation of imperfection data. Special thanks go to both Professor Rotter and Dr Ding for all their support and help. Thanks also go to Professor A. Combescure of INSA Lyon, France, for his advices on the simulation of welding processes.

The author wishes to thank Professors J.M. Ko and Y.S. Li, Heads of the Department of Civil and Structural Engineering at The Hong Kong Polytechnic University (during different periods of this candidature), who made available all facilities of the Department.

The author is deeply indebted to the technical staff in the Heavy Structures Laboratory of the Department, particularly, Messrs K. Tam, K.H. Wong, S.W. Liauw, H.Y. Yau and C.K. Kai, for their support and assistance during the experimental part of the project.

Thanks are also due to my friends and colleagues in the Department of Civil and Structural Engineering, The Hong Kong Polytechnic University. In particular, I wish to thank Tao

Hong, Yang Zhao, Chang-Yong Song, Jian Yao, Hon-Ting Wong, Xing-Fei Yuan, Yuan-Feng Duan and Zeng-Chun Wang for helpful discussions during my study. In addition, Yang Zhao is thanked for leaving me with his shell buckling test rig in good shape, for sharing his experience with me and for providing me with several diagrams of his shell buckling test rig for inclusion in this thesis.

This research project was financially supported by the Research Grants Council of the Hong Kong Special Administrative Region (Project No. 5045/98E) and The Hong Kong Polytechnic University. The author is grateful to both organisations for their financial support.

LIST OF PUBLICATIONS

The following three papers have been published during this candidature:

1. Lin, X. and Teng, J.G. (2003). "Iterative fourier decomposition of imperfection measurements at non-uniformly distributed sampling points". *Thin-Walled Structures*, 41(10): 901-924.

2. Teng, J.G. and Lin, X. (2002). "Fabrication of small models of large cylinders with extensive welding for buckling experiments". *Proceedings, 2002 Annual Stability Conference, Structural Stability Research Council*, April 24-27, 2002, Seattle, Washington, USA, pp245-266.

3. Lin, X. and Teng, J.G. (2002). "Buckling behaviour of extensively-welded steel cylinders under axial compression". *Advance in Steel Structures, Proceedings, Third International Conference on Advances in Steel Structures*, 9-11, December 2002, Hong Kong, China, Elsevier, pp737-744.

CONTENTS

DECLARATION.....I
ABSTRACT.....II
ACKNOWLEDGMENTS.....V
LIST OF PUBLICATIONS.....VII
CONTENTS.....VIII
NOTATION.....XV

CHAPTER 1 INTRODUCTION.....1
1.1 BACKGROUND.....1
1.2 BEHAVIOR OF AXIALLY COMPRESSED PERFECT AND IMPERFECT THIN CYLINDRICAL SHELLS.....3
1.3 APPROACHES FOR EXPLORING THE BEHAVIOUR OF THIN CYLINDRICAL SHELLS.....5
1.4 OBJECTIVES, RESEARCH STRATEGY, AND SCOPE OF THIS WORK.....7

CHAPTER 2 LITERATURE REVIEW.....14
2.1 INTRODUCTION.....14
2.2 BUCKLING OF ISOTROPIC CYLINDRICAL SHELLS UNDER AXIAL COMPRESSION.....14
2.2.1 Historical Note.....14
2.2.2 Effect of Prebuckling Deformations.....17
2.2.3 Effect of Boundary Conditions.....17
2.2.4 Imperfection Sensitivity.....18
2.2.5 Effect of Internal Pressurization.....19
2.2.6 Cylindrical Shells with Axisymmetric Imperfections.....20

2.2.7 Steel Cylinders Constructed from Many Welded Panels.....22
2.3 GEOMTRIC IMPERFECTIONS IN CYLINDRICAL SHELLS.....23
2.4 GEOMETRIC IMPERFECTIONS IN SHELL BUCKLING ANALYSIS.....24
2.4.1 Idealized Geometric Imperfections.....25
2.4.2 Localized Realistic Geometric Imperfections.....25
2.4.3 Equivalent Geometric Imperfections.....26
2.4.4 Equivalent Imperfections with Consistent Residual Stresses.....28
2.4.5 Equivalent-Load Geometric Imperfections.....29
2.4.6 Real Geometric Imperfections Represented by Fourier Series.....30
2.5 STABILITY DESIGN OF CYLINDRICAL SHELLS IN STEEL SILOS AND TANKS.....32
2.5.1 Introduction.....32
2.5.2 Fabrication Quality and Initial Geometric Imperfections.....33
2.5.3 Elastic Buckling under Axial Compression.....35
2.5.4 Elastic Buckling under Axial Compression and Low Internal Pressure.....37
2.5.5 Plastic Collapse under Axial Compression and High Internal Pressure.....38
2.5.6 Unified Expression for the Elastic Plastic Buckling Stress.....39
2.6 TECHNIQUES FOR SHELL BUCKLING EXPERIMENTS.....40
2.6.1 Introduction.....40
2.6.2 Model Fabrication.....41
2.6.3 Techniques for Imperfection Measurements.....43
2.6.4 Boundary and Loading Conditions.....46
2.7 NUMERICAL TECHNIQUES FOR SHELL BUCKLING ANALYIS.....47
2.8 CONCLUSIONS.....49

CHAPTER 3 ITERATIVE FOURIER DECOMPOSITION OF IMPERFECTION MEASUREMENTS WITH NON-UNIFORM INTERVALS.....55
3.1 INTRODUCTION.....55
3.2 FOURIER DECOMPOSITION OF UNIFORMLY-SPACED DATA POINTS.....57
3.3 FOURIER DECOMPOSITION OF NON-UNIFORMLY SPACED DATA POINTS.....60

3.4 ITERATIVE FOURIER DECOMPOSITION.....61
3.5 NUMERICAL EXAMPLES.....63
3.5.1 Example 1.....63
3.5.2 Example 2.....64
3.6 CONCLUSIONS.....64
APPENDICES.....78
A3.1 EXAMPLE DERIVATIONS OF FOURIER COEFFICIENTS.....78
A3.2 EXPRESSIONS OF $E_i(\delta)$ (i = 1-20).....80

CHAPTER 4 ANALYSIS OF GEOMETRIC IMPERFECTIONS IN LARGE EXTENSIVELY WELDED STEEL CYLINDERS.....83

4.1 INTRODUCTION.....83
4.2 PERFORMANCE OF FOURIER SERIES IN IMPERFECTION REPRESENTATIONS.....86
4.3 COMMENTS ON FORMS OF FOURIER SERIES USED IN PREVIOUS STUDIES.....88
4.4 MODAL AMPLITUDES OF VARIOUS FOURIER SERIES.....90
4.5 GEOMETRIC IMPERFECTIONS IN STEEL SILOS.....93
4.5.1 General.....93
4.5.2 Best-Fit Cylinders and "Real" Imperfections.....95
4.5.3 'Real' Imperfections in Ding's Silos at Port Kembla.....99
4.6 EFFECT OF LINEAR INTERPOLATIONS OVER ZONES OF MISSING DATA ON FOURIERDECOMPOSITION.....101
4.7 DECOMPOSITION OF GEOMETRIC IMPERFECTIONS USING 1D FOURIER SERIES.....103
4.8 DECOMPOSITION OF GEOMETRIC IMPERFECTIONS USING 2D FOURIER SERIES.....105
4.9 CONCLUSIONS.....109

APPENDICES.....140
A4.1 ELEMENTS OF MATRIX $[H]$.....140
A4.2 ELEMENTS OF MATRIX $[J^{j-1}]$.....140

CHAPTER 5 BUCKLING BEHAVIOR OF LARGE EXTENSIVELY WELDED STEEL CYLINDERS WITH MEASURED GEOMETRIC IMPERFECTIONS.....143
5.1 INTRODUCTION.....143
5.2 IMPERFECTION REPRESENTATIONS.....144
5.3 FINITE ELEMENT MODELS.....146
5.3.1 Shell Elements in ABAQUS.....146
5.3.2 Shell Dimensions and Material Properties.....147
5.3.3 Mesh Convergence Studies using a Sector Model.....147
5.4 LINEAR BUCKLING ANALYSES.....149
5.5 NON-LINEAR ANALYSES.....149
5.6 DOMINANT IMPERFECTION COMPONENTS.....151
5.7 FABRICTAION QUALITY CLASSES OF THE THREE SILO SHELLS.....154
5.7.1 General.....154
5.7.2 Meridional Measurement of Dimple Depths.....155
5.7.3 Circumferential Measurement of Dimple Depths.....156
5.7.4 Imperfection Parameters and Quality Classes.....158
5.8 BUCKLING STRENGTH COMPARISON.....161
5.9 CONCLUSIONS.....162

CHAPTER 6 TECHNIQUES FOR BUCKLING EXPERIMENTS ON EXTENSIVELY WELDED STEEL CYLINDERS.....197
6.1 INTRODUCTION.....197
6.2 EXISTING TEST RIG.....198
6.2.1 Loading and Supporting Systems of the Test Rig.....198
6.2.2 Measurement System of the Test Rig.....198
6.2.2.1 Measurement Device.....198

6.2.2.2 Laser Meter Movements, Data Acquisition, and Computer Control.....199
6.2.2.3 Calibration of the Measurement System.....200
6.3 MODIFICATIONS TO THE EXISTING TEST RIG.....201
6.3.1 General.....201
6.3.2 Modifications to the Loading System.....201
6.3.3 Modifications to the Measurement System.....202
6.4 FABRICATION OF SMALL MODELS.....204
6.4.1 General.....204
6.4.2 New Method for Model Fabrication.....205
6.4.3 Experimental Set-up for Stage I Operation.....206
6.4.4 Experimental Set-up for Stage II Operation.....207
6.4.5 Fabrication Process of a Model Specimen.....208
6.5 AXIAL COMPRESSION BUCKLING EXPERIMENTS.....211
6.6 CONCLUSIONS.....211

CHAPTER 7 BUCKLING EXPERIMENTS ON EXTENSIVELY WELDED STEEL CYLINDERS.....227
7.1 INTRODUCTION.....227
7.2 SPECIMENS AND MATERIALS.....228
7.2.1 Specimens.....228
7.2.2 Material Properties.....230
7.3 GEOMETRIC IMPERFECTIONS AND THEIR CHARACTERISTICS.....231
7.3.1 General.....231
7.3.2 Initial Surfaces of Model Shells.....232
7.3.3 Fourier Decomposition of Geometric Imperfections.....233
7.4 BUCKLING AND POST-BUCKLING BEHAVIOR.....236
7.4.1 General.....236
7.4.2 Experimental Results and Observations.....237
7.4.2.1 Specimen 09SC.....237
7.4.2.2 Specimen 09QC04.....238
7.4.2.3 Specimen 09P0408.....240

7.4.3 Variations of Radial Deformations.....241
7.4.3.1 Radial Deformations during Loading.....241
7.4.3.2 Growth of Fourier Series Coefficients during Loading.....243
7.4.4 Post-buckled Shapes.....246
7.5 CONCLUSIONS.....247

CHAPTER 8 FINITE ELEMENT MODELLING OF BUCKLING EXPERIMENTS ON EXTENSIVELY WELDED STEEL CYLINDERS.....308
8.1 INTRODUCTION.....308
8.2 SOME GENERAL ISSUES OF NUMERICAL MODELLING.....308
8.3 MESH CONVERGENCE STUDY.....309
8.4 RESULTS FROM LINEAR BUCKLING ANALYSES.....311
8.5 RESULTS FROM NON-LINEAR ANALYSES.....311
8.6 CONCLUSIONS.....314

CHAPTER 9 EXTENSIVELY WEDLED STEEL CYLINDERS UNDER COMBINED AXIAL COMPRESSION AND INTERNAL PRESSURE.....328
9.1 INTRODUCTION.....328
9.2 PREVIOUS STUDIES.....329
9.3 FINITE ELEMENT ANALYSIS.....331
9.4 FINITE ELEMENT RESULTS.....332
9.5 COMPARISON WITH CODE PREDICTIONS.....334
9.6 DESIGN PROPOSAL.....335
9.7 CONCLUSIONS.....336

CHAPTER 10 CONCLUSIONS.....356
10.1 INTRODUCTION.....356
10.2 FOURIER REPRSENTATIONS OF IMPERFECTION MEASUREMENTS WITH NON-UNIFORM INTERVALS.....357
10.3 ANALYSIS OF GEOMETRIC IMPERFECTIONS IN LARGE EXTENSIVELY WELDED STEEL SILOS.....358

10.4 BUCKLING BEHAVIOR OF LARGE EXTENSIVELY WELDED STEEL CYLINDERS WITH MEASURED GEOMETRIC IMPERFECTIONS.....360
10.5 TECHNIQUES FOR BUCKLING EXPERIMENTS ON EXTENSIVELY WELDED STEEL CYLINDERS.....362
10.6 BUCKLING EXPERIMENTS ON EXTENSIVELY WELDED STEEL CYLINDERS.....363
10.7 FINITE ELEMENT MODELLING OF BUCKLING EXPERIMENTS ON EXTENSIVELY WELDED STEEL CYLINDERS.....365
10.8 EXTENSIVELY WEDLED STEEL CYLINDERS UNDER COMBINED AXIAL COMPRESSION AND INTERNAL PRESSURE.....366
10.9 FUTURE RESEARCH 367

11 REFERENCES.....368

NOTATION

The main symbols used in this thesis have the following meanings, unless otherwise specified in the text. In most cases, only one meaning has been assigned to each symbol, but where this is not the case, the correct one will be evident from the context in which it is used. Roman characters are given first, followed by Greek characters and commonly used subscripts and superscripts. All symbols are defined in the text when they first appear. The less frequently used symbols are not given here, as their definitions are evident from the context.

A_{mn}, B_{mn},	
C_{mn}, D_{mn}	Fourier coefficients
a_0, a_j, b_j	Fourier coefficients of one-dimension Fourier series
a_n, b_n	Coefficients of one dimensional Fourier series for imperfections on a shell circumference
Δa_0^r, Δa_j^r,	
Δb_j^r	Coefficients of one dimensional Fourier series deduced at r th iteration
d	Dimple depth from straight gauge measurement
$d_{\max}$	Maximum measured internal diameter
$d_{\min}$	Minimum measured internal diameter
d_{nom}	Nominal internal diameter.
E	Young's modulus
e_a	Accidental eccentricity
f_y	Yield Stress
E	Young's modulus
$E_i(\delta)$	Representation error due to non-uniform intervals
$er(v_i, \theta_i)$	Error of Fourier representation at sampling points

$F(\theta)$	One-dimensional Fourier series
$F(v)$	One-dimensional Fourier series for shell in the meridional direction
$F(v,\theta)$	Two-dimensional Fourier series
$F_r(\theta)$	Accumulated Fourier series at rth iteration
$\Delta F_r(\theta)$	Fourier series deduced at rth iteration
j	Harmonic number of one-dimensional Fourier series
l_m	Meridional wavelength of an imperfection harmonic mode
l_c	Circumferential wavelength of an imperfection harmonic mode
m	Harmonic number for the meridional direction
N_f	Number of Fourier terms
N_j	Highest harmonic number adopted
N_m	Meridional harmonic number of the highest Fourier term adopted
N_n	Circumferential harmonic number of the highest Fourier term adopted
N_s	Number of sampling points
n	Harmonic number for circumferential direction
k	Harmonic number of the source function
l_{gx},	
l_{gw} , $l_{g\theta}$	Gauge lengths for dimple measurements
P	Period of Fourier series
p	Internal pressure
$\overline{p}$	Normalized internal pressure with respect to σ_{xRc}
$\overline{p}_y$	Normalized internal pressure with respect to f_y
Q	Fabrication quality parameter
R	Radius of cylindrical shell middle surface
r	Iteration number in iterative Fourier decomposition
s	Sampling point number with offset
R_{r1}	Convergence parameter in 1D Fourier decomposition
R_{r2}	Convergence parameter in 2D Fourier decomposition

t	Shell wall thickness
$t_{\min}$	Thickness of thinner plate at a joint
Tol	Pre-defined tolerance
U_{0x},	
$U_{0\theta}, U_{0w}$	Dimple tolerance parameters
U_e	Accidental eccentricity parameter
U_r	Out-of –roundness parameter
V	Height of the shell segment between chosen boundaries
v	Meridional coordinate used in imperfection analysis
w	Weld depression
w_i	Real imperfection deduced from a 'best-fit' cylinder procedure
w_k, z_k	Coordinates of sampling point K in meridional dimple depth measurement
w_l, z_l	Coordinates of sampling point L in meridional dimple depth measurement
w_{se}, w_{te}	Imperfection values at two edges of a shell
$w(v_i, \theta_i)$	Imperfection value at a sampling point
Δw_0	Dimple depth from arc gauge measurement
Δw_k	Characteristic imperfection amplitude defined in Eurocode 3
$\Delta w_{0x}, \Delta w_{0\theta}$,	
Δw_{ow}	Dimple depths
x_0, y_0	Coordinates of origin of cylinder axis
x_c, y_c	Coordinates of arc gauge center
x_l, y_l	Coordinates of sampling point L in circumferential dimple measurement
x_k, y_k	Coordinates of sampling point K in circumferential dimple measurement
x_s, y_s	Coordinates of a sampling point
Z	Meridional coordinate from the lower end of a chosen shell segment
$\overline{Z}$	Meridional coordinate from the lower end of a silo cylinder

α , β , γ	Orientation angles in the $O'X'Y'$ coordinate system
α_x	Elastic imperfection factor
α_{xp}	Imperfection factor with the effect of internal pressurization
α_{xpe}	Elastic imperfection factor with the effect of internal pressurization
α_{xpp}	Plastic imperfection factor with the effect of internal pressurization
β	Plastic range factor in Chapter 2
Δ_{mn}	Modal amplitude of 2D Fourier series
δ	Offset in sampling interval
δ_0	Amplitude of weld depression
ε	Strain
η	Interaction exponent as defined in Eurocode 3
θ	Circumferential coordinate on the shell (in radians), or variable in a Fourier series in Chapter 3
θ_i	Angular coordinate of *i*th sampling point
θ_s	Angular coordinate of a sampling point
$\Delta\theta_i$	Length of the *i*th interval.
λ	Shell meridional bending halfwave length
$\bar{\lambda}_0$	Squash limit slenderness
$\bar{\lambda}_p$	Plastic limit relative slenderness
$\bar{\lambda}_x$	Non-dimensional shell slenderness parameter
ν	Poisson ratio
σ	Stress
σ_{cl}	Classical buckling stress
σ_{xRc}	Critical meridional buckling stress of shells as defined in Eurocode 3
Φ	Phase angle from trigonometric transformation
Φ_n	Phase angle from trigonometric transformation
χ	Stability reduction factor

Subscripts and superscripts

cl	Classical buckling
cr	Critical
e	Elastic
i	i th sampling point
j	j th harmonic number
m	m th harmonic number
n	n th harmonic number
k	Point K
l	Point L
p	Plastic
r	r th iteration

CHAPTER 1

INTRODUCTION

1.1 BACKGROUND

Silos have been used for storing bulk solids in a great variety of industries such as mining and mineral processing, chemical processing, thermal power generation, agricultural production and processing, food processing, and manufacturing industries. Modern silos are made of either concrete or steel, with steel silos accounting for more than half of all silos as steel silos have many advantages over concrete silos in many situations. Silos usually have a circular shape in cross section but rectangular silos are also used in many applications. A silo may be either elevated, as shown in Figure 1.1 or directly supported on the ground, as shown in Figure 1.2, depending on the function of the silo. In recent decades, as a result of rapid industrial expansions, large silos have found increased applications all over the world. For instance, elevated steel silos with a unit capacity of 10,000 tonnes have been built in large numbers for storing grains (Jensen and Turnell, 1997), while the largest ground-supported silos have a unit storage capacity exceeding 100,000 tonnes.

The failure rate of silos is much higher than that of almost all other engineered structures. It was estimated that silos fail at a frequency being between 100 and 1000 times that of buildings (Weare, 1989). Jenkyn and Goodwill (1987) estimated that about 1000 structural failures occur in silos every year in North American alone, and failures are also common elsewhere in the world (e.g. Mclean 1984; Wood, 1997). Failure of a silo often results in severe consequences: (a) losses of the structure; (b) possible losses of lives; (c) great economic losses as a result of the disruption of industrial processes.

Failure of silos generally includes the total collapse of the structure, cracking of concrete silos, and buckling of steel silos. In the case of steel silos, most failures are caused by

buckling (Figure 1.3), as steel silos generally have much thinner walls compared to concrete silos. As circular steel silos are the predominant form of steel silos over the world, this dissertation therefore deals only with circular steel silos. It is well known that circular steel silos present some of the most complicated buckling phenomena as a result of the following three factors: firstly, the cylindrical shell is subject to complicated support conditions as well as complicated loading conditions; secondly, the axial buckling failure, which is the primary failure mode for circular steel silos, is acutely sensitive to both the form and the amplitude of imperfections in the silo wall (see review by Teng, 1996), while the form of imperfections depends on the fabrication process (Arbocz, 1982; Chryssanthopoulos *et al.*, 1991a; Rotter *et al.*, 1992); thirdly, the imperfections in circular steel silos are very complicated as a result of their unique fabrication process.

The diameters of thin cylindrical shells in large circular steel silos often range from 10m to the order of 100m. For such large cylinders, the technique of rolling a single sheet and joining the edges by welding or bolting is neither suitable for fabrication in a factory nor easy for transportation to the site; therefore, they are generally fabricated from joining a great number of rolled panels with many circumferential and meridional welds (referred to as the panel method later). A large circular steel silo constructed from many welded panels is shown in Figure 1.4. The extensive use of welding in silo fabrication leads to unique fabrication imperfections (both geometric imperfections and residual stresses). These geometric imperfections (Figures 4.11-4.13), which take the form of inward depressions at the circumferential welds and oscillating patterns of deviations at the meridional welds (Ding, 1992), may be very detrimental to the axial buckling strength of the steel silo because they may assume a pattern close to the potential buckling mode, and at the same time the associated residual stresses may further reduce the buckling strength.

However, this unique form of imperfections has rarely been addressed by researchers. The lack of research on the effect of these imperfections on the buckling behavior of cylindrical shells may be attributed to the scarce information available on the detailed distributions and amplitude of imperfections in steel silos as well as the great difficulties with accounting for such complicated imperfections accurately in analyses. The paucity of research on the buckling behavior of these steel silos and hence the inadequacy of relevant design recommendations may be the cause of some of the many structural failures in steel silos. The severe deficiency of existing knowledge on the behaviour steel silos made the

steel silo an area in strong need of research. This situation was reflected in a survey of research needs for metal structures conducted among engineers (Pham and Mansell, 1985) some 20 years ago which placed "bins and silos" as second only to the general category "building" as an area needing research, consistently exceeding the needs for research on bridges, offshore structures, cranes, towers, scaffolding and long-span roofs. Although a large amount of research has been conducted on steel silos since then, clarifying many uncertainties, there are still many issues that need extensive further research. This thesis is concerned with one of the major problems, the buckling strength of axially compressed cylindrical shells in steel silos.

1.2 BEHAVIOR OF AXIALLY COMPRESSED PERFECT AND IMPERFECT THIN CYLINDRICAL SHELLS

Figure 1.5 shows typical load-displacement paths, or equilibrium paths, for axially compressed thin cylindrical shells (Bushnell, 1981; Bushnell, 1982; Bushnell, 1985). The solid curves are the equilibrium paths for perfect shell structures, while the dashed curve is for imperfect ones. The imperfect shell deforms along a different path from those of the perfect shell because of the influence of imperfections.

The perfect axially loaded thin cylindrical shell is susceptible to instability failures in two ways, namely, snap-through buckling and bifurcation buckling. The cylindrical shell may deform along path OAC in which the deformation of the shell grows steadily with the applied axial load until point A is reached. The structure will collapse at this load level if the axial load is not sufficiently relieved. Point A is thus called the limit point and its corresponding load level is called the limit point load. This failure phenomenon is referred to as snap through buckling or limit point buckling. Paths OA and AC in this load-deformation relationship denote the pre-buckling equilibrium path and the post-buckling equilibrium path, respectively.

The second situation is that the perfect shell deforms along path OBD with a turning point at B. The turning point B represents a bifurcation point where the structure changes both the pattern and the path of its deformation. The deformation of the shell increases with the load along the path OB, and at B a new pattern of deformation that is orthogonal to the

original pattern of deformation appears. Afterwards, the shell follows the equilibrium path BD with increasing deformation in the transformed deformation pattern. The stable path OB is called the fundamental or pre-buckling path, while the unstable path BD is called the secondary or post-buckling path. This kind of failure is referred to as bifurcation buckling with the load at point B being called the bifurcation buckling load.

In any real shell structure, imperfections are unavoidable. The imperfections include geometric imperfections, residual stresses, and other imperfections. Because of such imperfections, the structure will follow path OEF with a snap-through buckling failure at the limit point E. Similar to those of the perfect shell, the paths OE and EF are respectively termed the pre-buckling path and the post-buckling path. It can be seen from Figure 1.5 that there is a difference in load as well as deformation between the bifurcation point of the perfect structure and the limit point of the imperfect structure, where the difference depends on the amplitude of initial imperfections. For a slightly imperfect structure, the limit point E is close to the bifurcation point B of its perfect counterpart. The bifurcation buckling analytical model is therefore valid in the sense it is a convenient and good approximation of the limit point failure in a real structure, though true bifurcation buckling in a real structure does not exist.

The buckling behavior of an axially compressed thin cylindrical shell is imperfection sensitive, as evident in many observations. Imperfection-sensitive buckling behavior generally displays the following three features as summarized by Calladine (1995):

(a) buckling loads which fall far short of the predictions of 'classical' buckling theory;
(b) unpredictability of buckling strength, as evidenced by the wide 'scatter' of experimentally observed buckling load; and
(c) unstable, dynamic, behaviour of the shell after the maximum load has been reached-leading to catastrophic failure in some circumstances.

The imperfections pertinent to this distinct behaviour are geometric imperfections, variations in wall thickness, pre-buckling stresses, material properties, loading conditions, and boundary conditions. Of all the items listed above, the most important is the geometric imperfections (e.g. Koiter, 1945; Budiansky & Hutchinson, 1964; Babcock, 1983); a relatively small deviation in shell geometry may result in dramatic reduction in the

buckling strength. For this reason, the effects of geometric imperfection on the buckling behavior of shells have attracted a great amount of attention of the research community.

1.3 APPROACHES FOR EXPLORING THE BEHAVIOUR OF THIN CYLINDRICAL SHELLS

Since initial geometric imperfections are the single dominant factor that influences the buckling behavior of axially compressed thin cylindrical shells, a reliable evaluation of the shell buckling behavior must take the geometric imperfections into proper account. One may also take other imperfections such as residual stresses into account in order to get a better prediction of shell buckling behavior. In this sense, the prediction of shell buckling behavior in a real structure is a serious challenge to researchers, because it requires researchers not only to possess a profound insight into the characteristics of the real imperfection that is generally unknown at the design stage, but also to have considerable knowledge of the mechanical behavior of the imperfect thin shell. Various techniques have been developed to study the buckling behavior of axially compressed thin cylindrical shells, they fall into three categories: experimental approach, analytical approach, and numerical approach.

The experimental approach is the oldest tool for studying the behavior of axially compressed cylinders. This approach can provide researchers with intuitive understanding of buckling and post-buckling behavior of the cylindrical shell under axial compression and thus has found many applications in investigations into the behavior of aeronautical structures, offshore structures, and civil engineering structures. Nowadays, the role of experimental approach has been extended from simple empirical evaluation of the load-bearing capacity of a shell to the verification of results from other approaches and the discovery of new phenomena. In many cases, fabrication imperfections such as geometric imperfections and residual stresses in the real structure can be reasonably well simulated in the test specimen. However, this is not the case for large civil engineering shells; great difficulties exist with simulating imperfections in large structures such as silos and tanks fabricated from a large number of welded panels in a small laboratory specimen. A novel fabrication technique for small scale specimens of large civil engineering shells is presented in this thesis to overcome the associated difficulties.

The analytical approach involves establishing differential governing equations and then solving them either analytically or numerically. Historically, the analytical approach has played an important role in the stability research of shell structures and has led to marked advances in the knowledge and understanding of many aspects of the buckling and post-buckling behavior of shells. Nevertheless, this approach has its limits; it can only deal with shells with geometric imperfections, loading conditions, and boundary conditions of simple forms. In general, only highly idealized conditions are considered but such conditions are generally not found in the real structures. Common situations that are beyond analytical solutions are shells with complex geometric shapes or complex forms of imperfections and shells subject to complicated loading and boundary conditions. For such situations, the numerical approach offers a powerful alternative.

The numerical approach is probably now the most commonly used tool for studying shell buckling problems. In the past three decades, great advances in finite element method in conjunction with the rapidly increasing power of modern computers have made it possible to predict the buckling and post-buckling behavior of complex imperfect shells numerically. The historical difficulties of tracing the load-deformation path in the vicinity of the limit point and beyond have been overcome using path following techniques such as the arc-length method (Ramm, 1981; Crisfield, 1981) based on earlier work by Riks (1979) and Wempner (1971). The bifurcation points of shells can be easily found numerically using either the branch-switching method (Wagner and Wriggers, 1988; Fujii and Choong, 1992) or the extended system solving technique (Wriggers *et al*, 1987). Various computer codes that include the above techniques are available for handling the buckling and post-buckling analyses of thin shell structures. A well-known general-purpose computer code is ABAQUS (Hibbitt, Karlsson & Sorensen, 1998) which has been used extensively for these types of problems. The significant advances in numerical approach have changed the picture of shell buckling research: a large number of complicated shell buckling tests which are rather consuming in both money and effort in the past are now replaced by a small number of well-planned shell buckling tests together with many numerical parametric studies to save both money and time.

1.4 OBJECTIVES, RESEARCH STRATEGY, AND SCOPE OF THIS WORK

As noted above, the buckling behavior of thin cylindrical shells is strongly dependent on the imperfections present in the shell wall. It should be noted, since this thesis is mainly concerned with geometric imperfections in shells, unless otherwise stated, the term 'imperfections' is reserved for geometric imperfections hereafter. A great number of studies on the behavior of axially compressed imperfect cylinders have led to a large amount of knowledge on the effect of imperfections on the buckling behavior of cylindrical shells, however, few of them have dealt with imperfections due to the fabrication process of steel silos in which a large number of rolled panels are joined by many circumferential and meridional welds. These imperfections are believed to have serious consequences for steel silos and to be partly responsible for the rather high failure rate of silo structures. The thesis is aimed at correcting this deficiency in existing knowledge the following two specific objectives:

(a) To develop the first accurate numerical buckling strength model for steel cylindrical shells constructed using a large number of curved panels joined by both circumferential and meridional welds;
(b) Using the numerical model from (a) to carry out a parametric study on the buckling strength of such shells under axial compression (with or without internal pressure) to supplement the limited experimental results from the project, so that an improved design method can be formulated.

The research strategy adopted combines theoretical studies with experimental investigations. In the theoretical studies, residual stresses are not taken into account because the distributions and magnitudes of residual stresses in these extensively welded shells are unknown, but the effect of geometric imperfections is accurately modeled. The effect of residual stresses is however indirectly evaluated through a comparison of experimental results which include this effect and nonlinear finite element results which do not include this effect.

The thesis first presents an in-depth study on the characteristics of the geometric imperfections measured on three large steel silos (24m in diameter) located at Port Kembla,

Australia (Ding, 1992). This is followed by a thorough investigation into the behavior of these three steel silos under axial compression with the measured geometric imperfections accurately accounted for. A series of laboratory experiments are next described to study the buckling behavior of cylindrical shells in which both geometric imperfections and residual stresses are important. Numerical models of the test specimens are also presented in which the measured geometric imperfections are precisely represented. A comparison of the predictions of the numerical models and the experimental results is made to examine the effect of residual stresses on buckling behavior. Finally, results from a parametric study using the verified numerical models are presented and rational design equations proposed. A summary of each of the main chapters is given below.

Chapter 2 presents a literature review on topics to be discussed in the thesis. The chapter begins with a short retrospect on existing research on the buckling behaviour of axially compressed cylindrical shells, with special attention to the effects of various forms of imperfections. Methods for dealing with geometric imperfections in cylindrical shells are next discussed, followed by a summary of recent advances in the design of cylindrical shells in steel silos, with particular reference to ENV 1993-1-6 (1999) and ENV 1993-4-1 (1999). Finally, the chapter presents a review of experimental and numerical techniques for studying the buckling behavior of shells.

Chapter 3 is concerned with the accurate Fourier decomposition of geometric imperfections measured with non-uniform intervals, as such non-uniform intervals are often necessary in imperfection measurements on real shell structures. Traditional Fourier decomposition techniques do not lead to an accurate representation of such imperfections. The iterative Fourier decomposition technique is therefore proposed to deal with such imperfection measurements. The theoretical background for this method is detailed, followed by numerical demonstrations of the effectiveness of this method.

Chapter 4 deals with Fourier analyses of the geometric imperfections measured on the same three large steel silos. The chapter first discusses the mathematical basis of Fourier series representation and the effectiveness of various Fourier series in interpreting different forms of imperfections, leading to the choice of an appropriate form that can be used in these imperfection analyses. Comments are given on the choices of Fourier series made by previous researchers, highlighting their inappropriate choices on some occasions

and the consequences of such inappropriate choices. A general expression for the modal amplitude of a complicated Fourier series is given and the procedure for the determination of a 'best-fit' cylinder to obtain 'real' imperfections is explained. The characteristics of the imperfections in the three large steel silos are finally examined using both 1D and 2D Fourier series, and their relationship to the construction details identified.

In Chapter 5, the buckling behaviour of the imperfect cylindrical shells of the three large steel silos mentioned above is explored. Finite element models, in which the measured geometric imperfections are accurately represented, were built. The buckling and post-buckling behavior of these shells was studied by means of both linear and nonlinear analyses using the ABAQUS program. In addition, systematic studies were performed to determine the effect of various imperfection components on the shell buckling strength. It is shown that buckling strength reductions are mainly due to the combined effect of a group of components and that an imperfection component in the form of a single harmonic mode has only a very limited contribution to the total strength reduction despite that some of the harmonic modes have a pronounced amplitude. The silo fabrication quality class in terms of buckling-relevant geometric tolerances is determined for each silo using small computer programs developed according to stipulations in Eurocode 3 (ENV1993-1-6, 1999). The buckling strengths of the three shells predicted with the relevant code rule are compared with finite element results, indicating that the code is too pessimistic about the strength of poor quality shells but too optimistic about the strength of high quality shells.

Chapter 6 presents various techniques developed or adopted for a series of buckling experiments on small-scale welded steel cylindrical shells under axial compression both experimental set-ups and procedures. Modifications were made to an existing test rig to upgrade the facility for the present buckling experiments. An innovative technique is presented for the fabrication of small models of large steel cylindrical shells constructed from many welded panels as commonly found in large steel silos and tanks. The new technique consists of two stages: (as) production of a high quality model by rolling two sheets (or a single sheet) and welding along the meridional seams; and (b) 'welding' in the form of controlled heat input in a required pattern of circumferential and meridional 'welds' on the central portion of the shell surface.

Chapter 7 examines experimental buckling behavior of extensively welded cylindrical shells with different weld patterns under axial compression. The imperfections in the specimens before and after Stage II welding are carefully analyzed to reveal their characteristics. The buckling phenomenon is reported in detail, together with load-axial shortening and load-strain curves. The shapes of two selected circumferences of each model shell were monitored during loading and the results are interpreted using Fourier series. The buckling loads of these specimens are much lower than those of shells with imperfections of many other known patterns, demonstrating the severity of these imperfections in reducing the shell buckling load.

Chapter 8 describes a finite element study of the buckling experiments on extensively welded cylinders presented in Chapter 7. The finite element models included the precisely measured geometric imperfections but omitted the associated residual stresses and any welding effect on steel material properties. Both linear buckling analyses and non-linear analyses were carried out and the predictions from the numerical analyses are compared with the test results. The effects of welding-induced residual stresses and alterations of material properties on the buckling behaviour of the welded cylinder are clarified.

Chapter 9 presents a numerical investigation into the behaviour and strength of extensively welded steel cylindrical shells with precisely measured geometric imperfections subject to the combined action of axial compression and internal pressure. A series of geometrically and materially nonlinear analyses were carried out for the cylindrical shells of the same three Port Kembla silos covering ten different levels of internal pressurization. The results are discussed and compared with predictions of the relevant design rule in Eurocode 3 (ENV1993-1-6, 1999). Modifications to the existing rule are proposed for a safer design of cylindrical shells in silos.

The thesis closes with Chapter 10, where the conclusions drawn in the previous chapters are reviewed and areas in need of further research are discussed.

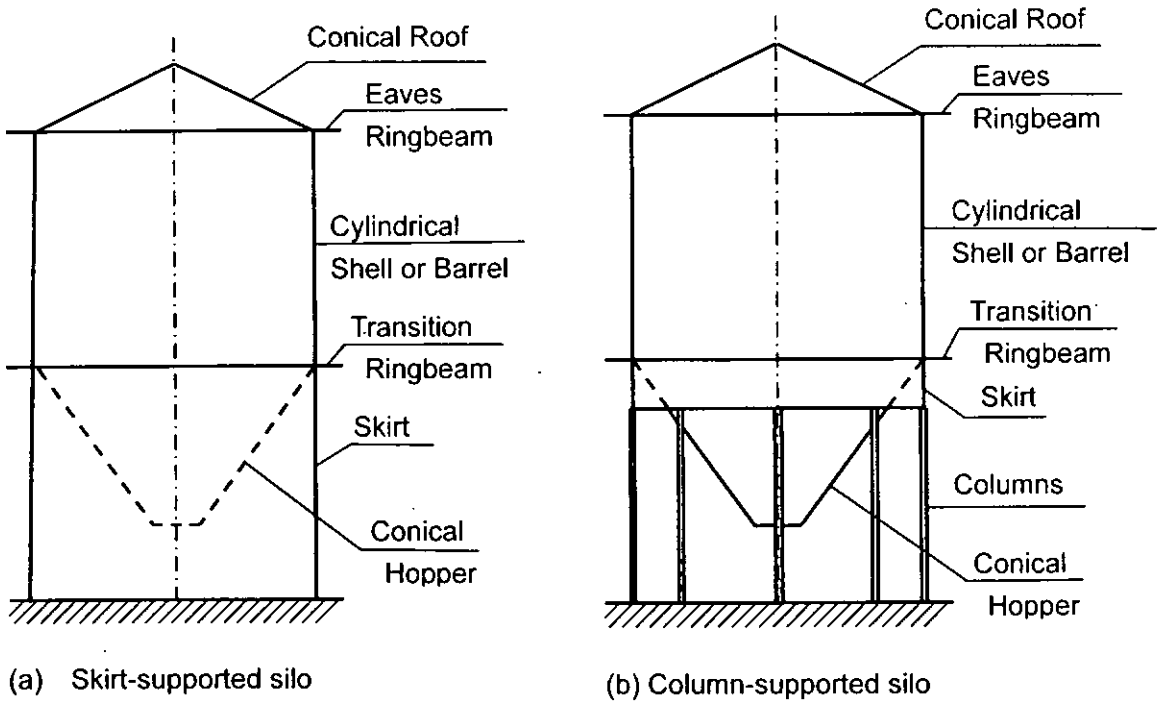

Figure 1.1 Elevated steel silos

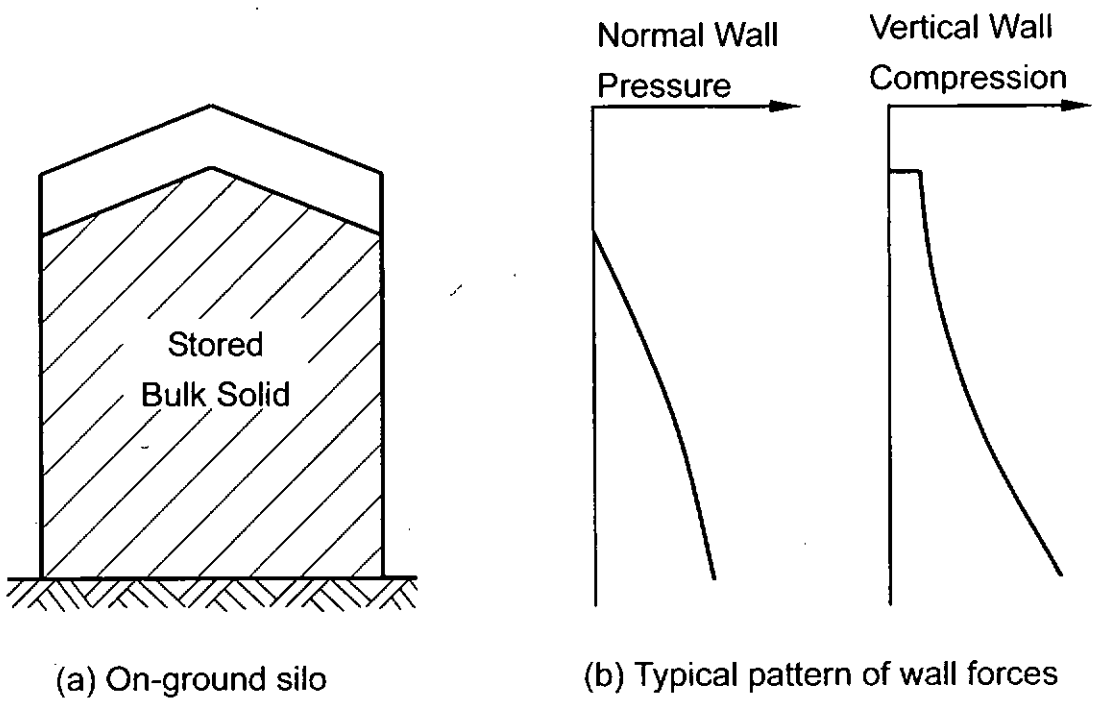

Figure 1.2 On-ground silo and wall loads (After Rotter *et al*, 1989)

Figure 1.3 Buckling failure of a steel silo (courtesy of Professor J.M. Rotter)

Figure 1.4 Steel silo constructed by the panel method

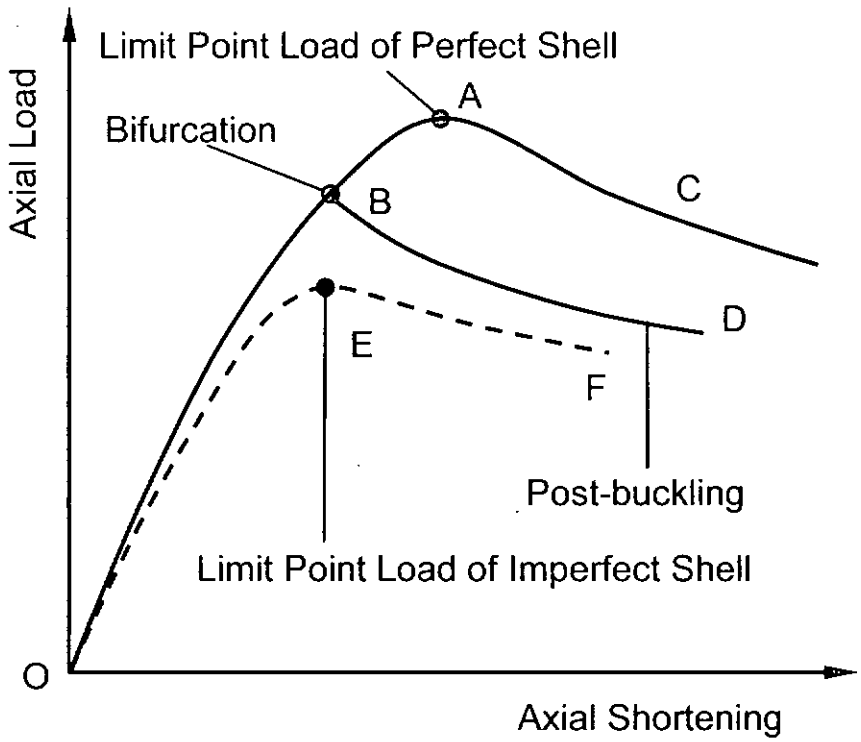

Figure 1.5 Load-deflection curves showing limit and bifurcation points

CHAPTER 2

LITERATURE REVIEW

2.1 INTRODUCTION

This chapter provides a review of existing knowledge pertinent to the buckling behavior of axially compressed cylindrical shells and the stability design of cylindrical shells in steel silos. The chapter begins with a glimpse of the existing work on the stability of isotropic cylindrical shells under axial compression. The effects of various factors on the buckling behavior of cylindrical shells are then reviewed with emphasis being given to the imperfection sensitivity of cylindrical shells under axial compression as well as axial compression combined with internal pressure. In addition, the methods of dealing with imperfections in the shell structure are summarized in some detail as they are of significant importance to the work presented in the thesis. Attention is then turned to recent advances in the stability design of cylindrical shells in steel silos with particular reference to ENV1993-1-6 and ENV1993-4-1. Finally, experimental techniques and the numerical techniques for shell buckling research are surveyed.

2.2 BUCKLING OF ISOTROPIC CYLINDRICAL SHELLS UNDER AXIAL COMPRESSION

2.2.1 Historical Note

The earliest studies on the buckling behavior of axially compressed cylindrical shells were probably the empirical tests carried out by Fairbairn and Hodgkinson in connection with the design of the Britannia and Conway Tubular Bridges (Clark, 1850) in 1845-1850, about six decades preceding the theoretical work by Lorenz (1908) and Timoshenko (1910) and Southwell (1914) who found the theoretical solution of the critical load for an axially

compressed cylindrical shell. These solutions were restricted to cylinders with perfect configurations and assumed simply supported boundary conditions, elastic material behavior, and a membrane stress distribution prior to buckling; the resulting critical buckling stress, which is commonly referred to as the "classical elastic buckling stress" and denoted as σ_{cl}, is given by

$$\sigma_{cl} = \frac{E}{\sqrt{3(1-\nu^2)}}\frac{t}{R} \approx 0.605\frac{Et}{R} \tag{2.1}$$

in which E is the Young's modulus, ν is the Poisson's ratio, the coefficient 0.605 is for steel with $\nu = 0.3$, t is the wall thickness, and R is the cylinder radius. As this equation provides a simple upper bound of the buckling load, σ_{cl} is widely used as a reference load level for axially compressed cylindrical shells undergoing buckling and postbuckling deformations.

Robertson (1928) found that there existed large discrepancies between theoretical solutions and experimental results in his first systematic experiments at the Royal Aircraft Establishment in 1915 and later at Manchester, reported a decade later. In the 1930s, widespread application of thin shells to airplane structures motivated much research on cylindrical shells under axial compression. Careful experiments were carried out by Lundquist (1933) and Donnell (1934) and others in which test results exhibited a wide scatter for ostensibly identical specimens; in the same period, tremendous efforts were spent in developing the linear shell buckling theory (e.g. Flügge, 1934; Timoshenko, 1936). It turned out that no matter how precise the applied linear theory was, its predictions were far from the test results as the latter were only 15%-60% of the values predicted by the former (Figure 2.1).

The unacceptable discrepancy between theoretical predictions and experimental results led to a re-evaluation of the linear shell buckling theory as well as the simplifying assumptions adopted in the early theoretical investigations. One of the most notable contributions on this aspect is the development of nonlinear shell buckling theories, the simplest of which is Donnell's theory (Donnell, 1934). Because of their relative simplicity, the Donnell equations have found more applications in shell stability analyses (e.g. Kármán and Tsien, 1941; Donnell and Wan, 1950) than any other nonlinear shell theories. Besides, attempts were made in an effort to attribute the discrepancy between theoretical

and experimental buckling loads to three sets of simplifying assumptions adopted in the classical approach: (a) the effect of prebuckling deformations (e.g. Fischer, 1965; Almroth, 1966; Yamaki, 1984), (b) the effect of boundary conditions (e.g. Ohira, 1961; Hoff and Soong, 1965), and (c) the effect of initial geometric imperfections (e.g. Kármán and Tsien, 1941; Donnell and Wan, 1950). It is now quite well accepted that the main cause of the poor correlation between theoretical predictions and experimental results and the wide scatter of experimental results is neither the prebuckling deformations nor the boundary conditions; it is due to the highly unstable post-buckling behavior of cylindrical shells under axial compression, which causes the shell to be very sensitive to initial geometric imperfections in the shell wall. Because of their historical importance in understanding the behavior of thin cylindrical shells under axial compression, these investigations are discussed in some detail in the following sub-sections.

There were also attempts to use the minimal postbuckling load of the perfect cylinder as a measure of the load carrying capacity for practical design purposes. Large deflection calculations of the minimum postbuckling load were conducted using Donnell equations by some researchers; examples include Leggett and Jones (1942), Michielsen (1948), Kempner (1954), and Almroth (1963). This attempt was ended with the work by Hoff *et al* (1966) who based on the same procedure as adopted in previous investigations but took more free parameters (i.e. more terms of Fourier series of the lateral displacement w) into account. They showed that the postbuckling minimum of a perfect shell was not a reasonable estimate of the actual buckling load as this minimum kept reducing as the number of free parameters used increased.

Since 1970s, the research on the stability of isotropic cylindrical shells under axial compression has been dominated by investigations into the effect of various forms of initial imperfections on the buckling behavior of axially compressed thin cylinders. The research in this area has been very active as evidenced by the large number of papers published in journals (e.g. AIAA Journal; Thin-Walled Structures; Journal of Engineering Mechanics, ASCE), and conference proceedings (e.g. Budiansky, 1976; Ramm, 1982; Jullien, 1991). As the number of papers is too large to be enumerated in a review of limited length, only selected papers directly relevant to the topic discussed in this thesis are summarized in the sub-sections below. It should be noted that with great advances of

numerical techniques especially the finite element method and remarkable improvements in computing power, much of the work conducted in this period relied heavily on various numerical approaches rather than analytical and experimental methods that were at one time the primary measures for exploring shell buckling behavior. Good examples of numerical studies of shell buckling behaviour include Rotter and Teng (1989), Teng and Rotter (1992), Pircher and Bridge (2001a, 2001b), Song (2002).

2.2.2 Effect of Prebuckling Deformations

The classical buckling theory assumes the prebuckling state of a shell being a pure membrane state. In the case of a cylindrical shell subject to axial compression, this means that the cylinder is free to expand transversely along its entire length before buckling. However, the ends of the cylinder are not completely free to expand in almost all practical cases, so the prebuckling state of a shell is expected to involve both membrane and bending deformation. The effect of prebuckling deformations on the buckling strength of axially compressed cylindrical shells was studied as early as 1932 by Flügge, and later by several researchers (e.g. Fischer, 1965; Almroth, 1966; Cohen, 1966; Gorman and Evan-Iwanowski, 1970; Yamaki and Kodama, 1972; Yamaki, 1984). Their studies revealed that the prebuckling deformations can reduce the buckling stress by only 8%-15% for cylindrical shells with the tangential displacements restrained at both ends; whereas for cylinders allowing free to displace along the circumference at both ends, the prebuckling deformations do not have any effect on the buckling strength. Obviously, the effect of prebuckling deformations is too small to explain the large discrepancy between theoretical and experimental buckling loads and the great scatter of experimental results.

2.2.3 Effect of Boundary Conditions

The effect of various boundary conditions, especially the in-plane boundary conditions, on the buckling strength of axially compressed cylindrical shells has been examined extensively in the 1960s (Ohira, 1961, 1963; Stein, 1962; Hoff, 1961, 1965; Hoff and Rehfield, 1965; Hoff and Soong, 1965, 1969; Hoff, 1966; Almroth, 1966, Cohen, 1966, Simmonds and Danielson, 1970). These studies showed that the boundary condition of a simple support with a free tangential displacement can lead to substantial reductions in the

shell buckling strength (Yamaki, 1984). However, this finding cannot account for the wide scatter of test results, nor can it explain the large discrepancy between the theoretical predictions and experimental results, as a unrestrained tangential displacements at the ends are unlikely to occur in experiments. Actually, a very small elastic restraint in the circumferential direction at the ends is sufficient to bring the buckling load of a cylindrical shell to approximately the same critical load of a shell with a full tangential restraint at both ends (Almroth, 1966; Cohen, 1966).

2.2.4 Imperfection Sensitivity

The most important contribution to understanding the imperfection sensitivity of cylindrical shells under axial compression was made by Kármán and Tsien (1941) who examined the large deformation behavior of a perfect cylinder under axial compression using the Donnell equations. They found that the post-buckling behavior of a perfect cylinder under axial compression was highly unstable which showed a dramatic drop after reaching the critical load (the solid curve in Figure 2.2). This situation contrasts sharply with that of a column for which the postbuckling path is one of a constant load with increasing deformation. In addition, they suggested the existence of a slightly deformed equilibrium state at a load far below the classical buckling load, but they did not explain why the applied load cannot reach the classical buckling load in the first place. The explanation to this question was given by Donnell and Wan (1950) who included initial imperfections in their large deformation analysis which revealed that initial imperfections resulted in significant reductions in the failure load (dotted curve in Figure 2.2).

At roughly the same time, Koiter (1945) created a general theory of initial postbuckling which focuses on elastic equilibrium at the bifurcation point itself and postbuckling configurations near the bifurcation point. He discovered that several different modes, which occur at the same classical buckling load, can interact to give an extremely unstable postbuckling behavior that had been suggested by Kármán and Tsien (1941). By including the first-order effects of small initial deflections in the shape of the classical buckling mode, he was able to get asymptotically exact estimates of the buckling load of imperfect cylinders. In particular, he related the buckling load to the amplitude of the initial imperfection and established a formula which is commonly referred to as "Koiter's first

formula". The Koiter's first formula shows that a small imperfection can greatly reduce the load-bearing capacity of shells, substantiating the conclusions drawn by Donnell and Wan (1950). Koiter (1963a) later extended his theory to the problem of finite deformations which is known as the "special theory", where a finite initial imperfection in the form of the axisymmetric buckling mode was considered in the analyses. He derived a simple formula for the upper bound load of a cylindrical shell bifurcating from an axisymmetric prebuckling state into a non-axisymmetric one when subject to axial compression. The predictions of the special theory not only matchs well with those of the general theory over a wide range of imperfection amplitudes, but also agree well with the test results of cylindrical shell specimens with axisymmetric sinusoidal imperfections (Tennyson and Muggeridge, 1969).

As a result of the work by many researchers and particularly by Kármán and Tsien (1941), Donnell and Wan (1950), Koiter (1945, 1963a), and Budiansky and Hutchinson (1966), the concept of imperfection sensitivity gained wide acceptance (e.g. Brush and Almroth, 1975). Intensive efforts then followed to examine the sensitivity of various forms of imperfections on shell buckling behaviour (e.g. Hutchinson *et al*, 1971; Amazigo and Budiansky, 1972; Arbocz and Sechler, 1974; Yamaki, 1984; Rotter and Teng, 1989).

2.2.5 Effect of Internal Pressurization

It is well known that the presence of an internal pressure can increase the buckling load of an imperfect cylindrical shell when subject to axial compression (e.g. Lo *et al*, 1951; Fung and Sechler, 1957; Lu and Nash, 1962; Hutchinson, 1965). The strength gains due to internal pressures depend significantly on the forms of imperfections (Hutchinson, 1965; Teng and Rotter, 1992).

Hutchinson'a study (1965) revealed that: for a shell with asymmetric imperfections but free of axisymmetric imperfections, the buckling load can approach the classical value at a relatively small internal pressure; whereas for a shell with axisymmetric imperfections, the buckling load remains much smaller than the classical value over the whole range of internal pressures for elastic buckling. These observations have been verified by tests for the case of asymmetric imperfections (e.g. Weingarten *et al*, 1965); as well as for the case

of predominantly axisymmetric imperfections (e.g. Bucklin *et al*, 1983; Rotter, 1985a). Hutchinson's theory (1965) was later re-examined by Rotter and Seide (1987) for pressurized cylinders with axisymmetric imperfections, and the low strengths predicted by Hutchinson's theory were confirmed for a wider range of variables, and a more precise approximation developed.

Teng and Rotter (1992) carried out a systematic investigation into the buckling strength of axially compressed internally pressurized elastic cylinders with three different form axisymmetric imperfections: repeated sinusoidal imperfections (Koiter, 1945, 1963a; Hutchinson, 1965); local inward depressions (Amazigo and Budiansky, 1972; Rotter and Teng, 1989); and outward bulges. It showed that among the three imperfection forms the sinusoidal imperfections lead to the slowest strength gains due to internal pressure, while the inward local depressions lead to the fastest strength gains, with outward local deviations being between the other two.

At higher internal pressures, an axially loaded internally pressurized thin cylindrical shell is prone to elastic-plastic collapse near the shell support. This failure mode is often referred to as "elephant foot" buckling, which features axisymmetric collapse and is less sensitive to the amplitude of initial imperfection. The load of the "elephant foot" failure can be either approximately obtained using a first-yield criterion proposed by Rotter (1983), or rigorously determined employing geometrically nonlinear elastic-plastic collapse calculations (Rotter, 1985a, 1990).

2.2.6 Cylindrical Shells with Axisymmetric Imperfections

Cylindrical shells in silos and tanks have been shown to possess imperfections that consist of both substantially uniform inward depressions at continuous circumferential welds and oscillating patterns of geometric imperfections due to short meridional welds (Ding, 1992). As axisymmetric imperfections generally lead to the largest reduction in the elastic buckling strength under pure axial compression (Koiter, 1963a; Yamaki, 1984), extensive studies on the effect of a single axisymmetric weld depression has been carried out in the past two decades as a first step toward a better understanding of the buckling behavior of cylinders constructed by the panel method. A single weld depression has also been proposed by some researchers as a substitute imperfection for relatively simple numerical

calculations (e.g. Rotter and Teng, 1989). A few early studies on axisymmetric imperfections were conducted around the end of 1960s (e.g. Tennyson and Muggeridge, 1969; Hutchinson *et al*, 1971; Amazigo and Budiansky, 1972), but axisymmetric imperfections were subsequently dismissed as being unimportant as such imperfections are not common in the context of aeronautical structures (Arbocz, 1974).

The effect of a single circumferential welded joint depression appears to have been first studied, only to a limited extent, by Bornscheuer *et al* (1983). The first systematic study of the effect of a single axisymmetric weld depression on the elastic buckling strength of cylindrical shells was carried out by Rotter and Teng (1989) who proposed two types of depressions for circumferential welds and predicted strength losses of up to 70% for an imperfection amplitude of one wall thickness. Rotter and Teng's (1989) theoretical predictions have been generally confirmed by experimental observations (Berry, 1997), although a more sophisticated comparison including the effects of yielding, residual stresses and unsymmetric patterns of imperfections in the theoretical model may change the picture. The two types of depressions proposed were verified and further developed by Pircher *et al* (2001) who used part of the imperfection data obtained from measurements made on real silos (Ding, 1992) to deduce depression models. Apart from studies concerned with a single axisymmetric weld depression, research has also been carried out on cylinders with multiple circumferential weld depressions, which is a situation commonly found in real structures. These studies showed that adjacent weld depressions may interact (Lock, 1989; Rotter, 1996, Pircher and Bridge, 2001a, 2001b), leading to a further reduction in the buckling strength of about 15% (Rotter, 1996, Pircher and Bridge, 2001a, 2001b). Residual stresses are always associated with welding, but no measurements have been undertaken. Several theoretical studies have been carried out to investigate the effect of residual stresses at circumferential welds, leading to contradictory conclusions: Bornscheuer *et al* (1983) used an assumed pattern of residual stresses to perform a limited number of calculations and reported a decrease of up to 10% due to the assumed residual stresses; Rotter (1996), Holst *et al* (2000), and Hübner *et al* (2003a), instead, adopted shrinkage models to induce residual stresses and found the residual stresses to be beneficial to the shell strength. Bornscheuer *et al*'s predictions may not be true, as the residual stresses they postulated do not satisfy equilibrium requirements. Assuming a pattern of residual stresses which is in equilibrium for an unloaded shell is difficult, because the stresses in a shell are complicated by their two dimensional nature

and the curvature of the shell surface. However, it is not difficult to assume a pattern of residual strains which automatically induces a complicated pattern of residual stresses satisfying equilibrium requirements everywhere. The latter strategy, which is commonly referred to as the shrinkage model, was proposed by Rotter (1996) and has found wide applications in recent studies (e.g. Holst *et al*, 1999, 2000; Holst and Rotter, 2002; Pircher and Bridge, 2001a, 2001b, Hübner *et al*, 2003a, 2003b) because of its simplicity.

2.2.7 Steel Cylinders Constructed from Many Welded Panels

The above studies on axisymmetric weld depressions neglected some realistic features that may have important influences on the buckling strength. First, as real structures have both circumferential and meridional welds, geometric imperfections associated with these welds are unsymmetric and may assume a pattern close to the potential buckling mode. Even in laboratory specimens manufactured with great care to achieve axisymmetric weld depressions, additional unsymmetric geometric imperfections do exist and may cause significant additional strength reductions (Berry, 1997). Second, welds in both directions lead to oscillating patterns of residual stresses over the shell surface; and these together with geometric imperfections of a matching pattern may produce severe consequences. This possibility has been confirmed by both the demonstration tests on two cylinders by Schmidt and Swadlo (1996) and recent theoretical investigations (Hübner *et al*, 2003a). In the Schmidt and Swadlo's tests (1996), one cylindrical specimen was constructed by rolling a single steel sheet and seaming it with a single meridional weld, while the other one was fabricated in an elaborate process resembling the panel method. The buckling load of the cylinder fabricated by the laboratory panel method is only 69% that of the one constructed from the rolling and seaming method. Similar conclusions were also drawn by Hübner *et al* (2003a), who examined the effect of different weld-induced imperfections. Their analyses were conducted using ABAQUS (Hibbitt, Karlsson & Sorensen, 1998) with weld-induced imperfections being modelled by a weld shrinkage procedure. While their work has led to advances in understanding the behavior of cylindrical shells with patterned welds, a great amount of further research is still needed before the buckling characteristics of a cylindrical shell built with many welds can be fully understood. This is because some realistic features, which may be important for the buckling behavior of shells, have been omitted in their study. As for the Schmidt and Swadlo's study, the laboratory panel method involved welding before rolling, contrary to the real situation where rolling is

performed before welding. Moreover, they did not provide any information on residual stresses in the sheet nor any numerical analyses. Hübner *et al* (2003a) were only concerned with depressions from weld-induced shrinkages, neglecting imperfections from other sources such as the plate rolling process.

2.3 GEOMTRIC IMPERFECTIONS IN CYLINDRICAL SHELLS

Careful and comprehensive measurements of real imperfections on cylindrical shells were initiated in late 1960s (e.g. Coppa, 1966; Arbocz, 1968; Shover, 1968; Arbocz and Babcock, 1969). In the years that followed, measurements of geometric imperfections were undertaken extensively as a result of the importance of geometric imperfections being recognized. For instance, imperfection measurements were conducted on small scale laboratory models (e.g. Singer *et al*, 1971; Walker and Sridharan, 1977; Singer *et al*, 1978; Singer *et al*, 1979, Pinkney *et al*, 1983; Abramovich *et al*, 1987; Berry, 1997), on large scale and full scale aeronautical structures (e.g. Arbocz and Williams, 1977; Horton, 1977), on offshore structures (e.g. Chryssanthopoulos *et al*, 1991a, 1991b; Chryssanthopoulos and Poggi, 1995), as well as on silo and tank structures (e.g. Schulz, 1970; Clarke and Rotter, 1988; Ding *et al*, 1991, 1995a, 1995b; Ding, 1992; Coleman *et al*, 1992; Rotter *et al*, 1992; Hornung and Saal, 2002).

When deducing geometric imperfections from measurement data, one has to define an imaginary reference cylindrical surface so imperfections are found as deviations from the reference surface. This can be achieved by finding the best-fit cylinder to the measured data using numerical techniques such as the least-square method (Arbocz and Babcock, 1969; Coleman *et al*, 1992). Figure 2.3 shows the definition of reference cylinder in Arbocz and Babcock (1969) which can be defined when the five parameters, i.e. the encentricities Y_1 and Z_1, the rigid body rotations α and β, and the mean radius R are determined by a least-square data reduction procedure. The geometric imperfections are then calculated as the deviations of sampling points from the reference cylinder. Existing studies on measured imperfections have shown that geometric imperfections are closely linked to the manufacturing process of shells (Arbocz, 1982; Singer, 1982a). In aeronautical structures, shells are generally constructed by joining rolled steel sheets along

longitudinal seams, so the resulting imperfection patterns are dominated by meridional welds in a non-axisymmetric form. Shells in civil engineering such as silos and tanks are built from a large number of rolled panels joined by many circumferential and meridional welds, so the geometric imperfections on these shells are quite different from those of aeronautical shells, featuring significant local axisymmetric imperfections at continuous circumferential welds and wavy patterns due to meridional welds.

Nowadays, geometric imperfections can be directly employed to assess the buckling behavior of shells using a nonlinear finite element analysis. In order to collect and evaluate the imperfection data obtained at different laboratories by different researchers, and more importantly, to facilitate the incorporation of realistic imperfection distributions into nonlinear analyses in shell buckling predictions, an international imperfection data bank was established with branches at the Delft University of Technology (Arbocz and Abramovich, 1979) and at the Technion in Haifa (Singer *et al*, 1978), respectively. Another imperfection data bank was subsequently set up for welded cylinders in offshore structures at Imperial College (Chryssanthopoulos *et al*, 1991b). Unfortunately, these data banks only include information for aerospace structures and offshore structures which is not applicable to civil engineering shell structures. As existing imperfection data for civil engineering shells (Ding, 1992; Hornung and Saal, 2002) are too limited for an imperfection data bank to be built, it is imperative to carry out additional extensive imperfection measurements on silos and tanks.

2.4 GEOMETRIC IMPERFECTIONS IN SHELL BUCKLING ANALYSIS

Today, there exist many approaches for dealing with geometric imperfections in shell buckling analysis which can be grouped into three categories, namely, the substitute imperfection approach (e.g. Donnell, 1934; Koiter, 1963a, 1963b; Teng and Rotter, 1992), the equivalent load approach (e.g. Calladine, 1972; Godoy, 1993), and real imperfection approach (e.g. Arbocz and Babcock, 1969; Hansen, 1977; Elishakoff and Arbocz, 1982, 1985). Among them the substitute imperfection approach has the longest history in shell buckling research. Many substitute imperfections such as idealized geometric imperfections, localized realistic imperfections, and equivalent imperfections in the shape of buckling or postbuckling mode, and equivalent geometric imperfections with consistent

residual stresses, were proposed and found effective in shell stability studies. In the following, these methods are reviewed one by one in some detail.

2.4.1 Idealized Geometric Imperfections

Early shell buckling studies usually adopted idealized geometric imperfections in the form of harmonic patterns (Donnell, 1934; Kármán and Tsien 1941; Koiter, 1945, 1963a, 1963b; Donnell and Wan, 1950). These kinds of geometric imperfections were assumed on the basis of intuition rather than knowledge of real imperfections, because there was little knowledge of geometric imperfections until imperfection measurements of shell structures commenced in late 1960s. Moreover, only imperfections in harmonic forms can be easily included in analytical models. Even nowadays, idealized geometric imperfections of harmonic forms are sometimes used for comparison purposes in research exploring the negative effects of different geometric imperfections on shell buckling. For instance, Teng and Rotter (1992) adopted a regular sinusoidal imperfection in comparison with two local axisymmetric imperfections (inward and outward) in which the sinusoidal imperfection was found to show the slowest strength gains with internal pressurization in comparison with the two local axisymmetric imperfections.

2.4.2 Localized Realistic Geometric Imperfections

Some simple forms of imperfections that are closely related to fabrication processes were explored by researchers as substitute imperfections. One of these examples is the localized circumferential weld depression for cylindrical shells in steel silos and tanks, as geometric imperfections on cylindrical shells in silos and tanks generally include substantial axisymmetric local depressions at circumferential welds in addition to imperfections more global in nature (Rotter, 1996). This form of substitute imperfection was first studied by Amazigo and Budiansky (1972), then by Bornscheuer and Hafner (1983). Rotter and Teng (1989) proposed two expressions to describe the shapes of two types of weld depressions.

The shape for TYPE A weld depression is given by them as:

$$w = \delta_0 e^{-\pi x/\lambda}\left(\cos\frac{\pi x}{\lambda} + \sin\frac{\pi x}{\lambda}\right) \tag{2.2}$$

while that for TYPE B weld depression is given by them as:

$$w = \delta_o e^{\pi x/\lambda} \cos\frac{\pi x}{\lambda} \tag{2.3}$$

where λ is the linear elastic meridional bending half-wavelength λ given by:

$$\lambda = 2.444\sqrt{Rt} \tag{2.4}$$

δ_0 is the amplitude of the depression

They found that a local depression of one wall thickness in amplitude can result in a 70% reduction in shell buckling strength under axial compression.

Rotter (1996) suggested several shapes such as "Open", "Closed", "Best", and "Final" to describe weld depressions measured on the three of the large silos at Port Kembla in Australia (Ding, 1992). Analyses were performed to explore the effect of a single weld depression as well as the interaction between adjacent weld depressions in the "Best" shape. In his study, a shell with adjacent circumferential weld joints at a spacing of 3000mm was modeled by a shell segment of 3000mm in height with either symmetric (S) or anti-symmetric (A) boundaries at 1500mm above and below the weld joint at mid-height. It was found that the condition S/S with the "Best" shape leads to a much higher buckling strength than a single weld depression in a long shell. Moreover, a depression of the "Best" profile gives a lower buckling stress than those predicted for the imperfections of either Amazigo and Budiansky (1972) or Rotter and Teng (1989) (TYPE A).

On the basis of imperfections surveyed on the Port Kembla silos (Ding, 1992), Pircher and his co-workers (Pircher *et al*, 2001), derived a new shape function for weld depressions. The new shape function agrees with the "TYPE A" and "TYPE B" weld depressions proposed by Rotter and Teng (1989) in that the latter two types were found to be special cases of the former. Pircher and Bridge (2001a, 200b) used the newly developed shape function to explore the influence of circumferential weld-induced imperfections on the buckling of silos and tanks, arriving at conclusions similar to those of Rotter (1996).

2.4.3 Equivalent Geometric Imperfections

In studying the buckling behavior of shells using a numerical approach, it is very important to take the effect of geometric imperfections into account. Apart from

imperfections measured on real structures or laboratory specimens, geometric imperfections in the shapes of buckling or postbuckling modes, among other forms of imperfections, are suitable choices for use in numerical buckling analysis. These imperfections, which are commonly known as "equivalent geometric imperfections", include: the linear buckling mode or non-linear buckling mode of perfect shells (e.g. Danielson, 1974; Brendel and Ramm, 1980; Combescure, 1986; Greiner and Derler, 1995; Guggenberger, 1995; Wunderlich and Albertin, 2000); a postbuckling deformation pattern of perfect shells (e.g. Greiner and Derler, 1995; Guggenberger, 1998); and a linear combination of eigenmodes (e.g. Arbocz, 1987; Teng and Song, 1999, 2001). The central difficulty with choosing the equivalent imperfection for a specific problem is the form of imperfection as there are many possibilities such as the bifurcation mode, postbuckling deformation patterns, or combinations of eigenmodes.

Some attempts were made in finding the 'worst' imperfection as the appropriate equivalent imperfection. For instance, Deml and Wunderlich (1997) developed a structurally stable procedure for the direct evaluation of the 'worst' imperfection shape in shell buckling. In their procedure, geometric imperfections are incorporated into the theory of shells and a shell finite element is developed, an extended system of nonlinear equations is then established with the imperfections being treated as additional degrees of freedom. Consequently, the 'worst' imperfection can be found by minimizing the buckling load with respect to the imperfection shape. This approach of determining the 'worst' imperfection is rather complex in that whether a specific imperfection form is the most deleterious form depends not only on the shell configuration but also on the stress state of the shell. In addition, the 'worst' imperfection deduced may sometimes be far beyond realistic possibilities, as real imperfections are produced by a practical fabrication process and are subject to practical constraints (Rotter, 1995a).

Equivalent geometric imperfections are also specified by the European code for steel shell structures (ENV1993-1-6, 1999), which forms part of Eurocode 3 and is often referred to as Eurocode 3 directly for brevity in this thesis. Eurocode 3 suggests that an equivalent geometric imperfection should have a pattern that has the most unfavorable effect on the buckling behavior of the shell. If the most unfavorable pattern cannot be readily identified beyond reasonable doubt, a sufficient number of analyses should be carried out for different imperfections to identify the worst case. The code recommends that the

eigenmode-affine pattern (the pattern in the form of a linear or nonlinear bifurcation mode) should be used unless a different unfavorable pattern can be justified, and the pattern of the equivalent geometric imperfection should conservatively reflect constructional details and boundary conditions. In addition, the Eurocode proposes that imperfection forms considered to be unrealistic because of the method of fabrication can be excluded from consideration whereas forms including realistic structural details such as axisymmetric weld depressions should be explored.

The amplitude of imperfections is also of critical importance in arriving at a realistic buckling load. Speicher and Saal (1991) proposed that the amplitude of an equivalent imperfection should be deduced according to the existing test results for cylindrical shells. The Eurocode, on the other hand, recommends that the amplitude of the adopted equivalent geometric imperfection be chosen according to the specified fabrication quality tolerance and be interpreted in a manner which is consistent with the gauge length method set out in the Eurocode.

2.4.4 Equivalent Imperfections with Consistent Residual Stresses

The concept of an equivalent imperfection with consistent residual stresses came from the weld shrinkage concept that was proposed by Rotter (1996) to overcome the difficulty in postulating equilibrium-state residual stresses in shells. Using the shrinkage model, Rotter (1996) was able to conduct the first rigorous investigation into the effect of residual stresses associated with circumferential weld depressions on the buckling strength of cylindrical shells, reporting the strengthening effect of residual stresses. This approach is simple to implement, but can be used to produce complicated realistic form imperfections in shell structures. As a result, it has been applied to cases other than welding induced imperfections. For example, this method was applied to study the effect of geometric imperfections in cylindrical shells resulting from fabrication misfits and the associated consistent residual stress field (Holst *et al*, 1999). Holst *et al* (2000) carried out a systematic study on shrinkage imperfections and buckling in cylindrical shells with consistent residual stresses. In his study, biaxial shrinkage on a square patch, uniaxial shrinkage on a square patch, uniaxial shrinkage on a meridional strip, uniaxial shrinkage on a circumferential strip, and the magnitude of the shrinkage strain, were all examined. A number of conclusions were reached in his studies, substantiating those drawn by Rotter

(1996). All of the above studies made use of a rectangular strain block on the shrinkage strip. Hübner *et al* (2003a) showed that there is a pronounced disadvantage with the rectangular strain block approach: the drastic changes in the initial strain at the edges of the block require the use of a very fine mesh near the edges which can be a significant disadvantage when a large number of welds need to be simulated. To overcome this problem, Hübner *et al* (2003a) adopted a trapezoidal strain block instead of the rectangular one in their weld shrinkage procedure which allows efficient modelling of imperfections (geometric imperfections and associated residual stresses) induced by various weld patterns (meridional welds, circumferential welds, and patterned welds). Using this modelling technique, the behavior of a shell segment under different loading conditions (axial compression, axial compression with internal pressure, and external pressure) were examined, and a number of important conclusions were drawn.

2.4.5 Equivalent-Load Geometric Imperfections

The concept of equivalent loads modeling geometric imperfections was first introduced by Calladine (1972). This method was further developed by Croll *et al* (1979b) in the analysis of geometrically imperfect cooling towers and was then advanced by Moy and Niku (1983) who deduced the equations for equivalent loads from equilibrium considerations.

The equivalent load analysis method, which is often implemented by an iterative procedure, is simpler than the method of direct imperfection modeling in some cases. For example, in the case of prismatic structural components with imperfections that destroy the prismatic condition, the equivalent load method preserves the prismatic conditions so that a semi-analytical finite element or finite difference analysis can still be undertaken. Similarly, it allows conventional computer codes for shells of revolution to be used to assess the influence of non-axisymmetric geometric imperfections (Godoy, 1993).

The equivalent load method was applied in a variety of structures such as cooling towers (Croll *et al*, 1979a, 1979b; Ellinas *et al*, 1980; Gupta and Al-Dabbagh, 1982; Hang and Tong, 1985), spherical shells (e.g. Godoy, 1987), cylindrical shells (e.g. Tam and Croll, 1988), and shallow shells (e.g. Godoy *et al*, 1988). However, this technique is applicable only when the imperfections are relatively simple. Moreover, it was found that the stresses in cooling towers with local imperfections of the shell wall thickness are considerably

underestimated by an equivalent load analysis (Hang and Tong, 1985). The problem was resolved by Godoy (1993) who derived the equivalent load from an initial strain expression of the imperfection including nonlinear terms.

2.4.6 Real Geometric Imperfections Represented by Fourier Series

Although equivalent-load imperfections and substitute geometric imperfections such as idealized geometric imperfections, localized realistic geometric imperfections, equivalent geometric imperfections, and equivalent imperfection with consistent residual stresses can capture many aspects of shell buckling behavior, an accurate prediction of shell buckling behavior should incorporate real geometric imperfections, as buckling of shells is highly dependent on the geometric imperfections in the shell walls.

Real geometric imperfections often take the form of irregular patterns in conjunction with some regular features. Real imperfections are generally represented using Fourier series, because a Fourier series representation not only provides a clear description of the characteristics of the geometric imperfections such as the identification of the 'critical modal components' (Arbocz and Babcock, 1969), but also provides a way of relating the components of the imperfections to the surface features of the shell wall and the associated fabrication process.

Two methods are available for the Fourier representation of real geometric imperfections in practice, i.e., the probabilistic method and the deterministic method. In the probabilistic method, the Fourier coefficients are treated as random variables. The probabilistic properties such as the mean vector and the variance-covariance matrix of the Fourier coefficients are calculated from the imperfection data by a special numerical procedure. Some of the examples of this approach include: Elishakoff and Arbocz (1982, 1985), Arbocz (1983), Arbocz and Hol (1991), Arbocz and Starnes Jr. (1991), Chryssanthopoulos *et al* (1991a, 1991b), Chryssanthopoulos and Poggi (1995). The probabilistic method is believed to be a viable approach which will lead to a safer structure, but its implementation relies heavily on the availability of extensive imperfection data measured on each type of shells constructed by a given fabrication process. This availability of imperfection data is unlikely to be ready in the near future for civil engineering shell structures; therefore, one shall focus on the deterministic method at the time being.

The deterministic analysis of geometric imperfections generally involves Fourier decomposition. In this approach, an appropriate Fourier series that can describe the imperfection on the shell wall is first chosen and the Fourier coefficients are then determined from the measured imperfection data using numerical integration techniques such as the trapezoidal rule. Subsequently, the relationship between the Fourier components of imperfections and the structural features resulted from the given fabrication process may be established. In particular, this approach allows different components of the imperfection to be selected for inclusion in subsequent numerical shell buckling analyses so that the effects of various imperfection components on the buckling behavior can be well understood. Example studies employing this approach are mentioned below. Arbocz and Babcock (1969) adopted three different double Fourier series, i.e. a full-wave general (including both sine and cosine terms) representation in both axial and circumferential directions, a half-wave cosine representation in the axial direction and a full-wave general representation in the circumferential direction, and a half-wave sine representation in the axial direction and full wave general representation in the circumferential direction, to interpret the imperfections as well as deformations measured on electroformed copper shell specimens; both the dominant components of the imperfections and the critical modal components were identified. Arbocz and Williams (1977) performed Fourier analyses on the imperfections surveyed on a 10-ft-diameter shell structure employing both a half-wave cosine representation and a half-wave sine representation in axial direction, with a full wave general representation in the circumferential direction in both cases. They also carried out multi-mode analysis to estimate the effect of initial imperfections by including some selected components of the imperfections in the analysis; Berry *et al* (2000) studied the components of geometric imperfections on their cylindrical specimens with a single weld depression using a one-dimensional (1D) Fourier series. Zhao and Teng (2001) used the 1D Fourier series to study the critical components of the geometric imperfections as well as the deformations on their cone-cylinder junction models. All these studies proved to be successful, demonstrating the effectiveness of the Fourier decomposition method in interpreting imperfections in shells. The Fourier series analysis was also used in the work presented in this thesis.

2.5 STABILITY DESIGN OF CYLINDRICAL SHELLS IN STEEL SILOS AND TANKS

2.5.1 Introduction

The behavior of circular steel silos is much more intricate than that of many other structures in civil engineering, because the cylindrical shells in steel silos show very complex behaviour, particularly when subject to complicated loading conditions. This is at least partly the reason why the failure rate of silo structures is the highest among all engineered structures for decades (Rotter, 1995a) as evidenced by many reports on the structural failures of silo structures (e.g. Ignatenko, 1978; Wood, 1980, 1997; Bushnell, 1981; Ravenet, 1981, 1983; Jenkyn and Goodwill, 1987; Allen, 1989; Guggenberger, 1997; Pavlovic, 1997). This section discuss the stability design provisions in the new Eurocode (ENV1993-1-6, 1999; ENV1993-4-1, 1999).

There are a number of publications on the design of bins and silos before ENV 1993-4-1 (1999) was issued, but few of them offer guidelines for the structural design of large steel silos. For example, the American standard ACI 313-97 (1998) is only concerned with concrete silos; the British code BS 5061 (1974) is for the design of farm silage silos; the Japanese Code JIS B8511 (1987) deals only with small aluminum silos; and some other standards such as AS 3774 (1990), ENV 1991-4 (1995), and ISO 11697 (1995) are for determination of loads on silo walls. Although a variety of publications providing information on the design of large steel silos (e.g Lambert, 1968; Wozniak, 1979; Trahair *et al*, 1983; Gaylord and Gaylord, 1984; Rotter, 1985b; Buzek, 1989) have been in existence for some time, they are not easy to follow in design, because some of the recommendations vary considerably from one to another. Furthermore, many important issues are not addressed by them. The ECCS recommendations (1988) for shell stability design may be useful for the design of large steel silos, but some ECCS rules may lead to unconservative results while other rules are more complicated than is necessary (Rotter, 1998a).

The time that no comprehensive code existed for the design of steel silos in the world ended when 'Eurocode 3: design of steel structures, Part 4-1: silos (ENV 1993-4-1, 1999)',

the first code for the structural design of steel silos, was published in 1999. In parallel with this publication, 'Eurocode 3: design of steel structures, Part 1-6: general rules: supplementary rules for shell structures (ENV 1993-1-6, 1999)' was also issued. The ENV 1993-4-1 (1999) document is an application standard that provides principles and application rules for the structural design of large steel silos, while ENV 1993-1-6 (1999) is a generic standard that deals with the strength and stability design for axisymmetric metal shells. Both of them were developed on the basis of a vast number of investigations carried out in the previous decades, reflecting the latest progress in shell stability research at that time. In the following, a brief review is given of recent advances in shell stability design, with particular reference to the two newly developed European codes, ENV 1993-1-6 (1999) and ENV 1993-4-1 (1999), and the background of their development. The review concentrates on those aspects directly relevant to the design of cylindrical shells under axial compression.

2.5.2 Fabrication Quality and Initial Geometric Imperfections

The initial geometric imperfections in a shell are closely related to the quality of construction, therefore the buckling strength of the shell is dependent on the shell fabrication quality. Odland (1978) was the first to suggest that cylindrical shells should be classed into different strength groups according to their construction qualities. This idea was then further developed by Rotter (1985d, 1995b), and is now quite well accepted (e.g. Poggi, 1996; Knoedel and Ummenhofer, 1996). ENV 1993-1-6 (1999) and ENV 1993-4-1 (1999) adopted the proposal of Rotter (1995b, 1998b) which defines the design value of imperfection by

$$\frac{\Delta w_k}{t} = \frac{1}{Q}\sqrt{\frac{R}{t}} \tag{2.5}$$

where Δw_k is the characteristic imperfection amplitude, t is the shell wall thickness, and Q is the fabrication quality parameter and takes values according to the classes of fabrication quality: for Class A (excellent quality), $Q = 40$; for Class B (High quality), $Q = 25$; and for Class C (Normal construction), $Q = 16$. Obviously, the amplitude of the initial imperfection decreases with an increase in the fabrication quality.

The Eurocodes define three types of geometric imperfections, namely, out-of-roundness, accidental eccentricity, and dimples, to determine the fabrication quality of cylindrical shells. In addition, the codes provide methods of measurements and allowable tolerances for the three types of imperfections.

Out-of-roundness is expressed in terms of the parameter U_r given by

$$U_r = \frac{d_{\max} - d_{\min}}{d_{nom}} \tag{2.6}$$

in which $d_{\max}$ is the maximum measured internal diameter, $d_{\min}$ is the minimum measured internal diameter, and d_{nom} is the nominal internal diameter.

The accidental eccentricity e_a refers to the accidental eccentricity perpendicular to the membrane compressive force, between the middle surfaces of the adjacent plates, but excluding the intended offset at a change of plate thickness. The accidental eccentricity is expressed in terms of the accidental eccentricity parameter U_a given by

$$U_a = \frac{e_a}{t_{\min}} \quad \text{or} \quad U_a = \frac{e_a}{t} \tag{2.7}$$

where $t_{\min}$ is the thickness of the thinner plate at the joint.

The measurements of dimples should be taken using a dimple measurement gauge at every position (Figure 2.4) along both the meridional and circumferential directions. The meridional gauge should be straight, whereas the circumferential gauge should have a curvature equal to the intended radius of the middle surface of the shell. The dimples in the shell wall should be measured using the gauges with the lengths given below:

(a) For positions with the presence of axial compressive stresses, including across welds, the length of gauge in both the meridional and circumferential directions is given by:

$$l_{gx} = 4\sqrt{Rt} \tag{2.8}$$

where R is the radius of the shell, and t is the thickness of the shell.

(b) Where circumferential compressive stresses or shear stresses are present, measurements along the circumferential direction should be made using the following gauge length:

$$l_{g\theta} = 2.3(l^2 Rt)^{0.25}, \text{ but } l_{g\theta} \leq R \tag{2.9}$$

(c) In addition, when the circumferential or meridional gauge crosses welds, the following gauge length should be used:

$$l_{gw} = 25t \text{ or } l_{gw} = 25t_{\min}, \text{ but with } l_{gw} \leq 500\,\text{mm} \tag{2.10}$$

The depth of initial dimples is expressed in terms of the dimple parameters U_{0x}, $U_{0\theta}$, U_{0w} given by:

$$U_{0x} = \Delta w_{0x} / l_{gx} \qquad U_{0\theta} = \Delta w_{0\theta} / l_{g\theta} \qquad U_{0w} = \Delta w_{0w} / l_{gw} \tag{2.11}$$

The tolerances for the three types of imperfections for different fabrication quality classes are given in Table 2.1. The parameters of the three types of imperfections shall have values smaller than or equal to their corresponding tolerances shown in Table 2.1.

2.5.3 Elastic Buckling under Axial Compression

Cylindrical shells in steel silos are subject to compressive stresses induced by stored solids; elastic buckling under axial compression is the common failure mode and often dominates their design because the shells have very thin walls (Rotter, 1985c, Rotter and Seide, 1987). Elastic buckling of cylindrical shells under pure axial compression is commonly major focus when developing shell stability design codes. ECCS (1988) suggests that the knock-down factor accounting for the effect of imperfections in axially compressed shells is dependent on R/t. However, theoretical studies have shown that this imperfection reduction factor is independent of R/t (e.g. Yamaki, 1984; Rotter and Teng, 1989; Teng and Rotter, 1992; Rotter, 1998c). In addition, ECCS (1988) provides four separate expressions, two for the full strength rule and two for the half strength rule, for the imperfection reduction factor, which is more complicated than is necessary.

The four separate expressions in ECCS (1988), though algebraically different from each other, in fact give much the same results for imperfections larger than one wall thickness. In an attempt to find a single simple relationship which is not too different in prediction from those of ECCS (1988), Rotter (1995b, 1998a) tried a variety of expressions and finally chose the following single equation to express the relationship between the

unpressurised elastic imperfection reduction factor α_x and the imperfection amplitude for all slenderness (R/t):

$$\alpha_x = \frac{0.83}{1+1.91\left(\frac{\Delta w_k}{t}\right)^{1.44}} \tag{2.12}$$

This formula matches well with the full strength rule, but gives slightly higher buckling strengths than those predicted by the half strength rule for cylinders with low R/t ratios. This means that the predictions of the formula may be slightly less safe than those of the half strength rule for the case of very imperfect thick cylinders, but this slight difference is insignificant as thick cylinders are controlled by plasticity rather than elastic buckling. For a 'perfect' shell, Eqn 2.11 gives $\alpha_x = 0.83$, retaining the denominator in the ECCS (1988) full strength rule.

The new Eurocodes (ENV 1993-1-6, 1999; ENV1993-4-1, 1999) adopt this relationship but also incorporate an additional safety factor γ ($\gamma = 4/3$) to consider detrimental factors other than geometric imperfections, such as non-uniform stresses, imperfections in boundary conditions, and residual stresses.

With the inclusion of the additional safety factor $\gamma = 4/3$, Eqn 2.12 becomes

$$\alpha_x = \frac{0.62}{1+1.91\left(\frac{\Delta w_k}{t}\right)^{1.44}} \tag{2.13}$$

Eqn 2.13 shows the relationship between the imperfection reduction factor and the imperfection amplitude for elastic buckling of cylindrical shells under pure axial compression, and was codified into the new Eurocodes. This relationship has the merit of explicitly considering the fabrication quality in the design, paving the way for the inclusion of fabrication tolerance into contract specifications.

2.5.4 Elastic Buckling under Axial Compression and Low Internal Pressure

Cylindrical shells in civil engineering are often subject to the combined action of axial compression and internal pressure. For example, the granular solids stored in steel silos not only exert axial compression, but also produce internal pressure on the shell wall. Internal pressurization reduces the imperfection sensitivity and increase the shell elastic buckling strength from the unpressurized value towards the classical elastic critical stress σ_{cl} in an asymptotical manner (Rotter, 1995b). Exploitation of this beneficial effect can lead to much lighter design.

This effect is covered by the ECCS recommendations (1988) in which an empirical formula based on a lower bound fit to available experimental results (e.g. Weingartten *et al*, 1965; Saal, 1977; Saal, 1979). The experimental data were obtained from tests on laboratory specimens fabricated by rolling a single sheet around a mandrel with one meridional seam in which the imperfections are expected to have been dominated by asymmetric forms. By contrast, large cylindrical shells in civil engineering structures such as steel silos and tanks are generally made by joining together many circular strakes with continuous circumferential welds between the adjacent strakes, which leads to approximately axisymmetric imperfections at circumferential welds (e.g. Bornscheuer *et al*, 1983; Rotter, 1988; Ding, 1992). Hutchinson (1965) showed theoretically that the strength gains from internal pressurization is strongly dependent on whether the imperfections are predominantly asymmetric or axisymmetric; axisymmetric imperfections were shown to lead to the lowest strength gains due to internal pressurization. This indicates that the ECCS (1988) rule is unconservative for practical structures in civil engineering (Rotter and Seide, 1987; Rotter and Teng, 1989).

Further theoretical analyses carried out on this subject mostly adopted axisymmetric imperfections and found lower strength gains than the ECCS predictions (Teng and Rotter, 1992; Rotter, 1996, 1997). On the basis of these calculations, the new Eurocodes (ENV 1993-1-6, 1999; ENV 1993-4-1, 1999) provide a more conservative design rule than that given in ECCS (1988), in which α_{xpe} is related to α_x as follows

$$\alpha_{xpe} = \alpha_x + (1-\alpha_x)\left(\frac{\bar{p}}{\bar{p} + 0.3/\sqrt{\alpha_x}}\right) \tag{2.14}$$

$$\bar{p} = \frac{pR}{t\sigma_{xRc}} \tag{2.15}$$

where α_{xpe} is the imperfection reduction factor with the effect of internal pressurization included, p is the minimum reliable local value of internal pressure, guaranteed to coexist with the meridional compression, and σ_{xRc} is the elastic critical meridional buckling stress given by Eqn 2.1 in which σ_{cl} is used instead of σ_{xRc}.

2.5.5 Plastic Collapse under Axial Compression and High Internal Pressure

If the level of internal pressure is high, the cylindrical shell may fail by local plastic collapse which is often axisymmetric pattern has the shape of an elephant's foot; it is therefore referred to as the 'elephant foot' failure. This failure mode often occurs in local bending zones near a boundary condition, in the vicinity of a ring, at a thickness change or local imperfections. ECCS (1988) makes no direct reference to this type of failure but recommends a complicated iterative procedure without a rational basis.

This failure mode was first theoretically investigated by Rotter who examined this failure mode near a boundary (Rotter, 1985d; 1990), and then at a local axisymmetric imperfection (Rotter, 1988; 1996). Teng (1994) studied this failure mode at a lap joint. These studies revealed that failure near a boundary or stiff ring stiffener appears to be the most deleterious to shell strength, but much further work needs to be carried out for a more refined assessment. The Eurocodes adopt a semi-empirical formula proposed by Rotter (1990):

$$\alpha_{xpp} = \left(1 - \frac{\bar{p}}{\bar{\lambda}_x}\right)\left(1 - \frac{1}{1.12 + s^{3/2}}\right)\left(\frac{s^2 + 1.21\bar{\lambda}_x^2}{s(s+1)}\right) \tag{2.16}$$

$$\bar{p} = \frac{pR}{t\sigma_{xRc}} \tag{2.17}$$

$$s = \frac{1}{400}\frac{R}{t} \tag{2.18}$$

in which: α_{xpp} is a factor accounting for pressure-induced plastic destabilization, p is the maximum local value of internal pressure, which is possibly coexistent with the

meridional compression, $\bar{\lambda}_x$ is the non-dimensional shell slenderness parameter given by $\bar{\lambda}_x = \sqrt{f_y / \sigma_{xRc}}$, and f_y is the yield stress.

In assessing the buckling strength of axially compressed cylinders with internal pressure, the strength reduction factor α_{xp} should be taken as the smaller of α_{xpe} and α_{xpp}.

2.5.6 Unified Expression for the Elastic Plastic Buckling Stress

Following the general procedure by many national and international standards for metal structures, the Eurocodes (ENV 1993-1-6, 1999; ENV 1993-4-1, 1999) adopted a unified expression of reduction factor for the elastic-plastic buckling strength in which the yield-stress related stability reduction factor χ is expressed as a function of the shell non-dimensional slenderness $\bar{\lambda}$ ($\bar{\lambda} = \sqrt{f_y / \sigma_{Rc}}$, σ_{Rc} is the critical buckling strength of a perfect shell) as follows:

$$\chi = 1 \qquad \text{when} \qquad \bar{\lambda} \le \bar{\lambda}_0 \tag{2.19}$$

$$\chi = 1 - \beta \left(\frac{\bar{\lambda} - \bar{\lambda}_0}{\bar{\lambda}_p - \bar{\lambda}_p} \right)^{\eta} \qquad \text{when} \qquad \bar{\lambda}_0 < \bar{\lambda} < \bar{\lambda}_p \tag{2.20}$$

$$\chi = \frac{\alpha}{\bar{\lambda}^2} \qquad \text{when} \qquad \bar{\lambda}_p < \bar{\lambda} \tag{2.21}$$

in which α is the elastic imperfection reduction factor, β is the plastic range factor, η is the interaction exponent describing the shape of the elastic-plastic buckling interaction between $\bar{\lambda}_0$ and $\bar{\lambda}_p$, $\bar{\lambda}_0$ is the squash limit slenderness defining the 'plastic plateau' of the buckling curve, and $\bar{\lambda}_p$ is the plastic limit relative slenderness given by

$$\bar{\lambda}_p = \sqrt{\frac{\alpha}{1-\beta}} \tag{2.22}$$

The shell characteristic buckling strength, with the effect of initial imperfections and plasticity duly considered, is determined as the product of the characteristic yield strength and the reduction factor:

$$\sigma_{xRk} = \chi f_y \tag{2.23}$$

The variation of the stability reduction factor χ with the non-dimensional shell slenderness $\bar{\lambda}$ as described above is illustrated in Figure 2.5. It clearly shows that the design of stocky shells ($\bar{\lambda} \leq \bar{\lambda}_0$) is controlled by plastic failure, slender shells ($\bar{\lambda}_p < \bar{\lambda}$) fail by elastic buckling, and shells of medium slenderness ($\bar{\lambda}_0 < \bar{\lambda} < \bar{\lambda}_p$) fail by elastic-plastic buckling. The values of buckling parameters $\bar{\lambda}_0$, β, and η are given in ENV 1993-1-6 (1999) for some basic shell buckling cases. For example, $\bar{\lambda}_0 = 0.20$, $\beta = 0.6$, $\eta = 1.0$ for cylindrical shells under axial compression (ENV1993-1-6, 1999).

The advantage of this single unified curve for stability design is that the format of the design rule is compatible with that of other stability cases in Eurocode 3. In addition, the reduction factor χ is in a form suitable for future refinement.

2.6 TECHNIQUES FOR SHELL BUCKLING EXPERIMENTS

2.6.1 Introduction

Buckling experiments on shells are far more complicated than those on columns or plates: firstly, the buckling and postbuckling behavior of shells, which has been previously discussed, is much more complex than that of columns or plates; secondly, the experimental set-up for shell buckling tests is generally more sophisticated than those for columns or plates. For these reasons, buckling experiments of shells, though with a history of more than one century, is still a serious challenge to researchers. Comprehensive reviews of experimental work on shell buckling have been given by Babcock (1974), Singer (1982a, 1982b, 1997), Amiro and Zarutskii (1996), and Singer et al (2002). Several important issues of thin shell buckling experiments pertinent to the present study are disscussed in this section.

2.6.2 Model Fabrication

Fabrication of good quality models is critical to shell buckling experiments, as the buckling behavior of a shell is often acutely sensitive to small details, especially, the initial imperfections in the shell. In making experimental models, issues such as model sizes, materials, fabrication techniques need careful consideration. The model shall not be too large to avoid inconvenience in laboratory tests nor too small to avoid difficulty in achieving the required radius-to-thickness ratio of the prototype structure. In addition, the material chosen shall be able to reproduce the buckling behavior of real structures. Extreme care shall be exercised in the model fabrication process so that the influence of unwanted imperfections is less than that of parameters under investigation.

Many techniques have been developed for the fabrication of small-scale shell models, among which are electroforming of nickel or copper, rolling and seaming of mylar sheets, thermal vacuum forming of plastics (such as PVC, polyethylene, Lexan, and other thermal forming plastics), spin casting of plastics (such as polymer and epoxy resins), semi-casting of resins, and cold working (such spinning, explosive forming, and hydroforming) of metal, and machining and special forging, etc. For more detailed information, Babcock (1974) and Singer *et al* (2002) should be consulted. Most of these fabrication techniques have been used to produce nearly-perfect specimens for laboratory tests. For instance, Tennyson (1964), by using the spinning-casting technique with meticulous care, was able to manufacture nearly perfect shells that buckle at loads close to the critical load predicted by a linear theory.

Apart from efforts aimed at the fabrication of nearly perfect specimens, researchers have also pursued the fabrication of realistic specimens, not only in material, but also in the fabrication technique. Realistic model fabrication is important for the development of design rules for civil engineering structures and offshore structures, which are generally built by the rolling and welding of steel sheets. To achieve a realistic specimen, the method of rolling thin steel sheets followed by connection welding (referred to as the rolling and seaming method hereafter) is commonly adopted in laboratory testing to study the behaviour offshore and civil engineering steel shell structures. Examples of studies in which this fabrication technique was employed include Dowling and Harding (1982), Dowling *et al* (1982), Green and Nelson (1982), Miller (1982), Walker *et al* (1982), Scott

et al (1987), Knoedel *et al* (1995), Berry (1997), Chryssanthopoulos *et al* (1997), Schmidt and Swadlo (1996, 1997), Schimdt and Winterstetter (1999), Berry *et al* (2000), Chryssanthopoulos and Poggi (2001). The aim of realistic model fabrication shall be to produce models with geometric imperfections and weld-induced residual stresses which are as close as possible to those in real structures.

In model fabrication using the rolling and seaming method, a forming mandrel or former is commonly employed to control the fabrication quality of the specimen (Babcock, 1974; Singer *et al*, 2002). The forming mandrel or former is important for the fabrication of high quality models for civil engineering shell structures such as silos and tanks, because model shells with a wall thickness as small as less than 1.0mm are susceptible to shape distortions without the support of a former. Such a small thickness is necessary to achieve a typical radius-to-thickness ratio ranging from 500 to 2000 without using a much larger diameter. Berry (1997) designed a forming mandrel for his cylindrical small models with wall thicknesses of 0.6mm, 0.7mm, 0.8mm, and 0.9mm, respectively. The mandrel consisted of four collapsible cylindrical segments that could collapse inward to release the specimen from the mandrel. The forming mandrel was a complete cylinder used to support the rolled steel sheets for alignment and welding during fabrication. Two rings were attached to both ends of the specimen to maintain its circularity after welding before being released from the mandrel. Teng *et al* (2001) set up a wooden former for fabricating their cone-cylinder junction models. The former was divided into two parts, i.e. a cone and a short cylinder, for ease of releasing the small model from the former.

Another important factor that controls the quality of model fabrication by the rolling and seaming method is the welding technique. TIG (Tungsten-Insert-Gas) welding has been employed in many studies (e.g. Green and Nelson, 1982; Walker *et al*, 1982; Scott *et al*, 1987), and proved to be suitable for model shells made of thin steel sheets. Later, pulsed TIG welding, which was developed specially for very thin sheet metals, was used to achieve quality welding on very thin model steel shells, producing specimens of superior quality (Knoedel *et al*, 1995; Berry, 1997; Teng *et al*, 2001). The pulse TIG welding technique has the advantages of lower total heat input and better heat dissipation and is thus one of the most suitable welding techniques for very thin sheet metals. In order to improve the consistency of welding quality, Berry (1997) developed an automatic welding device in which the welding torch was mounted on a spring-loaded carriage driven by two

DC motors so that welding could be performed automatically in both the circumferential and meridional directions. As a further measure to achieve high quality welding, the former should be covered with copper sheets in areas where welding will be carried out, to provide a non-sticky backing as well as a heat sink to reduce welding distortions and welding residual stresses (e.g. Berry, 1997; Teng *et al*, 2001).

2.6.3 Techniques for Imperfection Measurements

Although imperfection measurement on shells has a long history, its importance was properly recognized only several decades ago, when it became well accepted that knowledge of real imperfections is a necessity for applying the theory of imperfection sensitivity with confidence. Nowadays, geometric imperfection measurements have become an integral part of shell buckling experiments. Consequently, extensive measurements of geometric imperfections were carried out both on laboratory specimens and on full scale structures. In conjunction with this trend, a variety of imperfection measurement techniques have been developed. Reviews of these techniques have been provided by Singer and Abramovich (1995) and Singer *et al* (2002).

The first imperfection surveys on cylindrical shells were carried out in the context of studying the collapse pressures of the Bessemer steel lap-welded tubes by Stewart (1906) who designed a special device to measure the out-of-roundness of the tubes. Several others also performed circumferential scans on cylindrical and spherical shells under external pressure, to determine the magnitude of out-of-roundness but did not present details of measured shapes (e.g. Jasper and Sullivan, 1931; Galletly and Bart, 1956), and the concept of 'maximum out-of-roundness' was regarded as the criterion of shell imperfection level (e.g. Holt, 1952). Axial imperfection scans were also carried out in the fifties and sixties (e.g. Lunchick and Short, 1957; Babcock and Sechler, 1963). However, all of these early imperfection surveys were incomplete and without a perfect reference cylinder, so the data could not be used easily for detailed interpretations.

Complete and automated imperfection surveys were introduced in the late sixties and early seventies. The earliest systems were those developed simultaneously at GALCIT (Graduate Aeronautical Laboratories, California Institute of Technology) and at Stanford University in 1968. The GALCIT system (e.g. Arbocz and Babcock, 1968; Singer *et al*,

1971) used punched card recording and a perfect reference cylinder obtained by a least-square fit of the measured imperfection data, while the Stanford system adopted analog recording with AD conversion and digital data reduction (Shover, 1968).

There were important advances in imperfection measurement in the late seventies when the importance of imperfection measurements was well recognized. A number of imperfection surveys were carried out on laboratory scale as well as full scale shell structures; these were accompanied by the development of a number of measuring systems (Singer, 1982a, 1982b; Singer *et al*, 2002). One notable study involved an imperfection survey on a full-scale aluminium alloy stiffened shell with a diameter of 3.05m (10ft) conducted at the NASA Langley Center (Arbocz and Williams, 1977). In the system employed for this survey, an aluminium guide rail was supported on the outside diameter of the two steel end rings and a DCDT (Direct Current Differential Transformer) was installed on a trolley car which was spring-loaded to be in continuous contact with the guide rail. The trolley car was driven along the guide rail by an electric motor and the guide rail was moved stepwise around the cylinder circumference in 5^0 increments.

Another notable system was developed at the Chicago Bridge and Iron Co. for experiments on welded steel torispherical domes with a diameter of 4877mm under internal pressure (Miller and Grove, 1986). In this system, a frame was specially designed for geometric measurements. The frame included a precisely machined rotating arm for the mounting of 15 LVDTs (Linear Variable Differential Transformers), a support truss and a computer-controlled stepping motor for positioning the arm. As the arm was rotated around the shell, the LVDTs measured the shape of the shell with reference to the machined surface of the arm so that the initial shell shape as well as shape changes during a test could be measured.

LVDTs or other contact probes were employed in most imperfection measurements on small stiffened shells and large shells mentioned above. However, for shells with a very thin wall, even the small probe force may lead to distortions of the shell surface; therefore non-contact probes are preferable. Several non-contact techniques such as reluctance pickup and capacitance pickup were developed (Singer *et al*, 2002), but these are difficult to use in imperfection measurements. A special servo-system was set up for very accurate

non-contact mapping and was used in a multipurpose scanning and measurement system for imperfections and vibrations (Singer and Abramovich, 1995; Singer *et al*, 2002). Some other non-contact techniques such as holographic interferometry (Evans *et al*, 1987) and photoreflective moiré method (Foster, 1986; Krishnakumar and Foster, 1989) were also attempted, but they are unsuitable for imperfection surveys as the operation procedures are too complicated and the scope of application is restricted.

The laser displacement meter, which can provide high speed measurements with excellent accuracy, has positioned itself as the best solution to non-contact measurements. A number of recent experimental studies on shell buckling have employed one or more laser displacement meters mounted on a specially designed motion device (Berry *et al*, 1996; Esong *et al*, 1998; Bisagni, 1999; Lancaster *et al*, 2000, Teng *et al*, 2001). The motion device, which was driven by motors, allowed the sensor head of the laser meter to move up and down and rotate around the specimen, so that a three-dimensional survey of a specimen surface could be achieved. Some of the systems used an outside measurement scheme in which the measurement devices were installed outside the specimen (Berry *et al*, 1996; Lancaster *et al*, 2000; Teng *et al*, 2001) while others used an inside measurement scheme (Esong *et al*, 1998; Bisagni, 1999). The choice of one of these two schemes depends on the particular conditions experimental set-up and conditions. Options vary on number of laser meters: Berry *et al* (2001) and Teng *et al* (2001) used only one laser meter in terms of sensor, but Esong *et al* (1998) and Lancaster *et al* (2000) employed two laser sensors, while Bisagni (1999) adopted five sensors. Adopting more than one laser sensor shortens that the measurement time. Various types of laser displacement meters were used in these five systems; and their resolutions were different, i.e, 0.5 microns for Berry *et al*' system, 12 microns for Esong *et al*'s system, 15 microns for Bisagni's system, 50 microns for Lancaster *et al*'s system, and 0.5 microns and 3 microns for Teng *et al*'s system during their different periods of their experimental program.

Apart from the techniques discussed above for imperfection surveys in the laboratory, many techniques have also been developed to measure imperfections in large silos and tanks in service. Among them are the measurement rod method (e.g. Bornscheuer and Hafner, 1983), photogrammetry (e.g. Shmutter and Ethrog, 1971; Chisholm, 1977; Papo and Shmutter, 1978; Ethrog, 1986), the geodetic method (e.g. Moss, 1990), and a specially-designed profile measurement system (Coleman et al, 1992; Ding, 1992). Rotter

et al (1992) gave a brief review of these methods. Jullien (1996) proposed several other methods for measuring geometric imperfections, however, only the method of stereophotogrammetry is industrially usable so far. ECCS (1988) and ENV 1993-1-6 (1999) adopted the measurement rod (gauge) method to determine the magnitude of local geometric imperfections.

2.6.4 Boundary and Loading Conditions

As noted earlier in the chapter, boundary conditions have a considerable influence on the buckling load of a shell (e.g. Hoff and Soong, 1965). It is therefore crucial that the desirable boundary conditions are reliably achieved in shell buckling experiments. Early experimentalists generally adopted a simply supported boundary condition as the experimental results could be readily compared with theoretical predictions that were available only for this boundary condition. Theoretical advances over many decades have made it possible to obtain numerical solutions for all kinds of boundary and loading conditions. The simply supported condition is no longer a good choice as it is hard to implement in experiments (Berry, 1997). The fully clamped condition, which can be easily realized in experiments as well as easily modeled in numerical analysis, is probably the best choice (Babcock, 1974; Berry, 1997). The fully clamped boundary condition can be realized in experiments by casting the shell end into suitable materials such as a low-melting temperature alloy or epoxy (Babcock, 1974; Singer, 1982b). Berry (1997) adopted an alloy with a melting point of $73^{\circ}C$ and two rigid steel rings for clamping the shell ends, because epoxy is difficult to clean and re-use (Babcock, 1974; Berry, 1997). Other methods such as attaching the shell ends to some end fixtures by mechanical fasteners or tensioned bands, were suggested but proved to be unreliable, as they may sometimes result in erratic load transfer (Babcock, 1974).

Shell buckling experiments are usually performed using a standard testing machine or a special-purpose machine. Loading needs to be applied carefully to ensure its proper transfer to the test specimen. A good load transfer is usually much harder to achieve than reliable end fixity (Babcock, 1974). In order to achieve the desired loading condition, some load transferring devices usually need to be employed. For example, Berry (1997) designed for his experiments a universal joint and two conical platens that enabled the

point load of the actuator to be effectively transformed into an uniform annular load of 1000 mm diameter exerted on the cylindrical shell specimen.

In shell buckling experiments, either load control or displacement control may be used. The difference between these two control modes has been a subject of debate for many years. It is now quite well accepted that the control mode has little effect on the buckling load in a normal laboratory environment, but the control mode is important for the determination of the post-buckling path (Babcock, 1974). For the case of a cylindrical shell under axial compression, displacement control is necessary for testing in its postbuckling range as the postbuckling behavior of the shell is highly unstable. Berry (1997) used a MTS servo-controlled hydraulic actuator system to accomplish fine automated displacement control in his experiments.

2.7 NUMERICAL TECHNIQUES FOR SHELL BUCKLING ANALYIS

In recent years, the great advances in the finite element technology, coupled with the rapid development in computer technology have made computer-based numerical techniques an important tool for studying the buckling behavior of shells. Many different types of buckling analyses, which are summarized in Table 2.2 (ENV 1993-1-6, 1999), are available. A number of general purpose finite element programs have been developed for the analysis and design of a wide variety of structures. One of these programs is the famous ABAQUS general-purpose finite element package (Hibbit, Karlsson and Sorensen, 1998), which includes techniques such as eigenvalue buckling analysis and unstable collapse and postbuckling analysis. All the different types of buckling analysis listed in Table 2.2 can be accomplished using ABAQUS. Due to its capability, ABAQUS was used in a vast number of recent studies on shell stability (e.g. Holst *et al*, 1999, 2000; Goto and Zhang, 1999; Mandal and Calladine, 2000; Pircher and Bridge, 2001a, 2001b; Teng and Song, 2001; Zhao and Teng, 2001; Zhu *et al*, 2002).

An eigenvalue buckling analysis can be used to find the critical load (bifurcation load) of a shell structure. Two types of eigenvalue buckling analyses can be employed: linear bifurcation analysis nonlinear bifurcation analysis. The linear bifurcation analysis is the buckling analysis that is performed on the shell structures with either a load-free base state

or a linearly elastically pre-loaded one. The linearly elastically pre-loaded is usually used to overcome the numerical problems in the structures with many closely spaced eigenvalues such as the case of cylindrical shells under axial compression. In many situations, a series of clustered eigenvalues indicate the structures are imperfection sensitive. A linear bifurcation analysis will not predict accurate bifurcation load of the imperfection sensitive structures; a nonlinear bifurcation analysis should be used instead. The nonlinear bifurcation analysis is the buckling analysis performed on the nonlinearly deformed elastic shell structures which are preloaded to a base state which is sufficiently close to the buckling state. For all of these calculations, the bifurcation modes are described by the eigenvectors extracted, while the bifurcation loads of the shells P_{cr} are determined by:

$$P_{cr} = P_0 + \lambda Q \tag{2.24}$$

where P_o is the preload at the base state, λ is the eigenvalue extracted, and Q is the incremental load applied in the eigenvalue extracting process.

As noted previously, the initial postbuckling response of cylindrical shells under axial compression is highly unstable. Several approaches are available for modeling unstable postbuckling behavior. A commonly adopted approach, which is also available within ABAQUS (Hibbitt, Karlsson & Sorensen, 1998), is the 'modified Riks method' (Riks, 1979), which is capable of tracing an unstable static equilibrium path in a space defined by a proportional loading parameter and displacements. In the modified Riks procedure, the magnitude of load is used as an additional unknown computed as a load proportionality factor multiplying the reference loads; an artificial parameter, the arc-length, is introduced to measure the progress of the solution. Both parameters are part of the solution. Several parameters need to be specified by the user, some of which such as the initial increment in arc length, the minimum arc length increment, and the maximum arc length increment, are used to control the direction and progress of the calculation, while some other parameters such as the maximum value of the load proportionality factor, the maximum displacement at a node, and the total arc length scale factor are used to terminate the solution process when analysis of these limits is exceeded. In any case, the analysis will end when another user-specified parameter, the maximum number of increments for the step, is exceeded.

For the post-bifurcation analysis of perfect shells, the modified Riks method cannot be directly employed, because of the discontinuous response in terms of slope at the point of bifurcation buckling. To overcome this difficulty, the discontinuous response needs to be turned into a continuous response by introducing a geometric imperfection of a small amplitude into the perfect geometry.

2.8 CONCLUSIONS

This chapter has provided a review of existing research relevant to the work presented in this thesis. Based on this review, it is clear that the buckling behavior of thin cylindrical shells is strongly dependent on both the magnitude and form of imperfections in the shell. It is also clear that the form of imperfections depends strongly on the fabrication process. Existing research on the buckling response of axially compressed cylindrical shells has been concerned mainly with imperfections found in aeronautical shells or offshore structures, and with substitute imperfections, all of which are not representative of imperfections found in civil engineering shell structures such as silos and tanks which are generally constructed by the unique process of welding a large number of rolled panels (referred to as the panel method). The existing knowledge of the form of imperfections resulting from the panel method as well as the effect of these imperfections on the buckling strength of thin cylindrical shells under axial compression is very limited, a situation which has led to many structural failures of silo structures worldwide. It is therefore imperative to carry out rigorous investigations into these imperfections and their influence on the buckling behavior of cylindrical shells built using the panel method.

Table 2.1 Shell Fabrication Quality Classes and Tolerances

Fabrication Quality		Maximum Permitted Tolerance		
Quality	Description	$U_{r,max}$	$U_{e,max}$	$U_{0,max}$
Class A	Excellent	0.007	0.14	0.006
Class B	High	0.010	0.20	0.010
Class C	Normal	0.150	0.30	0.016

Table 2.2 Types of Shell Analysis According to ENV 1993-1-6

Type of Analysis	Abbreviation	Shell Theory	Material Law	Shell Geometry
Membrane theory of shells	-	Membrane equilibrium	Not applicable	Perfect
Linear elastic shell analysis	LA	Linear bending and stretching	Linear	Perfect
Geometrically nonlinear elastic analysis	GNA	Nonlinear	Linear	Perfect
Materially nonlinear analysis	MNA	Linear	Nonlinear	Perfect
Geometrically and materially nonlinear analysis	GMNA	Nonlinear	Nonlinear	Perfect
Geometrically nonlinear elastic analysis with imperfections	GNIA	Nonlinear	Linear	Imperfect
Geometrically and materially nonlinear analysis with imperfections	GMNIA	Nonlinear	Nonlinear	Imperfect

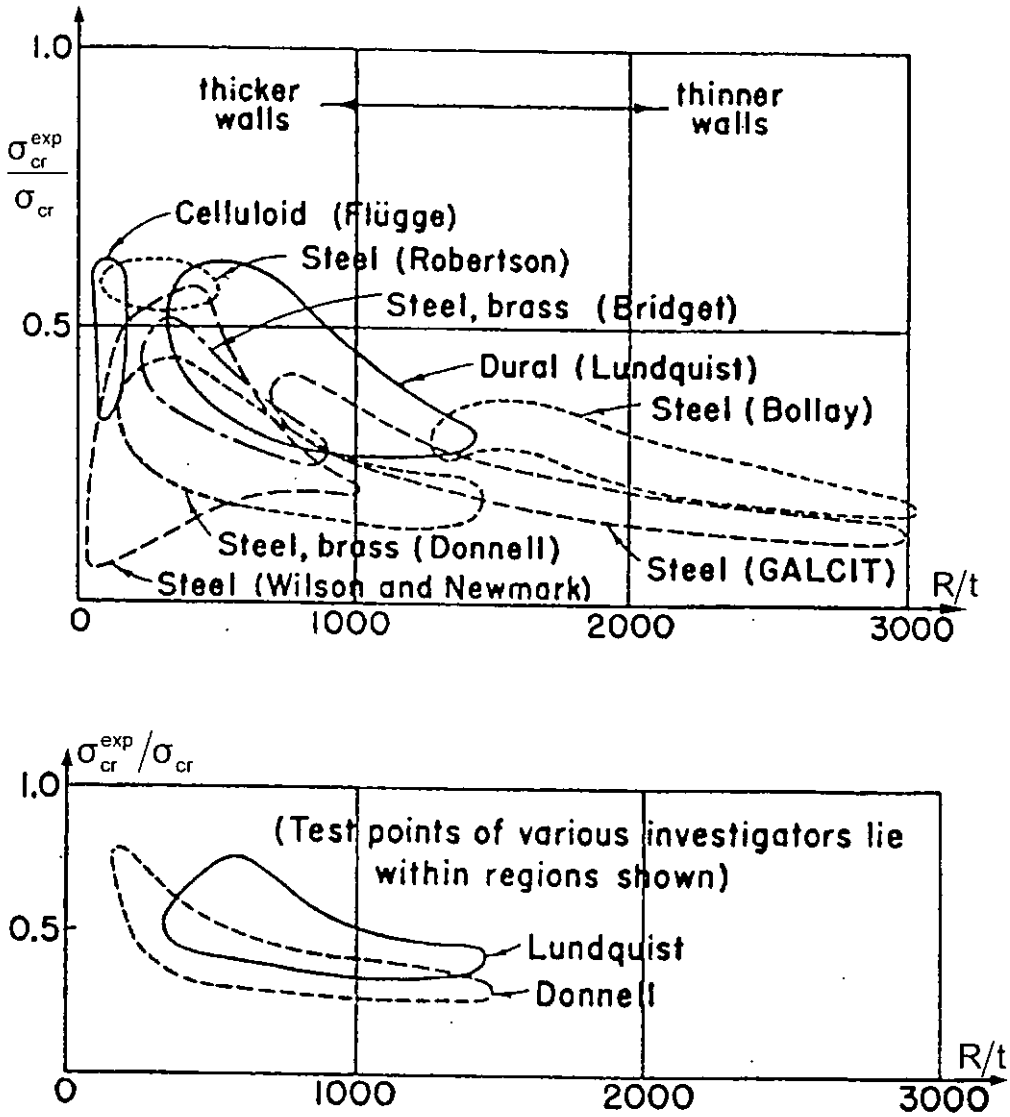

Figure 2.1 Test results on axially compressed cylindrical shells (After Donnell and Wan, 1950)

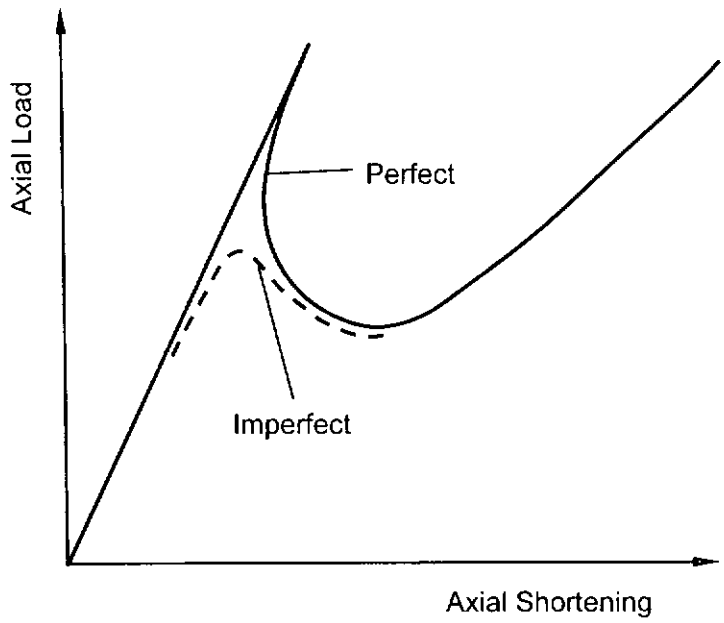

Figure 2.2 Behavior of cylindrical shells under axial compression

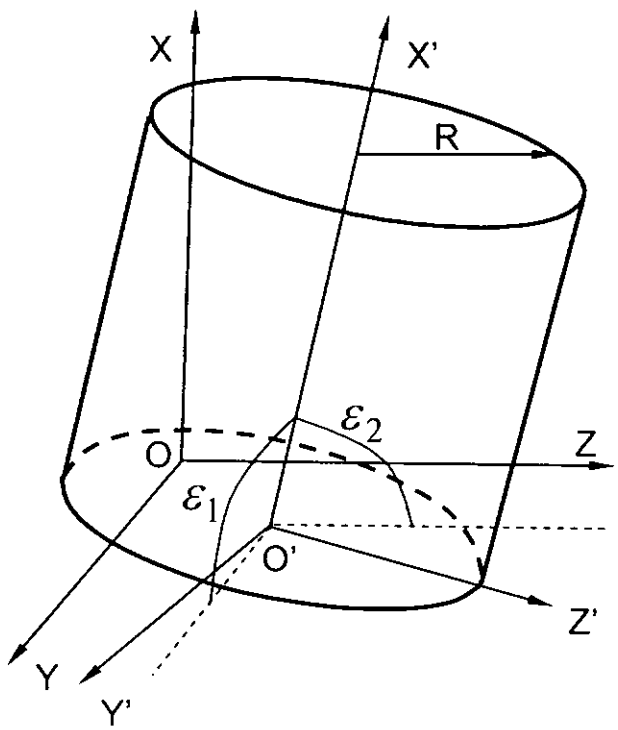

Figure 2.3 Definition of reference cylinder

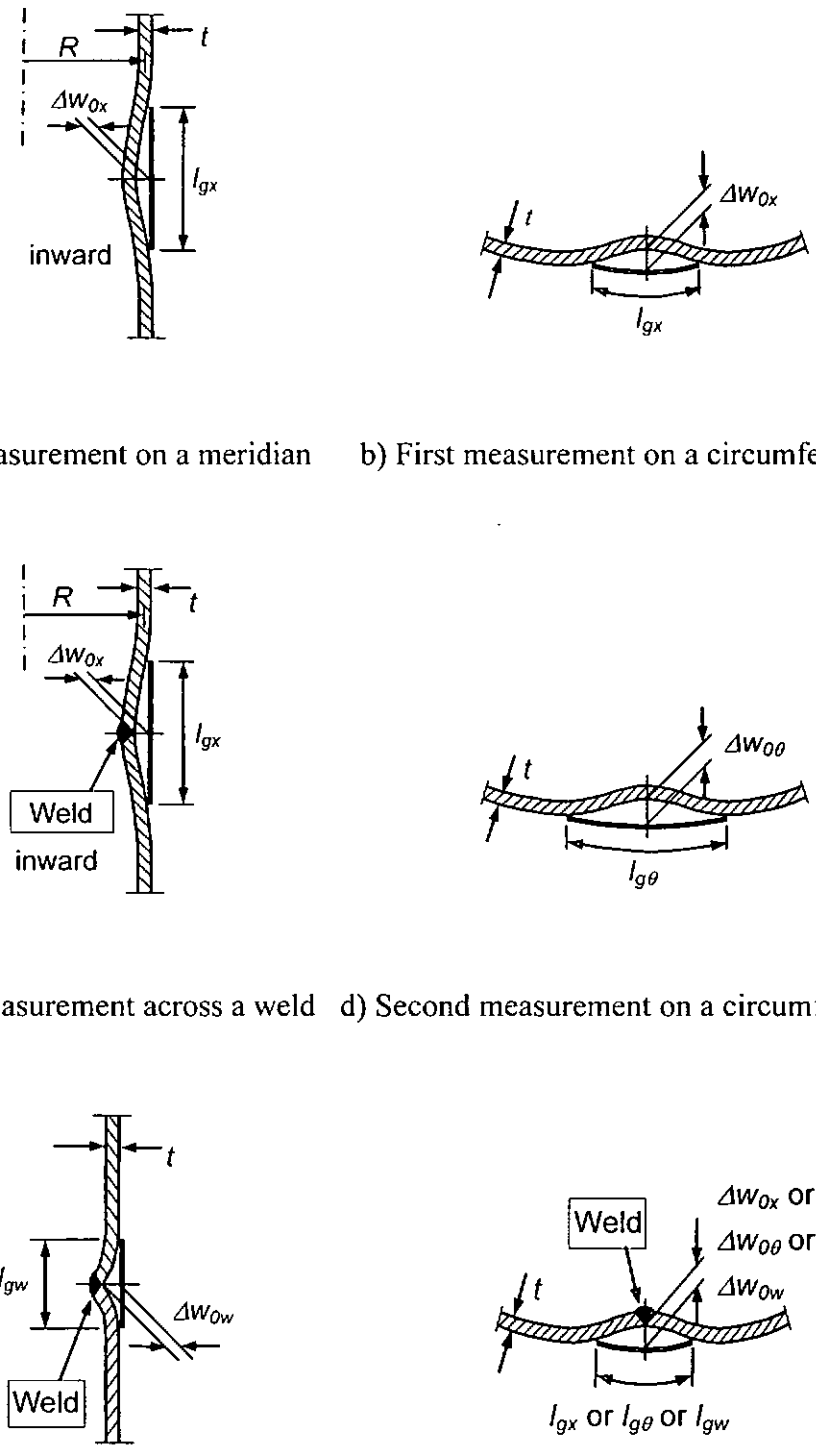

a) Measurement on a meridian

b) First measurement on a circumferential arc

c) First measurement across a weld

d) Second measurement on a circumferential arc

e) Second measurement across a weld with a special gauge

f) Measurements on a circumferential arc across a weld

Figure 2.4 Measurement of depths Δw_0 of initial dimples (After ENV1993-1-6, 1999)

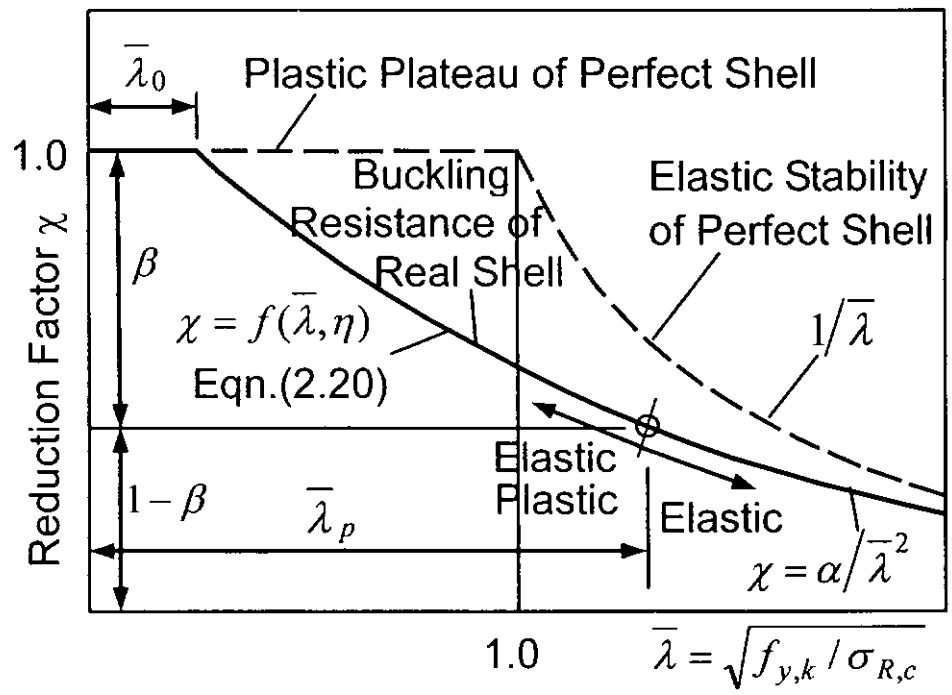

Figure 2.5 Stability reduction factor $\chi = f(\lambda)$ in ENV 1993-1-6 (After Schmidt, 2000)

CAHPTER 3

ITERATIVE FOURIER DECOMPOSITION OF IMPERFECTION MEASUREMENTS WITH NON-UNIFORM INTERVALS

3.1 INTRODUCTION

Buckling of shells subject to compressive stresses is often acutely sensitive to the form and amplitude of geometric imperfections present in the structure. For example, for axially compressed thin cylindrical shells, an imperfection with its amplitude being as small as one wall thickness may result in a 70% loss in the buckling strength. Both the form and the amplitude of geometric imperfections play an important role in reducing the buckling strength as discussed in Chapter 2. As a result, many attempts have been made to measure geometric imperfections in shells both in laboratory specimens and less frequently in full-scale structures.

Imperfection measurements are generally obtained at discrete points (i.e. the sampling points), as a result of the prevailing measurement technology available today. In the laboratory, a measurement grid with uniformly-distributed sampling points can always be used, although non-uniformly distributed sampling points in either or both of the meridional and circumferential directions of the shell surface may be more desirable for various reasons. For example, the sampling points may be chosen to be at the nodal positions of a subsequent finite element model which may use non-uniform nodal spacings in order to minimize computational cost. For imperfection measurements on full-scale structures, a common situation is that some parts of the structure are not accessible, due to the presence of accessories such as service ladders and pipes mounted on the structure. As a result, the use of a measurement grid with non-uniform intervals is generally unavoidable, and the difference between the largest and the smallest interval may be very large.

It has been well established that the form and amplitude of geometric imperfections are associated with the fabrication/construction process, and that the different components of an imperfection may have very different effects on the buckling strength of a shell (see Chapter 2 and Teng, 1996). Therefore, measured imperfections are generally interpreted using the well-known method of Fourier decomposition, so that the different harmonic components of imperfections can be more easily related to structural features such as positions of welds and their effects on buckling strength better understood. Fourier decomposition has been applied in many shell buckling studies (e.g. Arbocz and Babcock, 1969; Arbocz, 1982; Chryssanthopoulos *et al*, 1991a; Teng, 1996; Berry *et al*, 2000, Zhao and Teng, 2001). For imperfection measurements at uniformly distributed sampling points, two approaches have previously been employed: numerical integration, generally using the trapezoidal rule (Arbocz and Babcock, 1969; Arbocz, 1982; Chryssanthopoulos *et al*, 1991a; Teng, 1996; Berry *et al*, 2000) and the solution of a linear system of algebraic equations (Zhao and Teng, 2001). The latter method has been used only by Zhao and Teng (2001) in which the number of Fourier terms deducible is limited by the number of available data points. The former method is more versatile and has been the commonly used method. Both methods have been shown to perform well in existing studies where the imperfection measurements were all taken at uniformly distributed sampling points.

This chapter arose from the attempt to interpret discrete imperfection measurements made on large steel silos in service at non-uniformly distributed sampling points as presented in Chapter 4. It was found that the method of solving a system of linear algebraic equations leads to an ill-conditioned problem when the sampling points are non-uniformly distributed, and was thus not pursued further. This chapter is therefore focussed on the more versatile and commonly used numerical integration method.

The chapter first shows that for imperfection measurements at non-uniformly distributed sampling points, if the traditional Fourier decomposition method with numerical integration using the trapezoidal rule is adopted, the obtained Fourier series cannot represent the discrete imperfection data accurately. A method to overcome this difficulty, the iterative Fourier decomposition method, is next presented. The theoretical background of the proposed method is detailed, followed by a numerical demonstration of the effectiveness of the proposed method.

It should be noted that while the present chapter arose from a study of imperfection measurements on shells and is written within the context of interpreting such imperfections, the proposed method has applications far beyond the interpretation of imperfection measurements on shells. Indeed, the proposed method provides an effective way of Fourier decomposition of any type of discrete measurement data at non-uniformly distributed sampling points. For simplicity, only discrete data taken at sampling points in a one-dimensional space with a period of 2π is discussed in this chapter.

3.2 FOURIER DECOMPOSITION OF UNIFORMLY-SPACED DATA POINTS

Fourier decomposition refers to the process that a particular function $W(\theta)$ (referred to as the source function hereafter and is unknown in practice) is expressed as a suitable Fourier series (the deduced function) as follows (Kreyszig, 1999)

$$F(\theta) = \frac{a_0}{2} + \sum_{j=1}^{N_j} (a_j \cos j\theta + b_j \sin j\theta) \tag{3.1}$$

where a_j and b_j are the Fourier coefficients that are given by

$$a_j = \frac{1}{\pi} \int_0^{2\pi} W(\theta) \cos j\theta \, d\theta \,, \quad j = 0,1,2,3,\ldots,N_j \tag{3.2}$$

$$b_j = \frac{1}{\pi} \int_0^{2\pi} W(\theta) \sin j\theta \, d\theta \,, \quad j = 1,2,3,\ldots,N_j \tag{3.3}$$

where $W(\theta)$ is a function with a period of 2π. In practical applications of the Fourier decomposition method to interpret a discrete set of measurement data, the source function $W(\theta)$ is unknown, so the integration required to find a_j and b_j can only be done numerically. The simple trapezoidal rule is generally used for the numerical integration instead of the Simpson's rule which imposes the requirement that the number of data points to be used in the integration must be odd. No such restriction exists for the trapezoidal rule. This chapter is therefore concerned only with Fourier decomposition

using the trapezoidal rule, although the same problems as discussed in this chapter also exist if Simpson's rule is used instead (Kreyszig, 1999).

Using the trapezoidal rule, the Fourier coefficients can be found by

$$a_j = \frac{1}{\pi}\int_0^{2\pi} W(\theta)\cos j\theta\, d\theta \approx \frac{1}{\pi}\sum_{i=1}^{N_s-1}\frac{W(\theta_i)\cos j\theta_i + W(\theta_{i+1})\cos j\theta_{i+1}}{2}\Delta\theta_i \tag{3.4}$$

$$b_j = \frac{1}{\pi}\int_0^{2\pi} W(\theta)\sin j\theta\, d\theta \approx \frac{1}{\pi}\sum_{i=1}^{N_s-1}\frac{W(\theta_i)\sin j\theta_i + W(\theta_{i+1})\sin j\theta_{i+1}}{2}\Delta\theta_i \tag{3.5}$$

where θ_i is the angular coordinate of the ith sampling point and $\Delta\theta_i$ is the length of the ith interval. The accuracy of results from Eqns 3.4 and 3.5 for a set of discrete data taken at uniformly-spaced sampling points depends on the number of sampling points N_s relative to the harmonic number j, i.e. the number of complete waves over the range of 0 to 2π for θ. The performance of the numerical integration of Eqns 3.4 and 3.5 is examined in detail in the rest of this section, as a preparation for the discussions presented in the subsequent sections.

For a clear illustration, two sets of uniformly-spaced discrete data points are examined and the Fourier coefficients determined using Eqns 3.4 and 3.5. The first set of N_s data points have values given by the simple harmonic function $W_a(\theta) = A\cos k\theta$. An accurate Fourier decomposition procedure with a sufficient number of discrete data points is expected to reproduce this harmonic function. The second set of N_s data points lies on the curve of $W_b(\theta) = B\sin k\theta$, and again an accurate Fourier series representation should reproduce this simple source function.

The results of Fourier decomposition for these two sets of data differ depending on the number of data points, with $N_s = 2k+1$ being a threshold number. The results are thus listed for the following three cases in Table 3.1: $N_s < 2k+1$, $N_s = 2k+1$ and $N_s > 2k+1$. Appendix 3.1 shows the derivation of two coefficients for the case of $N_s < 2k+1$: a_o and

a_{k-p}. Such details for other coefficients and for the other two cases, which can be found in a similar manner, are omitted.

Table 3.1 shows that the source functions are only accurately reproduced by the Fourier decomposition method for case 3 where the number of data points available exceeds $2k+1$, k being the harmonic number of the source function. For the case of $N_s < 2k+1$, where the number of data points is $2k+1-p$ $(p < k)$, the deduced functions from exact decomposition are $\overline{F}_{1a}(\theta) = A\cos(k-p)\theta + A\cos k\theta$ and $\overline{F}_{1b}(\theta) = -B\sin(k-p)\theta + B\sin k\theta$ respectively for the source functions $W_a(\theta) = A\cos k\theta$ and $W_b(\theta) = B\sin k\theta$. In a practical numerical Fourier decomposition procedure such as that described later in the chapter, the decomposition process starts from the lower Fourier terms, and the accuracy of the deduced Fourier series is checked at the sampling points every time the next higher term is included. In such a numerical process, the deduced functions become $F_{1a}(\theta) = A\cos(k-p)\theta$ and $F_{1b}(\theta) = -B\sin(k-p)\theta$, as these functions pass through the discrete data points. In the present study, these truncated deduced functions are taken to be the results from a numerical Fourier decomposition process. Figures 3.1 and 3.2 show graphical comparisons of two sample problems for the case of $N_s < 2k+1$, where nine data points are shown and the two source functions are: $W_a(\theta) = 4\cos 5\theta$ and $W_b(\theta) = 4\sin 5\theta$, respectively. It is seen in both figures that the curve of the deduced function passes through the discrete data points. It should be noted that in the present discussion of the case of $N_s < 2k+1$, situations for which very few data points ($N_s \le k+1$) are available have been excluded. For the case of $N_s = 2k+1$, the deduced function for the source function $W_a(\theta)$ is twice the source function (Table 3.1, Figure 3.3), so the errors are as large as the original data, but for the source function $W_b(\theta)$, no function can be deduced (Table 3.1).

The above discussion shows that Fourier decomposition of discrete data points from source functions $W_a(\theta) = A\cos k\theta$ and $W_b(\theta) = B\sin k\theta$ can accurately reproduce the source functions only if the number of data points exceeds $2k+1$. Otherwise, the deduced functions contain significant errors. This has significant implications for the interpretation of imperfection measurements on shells: shell imperfections often contain significant

components in high harmonic modes, so for these modes to be accurately represented in the deduced Fourier series, a sufficient number of measurements need to be made available. In practice, the deduced Fourier series contains only a finite number of terms and the omission of some very high harmonic terms of small amplitude in the Fourier series is unavoidable. Nevertheless, a satisfactory Fourier representation is expected to pass through the discrete data points.

3.3 FOURIER DECOMPOSITION OF NON-UNIFORMLY SPACED DATA POINTS

A similar investigation into the behaviour of Fourier decomposition for a set of discrete data at non-uniformly distributed sampling points was also carried out and the results are presented in this section. Again, the results need to be discussed for the same three cases in terms of the number of data points available: i.e. $N_s < 2k+1$, $N_s = 2k+1$ and $N_s > 2k+1$. For simplicity, data sets which are uniformly spaced except for an offset δ in the abscissa of the sth data point are considered here. The results of Fourier decomposition of two sets of discrete data from the two source functions $W_a(\theta) = A\cos k\theta$ and $W_b(\theta) = B\sin k\theta$ respectively are given in Table 3.2. Appendix 3.1 shows the process of deriving the expression for a_0 in the case of $N_s < 2k+1$ for the source function $W_a(\theta)$. Such details for the other coefficients, which can be found in a similar manner, are omitted.

A comparison between the results given in Tables 3.1 and 3.2 reveals that the Fourier coefficients derived from data points with non-uniform intervals differ from their counterparts derived from uniformly-spaced data points, and this difference is a function of the offset δ. It is clear that a Fourier series derived from a set of non-uniformly spaced data points cannot represent the source function precisely, especially in those regions where the intervals vary in length or the data feature sharp changes, even if a sufficient number of data points are available. It should be noted that if δ approaches 0, the difference $E_i(\delta)$ vanishes, so the offset δ is solely responsible for the difference.

3.4 ITERATIVE FOURIER DECOMPOSITION

It is clear from the preceding discussion that for a set of non-uniformly spaced data points, the traditional Fourier decomposition method leads to a Fourier series with errors at the sampling points. As these errors are associated with the non-uniform data intervals, they cannot be reduced by the inclusion of additional Fourier terms. The only way to improve the Fourier representation is to refine the Fourier coefficients so that the deduced Fourier series passes through the discrete data points. To this end, an iterative Fourier decomposition method is proposed here, in which the errors in the deduced Fourier series at the sampling points are subject to another round of Fourier decomposition (referred to as an iteration hereafter). The method is described below.

In general, the proposed iterative Fourier decomposition method involves many iterations. The discrete data from measurements at non-uniformly distributed sampling points θ_i ($i = 1, 2, \ldots, N_s$) are denoted by $W(\theta_i)$, while the aim is to find a Fourier series $F(\theta)$ which can represent this set of discrete data accurately. In the rth iteration, the following iterative change in the Fourier series is found from the residual errors from the previous iteration $w_{r-1}(\theta_i)$, except for the first iteration, where $\Delta F_1(\theta)$ is deduced from the discrete measurement data $W(\theta_i)$ [i.e. $w_o(\theta_i) = W(\theta_i)$]:

$$\Delta F_r(\theta) = \frac{\Delta a_0^r}{2} + \sum_{j=1}^{N_r} (\Delta a_j^r \cos j\theta + \Delta b_j^r \sin j\theta) \tag{3.6}$$

where

$$\Delta a_j^r = \frac{1}{\pi}\int_0^{2\pi} w_{r-1}(\theta)\cos j\theta\, d\theta \approx \frac{1}{\pi}\sum_{i=1}^{N_s-1} \frac{w_{r-1}(\theta_i)\cos j\theta_i + w_{r-1}(\theta_{i+1})\cos j\theta_{i+1}}{2}\Delta\theta \tag{3.7}$$

$$\Delta b_j^r = \frac{1}{\pi}\int_0^{2\pi} w_{r-1}(\theta)\sin j\theta\, d\theta \approx \frac{1}{\pi}\sum_{i=1}^{N_s-1} \frac{w_{r-1}(\theta_i)\sin j\theta_i + w_{r-1}(\theta_{i+1})\sin j\theta_{i+1}}{2}\Delta\theta_i \tag{3.8}$$

and N_r is the number of the Fourier terms required in the rth iteration to minimise the errors represented by

$$R_{r1} = \sqrt{\sum_{i=1}^{N_s} w_r^2(\theta_i) \Big/ \sum_{i=1}^{N_s} W^2(\theta_i)} \tag{3.9}$$

where $w_r(\theta_i)$ is the residual error at each sampling point and is found from

$$w_r(\theta_i) = w_{r-1}(\theta_i) - \Delta F_r(\theta_i) \tag{3.10}$$

The Fourier series $F_r(\theta)$ found to represent the discrete data $W(\theta_i)$ after r iterations is given by

$$F_r(\theta) = \frac{a_0}{2} + \sum_{j=1}^{N_j} (a_j \cos j\theta + b_j \sin j\theta) \tag{3.11}$$

The Fourier coefficients are given by

$$a_j = \sum_{q=1}^{r} \Delta a_j^q \tag{3.12}$$

$$b_j = \sum_{q=1}^{r} \Delta b_j^q \tag{3.13}$$

where N_j is the highest harmonic number in the deduced Fourier series.

Convergence of the iterative process is deemed to have been achieved if the following condition is satisfied:

$$R_{r1} \leq Tol \tag{3.14}$$

where Tol is a pre-defined tolerance. The iterative process is alternatively stopped if the maximum number of iterations specified has been reached.

3.5 NUMERICAL EXAMPLES

A small computer program was written to implement the iterative Fourier decomposition method described in the preceding section. Two numerical examples are presented below to demonstrate the effectiveness of the proposed method.

3.5.1 Example 1

A cylindrical shell is considered here. From a shape survey, the initial deviations (discrete imperfection measurements) of 130 sampling points around a circumference of the cylinder are available (Figure 3.4). A Fourier series needs to be found to represent the variation of these initial deviations around the circumference. One of the intervals is 11.7°, but all other intervals are 2.7°. The iterative Fourier decomposition method was employed to find an accurate Fourier series for this set of data. Note that for a complete circumference, the first data point at $\theta = 0$ is the same as the last data point at $\theta = 2\pi$. That is, the number of data points used in the numerical integration was 131. However, for convergence checks, only the 130 physical sampling points were considered.

Figure 3.5 shows the errors in the representation of this set of data by the Fourier series deduced using the traditional Fourier decomposition method, namely after one iteration of the proposed iterative Fourier decomposition method. Significant errors are seen to exist, particularly at those sampling points associated with and near the single bigger interval. Figure 3.6 shows the variation of the value of R_{rl} with the number of iterations performed, indicating that after 13 iterations, R_{rl} falls below 10^{-3}. The reduction in errors is rapid in the first few iterations. That is, if the convergence tolerance for this problem is set as 10^{-3}, then 13 iterations are required. The number of iterations required depends on the accuracy expected. For a tolerance of 5×10^{-5}, 23 iterations are required for this problem. Figure 3.7 compares the predictions of the deduced Fourier series after 1, 13 and 23 iterations. It is obvious that the results after 13 iterations are already very accurate, with further iterations leading to little improvement. Figure 3.8 shows the errors in the deuced Fourier series after 13 and 23 iterations: the errors are very small after 13 iterations and are seen to have reduced further after 23 iterations.

The Fourier coefficients a_j and b_j deduced after 1 and 13 iterations are compared in Figures 3.9 and 3.10 respectively, while the differences between the Fourier coefficients after 1 and 13 iterations are shown in Figure 3.11. It appears that the improvement to the Fourier series representation occurred over the whole range of Fourier terms considered. Similar changes in both a_j and b_j resulted from the iterative process.

3.5.2 Example 2

Another set of discrete imperfection data from measurements around a circumference of a cylinder is considered here, which includes 95 physical sampling points (Figure 3.12). Five of the intervals are 14.4° starting from data point 50 and end at data point 55, with all other intervals being 3.2°. The errors in the deduced Fourier series at the sampling points after 1 iteration are quite large over the entire circumference, especially in the vicinity of sampling points with large intervals (Figure 3.13). Using the iterative Fourier decomposition method, convergence can be achieved after 19 iterations with $Tol = 0.001$ and in 30 iterations with $Tol = 5 \times 10^{-5}$. Figure 3.14 shows the variation of R_{rl} with the number of iterations performed, which is similar to that shown in Figure 3.6, showing rapid reductions in errors. Figure 3.15 compares the predictions of the deduced Fourier series after 1, 19 and 30 iterations. It is obvious that the results after 19 iterations are already very accurate, with further iterations leading to little improvement. The errors in the Fourier series at the sampling points after 19 and 30 iterations are shown in Figure 3.16. These errors are very small, with those after 30 iterations being much smaller than those after 19 iterations. Figures 3.17 and 3.18 compare the Fourier coefficients a_j and b_j respectively deduced after one and 19 iterations, while the differences between the Fourier coefficients after 1 and 19 iterations are shown in Figure 3.19. The Fourier coefficients a_j showed more changes than b_j as a result of the iterative process.

3.6 CONCLUSIONS

This chapter has been concerned with the interpretation of discrete imperfection measurements at non-uniformly distributed sampling points by the Fourier decomposition

method. The conventional method of Fourier decomposition has been shown to be inaccurate for such imperfection data. A new iterative Fourier decomposition method which provides an accurate Fourier representation has also been presented. While the work was carried out in the context of interpreting discrete imperfection measurements on shells, the results are generally applicable to the Fourier decomposition of any type of discrete data taken at non-uniformly distributed sampling points. The following conclusions can be drawn based on the results and discussions presented in this chapter:

1. For a set of uniformly-spaced discrete data, the conventional Fourier decomposition method leads to accurate representation of the discrete data only if the number of data points exceeds $2k+1$ if the discrete data are from source functions $A\cos k\theta$ and $B\sin k\theta$;
2. For a set of non-uniformly spaced discrete data, the conventional Fourier decomposition method does not provide an accurate representation of the discrete data even if the number of data points is sufficiently large.
3. An accurate Fourier series can be found for a set of non-uniformly spaced discrete data by an iterative procedure in which the residual errors in the Fourier series at the sampling points are further decomposed into Fourier series.

Table 3.1 Fourier decomposition of discrete data at uniformly distributed sampling points

Case	Number of data points N_s	Abscissas of the data points θ_i	Source function	Non-zero Fourier coefficients a_j, b_j	Deduced function	Errors at the sampling points
1	$N_s = 2k+1-p$ $(1 \le p < k)$	$\theta_i = \dfrac{2(i-1)\pi}{2k-p}$	$A\cos k\theta$	$a_{k-p} = A$ $a_k = A$	* $F_{1a}(\theta) = A\cos(k-p)\theta$	$\Delta_{1a} = A\cos k\theta_i - A\cos(k-p)\theta_i$ $= -2A\sin(i-1)\pi \sin\dfrac{(i-1)p\pi}{2k-p}$ $= 0$
			$B\sin k\theta$	$b_{k-p} = -B$ $b_k = B$	* $F_{1b}(\theta) = -B\sin(k-p)\theta$	$\Delta_{1b} = B\sin k\theta_i + B\sin(k-p)\theta_i$ $= 2B\sin(i-1)\pi\cos\dfrac{(i-1)p\pi}{2k-p}$ $= 0$
2	$N_s = 2k+1$	$\theta_i = \dfrac{(i-1)\pi}{k}$	$A\cos k\theta$	$a_k = 2A$	$F_{2a}(\theta) = 2A\cos k\theta$	$\Delta_{2a} = A\cos k\theta_i - 2A\cos k\theta_i$ $= -A\cos(i-1)\pi = \pm A$
			$B\sin k\theta$	0	$F_{2b}(\theta) = 0$	$\Delta_{2b} = B\sin k\theta_i - 0$ $= B\sin(i-1)\pi = 0$
3	$N_s = 2k+1+p$ $p \ge 1$	$\theta_i = \dfrac{2(i-1)\pi}{2k+p}$	$A\cos k\theta$	$a_k = A$	$F_{3a}(\theta) = A\cos k\theta$	$\Delta_{3a} = 0$
			$B\sin k\theta$	$b_k = B$	$F_{3b}(\theta) = B\sin k\theta$	$\Delta_{3b} = 0$

* These Fourier series are from a numerical procedure where the errors at the sampling points in the deduced Fourier series are checked every time a new Fourier term is included. The Fourier series from exact decomposition are different.

Table 3.2 Fourier decomposition of discrete data at non-uniformly distributed sampling points

Case	Number of data points N_s	Abscissas of the data points θ_i	Source function	Deduced Fourier coefficients a_j, b_j
1	$N_s = 2k+1-p$ $(1 \le p < k)$	$0, \frac{1\cdot 2\pi}{2k-p}, \ldots, \frac{(s-1)\cdot 2\pi}{2k-p}, \frac{s\cdot 2\pi}{2k-p}+\delta, \frac{(s+1)\cdot 2\pi}{2k-p}, \ldots, \frac{(2k-p-1)\cdot 2\pi}{2k-p}, 2\pi$	$A\cos k\theta$	$a_0 = E_1(\delta)$* $a_{k-p} = A + E_2(\delta)$ $a_k = A + E_3(\delta)$ $a_t = E_4(\delta)$, $if\ t \ne k-p, k$ $b_j = E_5(\delta)$
			$B\sin k\theta$	$a_j = E_6(\delta)$ $b_{k-p} = -B + E_7(\delta)$ $b_k = B + E_8(\delta)$ $b_t = E_9(\delta)$, $if\ t \ne k-p, k$
2	$N_s = 2k+1$	$0, \frac{\pi}{k}, \ldots, \frac{(s-1)\cdot\pi}{k}, \frac{s\pi}{k}+\delta, \frac{(s+1)\cdot\pi}{k}, \ldots, \frac{(2k-1)\cdot\pi}{k}, 2\pi$	$A\cos k\theta$	$a_k = 2A + E_{10}(\delta)$ $a_t = E_{11}(\delta)$, $if\ t \ne k$ $b_j = E_{12}(\delta)$
			$B\sin k\theta$	$a_j = E_{13}(\delta)$ $b_j = E_{14}(\delta)$
3	$N_s = 2k+1+p$ $(p \ge 1)$	$0, \frac{1\cdot 2\pi}{2k+p}, \ldots, \frac{(s-1)\cdot 2\pi}{2k+p}, \frac{s\cdot 2\pi}{2k+p}+\delta, \frac{(s+1)\cdot 2\pi}{2k+p}, \ldots, \frac{(2k+p-1)\cdot 2\pi}{2k+p}, 2\pi$	$A\cos k\theta$	$a_k = A + E_{15}(\delta)$ $a_t = E_{16}(\delta)$, $if\ t \ne k$ $b_j = E_{17}(\delta)$
			$B\sin k\theta$	$a_j = E_{18}(\delta)$ $b_k = B + E_{19}(\delta)$ $b_t = E_{20}(\delta)$, $if\ t \ne k$

* Expressions of $E_i(\delta)$ can be found in Appendix 3.2

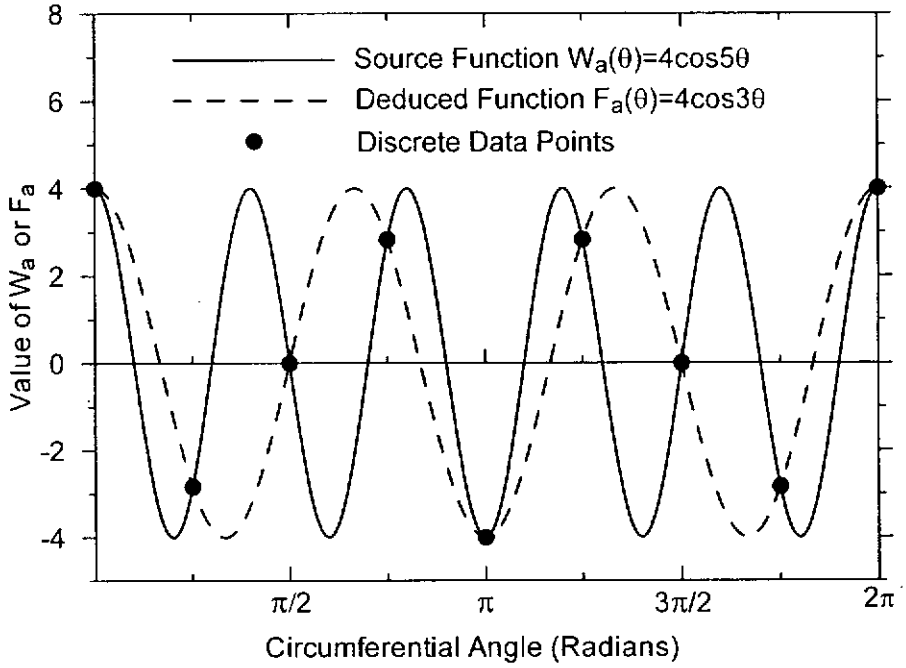

Figure 3.1 Comparison between the source function $W_a(\theta) = 4\cos 5\theta$ and the deduced function $F_a(\theta) = 4\cos 3\theta$ from a set of data points

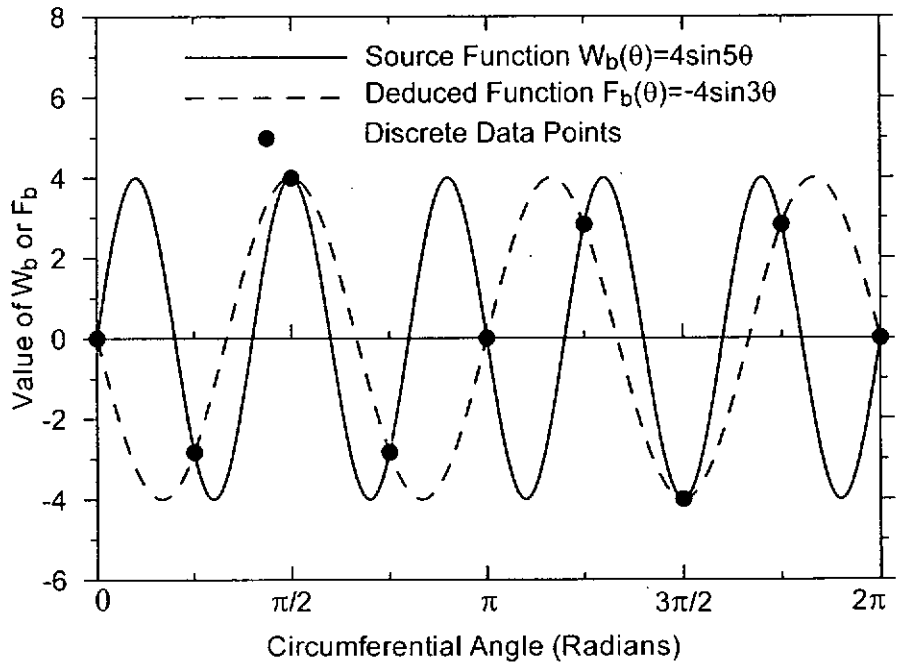

Figure 3.2 Comparison between the source function $W_b(\theta) = 4\sin 5\theta$ and the deduced function $F_b(\theta) = -4\sin 3\theta$ from a set of data points

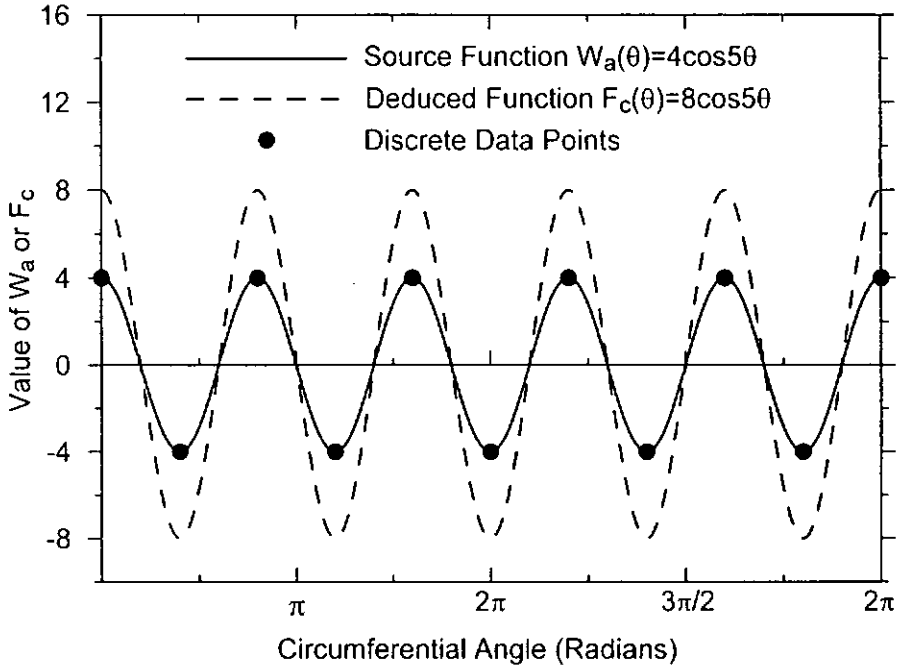

Figure 3.3 Comparison between the source function $W_a(\theta) = 4\cos 5\theta$ and the deduced function $F_c(\theta) = 8\cos 5\theta$ from a set of data points

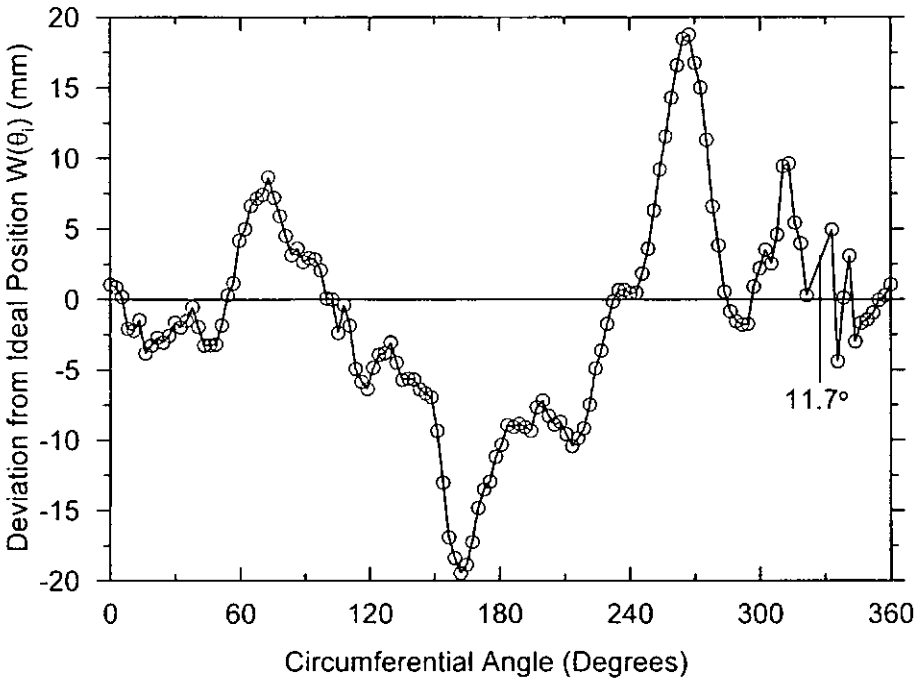

Figure 3.4 Imperfection measurements with one larger interval

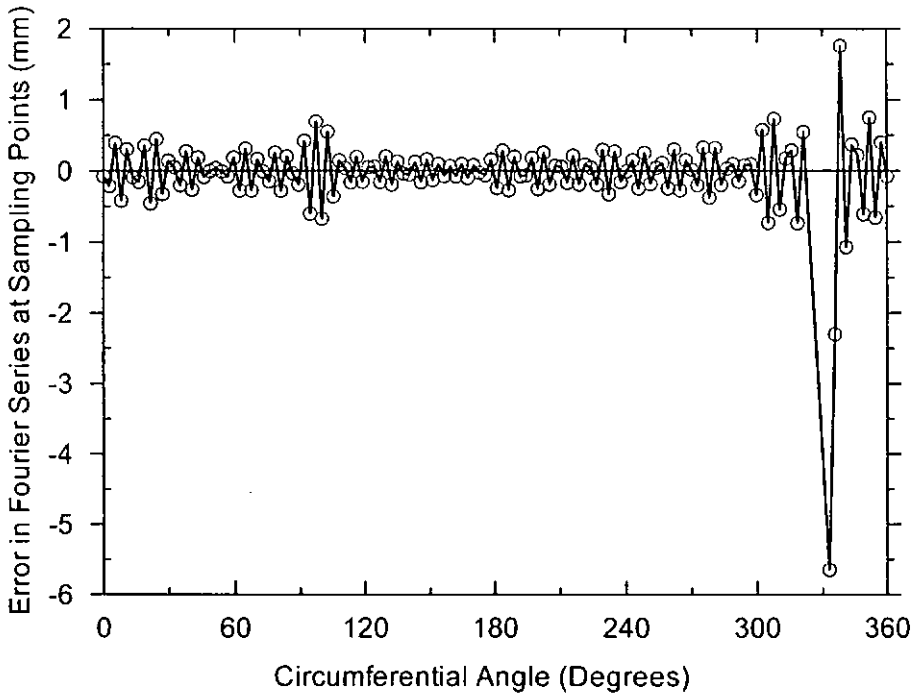

Figure 3.5 Error in Fourier representation at the sampling points after one iteration

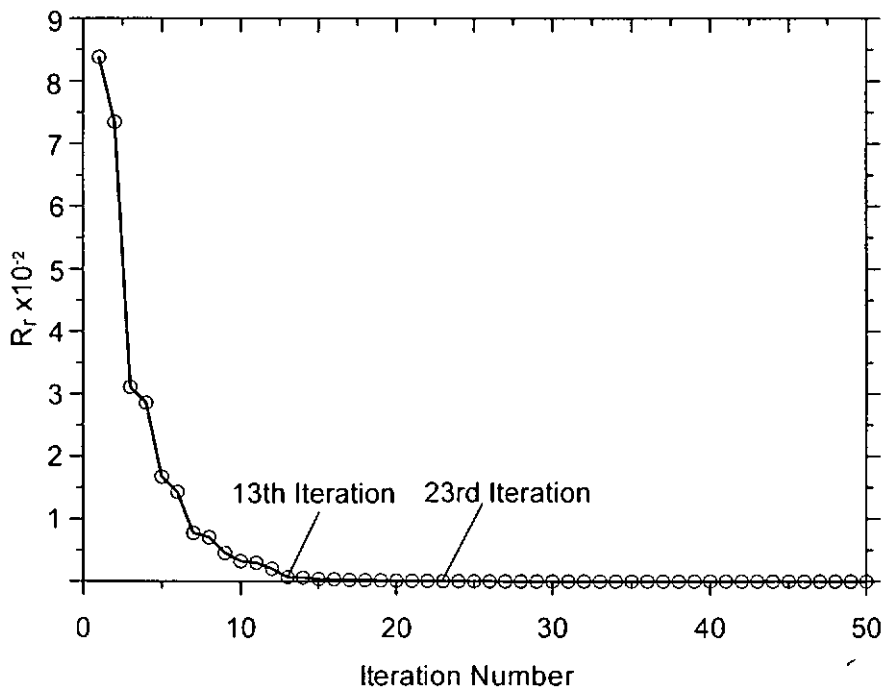

Figure 3.6 Variation of R_r with the iteration number

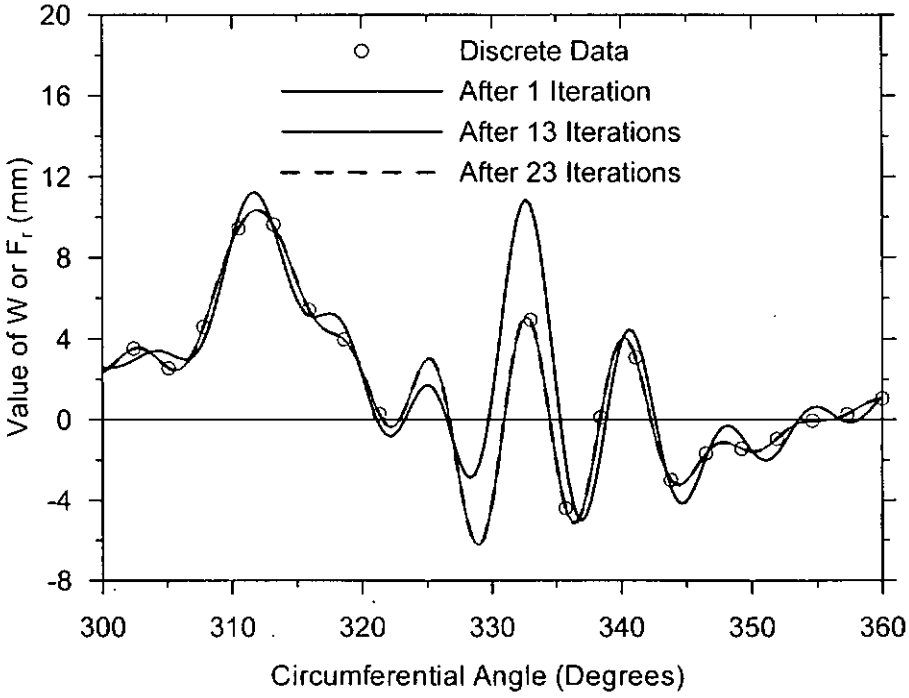

Figure 3.7 Accuracy of Fourier representation in the critical region after 1, 13 and 23 iterations

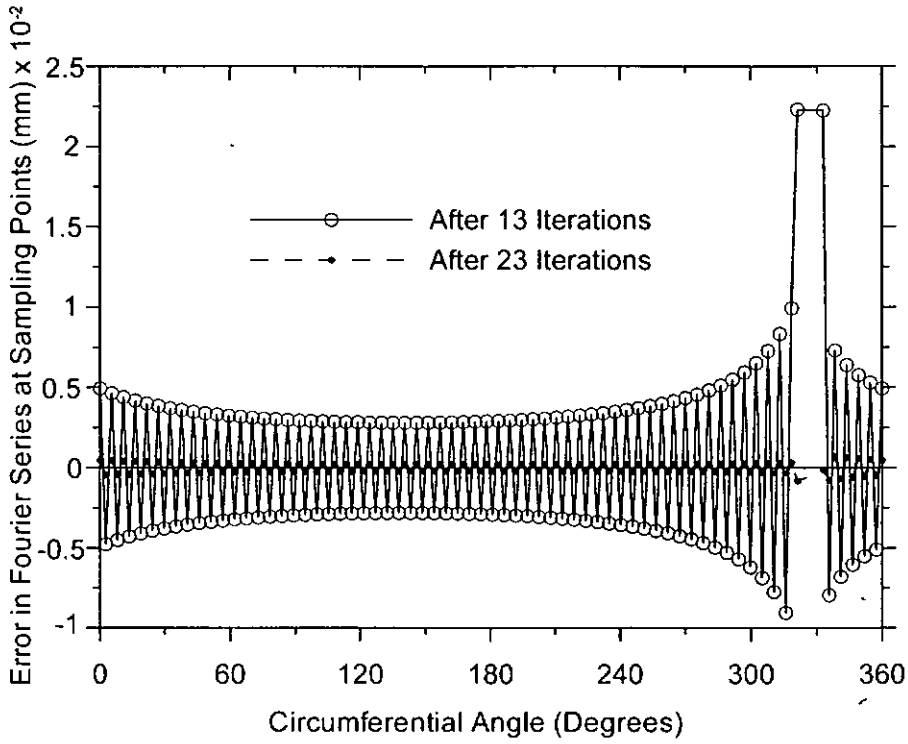

Figure 3.8 Error in Fourier representation at the sampling points after 13 and 23 iterations

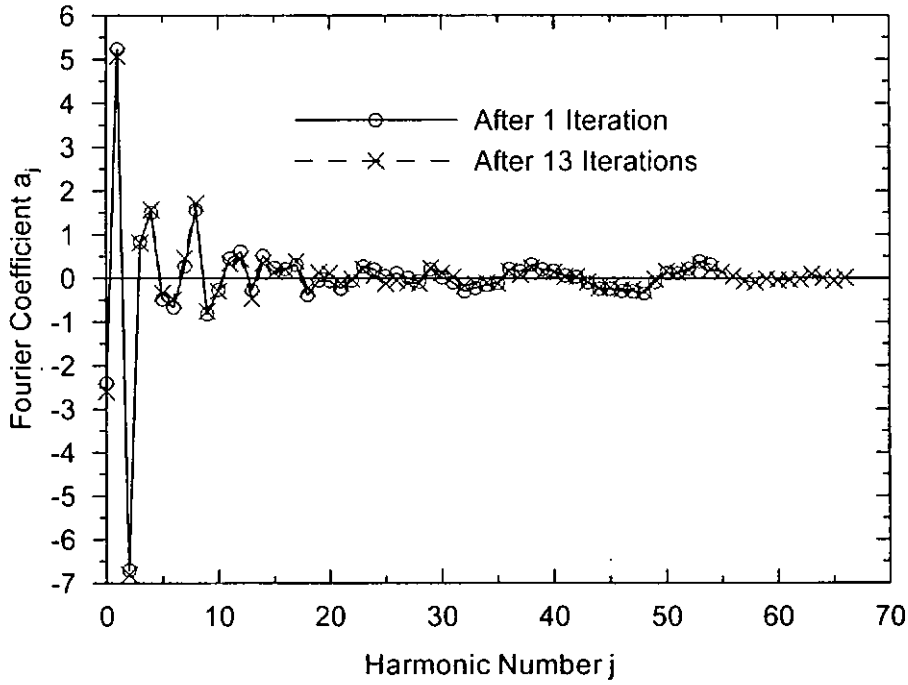

Figure 3.9 Fourier coefficient a_j deduced after 1 and 13 iterations

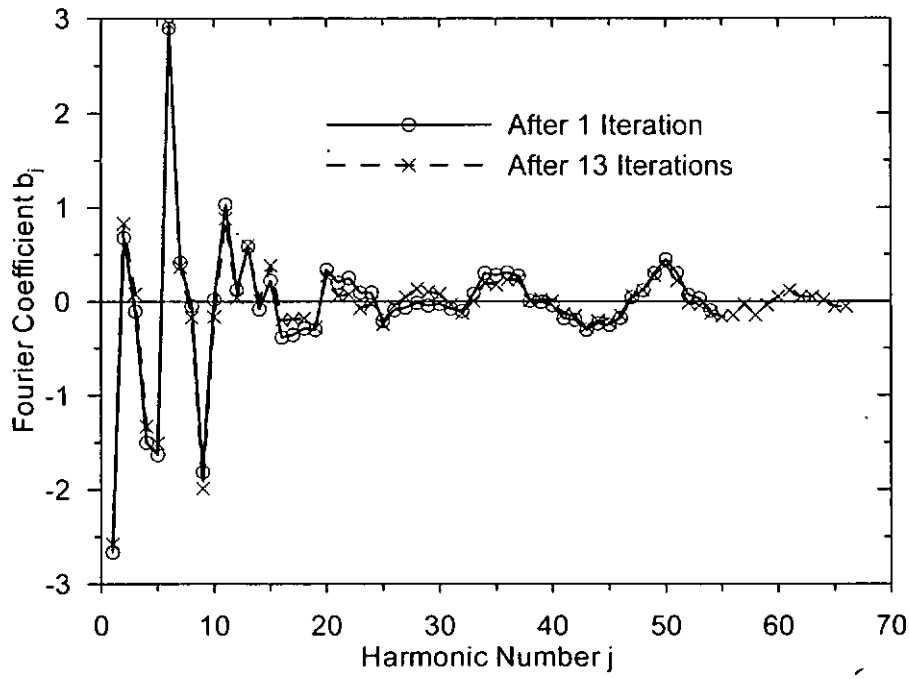

Figure 3.10 Fourier coefficient b_j deduced after 1 and 13 iterations

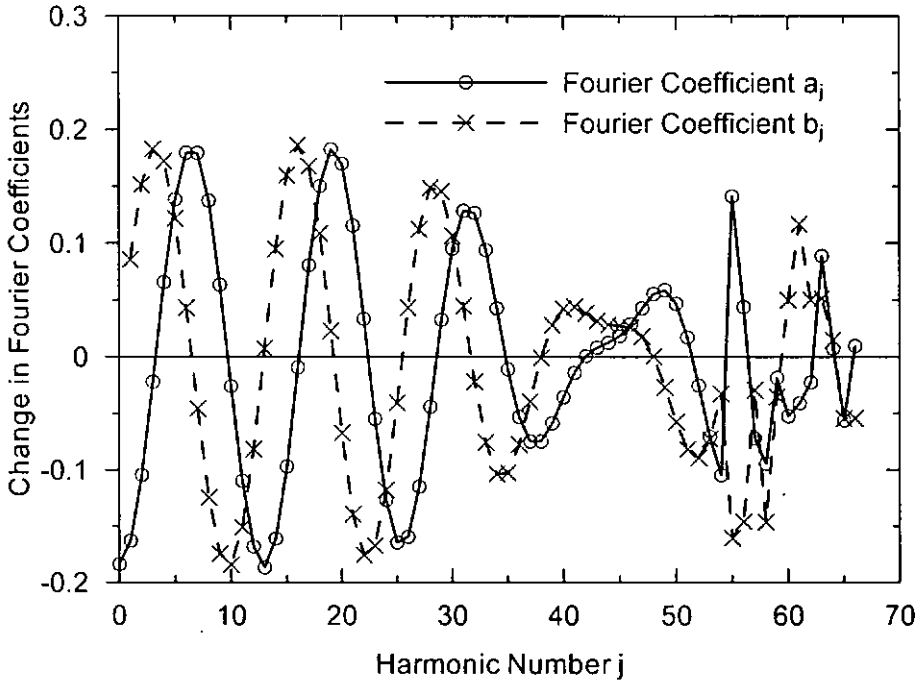

Figure 3.11 Change in the Fourier coefficients a_j and b_j between the 1st and 13th iteration

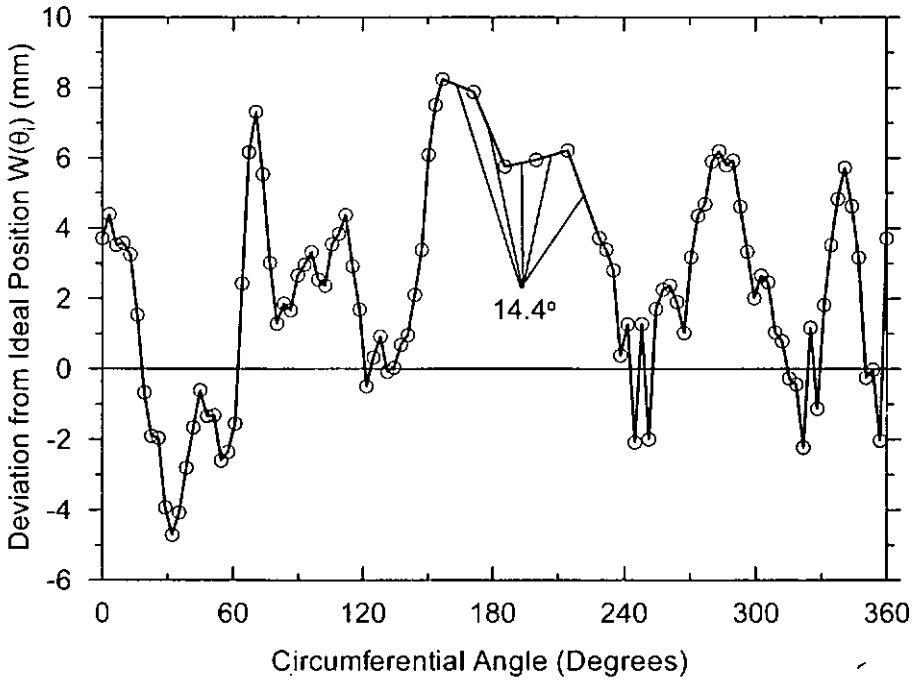

Figure 3.12 Imperfection measurements with five larger intervals

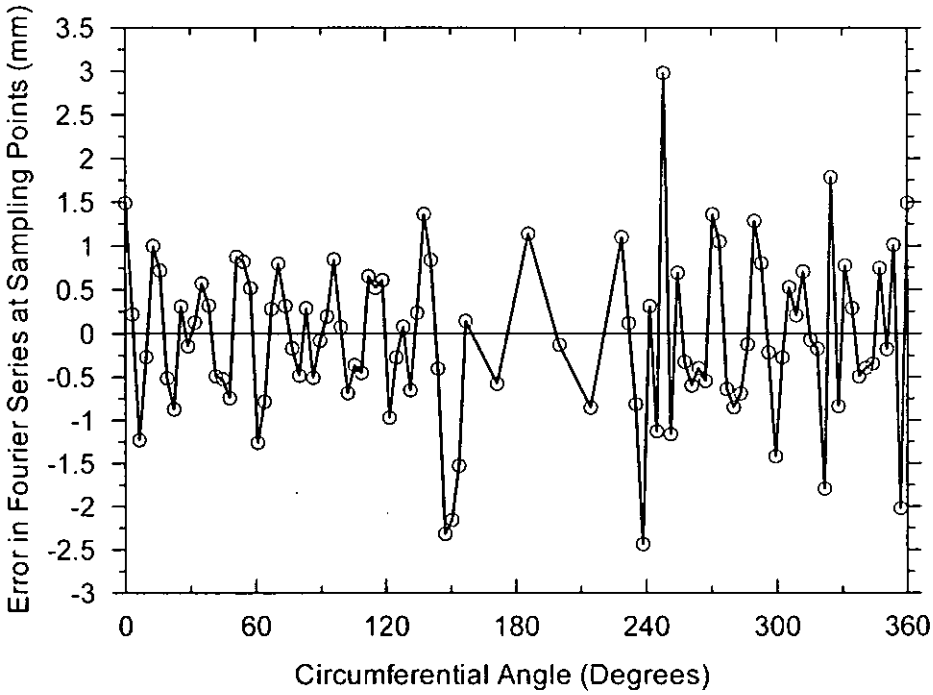

Figure 3.13 Error in the deduced Fourier series at the sampling points after one iteration

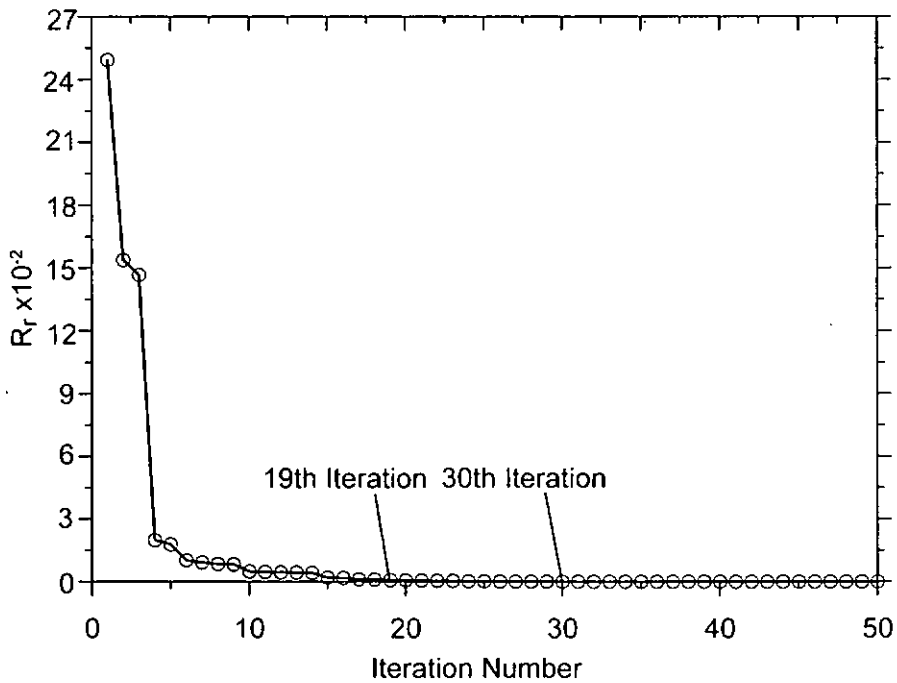

Figure 3.14 Variation of R_r with the iteration number

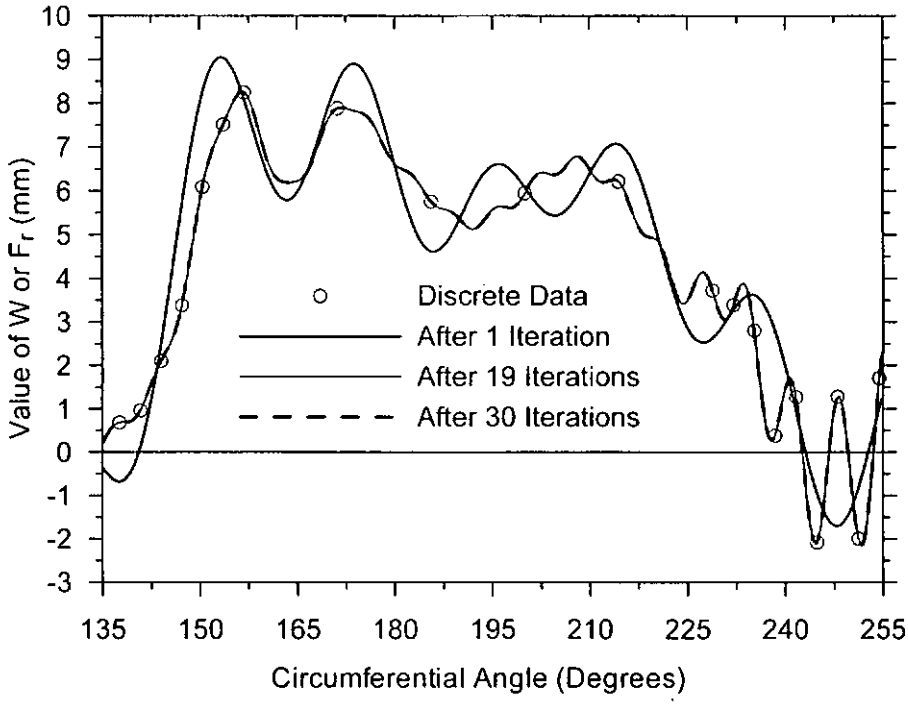

Figure 3.15 Accuracy of Fourier representation in the critical region after 1, 19 and 30 iterations

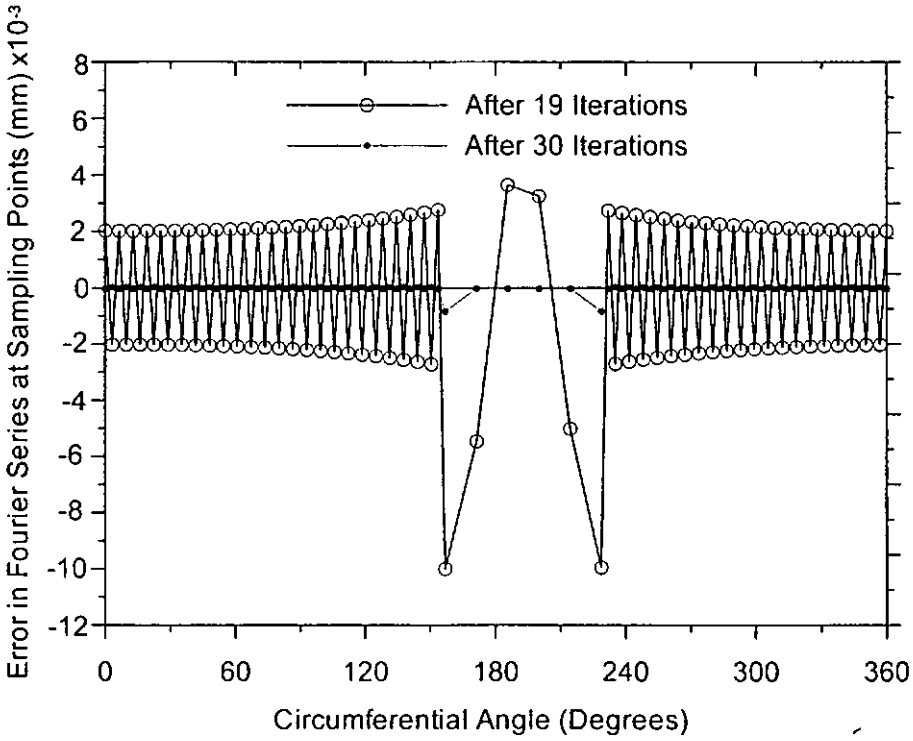

Figure 3.16 Error in the deduced Fourier series at the sampling points after 19 and 30 iterations

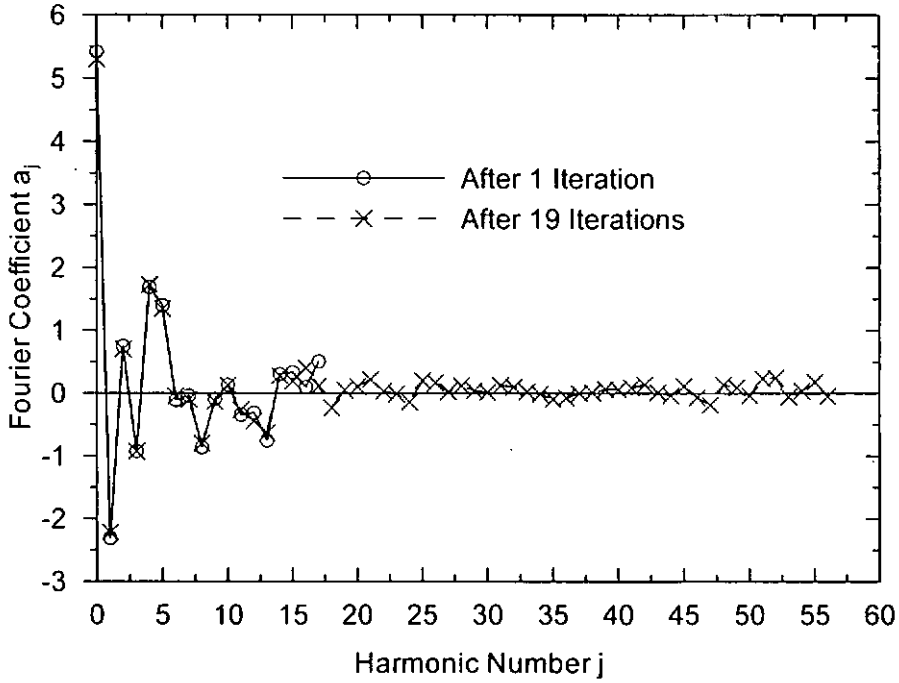

Figure 3.17 Fourier coefficient a_j deduced after 1 and 19 iterations

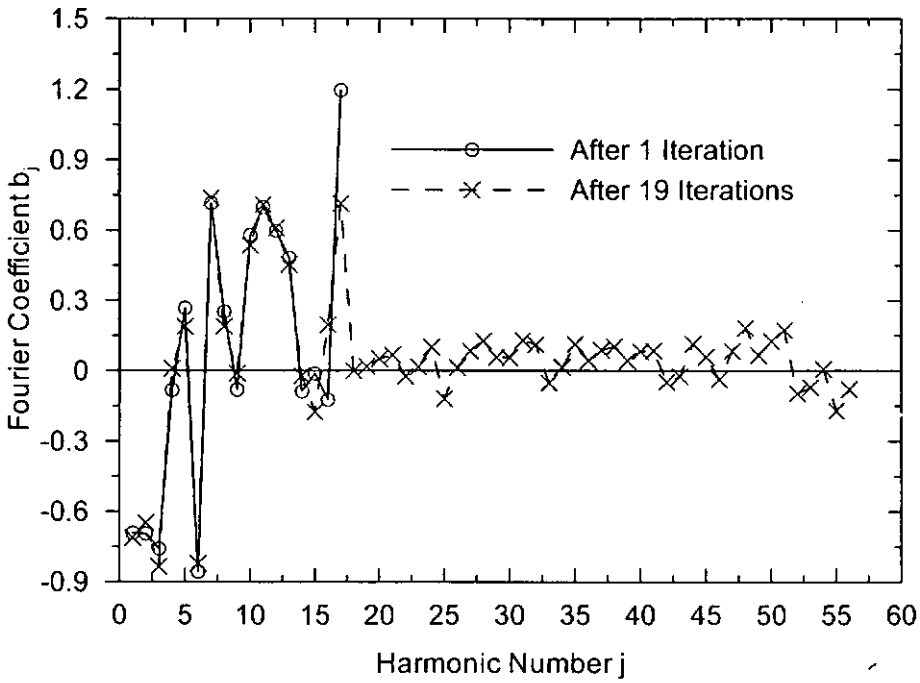

Figure 3.18 Fourier coefficient b_j deduced after 1 and 19 iterations

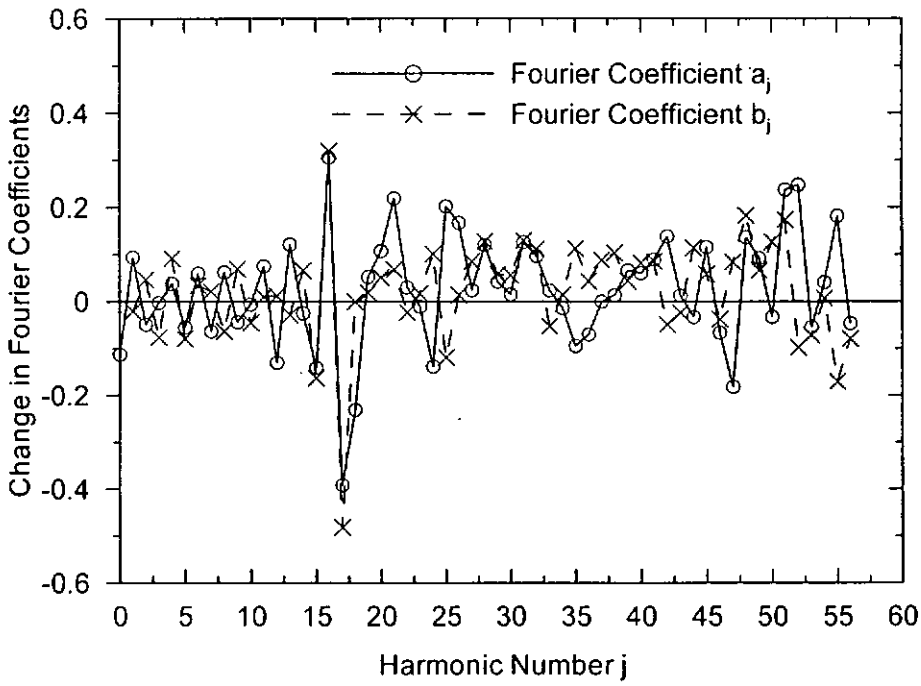

Figure 3.19 Change in the Fourier coefficients a_j and b_j between the 1st and 19th iterations

APPENDICES

A3.1 EXAMPLE DERIVATIONS OF FOURIER COEFFICIENTS

For a set of $2k+1-p$ ($p<k$) discrete data $W_a(\theta_i)$ from the source function $W_a(\theta)=A\cos k\theta$ at uniformly distributed sampling points, the Fourier coefficients a_0 and a_{k-p} can be derived as follows.

$$
\begin{aligned}
a_0 &= \frac{1}{\pi}\sum_{i=1}^{2k-p}\frac{W_a(\theta_i)+W_a(\theta_{i+1})}{2}\Delta\theta_i \\
&= \frac{A}{2k-p}[\cos 0 + 2\cos\frac{2k\pi}{2k-p} + 2\cos\frac{2\cdot 2k\pi}{2k-p} + 2\cos\frac{3\cdot 2k\pi}{2k-p} \\
&\quad + \ldots + 2\cos\frac{(2k-p-1)\cdot 2k\pi}{2k-p} + \cos 2k\pi] \\
&= \frac{A}{2k-p}[2 + \frac{\sin\frac{[2(2k-p-1)+1]k\pi}{2k-p} - \sin\frac{k\pi}{2k-p}}{2\sin\frac{k\pi}{2k-p}}] = 0
\end{aligned}
$$

and

$$
\begin{aligned}
a_{k-p} &= \frac{1}{\pi}\sum_{i=1}^{2k-p}\frac{W_a(\theta_i)\cos(k-p)\theta_i + W_a(\theta_{i+1})\cos(k-p)\theta_{i+1}}{2}\Delta\theta_i \\
&= \frac{A}{2k-p}[\cos^2 0 + 2\cos\frac{2k\pi}{2k-p}\cos\frac{2(k-p)\pi}{2k-p} + 2\cos\frac{2\cdot 2k\pi}{2k-p}\cos\frac{2\cdot 2(k-p)\pi}{2k-p} + \ldots \\
&\quad + 2\cos\frac{(2k-p-1)\cdot 2k\pi}{2k-p}\cos\frac{(2k-p-1)\cdot 2(k-p)\pi}{2k-p} + \cos 2k\pi\cos 2(k-p)\pi]
\end{aligned}
$$

$$= \frac{A}{2k-p}[2+(2k-p-1)+\frac{\sin\frac{[2(2k-p-1)+1]\cdot k\pi}{2k-p}-\sin\frac{k\pi}{2k-p}}{2\sin\frac{k\pi}{2k-p}}] = A$$

For a set of $2k+1-p$ ($p<k$) discrete data $W_a(\theta_i)$ at non-uniformly distributed sampling points from the source function $W_a(\theta) = A\cos k\theta$, the derivation of the Fourier coefficients differs slightly from that shown above. As an example,

$$a_0 \approx \frac{1}{\pi}\sum_{i=1}^{2k-p}\frac{W_a(\theta_i)+W_a(\theta_{i+1})}{2}\Delta\theta_i$$

$$= \frac{A}{2\pi}\{(\cos 0+\cos k\theta_1)\frac{2\pi}{2k-p}+(\cos k\theta_1+\cos k\theta_2)\frac{2\pi}{2k-p}+\ldots$$

$$+[\cos k\theta_{s-1}+\cos k(\theta_s+\delta)](\frac{2\pi}{2k-p}+\delta)+[\cos k(\theta_s+\delta)+\cos k\theta_{s+1}](\frac{2\pi}{2k-p}-\delta)$$

$$+(\cos k\theta_{s+1}+\cos k\theta_{s+2})\frac{2\pi}{2k-p}+\ldots+(\cos k\theta_{2k-p}+\cos 2k\pi)\frac{2\pi}{2k-p}\}$$

$$= \frac{A}{2\pi}\{(\cos 0+2\cos k\theta_1+2\cos k\theta_2+\ldots+2\cos k\theta_{s-1}+2\cos k\theta_s$$

$$+2\cos k\theta_{s+1}+\ldots+2\cos k\theta_{2k-p}+\cos 2k\pi)\frac{2\pi}{2k-p}$$

$$+(\cos k\theta_{s-1}-\cos k\theta_{s+1})\delta+2[\cos k(\theta_s+\delta)-\cos k\theta_s]\frac{2\pi}{2k-p}\}$$

$$= \frac{A\delta}{\pi}\sin\frac{2ks\pi}{2k-p}\sin\frac{2k\pi}{2k-p}-\frac{4A}{2k-p}\sin k(\frac{2s\pi}{2k-p}+\frac{\delta}{2})\sin\frac{k\delta}{2} = E_1(\delta)\neq 0$$

A3.2 EXPRESSIONS OF $E_i(\delta)$ (i = 1-20)

The following functions are used in this paper:

$$E_1(\delta)=\frac{A\delta}{\pi}\sin\frac{2ks\pi}{2k-p}\sin\frac{2k\pi}{2k-p}-\frac{4A}{2k-p}\sin k(\frac{2s\pi}{2k-p}+\frac{\delta}{2})\sin\frac{k\delta}{2}$$

$$E_2(\delta)=\frac{A\delta}{2\pi}\sin\frac{2ps\pi}{2k-p}\sin\frac{2p\pi}{2k-p}-\frac{2A}{2k-p}[\sin^2\frac{(2k-p)\delta}{2}+\sin(\frac{2ps\pi}{2k-p}+\frac{p\delta}{2})\sin\frac{p\delta}{2}]$$

$$E_3(\delta)=\frac{A\delta}{2\pi}\sin\frac{2ks\pi}{2k-p}\sin\frac{2k\pi}{2k-p}-\frac{2A}{2k-p}\sin(\frac{4ks\pi}{2k-p}+k\delta)\sin k\delta$$

$$E_4(\delta)=\frac{A\delta}{2\pi}[\sin\frac{2(k+t)s\pi}{2k-p}\sin\frac{2(k+t)\pi}{2k-p}+\sin\frac{2(k-t)s\pi}{2k-p}\sin\frac{2(k-t)\pi}{2k-p}]$$
$$-\frac{2A}{2k-p}[\sin(k+t)(\frac{2s\pi}{2k-p}+\frac{\delta}{2})\sin\frac{(k+t)\delta}{2}+\sin(k-t)(\frac{2s\pi}{2k-p}+\frac{\delta}{2})\sin\frac{(k-t)\delta}{2}]$$

$$E_5(\delta)=-\frac{A\delta}{2\pi}[\cos\frac{2(k+j)s\pi}{2k-p}\sin\frac{2(k+j)\pi}{2k-p}-\cos\frac{2(k-j)s\pi}{2k-p}\sin\frac{2(k-j)\pi}{2k-p}]$$
$$+\frac{2A}{2k-p}[\cos(k+j)(\frac{2s\pi}{2k-p}+\frac{\delta}{2})\sin\frac{(k+j)\delta}{2}-\cos(k-j)(\frac{2s\pi}{2k-p}+\frac{\delta}{2})\sin\frac{(k-j)\delta}{2}]$$

$$E_6(\delta)=-\frac{B\delta}{2\pi}[\cos\frac{2(k+j)s\pi}{2k-p}\sin\frac{2(k+j)\pi}{2k-p}+\cos\frac{2(k-j)s\pi}{2k-p}\sin\frac{2(k-j)\pi}{2k-p}]$$
$$+\frac{2B}{2k-p}[\cos(k+j)(\frac{2s\pi}{2k-p}+\frac{\delta}{2})\sin\frac{(k+j)\delta}{2}$$
$$+\cos(k-j)(\frac{2s\pi}{2k-p}+\frac{\delta}{2})\sin\frac{(k-j)\delta}{2}]$$

$$E_7(\delta)=\frac{B\delta}{2\pi}\sin\frac{2ps\pi}{2k-p}\sin\frac{2p\pi}{2k-p}+\frac{2B}{2k-p}[\sin^2\frac{(2k-p)\delta}{2}-\sin(\frac{2ps\pi}{2k-p}+\frac{p\delta}{2})\sin\frac{p\delta}{2}]$$

$$E_8(\delta)=-\frac{B\delta}{\pi}\sin\frac{4ks\pi}{2k-p}\sin\frac{4k\pi}{2k-p}+\frac{2B}{2k-p}\sin(\frac{4ks\pi}{2k-p}+k\delta)\sin k\delta$$

$$E_9(\delta) = -\frac{B\delta}{2\pi}[\sin\frac{2(k+t)s\pi}{2k-p}\sin\frac{2(k+t)\pi}{2k-p} - \sin\frac{2(k-t)s\pi}{2k-p}\sin\frac{2(k-t)\pi}{2k-p}]$$
$$+\frac{2B}{2k-p}[\sin(k+t)(\frac{2s\pi}{2k-p}+\frac{\delta}{2})\sin\frac{(k+t)\delta}{2}$$
$$-\sin(k-t)(\frac{2s\pi}{2k-p}+\frac{\delta}{2})\sin\frac{(k-t)\delta}{2}]$$

$$E_{10}(\delta) = -\frac{A}{k}\sin^2 k\delta$$

$$E_{11}(\delta) = \frac{A\delta}{2\pi}[\sin\frac{(k+t)s\pi}{k}\sin\frac{(k+t)\pi}{k} + \sin\frac{(k-t)s\pi}{k}\sin\frac{(k-t)\pi}{k}]$$
$$-\frac{A}{k}[\sin(k+t)(\frac{s\pi}{k}+\frac{\delta}{2})\sin\frac{(k+t)\delta}{2} + \sin(k-t)(\frac{s\pi}{k}+\frac{\delta}{2})\sin\frac{(k-t)\delta}{2}]$$

$$E_{12}(\delta) = \frac{A\delta}{2\pi}[\sin\frac{(k+j)s\pi}{k}\cos\frac{(k+j)\pi}{k} - \sin\frac{(k-j)s\pi}{k}\cos\frac{(k-j)\pi}{k}]$$
$$-\frac{A}{k}[\cos(k+j)(\frac{s\pi}{k}+\frac{\delta}{2})\sin\frac{(k+j)\delta}{2} - \cos(k-j)(\frac{s\pi}{k}+\frac{\delta}{2})\sin\frac{(k-j)\delta}{2}]$$

$$E_{13}(\delta) = -\frac{B\delta}{2\pi}[\cos\frac{(k+j)s\pi}{k}\sin\frac{(k+j)\pi}{k} + \cos\frac{(k-j)s\pi}{k}\sin\frac{(k-j)\pi}{k}]$$
$$+\frac{B}{k}[\cos(k+j)(\frac{s\pi}{k}+\frac{\delta}{2})\sin\frac{(k+j)\delta}{2} + \cos(k-j)(\frac{s\pi}{k}+\frac{\delta}{2})\sin\frac{(k-j)\delta}{2}]$$

$$E_{14}(\delta) = -\frac{B\delta}{2\pi}[\sin\frac{(k+t)s\pi}{k}\sin\frac{(k+t)\pi}{k} - \sin\frac{(k-t)s\pi}{k}\sin\frac{(k-t)\pi}{k}]$$
$$+\frac{B}{k}[\sin(k+t)(\frac{s\pi}{k}+\frac{\delta}{2})\sin\frac{(k+t)\delta}{2} - \sin(k-t)(\frac{s\pi}{k}+\frac{\delta}{2})\sin\frac{(k-t)\delta}{2}]$$

$$E_{15}(\delta) = \frac{A\delta}{2\pi}\sin\frac{4ks\pi}{2k+p}\sin\frac{4k\pi}{2k+p} - \frac{2A}{2k+p}\sin(\frac{4ks\pi}{2k+p}+k\delta)\sin k\delta$$

$$E_{16}(\delta) = \frac{A\delta}{2\pi}[\sin\frac{2(k+t)s\pi}{2k+p}\sin\frac{2(k+t)\pi}{2k+p} + \sin\frac{2(k-t)s\pi}{2k+p}\sin\frac{2(k-t)\pi}{2k+p}]$$
$$-\frac{2A}{2k+p}[\sin(k+t)(\frac{2s\pi}{2k+p}+\frac{\delta}{2})\sin\frac{(k+t)\delta}{2}$$
$$+\sin(k-t)(\frac{2s\pi}{2k+p}+\frac{\delta}{2})\sin\frac{(k-t)\delta}{2}]$$

$$E_{17}(\delta) = -\frac{A\delta}{2\pi}[\cos\frac{2(k+j)s\pi}{2k+p}\sin\frac{2(k+j)\pi}{2k+p} - \cos\frac{2(k-j)s\pi}{2k+p}\sin\frac{2(k-j)\pi}{2k+p}]$$
$$+\frac{2A}{2k+p}[\cos(k+j)(\frac{2s\pi}{2k+p}+\frac{\delta}{2})\sin\frac{(k+j)\delta}{2}$$
$$-\cos(k-j)(\frac{2s\pi}{2k+p}+\frac{\delta}{2})\sin\frac{(k-j)\delta}{2}]$$

$$E_{18}(\delta) = -\frac{B\delta}{2\pi}[\cos\frac{2(k+j)s\pi}{2k+p}\sin\frac{2(k+j)\pi}{2k+p} + \cos\frac{2(k-j)s\pi}{2k+p}\sin\frac{2(k-j)\pi}{2k+p}]$$
$$+\frac{2B}{2k+p}[\cos(k+j)(\frac{2s\pi}{2k+p}+\frac{\delta}{2})\sin\frac{(k+j)\delta}{2}$$
$$+\cos(k-j)(\frac{2s\pi}{2k+p}+\frac{\delta}{2})\sin\frac{(k-j)\delta}{2}]$$

$$E_{19}(\delta) = -\frac{B\delta}{2\pi}\sin\frac{4ks\pi}{2k+p}\sin\frac{4k\pi}{2k+p} + \frac{2B}{2k+p}\sin(\frac{4ks\pi}{2k+p}+k\delta)\sin k\delta$$

$$E_{20}(\delta) = -\frac{B\delta}{2\pi}[\sin\frac{2(k+t)s\pi}{2k+p}\sin\frac{2(k+t)\pi}{2k+p} - \sin\frac{2(k-t)s\pi}{2k+p}\sin\frac{2(k-t)\pi}{2k+p}]$$
$$+\frac{2B}{2k+p}[\sin(k+t)(\frac{2s\pi}{2k+p}+\frac{\delta}{2})\sin\frac{(k+t)\delta}{2}$$
$$-\sin(k-t)(\frac{2s\pi}{2k+p}+\frac{\delta}{2})\sin\frac{(k-t)\delta}{2}]$$

CHAPTER 4

ANALYSIS OF GEOMETRIC IMPERFECTIONS IN LARGE EXTENSIVELY WELDED STEEL CYLINDERS

4.1 INTRODUCTION

Metal silos are the chief means of storing granular products in many industries. Because the cost effectiveness increases as the silo capacity rises, many large metal silos, often exceeding 5,000 tonnes in capacity, are built to meet the increasing demands of modern industries all over the world. Of these structures, the 10,000 tonne steel silos at Port Kembla in New South Wales, Australia, may still be the largest column-supported silos in the world. When such large silos are constructed, the most common procedure is as follows. A large number of steel panels are rolled to a given curvature and then joined by vertical welds along their straight edges to form a strake (or course). These strakes are then stacked to construct a complete silo wall, each joined to the next by a continuous circumferential weld. The positions of the short vertical (meridional) welds are usually offset circumferentially from those of the adjacent strake by half a panel width, producing a brickwork-patterned silo wall (Figure 4.1).

Because rolling and welding are widely used in this silo construction procedure, a unique and rather well-defined set of geometric imperfections is produced in the silo wall. These fabrication-associated geometric imperfections are believed (Bornscheuer and Hafner, 1983; Rotter, 1985e, 1988, 1996, 2003; Rotter and Teng, 1989) to have a seriously detrimental effect on the buckling behavior of an axially compressed cylindrical shell, such as is found in a steel silo. It is therefore essential to study the effect of these imperfections with care.

Although there have been many studies into the effect of different forms of geometric imperfections on the axial compression buckling strength of cylindrical shells (Yamaki, 1984; Rotter, 2003), none of them has related directly to the 2D geometric imperfection pattern on the complete surface of a steel silo built in the common manner described above. Most previous work on the effect of imperfections on the buckling strength of metal shells was concerned either with imperfection forms found in aeronautical shells (e.g. Arbocz and Babcock, 1969; Singer *et al.* 1971; Arbocz and Williams, 1977; Arbocz, 1982, 1983; Singer, 1982b; Arbocz and Hol, 1991) or with those found in offshore structures or composite shells (e.g. Chryssanthopoulos and Poggi, 1995; Esong *et al.* 1998). The imperfections in these other types of shell are believed to be significantly different from those in the shells of metal silos and tanks because of the differences in the fabrication processes used. The only known work on 2D imperfection analysis of metal silos was carried out by Ding (1992) who studied the imperfections of shell sectors that he measured (Ding et al, 1991, 1996a and b; Coleman et al, 1992, Rotter et al, 1992) in the Port Kembla silos mentioned above. However, Ding's analysis of his measured imperfections unfortunately suffers from certain problems including the use of the same assumptions that had been used in many earlier studies, which can now be seen to be incomplete because these assumptions led to the adoption of a Fourier series that was too restricted. This shortcoming makes it desirable to study Ding's measurements of the imperfections in the Port Kembla silos again, to obtain a better understanding of both the characteristic components of imperfections in such silos and the relationship between the imperfection components and the fabrication process. It is also very necessary to perform a more careful Fourier analysis to determine the effect of these imperfection components on the buckling behaviour and strength of silo walls under axial compression.

The imperfection measurements made on three of the Port Kembla silos (Ding, 1992) were kindly made available to the author by Dr X.L. Ding and Prof. J.M. Rotter and are here used as the source data. The most effective tool for interpreting geometric imperfections in shells is currently a 2D Fourier series, so Fourier decompositions are employed to analyze these measured imperfections. Prior to the imperfection analyses themselves, the mathematical basis of Fourier series representations of different forms imperfections are examined. The performance of various forms of Fourier series in representing different forms of geometric imperfections is then discussed. This issue has received little previous attention, and is one of the reasons why this new study has been undertaken. Conclusions

are then drawn on the appropriate Fourier series that should be used to represent imperfections of a general form found in real structures or in laboratory models.

To explore the effectiveness of various Fourier series in representing different forms of imperfections, a short assessment is given of existing work on Fourier representations of imperfections in cylindrical shells, in which the use of inappropriate Fourier series and the consequences of these inappropriate choices are highlighted.

The geometric imperfections measured by Ding on three large steel silos at Port Kembla, Australia (Ding, 1992) are next analyzed using 2D Fourier decomposition. The "best-fit-cylinder" process is employed to deduce the real (or net) imperfections from the original imperfection data which are referred to as nominal imperfections. As imperfection data are not available for some parts of the complete silo surface due to obstructions that made them inaccessible to the measurement system, these zones are treated as measurement gaps and denoted Gap I, Gap II, and Gap III in Figures 4.9(a), 4.9(b), and 4.9(c). The measurement gaps lead to major differences in sampling spacings around the silo circumference. To enhance the accuracy of Fourier decomposition as well as to reduce the deviations of the deduced Fourier series in these gap zones from the overall trend of the imperfection distributions, additional conjectured sampled data were added in these zones to assist the Fourier decomposition. These extra conjectured points were obtained by a linear interpolation between the imperfection values at the two facing ends of the unsurveyed zone. In what follows, the effect of this linear interpolation on the main Fourier components is shown to be small.

Even with the use of these extra conjectured sampling points, the spacing of sampling points is non-uniform. As a result, Fourier decompositions of the imperfections were conducted using the iterative method presented in Chapter 3, because the traditional Fourier decomposition method cannot produce accurate results. Both 1D decompositions using both a 1D Fourier series and 2D decompositions using a double Fourier series are presented. The results of the Fourier decompositions are interpreted to identify the relationships between the main Fourier components and the fabrication method.

4.2 PERFORMANCE OF FOURIER SERIES IN IMPERFECTION REPRESENTATIONS

When analyzing geometric imperfections in shells, it is essential to choose a suitable Fourier series that can describe the geometric imperfections both in the interior and near the edges of the shell, as otherwise the imperfections cannot be accurately interpreted. As the imperfections in the interior of shells are generally smooth, they can generally be described well with a smooth Fourier series. The problem of Fourier representations is usually found near the edges of the shell, so this is a question that deserves clarification.

The measured imperfections are generally available over an interval or region, which is referred to herein as the definition interval of the imperfections. Let us consider a one-dimensional case with the imperfections (or imperfection function) being defined over the interval of $0 \le x \le L$ and assume that the values of imperfections at the two edges are w_{se} and w_{te}, respectively. For different values of w_{se} and w_{te}, the imperfections in this region may be classed into five cases (Figure 4.2):

(a) $w_{se} = w_{te} \neq 0$;

(b) $w_{se} = w_{te} = 0$;

(c) $w_{se} \neq w_{te}$, $w_{se} \neq 0$, $w_{te} \neq 0$;

(d) $w_{se} = 0$, $w_{te} \neq 0$; and

(e) $w_{se} \neq 0$, $w_{te} = 0$.

In representing these imperfections using Fourier series which are periodic trigonometric series, it is first necessary to decide whether the fundamental period of the Fourier series shall be L or $2L$. If the adopted Fourier series has a fundamental period of L, then the wavelength of the fundamental period is L, so the definition interval is equal to the full wavelength. Such a Fourier series is referred to as a full-wave (FW) series. Alternatively, if $2L$ is the fundamental period of the deduced Fourier series, then such a Fourier series is referred to as a half-wave (HW) series as the definition interval is equal to half the wavelength of the fundamental period.

If the full-wave option is adopted, then all five forms of imperfections shown in Figure 4.2 can be represented by a FW Fourier series which in general includes both a sine and a cosine term for each harmonic number as the imperfection function is generally neither symmetric nor anti-symmetric about the mid-interval point. Such a FW series is referred to as a full-wave general (FWG) series, to differentiate it from a full-wave sine (FWS) series containing sine terms only or a full-wave cosine (FWC) series containing cosine terms only. The deduced Fourier series represents a periodic function which is a simple periodic extension to the entire x axis of the original function over the definition interval of $0 \le x \le L$. This periodic extension of the original imperfection function leads to periodic discontinuities of the extended source function unless the two edge values of the imperfection function are identical, and hence inaccuracies in the Fourier representation near the edges. Of the five imperfection forms shown in Figure 4.2, the FW representation is only suitable for cases (a) and (b) (Figure 4.3).

In cases (c), (d), and (e), as the imperfection takes different values at the two edges of the definition region, to avoid discontinuities in the periodically extended source function, it is necessary to extend the data to the interval $-L \le x < 0$ so that a source function with the period of $2L$ is obtained and can subsequently be represented by a Fourier series with a fundamental period of $2L$. This procedure is referred to as "Half-Range Expansion" in the mathematical literature (Kreyszig, 1999). The imperfection function may either be extended as an even periodic function with a period of $P = 2L$ (Figures 4.4-4.6), which can be represented by a half-wave Fourier cosine (HWC) series, or it may be extended as an odd periodic function with a period of $P = 2L$ (Figures 4.4-4.6), which can be represented by a half-wave Fourier sine (HWS) series. It is important to note that the periodic function from an even extension is continuous in the value of imperfection for all five cases defined in Figure 4.2, but that from an odd extension features significant periodic jumps including those at the edges (or one of the edges) of the definition interval of $0 \le x \le L$, except when the edge values are both zero [case (b) of Figure 4.2]. As a result, except for case (b), the imperfections near one or both edges of the definition interval $0 \le x \le L$ cannot be closely represented. This leaves the HWC series as the only logical choice for the case of imperfections with different edges values. Case (b) is the only case which can be represented by a HWS series, though this case can be well represented by a FWG series.

In summary, the HWC series is a versatile series, as it can be applied to imperfections either with the same value at both ends or to those with different values at the two ends, because the imperfections. Half-wave general (HWG) series in the form of half-wave cosine series plus half-wave sine series should not be used for imperfection representations, because this implies an arbitrary extension of the imperfection function from the definition interval to the interval $-L \leq x < 0$. Such an arbitrary extension leads to unnecessary complication as an even (or odd if suitable) extension is much simpler.

Many numerical studies have shown that a large number of Fourier terms are needed to reduce the errors of a Fourier series representation. Even though the coefficients of higher terms of the series may individually be small when compared with those of lower terms, these higher terms play an important role. The number of Fourier terms, N_f, that can be adopted in the Fourier expansion is related to the number of sampling points, N_s, if the errors in the representation are to be minimized. The relationship between N_f and N_s, and the applicability of various different series, are summarized in Table 4.1. It shows that the total number of Fourier terms needed for either a HWC series or a HWS series is roughly equal to that of a FWG series, although the highest harmonic number used in the latter is roughly half that used in the former. Some negative comments have been made on the performance of HWC series (Rotter *et al*, 1992; Coleman *et al*, 1992). However, these only arise because the authors used an inadequate number of terms in their HWC series, leading to a poor representation of the complete imperfection pattern. In what follows, it is shown that HWC representations can capture all the necessary features of all forms of imperfection.

4.3 COMMENTS ON FORMS OF FOURIER SERIES USED IN PREVIOUS STUDIES

The imperfections in cylindrical shells inevitably have some non-zero, and usually have different values, at the two ends of the cylinder. This arises because the two ends cannot be perfectly circular, so there must be some non-zero values of imperfection at each end. Even where experimental models are fabricated with meticulous care, non-zero and different end values of imperfections always arise, though their values may be relatively

small. But real constructed shells have much larger imperfections at their ends, and the values are invariably different. This has been reported in many 3D plots of shell surfaces (e.g. Arbocz and Babcock, 1969; Singer *et al.* 1971; Arbocz and Williams, 1977; Arbocz, 1982, 1983; Singer 1982a; Arbocz and Hol, 1991; Chryssanthopoulos and Poggi, 1995; Cederbaum and Arbocz, 1996; Esong *et al.* 1998). When these imperfections are interpreted along each shell meridian, HWG and HWS series are inapplicable, because the coefficients of the former are very difficult to deduce while the latter have zero end values, and FWG series are inapplicable because it has the same end values. The only appropriate Fourier series for these forms of imperfections is the HWC series.

An improper choice of Fourier series to represent a set of imperfections can lead to very significant errors near the boundaries. This situation is illustrated in Figure 4.7, where both the FWG and HWS series give poor characterizations and have significant errors near the ends when representing quite simple imperfections with different non-zero values deduced from the simple source function of $w(x) = 0.2x + 1$. The number of harmonic terms was chosen to minimize the sum of the squares of the errors at the sampling points.

For the variation of the imperfections around the shell circumference, a FWG series can be used because w_{se} is necessarily equal to w_{te} since the starting point coincides with the ending point. Although a HWC series could be used, it has rarely been employed because a FWG series is a more self-contained series with a complete set of cosine series and sine terms.

From the above discussion, one may easily reach the conclusion that a double Fourier series of the following form is the best choice to obtain a good representation of imperfections in a shell.

$$F(v,\theta) = \sum_{m=0}^{N_m}\sum_{n=0}^{N_n} \cos\frac{m\pi v}{V}(A_{mn}\cos n\theta + B_{mn}\sin n\theta) \tag{4.1}$$

where

N_m the meridional harmonic number of the highest term adopted

N_n the circumferential harmonic number of the highest term adopted

v meridional coordinate on the shell

V the total height of the shell between boundaries

θ circumferential coordinate on the shell (in radians)

Unfortunately, many previous studies made poor choices of Fourier series to represent these imperfections. For example, a double Fourier series, with a HWS representation in the axial direction and FWG representation around the circumference, has often been employed. Examples of this choice include Arbocz and Babcock (1969), Singer *et al.* (1971), Arbocz and Williams (1977), Arbocz (1982, 1983), Singer (1982b), Arbocz and Hol (1991), Chryssanthopoulos and Poggi (1995), Cederbaum and Arbocz (1996), Esong *et al.* (1998). In addition to a double Fourier series with a HWS representation in the axial direction, Arbocz and Babcock employed another unsuitable double Fourier series with a FWG representation in both the axial and circumferential directions to evaluate the same imperfections. Although some studies (e.g., Arbocz and Babcock, 1969; Arbocz, 1982; and Singer, 1982b) also adopted a good choice of double Fourier series, with a HWC representation in the axial direction and a FWG representation around the circumference, they did not give a clear statement of the effectiveness of this series nor any analysis of the difference in the outcome of making different choices of series.

Apart from the aforesaid cases where poor choices were made, Ding (1992) used the alternative double Fourier series with a HWG series in both directions to represent his measurements of imperfections in shell sectors in the Port Kembla silos but these measurements have significant non-zero and different values at the two ends of the shell.

The above comments on previous work using Fourier series decompositions is intended to draw attention to the importance of a good choice of Fourier series to represent different forms of imperfection, so that future studies may make a better choice of series in tune with the imperfections in shells.

4.4 MODAL AMPLITUDES OF VARIOUS FOURIER SERIES

A Fourier series may contain more than one term at the same harmonic number. For example, in a one-dimensional Fourier series containing both sine and cosine terms, there are two terms in the series at a given harmonic number, and the coefficients of these terms are the Fourier coefficients. In analyses of geometric imperfections, it is often necessary to

discuss the importance of a given harmonic mode, corresponding to a specific harmonic number in a 1D Fourier series or to a combination of a meridional harmonic number and a circumferential number in a 2D Fourier series, in terms of the amplitude of this harmonic mode. To be able to evaluate this modal amplitude, a trigonometric transformation of the Fourier series from its elementary form to the modal form is required.

A simple example is a one dimensional full-wave Fourier series, which is commonly employed to represent the imperfection distribution around a shell circumference (e.g. Berry *et al*, 2000; Teng and Zhao, 2001):

$$F(\theta) = \sum_{n=0}^{N_n} (a_n \cos n\theta + b_n \sin \theta) \tag{4.2}$$

where

N_n the harmonic number of the highest term adopted

a_n, b_n coefficients of the terms of the Fourier series (i.e. Fourier coefficients)

θ circumferential coordinate on the shell (in radians)

The amplitudes of the individual harmonic modes of this series are given by $\sqrt{a_n^2 + b_n^2}$, which is obtained from the original series by the following transformation:

$$F(\theta) = \sum_{n=0}^{N_n} \sqrt{a_n^2 + b_n^2} \sin(n\theta + \Phi_n) \tag{4.3}$$

where

$$\Phi_n = arctg \frac{a_n}{b_n}$$

It should be noted that for the necessary differentiation in this thesis, these harmonic modes are also referred to as the harmonic terms (not Fourier terms) and the modal amplitudes are also referred to as the harmonic coefficients or the coefficients of the harmonic terms (not Fourier coefficients).

For more complicated forms of Fourier series, the amplitude deduction procedure is relatively complex. Presented below is an amplitude deduction procedure for a complicated double Fourier series in the form of a FWG series in both directions. Although this series is rarely used to represent imperfections in real shell structures for the reasons mentioned above, it is used here because the deduction procedure for finding its

amplitudes is typical of most 2D series. The double Fourier series in the form of a FWG series in both directions is given by:

$$F(v,\theta) = \sum_{m=0}^{N_m}\sum_{n=0}^{N_n}[\cos\frac{2m\pi v}{V}(A_{mn}\cos n\theta + B_{mn}\sin n\theta) +$$

$$\sin\frac{2m\pi v}{V}(C_{mn}\cos n\theta + D_{mn}\sin n\theta)] \tag{4.4}$$

where

N_m the meridional harmonic number of the highest term adopted

N_n the circumferential harmonic number of the highest term adopted

$A_{mn}, B_{mn}, C_{mn}, D_{mn}$ Fourier coefficients

v meridional coordinate on the shell

V the total height of the shell between boundaries

θ circumferential coordinate on the shell (in radians)

Eqn 4.4 can be expressed in the following form

$$F(v,\theta) = \sum_{m=0}^{N_m}\sum_{n=0}^{N_n}\Delta_{mn}[\cos\frac{2m\pi v}{V}\cdot\frac{A_{mn}\cos\theta + B_{mn}\sin n\theta}{\Delta_{mn}}$$

$$+\sin\frac{2m\pi v}{V}\cdot\frac{C_{mn}\cos n\theta + D_{mn}\sin n\theta}{\Delta_{mn}}] \tag{4.5}$$

Let

$$\sin\Phi = \frac{A_{mn}\cos n\theta + B_{mn}\sin n\theta}{\Delta_{mn}} \quad and \quad \cos\Phi = \frac{C_{mn}\cos n\theta + B_{mn}\sin n\theta}{\Delta_{mn}}$$

so that:

$$F(v,\theta) = \sum_{m=0}^{N_m}\sum_{n=0}^{N_n}\Delta_{mn}\sin[\frac{2m\pi v}{V} + \Phi(A_{mn}, B_{mn}, C_{mn}, D_{mn}, n, \theta)] \tag{4.6}$$

in which

$$\Delta_{mn} = \sqrt{(A_{mn}\cos n\theta + B_{mn}\sin n\theta)^2 + (C_{mn}\cos n\theta + D_{mn}\sin n\theta)^2}$$

$$\Phi = arctg \frac{C_{mn} \cos n\theta + D_{mn} \sin n\theta}{A_{mn} \cos n\theta + B_{mn} \sin n\theta}$$

and Δ_{mn} can be expressed as:

$$\Delta_{mn} = \sqrt{\frac{1}{2}(A_{mn}^2 + B_{mn}^2 + C_{mn}^2 + D_{mn}^2) + \Lambda_{mn} \sin[2n\theta + \varphi(A_{mn}, B_{mn}, C_{mn}, D_{mn})]}$$

where

$$\Lambda_{mn} = \sqrt{\frac{1}{4}(A_{mn}^2 + C_{mn}^2 - B_{mn}^2 - D_{mn}^2)^2 + (A_{mn}B_{mn} + C_{mn}D_{mn})^2} \tag{4.7}$$

$$\varphi = arctg \frac{\frac{1}{2}(A_{mn}^2 + C_{mn}^2 - B_{mn}^2 - D_{mn}^2)}{A_{mn}B_{mn} + C_{mn}D_{mn}}$$

The amplitude of the harmonic mode $j_m j_c$ in the double Fourier series can then be identified as:

$$\Delta_{mn} = \sqrt{\frac{1}{2}(A_{mn}^2 + B_{mn}^2 + C_{mn}^2 + D_{mn}^2) + \Lambda_{mn}} \tag{4.8}$$

Similar amplitude expressions for various Fourier series can be deduced, following a similar but simpler procedure, and are summarized in Table 4.2 for ease of reference.

4.5 GEOMETRIC IMPERFECTIONS IN STEEL SILOS

4.5.1 General

The three 10000-ton silos (marked by Ding as A, B and C) at Port Kembla were chosen as subjects for studying the imperfection characteristics of silos built from many welded panels, following access being given to this data by Dr. Ding. Following his description

(Ding, 1992), these silos have a diameter of 24m with a wall thickness that changes stepwise from 25mm to 16mm in the lower part of each silo, but this wall thickness is constant at 12mm above the level termed "8m" (it may be noted that this is 8m above the lower edge of the silo cylindrical wall, which is some 20m above the ground). The nominal coordinates of circumferential welds that join strakes are located at the vertical coordinates of $\overline{Z}$ =1.8m, 4.8m, 7.8m, 10.8m, 13.8m, 16.8m, and 19.8m (Figure 4.8).

Because there were a number of attachments to the walls, such as fumigating and water pipes running vertically from the bottom to the top of silo wall, the imperfection measurements (Ding, 1992) could not be made on the entire silo wall, but were taken over three separate zones (named Zone I, Zone II, and Zone III) on outer surface in Silo A and Silo B, and on two separate zones (named Zone I and Zone II) on the outer surface of Silo C (Figures 4.9(a), 4.9(b), 4.9(c)). In these zones, measurements were made by Ding at spacings of 50 mm for the vertical profiles and 500mm for the circumferential profiles. The numbers shown in the measured zones of silo walls (Figures 4.9(a), 4.9(b), 4.9(c)) indicate the number of profiles measured in each zone: the horizontally aligned value indicating the number of vertical lines of measurement, and the vertically aligned value indicating the number of circumferential lines of measurement. The numbers in brackets indicate the number of circumferential profiles that were analyzed in this study, which was confined to the hatched zone on each shell.

Examining the imperfections on the meridians of the silos, it was found that the imperfection often has a local aberrant value at each circumferential weld seam (Figure 4.10). These spurious values were ascribed to the protruding weld beads produced by the weld steel deposits. They were therefore deemed to be a surface effect and not a change in the position of the middle surface of the shell, so they were eliminated by using interpolation with a polynomial of degree 3. The coefficients of the polynomials were determined by taking two sampling points before and two sampling points after the point where the aberrant imperfection value was observed. Figure 4.10 shows nominal imperfections on the zero meridian of Silo A first before this interpolation and then after this interpolation. The spurious values of weld deposits are evidently removed, as shown in Figures 4.11-4.13. It should be noted that the word 'nominal' is used in Figures 4.11-4.13 to indicate that these imperfections are relative to a nominal reference cylinder with

the dimensions being those adopted in design, in contrast to "real" or "net" imperfections relative to a best-fit reference cylinder as explained later in the chapter.

4.5.2 Best-Fit Cylinders and "Real" Imperfections

If a surface is perfectly cylindrical, but not aligned with the reference axes being used, it may appear to depart from the cylindrical surface even though this is not the case. Thus, it is clear that the geometric imperfections that are discussed here must be only those components that differ from the closest perfect cylindrical surface to the complete set of observations. For this purpose, it is necessary to find the best-fit perfect cylinder to the full set of observations of the locations in space of the wall, and then to deduce the departures of the surface from this best-fit perfect cylinder as the "real" imperfections of the surface.

To determine these "real" imperfections, the best-fit perfect reference cylinder must first be found using the method of least-squares adjustment. The "real" imperfections can then be determined as the deviations of the surface from the imaginary cylinder surface (Arbocz and Babcock, 1969; Arbocz and Williams, 1977; Arbocz, 1982). The best fit can only be determined in relation to the sampling points, since these are the only points at which data is known. It should be recognized that the best-fit cylinder could therefore change if more or fewer sampling points are used.

A procedure was developed for deducing a best-fit cylinder and determining the "real" imperfections for a cylindrical shell. The best-fit cylinder was defined as a tilt cylinder with eccentricities at the origin of x_0 and y_0, an orientation $(\cos\alpha, \cos\beta, \cos\gamma)$, and a mean radius R (Figure 4.14). In previous studies, which were all concerned with imperfections in laboratory models rather than field observations of complete constructions, the axis of the best-fit cylinder was taken to coincide with one axis of the $O - X' Y' Z'$ coordinate system. This is because, in these studies of laboratory models, a reference cylindrical surface was defined by a rigid rail mounted on two very accurately machined end rings that were installed on the ends of the cylindrical specimen. Thus, the imperfections could be measured relative to this defining cylindrical reference system.

However, in the present field observations, the axes of the $O-X'Y'Z'$ coordinate system are not necessarily parallel to those of the reference coordinate system $O-XYZ$.

Thus, the present best-fit cylinder treatment differs from those of earlier researchers in that the coordinate system of the best-fit cylinder $O-X'Y'Z'$ is parallel to the reference coordinate system $O-XYZ$ but the axis of the best-fit cylinder has angles α,β,γ with respect to the axes $O'X'$, $O'Y'$, and $O'Z'$, respectively. The detailed procedure to determine the reference cylinder is as follows.

The equation for the axis $O'P'$ of the reference cylinder can be described by:

$$\frac{x-x_0}{\cos\alpha}=\frac{y-y_0}{\cos\beta}=\frac{z-z_0}{\cos\gamma} \tag{4.9}$$

Let $z_0=0$, then

$$x_z=x_0+\frac{\cos\alpha}{\cos\gamma}z \tag{4.10}$$

$$y_z=y_0+\frac{\cos\beta}{\cos\gamma}z \tag{4.11}$$

where x_z and y_z are the coordinates of the point at coordinate z on the cylinder axis $O'P'$.

Let $\frac{\cos\alpha}{\cos\gamma}=\zeta$, $\frac{\cos\beta}{\cos\gamma}=\rho$ then

$$x_z=x_0+\zeta z \tag{4.12}$$

$$y_z=y_0+\rho z \tag{4.13}$$

The reference cylinder is described by the equation

$$(x-x_z)^2+(y-y_z)^2=R^2$$

or $$(x-x_0-\zeta z)^2+(y-y_0-\rho z)^2=R^2 \tag{4.14}$$

The measure of deviation of a sampling point from the reference cylinder is given by

$$f_i(i,x_0,y_0,R,\zeta,\rho)=(x_i-x_z)^2+(y_i-y_z)^2-R^2$$

$$=(x_i-x_0-\zeta z_i)^2+(y_i-y_0-\rho z_i)^2-R^2 \tag{4.15}$$

$$g_i(i,x_0,y_0,R,\zeta,\rho)=f_i^2=[(x_i-x_0-\zeta z_i)^2+(y_i-y_0-\rho z_i)^2-R^2]^2 \tag{4.16}$$

The sum of the squares of the sampling point deviations can be used as an index to express the total deviations of the sampling points from the reference cylinder

$$G = \sum_{i=1}^{N_s} g_i = \sum_{i=1}^{N_s} f_i^2 \tag{4.17}$$

in which N_s is the number of sampling points. To minimize the total deviations, the first derivatives of G with respect to x_0, y_0, R, ζ, and ρ should be zero. That is

$$\frac{\partial G}{\partial x_0} = 0 \tag{4.18}$$

$$\frac{\partial G}{\partial y_0} = 0 \tag{4.19}$$

$$\frac{\partial G}{\partial R} = 0 \tag{4.20}$$

$$\frac{\partial G}{\partial \zeta} = 0 \tag{4.21}$$

$$\frac{\partial G}{\partial \rho} = 0 \tag{4.22}$$

As $\dfrac{\partial g_i}{\partial x_0} = -4[(x_i - x_0 - \zeta z_i)^2 + (x_i - x_0 - \rho z_i)^2 - R^2](x_i - x_0 - \zeta z_i)$

and writing $h_{1i} = [(x_i - x_0 - \zeta z_i)^2 + (y_i - y_0 - \rho z_i)^2 - R^2](x_i - x_0 - \zeta z_i)$ (4.23)

Eqn 4.18 becomes

$$\sum_{i=1}^{N_s} h_{1i} = 0 \tag{4.24}$$

Similarly, Eqns 4.19-4.22 can be respectively turned into

$$\sum_{i=1}^{N_s} h_{2i} = 0 \tag{4.25}$$

$$\sum_{i=1}^{N_s} h_{3i} = 0 \tag{4.26}$$

$$\sum_{i=1}^{N_s} h_{4i} = 0 \tag{4.27}$$

$$\sum_{i=1}^{N_s} h_{5i} = 0 \tag{4.28}$$

By now the following matrix can be defined,

$$[H] = \sum_{i=1}^{N_s} [h_{1i}\, h_{2i}\, h_{3i}\, h_{4i}\, h_{5i}]^T \tag{4.29}$$

with the detailed expressions of h_{1i}, h_{2i}, h_{3i}, h_{4i} and h_{5i} being given in Appendix 4.1

Eqns 4.24-4.28 form a nonlinear equation system with the following five parameters as the unknowns: x_0, y_0, R, ζ, and ρ. Because the equation system is nonlinear, it is necessary to solve it iteratively. It can be solved using the following well-known procedure:

$$\{\delta^j\} = \{\delta^{j-1}\} - [J^{j-1}]^{-1}[H^{j-1}] \tag{4.30}$$

where $\{\delta^j\}$ is the approximation of the five unknowns at the jth iteration given by

$$\{\delta^j\} = [x_0^j \; y_0^j \; R^j \; \zeta^j \; \rho^j]^T \tag{4.31}$$

where $[H^{j-1}]$ is the matrix $[H]$ at the (j-1)th iteration defined by

$$[H^{j-1}] = \sum_{i=1}^{N_s} [h_{1i}^{j-1} \; h_{2i}^{j-1} \; h_{3i}^{j-1} \; h_{4i}^{j-1} \; h_{5i}^{j-1}]^T \tag{4.32}$$

and $[J^{j-1}]$ is the Jacobian matrix at the (j-1)th iteration given by

$$[J^{j-1}] = \sum_{i=1}^{Ns} \begin{bmatrix} \partial h_{1i}/\partial x_0 & \partial h_{1i}/\partial y_0 & \partial h_{1i}/\partial R & \partial h_{1i}/\partial \zeta & \partial h_{1i}/\partial \rho \\ \partial h_{2i}/\partial x_0 & \partial h_{2i}/\partial y_0 & \partial h_{2i}/\partial R & \partial h_{2i}/\partial \zeta & \partial h_{2i}/\partial \rho \\ \partial h_{3i}/\partial x_0 & \partial h_{3i}/\partial y_0 & \partial h_{3i}/\partial R & \partial h_{3i}/\partial \zeta & \partial h_{3i}/\partial \rho \\ \partial h_{4i}/\partial x_0 & \partial h_{4i}/\partial y_0 & \partial h_{4i}/\partial R & \partial h_{4i}/\partial \zeta & \partial h_{4i}/\partial \rho \\ \partial h_{5i}/\partial x_0 & \partial h_{5i}/\partial y_0 & \partial h_{5i}/\partial R & \partial h_{5i}/\partial \zeta & \partial h_{5i}/\partial \rho \end{bmatrix}^{j-1} \tag{4.33}$$

The elements of the matrix $[J^{j-1}]$ are given in Appendix 4.2.

A parameter Δ was devised to control the convergence of the iteration procedure

$$\Delta = \left\| [J^{j-1}]^{-1}[H^{j-1}] \right\|_{\max} \le Tol \tag{4.34}$$

where Tol is the tolerance specified. Once Eqn 4.34 is satisfied, the iteration procedure may be stopped, and the values of the parameters x_0, y_0, R, ζ, and ρ are obtained. The reference cylinder is then described by Eqn 4.14.

The orientation ($\cos\alpha$, $\cos\beta$, $\cos\gamma$) of the reference cylinder axis $O'P'$ can be deduced from the following three equations:

$$\cos\alpha = \zeta \cos\gamma \tag{4.35}$$

$$\cos\beta = \rho \cos\gamma \tag{4.36}$$

$$\cos^2\alpha + \cos^2\beta + \cos^2\gamma = 1 \tag{4.37}$$

Eqn 4.37, which can be found in many mathematics texts, describes the relationship between the three orientation components. If Eqns 4.35 and 4.36 are substituted into Eqn 4.37, the value of γ may be obtained as

$$\cos\gamma = \pm\frac{1}{\sqrt{\cos^2\alpha + \cos^2\beta + 1}}$$

The two resulting values of γ differ from each other by 180° relative to the orientation of the reference cylinder axis, and this makes no difference for the reference cylinder. Thus only the positive value of γ needs to be chosen. It follows that

$$\cos\gamma = \frac{1}{\sqrt{\cos^2\alpha + \cos^2\beta + 1}} \tag{4.38}$$

Substituting Eqn 4.38 back into Eqns 4.35 and 4.36 yields

$$\cos\alpha = \frac{\zeta}{\sqrt{\cos^2\alpha + \cos^2\beta + 1}} \tag{4.39}$$

$$\cos\beta = \frac{\rho}{\sqrt{\cos^2\alpha + \cos^2\beta + 1}} \tag{4.40}$$

Once the reference cylinder has been found, the imperfections must be re-evaluated with respect to this reference cylinder so that the 'real' imperfections can be deduced. Figure 4.15 shows a sketch that outlines the method of computing the 'real' imperfections. The circle is the reference cylinder with $O_z(x_z, y_z)$ as its center, $S(x_s, y_s)$ is a sample point, $O(0,0)$ is the origin of the coordinate system, and $T(x_t, y_t)$ is the intersection between the line O_zS and the reference cylinder. The 'real' imperfections are then found as the deviation of S from the reference cylinder or $|ST|$, given by:

$$w_i = \sqrt{(x_s - x_z)^2 + (y_s - y_z)^2} - R \tag{4.41}$$

A computer program was coded to implement this procedure.

4.5.3 'Real' Imperfections in Ding's Silos at Port Kembla

In order to exclude the effect of wall thickness variations, only the imperfections in the hatched parts (Figures 4.8, 4.9(a), 4.9(b), and 4.9(c)) of the silos were analyzed in the present study. For simplicity, the hatched-parts in the three silos are referred to as Shell A, Shell B, and Shell C respectively. Using the computer program based on the procedure

presented above, the best-fit cylinder for each shell (Figures 4.9(a), 4.9(b), 4.9(c)) was determined and the "real" imperfections were obtained. Table 4.3 shows the eccentricities x_0 and y_0, the mean radius R, and the orientation $(\cos\alpha, \cos\beta, \cos\gamma)$ for each of the three shells that were deduced from the nominal imperfections. It shows that each of the best-fit cylinders is almost upright, with only small eccentricities in their centers, as well as small alterations in their radii. The "real" imperfections are therefore similar to the nominal imperfections, shifted by small values from the original ones. This situation can be seen clearly by examining an example, as shown in the Figure 4-16 where the "real" imperfections on Shell A is a integral shift from the original values. The term "real" is dropped hereafter so the term "imperfections" refer to the imperfections deduced by the above best-fit-cylinder process.

The imperfections on mid-strake circumferences at the heights of Z = 1.5m, 4.5m, and 7.5m are shown in Figures 4.17-4.19 for Shell A, Shell B, and Shell C respectively. The resulting imperfections on the circumferential weld seams at the heights of $Z = 0$m, 3m, 6m and 9m on Shell A, Shell B, and Shell C are shown in Figures 4.20-4.22 respectively. It can be seen that imperfections on these circumferences, though at different heights on the wall, are similar to each other within one shell, irrespective of whether they are on at the mid-strake position or on a circumferential weld. However, each shell clearly differs significantly from the others. From these figures, it seems that there is no clear correlation between the number of panels around the circumference (which is six) and circumferential imperfection distribution on these shells. Figures 4.23 to 4.25 show the imperfections down different meridians of Shell A, Shell B, and Shell C respectively. It can been seen that the imperfections down the meridians deviate significantly from each other, except that they jump slightly at each of the circumferential welds. In addition, there is not really a clear repeatable pattern to these imperfection profiles either on different meridians of the same shell or between the different shells. The imperfection patterns on these shells are very complicated but interesting. Fourier decompositions of the imperfections were therefore carried out in this study to investigate their characteristics using both one-dimensional and two dimensional Fourier series.

4.6 EFFECT OF LINEAR INTERPOLATIONS OVER ZONES OF MISSING DATA ON FOURIER DECOMPOSITION

The analysis of the imperfection forms in a complete full scale construction, such as a cylindrical shell, is an important concern of researchers. Laboratory models are relatively easy to measure and to describe comprehensively, but full scale prototypes are much more difficult to work with. As a result, it is quite common for the imperfections on small segments of the structure to be studied or reported (ECCS, 1988; Rotter, 1988, 1996; ENV 1993.1.6, 1999; Pircher *et al*, 2001). However, these small segments do not give a very reliable measure of the effect that the full imperfection set in the complete structure may have on the buckling strength. It is therefore critically important that the full 2 dimensional imperfection field should be evaluated using the entire circumference of the complete cylinder.

As Ding (1992) took his measurements on two or three separate zones, there is a remarkable disparity between the sampling point spacings in the parts that were measured and in those that were not around the circumferences. Analyses of these imperfections have shown that such large disparities may cause two problems in Fourier decompositions: first, it may be difficult to find an accurate Fourier representation for these imperfections even using the Iterative Fourier Decomposition Method (Lin and Teng, 2003). This method is generally very effective in deducing accurate Fourier representations of imperfections with non-uniform sampling intervals. The second problem is that the Fourier series representation may deviate significantly from the straight line connecting the facing end points in the zones that were not measured. An important objective of the Fourier decomposition is to achieve a fine mesh of imperfections to use in FE modeling for buckling analyses. However, if the Fourier series representation of the surface has serious deviations in the zone that was not measured, it is possible that buckling will be predicted to occur first in those zones, at a strength below that of the measured zones. Clearly, such an outcome would be most undesirable and meaningless. It is therefore important that the deduced recombined imperfections in the non-measured parts should not deviate very much from a linear interpolation between the two end points, so that these zones can be treated as having imperfections that do not strongly influence the buckling

strength. For these reasons, linear interpolations were applied in the non-measured zones before the Fourier decomposition was undertaken. This arrangement enhanced the accuracy of the Fourier representations and constrained the recombined Fourier curve in the non-measured zones.

To evaluate the effect of these linear interpolations on the Fourier decompositions, studies were carried out to explore the variations that occurred in the main imperfection components when different schemes were used for the linear interpolations in the measurement gaps on Shell A (Gap I, Gap II, and Gap III in Figures4.9a). These studies also considered the effect on the recombined Fourier series curves. The imperfections measured at the level of $Z = 5.1m$ in Shell A were chosen, because this set of data is one of the few whose imperfections can be accurately decomposed without adding any extra sampling points within the measurement gaps. Decompositions of the imperfections using the following interpolation schemes were studied:

(a) No interpolations in the non-measured zones (denoted as No Interpolation)
(b) Introduction of two additional points uniformly distributed in Gap III (denoted as Scheme I), leading to a spacing of 2664.5mm in Gap III.
(c) Introduction of nine additional points uniformly distributed in Gap III (denoted as Scheme II), leading to a spacing of 799.4mm in Gap III.
(d) Introduction of one additional point centrally located in Gap I, three equally spaced additional points in Gap II, and 15 equally spaced additional points in Gap III (Scheme III), leading to spacings of 450mm in Gap I, 500mm in Gap II, and 499.6mm in Gap III. These spacings are close to or equal to those in the measured zones.

In order to avoid the interference of different "best-fit" cylinder schemes, the nominal imperfections were used in these analyses. Figures 4.26 and 4.27 show typical results of the Fourier series deduced from the imperfections using different interpolation schemes.

The outcomes of these Fourier decompositions are presented here in terms of the amplitude spectrum of the Fourier series. Although the main components did not change much, the amplitude spectrum obtained without any introduced points within the measurement gaps was found to be somewhat different from that obtained from all the

different interpolation schemes where additional data points were introduced. The differences between the spectra deduced from the different schemes (Schemes I, II and III above) were fairly small (Figure 4.26). This suggests that the major differences may be attributed to the introduction of points in Gap III. This was verified by the fact that the curve deduced from the imperfections without any introduced points deviated significantly from the straight line between the adjacent end points in Gap III (Figure 4.27). This deviation is the very phenomenon that the analysis sought to avoid, for the reasons given above. Therefore the different schemes of adding additional data points in the non-measured parts (Gap I, Gap II, and Gap III in Figure 4.9(a), 4.9(b), and 4.9(c) are very necessary before Fourier decomposition is undertaken. Table 4.4 shows the different schemes of adding additional points and the spacings of the sampling points that were used in the following Fourier analyses.

4.7 DECOMPOSITION OF GEOMETRIC IMPERFECTIONS USING 1D FOURIER SERIES

Fourier series decompositions of one-dimensional data are simple but effective in analyzing the imperfection patterns on a silo structure. These 1D analyses were therefore undertaken first to investigate the characteristics of these series and the imperfections using the selected imperfection profiles shown in Figures 4.17-4.25.

To analyze the imperfection form on a circumference around a shell, the one-dimensional full-wave Fourier series of "cosine plus sine" set given by Eqn 4.2 was employed, because the first sampling point coincides the last one on each circumference. As the sampling intervals were non-uniform, the method of Iterative Fourier Decomposition (Lin and Teng, 2003) was employed to find accurate Fourier representations of these imperfections. Iterative Fourier Decomposition works extremely well here, as the errors in the Fourier representations at the sampling points decline to any chosen small value after a number of iterations. It was found that the larger modal amplitudes in the series are clustered at low harmonic numbers. The high harmonics, though important in capturing local details using Fourier representations, are individually fairly small. If all the model amplitudes are presented on a single figure, the values of many of the modal amplitudes are illegible because the smaller ones are much lower than the dominant ones (Figure 4.26). The

number of harmonic modes was therefore truncated to 30 or 40 in the figures hereafter, even though many more modes were calculated. The modal amplitudes deduced from the imperfections on the selected circumferences of Shell A, Shell B and Shell C (Figures 4.17-4.22) are shown in Figures 4.28-4.33.

It is evident that the modal amplitudes for harmonics $n = 0, 1$ are very much larger than those of other harmonics. If these low harmonics are excluded from the display, other harmonics with relatively large coefficients can be seen more clearly, and the dominant terms are found to be in harmonics 6, 12 and 24 in Shell A, harmonics 12 and 24 in Shell B, and harmonics 6 and 12 in Shell C. These terms dominate over their neighbours, and it is naturally significant that these values are integer multiples of the number of circumferential panels (six) on each circumference of the shell.

In addition to the analysis of these selected circumferences, Fourier decompositions were also performed on the imperfections on some selected meridians, using the single half-wave series given by Eqn 4.42. The HWC series was chosen because $w_{se} \neq w_{te}$ on these meridians.

$$F(v) = \sum_{m=0}^{N_m} a_m \cos\frac{m\pi v}{V} \tag{4.42}$$

Since Ding (1992) measured the imperfections down each meridian at a uniform sampling point spacing of 50mm, the Iterative Fourier Decomposition Method was not needed here. The maximum error given by the recombined Fourier series after analysis at any sampling point was found to be less than 0.02mm for all these imperfections. Thus the process yielded a high quality representation of the data. The modal amplitudes of the Fourier series deduced from the imperfections on the meridians of the three shells are shown in Figures 4.34- 4.36. It is clear that the amplitudes of harmonic 6 dominate those of other harmonics if the lower harmonics that reflect the tilt of the meridians and overwhelm all of the others, were excluded. The harmonic 6 may correlate with the number of the meridional panels that was chosen as 3 in the analyses.

The amplitudes decay roughly as $1/j$ (j is the harmonic number) for both imperfections around the circumference and those down each meridian. When considering the harmonics with an amplitude of larger than 1, it shows that the harmonic coefficients of the Fourier

Pao Yue-kong Library
PolyU • Hong Kong

series deduced from the imperfections around the circumferences of each shell are much richer than those deduced from the imperfections down the meridians of the shells. In all of these shells, the coefficients of low harmonics such as $n = 0,1$ for the circumferential Fourier decompositions and $m = 0,1$ for the meridional decompositions overwhelm all other harmonic coefficients in the Fourier series deduced. It is believed that these may result from some common factors during fabrication process. Apart from these coefficients, the panel-associated coefficients stand out as substantially larger than their neighbours. In order to confirm these findings, a two-dimensional Fourier analysis of these imperfections using a double Fourier series was carried out.

The Fourier analyses were carried out with two conditions: using the imperfections before "best-fit-cylinder" reductions and after those reductions. Comparisons of the results of the Fourier series using the imperfections before and after "best-fit-cylinder" reductions show that the difference between the two sets lies only in the coefficient a_0^c for circumferential decompositions, where the value of a_0^c does not necessarily equal the value of "best-fit-cylinder" shift, as there are also eccentricity adjustments involved. In the meridian, the differences are only found in the coefficients of a_0^m and a_1^m.

4.8 DECOMPOSITION OF GEOMETRIC IMPERFECTIONS USING 2D FOURIER SERIES

The double Fourier series shown in Eqn 4.1 was adopted for decompositions of the imperfections in these shells, where the modal amplitudes of the Fourier series are given by (Table 4.2):

$$\Delta_{mn} = \sqrt{A_{mn}^2 + B_{mn}^2} \tag{4.43}$$

while the errors of the Fourier series representations at the sampling points are defined as:

$$er(v_i, \theta_i) = w(v_i, \theta_i) - \sum_{m=0}^{N_m}\sum_{n=0}^{N_n}(A_{mn}\cos\frac{m\pi v_i}{V}\cos n\theta_i + B_{mn}\cos\frac{m\pi v_i}{V}\sin n\theta_i) \tag{4.44}$$

where

v_i, θ_i	coordinates of the ith sampling point
$w(v_i, \theta_i)$	imperfection value at the sampling point

Even if extra data points are added in the measurement gaps with interpolations, equally spaced sampling points cannot be achieved over the whole circumferences (because the spacings do not permit an integer sub-division). It can be seen from the Table 4.4 that the sampling point spacing in Gap I in both Shell A and Shell B is 450mm after linear interpolation, whereas that of the measured zones is 500 mm. In addition, we generally cannot get a spacing of 500mm in Gap III in either Shell A or Shell B or in Gap II in Shell C. As non-uniform sampling spacings are unavoidable, a traditional Fourier decomposition method cannot accurately decompose the data and the iterative Fourier decomposition method, which was described in Chapter 3, was employed here in 2D Fourier decompositions to get accurate representations of the imperfections.

The convergence parameter was chosen as

$$R_{r2} = \sqrt{\sum_{i=1}^{N_s} er^2(v_i, \theta_i) \Big/ \sum_{i=1}^{N_s} w^2(v_i, \theta_i)} \tag{4.45}$$

where

R_{r2} is the convergence parameter

$w(v_i, \theta_i)$ is the imperfection at the sampling point (v_i, θ_i)

It was found that the Iterative Fourier Decomposition Method worked very well for Shell A and Shell B but was less important for Shell C because the errors in Shell C are quite small by the first iteration, since sampling point intervals were fairly uniform after linear interpolation. Table 4.5 shows the variations of the maximum representation error and the convergence parameter during the iterative procedure. It may be noted that the point on the shell at which the maximum representation error occurs generally changes during the iteration process. Further iterations show little additional error reduction, because the small remaining errors are dominated by the imperfection forms down shell meridians in a

form of $\cos(90\frac{x}{L})$ (Figure 4.38) which cannot be interpreted using a cosine series with these 181 evenly-distributed sampling points. This situation has been explained in Chapter 3, where uniformly-spaced discrete imperfection values in the form of $A\cos k\theta$ cannot be deduced from 2k+1 sampling points. Figure 4.37 shows the error in the Fourier series representation at the sampling points on Shell A after one iteration, while Figure 4.38 shows the errors after 5 iterations. It can be seen that large errors gather in the vicinity of the zone that has non-uniform sampling intervals which is 450mm here. This observation was also found in Fourier decompositions of the imperfections on Shell B. It shows that the representation error is very sensitive to the non-uniformity of the sampling point intervals: a variation of 10% in sampling point interval can result in considerable errors near the ends of the non-uniform intervals. This phenomenon was pointed out in Chapter 3 in the context of one-dimensional Fourier representations: here it is verified for the case of two-dimensional Fourier representations.

The modal amplitudes of the Fourier series deduced from the imperfections in Shell A, Shell B and Shell C are shown in Figure 4.39, Figure 4.40, and Figure 4.41 respectively. It can be seen from these figures that some features of the imperfection wave patterns are similar in these three shells. For example, the large wave patterns around the circumference are more abundant than in the meridional direction with the dominant wave patterns clustered in the lower harmonic region. The coefficients of the harmonic modes $(m = 0, n = 1)$ and $(m = 0, n = 2)$ generally overwhelm all the others, indicating ovalisation and the overall imperfection being the most dominant form of imperfection in shells. If the term "marked harmonic modes" is defined as the harmonic modes larger than the neighbouring modes, but excluding the overwhelming low harmonic modes mentioned above, it is found that, around the circumference, the harmonic modes $(m = 0, n = 6, 24)$, $(m = 1, n = 12)$, and $(m = 2, n = 12, 24)$ in Shell A, $(m = 0, n = 12)$ and $(m = 1, 2, n = 24)$ in Shell B, and $(m = 0, n = 6, 12)$ and $(m = 6, 12, n = 0)$ in Shell C are the marked harmonic modes. Down the meridians of the shells, the modes $(m = 6, 12, 18, n = 0)$ in both Shell A and Shell B and the modes $(m = 0, n = 6, 12)$ in Shell C were the marked modes. These marked modes have a physical relationship to the numbers of panels in each direction, as the number around the circumference at all levels is 6, while the number down each meridian in the analyses is 3, as shown in the examples given below.

The length of the marked harmonic modes can be deduced from the corresponding wave number m and n in a manner similar to that of Ding (1992):

$$l_m = \frac{2V}{m} \tag{4.46}$$

$$l_c = \frac{2\pi R}{n} \tag{4.47}$$

where

l_m and l_c are the wavelength of the imperfection harmonic mode down each meridian and around each circumference of the shell, respectively;

R is the radius of the shell.

For the harmonic mode $(m = 6, n = 0)$,

$$l_m = \frac{2V}{m} = \frac{2 \times 9000mm}{6} = 3000mm \tag{4.48}$$

For modes $(m = 0, n = 12)$ or $(m = 1, n = 12)$,

$$l_c = \frac{2\pi R}{n} = \frac{2 \times 3.14 \times 12000mm}{12} = 6280mm \tag{4.49}$$

and

$$2l_c = 12560mm \tag{4.50}$$

These two wavelengths are clearly associated with the weld joints or the panel size, which is $3000mm \times 12500mm$.

Besides these imperfection features that are common in three shells, there are some distinct marked modes that cannot be explained by the association with the construction method of panel fabrication. These wave patterns may be caused by some other systematic

features of the fabrication process for these shells that are not easily identified without having more detailed information about the manner of their construction.

As mentioned above, Fourier decomposition of the nominal imperfections in the shells were also carried out. Comparisons of the modal amplitudes deduced from the "real" imperfections and those found from nominal imperfections show only one difference between the two sets of Fourier coefficients: the coefficient a_{00} deduced from the "real" imperfections is rather small, but the corresponding value deduced from the nominal imperfections is much larger. This is easily understood because the "best-fit" cylinder process caused all the values to be translated: the large a_{00} for the raw data can therefore be seen as an alignment error.

The imperfections surveyed on the three shells can be incorporated into finite element models to assess the buckling behavior under axial compression of these shells, which is well known to be sensitive to the forms and amplitudes of geometric imperfections. For other silos that have not been measured, where the same contractor used the same fabrication technique, it is scientifically credible to construct geometric imperfections using both the forms and the amplitudes of the imperfections decomposed in these analyses. To apply these imperfections to other silo structures or to future silo designs, it is desirable to establish a fuller Initial Imperfection Data Bank (e.g. Arbocz, 1982), based on a statistical assessment of many similar structures. However, the limited data currently available on the initial imperfections in silo structures is a serious impediment to the attainment of this goal in the near future. Thus, a major effort to establish an initial imperfection data bank and to analyze the characteristics of the imperfections related to this fabrication technique is still a very important research goal.

4.9 CONCLUSIONS

This chapter presented several analyses of imperfections in some large steel silos. The mathematical basis of a Fourier series representation was discussed, as well as the performance of various forms of Fourier series and their suitability to represent the different forms of imperfections. Conclusions were then drawn and an appropriate choice of Fourier series representation was made to represent the different forms of imperfections.

Comments were made on the choices made by previous researchers who used Fourier series to represent cylindrical shell imperfections, and the inappropriate choices made on some occasions were identified and their consequences highlighted. A typical amplitude deduction procedure for a complicated Fourier series was demonstrated and the amplitude expressions for various Fourier series were presented for ease of reference. In addition, the procedure of deriving the 'best-fit' cylinder to obtain the "real" imperfections with respect to the best-fit reference cylinder was presented.

Systematic Fourier decompositions of the imperfections measured by Ding (1992) in the three large steel silos at Port Kembla, Australia, were carried out. Imperfections forms and magnitudes around the circumference at selected levels on each silo were decomposed using 1D FWG series, while the imperfections on selected meridians on each shell were analyzed using 1D HWC series. In addition, the complete 2D imperfection form in a selected height range in each of the shells was decomposed using 2D Fourier series with a HWC representation in the axial direction and a FWG representation in the circumferential direction.

Based on the studies in this chapter, a number of conclusions can be drawn:

1. The FWG series taking the form of full-wave cosine series plus sine series can be used to represent imperfections with the same end values. An example is the case of the imperfection variation around the circumference of a cylindrical shell, where the starting and finishing values must necessarily be identical. The HWC series is a versatile Fourier series that can be used to represent every form of imperfection pattern with a high accuracy: this form of Fourier series is often used to represent imperfections with different end values. The HWS series may be used to interpret imperfections with zero end values: this form of Fourier series is often replaced by a FWG series because the latter is more complete with a full set of cosine and sine series. A HWG series in the form of a HWC series added with a HWS series should never be used. Neither FWC nor FWS series are suitable for the representation of imperfections, because the imperfections in cylindrical shells do not necessarily take the form of symmetric or anti-symmetric shapes with respect to the middle point of the region considered.

2. The number of terms used in a Fourier series should be chosen according to the number of data sampling points according to Table 4.1, so that the representation errors (in terms of the sum of the squares of the errors at the sampling points) can be minimized.
3. The Iterative Fourier decomposition method, which was proposed in the context of one-dimensional Fourier decompositions, is also very effective in 2D Fourier decompositions of cylindrical shell imperfections, when the data is obtained at non-uniformly distributed sampling points.
4. The higher terms of a Fourier series, whose coefficients may themselves seem small, play an important role in reducing the errors in Fourier representations and capturing important local features of the imperfection form.
5. Although there is little visual similarity between the global imperfection patterns on the three shells studied, the spectra of these imperfections in Fourier decompositions show some remarkable common features, such as the dominant wave patterns clustering in low harmonic modes of the Fourier spectrum and the circumferential wave patterns that are much richer than the meridional ones.
6. There are some very marked global features of the imperfections: the harmonic modes such as $\Delta_{0,1}, \Delta_{0,2}, \Delta_{1,1}, \Delta_{1,2}$ display overwhelmingly large amplitudes which may be attributed to the global imperfections such as out-of-roundness and meridional tilt in these shells.
7. In addition to these very large amplitudes in large scale shape errors, there exist some pronounced wave patterns of imperfections that are closely related to the number of panels in each silo shell, indicating the dependence of the geometric imperfection patterns on the fabrication process for the structure.

Table 4.1 Performance of Fourier series in representing various forms of imperfections

Case	Form of imperfection	Form of Fourier series	Relationship between N_f and N_s
(a)	$w_{se} = w_{te} \neq 0$	FWG	$N_f = (N_s - 2)/2$, *if* N_s *is an even number* $N_f = (N_s - 1)/2$ *or* $N_f = (N_s - 3)/2$, *if* N_s *is an odd number*
		HWC	$N_f = N_s - 1$ or $N_f = N_s - 2$
(b)	$w_{se} = w_{te} = 0$	FWG	$N_f = (N_s - 2)/2$, *if* N_s *is an even number* $N_f = (N_s - 1)/2$ *or* $N_f = (N_s - 3)/2$, *if* N_s *is an odd number*
		HWS	$N_f = N_s - 1$ or $N_f = N_s - 2$
(c)	$w_{se} \neq w_{te}$, $w_{se} \neq 0$, $w_{te} \neq 0$	HWC	
(d)	$w_{se} = 0$, $w_{te} \neq 0$		
(e)	$w_{se} \neq 0$, $w_{te} = 0$		

Table 4.2 Amplitudes of various Fourier series

Form of Fourier Series	Definition Interval*	Modal Amplitude
Double FWG: $\sum_{m=0}^{N_m}\sum_{n=0}^{N_n}[\cos\frac{2m\pi v}{V}(A_{mn}\cos m\theta + B_{mn}\sin n\theta) + \sin\frac{2m\pi v}{V}(C_{mn}\cos m\theta + D_{mn}\sin n\theta)]$	$0 \le v \le V$ $0 \le \theta \le 2\pi$	$\Delta_{mn} = \sqrt{\frac{1}{2}(A_{mn}^2 + B_{mn}^2 + C_{mn}^2 + D_{mn}^2) + \Lambda_{mn}}$ where Λ_{mn} refer to Eqn.(4-7)
Meridional: HWS, Circumferential: FWG: $\sum_{m=0}^{N_m}\sum_{n=0}^{N_n}\sin\frac{m\pi v}{V}(A_{mn}\cos m\theta + B_{mn}\sin n\theta)$	$0 \le v \le V$ $0 \le \theta \le 2\pi$	$\Delta_{mn} = \sqrt{A_{mn}^2 + B_{mn}^2}$
Meridional: HWC, Circumferential: FWG: $\sum_{m=0}^{N_m}\sum_{n=0}^{N_n}\cos\frac{m\pi v}{V}(A_{mn}\cos m\theta + B_{mn}\sin n\theta)$	$0 \le v \le V$ $0 \le \theta \le 2\pi$	$\Delta_{mn} = \sqrt{A_{mn}^2 + B_{mn}^2}$
Meridional: HWS, Circumferential HWC: $\sum_{m=1}^{N_m}\sum_{n=0}^{N_n}A_{j_m j_c}\sin\frac{m\pi v}{V}\cos\frac{n\pi u}{U}$	$0 \le v \le V$ $0 \le u \le U$	A_{mn}
Double HWC: $\sum_{m=0}^{N_m}\sum_{n=0}^{N_n}A_{mn}\cos\frac{m\pi v}{V}\cos\frac{n\pi u}{U}$	$0 \le v \le V$ $0 \le u \le U$	A_{mn}

*where: v meridional coordinate, V the considered height of the shell

u circumferential coordinate, U the considered arc-length of the shell circumference

Table 4.3 Parameters of the best-fit cylinders for the three shells

Shell	$x_0(mm)$	$y_0(mm)$	$R(mm)$	$\cos\alpha$	$\cos\beta$	$\cos\gamma$
Shell A	-0.53	-0.51	11996.1	1.1×10^{-4}	9.6×10^{-5}	1.0
Shell B	0.05	-0.08	12000.9	1.3×10^{-5}	-2.6×10^{-5}	1.0
Shell C	0.28	-0.32	11999.0	-2.8×10^{-5}	3.9×10^{-5}	1.0

Table 4.4 Spacings of the sampling points used in Fourier decomposition

Shell		Shell A	Shell B	Shell C
Sampling Spacing for the Surveyed Zones (mm)		500.0		
Gap I	Number of Points from Interpolation	1	1	
	Spacing (mm)	450.0	450.0	
Gap II	Number of Points from Interpolation	3	3	3
	Spacing (mm)	500.0	500.0	500.0
Gap III	Number of Points from Interpolation	16	18	50
	Spacing (mm)	499.6	499.6	497.9

Table 4.5 Values of maximum error and convergence parameter during iterative Fourier decomposition

Iteration	Shell A		Shell B		Shell C	
	Max. Error (mm)	R_{r2}	Max.. Error (mm)	R_{r2}	Max. Error (mm)	R_{r2}
1	1.16mm	5.04×10^{-3}	1.61mm	1.10×10^{-2}	-0.06mm	1.87×10^{-3}
2	-0.32mm	2.04×10^{-3}	0.32mm	3.95×10^{-3}	0.03mm	1.07×10^{-3}
3	-0.12mm	1.29×10^{-3}	0.13mm	2.04×10^{-3}		
4	0.06mm	1.15×10^{-3}	0.06mm	1.60×10^{-3}		
5	-0.05mm	1.13×10^{-3}				

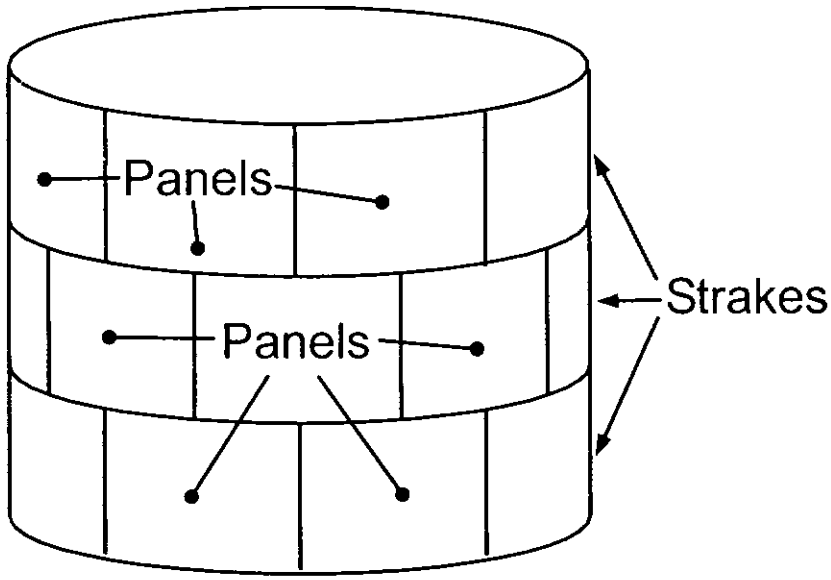

Figure 4.1 Silo construction

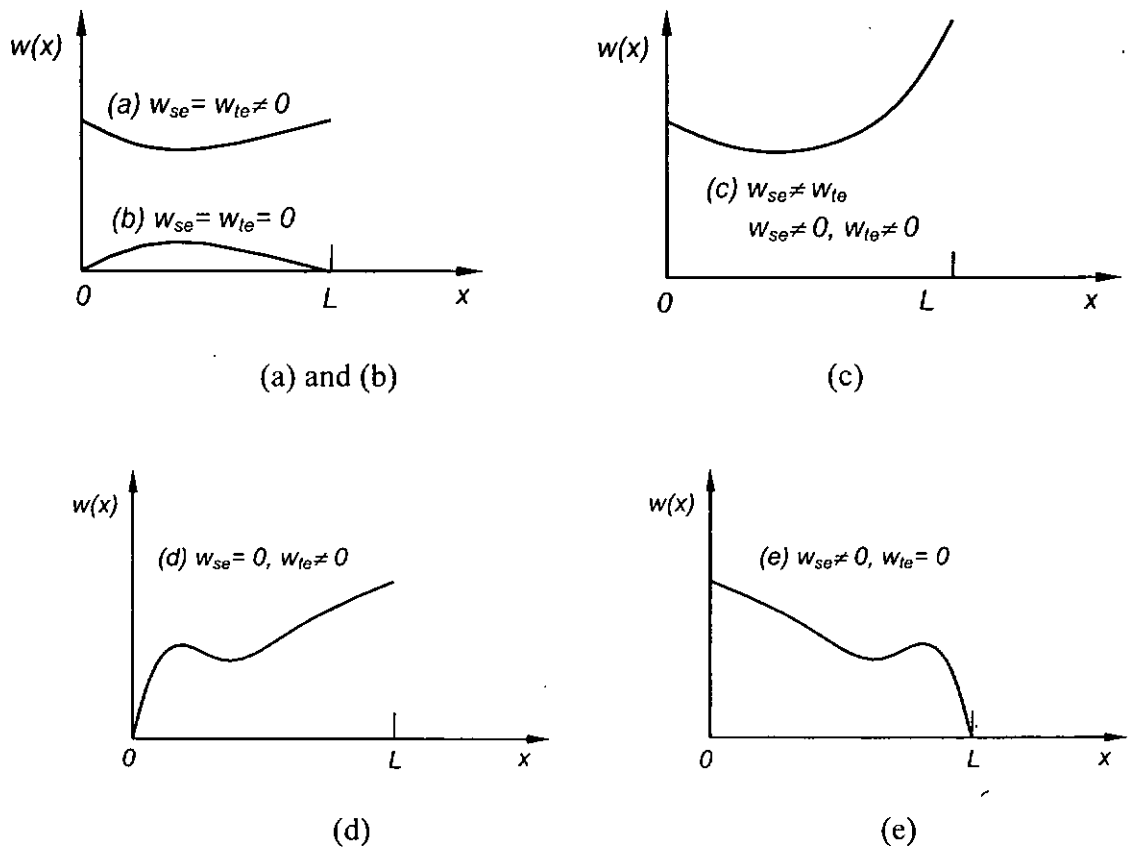

Figure 4.2 Possible edge conditions of imperfection functions

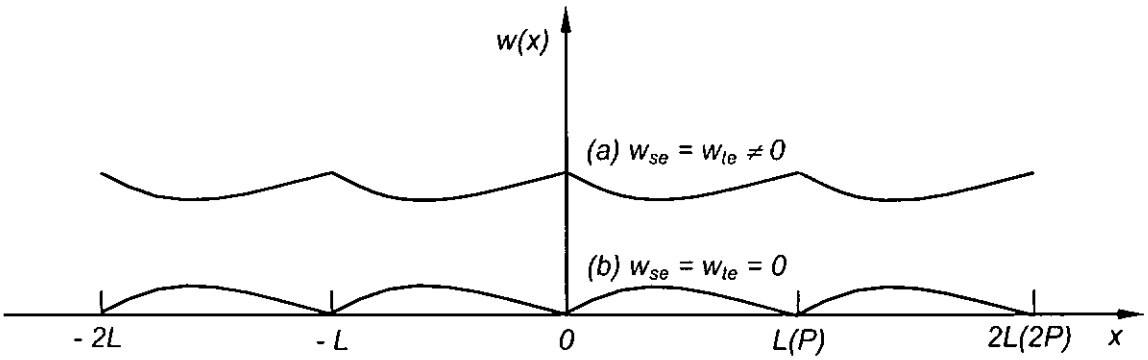

Figure 4.3 Periodic extension of an imperfection function with identical edge values

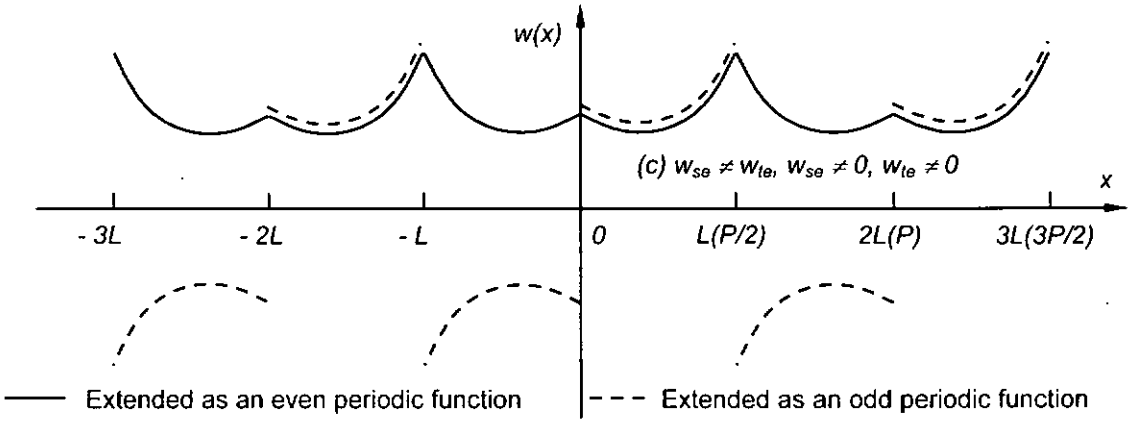

Figure 4.4 Imperfection function of case (c) and its even/odd extension

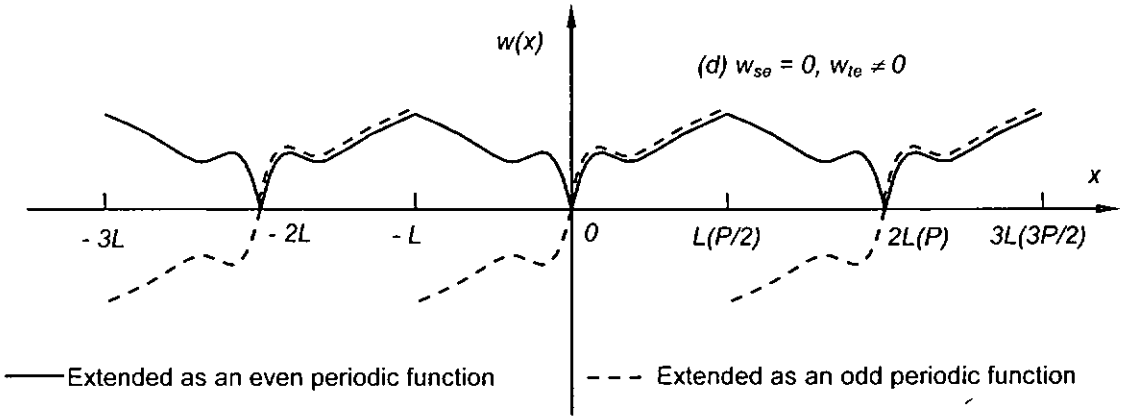

Figure 4.5 Imperfection function of case (d) and its even/odd extension

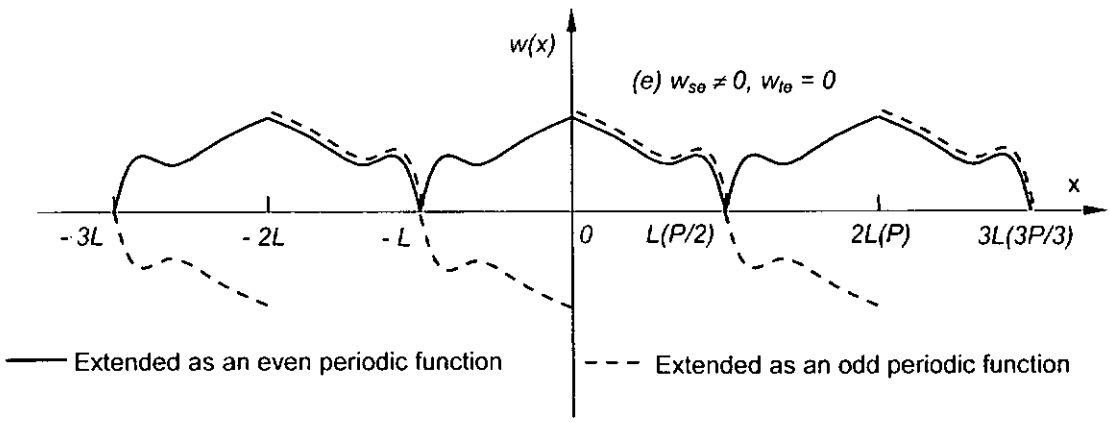

Figure 4.6 Imperfection function of case (e) and its even/odd extension

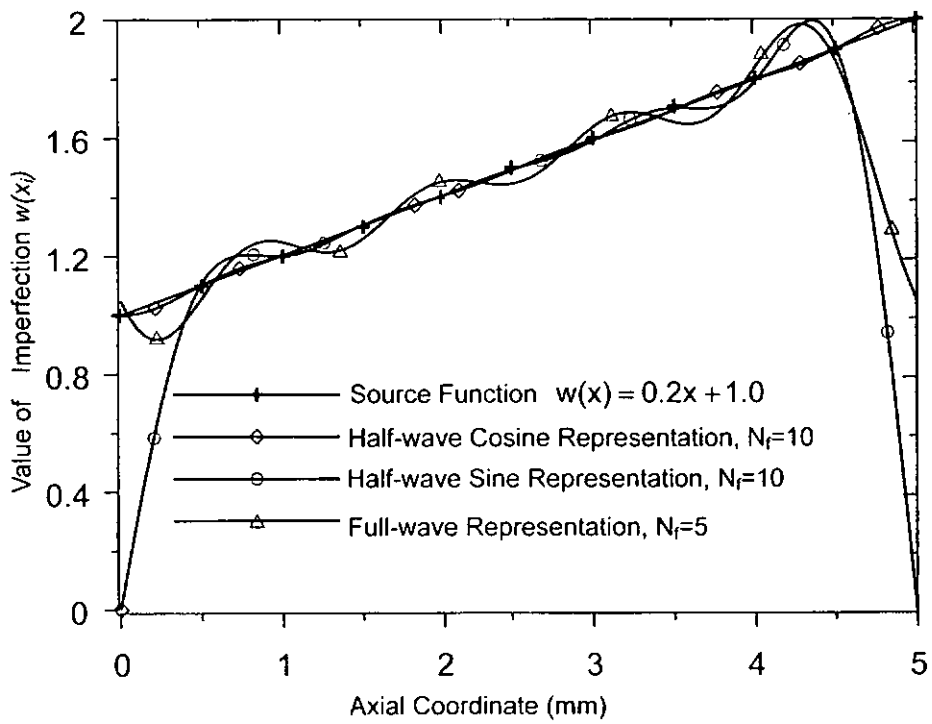

Figure 4.7 Different Fourier representations of an imperfection function with different edge values

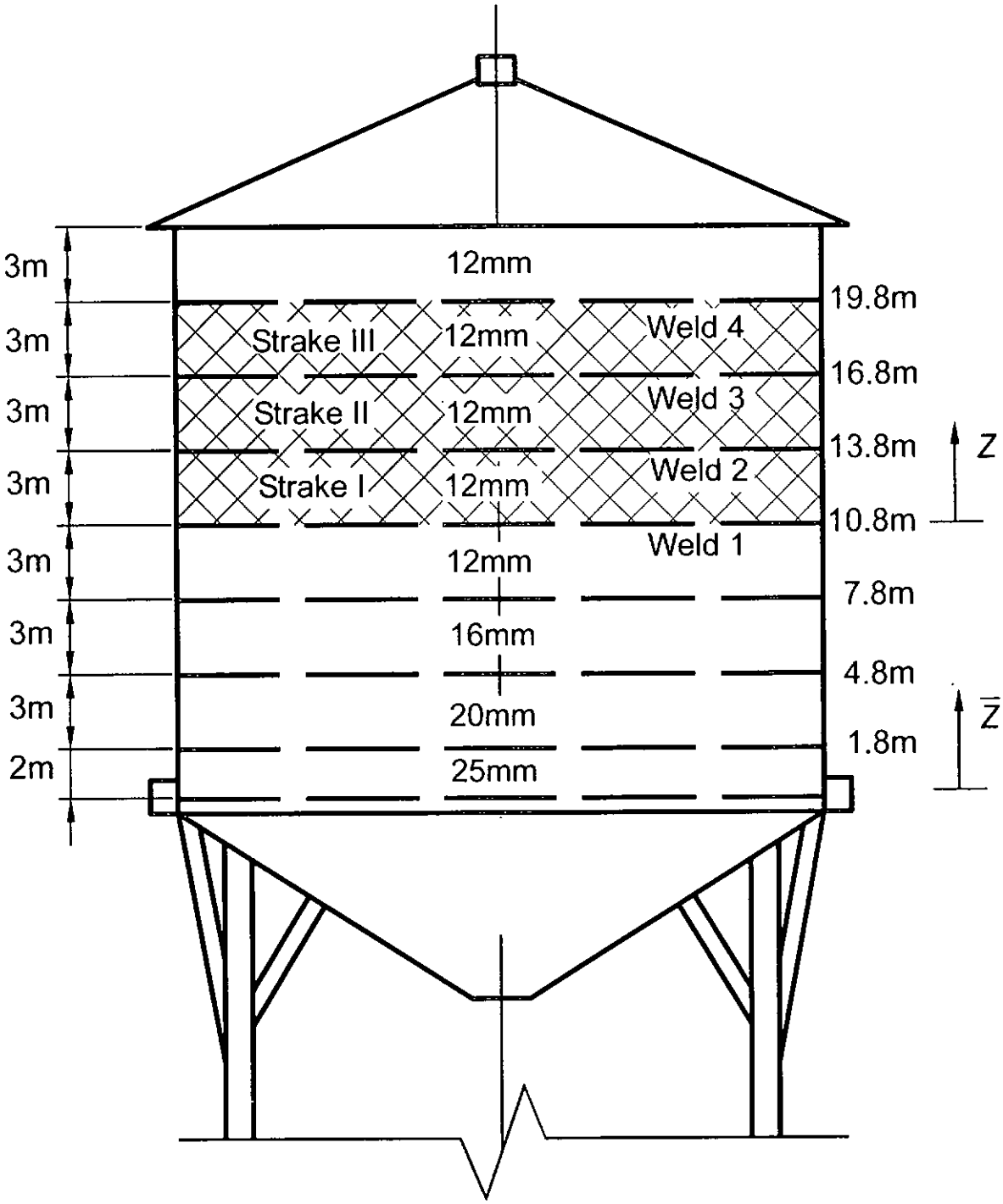

Figure 4.8 Height and wall thickness of the subject silos (After Ding, 1992)

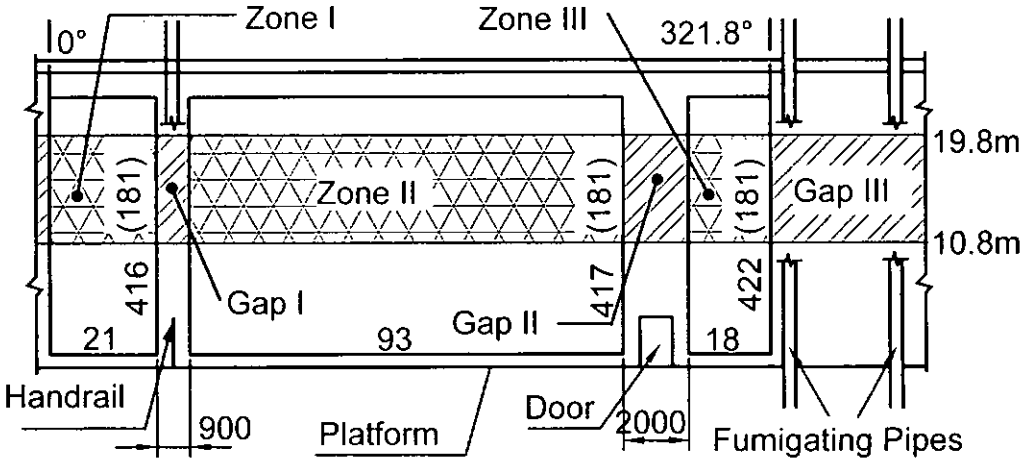

(a) Silo A

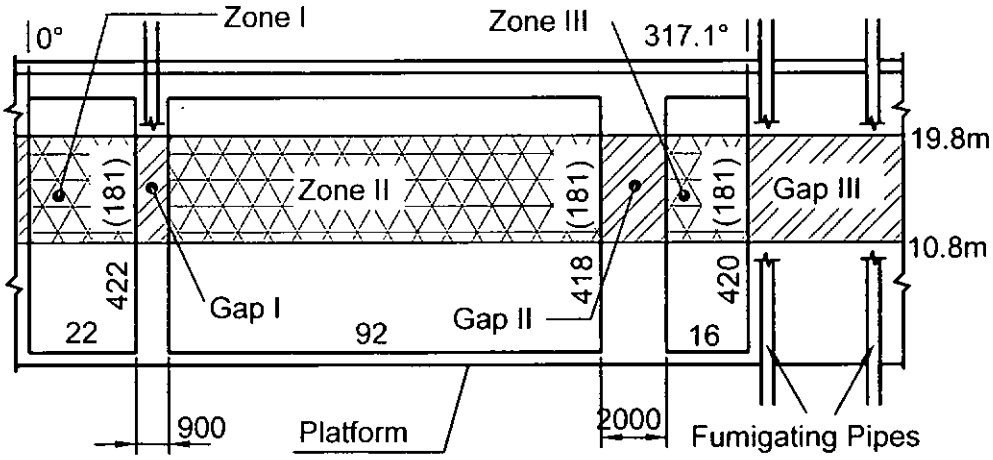

(b) Silo B

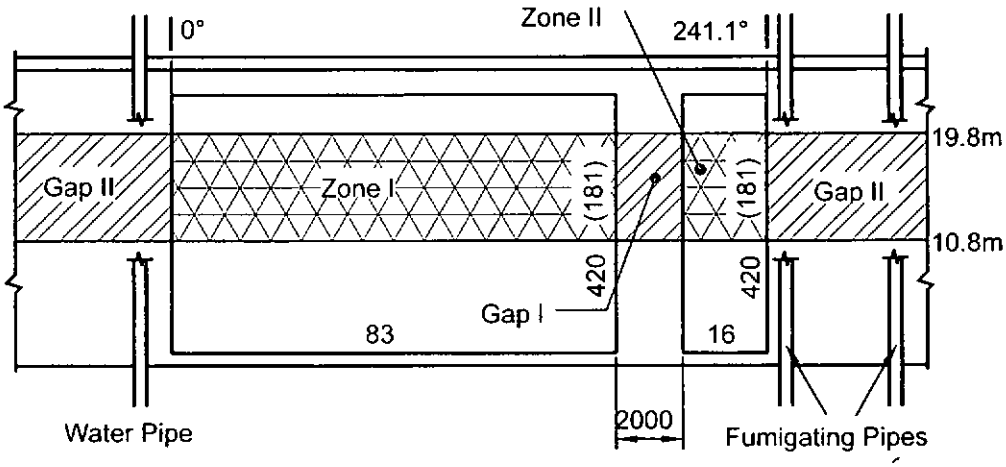

(c) Silo C

Figure 4.9 Measured zones and gaps on the three silos

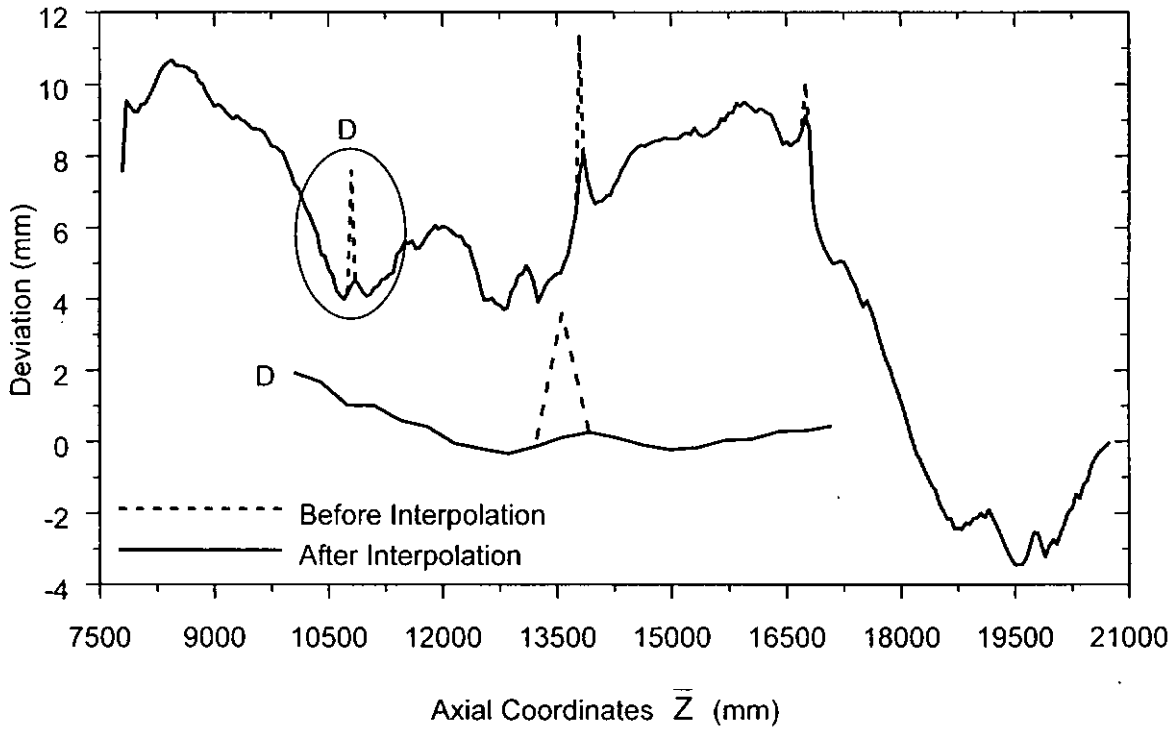

Figure 4.10 Imperfections on 0^0 meridian of Silo A before and after interpolation.

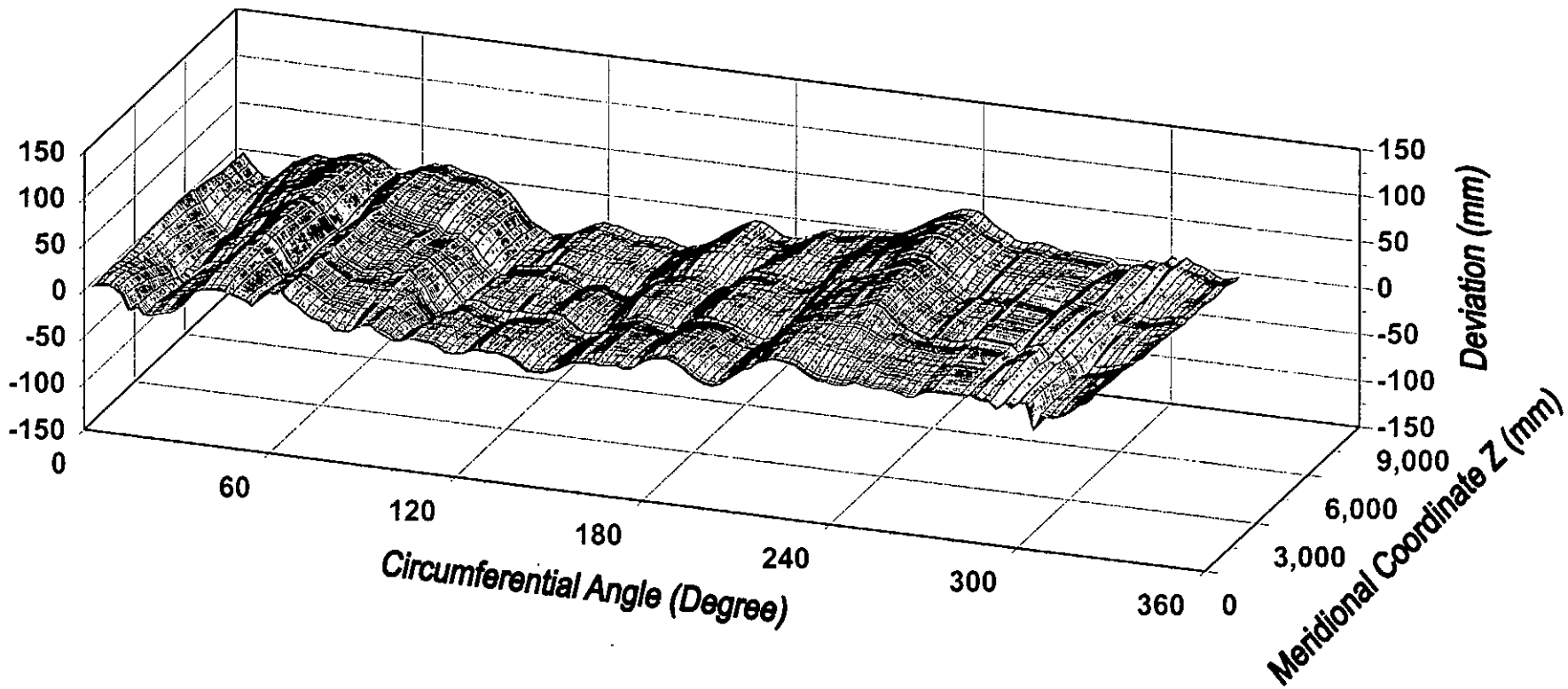

Figure 4.11 Nominal imperfections in shell A

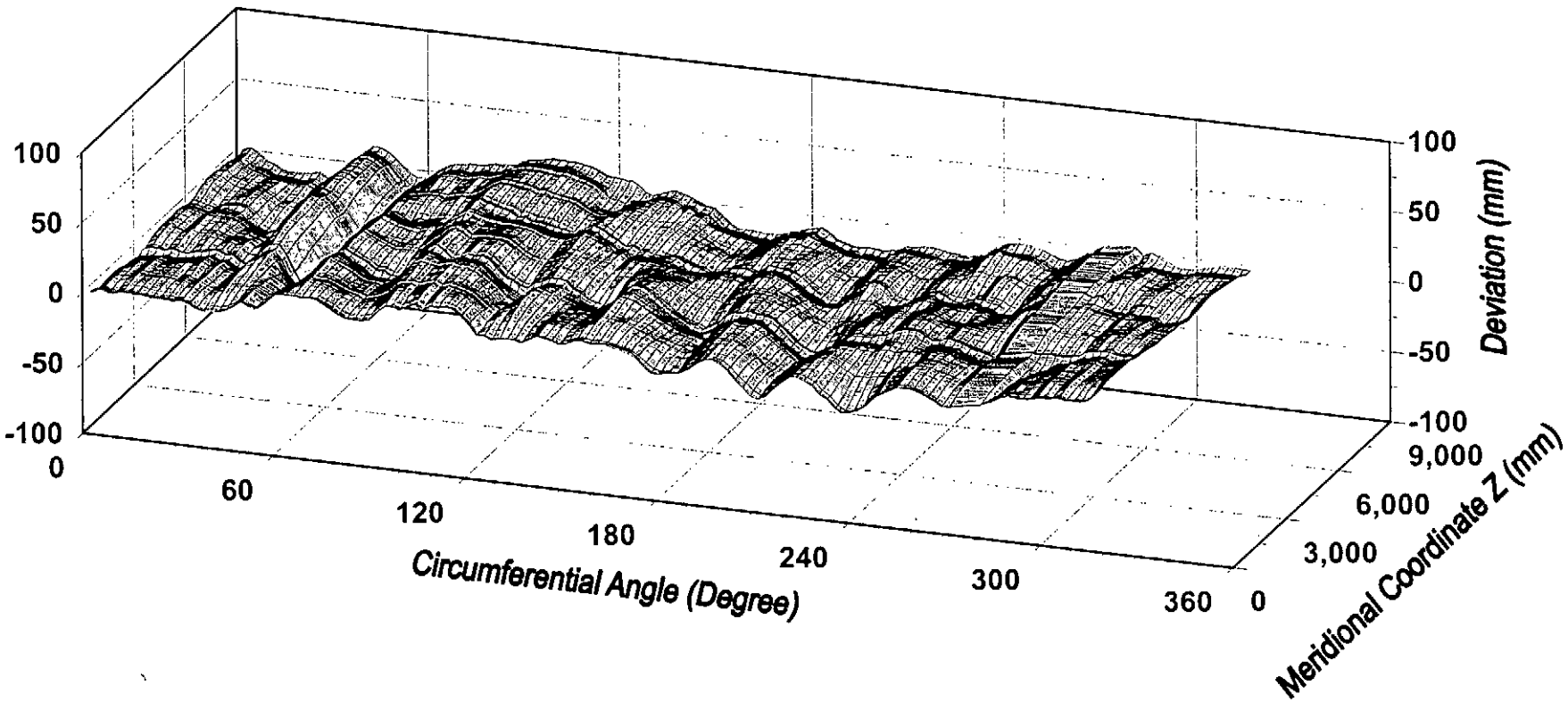

Figure 4.12 Nominal imperfections in Shell B

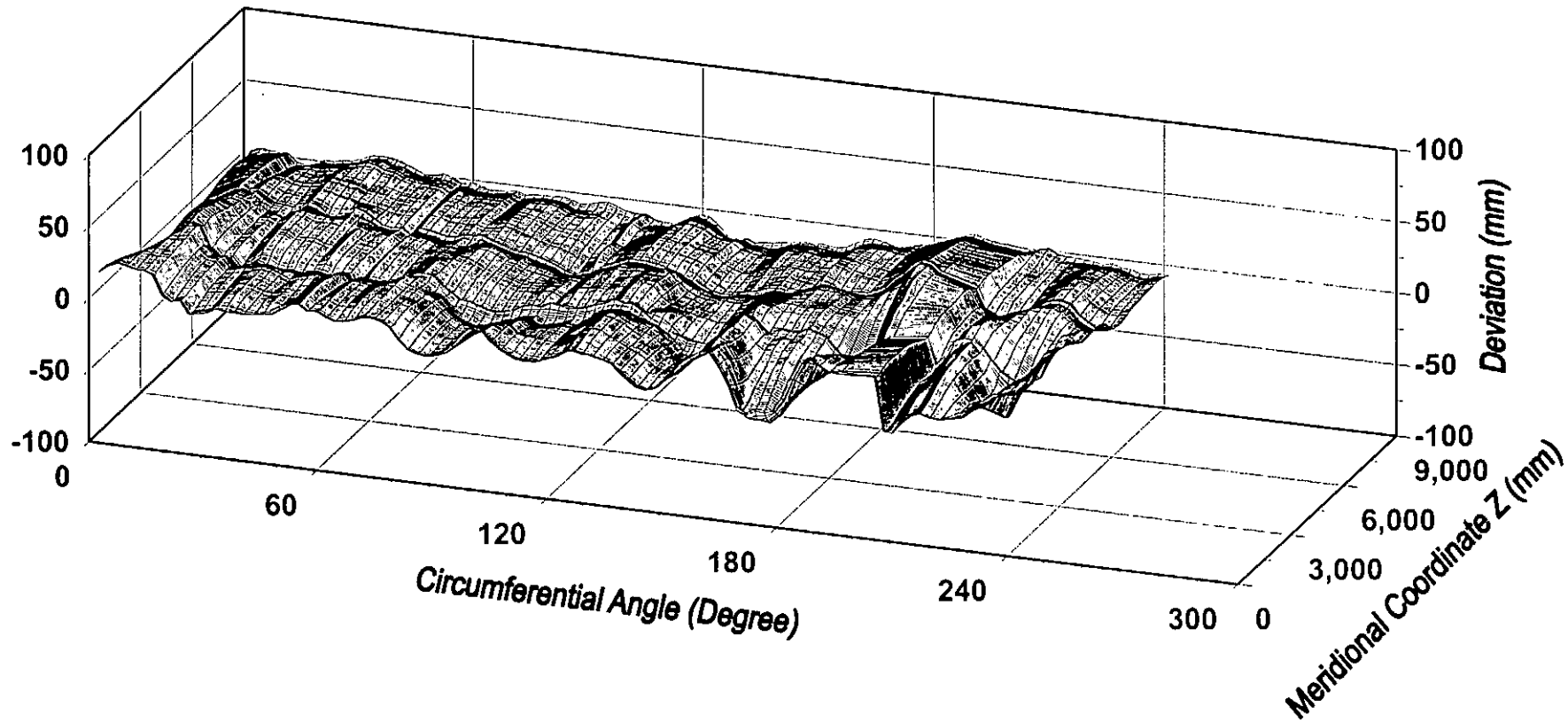

Figure 4.13 Nominal imperfections in Shell C

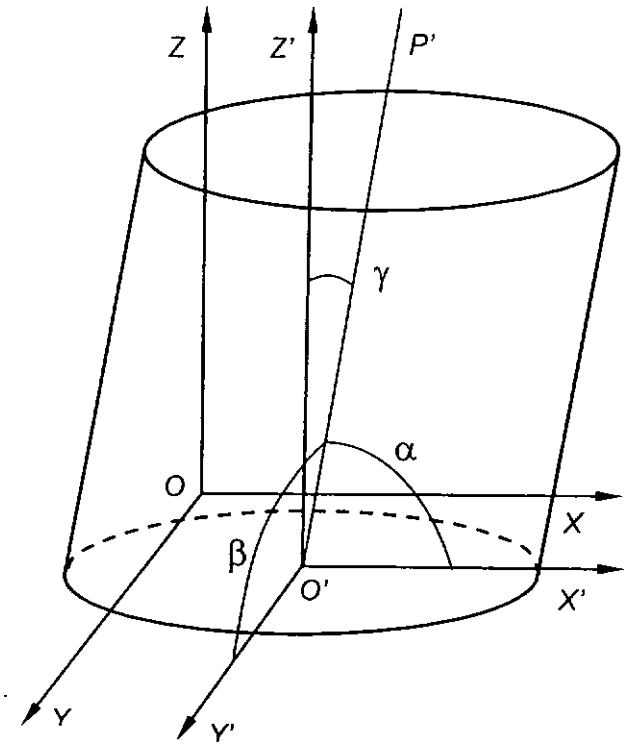

Figure 4.14 Definition of a best-fit cylinder

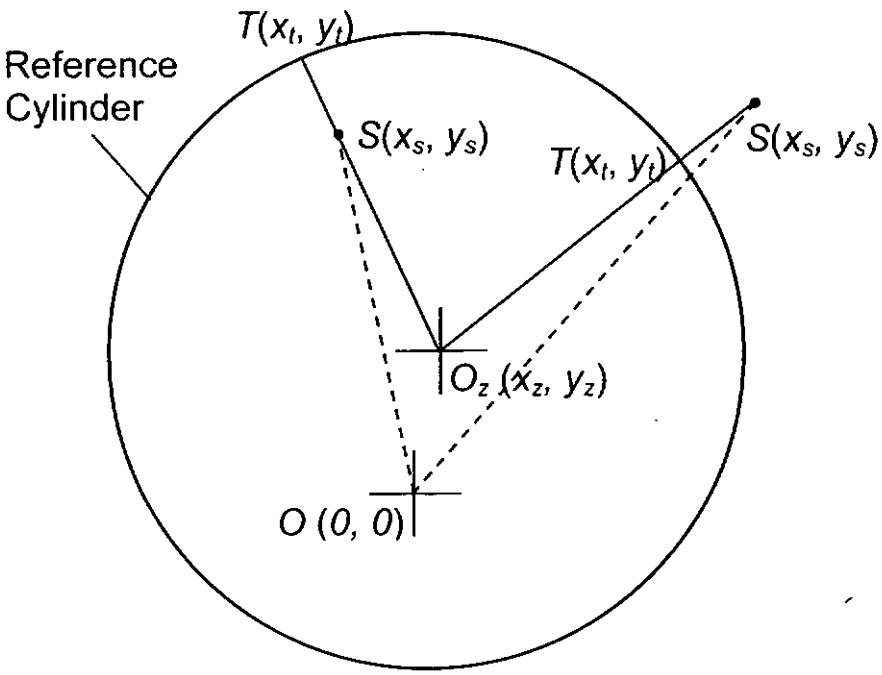

Figure 4.15 Deduction of 'real' imperfections

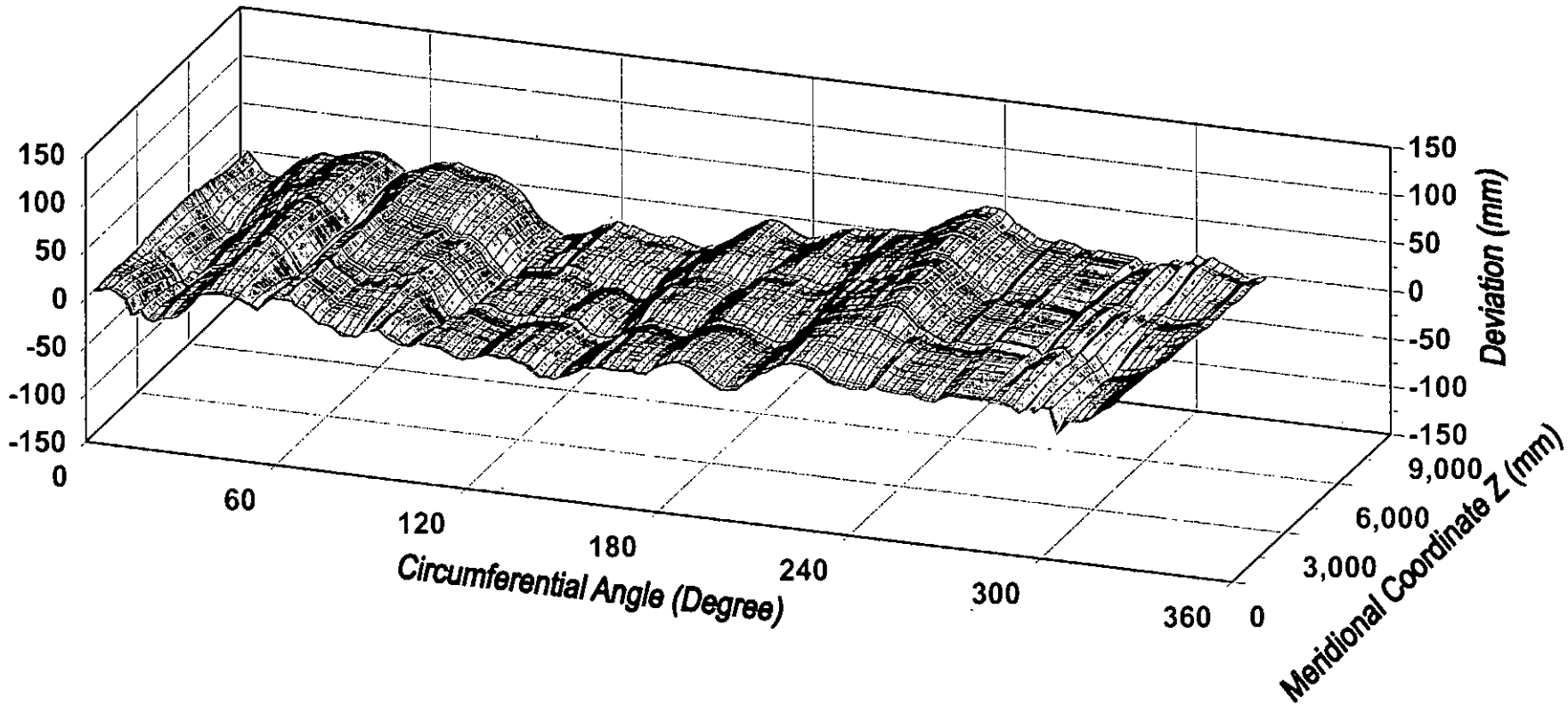

Figure 4.16 Real imperfections in Shell A

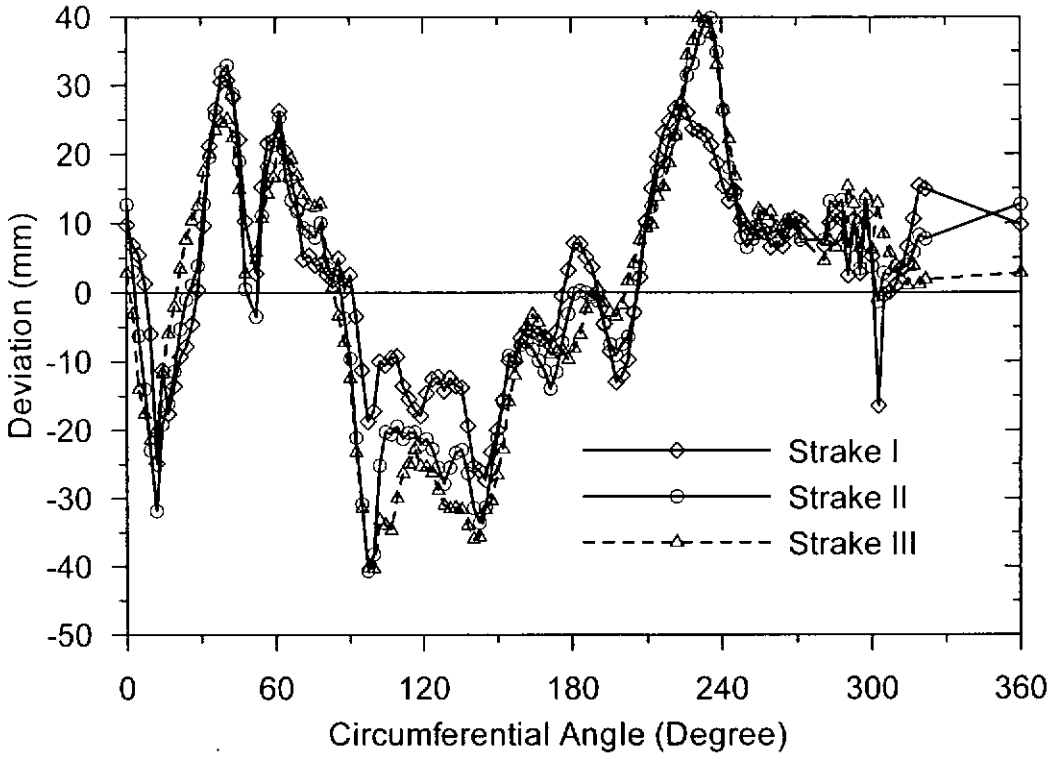

Figure 4.17 Imperfections on mid-strake circumferences of Shell A

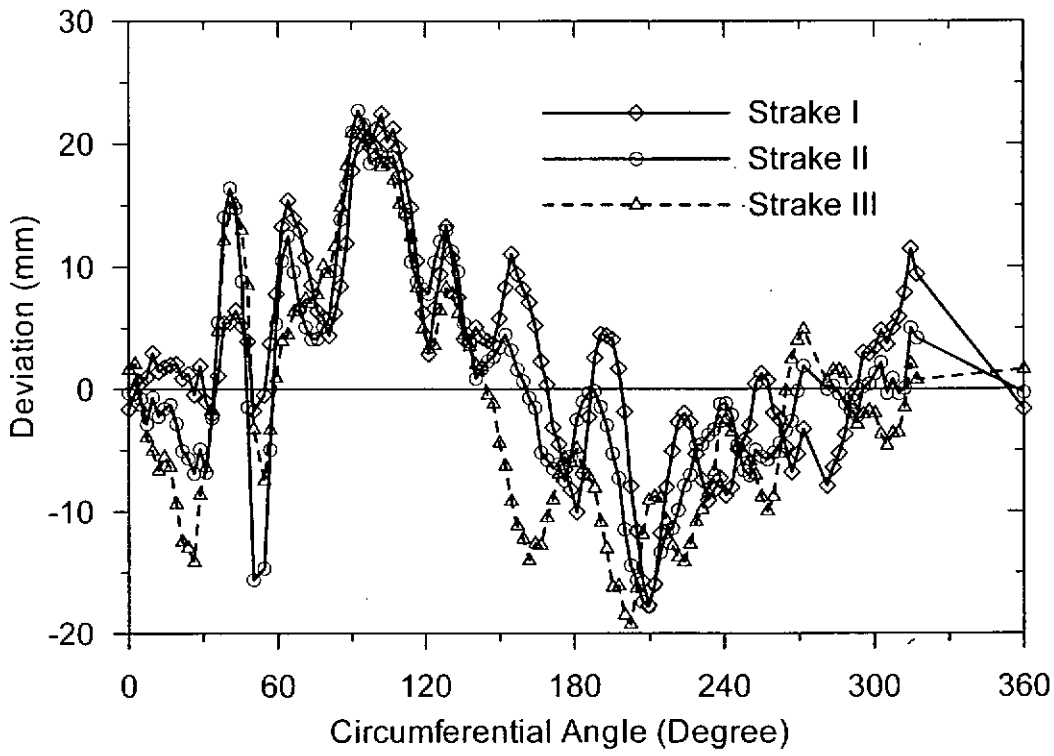

Figure 4.18 Imperfections on mid-strake circumferences of Shell B

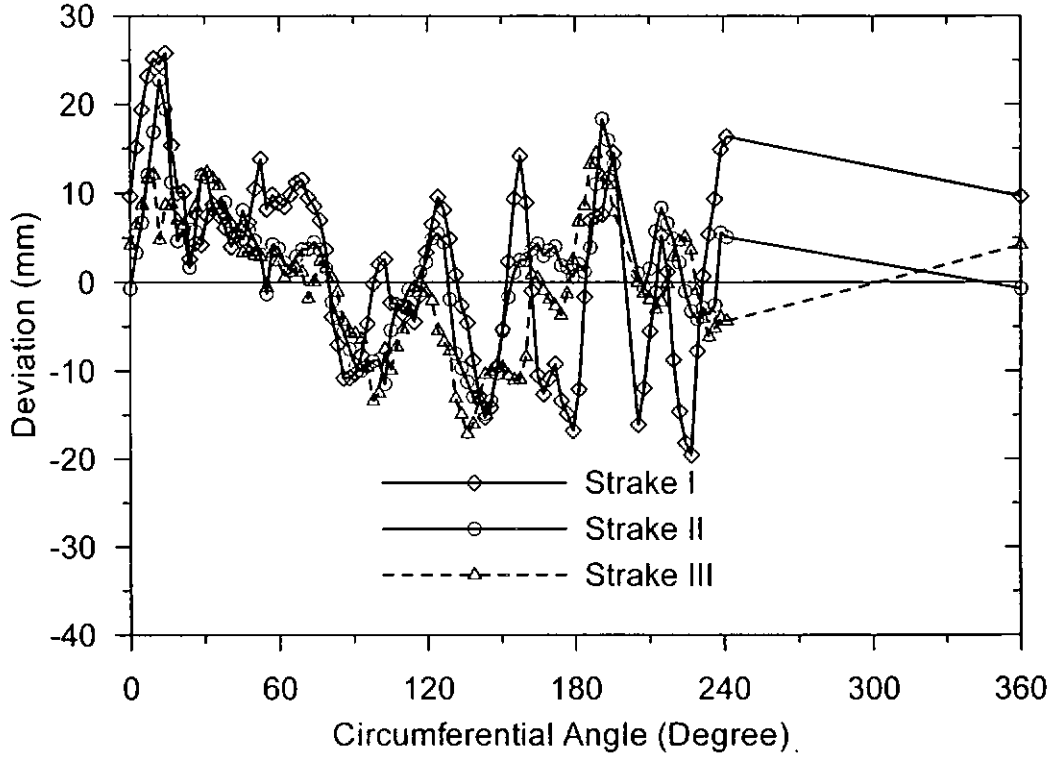

Figure 4.19 Imperfections on mid-strake circumferences of Shell C

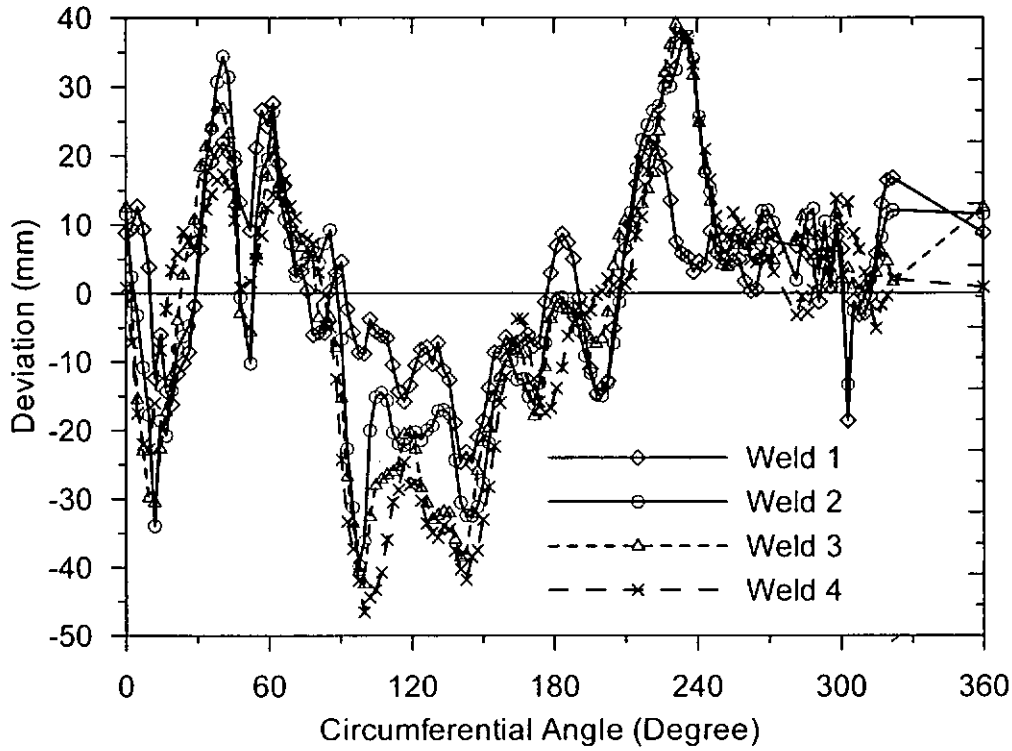

Figure 4.20 Imperfections on circumferential weld seams of Shell A

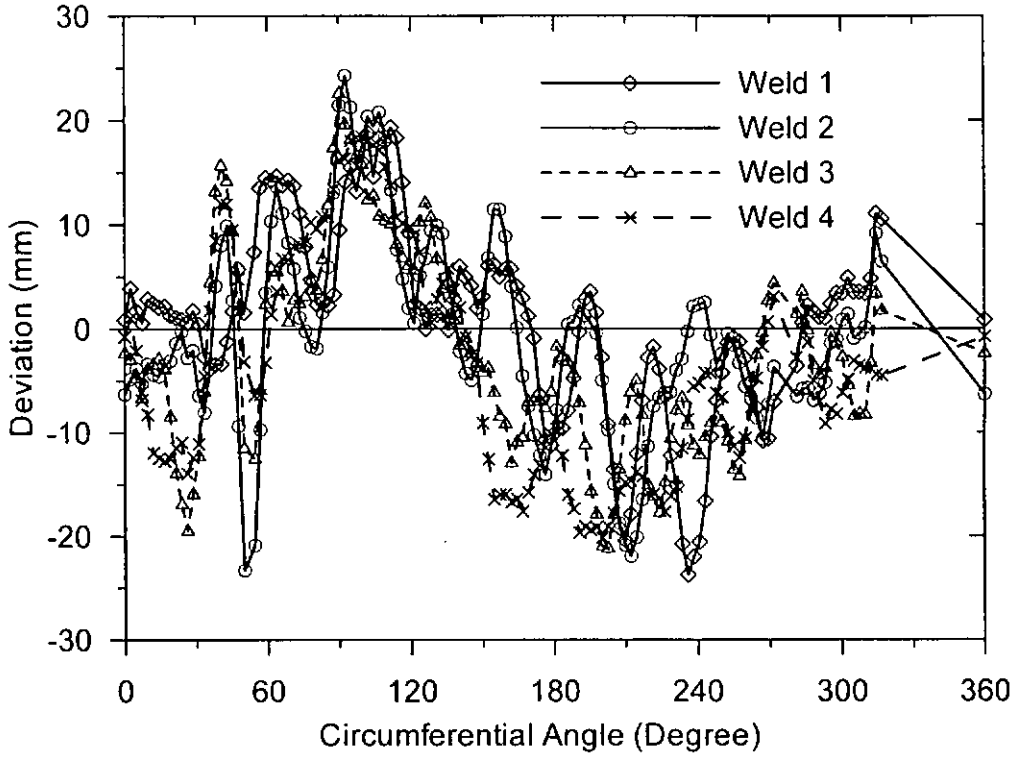

Figure 4.21 Imperfections on circumferential weld seams of Shell B

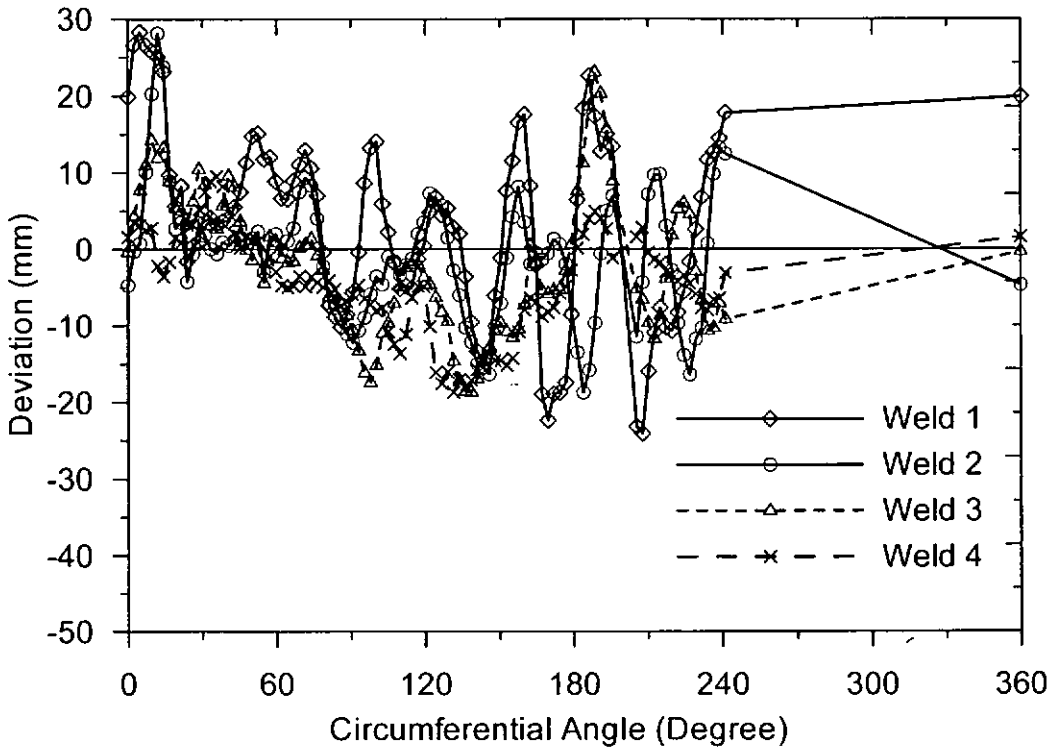

Figure 4.22 Imperfections on circumferential weld seams of Shell C

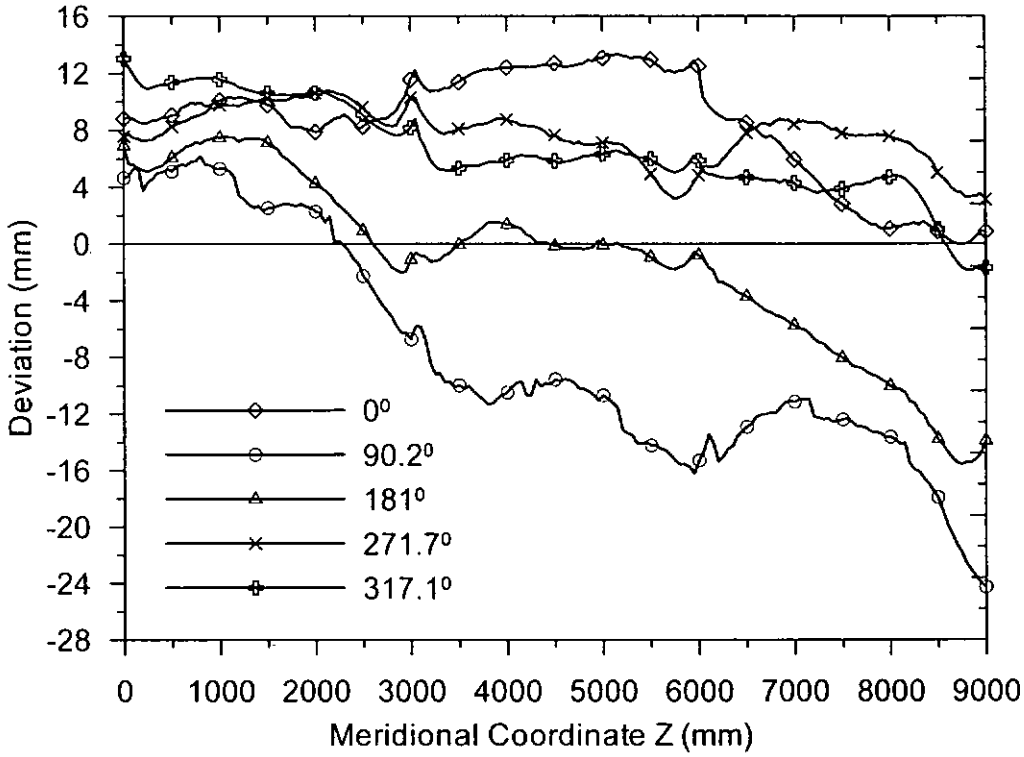

Figure 4.23 Imperfections on selected meridians of Shell A

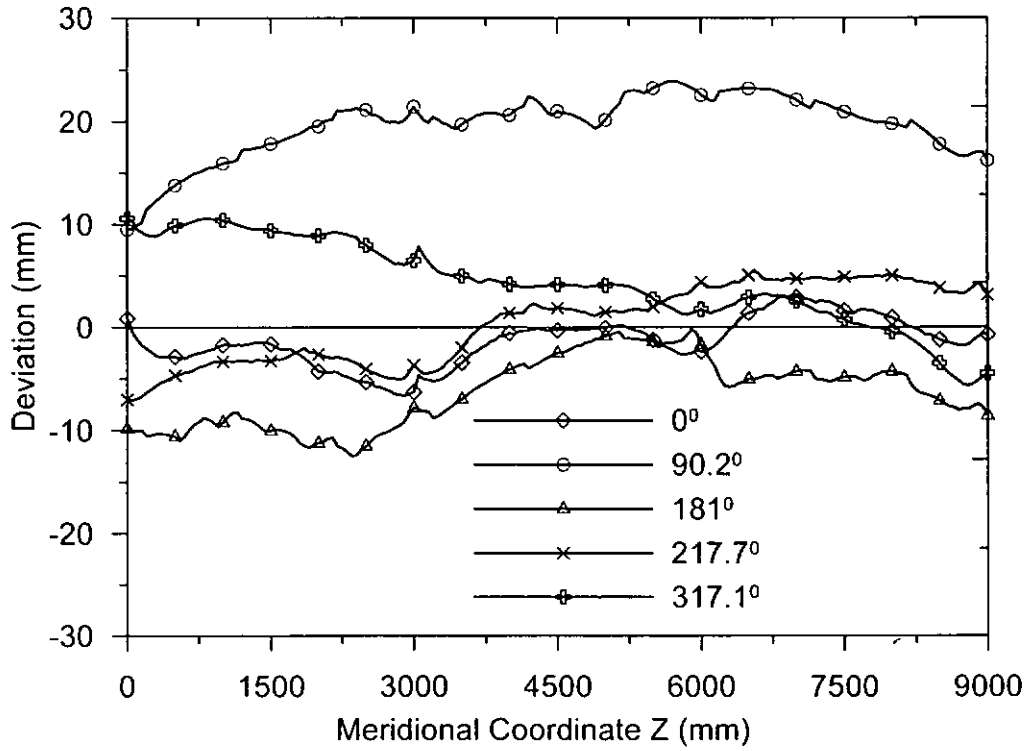

Figure 4.24 Imperfections on selected meridians of Shell B

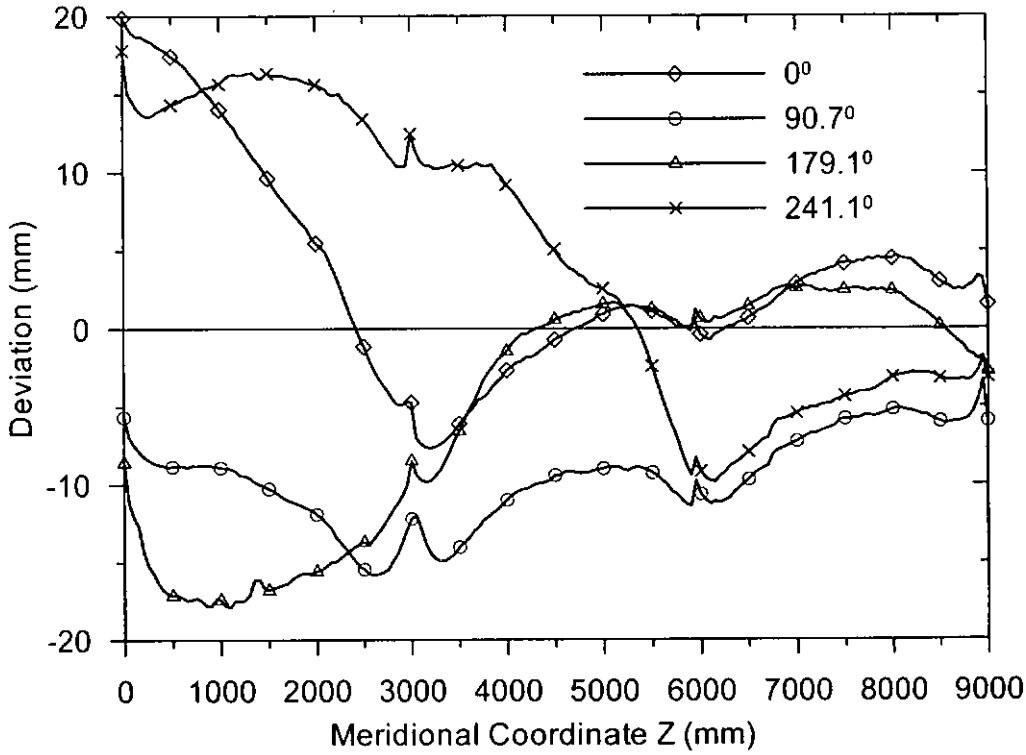

Figure 4.25 Imperfections on selected meridians of Shell C

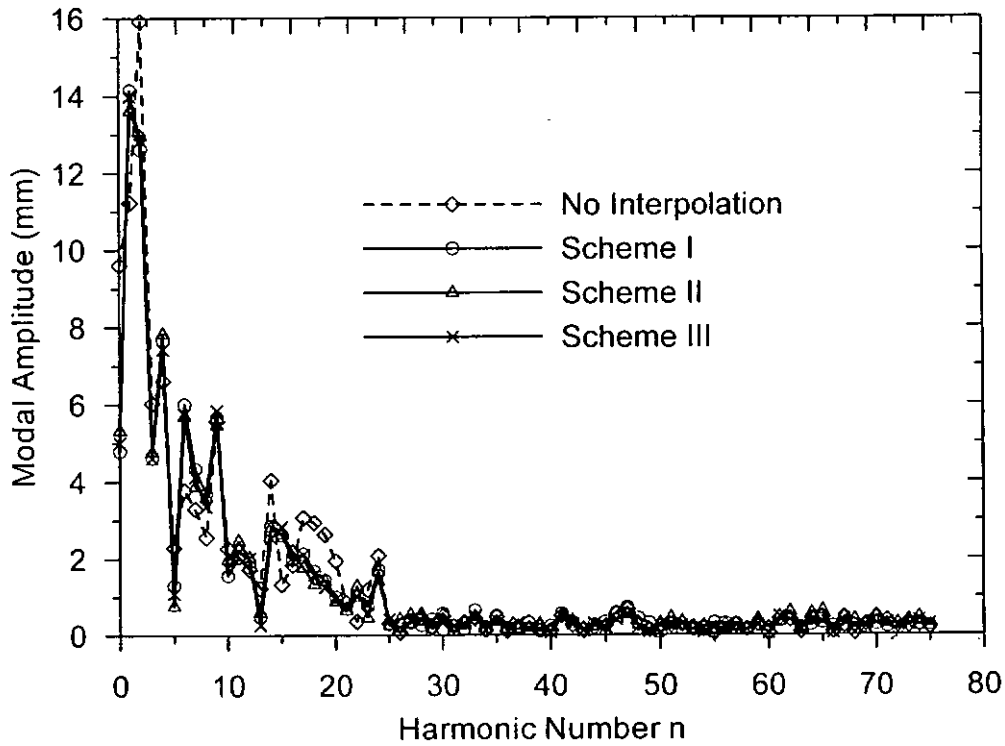

Figure 4.26 Spectra of Fourier series representing imperfections on Z=5.1m circumference of Shell A with different interpolation schemes

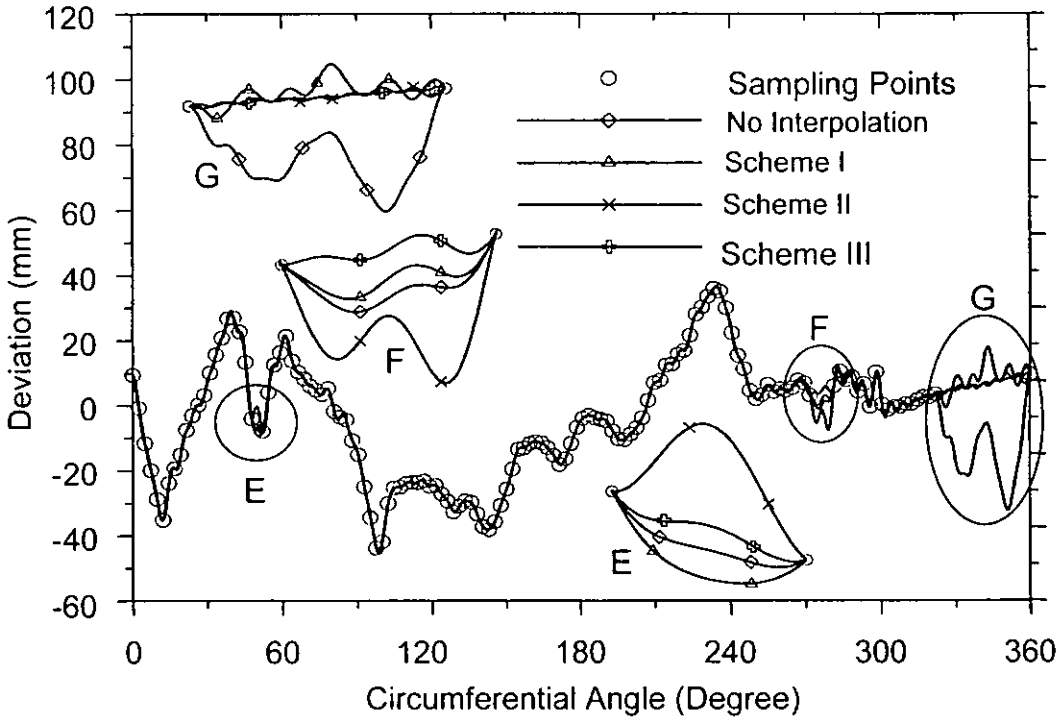

Figure 4.27 Circumferential distributions of Fourier series representing imperfections at the Z=5.1m circumference of Shell A with different interpolation schemes

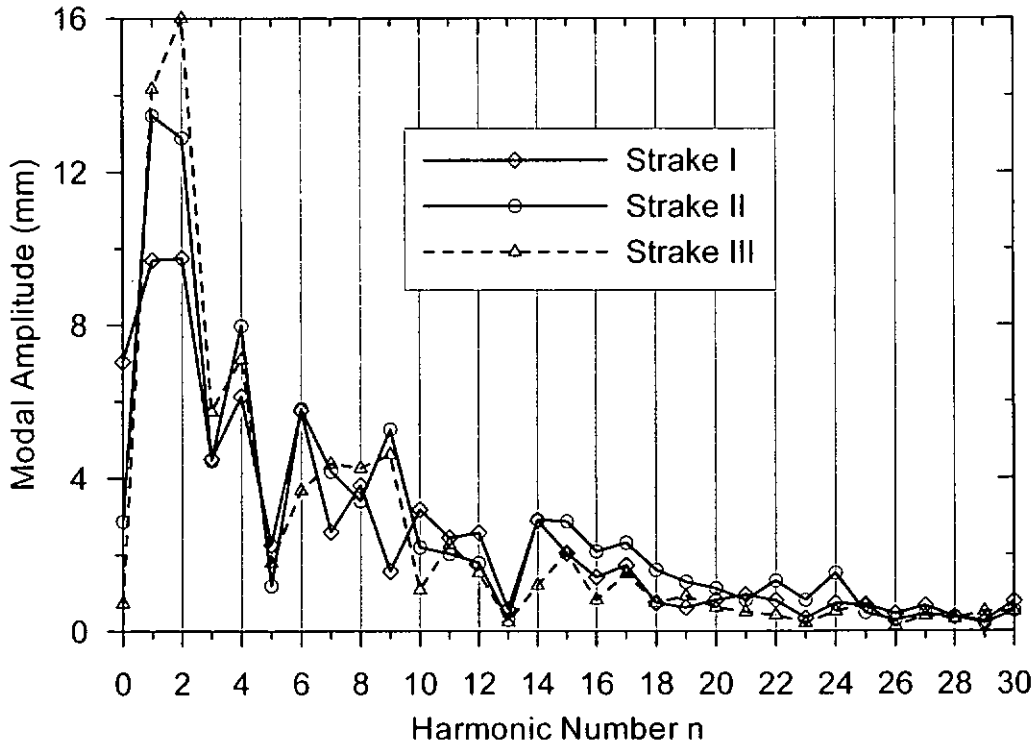

Figure 4.28 Spectra of Fourier series representing imperfections on the mid-strake circumferences of Shell A

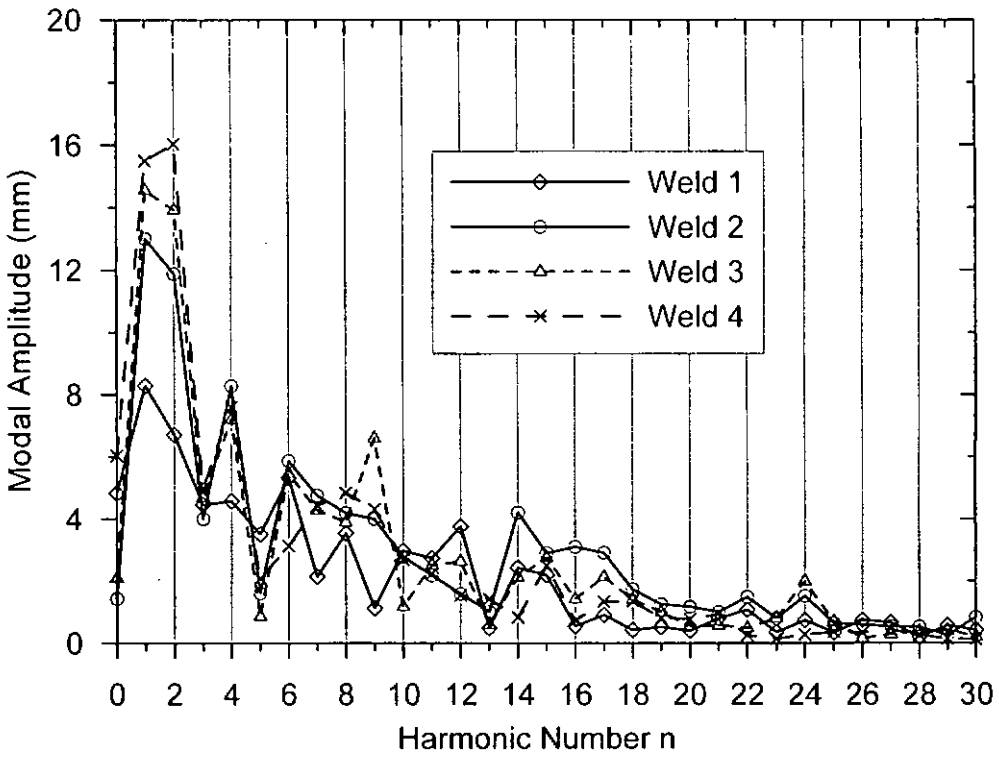

Figure 4.29 Spectra of Fourier series representing imperfections on the circumferential weld seams of Shell A

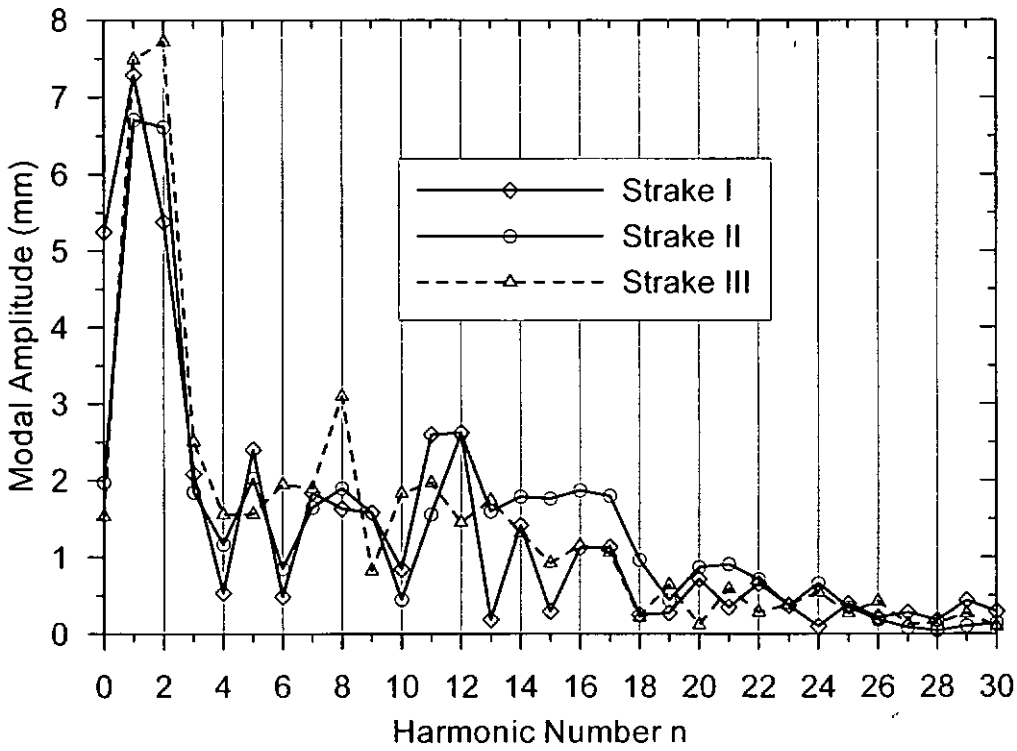

Figure 4.30 Spectra of Fourier series representing imperfections on the mid-strake circumferences of Shell B

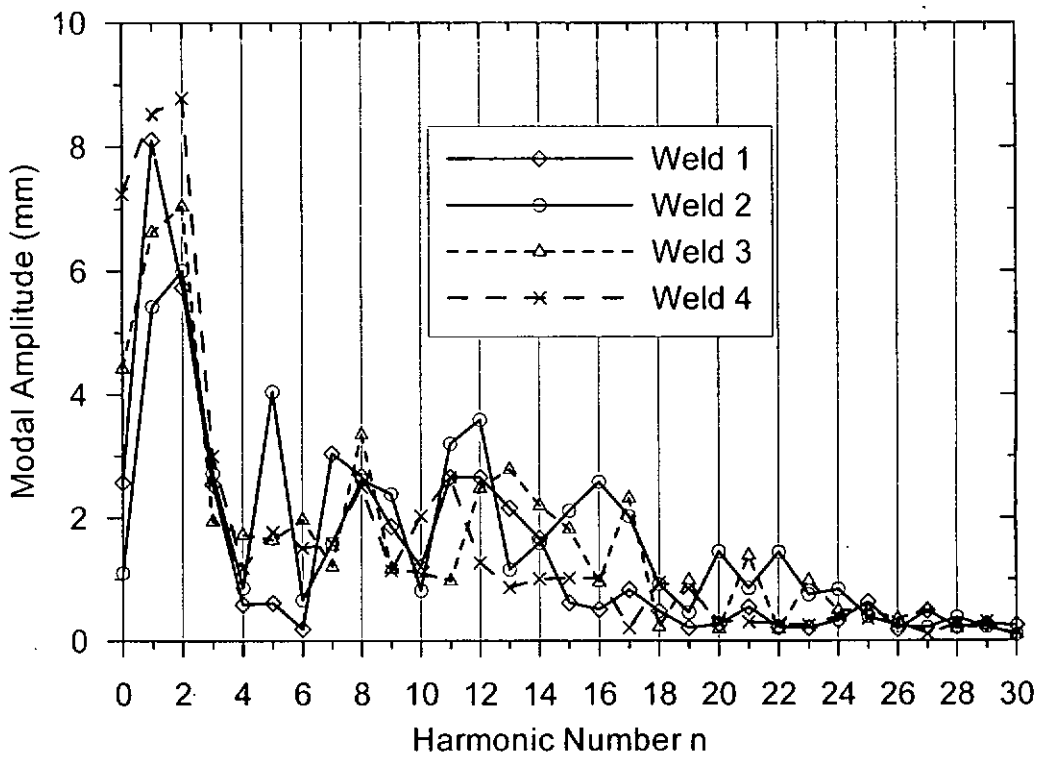

Figure 4.31 Spectra of Fourier series representing imperfections on the circumferential weld seams of Shell B

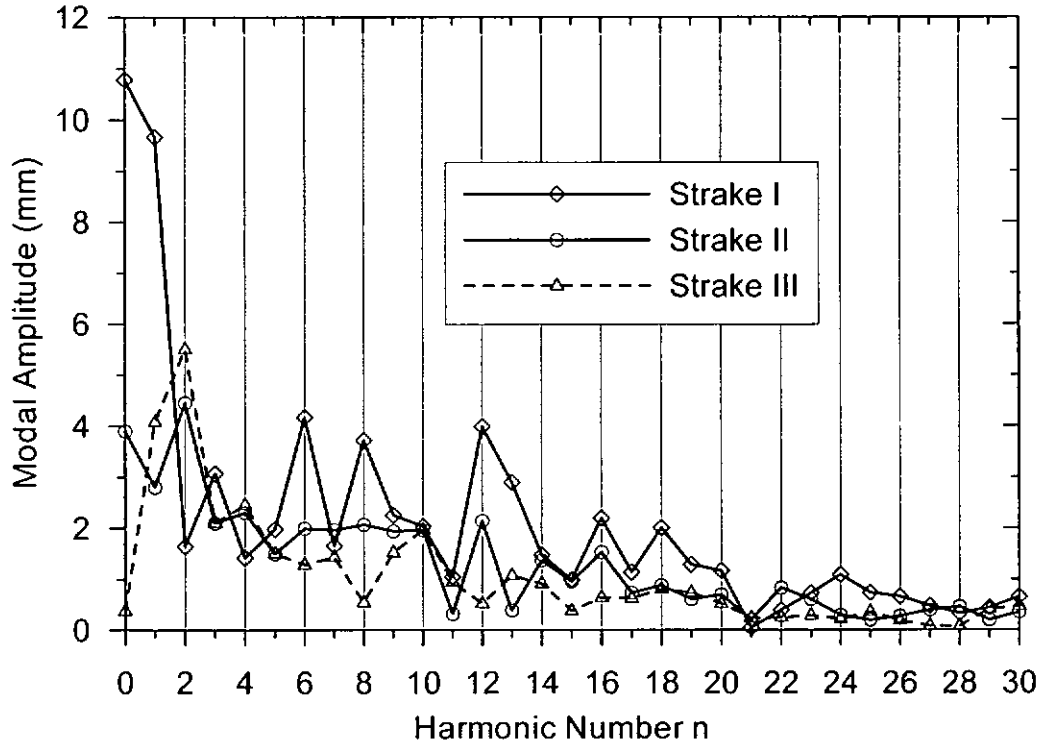

Figure 4.32 Spectra of Fourier series representing imperfections on the mid-strake circumferences of Shell C

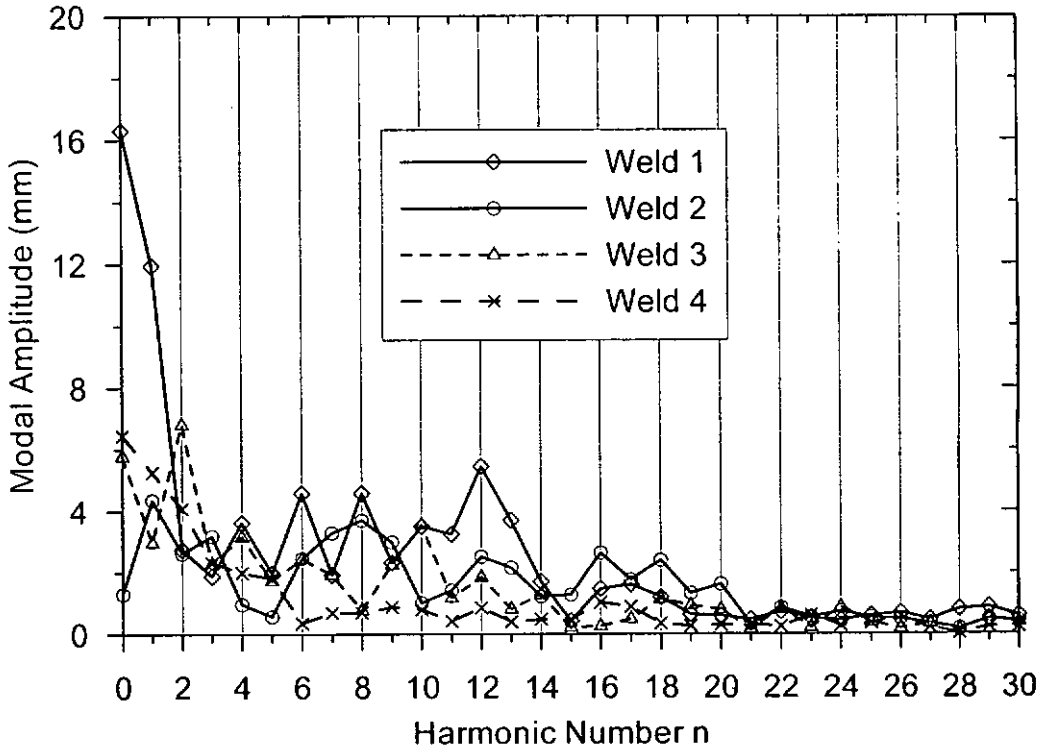

Figure 4.33 Spectra of Fourier series representing imperfections on the circumferential weld seams of Shell C

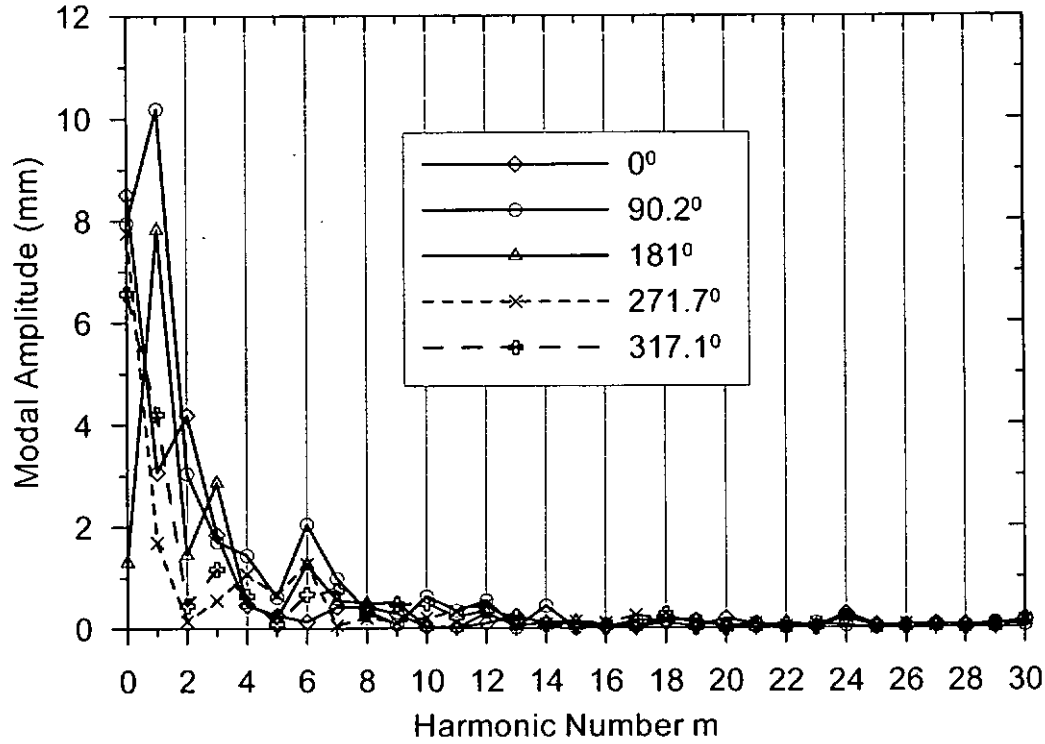

Figure 4.34 Spectra of Fourier series representing imperfections on selected meridians of Shell A

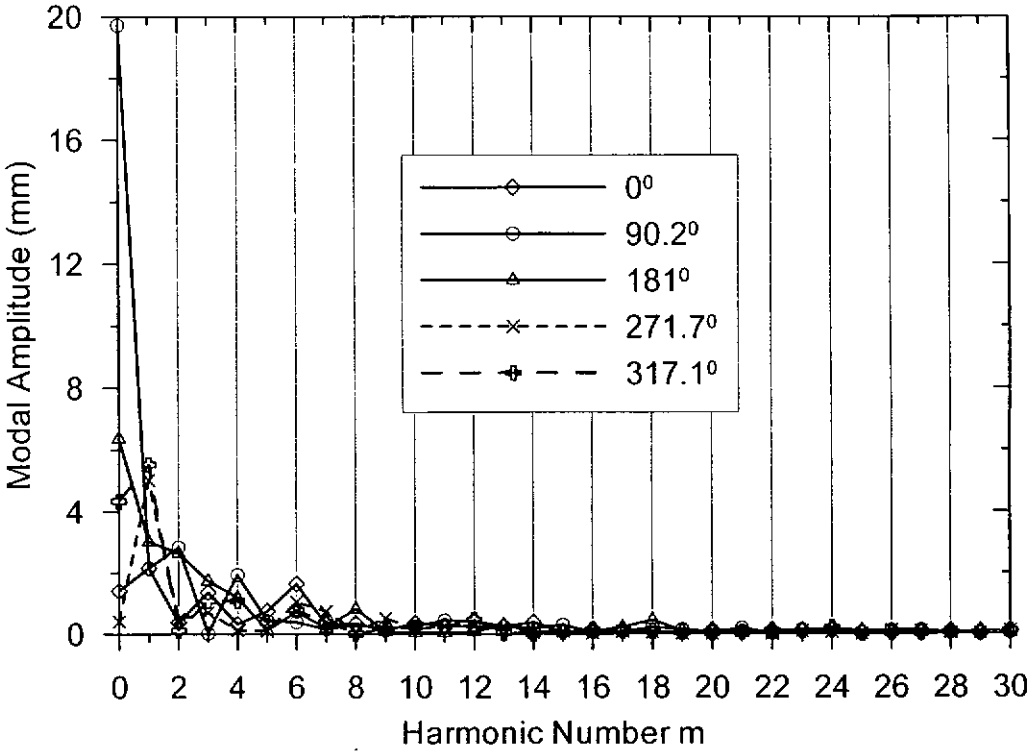

Figure 4.35 Spectra of Fourier series representing imperfections on selected meridians of Shell B

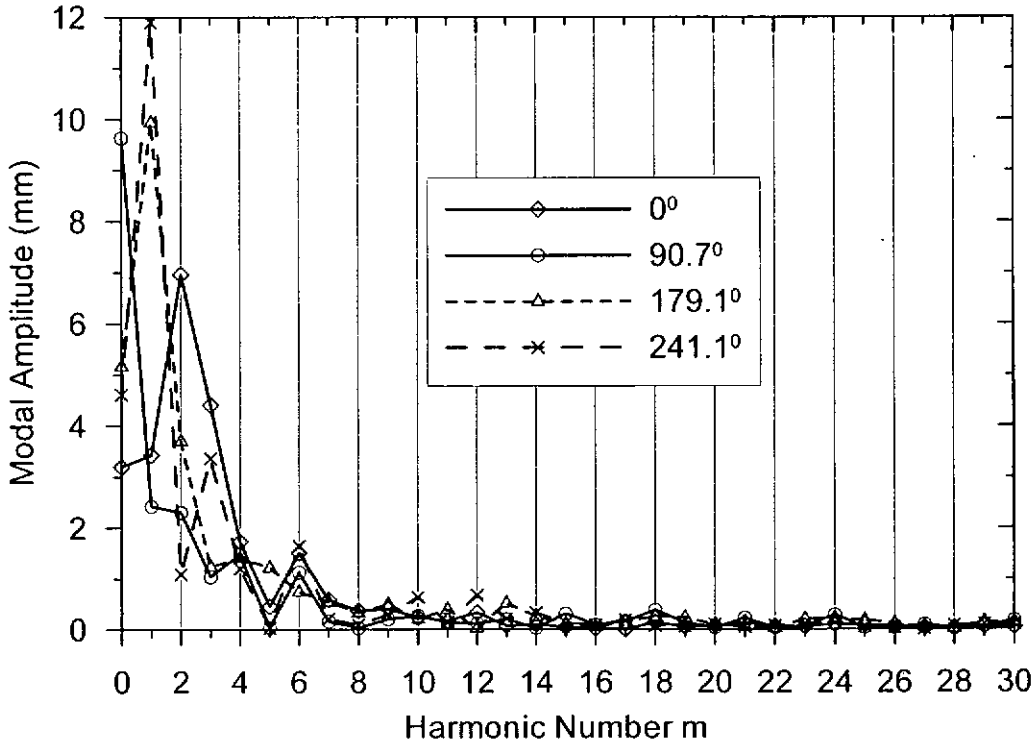

Figure 4.36 Spectra of Fourier series representing imperfections on selected meridians of Shell C

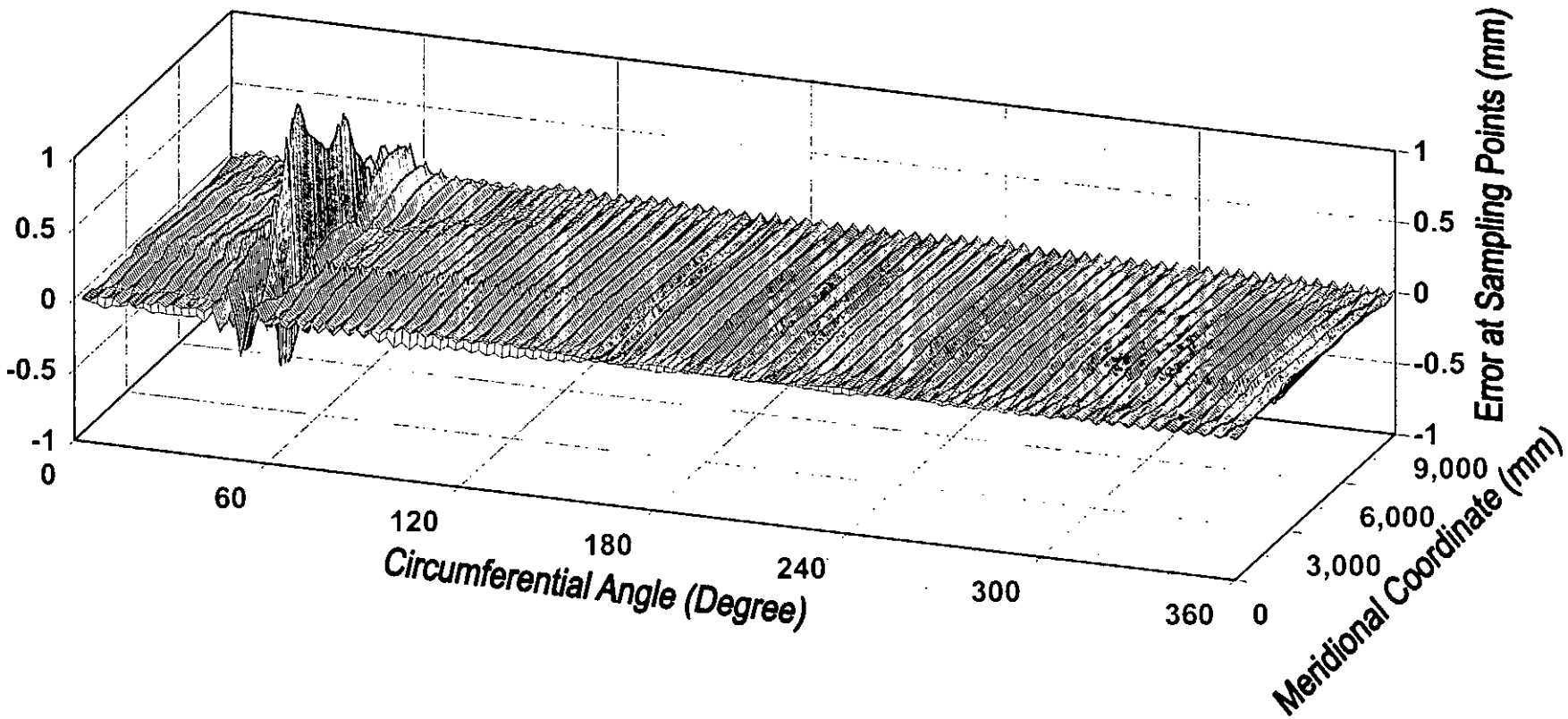

Figure 4.37 Errors of the Fourier series at the sampling points of Shell A after one iteration

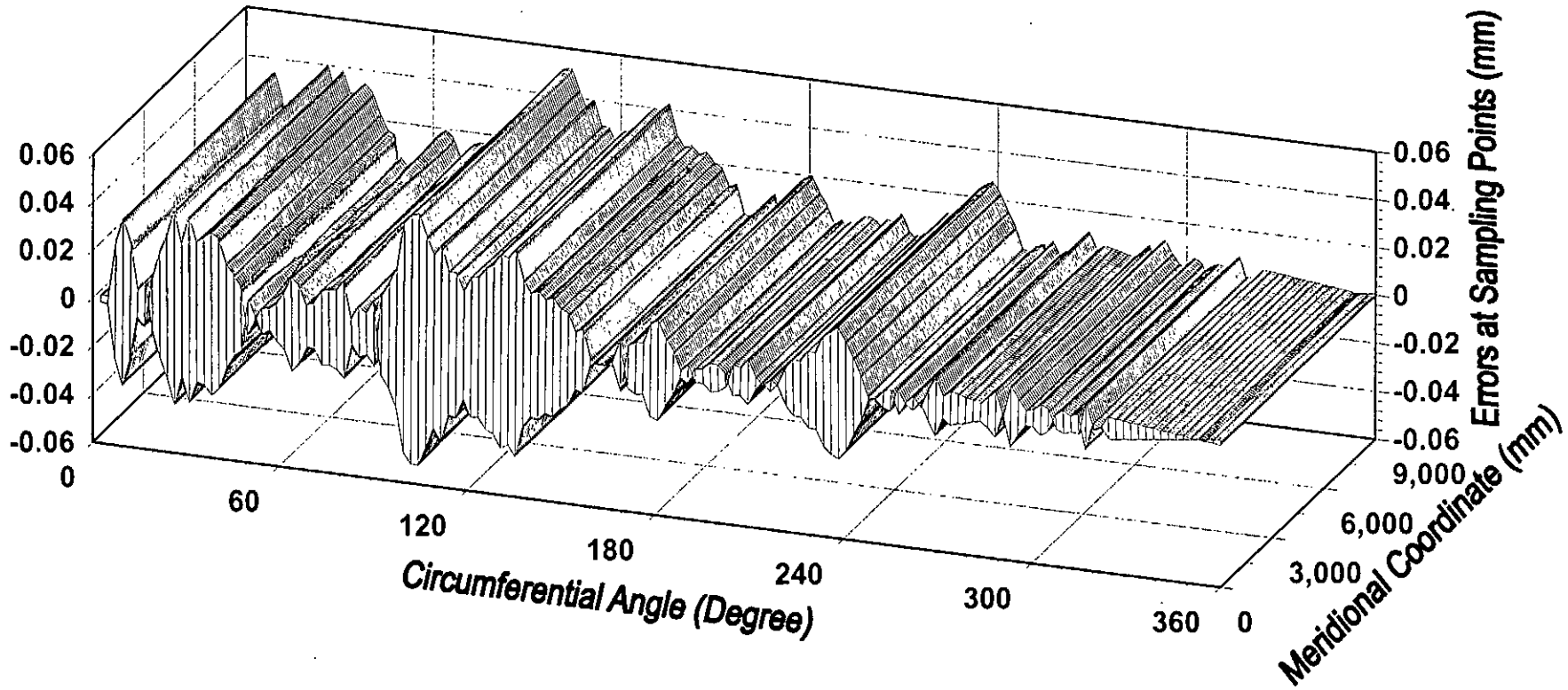

Figure 4.38 Errors of the Fourier series at the sampling points of Shell A after 5 iterations

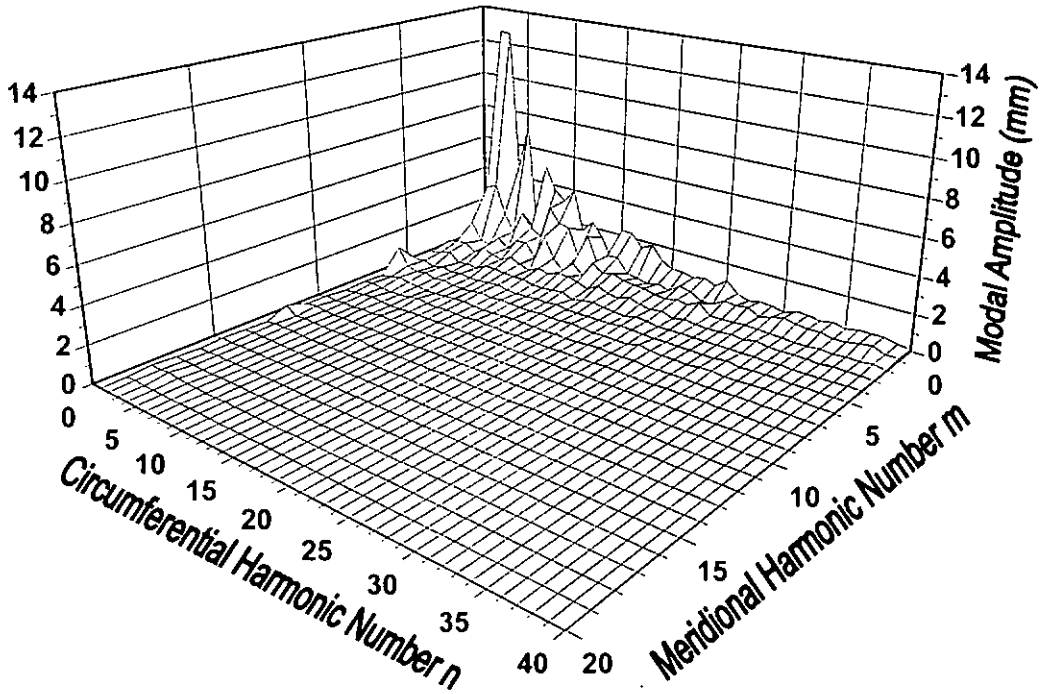

Figure 4.39 Spectrum of the double Fourier series representing imperfections in Shell A

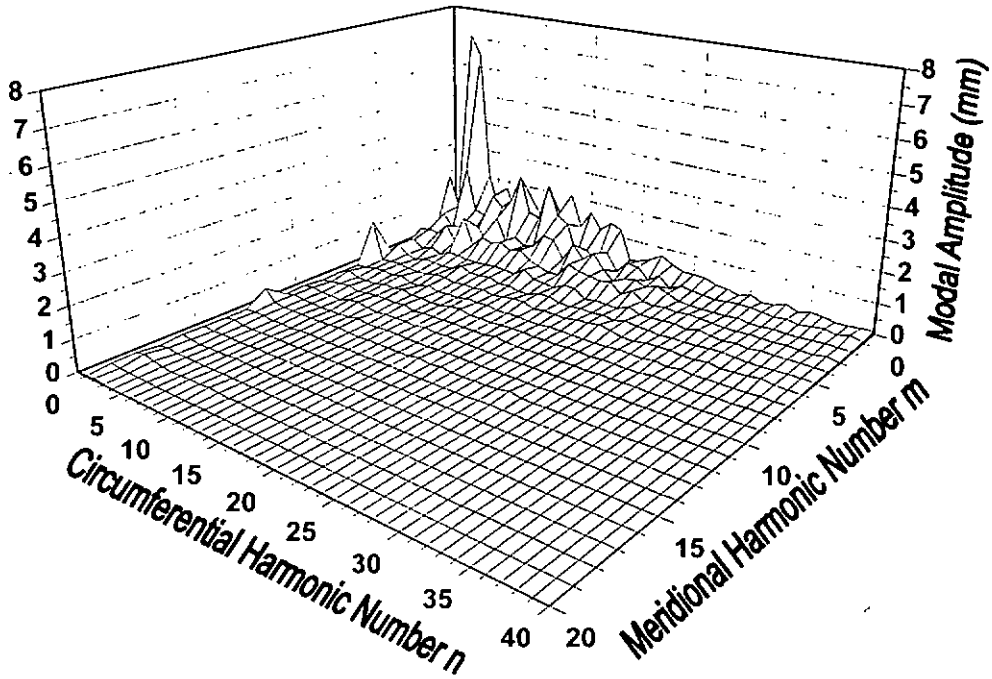

Figure 4.40 Spectrum of the double Fourier series representing imperfections in Shell B

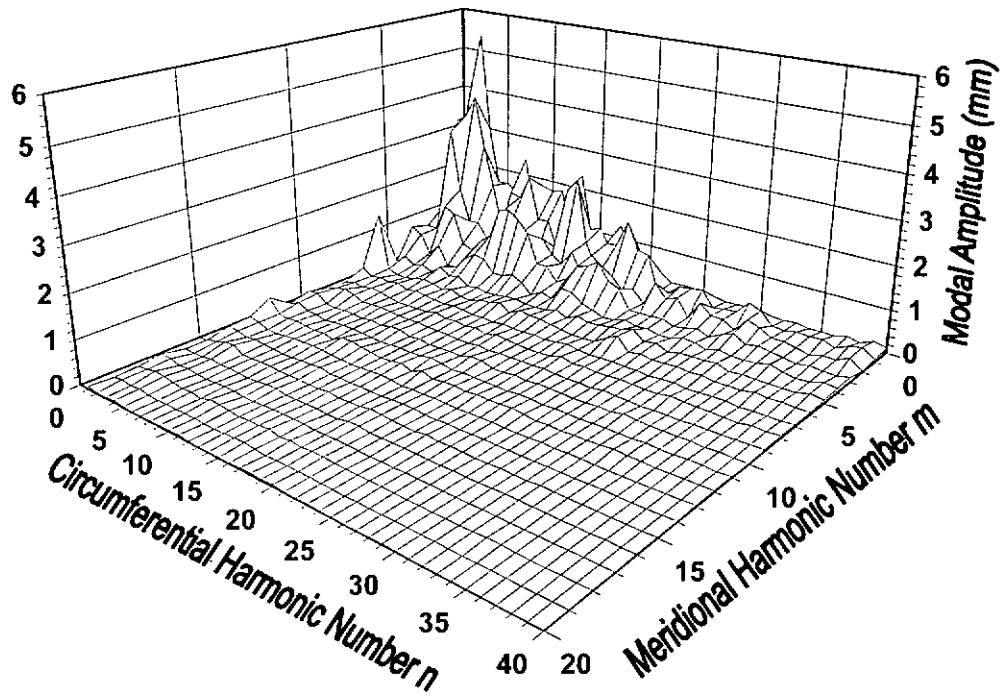

Figure 4.41 Spectrum of the double Fourier series representing imperfections in Shell C

APPENDICES

A4.1 ELEMENTS OF MATRIX $[H]$

$$h_{1i} = [(x_i - x_0 - \varsigma z_i)^2 + (y_i - y_0 - \rho z_i)^2 - R^2](x_i - x_0 - \varsigma z_i)$$

$$h_{2i} = [(x_i - x_0 - \varsigma z_i)^2 + (y_i - y_0 - \rho z_i)^2 - R^2](y_i - y_0 - \rho z_i)$$

$$h_{3i} = [(x_i - x_0 - \varsigma z_i)^2 + (y_i - y_0 - \rho z_i)^2 - R^2]R$$

$$h_{4i} = z_i[(x_i - x_0 - \varsigma z_i)^2 + (y_i - y_0 - \rho z_i)^2 - R^2](x_i - x_0 - \varsigma z_i)$$

$$h_{5i} = z_i[(x_i - x_0 - \varsigma z_i)^2 + (y_i - y_0 - \rho z_i)^2 - R^2](y_i - y_0 - \rho z_i)$$

A4.2 ELEMENTS OF MATRIX $[J^{j-1}]$

$$\frac{\partial h_{1i}^{j-1}}{\partial x_0} = -3(x_i - x_0^{j-1} - \varsigma^{j-1} z_i)^2 - (y_i - y_0^{j-1} - \rho^{j-1} z_i)^2 + (R^{j-1})^2$$

$$\frac{\partial h_{1i}^{j-1}}{\partial y_0} = -2(x_i - x_0^{j-1} - \varsigma^{j-1} z_i)(y_i - y_0^{j-1} - \rho^{j-1} z_i)$$

$$\frac{\partial h_{1i}^{j-1}}{\partial R} = -2R^{j-1}(x_i - x_0^{j-1} - \varsigma^{j-1} z_i)$$

$$\frac{\partial h_{1i}^{j-1}}{\partial \varsigma} = -3z_i(x_i - x_0^{j-1} - \varsigma^{j-1} z_i)^2 - z_i(y_i - y_0^{j-1} - \rho^{j-1} z_i)^2 + z_i(R^{j-1})^2$$

$$\frac{\partial h_{1i}^{j-1}}{\partial \rho} = -2z_i(x_i - x_0^{j-1} - \varsigma^{j-1} z_i)(y_i - y_0^{j-1} - \rho^{j-1} z_i)$$

$$\frac{\partial h_{2i}^{j-1}}{\partial x_0} = -2(x_i - x_0^{j-1} - \varsigma^{j-1} z_i)(y_i - y_0^{j-1} - \rho^{j-1} z_i)$$

$$\frac{\partial h_{2i}^{j-1}}{\partial y_0} = -(x_i - x_0^{j-1} - \varsigma^{j-1} z_i)^2 - 3(y_i - y_0^{j-1} - \rho^{j-1} z_i)^2 + (R^{j-1})^2$$

$$\frac{\partial h_{2i}^{j-1}}{\partial R} = -2R^{j-1}(y_i - y_0^{j-1} - \rho^{j-1} z_i)$$

$$\frac{\partial h_{2i}^{j-1}}{\partial \varsigma} = -2z_i(x_i - x_0^{j-1} - \varsigma^{j-1} z_i)(y_i - y_0^{j-1} - \rho^{j-1} z_i)$$

$$\frac{\partial h_{2i}^{j-1}}{\partial \rho} = -z_i(x_i - x_0^{j-1} - \varsigma^{j-1} z_i)^2 - 3z_i(y_i - y_0^{j-1} - \rho^{j-1} z_i)^2 + z_i(R^{j-1})^2$$

$$\frac{\partial h_{3i}^{j-1}}{\partial x_0} = -2R^{j-1}(x_i - x_0^{j-1} - \varsigma^{j-1} z_i)$$

$$\frac{\partial h_{3i}^{j-1}}{\partial y_0} = -2R^{j-1}(y_i - y_0^{j-1} - \rho^{j-1} z_i)$$

$$\frac{\partial h_{3i}^{j-1}}{\partial R} = (x_i - x_0^{j-1} - \varsigma^{j-1} z_i)^2 + (y_i - y_0 - \rho^{j-1} z_i)^2 - 3(R^{j-1})^2$$

$$\frac{\partial h_{3i}^{j-1}}{\partial \varsigma} = -2z_i R^{j-1}(x_i - x_0^{j-1} - \varsigma^{j-1} z_i)$$

$$\frac{\partial h_{3i}^{j-1}}{\partial \rho} = -2z_i R^{j-1}(y_i - y_0^{j-1} - \rho^{j-1} z_i)$$

$$\frac{\partial h_{4i}^{j-1}}{\partial x_0} = -3z_i(x_i - x_0^{j-1} - \varsigma^{j-1} z_i)^2 - z_i(y_i - y_0^{j-1} - \rho^{j-1} z_i)^2 + z_i(R^{j-1})^2$$

$$\frac{\partial h_{4i}^{j-1}}{\partial y_0} = -2z_i(x_i - x_0^{j-1} - \varsigma^{j-1} z_i)(y_i - y_0^{j-1} - \rho^{j-1} z_i)$$

$$\frac{\partial h_{4i}^{j-1}}{\partial R} = -2z_i R^{j-1}(x_i - x_0^{j-1} - \varsigma^{j-1} z_i)$$

$$\frac{\partial h_{4i}^{j-1}}{\partial \varsigma} = -3z_i^2(x_i - x_0^{j-1} - \varsigma^{j-1} z_i)^2 - z_i^2(y_i - y_0^{j-1} - \rho^{j-1} z_i)^2 + z_i^2(R^{j-1})^2$$

$$\frac{\partial h_{4i}^{j-1}}{\partial \rho} = -2z_i^2(x_i - x_0^{j-1} - \varsigma^{j-1} z_i)(y_i - y_0^{j-1} - \rho^{j-1} z_i)$$

$$\frac{\partial h_{5i}^{j-1}}{\partial x_0} = -2z_i(x_i - x_0^{j-1} - \varsigma^{j-1} z_i)(y_i - y_0^{j-1} - \rho^{j-1} z_i)$$

$$\frac{\partial h_{5i}^{j-1}}{\partial y_0} = -z_i(x_i - x_0^{j-1} - \xi^{j-1} z_i)^2 - 3z_i(y_i - y_0^{j-1} - \rho^{j-1} z_i)^2 + z_i(R^{j-1})^2$$

$$\frac{\partial h_{5i}^{j-1}}{\partial R} = -2z_i R^{j-1}(y_i - y_0^{j-1} - \rho^{j-1} z_i)$$

$$\frac{\partial h_{5i}^{j-1}}{\partial \varsigma} = -2z_i^2(x_i - x_0^{j-1} - \varsigma^{j-1} z_i)(y_i - y_0^{j-1} - \rho^{j-1} z_i)$$

$$\frac{\partial h_{5i}^{j-1}}{\partial \rho} = -z_i^2(x_i - x_0^{j-1} - \varsigma^{j-1} z_i)^2 - 3z_i^2(y_i - y_0^{j-1} - \rho^{j-1} z_i)^2 + z_i^2(R^{j-1})^2$$

CHAPTER 5

BUCKLING BEHAVIOR OF LARGE EXTENSIVELY WELDED STEEL CYLINDERS WITH MEASURED GEOMETRIC IMPERFECTIONS

5.1 INTRODUCTION

Cylindrical shells in steel silos are subject to axial compressive stresses in the wall, and buckling under axial compression is normally the controlling failure mode. As noted previously, the buckling behavior of cylindrical shells is strongly dependent on both the form and amplitude of the imperfection in the shell. The analysis of imperfections in the cylindrical shells in the three large steel silos at Port Kembla in Australia presented in Chapter 4 revealed that the imperfections in such shells are very complicated as the shells are constructed by the panel method, in which a large number of rolled panels are connected with many short meridional welds and continuous circumferential welds. Most existing studies have been concerned with either asymmetric imperfections due to meridional welds (e.g. Arbocz and Babcock, 1969; Arbocz, 1974) or axisymmetric imperfections due to circumferential welds (e.g. Rotter and Teng, 1989; Pircher and Bridge, 2001b). Two existing studies on the buckling behavior of shells built with the panel method suggested that imperfections in such shells are more detrimental to the buckling strength than those of other forms (Schmidt and Swadlo, 1996; Hübner *et al*, 2003a). Nevertheless, Schmidt and Swadlo adopted an unrealistic process in the fabrication of their test specimens, while Hübner *et al* omitted imperfections from sources other than welding. Therefore, further studies need to be carried out to explore the effect of this form of imperfections on the buckling behavior of cylindrical shells. This chapter presents the first systematic study into the buckling behavior of such shells, and this is accomplished by analyzing the buckling behavior of the cylindrical shells in the three

large steel silos at Port Kembla, using the precisely measured geometric imperfections in these silos (Ding, 1992).

In this chapter, Fourier representations of the measured imperfections for use in finite element analysis are first discussed. Results from both linear and nonlinear finite element buckling analyses are next presented to study the effect of these real imperfections on buckling behavior. The finite element results were obtained using the general-purpose finite element package ABAQUS (Hibbit Karlsson & Sorensen, 1998), which has been employed in many shell buckling studies (e.g. Holst *et al*, 1999, 2000; Goto and Zhang, 1999; Mandal and Calladine, 2000; Pircher and Bridge, 2001a, 2001b; Teng and Song, 2001; Zhao and Teng, 2001; Zhu *et al*, 2002). In addition, a systematic investigation to identify those imperfection components which are responsible for most of the shell buckling strength reduction is also presented.

In Eurocode 3, the buckling strength of a shell is related to its fabrication quality characterized by three types of tolerance parameters. In this chapter, a numerical procedure for the determination of quality classes of the three Port Kembla silos using the measured imperfections is presented and the quality classes of these shells clarified. Buckling load predictions are then made using the Eurocode and these are compared with predictions from numerical buckling analyses.

5.2 IMPERFECTION REPRESENTATIONS

The detailed configurations of the three large steel silos (referred to as silos A, B and C) are given in Chapter 4. Due to the presence of various accessories on the walls, the imperfections in some parts of the silo surfaces were not measured. For silos A and B, imperfections were measured on the outer surface in three zones (namely, Zone I, Zone II, and Zone III), while for silo C, imperfections were measured in two zones (namely, Zone I and Zone II). The measurements were taken at a meridional spacing l_{mx} of 50 mm ($l_{mx}/\sqrt{Rt} = 0.132$) and a circumferential spacing $l_{m\theta}$ of $500mm$ ($l_{m\theta}/\sqrt{Rt} = 1.318$) (Ding, 1992). The surveyed zones measured and the un-surveyed zones (referred to as

gaps) between the measured zones are indicated in Figures 4.9(a), 4.9(b), and 4.9(c) as well as in Table 5.1.

In the present study into the buckling behavior of the silo shells, only the segment of the cylindrical wall in each silo with a constant thickness of 12mm is considered (the hatched zone in the Figure 5.1). The upper and lower ends of this segment are at 20.75m and 8.5m from the datum line located at 0.2m from the lowest circumferential weld shown in Figure 5.1. The upper edge of the segment corresponds to the highest point in the shell for which imperfection data exist for all three silos. The lower edge was chosen to cover the 12 mm panels as much as possible and to give an appropriate number of imperfection sampling points over the height of this segment for ease of subsequent finite element discretization. The chosen segment contains 241 sampling points over its height at an interval of 50mm, which can be used for four meshes with nearly square elements of $50mm$, $100mm$, $150mm$ and $200mm$ in size in finite element modeling. The three cylindrical segments from Silos A, B and C are directly referred to as Shells A, B and C respectively in subsequent discussions. It should be noted that these three shells are now slightly different from those defined in Chapter 4 where the emphasis was on the relationship between the patterns of welds and the distributions of imperfections.

The double Fourier series of Eqn 4.1 was employed to represent the imperfections in the three silo shells. Before undertaking the Fourier decomposition, polynomial interpolations were employed to filter out jumps in the imperfection data due to the deposited welding beads and linear interpolations were applied to produce data points in the gaps as explained in Chapter 4. The Iterative Fourier Decomposition Method presented in Chapter 3 was used to reduce the significant errors associated with conventional Fourier decompositions as a result of non-uniform intervals of sampling points around the circumference. Table 5.2 shows the maximum errors of the Fourier representations at the sampling points for the three silos during the iterative process. It can be seen that the errors became very small after several iterations, and the deduced Fourier series can be regarded as accurate representations of the imperfection data. Figures 5.2-5.4 show the spectra of the Fourier series representing the imperfections in Shells A, B, and C respectively. A comparison between these figures and Figures 4.39-4.41 shows that the spectra of the two sets of Fourier series are similar, despite the fact that the zones of imperfection measurements considered in the two cases are somewhat different.

5.3 FINITE ELEMENT MODELS

5.3.1 Shell Elements in ABAQUS

Buckling analyses of the three shells were carried out using the commercial finite element software package ABAQUS (Hibbit Karlsson & Sorensen, 1998). Three categories of curved shell elements are available in ABAQUS: (a) general-purpose shell elements (S4 and S4R); (b) thin shell elements (S4R5, S8R5, and S9R5); and (c) thick shell elements (S8R). The nomenclature for shell elements in ABAQUS complies with the following rules: the first character 'S' indicates that this is a stress/displacement shell element, the second character gives the number of nodes in a shell element, the third character 'R' is optional and denotes the use of reduced (lower-order) integration in forming the element stiffness matrix, and the last character is also optional and denotes the number of degrees of freedom (DOFs) per node. The thin shell elements are only applicable to thin shell problems in which transverse shear deformation can be neglected. The thick shell element is applicable only to thick shell problems for which transverse shear flexibility cannot be ignored. The general-purpose shell elements are suitable not only for thin shell problems but also for thick shell problems as these shell elements allow transverse shear deformations but also perform well in solving thin shell problems.

While both the thin elements (S4R5, S8R5, and S9R5) and the general-purpose elements (S4 and S4R) are suitable for thin shell problems, elements S8R5, S9R5, and S4R5 have been reported to experience spurious modes in buckling analyses (Song, 2002), while element S4 is recommended over S4R (Hibbit Karlsson & Sorensen, 1998) to ensure accurate solutions for problems prone to spurious modes and with significant in-plane bending. Based on these considerations, the general-purpose doubly-curved shell element S4 was used in all buckling analyses presented in this thesis. This is a robust element without shear locking and spurious modes problems, with the only shortcoming being that it is computationally less efficient. Integration across the shell wall thickness was achieved using Simpson's rule with 9 integration points as some problems with ABAQUS have been found when fewer than 7 points were used (Hübner *et al*, 2003b).

5.3.2 Shell Dimensions and Material Properties

In the finite element analyses presented here, the imperfect surfaces of the three shells cut from the three large Port Kembla silos were modeled by the specification of a perfect reference cylinder with a radius of 12m and a wall thickness of 12mm, followed by the superposition of the imperfections (deviations) obtained from measurements and interpolations. The steel of the shells was assumed to be elastic-perfectly plastic with an elastic modulus $E = 2.0 \times 10^5$ MPa, a yield stress σ_y = 250MPa and a Poisson's ratio ν = 0.3. Both the bottom and top ends of the shells were provided with a classical simple support, with the top end left free to move vertically and to receive axial compression.

As the three imperfect shell surfaces do not possess symmetry or anti-symmetry about any meridian, the entire surface was modeled for reliable predictions of buckling behavior. Before undertaking buckling analyses in which the whole shell was modeled, mesh convergence studies were first carried out using sector models to arrive at accurate but economic meshes.

5.3.3 Mesh Convergence Studies using a Sector Model

In choosing a shell sector for a mesh convergence study, two factors need to be considered: one is that the shell sector shall be large enough to cover a sufficient number of buckling waves in both the meridional and circumferential directions; and the other is that the sector width and length shall allow easy FE discretization into elements of desirable sizes. Based on these considerations, for each of the three shells, a sector covering the entire length of the shell and 34.38° around circumference was cut from the shell for a mesh convergence study. These sectors are referred to as Sectors A, B and C for Shells A, B and C respectively. To simplify the problem further, two meridional edges of the sector model were imposed with symmetric boundary conditions.

Four different meshes, Meshes I, II, III and IV with element sizes of $50mm \times 50mm$, $100mm \times 100mm$, $150mm \times 150mm$, and $200mm \times 200mm$, were considered in the mesh convergence study for each of the three shells. In terms of the linear elastic meridional bending half-wavelength λ given by Eqn 2.4, these element sizes

are $\lambda/18.5$, $\lambda/9.3$, $\lambda/6.2$, and $\lambda/4.6$ respectively. As Mesh I is a very fine mesh, the result obtained with this mesh is treated as the converged reference solution here in evaluating the convergence of solutions obtained with the other three meshes.

Table 5.3 shows the linear buckling stresses of the three shell sectors and the differences between the results from Meshes II, III and IV and that obtained with Mesh I. It is seen that the differences between the results from different meshes are small, with the greatest difference being only 2.654% for Mesh IV of Sector A. Table 5.3 demonstrates that both Meshes II and III are sufficiently accurate for linear buckling analyses.

Non-linear analyses were also conducted on each of the three shell sectors using the four different meshes. In these analyses, the mid-point at the top of the sector was monitored in each case. Figures 5.5-5.7 show the load-displacement curves of the monitored point for Sections A, B and C respectively from nonlinear analyses. For all three shell sectors, the load-displacement curve predicted with Mesh II nearly coincides with that of Mesh I, and the curve of Mesh III lies close to that of Mesh I with only some small differences in the deep postbuckling stage. By contrast, the load-displacement curve of Mesh IV is close to that of Mesh I for Sections A and B but not for Sector C.

From the results of linear and non-linear buckling analyses of the three shell sectors presented above, it is clear that the element size of Mesh II is suitable for use in studying the buckling and postbuckling behavior of the three silo shells, and the element size of Mesh III is also of sufficient accuracy. For brevity, in the following discussions, the use of the element size of one of the meshes is simply stated as the use of that mesh. In the present study, Mesh II was adopted in both linear and non-linear buckling analyses of the whole-structure models of the three silo shells. This led to a finite element model with a total of 90,480 elements, with 754 elements around the circumference and 120 elements over the height. For the parametric studies that followed, Mesh III was used, leading to a model with 40,160 elements so that the computational time could be substantially reduced.

5.4 LINEAR BUCKLING ANALYSES

Linear buckling calculations of the three imperfect silo shells were first performed using Mesh II. The linear buckling stresses of Shells A, B and C are only 33%, 39.7%, and 38.7% of their classical buckling stress respectively. These results demonstrate that the unique imperfections in these shells are severely detrimental to their axial buckling strengths.

The linear buckling modes of these three shells are shown in Figures 5.8-5.10 respectively. These linear buckling modes indicate that the buckling deformations are localized, and the three buckling modes differ from each other as a result of their different geometric imperfections. In Shells A and C, the buckling deformations involve mainly the surveyed zones, but in Shell B, the predicted buckling mode covers the circumferential range between 43.9^0 and 60.6^0, within which the smallest measurement gap of the shell (Gap I) (Figure 5.9) falls. Despite this problem, the results of these linear analyses are believed to be convincing, because the buckling load of Shell B is not controlled by deformations in Gap I. The justification for this statement is given in the following section presenting the results from non-linear analyses.

5.5 NON-LINEAR ANALYSES

Although the results from linear buckling analyses presented above have shed significant light on the buckling behavior of the three imperfect silo shells, a thorough understanding of their behavior can only be gained from non-linear analyses considering both geometric and material nonlinearities although the effect of material nonlinearity is generally small in these shells. Therefore non-linear load-displacement analyses were conducted using the Riks technique available in ABAQUS. During these non-linear analyses, warning messages of a negative eigenvalue near the peak load of the nonlinear analysis were often issued by ABAQUS. Non-linear bifurcation analyses were thus carried out to check if a non-linear bifurcation point exists before the peak load for these shells. Such checks showed that the non-linear bifurcation loads are the same as the peak loads from the non-

linear analyses, indicating that no bifurcation point exists before the peak load is reached for all three shells.

Figures 5.11-5.13 show the load-displacement curves of selected top nodes of each shell for the three shells respectively. It should be noted that in plotting these curves, the results of some increments were omitted for better clarity. It can be seen that the buckling loads of the three shells range from $0.248\sigma_{cl}$ to $0.292\sigma_{cl}$, and their load-displacement paths are quite different from each other. The deformed shapes of the three shells at the peak load (Point D indicated in Figures 5.11-5.13) are shown in Figures 5.14-5.16, while their deformed shapes at a point in the post-buckling stage (Point E indicated Figures 5.11-5.13) are illustrated in Figures 5.17-5.19. It is not surprising to observe that the deformed shapes of the three shells are significantly different from each other, because the imperfections in the three silos, which have been discussed in the previous chapter, are considerably different despite the fact that the three silos were constructed with the same fabrication process. Figures 5.20-5.22 show the nonlinear bifurcation modes of the three shells. These modes are the incremental modes of deformed shapes of the shells at the peak load, and are thus the nonlinear counterparts of the linear buckling modes. The deformed shapes of the shells at the peak load include all deformations accumulated to that point.

It needs to be pointed out that most of the deformations controlling the buckling and postbuckling behavior of the shells occur at some distance from the measurement gaps, although the smallest gap, Gap I, of each of the three shells is involved in these deformations. It may be recalled that Gap I of Shell B also falls within the deformation zone of the linear buckling mode. Since the imperfections in Gap I of each shell was not surveyed, one may be concerned with the predicted buckling behavior when Gap I is involved in the controlling deformation zone. While this is a valid concern, it is nevertheless believed that this involvement of Gap I in the buckling/postbuckling deformations is not of consequence on the predicted behavior for the following reasons: (a) Gap I extends over a small part of the circumference ($1.8\,l_{m\theta}$ for Shells A and B, and $4\,l_{m\theta}$ for Shell C), and linear interpolations were already applied to these gaps before the Fourier decomposition so any imperfections in Gap I are reasonably well represented; (b) The linear buckling mode, the non-linear deformed shape at the peak load and the non-linear bifurcation mode do not all involve Gap I; (c) The largest deformations of the linear

buckling mode and the non-linear bifurcation mode do not appear in Gap I. The above observations indicate that Gap I in each shell is not the critical location controlling the buckling and postbuckling behavior of the shell. It is therefore believed that the results presented here are the reliable predictions of the buckling and post-buckling behavior of the three silo shells.

5.6 DOMINANT IMPERFECTION COMPONENTS

The Fourier representations of imperfections in the three shells contain many individual harmonic terms (or harmonic modes), with the meridional terms ranging from harmonic 0 to harmonic 239 and the circumferential terms ranging from harmonic 0 to harmonic 75. Those terms with significant amplitudes are however concentrated in the zone of low harmonic numbers (Figures 5.2-5.4). In particular, most of the terms with amplitudes larger than 1.0 mm (i.e. one twelfth of the shell wall thickness), are associated with a meridional harmonic number m from 0 to 2 and a circumferential harmonic number n from 0 to 18, with few exceptions. To understand which of the large number of the harmonic modes are important to the buckling strength, either individually or collectively, a parametric study was conducted in which imperfections composed of different combinations of harmonic modes were considered.

Since the parametric study required a large number of calculations, only linear buckling analyses with Mesh III (element sizes of $150mm \times 150mm$) were conducted to save the computational effort. Before presenting the finite element results, the terminology adopted here in describing selected imperfection components needs to be explained. Figure 5.23 shows what may be referred to as the imperfection map, where m is the meridional harmonic number defining the rows and while n is the circumferential harmonic number defining the columns. The intersection between a row and a column defines a single harmonic mode of the double Fourier series.

When an imperfection component includes a single meridional harmonic but all associated circumferential harmonics, it is referred to as a 'row' imperfection. By contrast, an imperfection component containing only a single circumferential harmonic but all associated meridional harmonics is referred to as a 'column' imperfection. An

imperfection containing a single harmonic mode of the double Fourier series is referred to as a single-mode imperfection. If, however, a number of terms are included, then the imperfection is referred to as a block imperfection. In exploring the effect of different components of the measured imperfections, finite element linear buckling analyses were carried out for the three shells with different selections of imperfection components from the double Fourier representations.

Attempts were initially made to examine the effect of individual harmonic terms with a pronounced amplitude in the block of $m = 0-2$ and $n = 0-18$ but it was soon realized that a single-term imperfection has little effect on the buckling strength. Attention was next turned to the effect of other imperfection components. Row and column imperfections were next examined. However, the use of row or column imperfections was also found to be ineffective, as the effect of a single row or column imperfection may be substantially different from that of the combination of some rows and some columns. For example, the column imperfection of $n = 6, m = 0-239$ in Shell A has a detrimental effect on the shell buckling strength when it is the only imperfection in the shell, but becomes beneficial to the buckling strength when it co-exists with a block imperfection (Figure 5.25). The same is true for the column imperfection of $n = 13, m = 0-239$. Furthermore, this approach involves a vast amount of computation, because every row ($m = 0-239$) and every column ($n = 0-75$) of the imperfection map need to be checked.

A more reasonable approach was subsequently adopted, in which two series of computations are conducted using block imperfections with rows or columns of the lower harmonic terms being progressively eliminated. For example, the first series computations are conducted, sequentially, for the block imperfections of ($m = 1-239$, $n = 0-75$), ($m = 2-239, n = 0-75$), ($m = 3-239, n = 0-75$), ..., while the second series of computations are conducted, sequentially, for the block imperfections of ($m = 0-239, n = 1-75$), ($m = 0-239, n = 2-75$), ($m = 0-239, n = 3-75$). These calculations can reveal the effect of a row or column imperfection together with the others on the buckling strength so that the rows and columns that dominate the strength degradation can be identified. Consequently, the dominant block imperfection is found to consist of those harmonic terms located at the intersections of the identified rows and columns.

The results of the two series of computations for the three shells are plotted in Figures 5.24-5.29 which show that the lower harmonic terms play an important role in the strength reduction. Figures 5.24, 5.26 and 5.28 show that of the 240 meridional harmonic terms (i.e. 240 row imperfections), the first 26 rows (i.e. $m < 26$) are responsible for more than 95% of the strength reduction.

Of the 76 circumferential harmonic terms (i.e. 76 column imperfections), the lower terms are again seen to contribute more significantly to the buckling strength reduction, but their contribution to the strength reduction is not as large as that of the lower meridional harmonic terms (Figures 5.25, 5.27, and 5.29). Calculations conducted with several block imperfections excluding the first 20 or more column imperfections indicated that further exclusions of column imperfections led to very small buckling strength variations.

It is reasonable to assume that an important row or column imperfection shall lead to a pronounced strength variation when it is excluded from block imperfection. In identifying the influential row and columns of the imperfection map, a threshold value for the strength variation was set as $0.02\sigma_{cl}$. That is, an influential row or column imperfection should lead to a strength increase of 2% or more when it is excluded from the block imperfection. Based on this criterion, the following rows of the imperfection map were identified as the influential ones: $m = 8-25$ for Shell A, $m = 0-24$ for Shell B, and $m = 3-26$ for Shell C. Similarly, the influential columns of the imperfection map are: $n = 0-15$ for Shell A, $n = 0-20$ for Shell B, and $n = 0-16$ for Shell C.

Based on the identified rows and columns of the imperfection map for each shell, the critical block imperfection can be easily identified to be: ($m = 8-25$, $n = 0-15$) for Shell A, ($m = 0-24$, $n = 0-20$) for Shell B, and ($m = 3-26$, $n = 0-16$) for Shell C. The selected columns and rows of the imperfection maps of the three shells show some similarity, except that the rows of $m = 0-2$, which are the rows with large associated amplitudes, are important for Shell B but not for Shells A and C. The differences between the selected block imperfections of the three shells are clearly seen in the three-dimensional plots shown in Figures 5.30-5.32: the block imperfection of Shell A (Figure 5.30) feature short waves of a uniform pattern over the entire surface, that of Shell B features circumferential waves of large amplitudes in combination with two-way short

waves (Figure 5.31), and that of Shell C features local large waves at the bottom with small waves elsewhere (Figure 5.32). It is clear that the dominant block imperfection of Shell A is significantly axisymmetric, while those of Shell B and C are considerably non-symmetric. A comparison of these plots with those in Figures 4.11-4.13 including all imperfection components shows that the surfaces of the selected block imperfections are much smoother because the higher harmonic terms have been excluded.

Linear buckling analyses with the selected block imperfections found that the linear buckling stresses of the three shells are $0.33576\sigma_{cl}$, $0.42902\sigma_{cl}$, and $0.42947\sigma_{cl}$, respectively. These results differ from their counterparts obtained with all imperfection components taken into account by only -0.068%, 7.98%, and 8.8%. Figures 5.33-5.35 show the linear buckling modes of the shells with these block imperfections. It is seen that the buckling modes of Shells A and B are identical to those found with all imperfection components included (Figures 5.8-5.9), while the buckling mode of Shell C is similar to that found with all imperfection components included (Figure 5.10). It can therefore be safely concluded that the block imperfection method is an effective method for locating those imperfection components that dominate the shell strength reduction, and only a limited number of the lower harmonics of the imperfection is responsible for the almost all the buckling strength reduction.

5.7 FABRICTAION QUALITY CLASSES OF THE THREE SILO SHELLS

5.7.1 General

As mentioned in Chapter 2, the new Eurocode 3 relates the buckling strength of a shell to its fabrication quality which is divided into three classes: Class A, Class B, and Class C. The fabrication quality class of a shell is determined according to the following three imperfection tolerance parameters: accidental eccentricity, out-of-roundness and dimple depth. Once the quality class of a shell is known, the buckling strength of the shell can be predicted using rules in this code. The code also provides simple measurement methods for evaluating the values of these three imperfection parameters (see Chapter 2), but the practical application of these methods is subject to subjective judgment and interpretation.

In this and the next section, a study is presented to clarify two issues: (a) What quality classes do these three silo shells belong to? (b) Are the predictions of buckling strength based on the design rule of the code reliable? The work presented here is concerned only with dimples, as accidental eccentricities cannot be found from the imperfection measurements made on the outer surface of the shell alone. The parameter of out-of-roundness is also not addressed as it is a very simple parameter (Eqn 2.6). It is believed that both the accidental eccentricity and out-of-roundness are unimportant for the buckling strengths of the three silo shells.

5.7.2 Meridional Measurement of Dimple Depths

The determination of dimple depths in the meridional direction involve moving a straight gauge of a specific length across the shell surface meridionally and then evaluating the distances sampling points on the dimple profile to the gauge. A diagrammatic sketch of the meridional measurements is shown in Figure 5.36, where the curve *PQ* is the shell meridional profile, the evenly distributed dots are the sampling points, and the line *MN* is the measuring gauge that is in contact with the shell surface at the sampling points *K* and *L*. For ease of manipulation, the gauge shall be divided into many sub-divisions of certain length according to the length of the gauge, and the interval of the sampling points/nodes shall be the same as the length of the gauge sub-divisions so that the two sets of points can be properly matched when the gauge moves stepwise. The positions of the sampling points of the shell profile at the required interval can be easily obtained from the Fourier series representing the imperfection surface of the shell.

The straight gauge is idealized as Line *MN* described by the following equation:

$$\frac{z - z_k}{z_l - z_k} = \frac{w - w_k}{w_l - w_k}$$

or

$$w - \left(\frac{w_l - w_k}{z_l - z_k}\right) z + \left(\frac{w_l - w_k}{z_l - z_k}\right) z_k - w_k = 0 \tag{5.1}$$

Let $A = 1$, $B = -\left(\frac{w_l - w_k}{z_l - z_k}\right)$, and $C = \left(\frac{w_l - w_k}{z_l - z_k}\right) z_k - w_k$, then Eqn 5.1 becomes

$$w + Bz + C = 0 \tag{5.2}$$

or

$$w = -Bz - C \tag{5.3}$$

The depth of a sampling point of a dimple can be defined as the perpendicular distance of the sampling point to the measuring gauge placed over the dimple with two of the nodes on the gauge being in contact with the two end points of the dimple. The depth can be obtained from the equation for the point-to-line distance given by:

$$d = \frac{|Aw_i + Bz_i + C|}{\sqrt{A^2 + B^2}} = \frac{|w_i + Bz_i + C|}{\sqrt{B^2 + 1}} \tag{5.4}$$

Using the equations given above, a small computer program called MMDD (Meridional Measurement of Dimple Depths) was written to provide an automated procedure of "measuring" dimple depths in the meridional direction.

5.7.3 Circumferential Measurement of Dimple Depths

Figure 5.37 illustrates the measurement of dimple depths in the circumferential direction, in which a circular arc gauge of a specific length moves around the shell and the depths of the sampling points are measured with respect to the gauge. The depth of a sampling point on the profile of a dimple is defined as the perpendicular distance of the sampling point to the tangent to the arc gauge at a corresponding point. Although the measurement of dimple depths around the circumference is quite similar to that along the shell meridian in principle, the detailed aspects of these measurements are significantly different. Described below is the derivation of the equations for the arc gauge and the determination of dimple depths.

As shown in Figure 5.37, an arc gauge is assumed to be in contact with two sampling points $K(x_k, y_k)$ and $L(x_l, y_l)$ of a circumferential dimple. The position of the arc gauge is then given by two simultaneous equations with the coordinates of the arc center being the unknowns:

$$(x_k - x_c)^2 + (y_k - y_c)^2 = R^2 \tag{5.5}$$

$$(x_l - x_c)^2 + (y_l - y_c)^2 = R^2 \tag{5.6}$$

or

$$x_k^2 + x_c^2 - 2x_k x_c + y_k^2 + y_c^2 - 2y_k y_c - R^2 = 0 \tag{5.7}$$

$$x_l^2 + x_c^2 - 2x_l x_c + y_l^2 + y_c^2 - 2y_l y_c - R^2 = 0 \tag{5.8}$$

where x_c and y_c are the coordinates of the arc center; and R is the intended radius of curvature that is equal to the nominal radius of the shell.

Subtracting Eqn 5.7 from 5.8 yields:

$$y_c = \frac{(x_l^2 - x_k^2) + (y_l^2 - y_k^2) - 2(x_l - x_k)x_c}{2(y_l - y_k)} \tag{5.9}$$

Substituting Eqn 5.9 into 5.5 gives:

$$\frac{(x_l - x_k)^2 + (y_l - y_k)^2}{(y_l - y_k)^2} x_c^2 - \frac{(x_l + x_k)[(x_l - x_k)^2 + (y_l - y_k)^2]}{(y_l - y_k)^2} x_c +$$

$$\frac{[(x_l^2 - x_k^2) + (y_l - y_k)^2]^2}{4(y_l - y_k)^2} + x_k^2 - R^2 = 0 \tag{5.10}$$

Let $D = \frac{(x_l - x_k)^2 + (y_l - y_k)^2}{(y_l - y_k)^2}$, $E = -\frac{(x_l + x_k)[(x_l - x_k)^2 + (y_l - y_k)^2]}{(y_l - y_k)^2}$, and

$F = \frac{[(x_l^2 - x_k^2) + (y_l - y_k)^2]^2}{4(y_l - y_k)^2} + x_k^2 - R^2$, then

$$D x_c^2 + E x_c + F = 0 \tag{5.11}$$

If $\Delta = \sqrt{E^2 - 4DF} \geq 0$, the roots of equation (5-11) are given by

$$x_{c1,c2} = \frac{-E \pm \sqrt{E^2 - 4DF}}{2D} \tag{5.12}$$

Substituting equation (5-12) into equation (5-9) gives

$$y_{c1,c2} = \frac{(x_l^2 - x_k^2) + (y_l^2 - y_k^2) - 2(x_l - x_k)x_{c1,c2}}{2(y_l - y_k)} \tag{5.13}$$

If $\Delta = 0$, only one solution exists; in other words, (x_{c1}, y_{c1}) coincides with (x_{c2}, y_{c2}). If $\Delta > 0$, two solutions are available; that is, $C_1(x_{c1}, y_{c1})$ and $C_2(x_{c2}, y_{c2})$ co-exist for the simultaneous Eqns 5.5 and 5.6. Of these two solutions, one defines a point outside the shell surface and should be discarded, while the other defines a point inside the shell and is the valid solution. Therefore, the valid solution, denoted by (x_c, y_c), should satisfy the following relationship:

$$x_c^2 + y_c^2 < R^2 \tag{5.14}$$

As the radius at any point of the arc gauge is perpendicular to the tangent to the arc at that point, the depth of a sampling point on the profile of a dimple, which is equal to the length of segment ST lying on the radial path that goes through the sampling point, can be obtained by:

$$\Delta w_0 = R - d_{cs} \tag{5.15}$$

where d_{cs} is the length of the segment CS given by:

$$d_{cs} = \sqrt{(x_s - x_c)^2 + (y_s - y_c)^2} \tag{5.16}$$

Before the depth of any sampling point can be determined, the magnitude of the geometric imperfection in the direction normal to the shell surface at the sampling point under consideration shall be transformed into the x-y coordinates of the sampling point as follows:

$$x_s = (R + w_s)\cos\theta_s \tag{5.17}$$

$$y_s = (R + w_s)\sin\theta_s \tag{5.18}$$

where (x_s, y_s) are the x-y coordinates of the sampling point; w_s is the geometric deviation at the sampling point; and θ_s is the angular coordinate of the sampling point. Based on the procedure described above, a small computer program called CMDD (Circumferential Measurement of Dimple Depths) was written for automated circumferential measurements of dimple depths.

5.7.4 Imperfection Parameters and Quality Classes

Apart from the two small programs CMDD and MMDD mentioned above, a small program called MSOR (Measurement of Shell Out-of-Roundness) was also developed. Using these three programs, the values of two imperfection tolerance parameters, namely out-of-roundness and dimple depths, were determined for the three silo shells.

Figures 5.38-5.40 show the meridional variations of the out-of-roundness parameter U_r for the three shells. Despite that the three shells were fabricated by the same process, the variations of U_r are significantly different. In both Shells A and B, the maximum value of U_r occurs in the mid-height region and the smallest value occurs at the lower end; the value at the upper end is also much smaller than the maximum value. In Shell C, the

maximum value of U_r occurs at the lower end and the smallest value occurs at the upper end. The maximum values of U_r for the three shells, which are used for the assessment of shell fabrication quality, are given in Table 5.4. Although the values of $U_{r,\max}$ for the three shells differ considerably, all three shells fall into fabrication quality Class A according to the tolerances specified in ENV 1993-1-6 (1999).

For the measurement of dimple depths, ENV1993-1-6 stipulates that measurements along shell meridians and circumferences should be carried out using three different gauge lengths as given by Eqns 2.8, 2.9, and 2.10. Circumferential measurements using the gauge length given by Eqn 2.9 is not applicable here, as the primary stress state in the shells is axial compression. Circumferential measurements across welds using the gauge length given by Eqn 2.10 are also not possible as the locations of the short meridional welds cannot be ascertained in Figures 4.11-4.13. Moreover, the gauge length specified by Eqn 2.9, which is $25t_{\min}$ or 300mm, is much smaller than that of $4\sqrt{Rt}$ specified by Eqn 2.8. Meridional measurements using the gauge length given by Eqn. 2.10 were also not conducted for the same consideration that the length given by Eqn 2.10 is considerably smaller than that of Eqn 2.8. Based on these considerations, the gauge length of $4\sqrt{Rt}$ specified by Eqn 2.8 is the only gauge length applicable to both meridional and circumferential measurements of dimple depths. As the three silos have the same geometry of $R = 12000mm$ and $t = 12mm$, the gauge length $l_{gx} = 4\sqrt{Rt} \approx 1518mm$. For simplicity of numerical operation, the gauge length was rounded to 1500mm which was divided into 10 sub-divisions of 150mm. To match this gauge length, the sampling points of the imperfection surface were evenly distributed at a spacing of 150 mm in both the meridional and circumferential directions and the magnitudes of imperfections at the sampling points were obtained from the Fourier series deduced earlier.

Figures 5.41-5.46 show the three-dimensional plots of the dimple depths found from the above numerical procedure for the three shells. Every sampling point on the shell was numerically measured many times as the circumferential and meridional gauges moved across so only the maximum measured depth is shown in these figures. The ring strakes of the shells are clearly visible in the results of meridional measurements, with the wave crests being at the circumferential weld joints.

The results of circumferential measurements show few waves in certain regions. These are regions for which the imperfections were not surveyed and linear interpolations were used to produce data points. Results for these regions should thus not be taken too seriously. In addition, large waves are seen to appear in some circumferential regions over the entire height of the shell, which implies the possibility of local deviations due to the matching of strakes at the circumferential joints as the shells were built by stacking up the strakes from the bottom to the top. Long-wave global imperfection components have been completely excluded from all these measurement results. These local measurements thus provide reliable local imperfections in the shells.

The maximum dimple depths, which are the most important results of these measurements, are given in Table 5.4, as they determine the fabrication quality classes of these shells. The maximum values of the out-of-roundness parameters of the three shells are all below the tolerance value of 0.007 stipulated in ENV1993-1-6 for Class A shells, so based on this parameter, all three shells are Class A shells. However, according to the maximum dimple depths, strictly speaking the fabrication quality of Shell A is worse than Class C, that of Shell B belongs to Class B and that of Shell C belongs to Class C. Coincidentally, the maximum values of the dimple depths of Shells A, B and C are close (but exceed) the tolerances specified for Classes C, A and B. For ease of comparison in checking the reliability of code predictions of buckling strengths, these three shells are taken as shells of Classes C, A and B respectively.

It may be noted that for a given shell, the fabrication quality class derived from one imperfection parameter may be different from that based on another parameter. The dimple depths measured meridional and circumferentially however lead to consistent results (Table 5.4).

5.8 BUCKLING STRENGTH COMPARISON

As mentioned earlier, ENV1993-1-6 (1999) stipulates that the characteristic amplitudes of initial imperfections in shells be determined on the basis of their fabrication quality classes according to the following equation:

$$\frac{\Delta w_k}{t} = \frac{1}{Q}\sqrt{\frac{R}{t}} \tag{5.19}$$

where Q is the meridional compression quality parameter: for quality Class A (Excellent quality), Q=40; for quality Class B (High quality), Q=25; and for quality Class C (Normal), Q=16.

The meridional elastic imperfection factor can then be obtained from:

$$\alpha_x = \frac{0.83}{1+1.91(\Delta w_k / t)^{1.44}} \tag{5.20}$$

Based on Equations (2-5) and (2-12), the buckling strengths of the three silo shells can be determined according to the rules of ENV1993-1-6 (1999).

Table 5.5 lists the buckling loads of the three shells predicted by both finite element analyses and the design rules in the code (ENV1993-1-6, 1999) for all three fabrication quality classes. Compared to the finite element results predicted using linear bucking analyses, the Eurocode predictions are rather conservative. This observation is not surprising as linear buckling analyses are known to overestimate the buckling loads of such shells. The differences between the results from nonlinear finite element analyses and the code predictions are reasonably small. It is important to note that Shell B, which is a Class A shell, has a finite element buckling load significantly below that predicted by the code. For the other two shells, the code predictions are significantly conservative. These results indicate that the current rules of the Eurocode are too optimistic for Class A shells but too pessimistic for Classes B and C. It is also significant that Shell A falls outside of the three classes defined in the code although its buckling strength is much higher than the code prediction for a Class C shell.

5.9 CONCLUSIONS

This chapter has been concerned with the buckling and postbuckling behavior of three shells taken from the three Port Kembla silos with measured geometric imperfections. The measured imperfections were accurately represented and incorporated into linear and nonlinear finite element buckling analyses using ABAQUS. A block imperfection

approach was suggested and found to be effective in identifying the critical imperfection components that are responsible for most of the shell buckling strength reduction. In this approach, finite element analyses are carried out for a series of block imperfections obtained by progressively excluding the lower harmonic terms of the imperfection to determine the effect of the imperfection components represented by the lower harmonic terms. Moreover, automated computer procedures were developed to numerically "measure" dimple depths in both the meridional and the circumferential directions. These dimple depths together with values of the out-of-roundness parameter allowed the determination of the fabrication quality classes of the three shells according to the stipulations in ENV1993-1-6 (1999). Finally, the finite element linear and nonlinear buckling loads were compared with appropriate code predictions.

The results and discussions presented in this chapter allow the following major conclusions to be made about the behavior of the three silo shells (Shells A, B and C for Silos A, B and C respectively):

1 Geometric imperfections arising from the panel method of construction are severely detrimental to the shell buckling strength. Despite that the three shells were constructed by the same method and had the same geometric and material properties, they differ significantly in their buckling and post-buckling behavior as a result of the different geometric imperfections in the three shells.
2 Although the Fourier series representing the imperfections contain a large number of harmonic terms, the lower terms in both the meridional and circumferential directions dominate the buckling strength. There are significant differences between the dominant components of the three shells.
3 Based on the stipulations in ENV1993-1-6 (1999), the fabrication quality classes of the three shells are all controlled by their dimple depths rather the out-of-roundness parameter. According to the maximum dimple depths, the fabrication quality of Shells A, B and C is close to the worst of Classes C, A and B respectively. That is, the same construction procedure led to a spread of quality over all three quality classes defined by the Eurocode (ENV1993-1-6 1999).
4 A comparison of code predictions of buckling strengths with nonlinear finite element results indicate that the current rules of the Eurocode are too optimistic for Class A shells but too pessimistic for other shells. It is also significant that strictly speaking,

Shell A falls outside of the three quality classes defined in the code although its buckling strength is much higher than the code prediction for a Class C shell. The relationship between buckling strengths and quality classes requires further research.

The theoretical work presented in this chapter has led to a good understanding of the buckling and post-buckling behavior of real imperfect cylindrical shells in steel silos when subject to axial compression for the first time. In this theoretical work, residual stresses, which always co-exist with the geometric imperfections in these shells, have been ignored. Since residual stresses in thin shells can hardly be measured, their effect of buckling strengths has been studied only on the basis of assumed residual stresses (Rotter, 1996; Holst *et al*, 2000; Hübner *et al*, 2003a). Such studies are however inconclusive.

The most reliable approach for assessing the effect of residual stresses is to carry out buckling experiments on shells in which both geometric imperfections and residual stresses are realistically replicated. As the effect of geometric imperfections can be expected to be closely predicted by a finite element model which includes precisely measured geometric imperfections in the test shell, a comparison between the finite element predictions and the test result can reveal the overall effect of residual stresses and other effects (e.g. unintended non-uniformity in loading). If the finite element buckling load is in close agreement with the test buckling load, it can then be concluded that the effect of residual stresses in the shell is unimportant to the buckling strength. Such an experimental study will be presented in the next two chapters.

Table 5.1 Surveyed zones and gaps in imperfection measurements

Silo		Zone I	Gap I	Zone II	Gap II	Zone III	Gap III
A	Circumferential Range	0^0 – 47.7^0	47.7^0 – 52^0, $1.8\,l_{m\theta}$	52° – 271.7°	271.7° – 281.2^0, $4\,l_{m\theta}$	281.2° – 321.8°	321.8° – 360^0 $16\,l_{m\theta}$
	Number of Meridional Profiles	21		93		18	
B	Circumferential Range	0° – 50.1°	50.1° – 54.4^0, $1.8\,l_{m\theta}$	54.4° – 271.7°	271.7° – 281.2^0, $4\,l_{m\theta}$	281.2° – 317.1°	317.1° – 360^0, $18\,l_{m\theta}$
	Number of Meridional Profiles	22		92		16	
C	Circumferential Range	0° – 195.7°	195.7° – 205.3^0, $4\,l_{m\theta}$	205.3° – 241.1°	241.1° – 360^0, $49.8\,l_{m\theta}$		
	Number of Meridional Profiles	83		16			

Table 5.2 Variation of the maximum error in the imperfection representation during the iterative procedure

Iteration	Shell A	Shell B	Shell C
1	1.323mm	1.556mm	0.066mm
2	-0.351mm	0.318mm	0.029mm
3	-0.131mm	0.142mm	
4	-0.068mm	0.075mm	
5		0.035mm	

Table 5.3 Linear buckling stresses from different meshes, σ_{cl} =121MPa

Mesh		I	II	III	IV
Sector A	$\sigma_{cr}^{(i)}/\sigma_{cl}$	0.44996	0.44954	0.45639	0.46190
	$(\sigma_{cr}^{(i)}-\sigma_{cr}^{(I)})/\sigma_{cr}^{(I)}$	0%	-0.093%	1.429%	2.654%
Sector B	$\sigma_{cr}^{(i)}/\sigma_{cl}$	0.55724	0.56707	0.56786	0.55236
	$(\sigma_{cr}^{(i)}-\sigma_{cr}^{(I)})/\sigma_{cr}^{(I)}$	0%	1.764%	1.906%	-0.876%
Sector C	$\sigma_{cr}^{(i)}/\sigma_{cl}$	0.46547	0.46492	0.46716	0.47431
	$(\sigma_{cr}^{(i)}-\sigma_{cr}^{(I)})/\sigma_{cr}^{(I)}$	0%	-0.118%	0.363%	1.899%

Table 5.4 Fabrication tolerance parameters and quality classes of the three shells

Shell	Out-of-roundness Tolerance		Meridional Dimple Tolerance		Circumferential Dimple Tolerance		Overall Fabrication Quality Class
	$U_{r,\max}$	Quality Class	$U_{0m,\max}$	Quality Class	$U_{0c,\max}$	Quality Class	
Shell A	0.004	Class A	0.012	Class C	0.018	worse than Class C	worse than Class C
Shell B	0.003	Class A	0.006	Class A	0.007	Class B	Class B
Shell C	0.003	Class A	0.011	Class C	0.010	Class B	Class C

Table 5.5 Buckling loads of the three shells from finite element analyses and the Eurocode, σ_{cl} =121MPa

Shell	Representative Quality class	Linear Buckling Load $\sigma_{cr}^{l}/\sigma_{cl}$	Non-linear buckling Load $\sigma_{cr}^{nl}/\sigma_{cl}$	Eurocode Prediction
Shell A	Class C	0.330	0.248	0.136
Shell B	Class A	0.392	0.292	0.351
Shell C	Class B	0.387	0.278	0.226

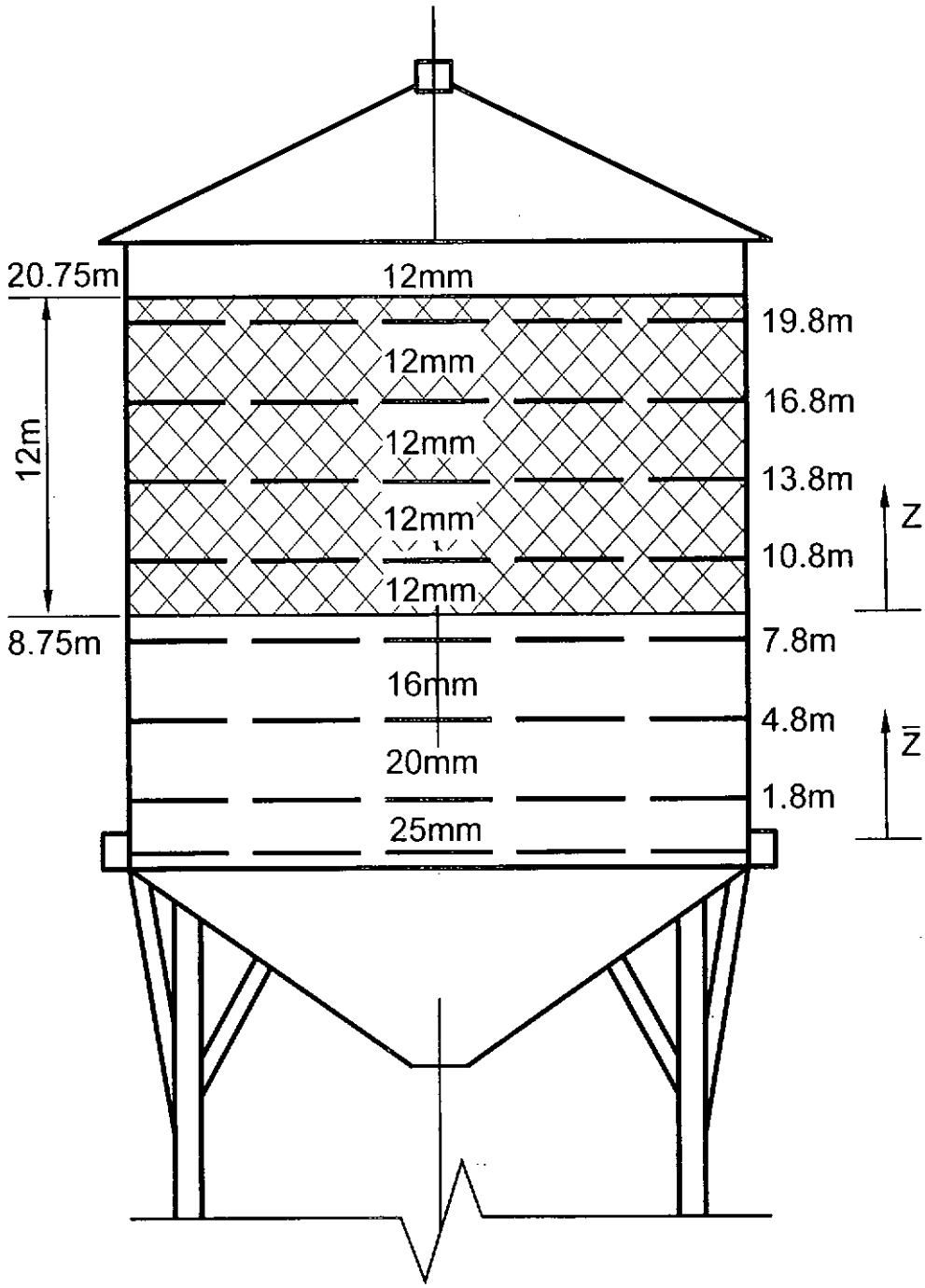

Figure 5.1 Wall thicknesses of Port Kembla silos (After Ding, 1992)

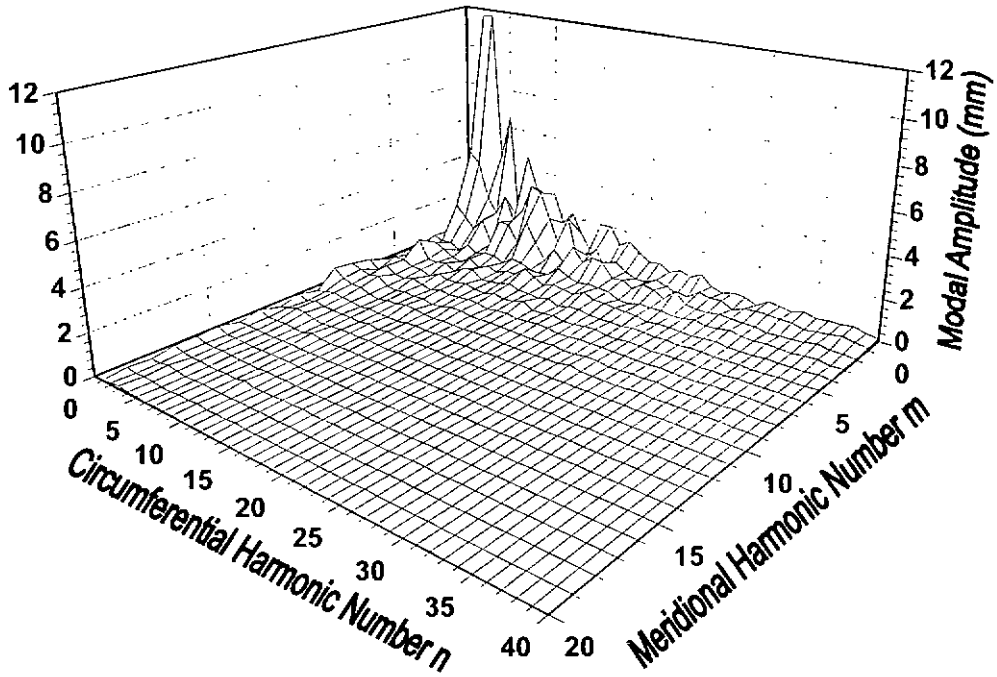

Figure 5.2 Spectrum of imperfections in Shell A

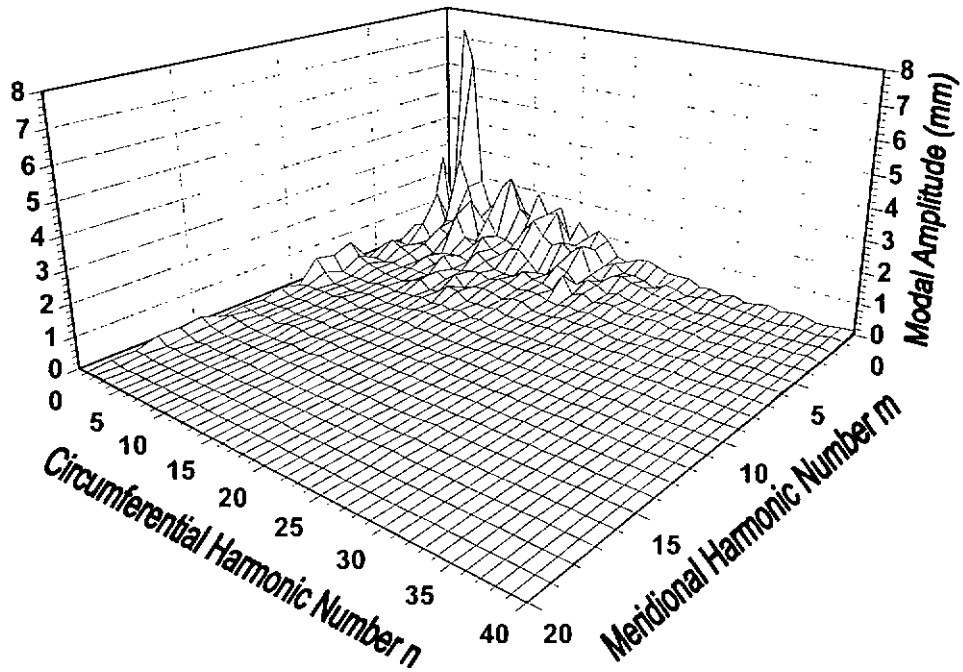

Figure 5.3 Spectrum of imperfections in Shell B

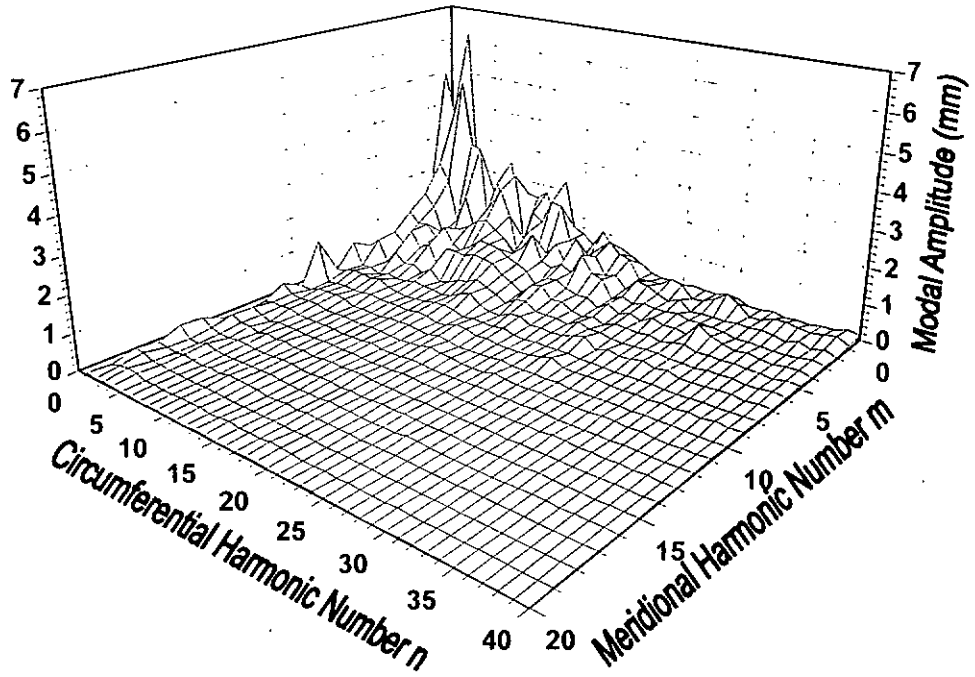

Figure 5.4 Spectrum of the imperfections in Shell C

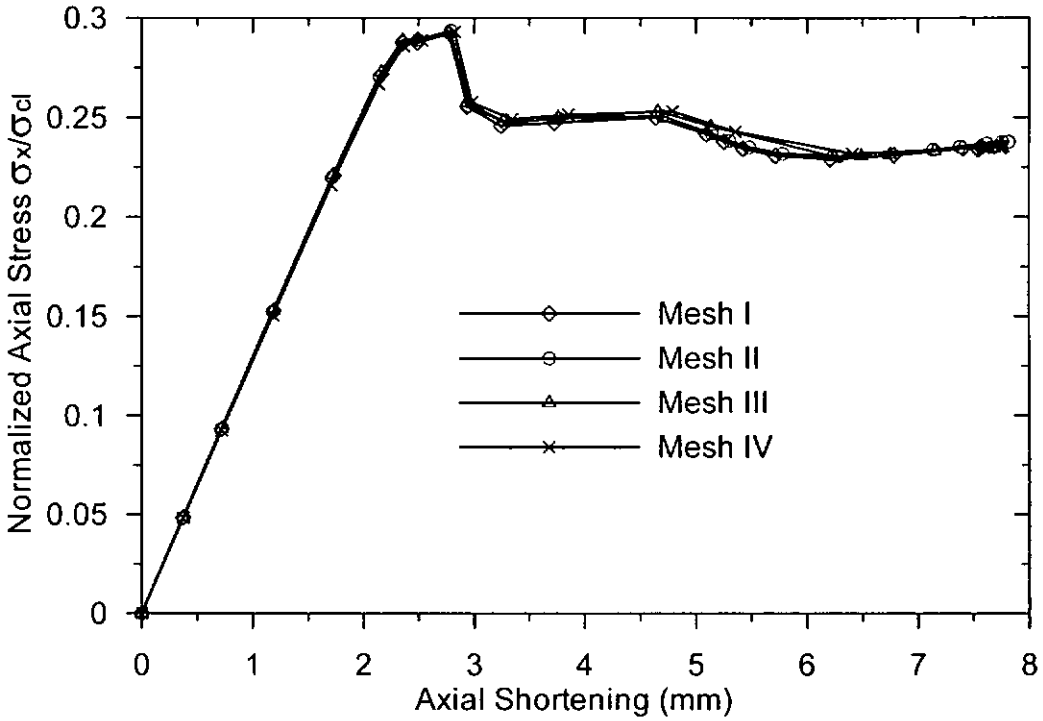

Figure 5.5 Load-displacement curves of the top middle node of Sector A

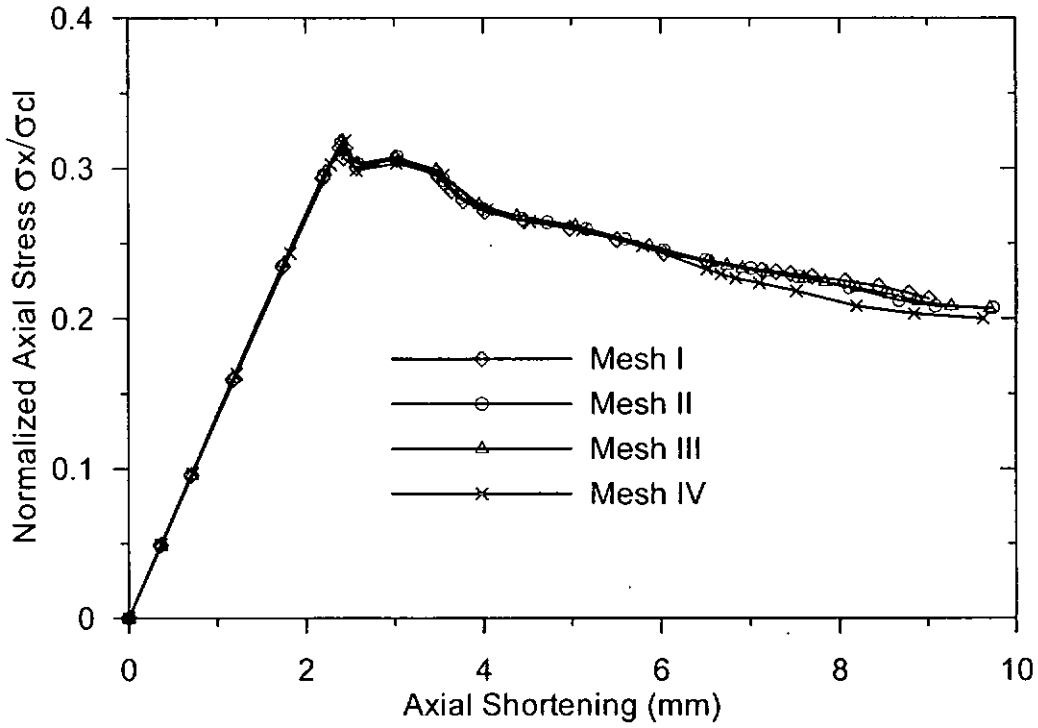

Figure 5.6 Load-displacement curves of the top middle node of Sector B

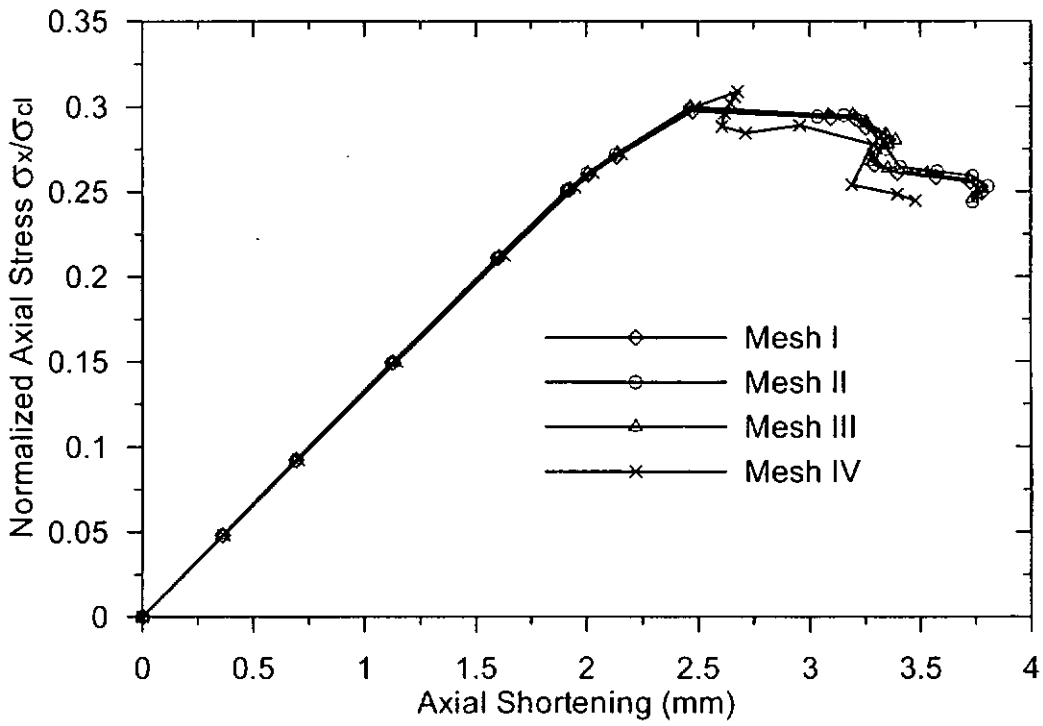

Figure 5.7 Load-displacement curves of the top middle node of Sector C

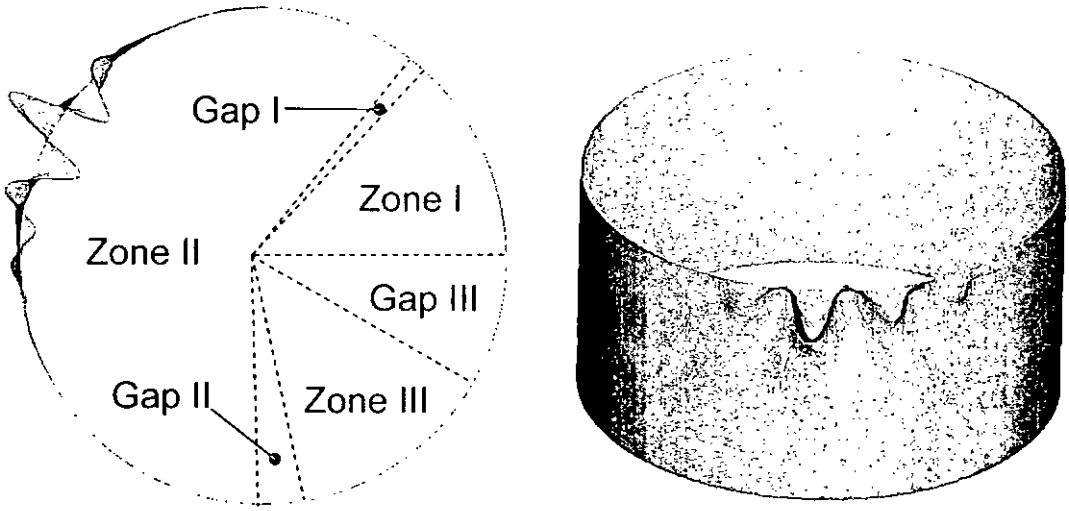

(a) Plan view (b) Perspective view

Figure 5.8 Linear buckling mode of Shell A

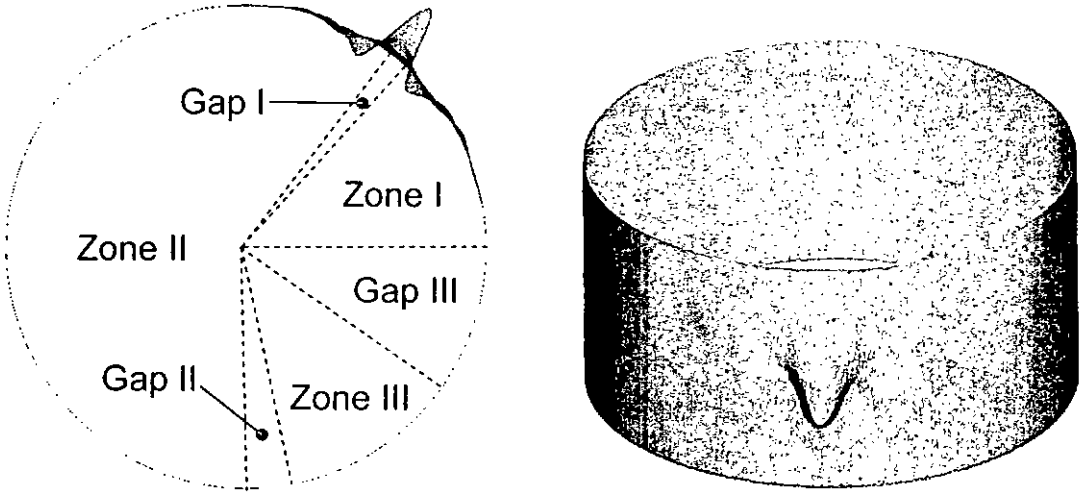

(a) Plan view (b) Perspective View

Figure 5.9 Linear buckling mode of Shell B

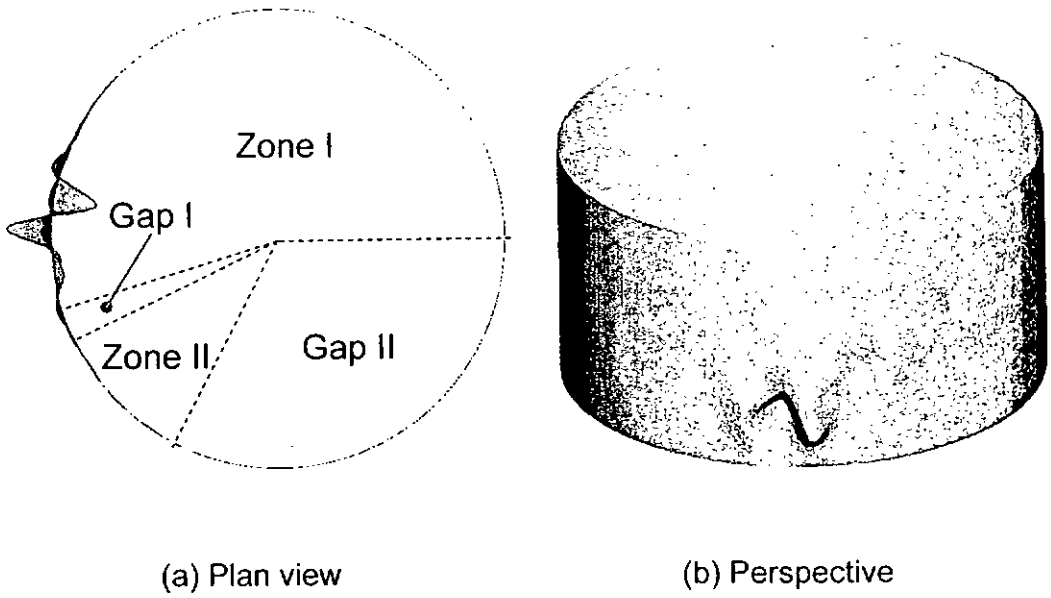

Figure 5.10 Linear buckling mode of Shell C

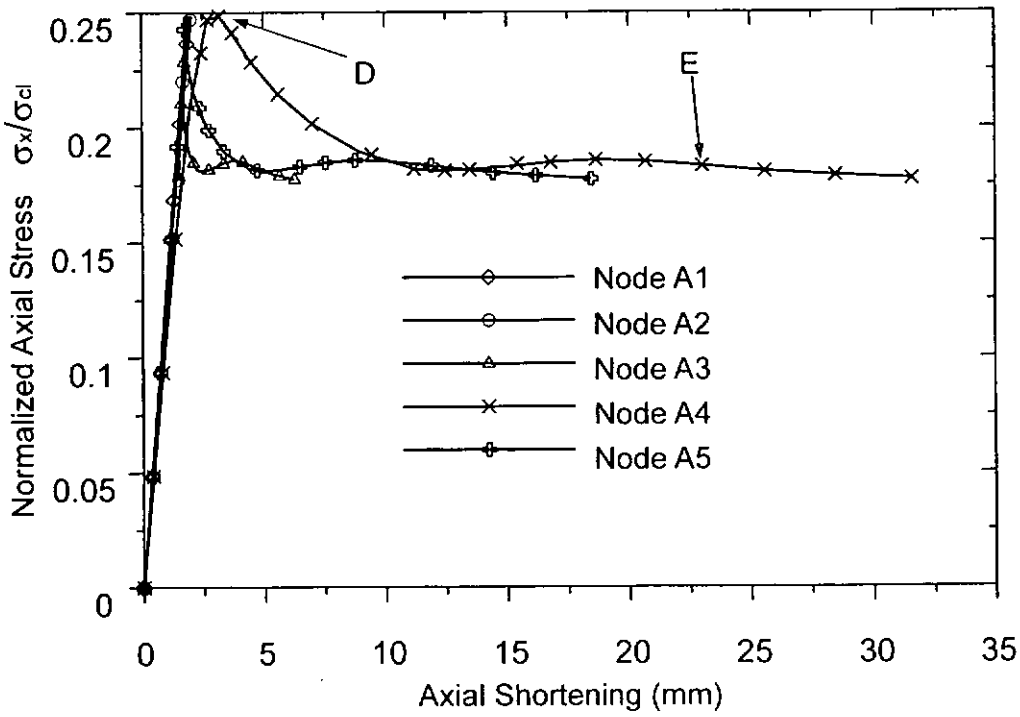

Figure 5.11 Load-displacement curves of selected nodes on upper end of Shell A

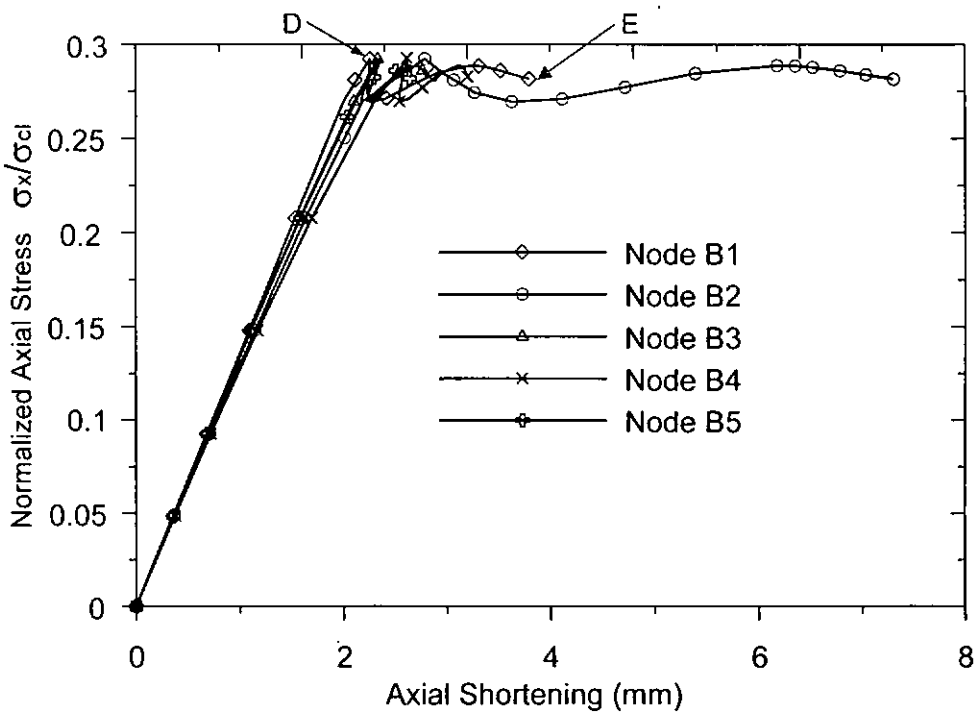

Figure 5.12 Load-displacement curves of selected nodes on upper end of Shell B

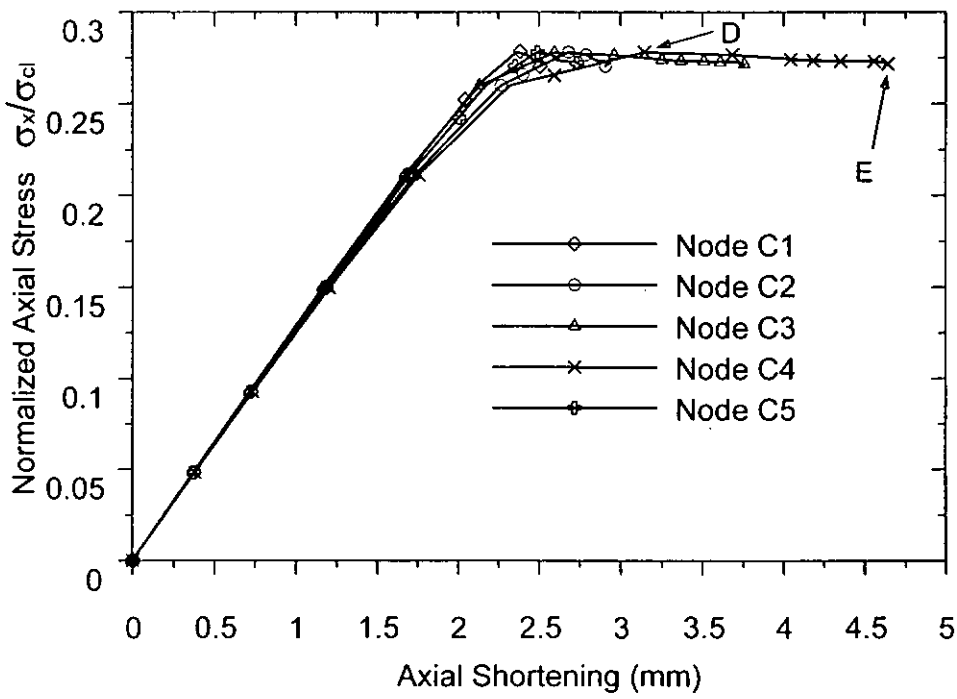

Figure 5.13 Load-displacement curves of selected nodes on upper end of Shell C

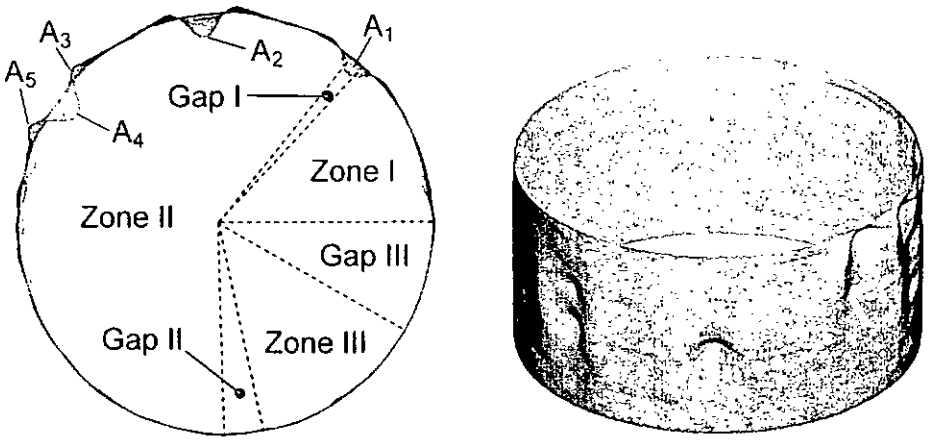

(a) Plan view (b) Perspective view

Deformation scaled by a factor of 50

Figure 5.14 Deformed shape of Shell A at point D of Figure 5.11

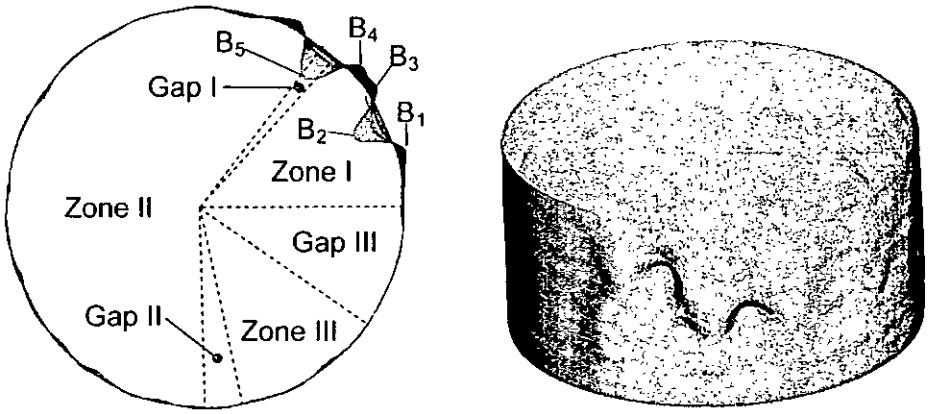

(a) Plan view (b) Perspective view

Deformation scaled by a factor of 50

Figure 5.15 Deformed shape of Shell B at point D of Figure 5.12

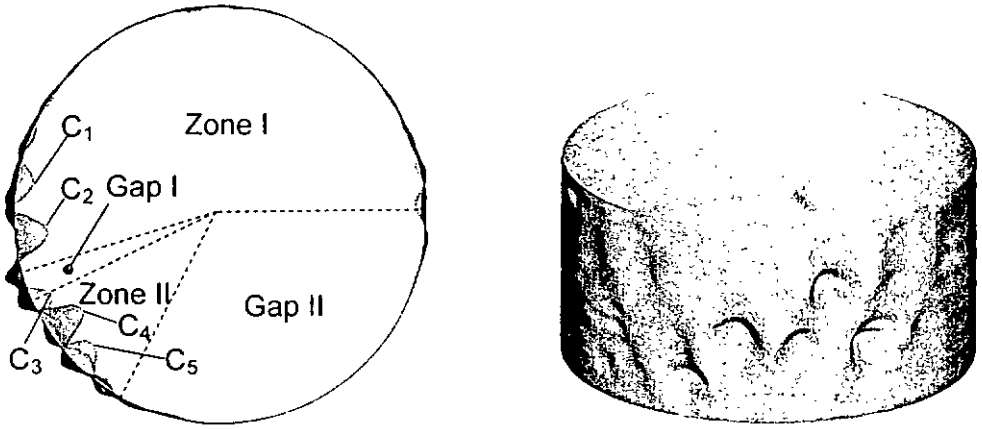

(a) Plan view (b) Perspective view

Deformation scaled by a factor of 50

Figure 5.16 Deformed shape of Shell C at point D of Figure 5.13

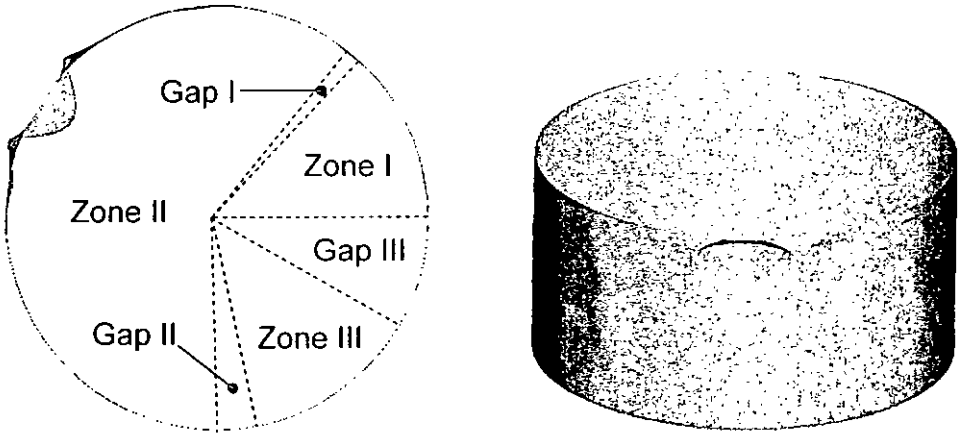

(a) Plan view (b) Perspective view

Deformation scaled by a factor of 10

Fig. 5.17 Deformed shape of Shell A at point E of Figure 5.11

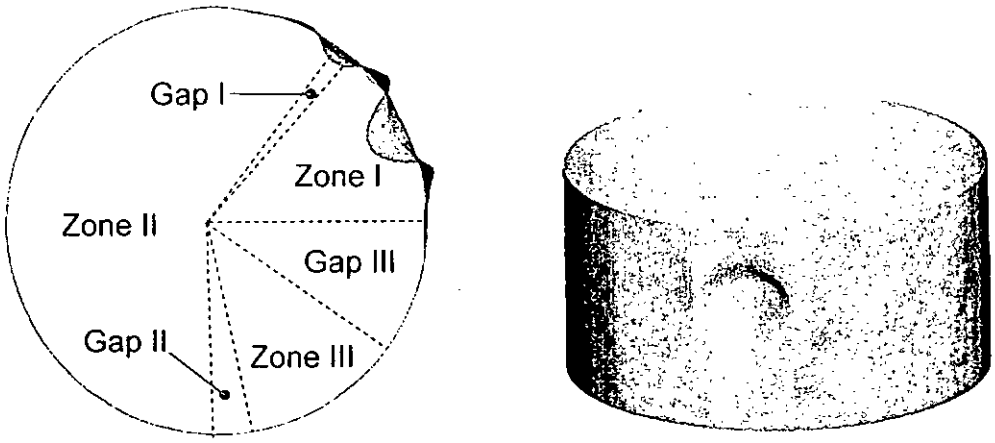

(a) Plan view (b) Perspective view

Deformation scaled by a factor of 15

Figure 5.18 Deformed shape of Shell B at point E of Figure 5.12

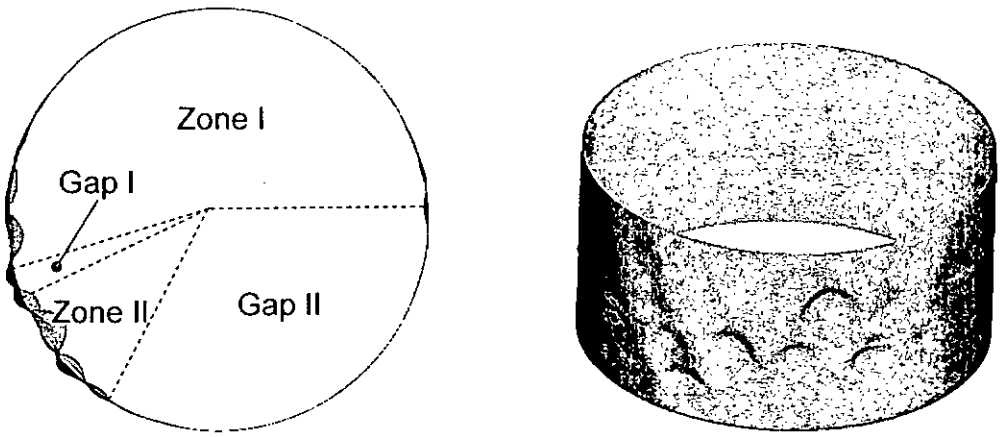

(a) Plan view (b) Perspective view

Deformation scaled by a factor of 20

Figure 5.19 Deformed shape of Shell C at point E of Figure 5.13

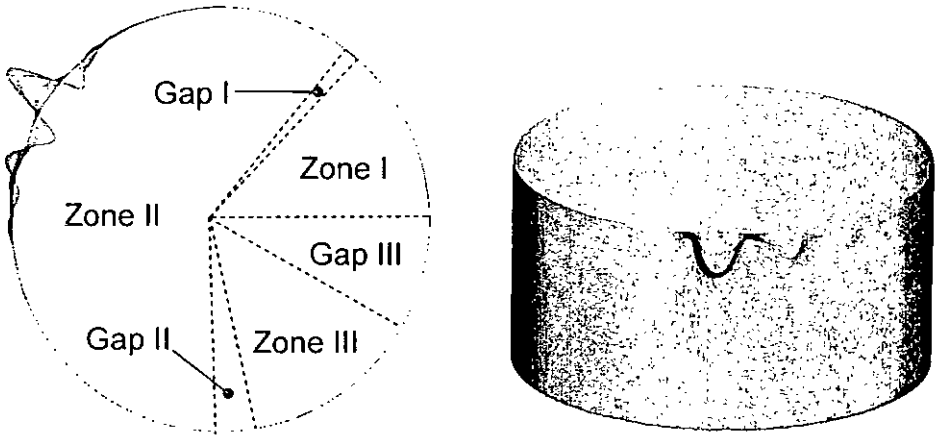

(a) Plan view (b) Perspective view

Figure 5.20 Nonlinear bifurcation mode of Shell A

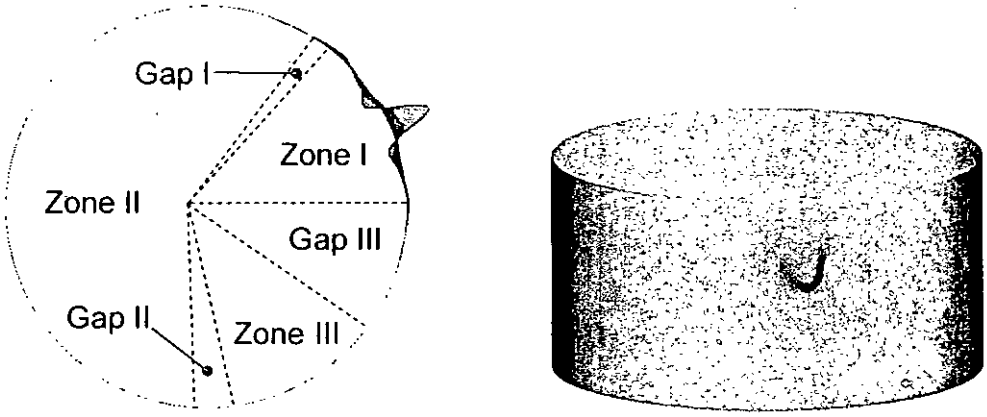

(a) Plan view (b) Perspective view

Figure 5.21 Nonlinear bifurcation mode of Shell B

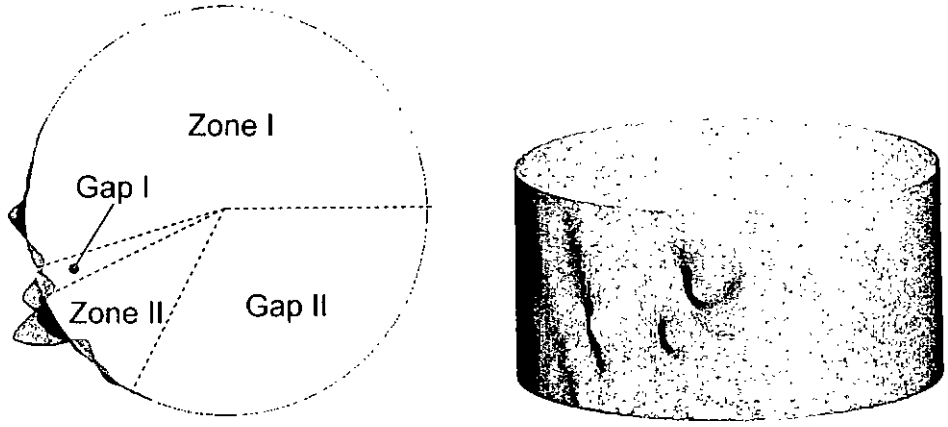

(a) Plan view (b) Perspective view

Figure 5.22 Nonlinear bifurcation mode of Shell C

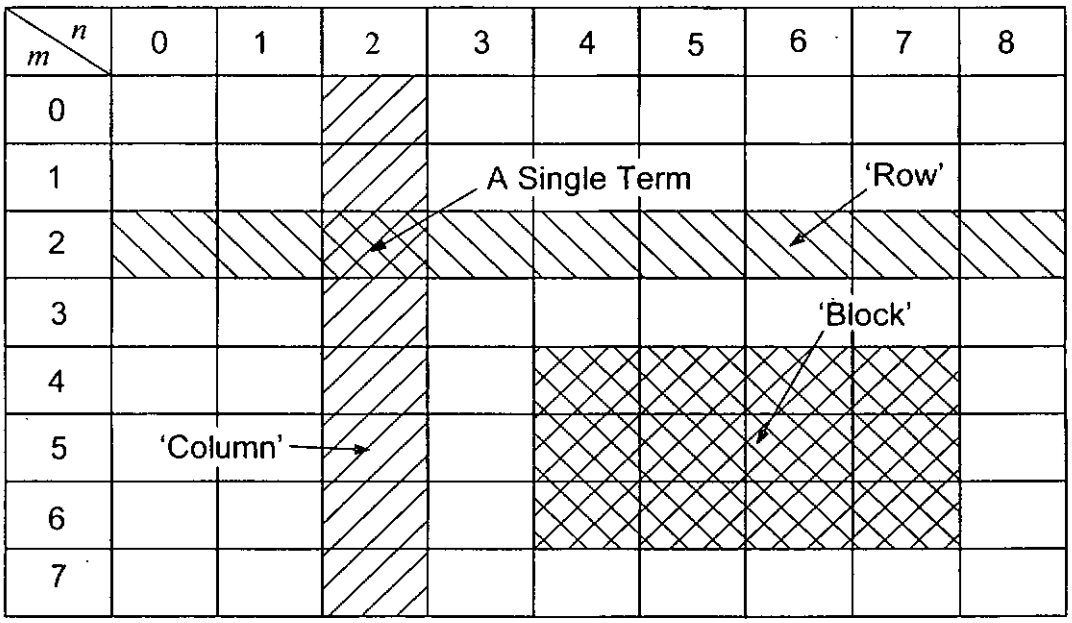

Figure 5.23 Imperfection map

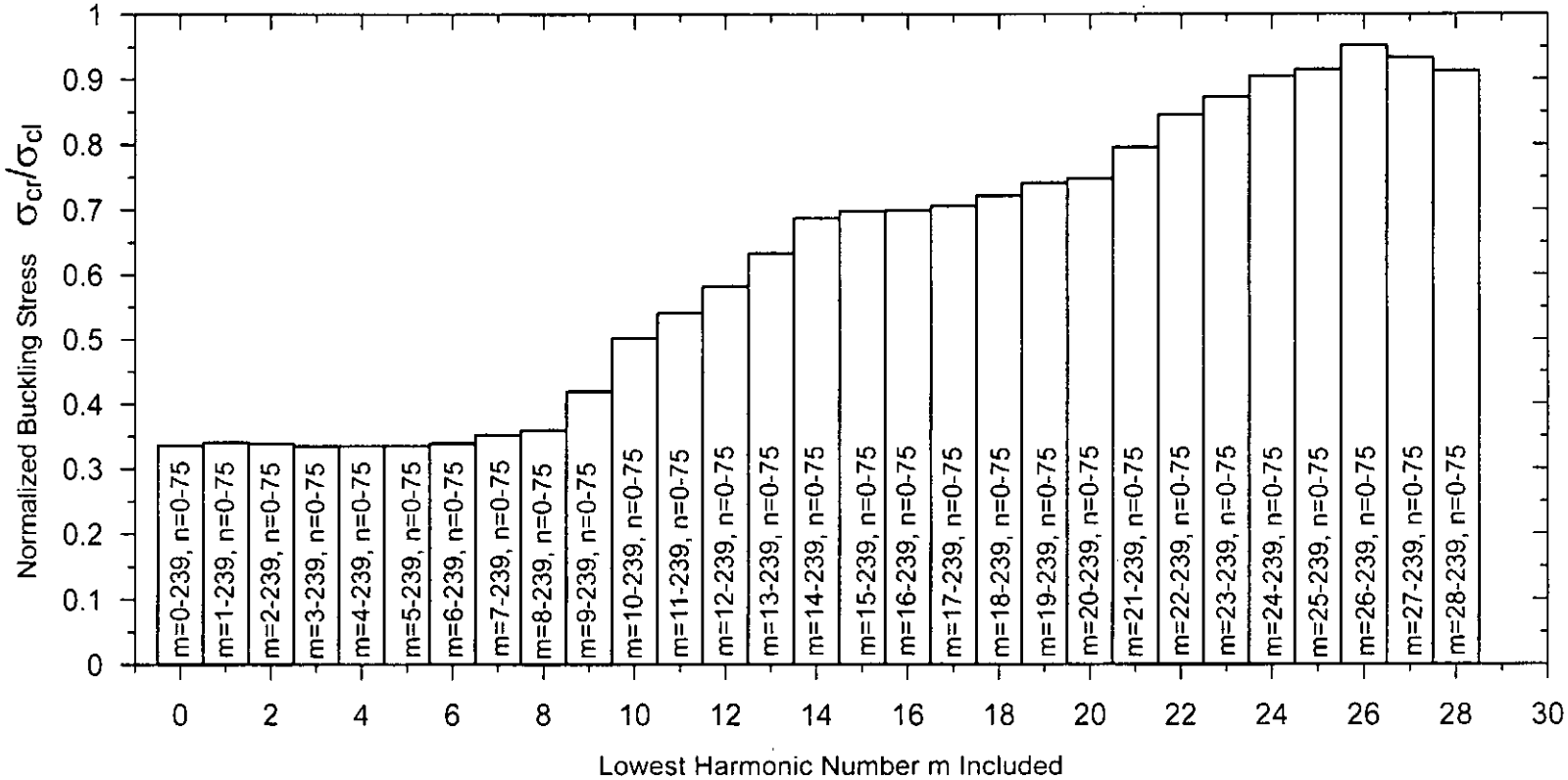

Figure 5.24 Linear buckling stresses of Shell A with selected block imperfections: effect of progressive exclusion of row imperfections

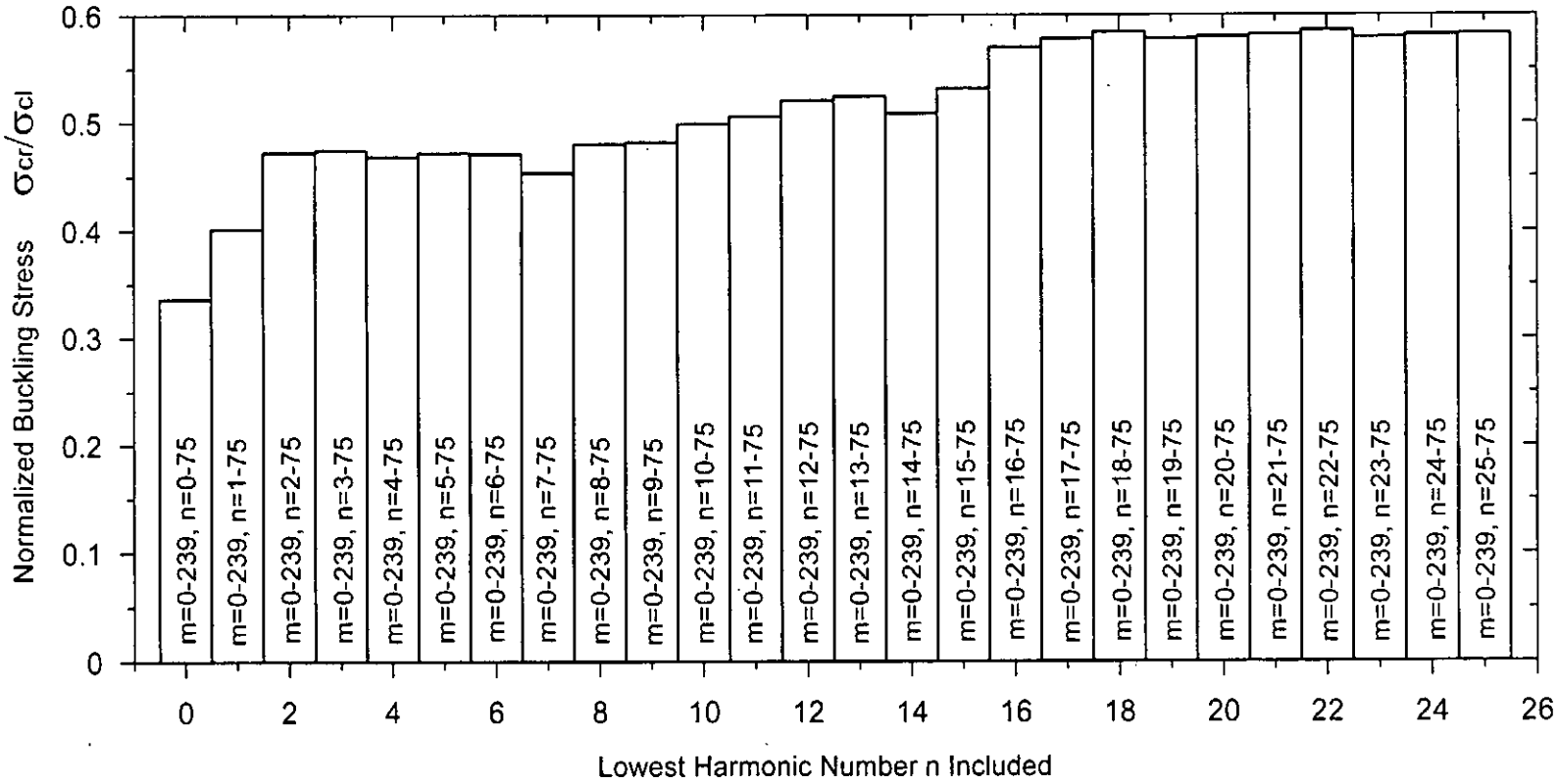

Figure 5.25 Linear buckling stresses of Shell A with selected block imperfections: effect of progressive exclusion of column imperfections

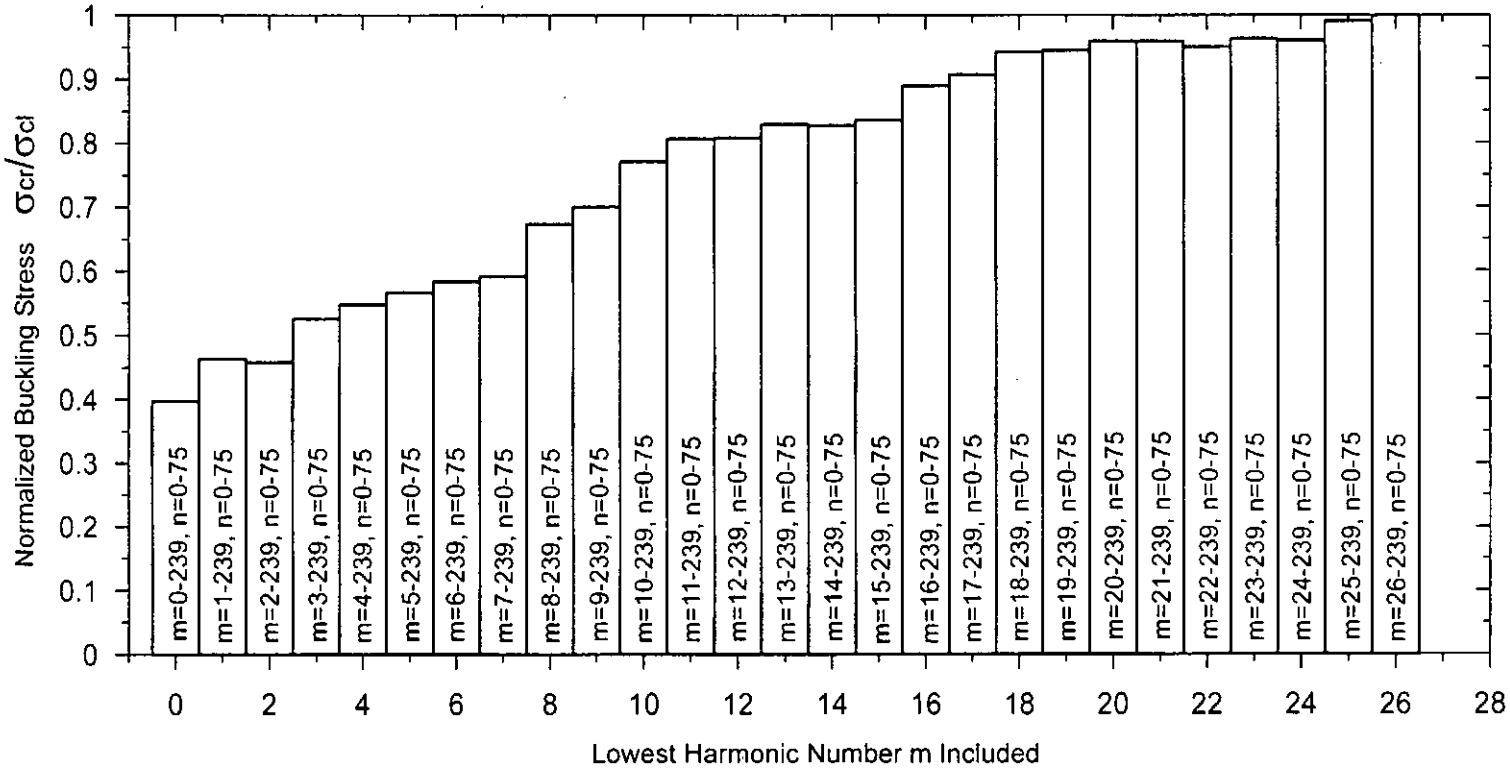

Figure 5.26 Linear buckling stresses of Shell B with selected block imperfections: effect of progressive exclusion of row imperfections

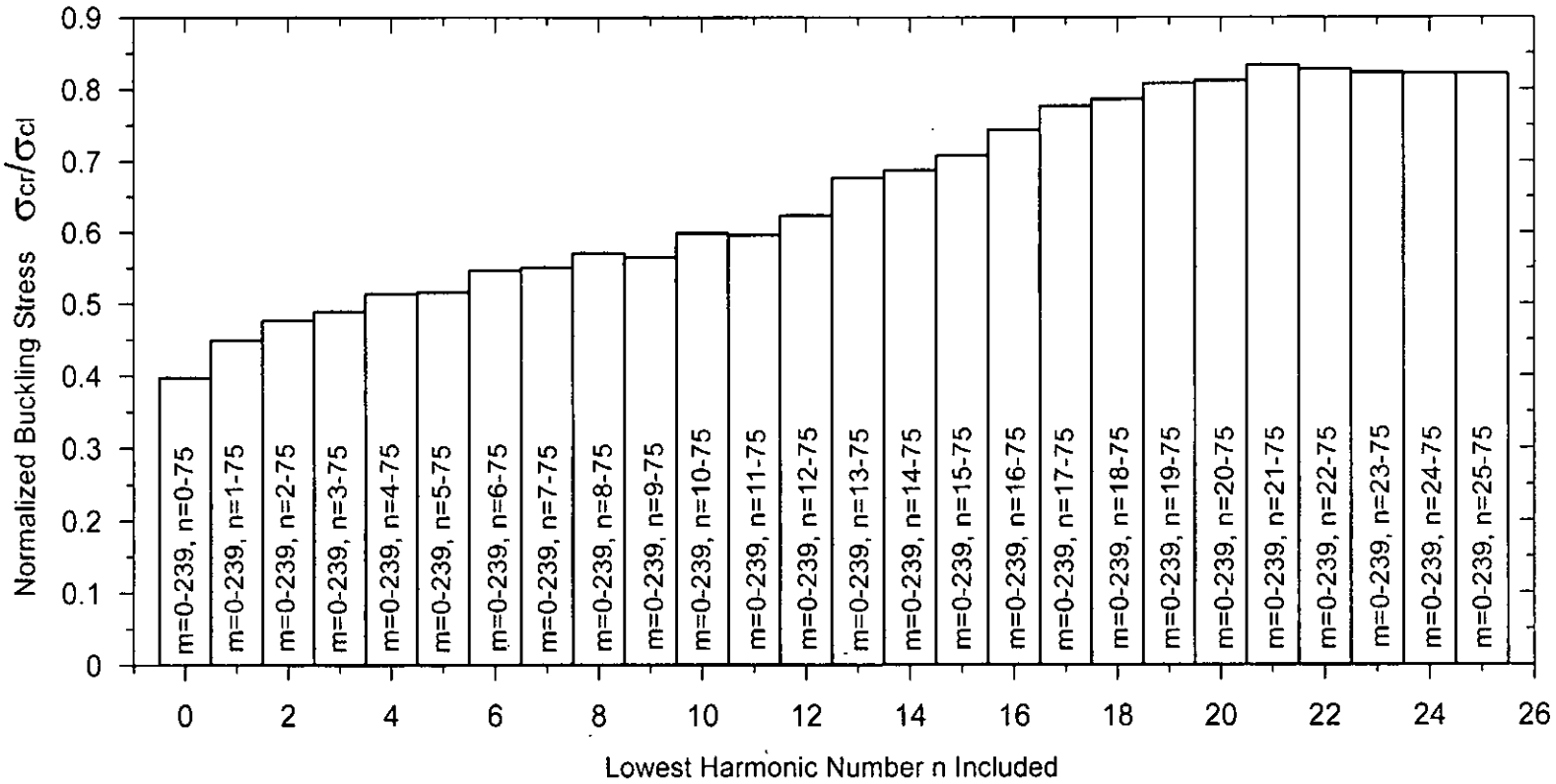

Figure 5.27 Linear buckling stresses of Shell B with selected block imperfections: effect of progressive exclusion of column imperfections

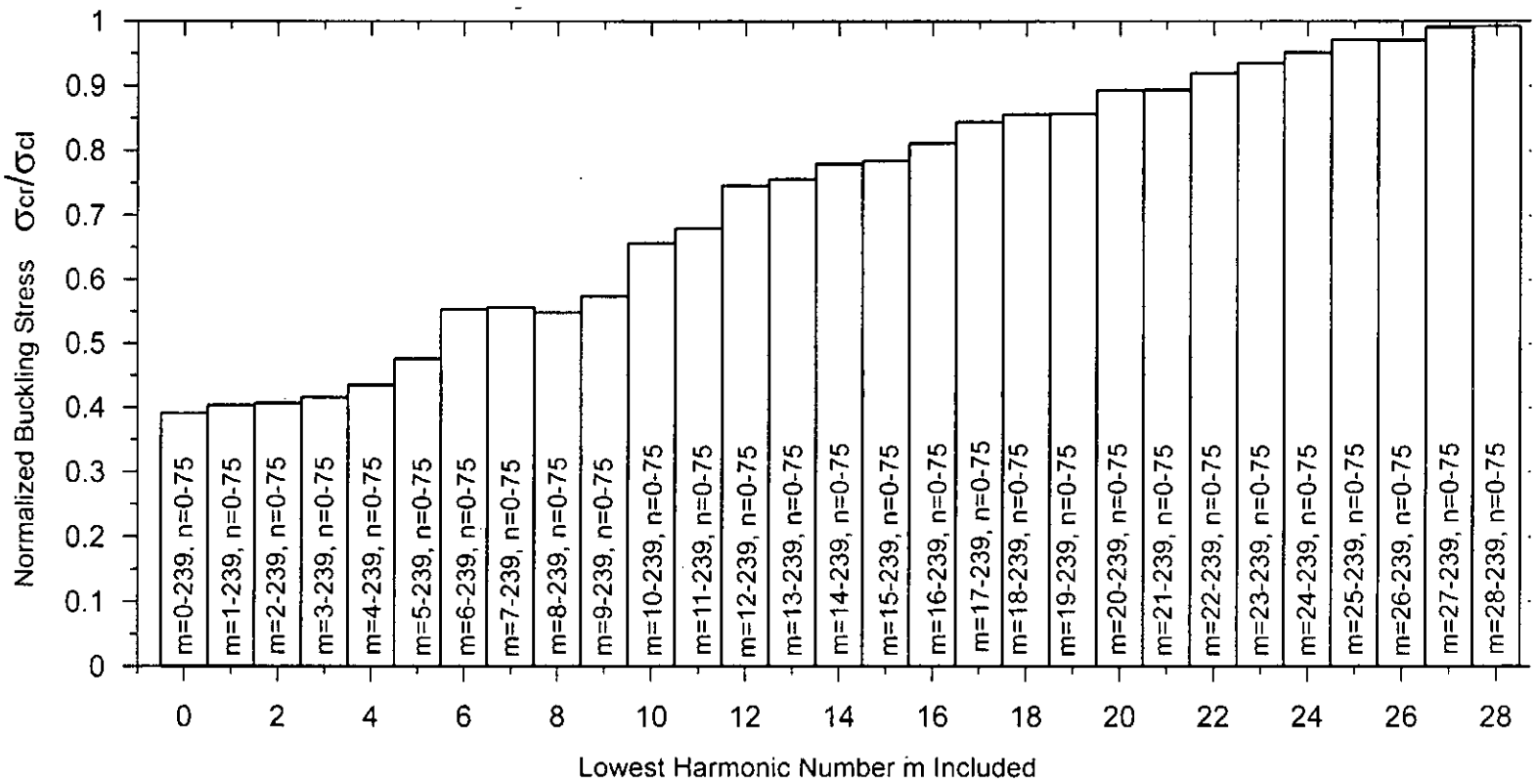

Figure 5.28 Linear buckling stresses of Shell C with selected block imperfections: effect of progressive exclusion of row imperfections

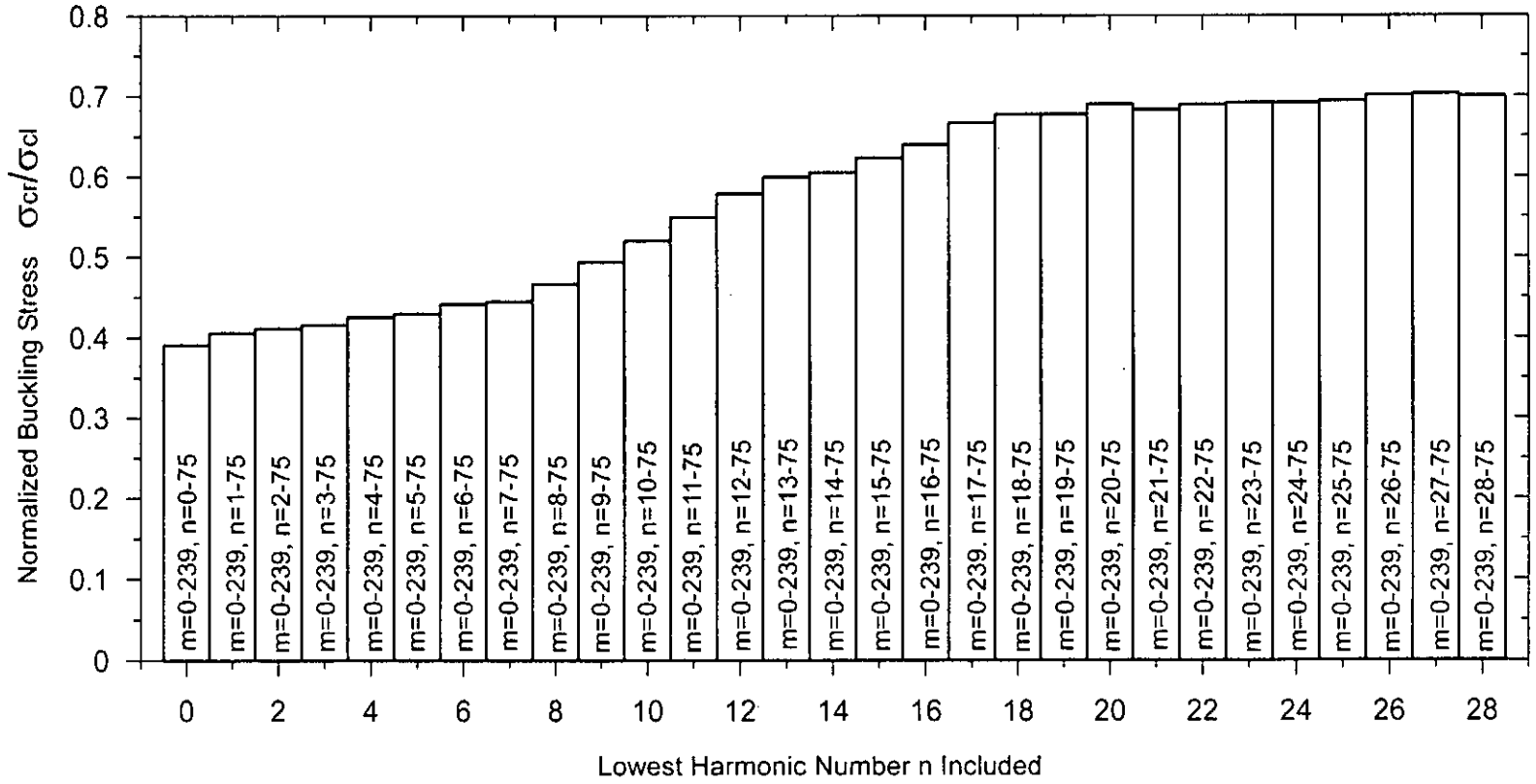

Figure 5.29 Linear buckling stresses of Shell C with selected block imperfections: effect of progressive exclusion of column imperfections

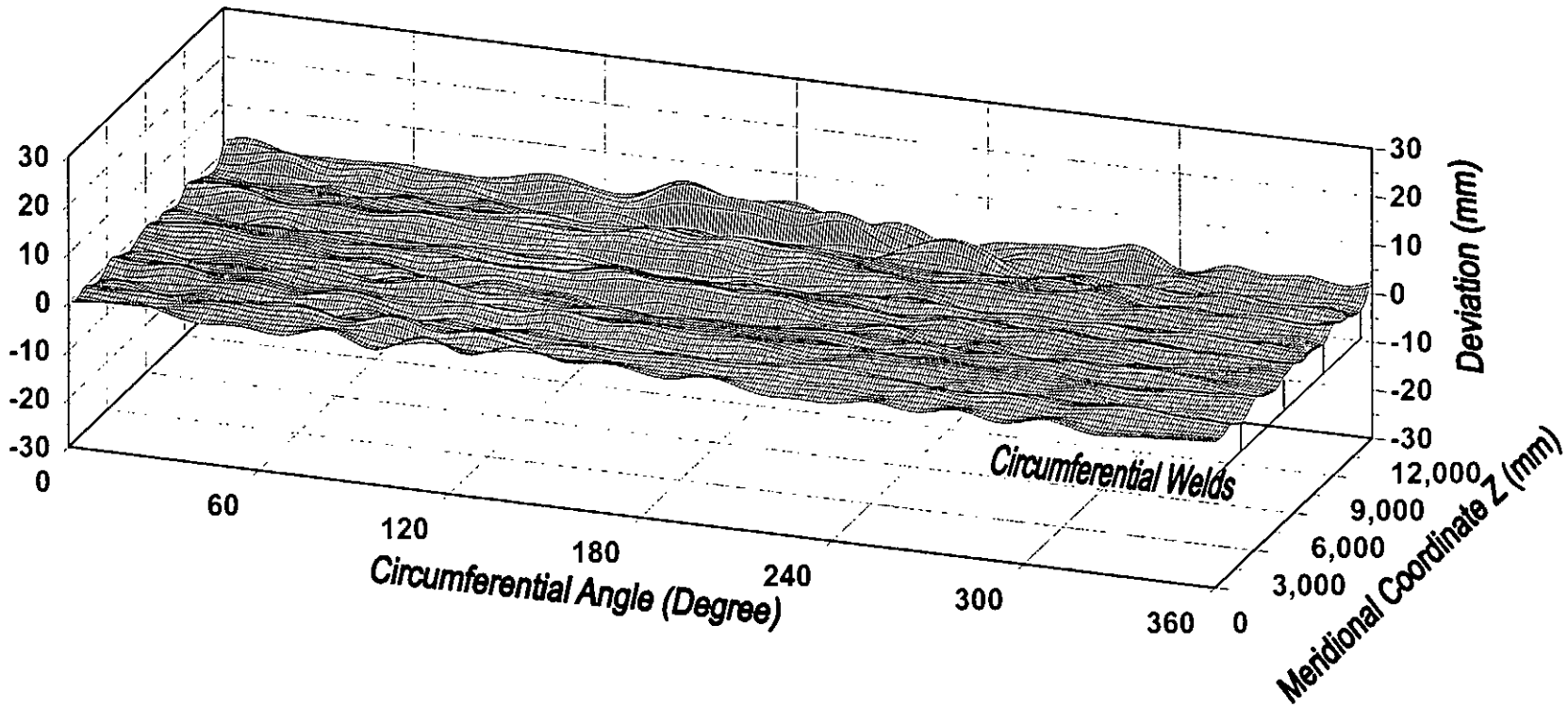

Figure 5.30 Three-dimensional plot of the critical block imperfection in Shell A

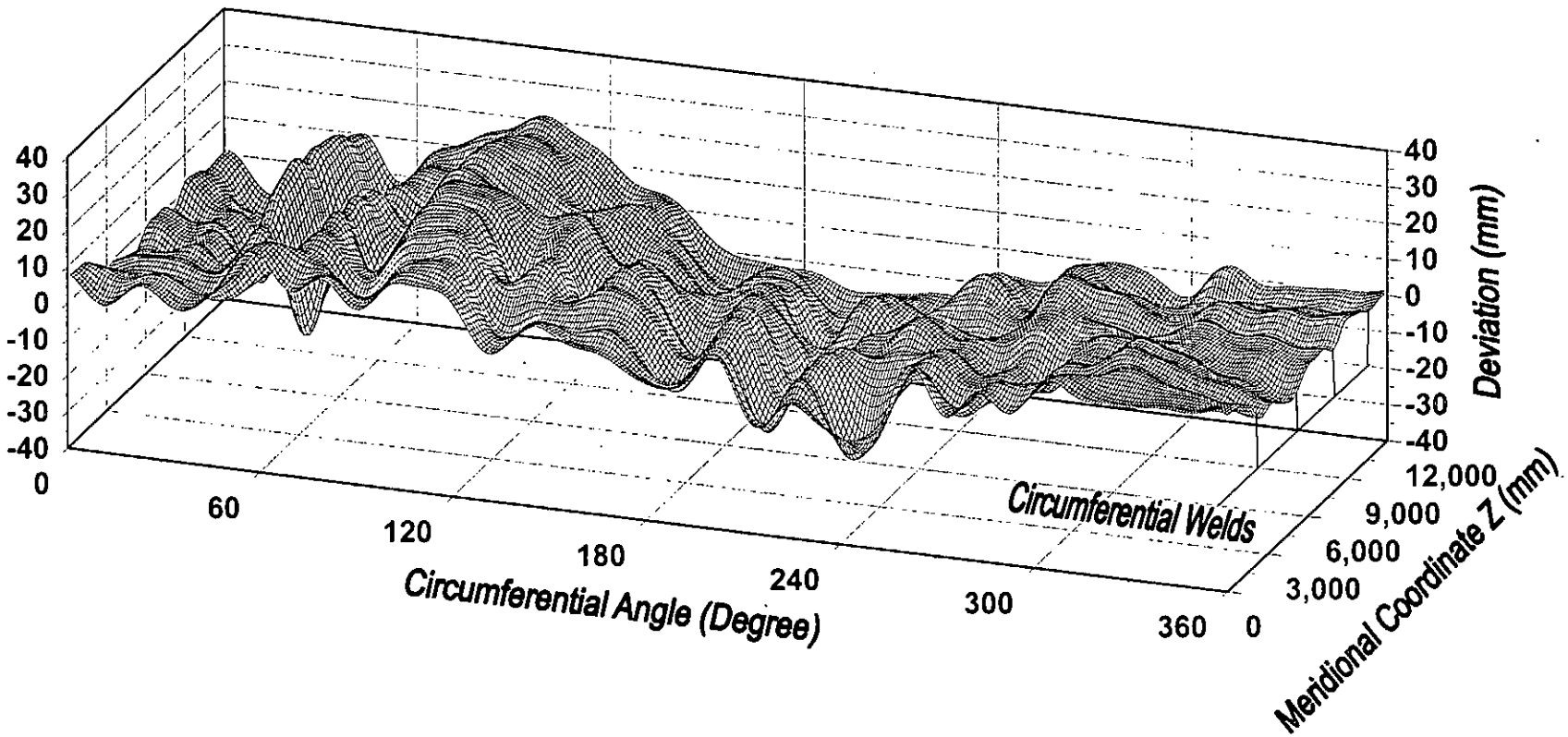

Figure 5.31 Three-dimensional plot of the critical block imperfection in Shell B

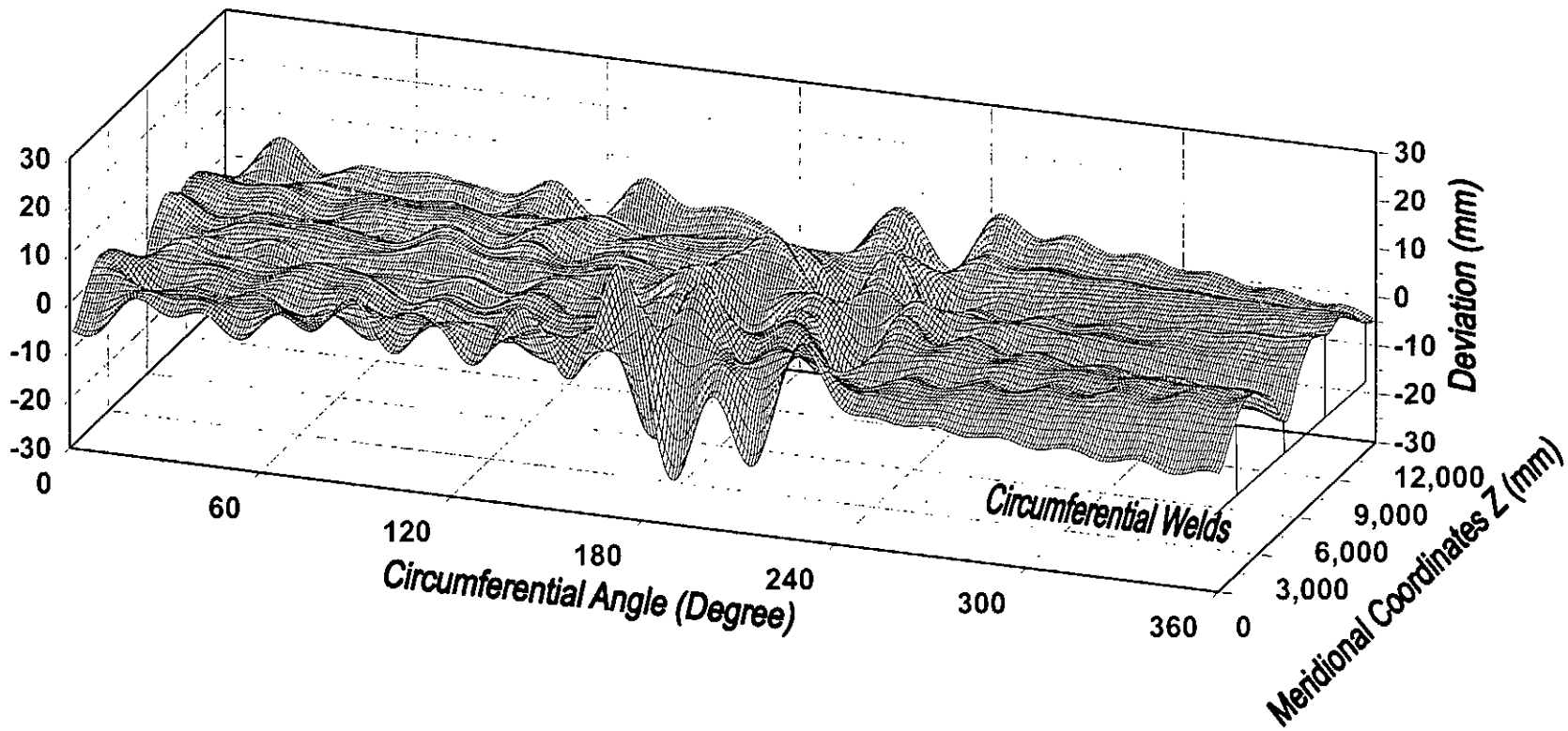

Figure 5.32 Three-dimensional plot of the critical block imperfection in Shell C

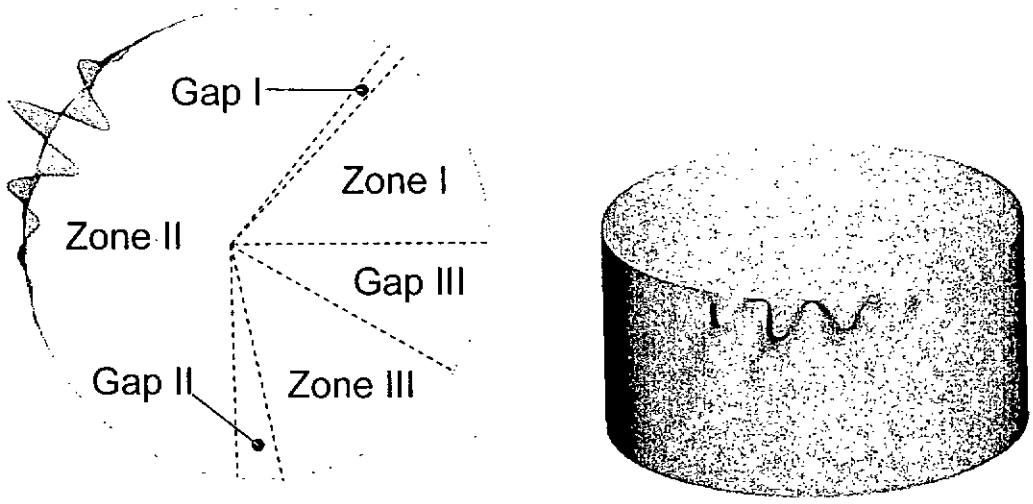

(a) Plan view (b) Perspective view

Figure 5.33 Linear buckling mode of Shell A with the critical block imperfections

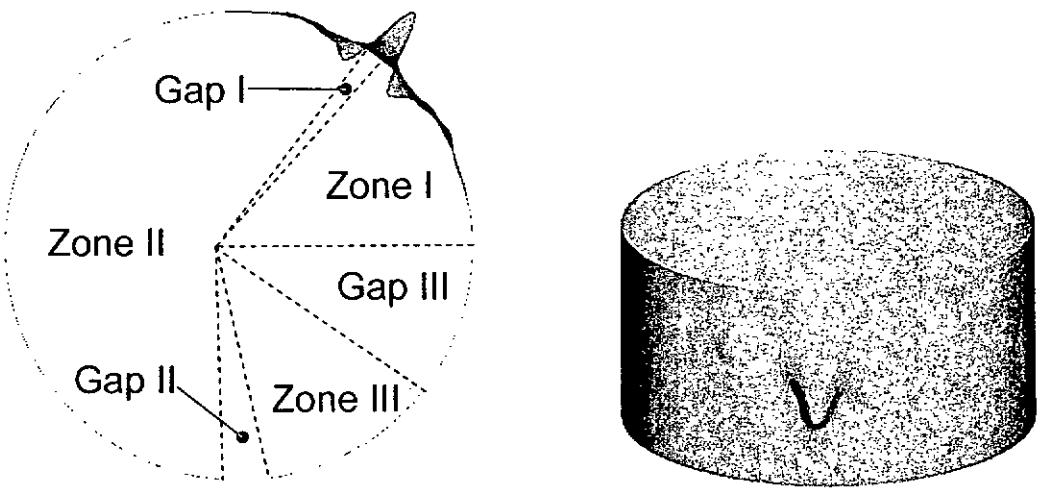

(a) Plan view (b) Perspective view

Figure 5.34 Linear buckling mode of Shell B with the critical block imperfections

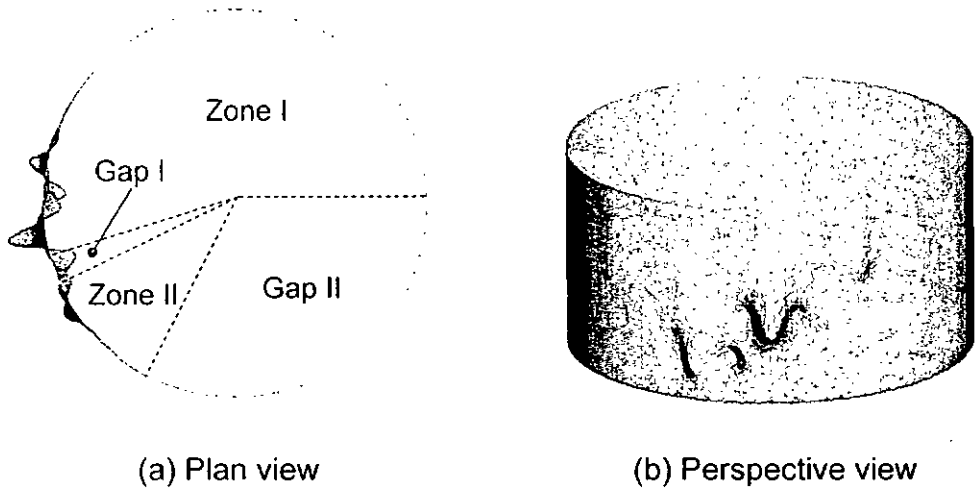

Figure 5.35 Linear buckling mode of Shell C with the critical block imperfections

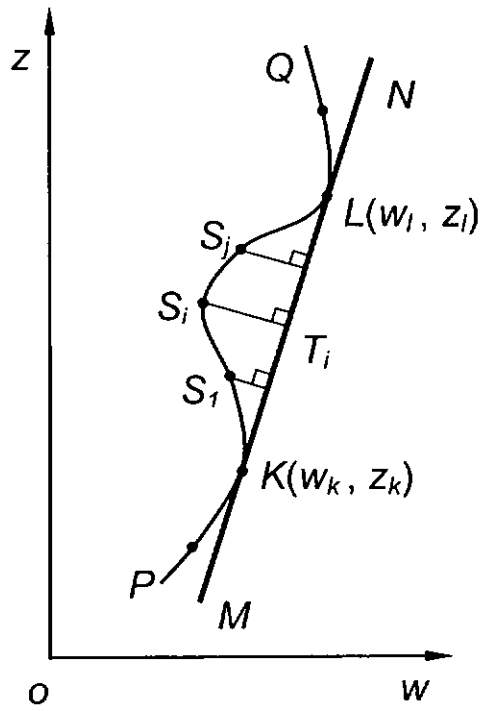

Fig. 5.36 Schematic of meridional measurement of dimple depths

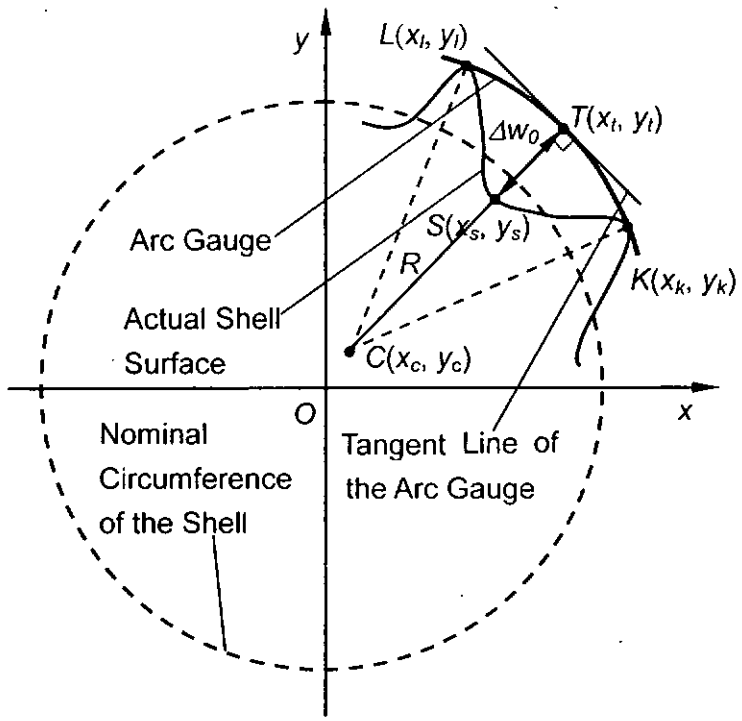

Fig.5.37 Schematic of circumferential measurement of dimple depths

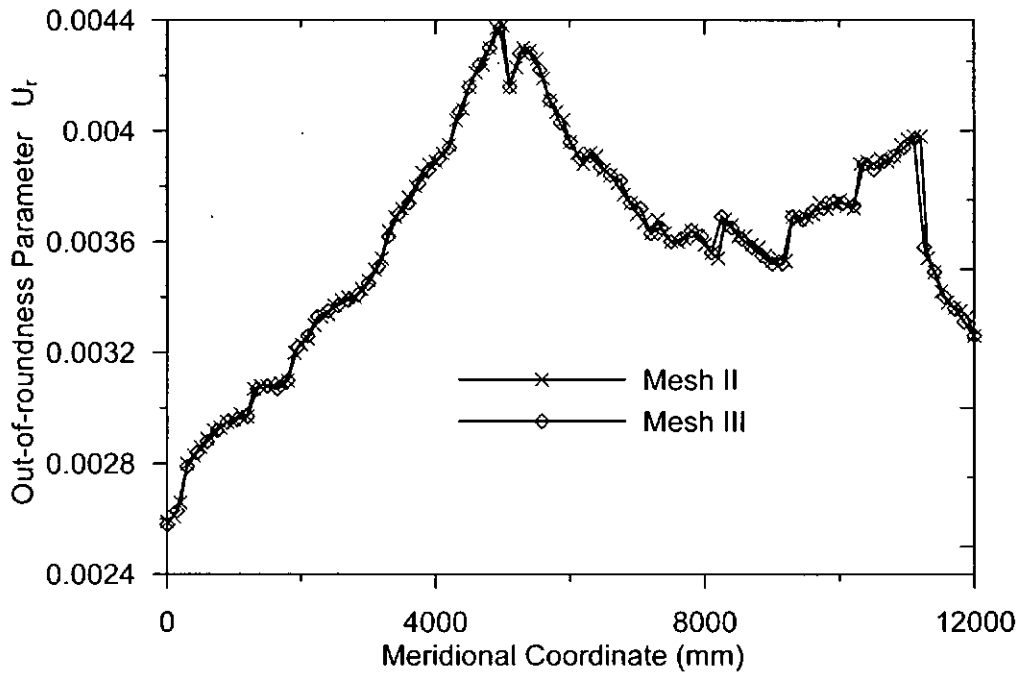

Fig. 5.38 Variation of the out-of-roundness parameter over the height of Shell A

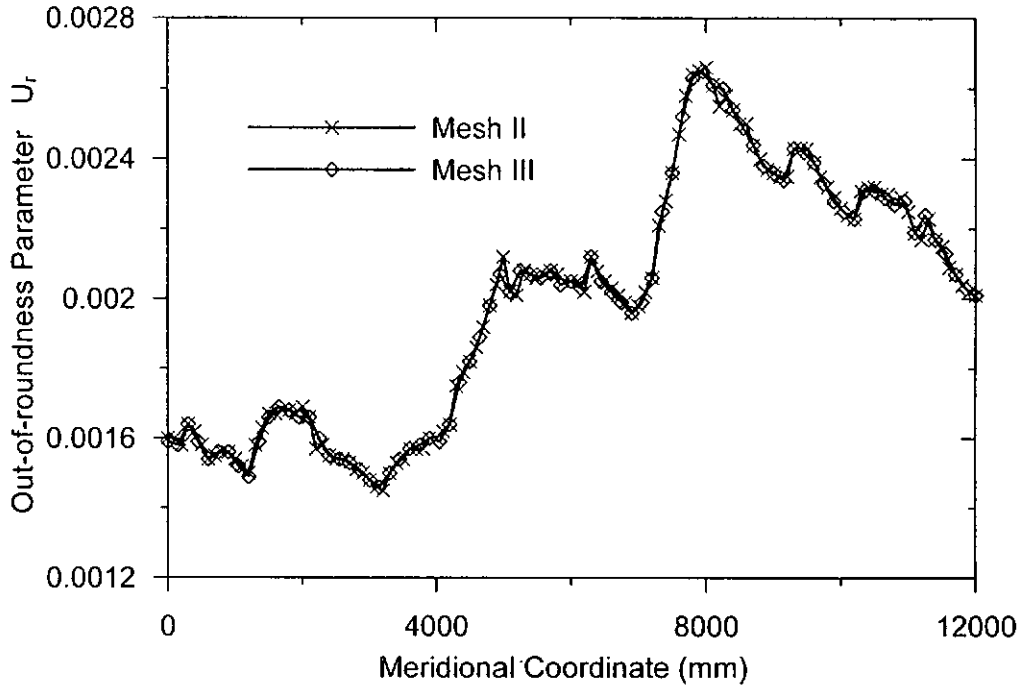

Fig. 5.39 Variation of the out-of-roundness parameter over the height of Shell B

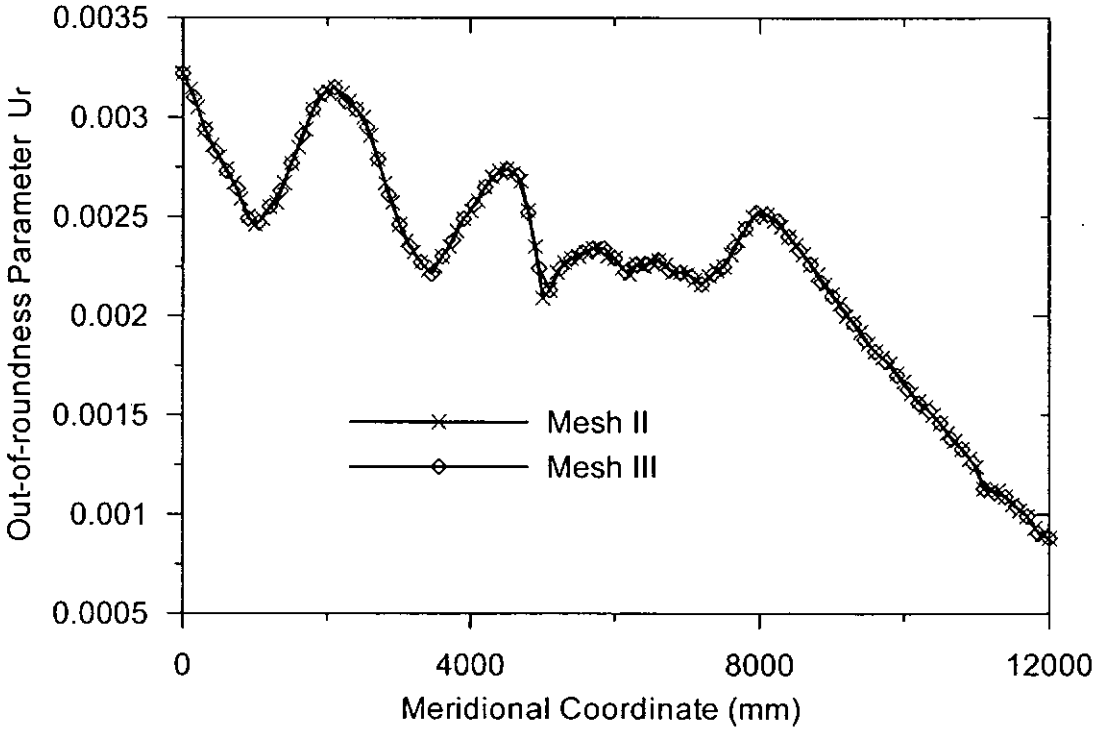

Fig. 5.40 Variation of the out-of-roundness parameter over the height of Shell C

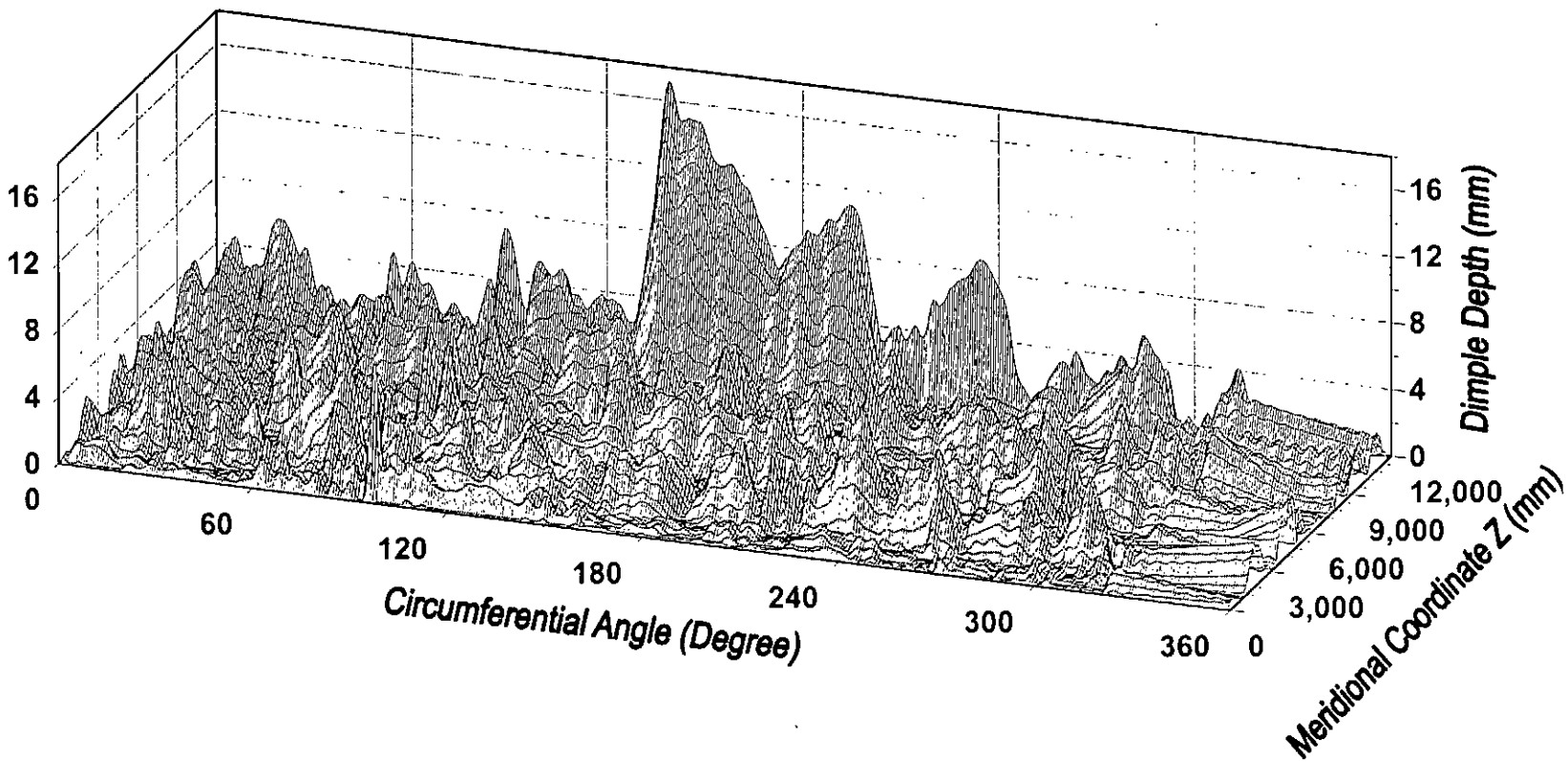

Figure 5.41 Dimple depths of Shell A from meridional measurements

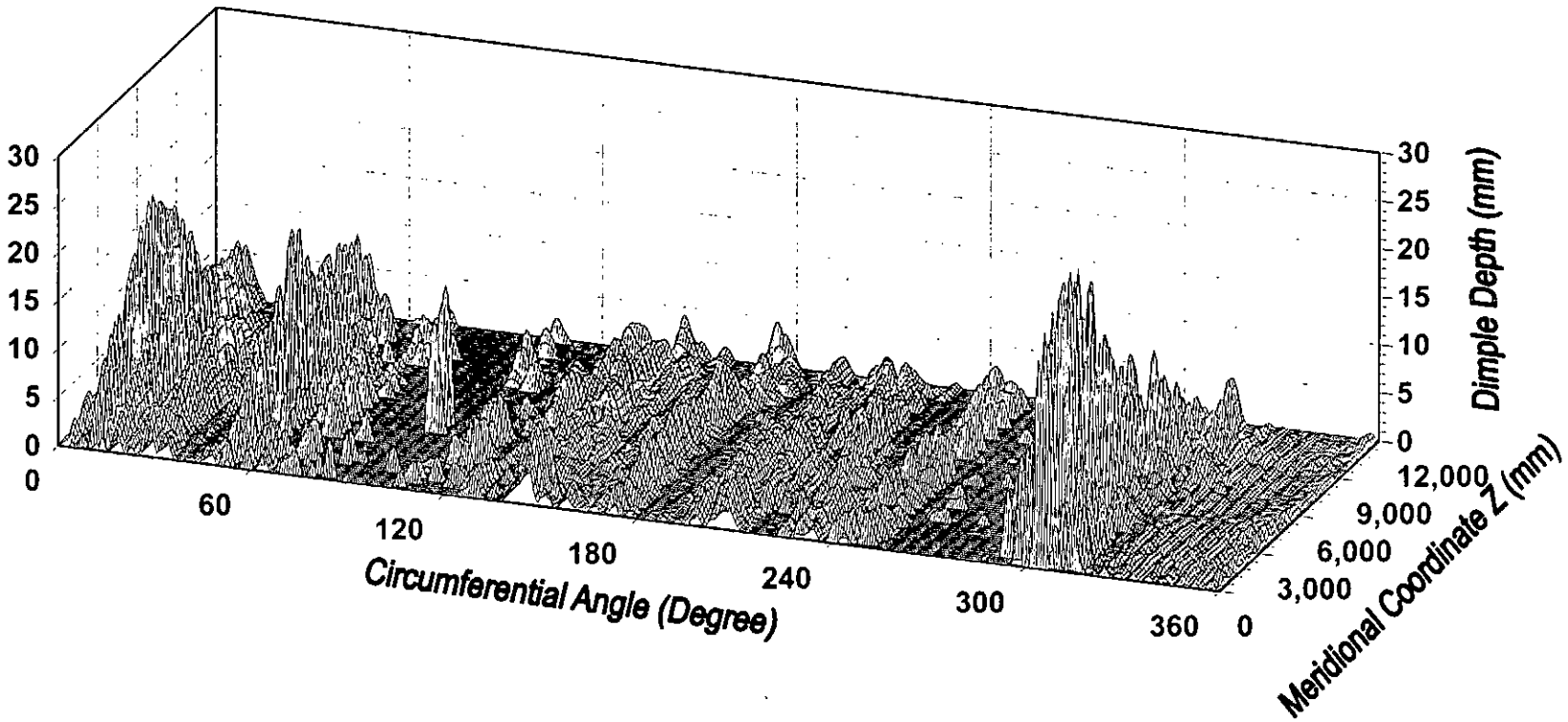

Figure 5.42 Dimple depths of Shell A from circumferential measurements

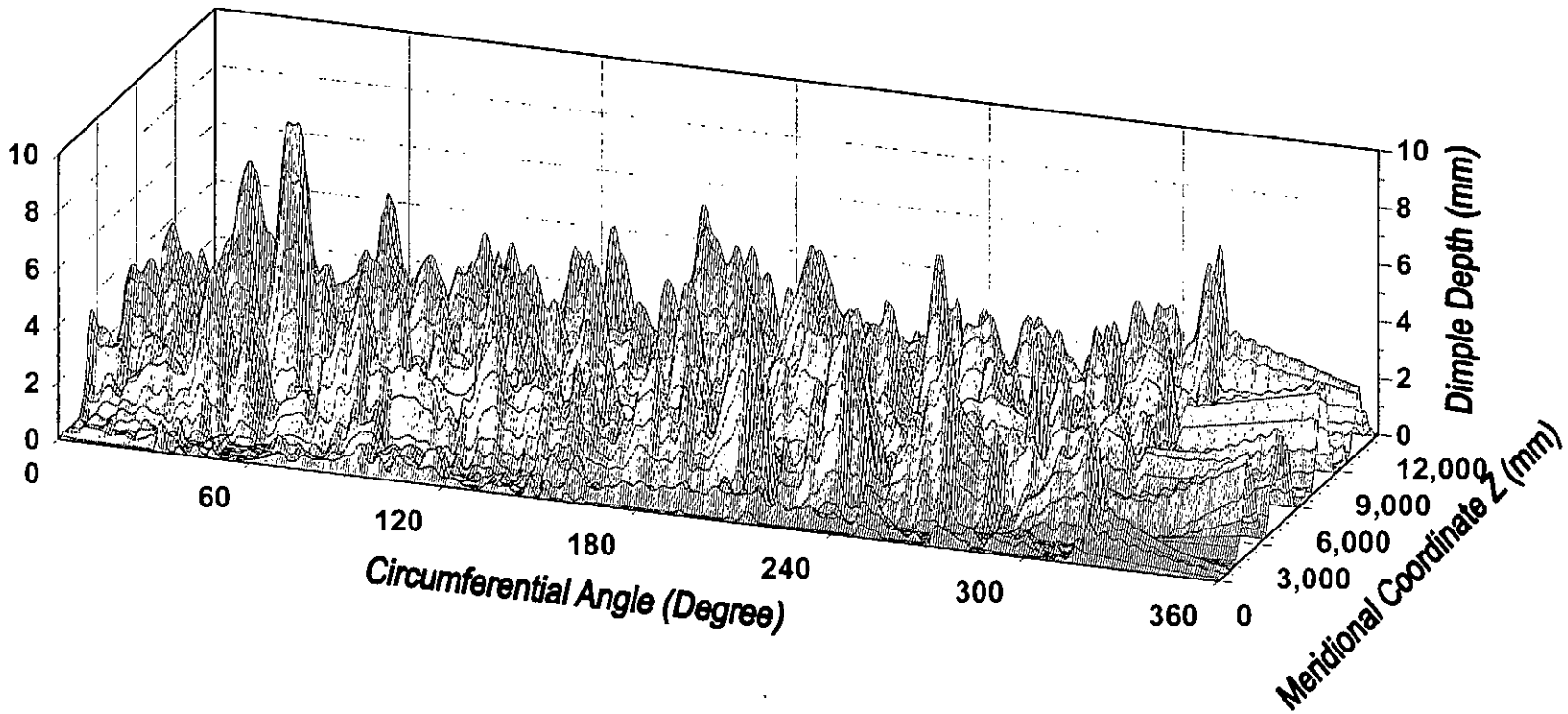

Figure 5.43 Dimple depths of Shell B from meridional measurements

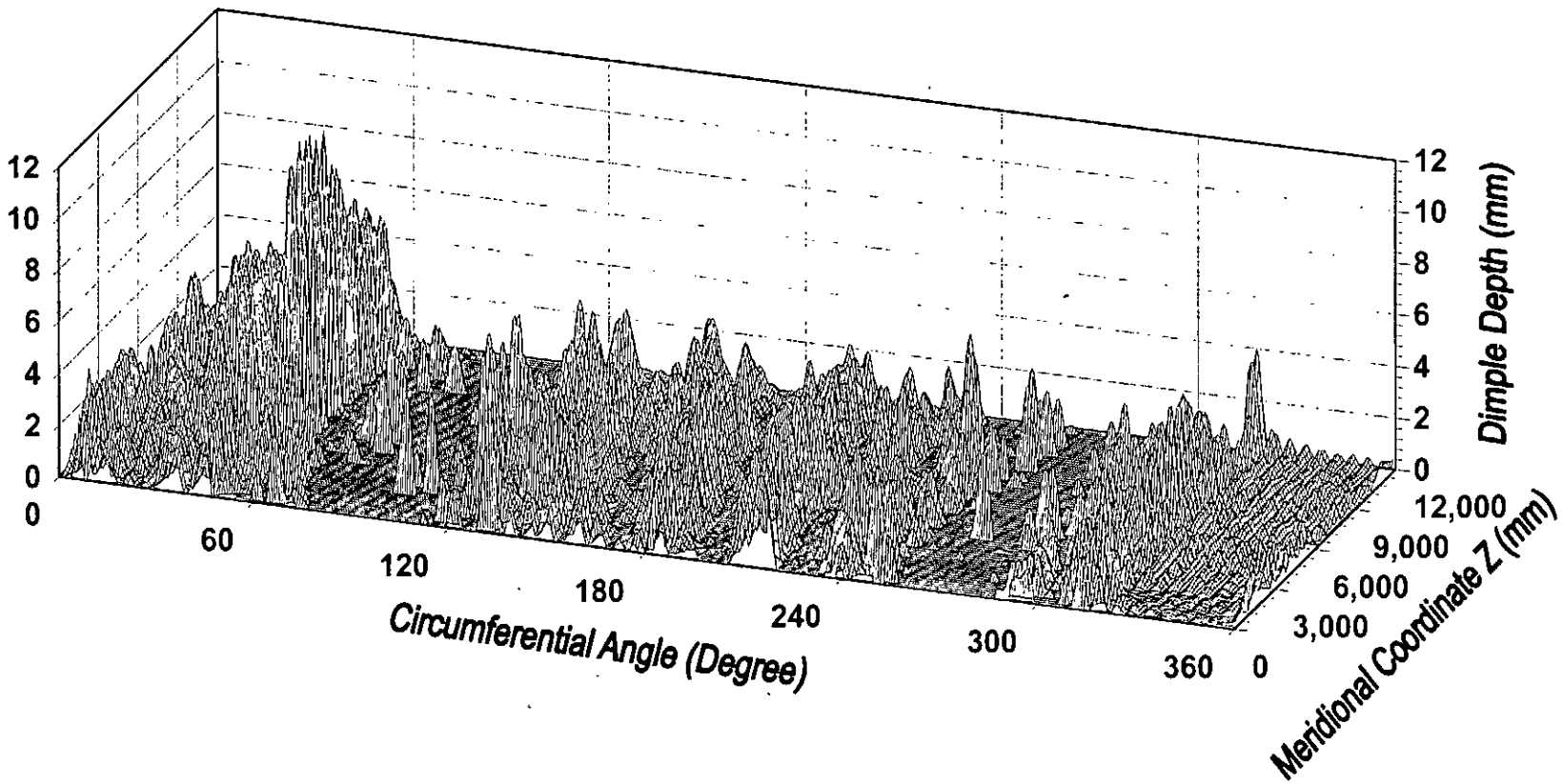

Figure 5.44 Dimple depths of Shell B from circumferential measurements

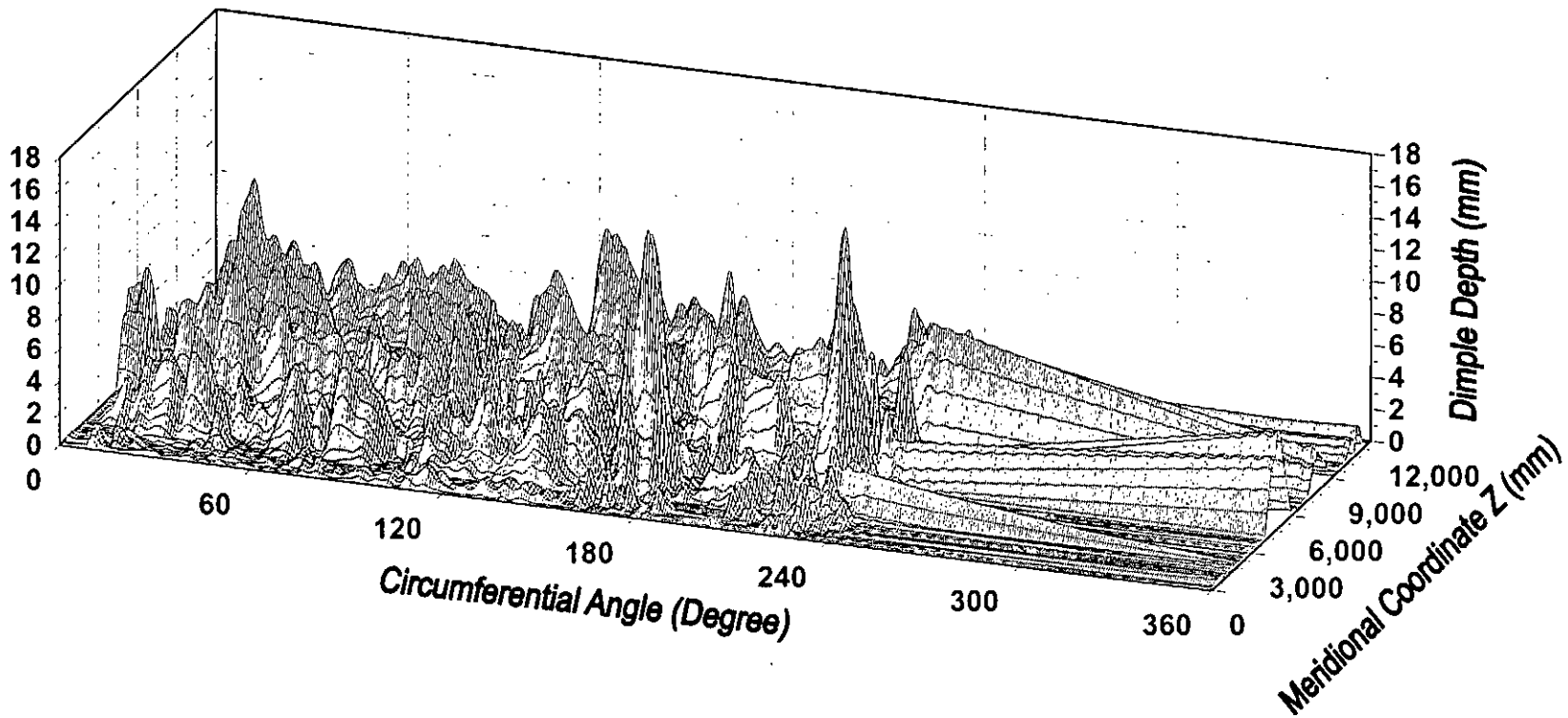

Figure 5.45 Dimple depths of Shell C from meridional measurements

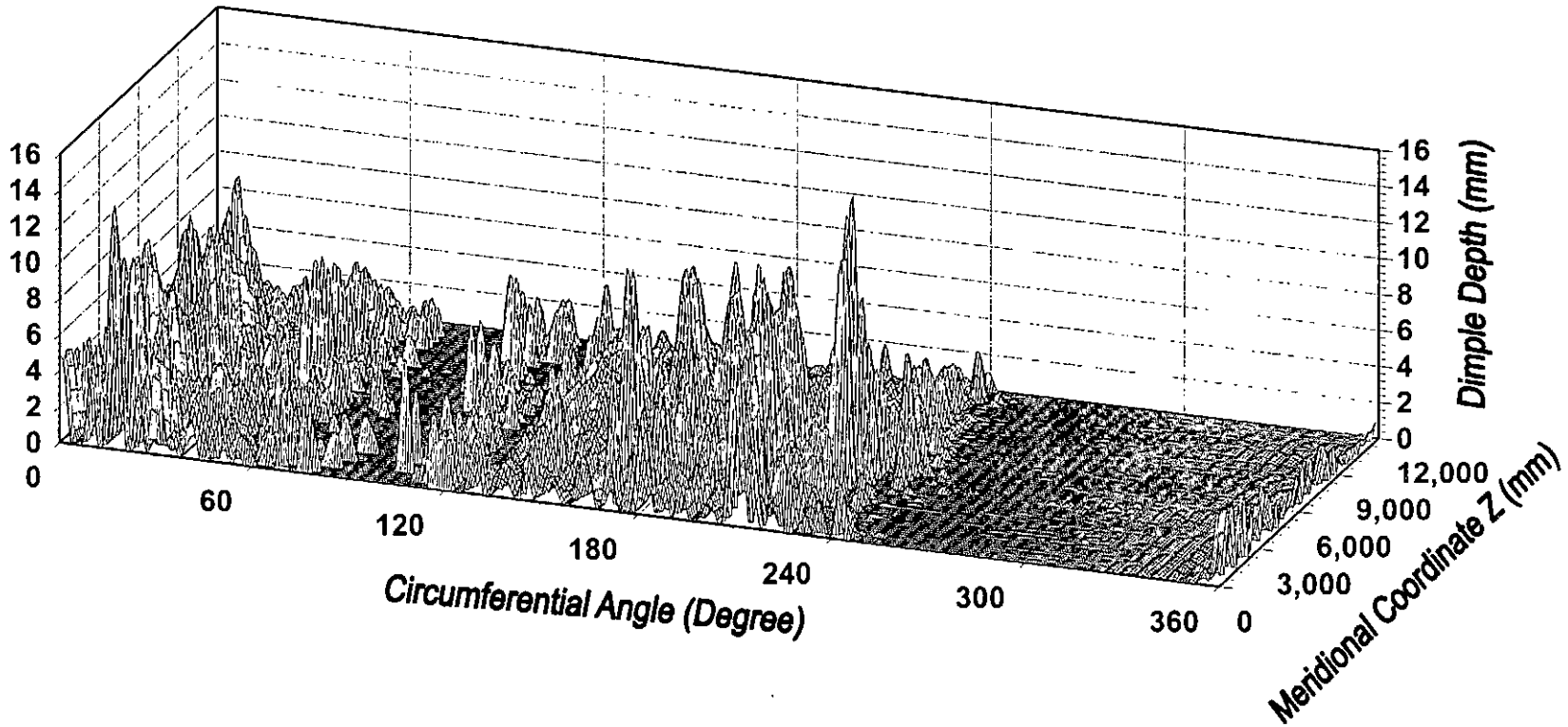

Figure 5.46 Dimple depths of Shell C from circumferential measurements

CHAPTER 6

TECHNIQUES FOR BUCKLING EXPERIMENTS ON EXTENSIVELY WELDED STEEL CYLINDERS

6.1 INTRODUCTION

As explained in the preceding chapter, to quantify the welding-associated factors other than geometric imperfections, it is necessary to conduct careful experiments on model cylindrical shells with a large number of welds as found in real shells in steel silos and tanks. Buckling experiments on cylindrical shells subject to axial compression are challenging because for such experiments to be of any value, the loading and support conditions need to be carefully controlled to achieve uniform axial compression in the shell and the initial geometric imperfections in the shell (and preferably some deformed shapes) need to be precisely measured. Furthermore, depending on the purpose of the experiment, the magnitude and form of imperfections in the shell need to be controlled; in cases where the test is expected to represent a real shell, then the imperfections need to be representative of those in real shells at least in terms of overall effect. It is also desirable to control the loading by displacements in the post-buckling stage so that the descending load-displacement path can be followed, although this is not essential if the buckling load is the main concern.

For experiments on model cylindrical shells simulating large real shells constructed from a large number of panels, with the effect of welding residual stresses appropriately reflected, the fabrication of the model shells is an additional challenge. The method of welding a large number of rolled panels to form a cylindrical shell, as is done in real construction, is not feasible for fabricating small models with a diameter of 1 meter and a wall thickness as small as or less than $1mm$. Models of a much greater size may be easier to fabricate

using this method, but they will very difficult to test in normal structural laboratory. To overcome this great problem, a novel fabrication was developed in the present work.

This chapter presents the techniques adopted or developed in the present work to overcome the difficulties mentioned above. A shell buckling test facility developed in a previous research project is first introduced, followed by a description of necessary modifications to this existing facility for the present experiments. A novel method for the fabrication of small model shells that simulate real shells constructed from many welded panels is next presented.

6.2 EXISTING TEST RIG

6.2.1 Loading and Supporting Systems of the Test Rig

The existing test rig was developed in a previous project for experiments on steel silo transition junctions (Zhao, 2001). The test rig consisted of three parts: a loading system, a supporting system, and a measurement system (Figures 6.1 and 6.2). The loading system comprised of a hydraulic jack and a rigid circular plate, with which the load from the hydraulic jack was transferred to the sand infill in the model steel silo transition junction to exert both internal pressures and wall frictions the model junction. The supporting system consisted of a thick circular support plate on a solid cylinder. The thick circular plate was provided with 12 radial stiffeners to enhance its bending rigidity. The supporting system not only provided a support for the test model, but also transmitted the load from the hydraulic jack to the base of the test rig; it can therefore be regarded as part of the loading system. As the measurement system is the key component of the test rig, it is described in the next sub-section in some detail.

6.2.2 Measurement System of the Test Rig

6.2.2.1 Measurement Device

The measurement system included a laser displacement meter, a rotating frame, a supporting frame, and a computer for data acquisition and automatic control. A laser displacement

meter of model KENYENCE LK-081, which had a resolution of 3 microns and a response time of 0.001 second, was used to ensure a high-speed non-contact measurement of high accuracy. The measurement range of this laser displacement meter was $80 \pm 15\,mm$, which was sufficient for the measurement of imperfections as well as deformations until in the deep post-buckling stage. An analog-to-digital converter of model KENYENCE RD-50R was employed to convert the analog signals from the laser meter to digital signals so that the data could be recorded by the computer.

The sensor head of the laser displacement meter was mounted on an aluminum rectangular rotating frame that sat on two bearings installed on a supporting frame. The two bearings were placed respectively on the top and bottom of the rotating frame at its vertical axis of symmetry so that the rotating frame could rotate around this axis. For accurate measurements, the measurement system was designed to be independent of the loading system. This was achieved by using a separate supporting frame and a tubular rotating shaft with an inner diameter of 110mm. The hollow rotating shaft allows the load to pass through the axis of the rotating frame without any interference with the measurement system.

6.2.2.2 Laser Meter Movements, Data Acquisition, and Computer Control

The circumferential movements of the laser meter were effected by the rotational movements of the rotating frame; these movements provided the circumferential coordinates. An ORIENTAL UPK564A-PG36 5-phase stepping motor with a step angle of 0.72^0 was used to drive the rotating frame. A gear with a gear ratio of $1:36$ was attached to the stepping motor to increase the resolution of the step angle. The transmission between the shaft of the gear and that of the rotating frame was implemented by a small pulley connected by a timing belt. The small pulley had a reduction ratio of $1:3$, leading to a further increase in the step angle resolution. The final resolution of the step angle is 0.0067^0, which corresponds to a circumferential distance of 0.058mm for a cylinder with a diameter of 1000 mm.

The vertical movements of the laser displacement meter, provided the meridional coordinates, was implemented by a lead-screw system (Figure 6.3) which could transform every 360° rotation of the lead-screw into a 5mm linear movement in the laser meter, as the

lead-screw had a pitch of 5mm. The lead-screw was driven by a 2-phase stepping motor of model ORIENTAL UMK243A with a step angle of 1.8^0, leading to a linear resolution of 0.025mm per step. To prevent the swinging of the lead-screw from interfering with the linear movement, two separate sliding blocks, with the lower block connected to the nut of the lead-screw system and the upper one attached to two guide rods via two small bushing bearings, were employed. This installation allowed horizontal sliding between the two blocks so that only the vertical movement of the lower block was transmitted to the upper block while the swinging motions were isolated. As the laser meter was mounted on the upper sliding block, the rotational motion of the lead-screw was transformed into a stable and smooth linear movement of the laser meter along the guide rods.

Both the measurements and the movements were controlled by a computer, where the communications between the measurement system and the computer were implemented through two passages. One was a Digital I/O Card and a 20-Pin Flat Cable for the communications between the computer and the stepping motors, while the other was an RS232C interface for the communications between the computer and the laser displacement meter. The procedure of measurements was implemented as the follows (Figure 6.4): First the digital signals were sent to the stepping motors to drive the laser meter to the required position via the Digital I/O Card and the 20-Pin Flat Cable, then the instruction of taking measurement was sent to the laser displacement meter and the measurement reading was sent back to the computer for storage via RS232C interface. In fact, the movement of the laser meter was continuous but the readings were taken at discrete points. All of these processes were accomplished semi-automatically using a program written in QBASIC.

6.2.2.3 *Calibration of the Measurement System*

The measurement system rotated the laser displacement meter around and moved it up and down the test specimen, producing a three dimensional surface of the test specimen. However, a surface so produced is not the exact surface of the specimen because it includes errors of the measuring system. To exclude these errors, a corresponding surface survey needed to be performed on a reference cylinder with a diameter of 1000mm, which was precisely machined to provide a calibration surface for the specimen. The results of the specimen survey could then be compared with those of reference cylinder surveyed with the

same measurement grid of the specimen. The errors of the measurement system were removed and the real surface of the specimen was found.

6.3 MODIFICATIONS TO THE EXISTING TEST RIG

6.3.1 General

Several aspects of the existing test rig were found to be unsuitable for the buckling experiments on axially compressed welded cylindrical shells planned for the present project. First, the methods of load transfer and load control were incapable for capturing the likely unstable post-buckling deformations in the present tests. Second, the semi-automatic measurement procedure of the original system, which was suitable for making measurements on a relatively small zone in the silo transition junction tests, was not feasible for the planned surface measurement of a complete cylinder, because the latter was found to be very time-consuming. Third, the original reference cylinder, which was only 500mm in height, was too short for the present cylindrical shell specimens with a height of 850mm. Modifications were therefore planned and implemented to the original test rig. A new reference cylinder with a height of 1000mm was precisely machined to replace the original one for specimen surface calibration. Details of other modifications are given below.

6.3.2 Modifications to the Loading System

For the loading system, the hydraulic jack was removed and the girders of the reaction frame that supported the jack were raised to make clearance for installing a MTS actuator. The MTS actuator was used because it provided programmable controllers not only for displacement but also for load. The base of the MTS actuator was connected to a stiffened steel beam that was mounted the girders of the reaction frame, while the swivel head of the MTS actuator was joined to a specially designed load transfer system, where the point load of the actuator was transferred uniformly to an annular line load on a test specimen of 1000mm in diameter.

The load transfer system consisted of a load transfer cylinder with end plates, a universal joint, a loading cone, and a loading ring (Figure 6.5); all these elements were joined together

using bolts and were capable of resisting both tension and compression. The load transfer cylinder, which had a diameter of 90mm, passed through the top tubular shaft of the test rig with a clearance of 10mm between the cylinder and the tube, while the end plates of the load transfer cylinder were connected to the swivel head of the MTS actuator and the universal joint at the top and the bottom, respectively. As a result, the point load of the actuator was effectively transmitted to the universal joint without any disturbances to the measurement system. The universal joint was used to make sure that only a vertical point load was transmitted to the loading cone; this was achieved by incorporating a spherical bearing into the joint to provide a biaxial rotational freedom. The shallow loading cone, which was designed as a truncated cone with a thick circular plate at the top and a strong ring at the bottom, provided a uniform and stiff device for distributing the concentrated load from the universal joint to an annular line load. Two holes of 22mm in diameter were drilled symmetrically on the cone for the cables and wires to pass through. The loading ring with a knife edge was designed to achieve uniform axial compression on the end ring of a shell specimen. In conjunction with this design, a V-groove was incorporated into the bottom ring of the loading cone match the knife edge of the loading ring. The rectangular groove at the bottom of loading ring was designed to mate the end ring of the shell specimen.

6.3.3 Modifications to the Measurement System

During circumferential measurements, there existed an inevitable small gear clearance between the driving gear and the gear being driven, which was amplified remarkably by the transmission system and the long arm of the rotating frame, leading to a positional error of around 8 mm at the end of a complete circumferential motion around a cylinder of 1000 mm in diameter. This was a major problem for the implementation of an automated surface survey in which the laser displacement meter was required to move continuously around the shell in the clockwise and the anti-clockwise directions alternately from the same starting point at successive meridional positions. The alternate movements in the clockwise and the anti-clockwise directions were required so that the connected wires could be wound and unwound alternately. In the previous project (Zhao, 2001), a semi-automatic measurement procedure was adopted to overcome this problem, in which the gear clearance was eliminated by adjusting the rotating frame manually at the start of each round of circumferential measurements. This semi-automated procedure was too time-consuming for the present tests.

During this project, many attempts were initially made to eliminate the gear clearance problem by sending a few additional signals (pulses) to the rotational stepping motor. This approach was however found to be ineffective, as the number of pulses required for the elimination of this problem was found to vary for each round of circumferential measurements. Later attempts found that by starting and stopping the rotational motion gradually in a proper manner, the gear clearance problem could be effectively eliminated. For a 360^0 circumferential motion of the rotating frame, an acceleration of the rotational speed from zero to about $0.015 rad/s$ within the range of $0^0 - 15^0$ combined with a gradual deceleration of the rotation speed from $0.015 rad/s$ to zero within the range of $340^0 - 360^0$ were found to enable the ending position to coincide with the starting position.

Similar to those in Teng and Zhao (2001), repeatability tests were carried out to examine the stability of the measurement system. It was found that the largest difference between two sets of meridional measurements at an interval of 1mm over a range of 500mm was only $21\mu m$, while the biggest difference between two sets of circumferential measurements at an interval of 1^0 over a range of 360^0 was within $38\mu m$ for both the clockwise and the counter-clockwise measurements. These results demonstrated not only the excellent repeatability of the measurement system but also the effectiveness of the procedure adopted for eliminating the gear clearance problem.

With the problem of gear clearance resolved, automated measurements on a complete shell surface could be easily made. The automated measurement procedure was as the follows and was implemented by a computer program written in QBASIC.

(1) The laser displacement meter was positioned manually at a chosen starting point for measurements;

(2) The control computer sent an instruction to the laser meter to take the first reading that was subsequently recorded in the computer;

(3) The control computer sent an instruction to the rotating stepping motor to drive the laser meter counter-clockwise to the desired next circumferential position and another reading was taken and recorded by the computer. This procedure was repeated until the laser meter returned to the starting point of this circumference.

(4) The computer instructed the stepping motor for linear movements to drive the laser meter meridionally to the starting point of the second circumference and the measurement of the second circumference began; this time the laser displacement meter was rotated clockwise so that the cables that were wound around the rotating shaft during the first round of circumferential measurements were un-wound;

(5) The counter-clockwise measurements and the clockwise measurements were undertaken alternately around circumferences until measurements of the complete surface of the shell were completed.

6.4 FABRICATION OF SMALL MODELS

6.4.1 General

As explained earlier, one of the challenges of shell buckling experiments is to fabricate small specimens with desired characteristics. In the present work, the aim was to produce small models which were representative of real shells. In real construction using the panel method, flat plates of relatively small sizes are rolled into circular panels and then joined to form circular strakes. These circular strakes are then assembled to form the complete cylinder using circumferential welds. The extensive use of welding to join many panels results in oscillating patterns of geometrical imperfections and associated residual stresses. These are the key features the laboratory model should reproduce.

The exact process of welding a large number of small rolled panels to form a cylinder is however impractical for small model fabrication, because the wall thickness is so small that this method will lead to excessive mismatching, welding and random imperfections at the joints and consequently the effect of welding-induced fabrication imperfections cannot be easily isolated as the other imperfections may dominate the behavior. The very time-consuming nature of the process is another obstacle. The small thickness of the shell model is dictated by the desirable size of the test specimen and a realistic radius-to-thickness ratio. For example, a cylindrical specimen of 1000mm in diameter, which is an upper limit for convenient testing in laboratory, will have a wall thickness as small as less than 1mm in order to achieve a representative value of the radius-to-thickness ratio (R/t)

in real shell structures. The radius-to-thickness ratio, which is the geometric parameter for shell slenderness, often falls in the range between 500-1000 for cylindrical shells in elevated steel silos. This is the key parameter that the test specimen shall follow, because it significantly affects the buckling behavior and the interaction between buckling and yielding.

In the first and only existing attempt at simulating this construction process in the laboratory, Schmidt and Swadlo (1996) adopted the process of cutting a flat sheet into many square (or rectangular) pieces, which were then joined together to form a flat plate again by orthogonal welds. Furthermore, the panel was cold straightened to reduce the level of geometric imperfections. The flat sheet was then rolled into a cylinder and joined by an additional meridional weld. This process, although both quicker and easier to realize in the laboratory than the actual panel method, is still time consuming. More importantly, the unrealistic feature that welding is performed before rolling is a serious drawback, as the different responses of the shell to circumferential welding and meridional welding cannot be properly reflected. Rolling residual stresses are also induced in the welds, although these are of the bending type and may not have a strong influence on the buckling strength. Cold straightening is another unrealistic feature of the process. This section presents an innovative technique for fabricating small laboratory models for large cylinders with many welds as found in large steel silos and tanks.

6.4.2 New Method for Model Fabrication

A new method was developed in the present project for fabricating small-scale models for large welded cylinders for laboratory bucking experiments. The specimen size studied has a diameter of 1 m and may have a thickness of 0.6 mm to 1 mm. This specimen size avoids the inconvenience associated with the testing of large models in laboratory, and in the meantime allows high radius-to-thickness ratios as found in large steel silos and tanks to be achieved. This specimen size also conforms to the requirement of a shell buckling test facility developed in a previous project (Teng *et al.* 2001).

The new method is an innovative two-stage fabrication method that retains all the essential characteristics of a cylinder constructed by the panel method. In Stage I, two sheets of steel (or a single sheet) are rolled into a cylindrical surface and then joined with two

meridional welds to form a cylinder. Ring stiffeners providing radial restraints are then added to both ends to maintain circularity before the Stage II operation. In Stage II, 'welding' in the form of controlled heat input in a required pattern of circumferential and meridional 'welds' (the quotation marks are dropped hereafter) is then carried out on the central portion of the shell surface, producing a specimen with its central portion being similar to the cylindrical shell in a real steel silo or tank. Details of the two stages are described in the next section.

This new method of fabrication has many advantages: (a) it avoids joint mismatching between the large number of panels and the need for cold straightening, but includes small random geometric imperfections from the rolling process; (b) it leads to great savings in fabrication time; (c) different patterns of welds can be easily applied to the shell surface to vary the 'panel' size and aspect ratio; (d) rolling of the sheet is applied before welding, the process is more realistic than the approach of Schmidt and Swadlo (1996), and the effects of meridional and circumferential welds are properly captured. Inspiration for this approach came from Berry (1997) who produced cylinders with a single (almost) axisymmetric imperfection by suitable heat input around a circumference at the mid-height of a cylinder when he found it difficult to fit together perfectly even only two half-length cylinders.

6.4.3 Experimental Set-up for Stage I Operation

The model fabrication set-up for the Stage I operation included a three-roller bending machine, a plasma electric cutting installation, a TRANSTIG 16Pi Pulsed TIG (Tungsten Inert Gas) welding machine, a collapsible former with a former stand, and two rigid end rings. The bending machine, the plasma electric cutting installation, and the TIG welding machine were all existing equipment available in the workshop, but the former, the stand (Figure 6.6) and the two end rings were designed and manufactured specifically for the present project.

The collapsible former represents an improvement to that designed by Berry (1997) in that the former had eight built-in control screws which enabled it to be expanded or collapsed easily by only one person. The former was designed as a four-segment integrated cylinder (Figure 6.7) with a diameter of 999 mm and was held by the former stand. The former

provided support to the two half-cylinders during welding along the two meridional seams to produce good quality models in Stage I. It should be noted that the shell model from Stage I should be of high quality so that the shell is sensitive to the effect of the Stage II operation, namely the simulated pattern welding process. A model shell with excessive geometric deformations is unlikely to show significant further degradation in buckling strength as a result of imperfections due to the patterned welds. Two meridional strips of copper at 180° apart were inlaid in the former and their surfaces were machined to match the surface of the former. In the Stage I operation, the two meridional seams of the cylinder were placed against the copper strips which provided heat sinks during welding to reduce welding distortions and ensured that the cylinder stayed separate from the former after welding.

The four segments of the cylinder could collapse towards the central shaft (Figure 6.7b) in a controlled manner. A specially designed control screw together with a sliding plate was installed on both the top and bottom of each segment. The control screws drove the sliding plates to move in the guideways with a swallow tail section shape (Figure 6.7), which could either collapse or expand the former. In addition, positioning pins were included to ensure that the segments could be unfurled to their correct positions.

The stand held the central shaft of the former with pivot housings at its top and bottom, allowing the former to revolve around its central shaft. A specially designed electric stove used to heat up the ring also provided the support to the ring. A specially designed screw jack consisting of three tubes was developed to support the former and to adjust the elevation of the former. The former ascended or descended (Figure 6.8) when the intermediate tube was turned.

6.4.4 Experimental Set-up for Stage II Operation

For the Stage II operation which mainly involves heat input on the surface of the cylinder to simulate pattern welding, an automatic welding device was set up on an existing shell buckling test facility to induce imperfections in the model shell (Figure 6.9). Figures 6.9b and 6.10b show an early specimen in the test facility during automatic welding. As mentioned earlier, the existing shell buckling facility included a rotating frame with a lead-screw system on one of the arms for vertical moment of a laser displacement meter

(Teng *et al.* 2001). The laser displacement meter could thus be driven around and moved up and down the model shell for three-dimensional surveys of initial shapes as well as deformed shapes. For the present purpose of pattern welding, a lead-screw system was installed on the other arm of the rotating frame to support the welding carriage so that the welding torch could be moved around and up and down the shell (Figure 6.10b). The rotation of the lead-screw system was driven by an additional 2-phase (ORIENTAL PK264-02A) with a step angle of 1.8^0. Another computer program was composed in QBASIC to control both the stepping motor and the TIG welding machine. The communications between the computer and the additional stepping motor and those between the computer and the welding machine were effected via two spare channels in the existing I/O card and the 20-pin flat cable (Figure 6.11). The computer program was set to turn on the welding machine before the welding torch started to move, with allowance for the arc ignition time.

The welding torch was mounted on a spring-loaded welding carriage (Figures 6.10) in order to maintain a constant gap between the welding torch and the shell surface, which was necessary to achieve a uniform heat input and to prevent the welding torch from direct contact with the welding-distorted shell surface. Pattern welding was limited only to the central portion of the cylinder to limit the subsequent finite element model. A sufficient number of welds were nevertheless included to properly capture interactions between welds.

6.4.5 Fabrication Process of a Model Specimen

Using the technique proposed and the experimental set-ups developed, a model specimen simulating a real cylinder constructed using the panel method could be fabricated. The complete fabrication process of a model specimen involved the cutting of two steel panels, the rolling of the two steel panels into two half-cylinders, the welding of the rolled panels to form a complete cylinder with two continuous meridional welds, the attachment of two rigid end rings to stiffen the cylindrical shell, and the execution of patterned welds through controlled heat input to the specimen. A typical implementation of the fabrication procedure in the present work is given below.

Two rectangular steel panels of $782mm \times 1673mm$ were first cut from steel sheets of $1200mm \times 2400mm$ in size using the plasma electric cutting installation, with a $2mm$ allowance at both cutting edges. The coarse cutting edges were then carefully smoothened by grinding and the size of the panels became $780mm \times 1671mm$, which was appropriate for the production of a cylindrical shell with a diameter of 1000 mm and a height of 780 mm. The three-roller bending machine was employed to roll these sheets into the desired curvature. However, rolling by this bending machine led to flat portions of roughly 40mm width at both the leading and the trailing edges of the rolled panel, because of the gap between the clamping rollers and the bending roller in this machine. In order to avoid this type of imperfection, an excess length of 100 mm was included in the 1671 mm circumferential length mentioned above so that the flat ends could be removed after rolling. The flat portions of the first panel were removed by cutting away strips of 50mm in width at both ends. For the second panel, a 50 mm wide strip was first cut away from one end and the excess width to be cut away from the other end worked out by placing both panels on the former.

Before the former was installed on the stand, the electric stove and one rigid ring with its groove filled with solder of a low meting point of 95^0C was first placed on the stand. A set of fine screws were used to level the ring before the former was in place. Then the former was installed, and another set of fine screws was used to adjust the positions of the stove and the ring to ensure the co-axiality of the ring with the former. This was followed by clamping the two rolled panels onto the former using tension straps and ratchets. The vertical edges of the panels were placed on the inlaid copper strips on the former, while the horizontal edges protruded by 20 mm out of the former to allow them to be secured in the two rigid end rings with a groove. After spot-welds that connected the two panels were conducted, the tension straps were removed and the continuous welds joining the two rolled panels to form a complete cylinder were performed with great care. The excessive weld deposits at the two meridional welds were eliminated by grinding in a meticulous way and a good quality cylinder was fabricated. This welding and the patterned welding of Stage II were performed using a TRANSTIG 16Pi Pulsed TIG (Tungsten Inert Gas) welding machine noted above. The pulsed TIG welding machine is highly suitable for welding work on light gauge steel sheets for lower welding distortions, because the pulsed

currents can significantly reduce heat input so that excessive heat buildup during welding can be prevented.

Next, the solder in the groove of the ring was melted using the electric stove below it (Figure 6.8). The former was then lowered by turning the intermediate tube of the screw jack, and the specimen placed in the groove filled with melted solder. When the solder solidified, the lower end of the specimen was firmly clamped by the ring (Figure 6.12). The specimen together with the former was next lifted out of the stand, turned upside down and placed on the stand again (Figure 6.13), and the lower end clamped in the second ring which was placed on the stand when the specimen was removed.

Once both end rings were attached, the former was collapsed (Figure 6.14) and the specimen, whose ends were now secured in the rings was released by lifting it out of the stand using a crane. The specimen was then moved to the shell buckling test facility. A three dimensional survey of the surface of the model shell was next carried out using the laser displacement meter, before pattern welding. Pattern welding to the central portion of the cylinder followed, leading to a specimen (Specimen 09P0408) as shown in Figure 7.3. The welding parameters for use in this pattern welding, such as the welding pulse, the gap between the welding torch and the cylinder, the movement speed of the welding torch, were decided in systematic pre-test runs of the welding set-up. A three-dimensional survey of the initial shape of the specimen was again conducted following pattern welding. The specimen (09P0408) was now ready for the buckling test. The nominal radius of the middle surface of the model specimen was 500 mm, while the height of the model was 750 mm (excluding end portions in the rings). The circumferential welds were spaced at 85 mm ($\approx 4\sqrt{Rt}$) while the meridional welds were placed at 175mm ($\approx 8\sqrt{Rt}$). The meridional welds on one 'strake' were offset from those on the next 'strake' by half a panel width. The circumferential welds were symmetrically positioned about the mid-height of the cylinder.

6.5 AXIAL COMPRESSION BUCKLING EXPERIMENTS

Figure 6.15 shows the general layout of the experimental set-up for loading tests, while its general overall view is shown in Figure 6.16. The point load of the MTS actuator was transferred through a load transfer cylinder, a universal joint, a shallow loading cone, and a loading ring with a knife edge to ensure uniform loading on the end ring of the specimen. In order to control the progress of the highly unstable post-buckling behavior of the shell, the top ring of the specimen was firmly connected to the loading cone using 12 uniformly distributed bolts while the bottom ring of the specimen was connected to the base support table in a similar way. The loading from the MTS actuator was effected through a MTS control panel which was set to apply a stroke of 0.04*mm*/minute during the initial linear stage of deformation and a stroke of 0.02*mm*/minute afterwards. Before each test, the specimen was preloaded to 10% of the buckling load from a nonlinear finite element analysis.

During the test, the surface deformations of the specimen were monitored at selected load levels using the laser displacement meter. At the same time, the data of loads, strains, and axial shortening were taken via the data logger system and recorded in another computer that was connected to the data logger system. To avoid any interference with the shape surveys on the external surface, four transducers that measured the relative displacements between the two end rings (i.e. axial shortening) were installed inside the test specimen at an approximate separation angle of 90^0 (Figure 6.17). For the same reason, the strain gauges were also placed on the inner surface of the cylinder. Two holes were drilled on the loading cone for the cables of transducers and the wires of the strain gauges to pass through.

6.6 CONCLUSIONS

This chapter has presented the modifications made to an existing test rig to upgrade the facility for the planned buckling experiments on welded cylinders under axial compression. An MTS actuator was employed to achieve displacement-control loading. A load transfer

system, which consisted of a load transfer cylinder, a universal joint, a flat loading cone, and a loading ring with a sharp edge, was designed to transform the point load of the MTS actuator into a uniform ring load on the shell specimen. Moreover, the problem of gear clearance in the rotational movement of the measurement system was eliminated so that the imperfection survey of the entire surface of a cylindrical shell specimen could be carried out automatically, reducing significantly the measurement effort. The overall experimental set-up for these buckling experiments has also explained. Transducers and strain gauges were installed inside the model shell to avoid any interference with shape surveys on the external surface of the shell surface.

An innovative technique has been presented for the fabrication of small models of large steel cylindrical shells constructed from many welded panels as commonly found in large steel silos and tanks. The new technique consists of two stages: (as) production of a high quality model by rolling two sheets (or a single sheet) and welding along the meridional seams; and (b) 'welding' in the form of controlled heat input in a required pattern of circumferential and meridional 'welds' on the central portion of the shell surface. The experimental set-ups and the detailed fabrication procedure have been described. The proposed technique for the first time provides a feasible method for the production of realistic small-scale models of large cylindrical shells in steel silos and tanks. It is believed that the technique will greatly facilitate future experimental research on the buckling behavior of cylindrical shells built by the panel method under many loading conditions, including axial compression with or without internal pressure, external pressure, shear and torsion, non-uniform pressures on silos from various sources and local loads such as column support reaction forces.

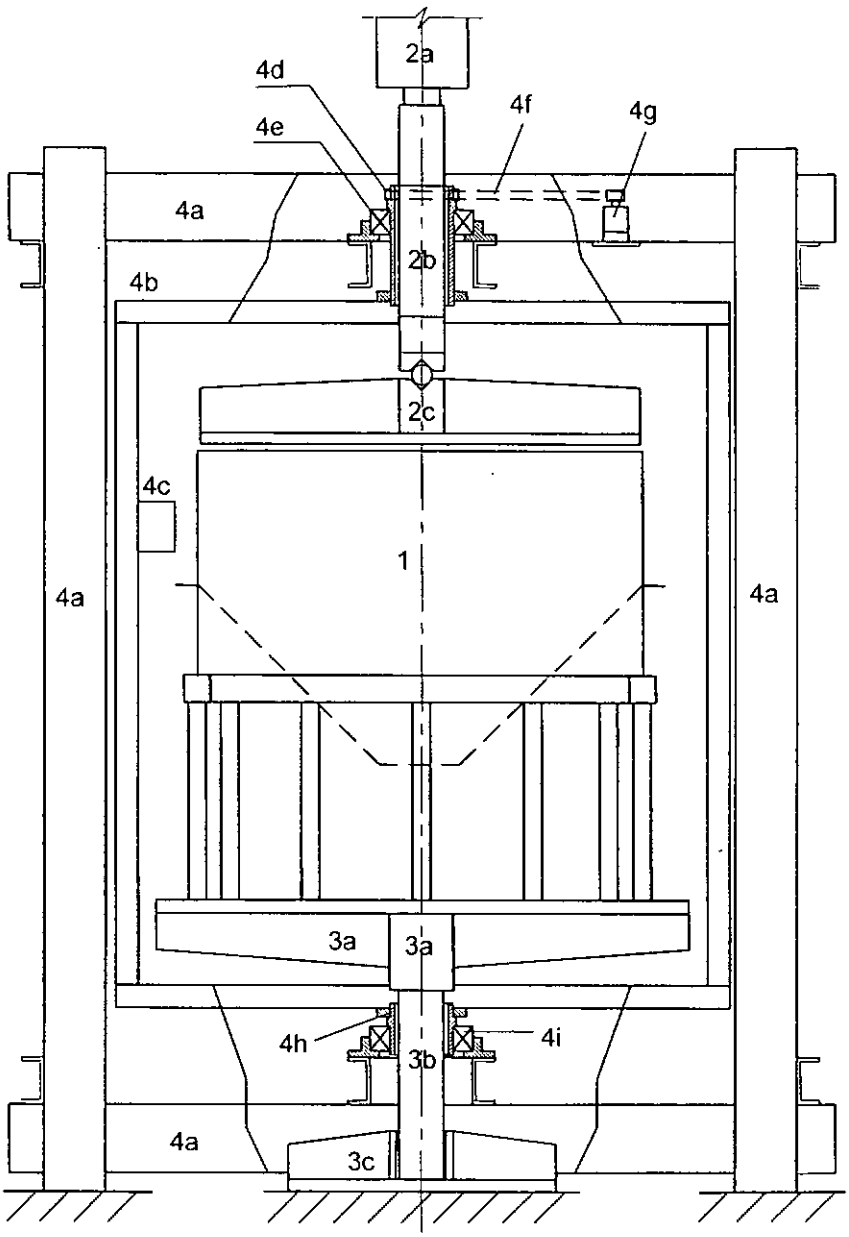

1 Silo Specimen
2 Loading System: 2a Hydraulic jack, 2b Load transfer cylinder,
2c Rigid circular plate
3 Supporting System: 3a Circular support plate, 3b Solid cylinder, 3c Base
4 Measurement System: 4a Supporting frame; 4b Rotating frame,
4c Laser meter, 4d Upper rotating shaft,
4e Upper roller bearing, 4f Timing belt,
4g Stepping motor, 4h Lower rotating shaft,
4i Lower roller bearing

Figure 6.1 General layout of existing test rig

(After Zhao, 2001)

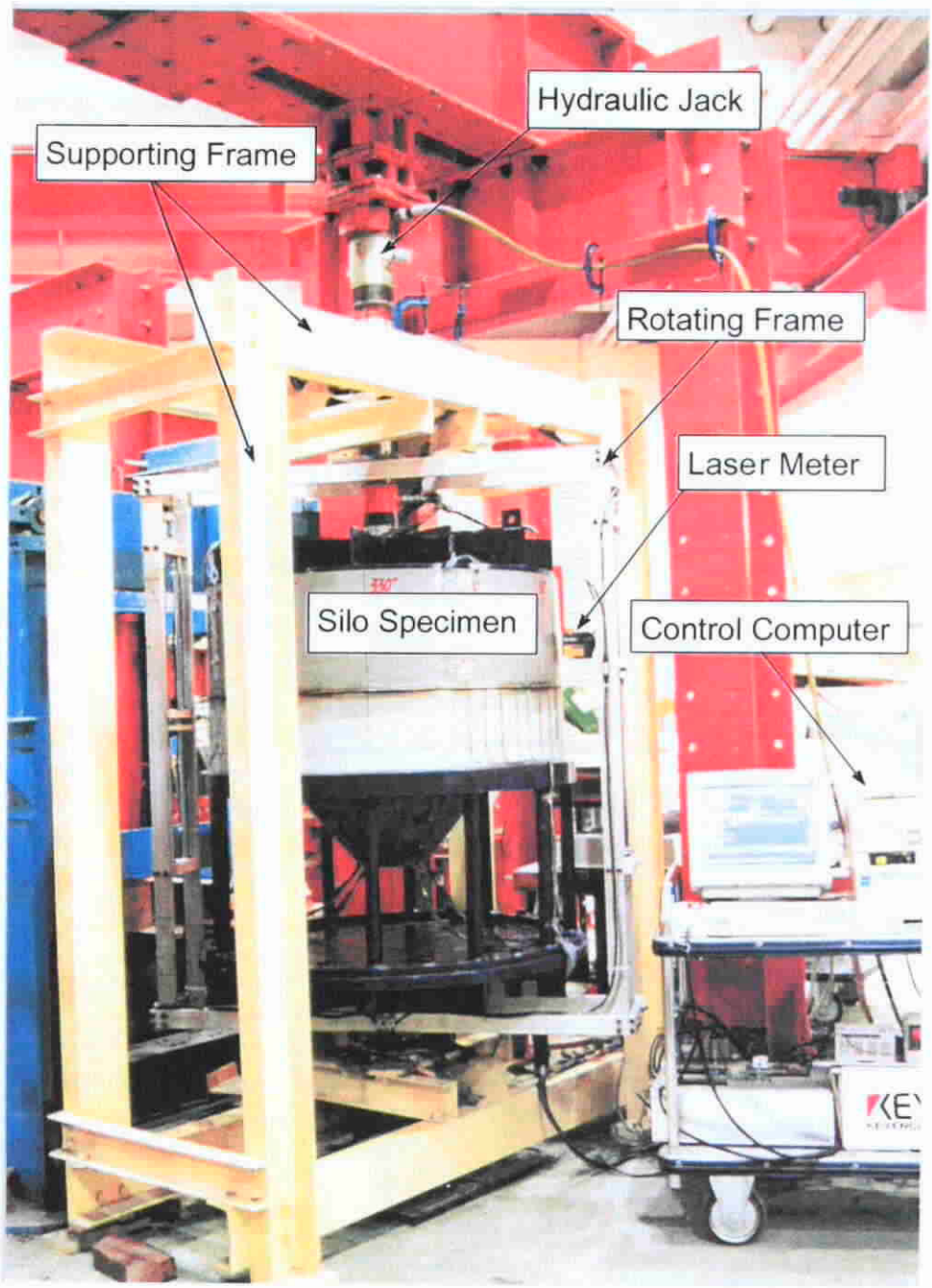

Figure 6.2 Overall view of existing test rig for silo junction experiments (After Zhao, 2001)

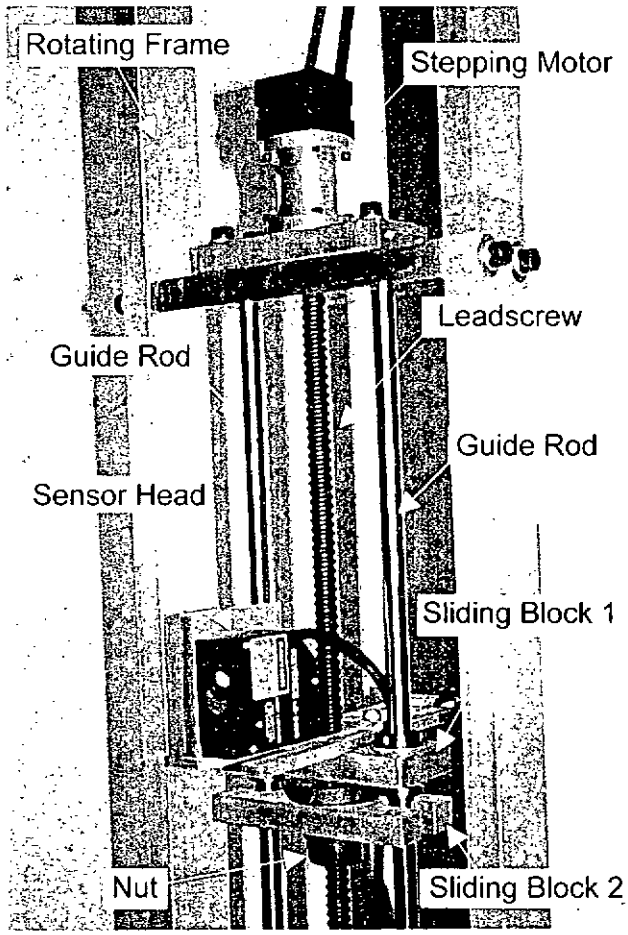

Figure 6.3 Leadscrew system for linear movement

(From Zhao, 2001)

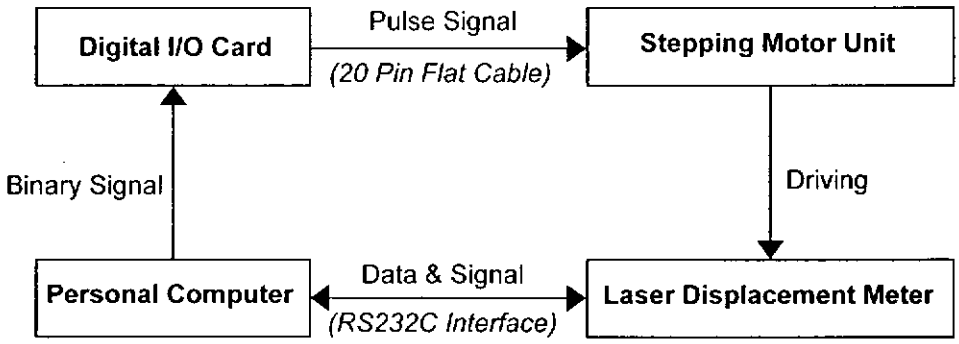

Figure 6.4 Flow chart of measurement system operations

(From Zhao, 2001)

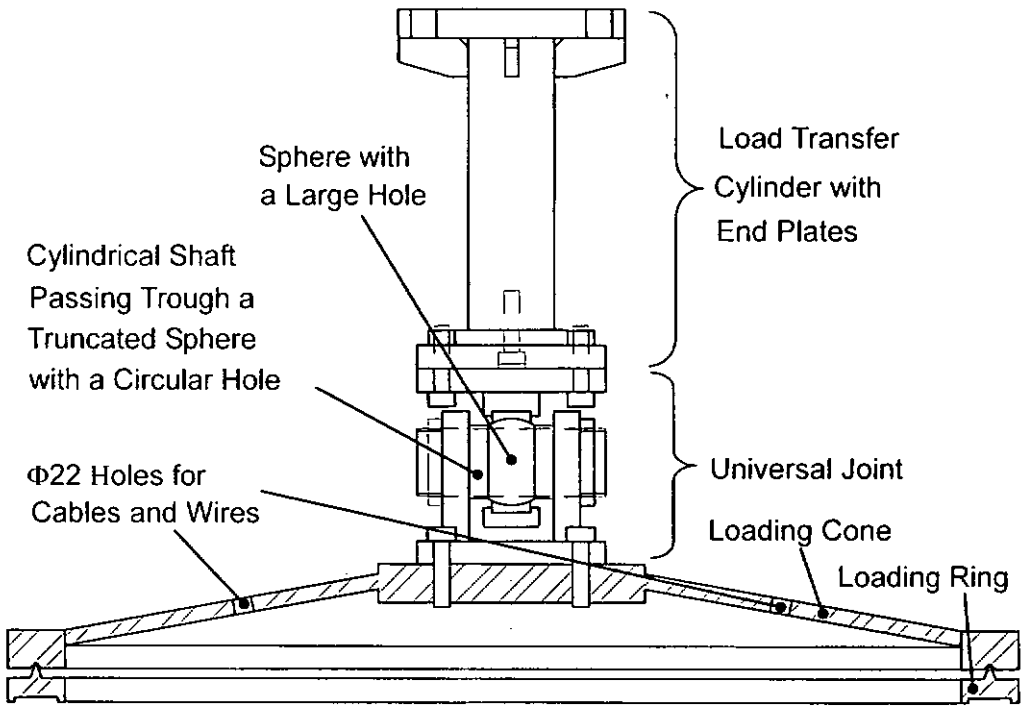

Figure 6.5 Load transfer system

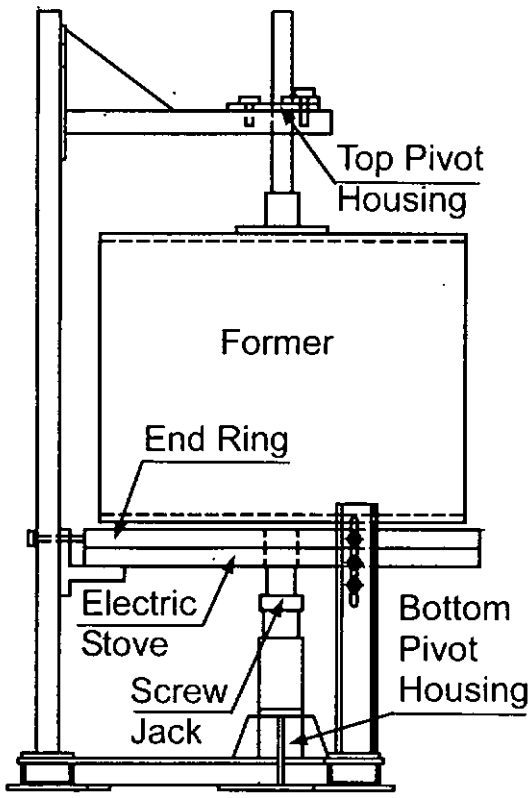

Figure 6.6 The former held by the stand

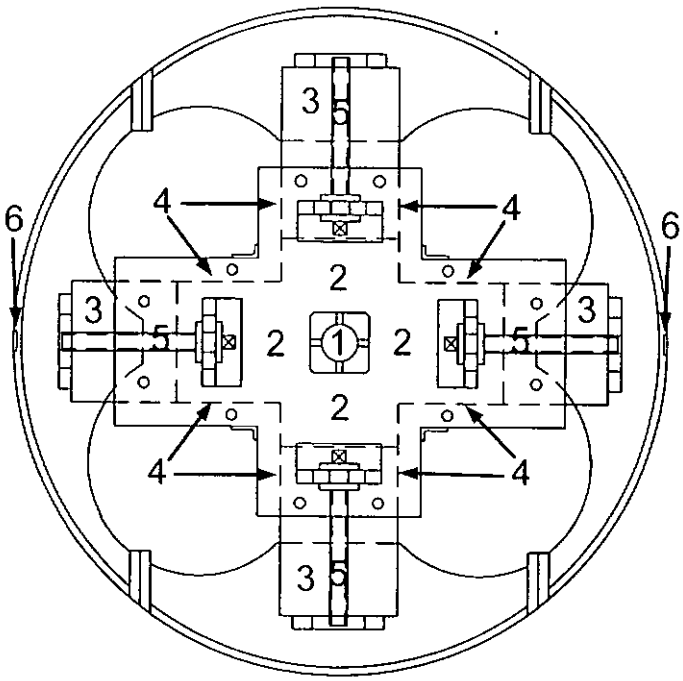

(a) Expanded

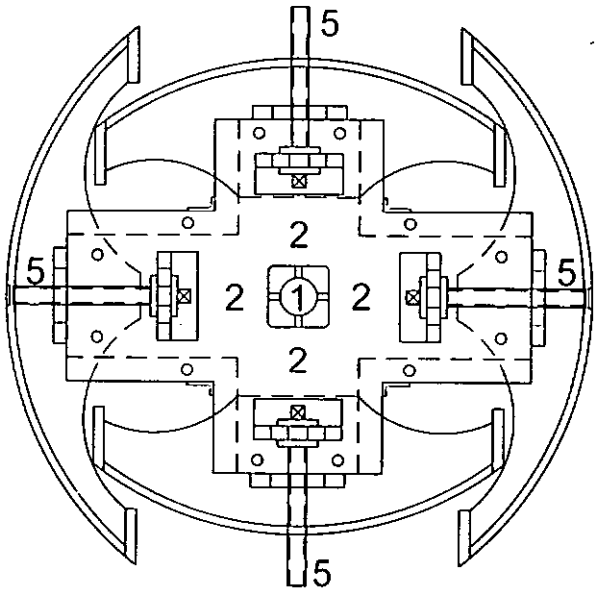

(b) Collapsed

1-Central Shaft 2-Bearer 3-Sliding Plate 4-Guideway 5-Control Screw
6-Copper Strip

Figure 6.7 Plan view of the collapsible former

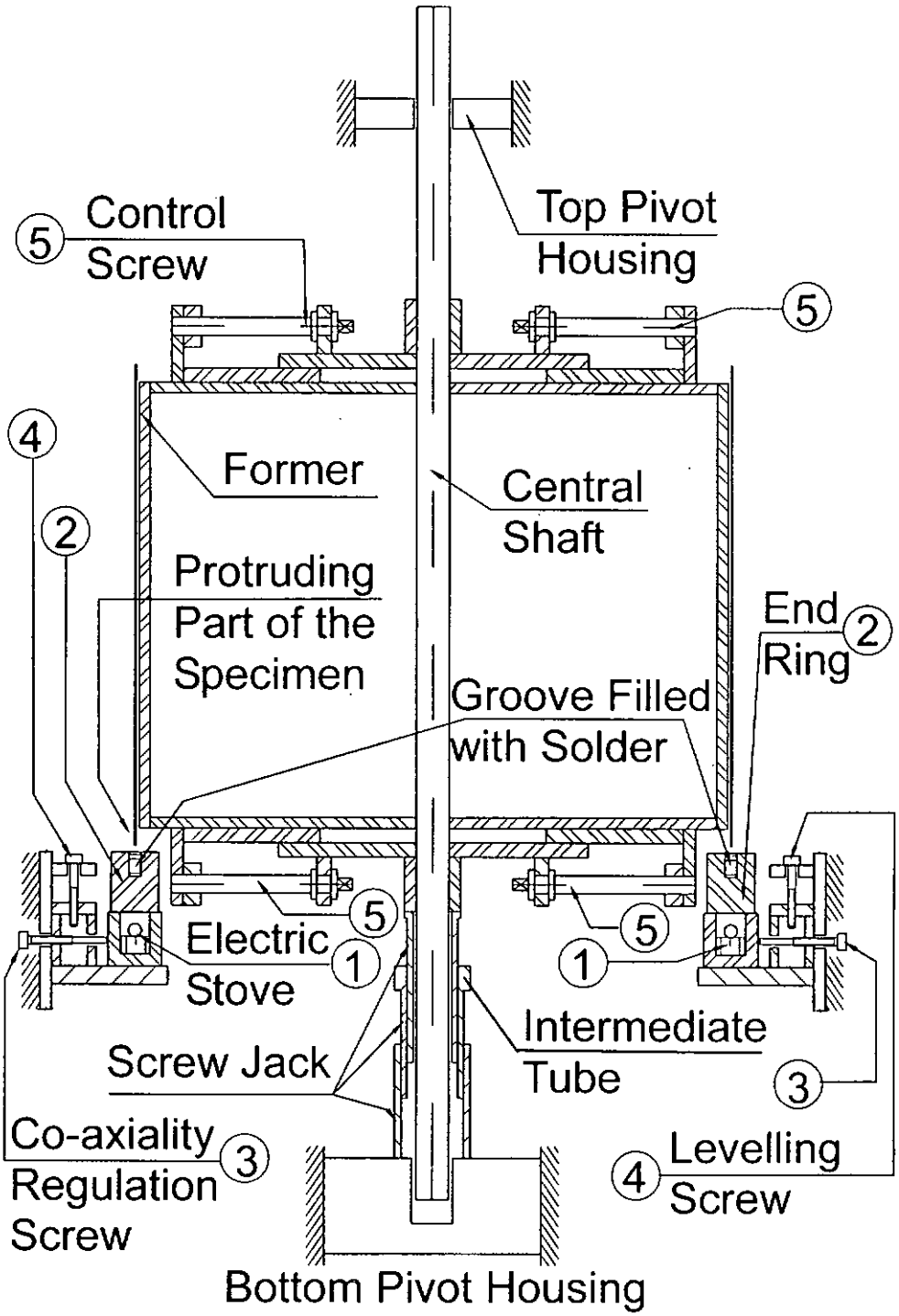

Figure 6.8 Placement of a shell model in an end ring

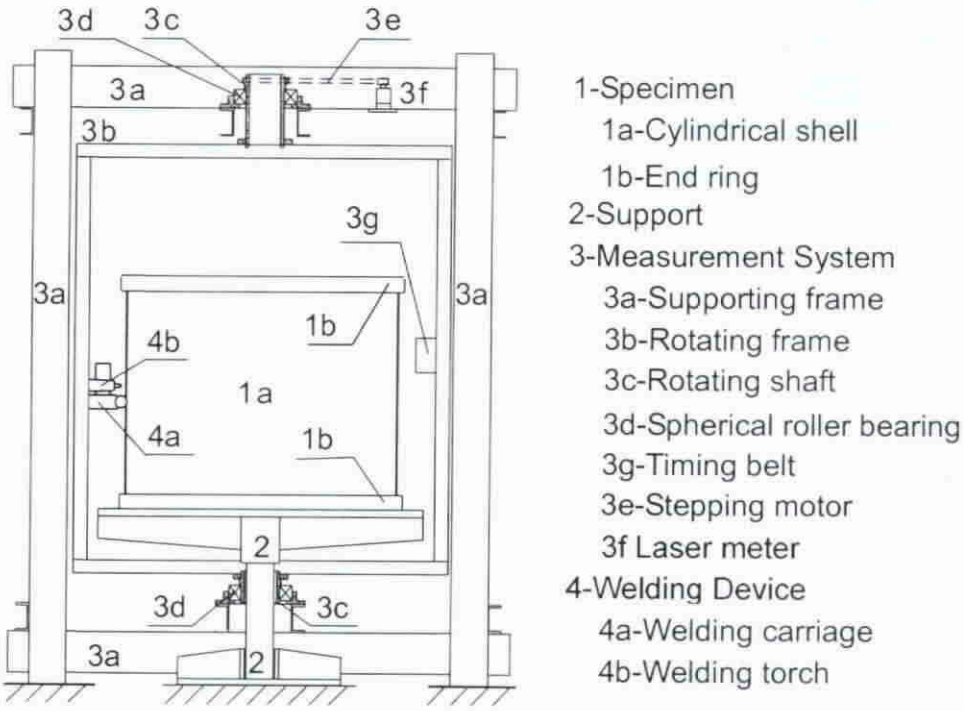

(a) Schematic drawing

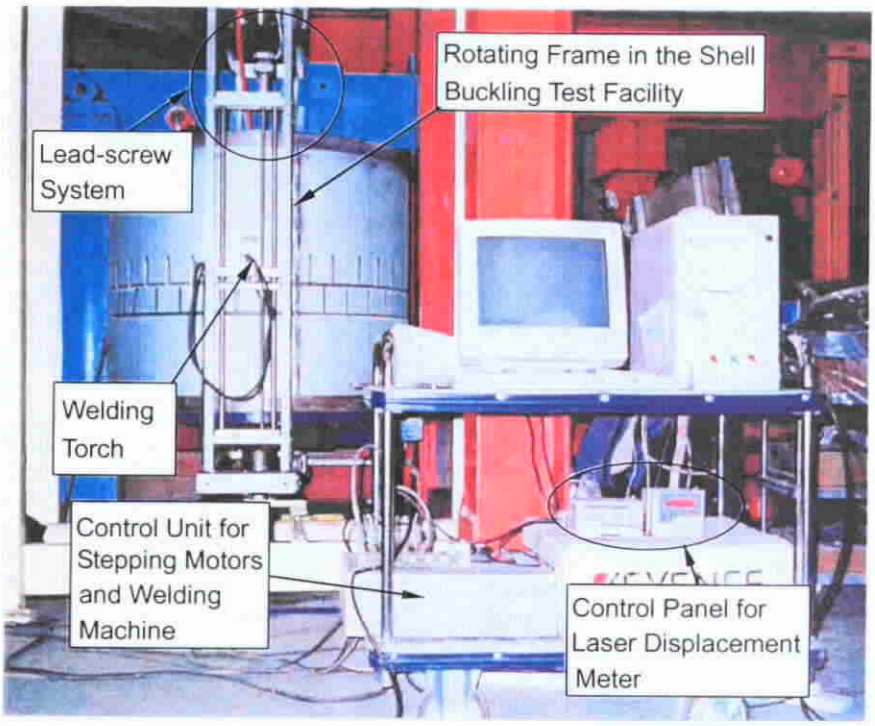

(b) Photo

Figure 6.9 Automatic welding device during pattern welding

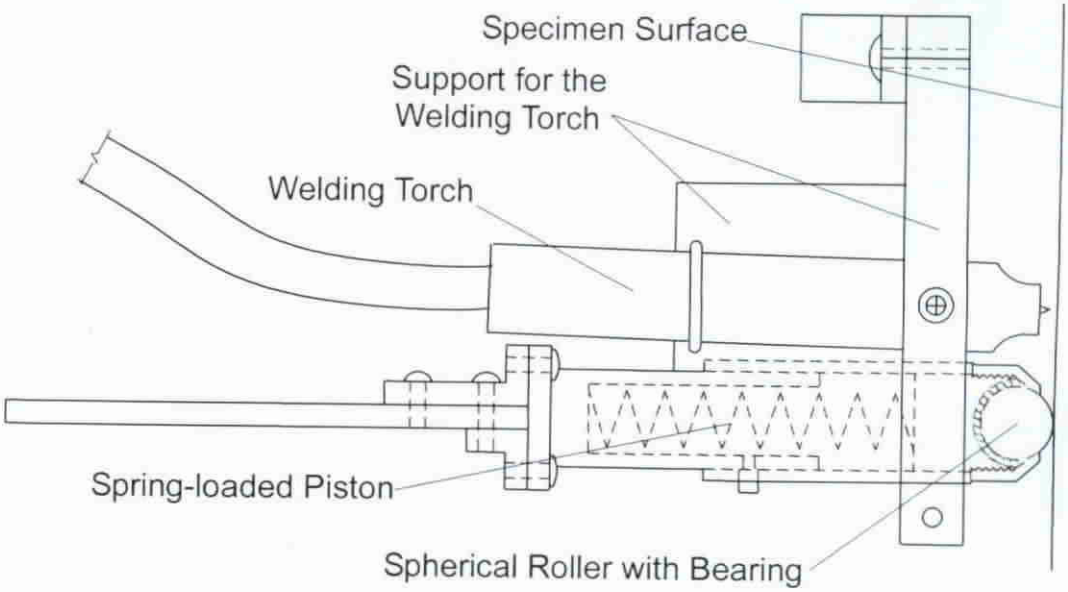

(a) Schematic drawing

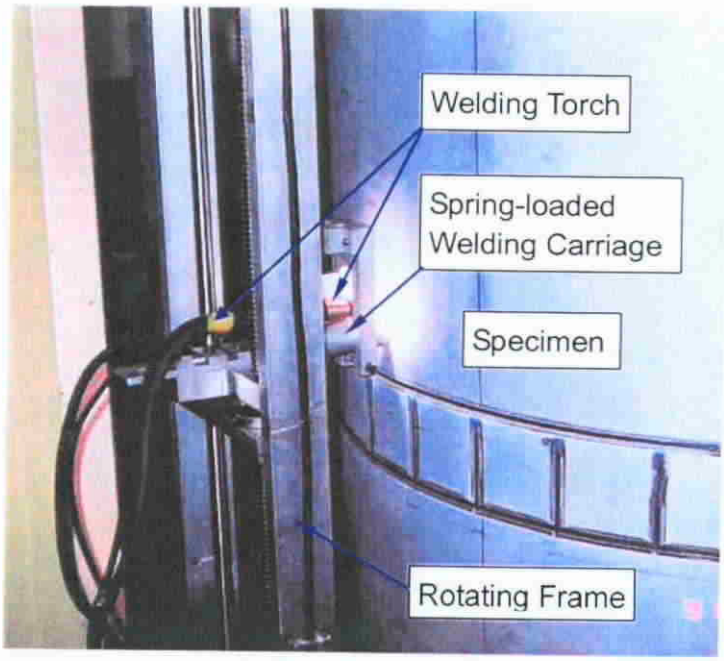

(b) Photo

Figure 6.10 Welding torch on a spring-loaded welding carriage

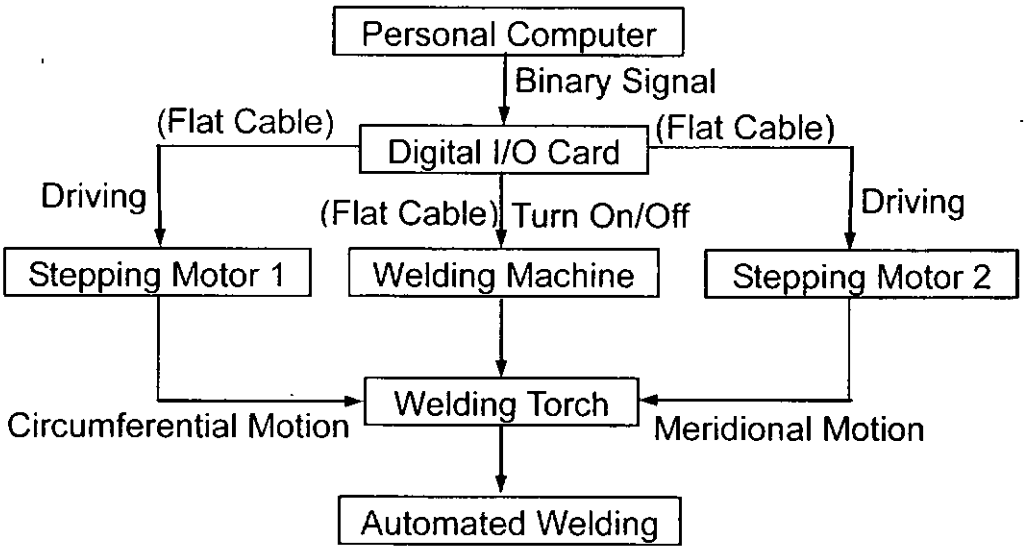

Figure 6.11 Operation flow chart of automated welding

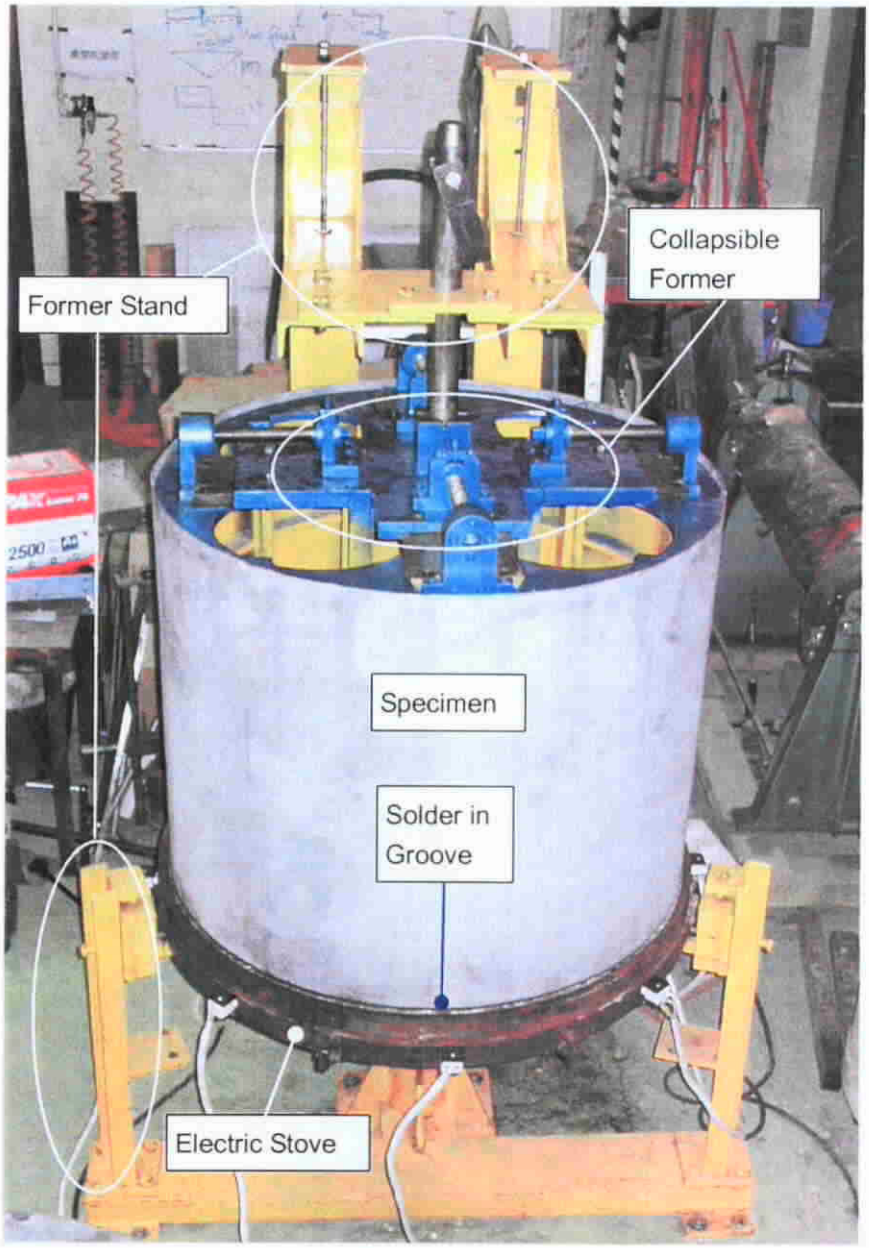

Figure 6.12 Specimen clamped in one end ring

Figure 6.13 Specimen turned upside down for placement into the second end ring

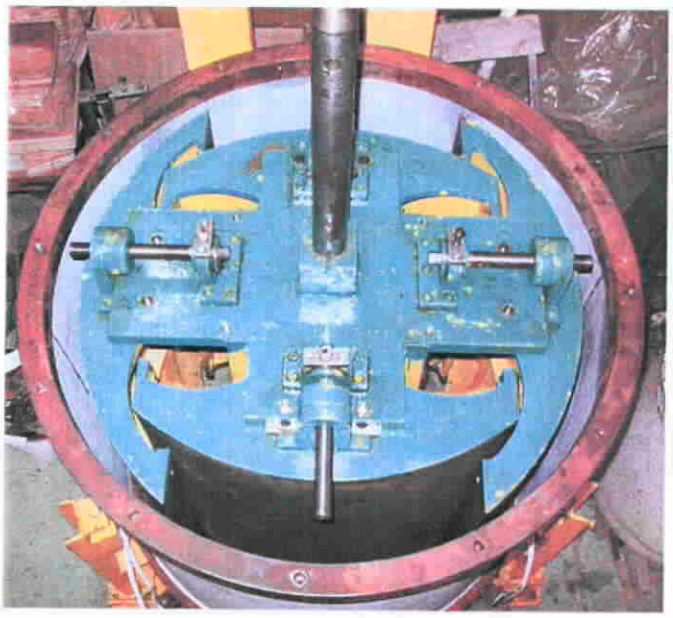

Figure 6.14 Collapsed former with the specimen ready for removal

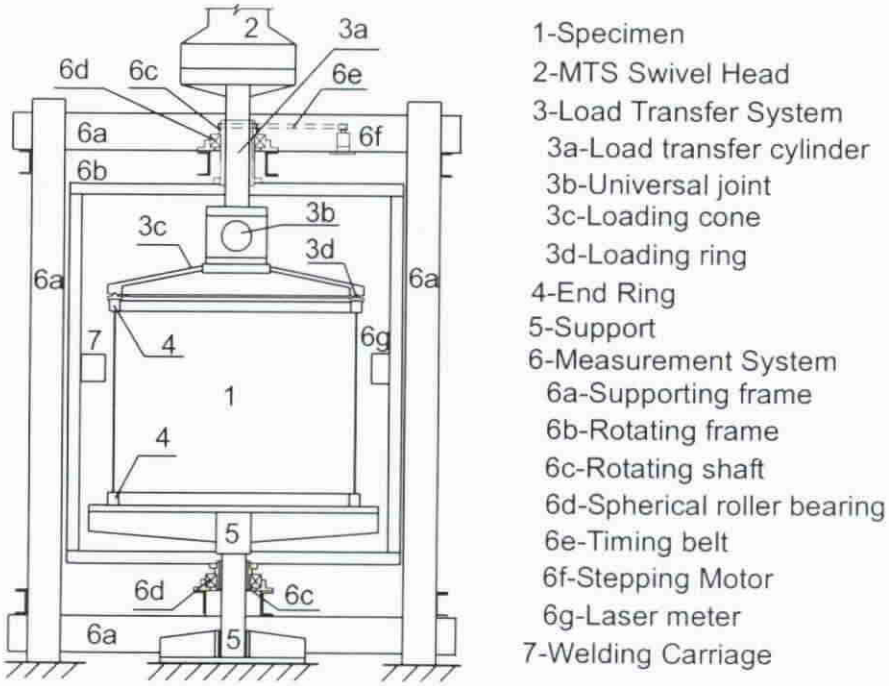

Figure 6.15 General layout of experimental set-up

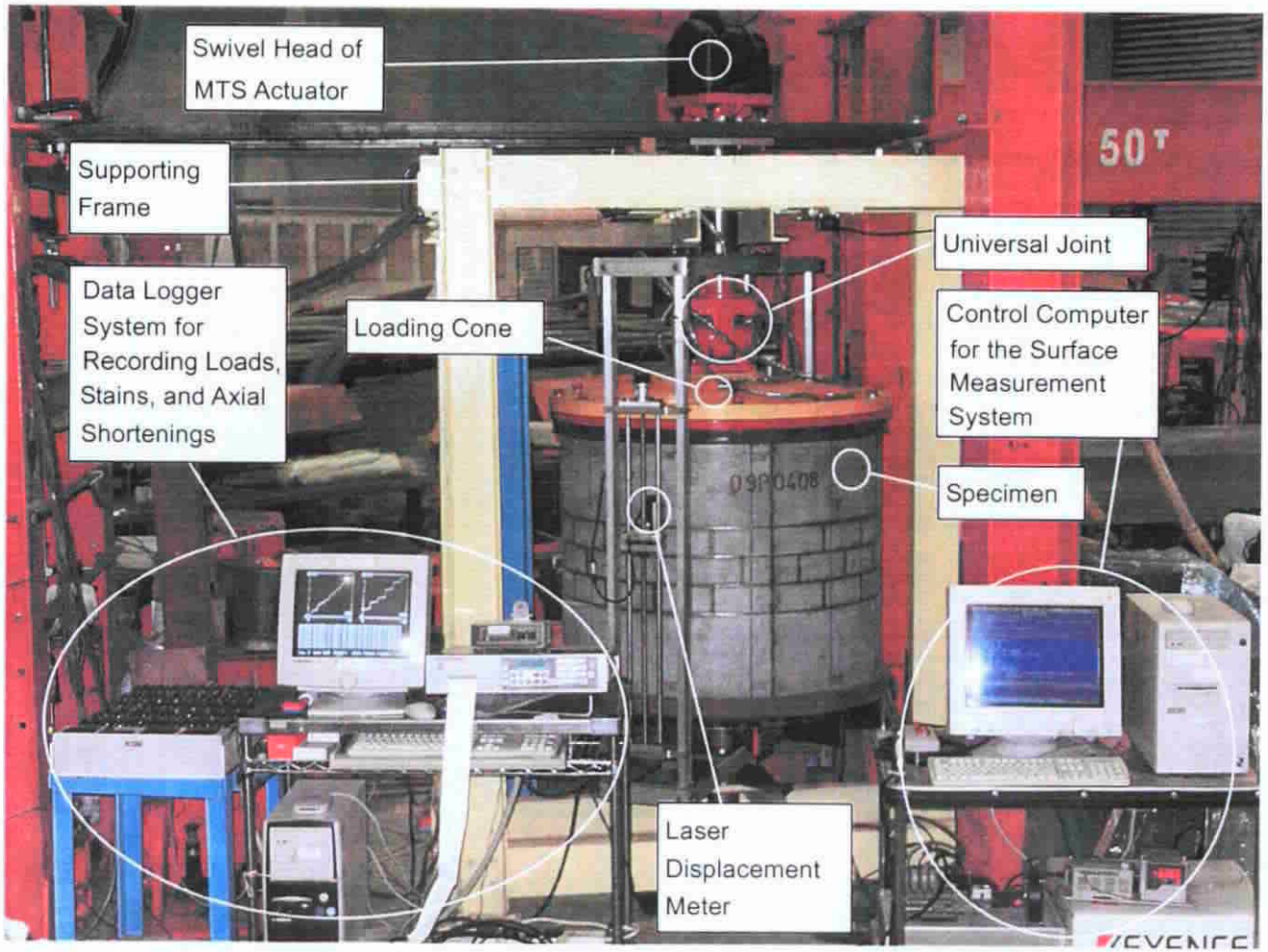

Figure 6.16 Overall view of the experimental set-up

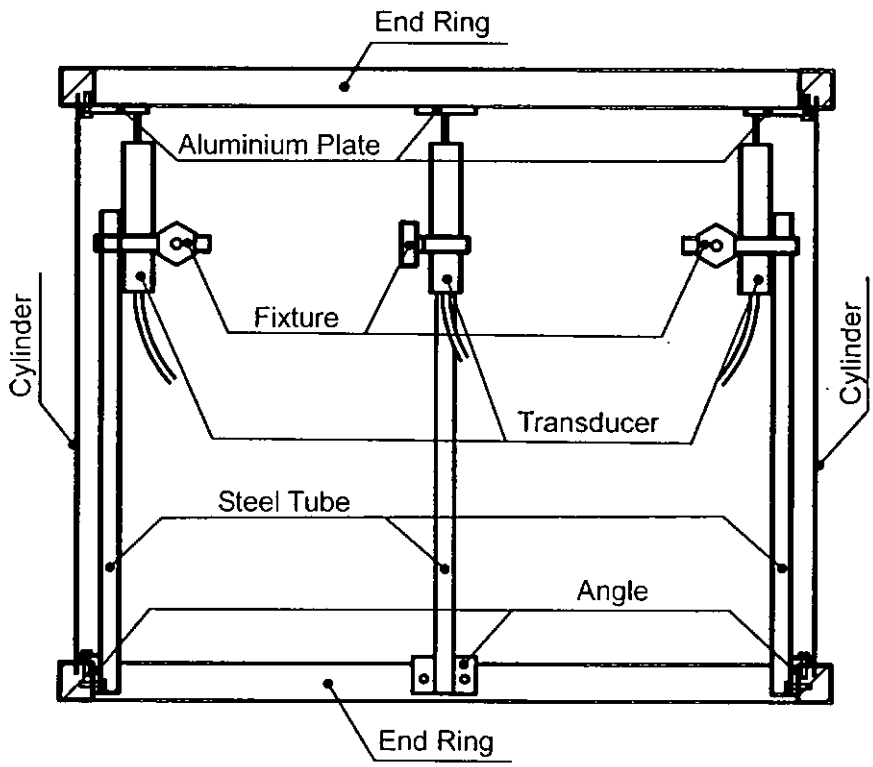

Figure 6.17 Transducers inside a specimen

CHAPTER 7

BUCKLING EXPERIMENTS ON EXTENSIVELY WELDED STEEL CYLINDERS

7.1 INTRODUCTION

While the numerical study on the buckling of the real cylindrical shells of the three large steel silos at Port Kembla presented in Chapter 5 has shed considerable light on the nature of geometric imperfections in the shell walls and on their effect on the buckling behaviour of these shells under axial compression, the issue of residual stresses were ignored in that study. In such welded shells, a major cause of the geometric imperfections is the weld connections, and welding also leads to residual stresses near the welds. A difficulty with quantifying the effect of residual stresses in thin shells is that it is impossible to measure them precisely enough to produce residual stress patterns for use in a numerical study, as six stress resultants are involved and they must form a self-equilibrium stress system on the curved surface. As a result, even the direct assumption of a certain residual stress pattern that satisfies the above requirement is a difficult task. Residual stresses not in self-equilibrium will lead to deformations before any loading is applied, thereby changing the shape and magnitude of the initial geometric imperfection specified (Rotter, 1996). Such a situation will unnecessarily complicate the numerical modeling process. A successful existing approach of specifying imperfections is to use shrinkage strains (Rotter, 1996; Holst *et al*, 2000; Pircher and Bridge, 2001a; Hübner *et al*, 2003a) which will lead to both residual stresses and geometric imperfections in the shell. These studies have shown that the effect of residual stresses is beneficial to the buckling strength of axially compressed cylinders. There is however still considerable uncertainty on the representativeness of these numerically-simulated welding imperfections and residual stresses, particularly when a large number of welds as in real silos are present, so the existing findings are inconclusive. No experimental study has been conducted focusing specifically on the

effect of residual stresses on the buckling strength, understandably due to the difficulty with the measurement of residual stresses.

This chapter and the next chapter aim to clarify the effect of residuals stresses in extensively welded cylinders subject to axial compression using an alternative experimental approach in which the direct measurement of residual stresses is avoided but their effect is indirectly but nevertheless conclusively evaluated. To this end, a series of three careful tests were conducted on model shells with simulated welds of different patterns. The geometric imperfections in these specimens were precisely surveyed and incorporated into nonlinear finite element analyses. The discrepancies between the test results and the nonlinear finite element analyses can then be attributed to factors not modeled in the nonlinear finite element analyses, the most obvious of these factors being the residual stresses. These test results also provide an experimental exposition of the buckling behavior of axially-compressed cylindrical shells with patterned welds for the first time. The experimental findings are presented in this chapter, while the finite element results are given in Chapter 8.

7.2 SPECIMENS AND MATERIALS

7.2.1 Specimens

The experimental program consisted of three specimens, which are identified as 09SC, 09QC04, and 09P0408, respectively. The configurations for these three specimens are as the follows: the nominal wall thickness of the models is 0.9mm, the nominal middle-surface radius of the models is 500mm, and the nominal height of the models is 750mm (excluding the end portions in the rings). The nomenclature for these specimens complies with the following rules: the first two digits stand for the shell wall thickness given in one-tenth of a millimeter, while the characters that follow denote the different welding patterns: 'SC' refers to the specimen with a single circumferential weld; 'QC04' refers to the specimen with four circumferential welds at a meridional spacing of $4\sqrt{Rt}$ (a quaternary of welds); and 'P0408' refers to the specimen with patterned welds dividing the shell surface into rectangular "panels" with a height of $4\sqrt{Rt}$ and a width of $8\sqrt{Rt}$, where

R and t are the radius and wall thickness of the specimen, respectively. In addition to the loading tests, the geometric imperfections in these specimens were surveyed and analyzed using Fourier series.

The circumferential welds were symmetrically positioned about the mid-height of the cylinder: the single circumferential weld in specimen 09SC was at the mid-height (Figure 7.1); the four circumferential welds in specimen 09QC04 were located at the heights of 247.5mm, 332.5mm, 417.5mm, and 502.5mm from the lower end, respectively (Figure 7.2); the circumferential welds in specimen 09P0408 were at the same 4 heights as in specimen 09QC04, and in addition, specimen 09P0408 had short meridional welds at a spacing of $8\sqrt{Rt}$, with the meridional welds on one strake being offset from those on the next strake by half a panel width (Figure 7.3).

In determining the appropriate spacing to be adopted for the circumferential welds in specimens 09QC04 and 09P0408, a numerical study on the effect of weld spacing on the non-linear bifurcation buckling strength of an axially compressed cylinder was carried out. The subject shell had the geometry as the test specimens except that the top and bottom ends of the shell were not reinforced with a ring. To save the computational effort, only a 90^0 shell sector of full height that was cut from the original cylindrical shell was studied. The two meridional edges were imposed with symmetry conditions while both the top and bottom ends were provided with a classical simple support but the top end was allowed to move vertically so that axial compression could be exerted there. The shell sector was believed to be sufficient for representing the whole cylindrical shell closely as it covers one quarter of the shell circumference. Two weld depressions of various spacings in the form of TYPE-A depression of Rotter and Teng (1989) were imposed in the middle portion of the shell sector. The numerical study revealed that two adjacent weld depressions at a spacing of $4\sqrt{Rt}$ have strong interactions (Figure 7.4), leading to a further reduction of 12.1% in the axial buckling load compared to that of a shell with a single weld depression of TYPE-A (Rotter and Teng, 1989). It may be noted that this length coincides with the gauge length specified by Eurocode 3 (ENV 1993-1-6 1999) for measurement of local dimple depths based on the expected wavelength of a potential buckle. For the same reason, it was also used by Schmidt and Swadlo (1996) in their study.

As mentioned in Chapter 6, the two ends of the cylindrical shell specimens were clamped in two rigid end rings to maintain the circularity of the specimens and to provide well-defined boundary conditions for subsequent numerical modeling.

7.2.2 Material Properties

Material properties of the steel sheets used in these models were determined from tensile tests according to the British Standard (BSEN1002-1:2001). Tensile test specimens cut from the steel sheets before and after rolling were tested. Tests on coupons containing a weld were not conducted, because the material properties obtained from such tensile tests are not applicable to the compression-dominated model shells such as the cylindrical shell specimens in the present study; moreover, the width of the heat affected zone (HAZ) and the gradient of the material property variation within the HAZ are very difficult to determine.

Altogether, 16 tensile test coupons were prepared for as-supplied steel sheets. Eight of the coupons were cut from two randomly selected steel sheets before rolling, and another eight were cut from two randomly selected steel sheets after rolling. From each selected steel sheet, four coupons were cut: two coupons were cut along the meridional direction and two along the circumferential direction in terms of the rolled shape. The coupons are each given a five-character identifier: the characters in turn represent the nominal thickness in one-tenth of a millimeter, rolling status, sheet identifier, the cutting direction, and the coupon number of the same direction in the same sheet. Two strain gauges were adhered on the two sides of each coupon at the mid-length to obtain the average tensile strain, and the stress was calculated using the actual thickness measured.

Figure 7.5 shows a typical strain-stress curve obtained from these tensile tests. This curve is typical of curves obtained for steel sheets both before and after rolling, as rolling was found to have little effect on the stress-strain curve. Following the common practice, the upper yield stress is excluded from consideration, reducing the stress-strain curve to one consisting of an elastic portion followed by a long plastic plateau, a curve that is commonly referred to as elastic perfectly-plastic. The tensile test results of these coupons are summarized in Table 7.1 and Table 7.2 for the steel sheets before rolling and after rolling, respectively. Columns (4) and (7) lists the average Young's modulus and yield

stress of the two coupons of the same cutting direction from the same steel sheet, while columns (2), (5), and (8) show the overall average values of thickness, Young's modulus, and yield stress for the steel sheets either before or after rolling. It is clear that the material properties vary little regardless of the coupon cutting direction, the sample sheet, or the rolling status. The yield stress of the steel after rolling is nearly the same as that before rolling.

The largest difference between the material properties of the steel before rolling and those of the steel after rolling is seen to be with the Young's modulus, but even this difference is only 0.45%. Therefore the material properties of the steel after rolling were adopted in the finite element numerical analyses presented in Chapter 8.

7.3 GEOMETRIC IMPERFECTIONS AND THEIR CHARACTERISTICS

7.3.1 General

As described in Chapter 6, the model shell specimens were fabricated by a two-stage process: (a) fabricating the 'raw' model cylinder; and (b) performing Stage II welding to introduce desired imperfections. For each model shell, two three-dimensional surveys of the shell surface were conducted: one at the end of Stage I and the other at the end of Stage II. These measurements were compared with those conducted on a precisely machined calibration cylinder with an external diameter of 1000mm (Figure 7.6) with the same measurement grids to obtain the next imperfection surface of the specimen.

All measurements were taken on the external surfaces of the specimens, because the internal surfaces of the specimens were inaccessible to such measurements. In order to examine any thickness variations due to the Stage II welding, two small pieces were cut from specimen 09P0408 after testing, on each of which there was a circumferential weld and a meridional weld. Thickness measurements were performed on these two small pieces of steel sheets along 5 lines across each weld using a micrometer of 0.001mm in resolution. These measurements found little thickness variations at both welds, with the largest thickness variation being 1%-2% of the sheet thickness at locations adjacent to the centre of the circumferential weld. Local thickness increases, which were caused by

welding deposits and contained small voids, are believed to be unlikely to have affected the shell buckling behavior. It is thus reasonable to exclude these welding deposits in the numerical modeling of the buckling tests. Therefore the middle surfaces of the specimens, which are referred to as the initial surfaces of the specimens here, can be obtained by shrinking the external surfaces as defined by measurements by half a thickness of the steel sheets.

The surveys of the initial surfaces were taken with a measurement grid of 4.5mm along the shell meridian and 4.36mm or 0.5^0 around the shell circumferences. This led to 167 meridional stations and 720 circumferential stations, with a total of 120240 measurement stations in a single shell specimen. These measurement grids ensured that even very localized geometric variations of the shell surfaces were captured. Furthermore, as the measurement grid points were subsequently transformed into nodes in the finite element model, such a fine grid with a spacing of less than $\lambda/11.5$ (λ is the meridional bending half wave length of the shell) ensured that very local buckling deformations could be accurately modeled in finite element analysis. To avoid congestion, the three-dimensional plots of the shell initial surfaces shown in this chapter used only half of the grid points, i.e., 84 points for each meridian and 360 points for each circumference.

7.3.2 Initial Surfaces of Model Shells

Figures 7.7 and 7.8 show the initial surfaces of Specimen 09SC from the three dimensional surveys before and after circumferential welding, respectively. The depression due to the circumferential weld is clearly seen in Figure 7.9; this was obtained simply by subtracting the coordinates of the external surface before the Stage II circumferential welding from those of the external surface after circumferential welding. Similarly, Figures 7.10 and 7.11 show the initial surfaces of Specimen 09QC04 before and after circumferential welding respectively, and Figure 7.12 shows the depressions arising from the four circumferential welds. The three dimensional plots of the initial surfaces of Specimen 09P0408 are shown in Figures 7.13 and 7.14, respectively; while its geometric distortions associated with the patterned welds are displayed in Figure 7.15.

As shown in Figures 7.7, 7.10 and 7.13, the initial deviations of the model shell surfaces before Stage II welding are quite small except along the two meridional weld seams. Despite the meticulous care exercised in fabricating these specimens, all three specimens featured substantial distortions at the meridional welding seams, especially at the bottom of the second longitudinal weld seam in each specimen, which is in the vicinity of 90^0. These were caused by the strong contraction of the front welding pool, where the perfectly fitted edges were pushed outwards. The maximum wall deviations from the corresponding nominal perfect surface are 5.29mm for Specimen 09SC, 5.53mm for Specimen 09QC04, and 4.35mm for Specimen 09P0408, respectively. Apart from those along the meridional weld seams, most of the wall deviations fall within $\pm 0.6mm$.

The Stage II circumferential welding in the three specimens was performed with two passes in all cases, in order to introduce a sufficiently large circumferential weld depression so that their effect would dominate that of the imperfections at the two meridional welds. The circumferential welds produced nearly axisymmetric depressions plus some wrinkles near the meridional seams (Figures 7.9 and 7.12), whereas the patterned welds induced approximately axisymmetric depressions at the circumferential welds and the wave patterns associated with the short meridional welds (Figure 7.15). The distortions induced by the Stage II welds were mostly confined to the middle portion of the cylinder where the Stage II welds were applied. These were mainly inward distortions and closely associated with the welds. The maximum and the average weld depression amplitudes are 2.19mm (about $2.46t$) and 0.79mm (about $0.886t$), respectively, for Specimen 09SC. While the maximum weld depression amplitudes for Specimen 09QC04 are 1.0mm, 1.16mm, 0.94mm and 1.13mm for the four circumferential welds counting from the lowest one upwards, the average amplitudes of these weld depressions are 0.66mm, 0.64mm, 0.61mm and 0.63mm, which are equivalent to $0.74t$, $0.717t$, $0.684t$ and $0.706t$, respectively. These weld depressions were measured using a straight gauge with a length of $4\sqrt{Rt}$ as stipulated in ENV1993-1-6 (1999). The distortions due to the patterned welds in Specimen 09P0408 are mainly oscillating inward distortions and are closely associated with the welds. The maximum deviation due to pattern welding is 2.88mm and is inward.

7.3.3 Fourier Decomposition of Geometric Imperfections

In order to better understand the nature of the measured imperfections, the double Fourier series, which has been successfully employed to represent imperfections in the three large steel silos as presented in Chapter 4, was used to represent the imperfections measured on the three test specimens:

$$F(v,\theta)=\sum_{m=0}^{N_m}\sum_{n=0}^{N_n}\cos\frac{m\pi v}{V}(A_{mn}\cos n\theta+B_{mn}\sin n\theta) \tag{7.1}$$

Two choices of the imperfection regions were considered for imperfection interpretation: one is the complete shell surface, while the other includes only the middle region with a meridional length of $12\sqrt{Rt}$. The latter option was considered because the middle region is the critical region for these buckling experiments, where the Stage II welds were applied and the buckling deformations were concentrated. For each choice, Fourier decompositions were performed for both the imperfections before Stage II welding and those after Stage II welding to examine the effect of the Stage II welds on the distribution of the imperfection. Although the Fourier series deduced contain a large number of terms, only the lower harmonic terms are displayed as the higher harmonic terms are all very small.

Figures 7.16(a) and 7.16(b) show the spectra (amplitude of each harmonic mode plotted against the harmonic numbers in both directions) of the Fourier series representing the imperfections on the complete surface of Specimen 09SC before and after patterned welds, while Figures 7.17(a) and 7.17(b) show the corresponding spectra of the imperfections in the mid region of the specimen before and after patterned welds, respectively. An obvious observation of these figures is that the amplitudes of the harmonic modes ($m=0, n=0$), ($m=0, n=1$), ($m=1, n=1$) overwhelm those of other harmonic modes. However, these Fourier components are unlikely to have an important effect on shell buckling behavior, because they are associated with imperfections in the forms of out-of roundness and overall tilt. A second observation is that the harmonic modes of pronounced amplitudes are concentrated at the lower harmonic numbers. A comparison of the amplitudes of harmonic modes deduced from the imperfections in the shell before and after the Stage II single circumferential weld shows that the Stage II weld led to amplitude growths in the components of ($n=0$) and ($m=0, n=10$); the latter component is possibly due to the

circumferential wrinkles introduced by the Stage II welding. The amplitudes of the harmonic modes deduced from the imperfections on the complete shell surface and those in the middle region are substantially different, especially for the components of $n = 0$, which illustrates the importance of the proper choice of the imperfection region for a clear interpretation.

The amplitudes of the harmonic modes deduced from the imperfections on the complete surface of Specimen 09QC04, which are given in Figures 7.18(a) and 7.18(b), are similar to those of Specimen 09SC in the following two respects: first, the amplitudes of harmonic modes ($m = 0, n = 1$) and ($m = 1, n = 1$) dominate those of other terms; second, the Harmonic modes with large amplitudes amass in the lower harmonic numbers. An important feature of the Fourier series representing the imperfection after the Stage II welds is that the four circumferential welds led to many Harmonic modes with $n = 0$ having appreciable amplitudes, while some of the other Harmonic modes with $m = 0$ become small. The Fourier series deduced from the imperfections on the complete surface are somewhat similar to those deduced from the imperfections in the mid region of the specimen surface (Figs.7.18 and 7.19). Apart from the similarities, there is a significant difference in the Fourier series for the two cases: the four circumferential welds led to many pronounced harmonic terms at $n = 0$ when the complete surface was included in the analysis but when only the middle region was considered, the single harmonic mode of $m = 6$ at $n = 0$ stands out as the term with a large amplitude. Obviously, the harmonic mode ($m = 6, n = 0$) with a large amplitude from the middle region option is closely related to the three 'strakes' produced by the four welds. Therefore, the middle region option can better reveal the distinct characteristics of the imperfection arising from the Stage II welds than the complete surface option.

The spectra of the Fourier series deduced from the imperfections in Specimen 09P0408 are fairly simple compared with those deduced from the imperfections in Specimens 09SC and 09QC04 (Figures 7.20 and 7.21). The patterned welds on Specimen 09P0408 led to some Harmonic modes closely associated with the welds. For the Fourier series deduced from the imperfection over the complete shell surface, the most conspicuous components associated with the patterned welds are found in the Harmonic modes with $n = 0$ and $n = 18$, the former of which is related to the circumferential welds in a manner

similar to that in Specimen 09SC and 09QC04, while the latter is related to the 18 short meridional welds. The spectrum deduced from middle region option exhibits even more pronounced features associated with the patterned welds, such as the Harmonic modes ($m = 6, n = 0$), ($m = 2, n = 18$) and ($m = 4, n = 18$).

Although the spectrum of the Fourier series for the imperfection in Specimen 09P0408 (Figure 7.21(b)) does not closely resemble that of the Fourier series for the imperfection in a real large silo (Figures 4.39-4.41) in some respects, but both of them indicate that the imperfection is closely related to the pattern of welds. The differences between the two spectra are not surprising, as even between the spectra for the three real silos constructed by the same process, there are substantial differences. Compared to the real silos, the imperfection in Specimen 09P0408 contains much fewer components which are not related to the patterned welds. This is understandable, as the real process of assembly of panels into a shell is certainly to induce other geometric deviations than those associated with the shrinkage of welds simulated in the laboratory process.

7.4 BUCKLING AND POST-BUCKLING BEHAVIOR

7.4.1 General

The shell specimens described above were loaded in uniform axial compression to failure in the upgraded shell buckling test facility described in Chapter 6. The upgraded facility was designed for displacement control during loading using an MTS Actuator. Load transfer from the actuator to the cylinder was effected through a universal joint, a shallow loading cone and a loading ring with a knife edge to ensure uniform loading on the end ring of the cylinder.

Four transducers were installed inside the test specimen to measure the relative displacements between the two end rings (i.e. axial shortening). Details of these transducers were given in Chapter 6. Strain gauges were placed on the inner surface of the cylinder to avoid any interference with shape surveys on the external surface. The markings of circumferential angles relative to the two continuous meridional welds on the

specimens could not be unified due to testing constraints. As a result, the transducer layout and the strain gauge arrangement for each specimen are somewhat different. Figures 7.22-7.24 show the layouts of both transducers and strain gauges for specimens 09SC, 09QC04, and 09P0408, respectively. The four transducers on each specimen are named D1, D2, D3 and D4, while the strain gauges on each specimen are simply numbered in Figures 7.22-7.24 but referred to elsewhere with a starting letter "S" to indicate that they are strain gauges. In formulating the strain gauge arrangements, finite element results from pre-test analyses of these specimens were taken into due account.

In order to provide a comprehensive picture of the buckling and post-buckling behavior of each specimen, the readings from all strain gauges and transducers are reported here, despite that some of the readings from non-critical locations may not be a great help in understanding the behavior.

7.4.2 Experimental Results and Observations

7.4.2.1 Specimen 09SC

The axial load on specimen 09SC increased steadily until 100kN, when the shell wall in the vicinity of the circumferential weld within the circumferential ranges of 0^0 to 45^0 and 330^0 to 360^0 became somewhat flat. The local wall flattening in the circumferential range of 330^0 to 360^0 is reflected in the readings of the strain gauges installed in this region (Figure 7.27). As the load was increased to 120kN, small dimples were found at the middle portions of the two circumferential ranges mentioned above. These dimples then grew larger with further loading and some other dimples emerged in regions near 0^0. When the load reached 177.7kN ($0.298\sigma_{cl}$), several 'pop' sounds were heard, and many of the dimples suddenly changed to big buckles at the middle part of the shell with the appearance of many other buckles elsewhere in the shell as well. Most of the buckles assumed a diamond form, with the circumferential weld depression passing through its centre. This is the typical buckling mode for a shell with a single axisymmetric depression as can be found in the published literature (e.g. Rotter and Teng, 1989, Berry *et al*, 2000). The specimen jumped from a pre-buckling state to a deep post-buckling state, during which the axial load dropped rapidly. The test set-up failed to capture the post-buckling

process of the specimen because the rigidity of the loading system was not sufficient due to various constraints. The load-axial shortening curves for the meridians at 30^0, 120^0, 210^0 and 300^0 are shown in Figure 7.25 to indicate the loading history of the test. The deep post-buckling state of the specimen is not included in Figure 7.25, as otherwise the it will be very difficult to show the pre-buckling curves clearly in the figure.

The load-strain curves from strain gauges S33, S34, S35, and S36, which are given in Figure 7.26, diverge at a load as low as 40kN, indicating the early local bending at the locations of S33 and S36. It is clear that the load-axial strain curves in Figure 7.26 are significantly different from the load-axial shortening curves in Figure 7.25. This can be easily understood, as the load-strain curves depict very local strain variations, whereas the load-axial shortening curves describe the overall state of the whole meridian being monitored.

The circumferential strains near the circumferential weld are shown in Figures 7.27 and 7.28 for the strain gauge groups of S1-S6 and S13-S18, respectively. It can be seen that compressive strains developed at the circumferential weld while tensile strains occurred at the circumference at a distance of λ (λ is the meridional bending halfwave length) from the circumferential weld. This phenomenon agrees well with the finite element predictions by Rotter and Teng (1989). By contrast, some of the circumferential strains at or near the intersection between the circumferential and one of the meridional welds (Figures 7.29 and 7.30) are tensile. This difference is due to the complex geometric imperfections at these locations (Figure 7.9). The effect of the complex geometric imperfections at these locations is also reflected by the diverging load-strain relationships for the strain gauge group of S26, S27 and S29 and the group of S30-S32 presented in Figures 7.31 and 7.32.

7.4.2.2 Specimen 09QC04

As indicated in Figure 7.33, the load increased steadily in Specimen 09QC04 before buckling, but then decreased in a more gradual manner than that of specimen 09SC so the postbuckling response could be recorded. During the loading process before buckling, the middle portion of the specimen within the circumferential ranges of 0^0 to 60^0 and 210^0 to 240^0 underwent some local flattening, which could be felt by hand. Buckling happened

suddenly with a 'pop' sound when the load level reached 169.0kN ($0.283\sigma_{cl}$), and buckles turned up at the third and fourth circumferential welds within the circumferential range of 120^0 and 165^0. The buckles continued to grow larger and propagated circumferentially and somewhat meridionally with a decreasing load during post-buckling deformation. Eventually, the buckles were found to cover almost the complete shell circumference ($0^0 - 220^0$ and $280^0 - 360^0$) in the middle region where the circumferential welds were located. While the buckles of Specimen 09QC04 are similar to those of Specimen 09SC in shape, the buckles in the former have the distinctive feature that the buckles centred at adjacent weld depressions are staggered. This phenomenon is due to the interaction of adjacent welds which has been studied by some researchers such as Lock (1989) and Rotter (1996). The study by Rotter (1996) suggested that the interaction between adjacent welds may reduce the buckling strength by about 15%. The conclusion is confirmed by the present experimental results: the buckling load of Specimen 09QC04 is about 5% lower than that of Specimen 09SC despite that the amplitude of the geometric imperfection in Specimen 09QC04 is much lower than that of the geometric imperfection in Specimen 09SC.

The load versus vertical strain curves from strain gauges S33-S36, shown in Figure 7.34, indicate that the load-vertical strain relationships at these locations are almost linear before buckling, despite that they diverge somewhat at the load level 60kN, but they become rather complicated after the buckling load is reached.

Figures 7.35 and 7.36 present the load-hoop strain responses from the strain gauge groups of S1-S6 and S13-S18, which are at some distance away from the two meridional welds. It is clear that the responses are linear up to the buckling load; strain gauges S1-S3 and S13-S15 located at the circumferential weld recorded compressive hoop strains while strain gauges S4-S6 and S16-S18 at a circumference away from the circumferential weld recorded tensile strains.

The trends shown by readings of the strain gauge groups S7-S12&S25 and S19-S24&S29 (Figures 7.37 and 7.38), which were installed in the vicinities of the intersections of the circumferential weld and the two meridional welds, are similar to those of strain gauges away from the meridional welds in that hoop strains away from the monitored

circumferential weld are tensile (strain gauges S10-S12 and S25, and S22-S24 and S29) and those at the monitored circumferential weld are compressive, except strain gauges S8 and S20 at the points of intersection between the monitored circumferential weld and the two meridional welds.

The meridional strains of the strain gauges S26-S28 and S30-S32 at in specimen 09QC04 (Figures 7.39 and 7.40) are different from those of their counterparts in specimen 09SC (Figures 7.31 and 7.32) in that the readings from strain gauges S27 and S31 are tensile. This indicates that at these locations where the monitored circumferential weld intersects the meridional welds, the wall was subject to bending that led to bending tensile strains on the external surface that exceeded the axial membrane compressive strains. The readings of strain gauges (strain gauges S8, S27 and S20, S31) at the intersections of the circumferential weld and the meridional ones can be attributed to the complicated geometric imperfections at these locations.

7.4.2.3 Specimen 09P0408

Compared to that of specimens 09SC and 09QC04, the load-displacement behaviour of specimen 09P0408 is rather different, because local buckling was observed in the early stage of the test. Figure 7.41 presents the load-axial shortening responses of the four monitored meridians in specimen 09P0408. It shows that the curves of the transducers D1 and D2 diverge at a load level as low as 65kN, because the panels in the vicinity of the 150^0 meridian underwent local flattening at this load level. When the load was increased to 100kN, some local buckles were observed in the two panels of the bottom strake around the 65^0 meridian, leading a turning point in the curve of transducer D1. As the load continued to increase, deformations developed slowly and new buckles appeared in the upper strake at the 300^0 meridian at a load level of about 110kN. Despite the development of so many local buckles in the shell wall, the shell was able to carry an increasing load until the specimen failed at a load of 166.6kN, which is only 27.9% of the classical buckling load of its perfect counterpart.

Similar to those in specimen 09QC04, the buckles in specimen 09P0408 generally assumed an inward diamond pattern, with the buckles centred at adjacent circumferential

welds being in a staggered pattern. Many of buckles spanned two or three panels in the circumferential direction as well as two strakes in the meridional direction, leading to a rough size with diagonal lengths of 300*mm* and 200*mm* respectively. Although the ultimate load of the specimen was not controlled by development of local buckles, but the local buckles were important in triggering the final collapse. The appearance of local buckles at the load of 100kN ($0.168\sigma_{cl}$) indicates the severity of the geometric imperfections and residual stresses induced by the patterned welds in this specimen.

Figures 7.42 and 7.43 show the load-meridional strain responses from strain gauges installed at panel centres (S25-S28) and at meridional welds (S29-S32). The readings of strain gauges S26 and S30 diverged from those of others at an axial load of about 65kN, when the panels in the vicinity of the 150^0 meridian experienced local flattening. As the load was increased to around 105kN, the readings of strain gauge S32 in Figure 7.43 started to increase more rapidly, because some buckles turned up there. The load-circumferential strain behaviour of the shell is complicated by the oscillating geometric imperfections induced by the short meridional welds. Most of the circumferential strain readings comply with the following rule before buckling: the strain gauges at mid-strake circumferences recorded tensile strains while their counterparts at circumferential welds recorded compressive strains. Examples included strain gauges S1-S6 in Figure 7.44, strain gauges S19-S24 in Figure 7.45, strain gauges S7, S9 and S10 in Figure 7.46, strain gauges S13, S15 and S18 in Figure 7.47. Nevertheless, strain gauges S8, S11, and S12 in Figure 7.46 and strain gauges S14, S16, and S17 in Figure 7.47 recorded almost no strains before buckling. This anomalous behaviour can be attributed to the complex imperfections produced by the meridional welds.

7.4.3 Variations of Radial Deformations

7.4.3.1 Radial Deformations during Loading

In order to monitor the growth of radial deformations during the test, circumferential surveys of two selected circumferences of each specimen were performed at certain load levels using the measurement system of the shell buckling test facility. The circumferences measured were chosen to be identical to the circumferences on which the circumferential

strain gauges were installed. The measurements were done at a circumferential spacing of 0.5^0 (or $4.36mm$) before loading, at selected levels of loading as well as for a deep post-buckling state. To avoid likely congestion of circumferential shapes at different load levels, the results of measurements for each monitored circumference are displayed in two separate graphs: one graph showing the shapes of the circumference before loading and at the selected load levels before buckling where the gradual changes in the shape of the circumference can be more clearly seen, and the another graph showing the same information given in the first graph plus the shape of the circumference of a deep post-buckling state where the post-buckled shape is contrasted with the pre-buckling shapes of the circumference. Also for clarity, the initial shape of the circumferences before loading is shown as a red thick solid line, the pre-buckling shapes are shown as black thin solid lines, and the post-buckled shape is shown as a dotted line.

In general, some of the dimples at the deep post-buckling stage fell beyond the measurement range of the laser displacement meter. In such a case, the monitored circumference at the deep post-buckling stage was measured twice: the first survey was done as usual while the second survey was done to provide missing data for the far parts of the dimples by positioning the laser meter closer to the shell surface; the results from the two survey were finally combined to produce the complete shape of the circumference.

Figures 7.48 and 7.49 show the shapes of the two monitored circumferences of specimen 09SC at the pre-buckling load levels of 0kN, 20kN, 40kN, 60kN, 80kN, 100kN, 125kN, 141kN, and 165kN. It is seen that deformations were induced by loading over nearly the entire circumference at the beginning of loading and they grew as the load was increased. The locations of the two meridional welds, though having initial geometric deviations, experienced little additional deformations during the test. These shapes are shown together with the post-buckled shapes of the two circumferences in Figures 7.50 and 7.51 respectively. A clear feature is that buckles developed within the circumferential ranges of 0^0 to 130^0 and 240^0 to 360^0, in which the pre-buckling deformations are relatively large. The buckles are seen to be predominantly inward and are fairly similar to the geometric imperfections in shape.

The shapes of two monitored circumferences of specimen 09QC04 at the pre-buckling load levels of 0kN, 30kN, 60kN, 90kN, 120kN, and 150kN are displayed in Figures 7.52 and 7.53, respectively. The deformations of the circumferences within the range of 0^0 to 180^0 are seen to be outward while those within the range of 180^0 to 360^0 are inward. The shapes of the two monitored circumferences at a post-buckling load of 122kN are respectively shown in Figures 7.54 and 7.55 respectively. The buckles cover almost the entire circumference in specimen 09QC04. Although the post-buckled shapes are somewhat similar to those of geometric imperfections, the similarity between them is much less than that observed in specimen 09SC.

The radial deformations of the two monitored circumferences in specimen 09P0408 are much more obvious than those of specimens 09SC and 09QC04, because the former experienced local buckling at a low load level. Figures 7.56 and 7.57 show the results of circumferential scans on the mid-strake circumference and the weld circumference of specimen 09P0408 at the pre-buckling load levels of 0kN, 30kN, 60kN, 90kN, 133kN, and 150kN, respectively. It is seen that the growth of radial deformations of the weld circumference is much larger than that of the deformations of the mid-strake circumference, with both of them generally assuming a pattern similar to the form of the geometric imperfections. The shapes of the two circumferences at a post-buckling load of 123kN are shown in Figures 7.58 and 7.59 in conjunction with corresponding pre-buckling shapes respectively. Obviously, the buckles are inward and take the form of the geometric imperfection in a way similar to that of Specimen 09SC. Despite that large pre-buckling deformations developed almost over the entire circumference, the buckles were concentrated within the circumferential ranges of 0^0 to 60^0 and 210^0 to 360^0, indicating these locations were critical to the strength of this shell.

7.4.3.2 Growth of Fourier Series Coefficients during Loading

In order to better understand the characteristics of the geometric imperfections in the test specimens and the role they played in the buckling failure, both the geometric imperfections and the deformations of the monitored circumferences of the specimens were interpreted by through Fourier decomposition. As only the variation of the imperfection/deformation around the circumference was concerned, a one-dimensional

Fourier representation (Eqn 7.2) was employed to describe the measured imperfections and deformations:

$$F(\theta) = \sum_{n=0}^{N_n} (a_n \cos n\theta + b_n \sin \theta) \tag{7.2}$$

where the amplitude (or coefficient) of each harmonic mode is given by:

$$A_n = \sqrt{a_{n_c}^2 + b_{n_c}^2} \tag{7.3}$$

Although the number of Harmonic modes deduced, which depend on the number of sampling points as explained in Chapter 4, is large, the coefficients of Harmonic modes larger than 50 are very close to zero. Therefore, only those harmonic modes with a harmonic number n being no less than 50 are discussed here. The harmonic terms 0 and 1, whose coefficients have large values, are also excluded from the figures, to make the coefficients of other harmonic modes more visible in the relevant figures. Harmonic terms 0 and 1 correspond to axisymmetric deformations and rigid-body horizontal shifts of the circumference, are unlikely to have appreciable effects on the development of short wave buckles observed in the tests.

Figures 7.60 and 7.61 show the growths of the amplitudes of Fourier series for the two monitored circumferences of specimen 09SC. The lower harmonic modes are seen to have large initial amplitudes and to experience appreciable growths, indicating that the lower harmonic modes played an important role in the buckling process. The distributions of the harmonic coefficients of the post-buckled shapes are significantly different for the two circumferences despite that their pre-buckling distributions are similar. Large amplitudes are found only in harmonic modes with the harmonic number n being below 15 for the above-weld circumference (Figure 7.62), whereas for the weld circumference, large amplitudes are found with some higher harmonic modes (Figure 7.63).

The growths of the amplitudes of harmonic modes deduced from the deformations of the two monitored circumferences of specimen 09QC04 are shown in Figures 7.64 and 7.65, respectively. Similar to those in specimen 09SC, appreciable growths in the amplitudes are also found in the lower harmonic modes, especially in harmonic term 4 for both circumferences. Nevertheless, the amplitude growths of for specimen 09QC04 are significantly different from those for specimen 09SC in that the growths of the lower harmonic terms in the former are through the amplification of initial geometric

imperfections but this is not the case for the latter. The harmonic coefficients of the post-buckled shapes of the two circumferences in specimen 09QC04 are plotted in Figures 7.66 and 7.67 respectively. In contrast to those of specimen 09SC, the spectra of the two post-buckled circumferences of specimen 09QC04 are quite similar, with both having its largest coefficient for harmonic term 11, followed by harmonic terms 4 and 12.

The growths of the harmonic coefficients in specimen 09P0408 are more complicated than those of specimens 09SC and 09QC04, except harmonic terms 18 and 36 for the mid-strake circumference and harmonic term 36 for the weld circumference, which are closely related to the pattern of short meridional welds (Figures 7.68 and 7.69). The complex geometric imperfections as well as the associated residual stresses are believed to be responsible for the complex deformation response. As shown in Figures 7.70 and 7.71, the spectra of the two Fourier series for the post-buckled shapes of the two monitored circumferences in specimen 09P0408 are very different. Nevertheless, they are similar in some respects, for example, large harmonic coefficients are confined to harmonic terms below 20, but the coefficients of these terms from pre-buckling deformations are small. The harmonic term 18 which has a large coefficient does not grow much during the post-buckling deformation. Moreover, some of the terms higher than 20, which have very small amplitudes in the pre-buckling stage, show visible growths.

The harmonic modes which show rapid amplitude growths are clearly important in the process of buckling failure. Although the spectra of the Fourier series for the imperfections/deformations in the three specimens are significantly different, they do share some common features. First, the growths in the harmonic coefficients of pre-buckling deformations are generally found in the harmonic terms below around 20 for which the harmonic coefficients of initial imperfections are relatively large, demonstrating the important role played by the short wave imperfections in the buckling process. Second, the spectra of the post-buckled deformations are significantly different from those of pre-buckling deformations, indicating mode changes during post-buckling deformations, which is a well known phenomenon of axially compressed cylinders.

7.4.4 Post-buckled Shapes

The photographs and the three-dimensional surface plots of the three specimens are shown in Figures 7.72-7.74 and Figures 7.75-7.77, respectively. Generally speaking, the three dimensional plot provides more details of the deformed surface than the photograph, as the plot displays the complete view of the shell surface. The surface scans for the three dimensional plot were done on the failed specimen after the load had released. For the three specimens, two different measurement grids were adopted: $10mm \times 0.5^0$ for specimens 09SC and 09P0408, and $9mm \times 0.5^0$ for specimen 09QC04. These measurement grids are believed to be sufficient for capturing the configurations of the post-buckled specimens which had much longer deformation waves than those of the geometric imperfections. Figures 7.75-7.77 show that most of the buckles were confined to the middle portion of the specimen where the Stage II welds were located, indicating that the Stage II welds led to the critical imperfections despite that these imperfections are much smaller than those associated with the two meridional welds.

The deformations of the post-buckled specimens were also interpreted using the double Fourier series (Eqn 4.1). The deduced Fourier series have very small coefficients for harmonic terms with the meridional harmonic number $m > 20$ or the circumferential harmonic number $n > 30$, the spectra of the Fourier series are displayed here only for harmonic numbers $m \leq 20$ and $n \leq 30$. Figures 7.78-7.80 show the truncated spectra of the Fourier series deduced from the deformations of the three post-buckled specimens respectively. Although post-buckled surfaces of the specimens 09SC and 09QC04 are significantly different, their spectra are rather similar, as both of them are dominated by the lower harmonic terms of columns of $n = 0$, $n = 1$, $n = 10$, and $n = 11$. The similarity of these two spectra is related to their similarity in their geometric imperfections. The Fourier spectrum of the post-buckled surface of specimen 09P0408 is very different from those of the other two specimens, because the dominant components of imperfections in specimen 09P0408 are in the block of harmonic terms with $m \leq 15, n \leq 20$ rather than the 'column' forms of imperfections in specimens 09SC and 09QC04.

7.5 CONCLUSIONS

This chapter has presented the results from careful buckling experiments on welded steel cylinders under axial compression. Three model shells, referred to as specimens 09SC, 09QC04, and 09P0408, were tested. Apart from the two meridional welds required to form the shell, Specimen 09SC had a single circumferential weld at the mid-height, specimen 09QC04 had four circumferential welds which were symmetrically located at a constant spacing within the mid-height region of the shell, while specimen 09P0404 had many short meridional welds in addition to the four circumferential welds, forming a typical pattern of welds as is generally present in a typical silo or tank; the welds divided the mid-height region of the shell wall into many rectangular panels.

The material properties of the as-supplied thin steel sheets were determined and the effects of rolling on the material properties were examined and found to be very small. The initial surfaces of the specimens were surveyed before and after the Stage II welding as well as after the tests. Two small pieces of the shell wall were cut from specimen 09P0408 after testing for thickness measurements and the thickness variations due to Stage II welding were very small. As a result, the middle surface of a test shell was deduced from the external surface as measured by shrinking it by half the thickness.

The imperfections in the specimens before and after Stage II welding were carefully analyzed to reveal their characteristics. A clear relationship was found to exist between the imperfections and the welds. These imperfection analyses confirmed the success of the model fabrication techniques presented in Chapter 6, as the imperfections had the desired characteristics associated with the welds introduced in the Stage II operation.

The buckles observed in specimens 09SC and 09QC04 were found to have a diamond shape, while the buckles in specimen 09P0408 had a pattern closely associated with the weld pattern. Fourier decompositions of the post-buckling deformations of the specimens showed that the dominant components of deformations are described by the lower harmonic terms.

The initial and deformed shapes of two selected circumferences were monitored during each test, and the results were represented by one-dimensional Fourier series. During loading, the modal amplitudes of the lower harmonics were found to grow rapidly, and these represent the controlling components of deformations. The important harmonic terms of the post-buckled circumferences are significant different from those of the pre-buckling circumferences, which confirms the phenomenon of mode changes during post-buckling deformation. In addition, the variations of axial shortenings and strain readings at the selected locations were reported. Most of the strain readings can be easily understood, but some of the readings, from gauges installed at intersections of welds, cannot be easily expected.

The buckling loads of these specimens are much lower than those of shells with imperfections of many other known patterns, demonstrating the severity of these imperfections in reducing the shell buckling load. For a fuller understanding of the buckling behavior of these cylinders, results from numerical models of these test specimens will be presented and compared with the test results in the next chapter.

Table 7.1 Material properties of steel sheets before rolling

Coupon	Thickness (mm)		Young's Modulus (MPa)			Yield Stress (MPa)		
	(1)	(2)	(3)	(4)	(5)	(6)	(7)	(8)
09NAM1	0.889	0.892	199022	198060	198034	317.2	310.5	311.0
09NAM2	0.886		197098			303.8		
09NAC1	0.904		197166	195805		317.4	312.0	
09NAC2	0.898		194443			306.6		
09NBM1	0.882		199214	199738		310.0	309.9	
09NBM2	0.887		200262			309.7		
09NBC1	0.907		197898	198533		312.9	311.6	
09NBC2	0.884		199167			310.3		

Table 7.2 Material properties of steel sheets after rolling

Coupon	Thickness (mm)		Young's Modulus (MPa)			Yield Stress (MPa)		
	(1)	(2)	(3)	(4)	(5)	(6)	(7)	(8)
09RAM1	0.897	0.892	195449	196705	197140	316.2	316.3	311.8
09RAM2	0.866		197960			316.4		
09RAC1	0.905		197133	197009		318.9	310.2	
09RAC2	0.882		196884			301.5		
09RBM1	0.895		198400	196448		320.3	315.3	
09RBM2	0.898		194495			310.5		
09RBC1	0.886		198667	198396		292.7	305.4	
09RBC2	0.906		198124			318.0		

Figure 7.1 Photograph of Specimen 09SC

Figure 7.2 Photograph of Specimen 09QC04

Figure7.3 Photograph of Specimen 09P0408

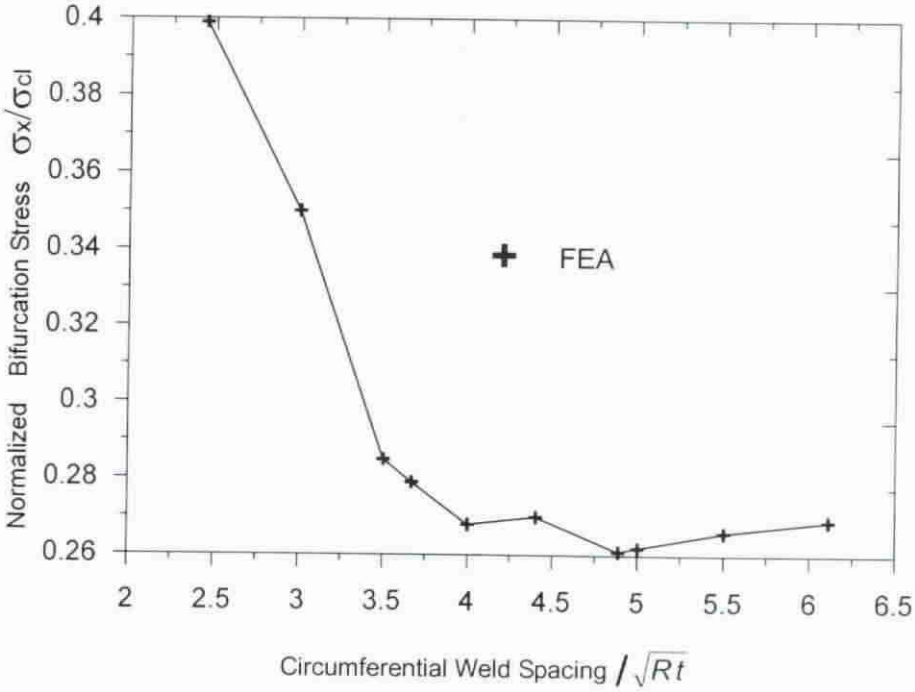

Figure 7.4 Effect of interaction between adjacent weld depressions

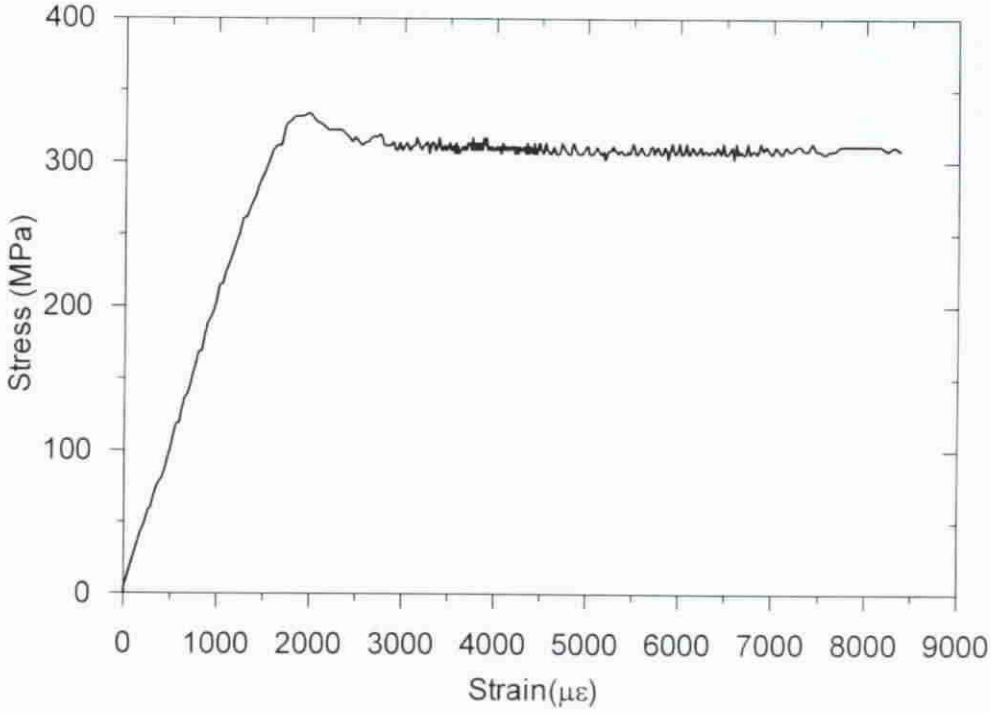

Figure 7.5 Typical strain-stress curve from a tensile test

Figure 7.6 Precisely machined steel cylinder for calibration

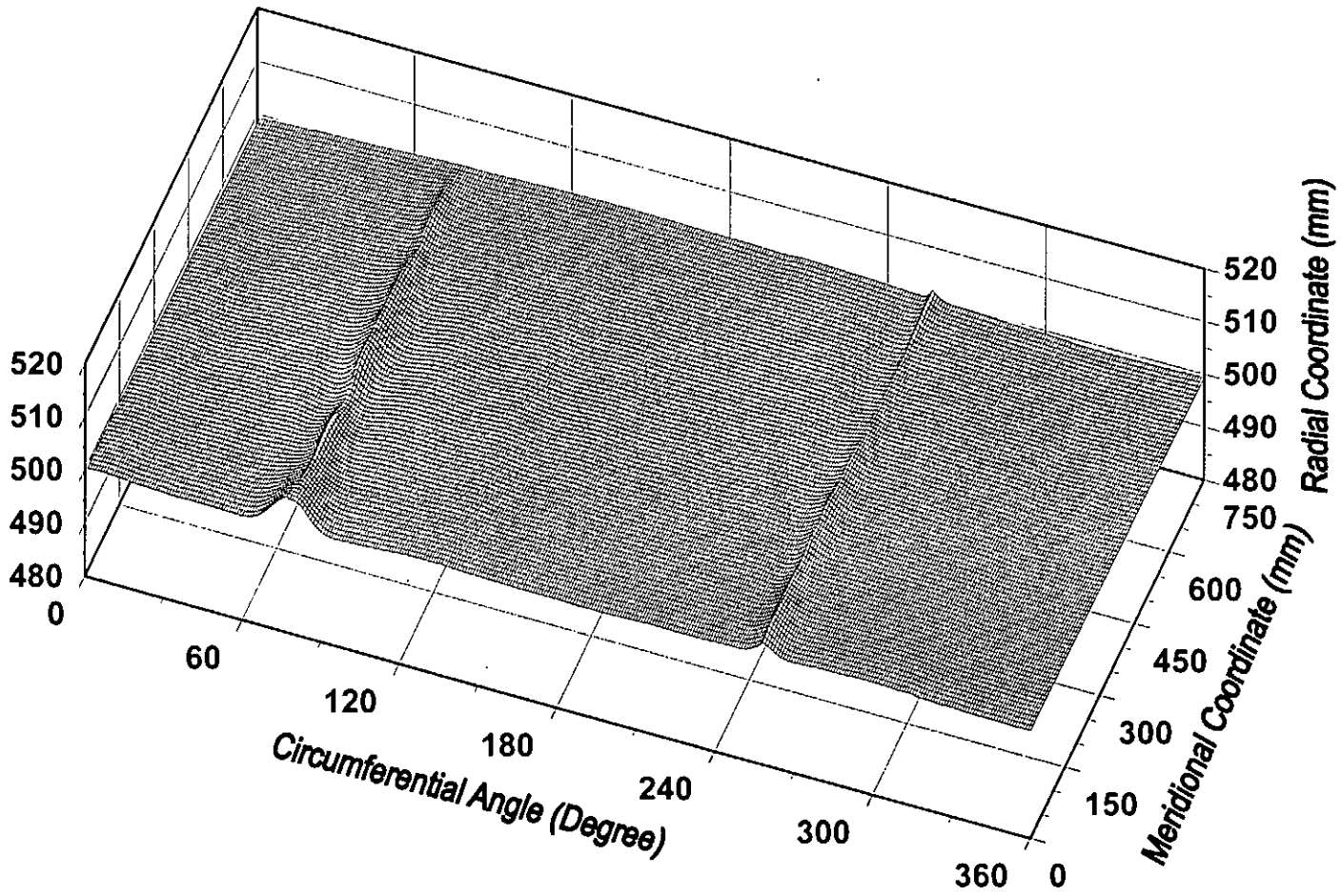

Figure 7.7 Initial surface of Specimen 09SC before Stage II welding

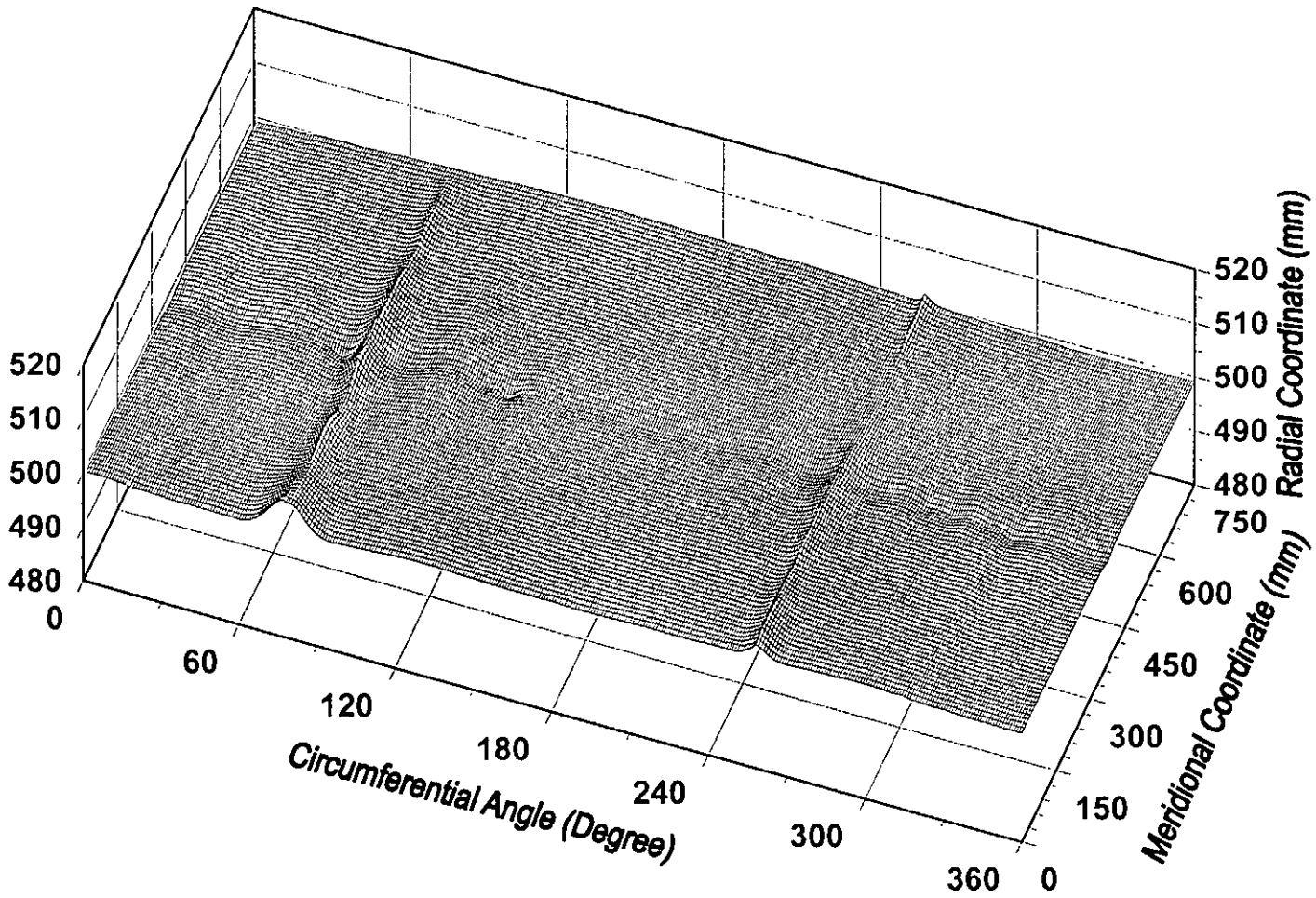

Figure 7.8 Initial surface of Specimen 09SC after Stage II welding

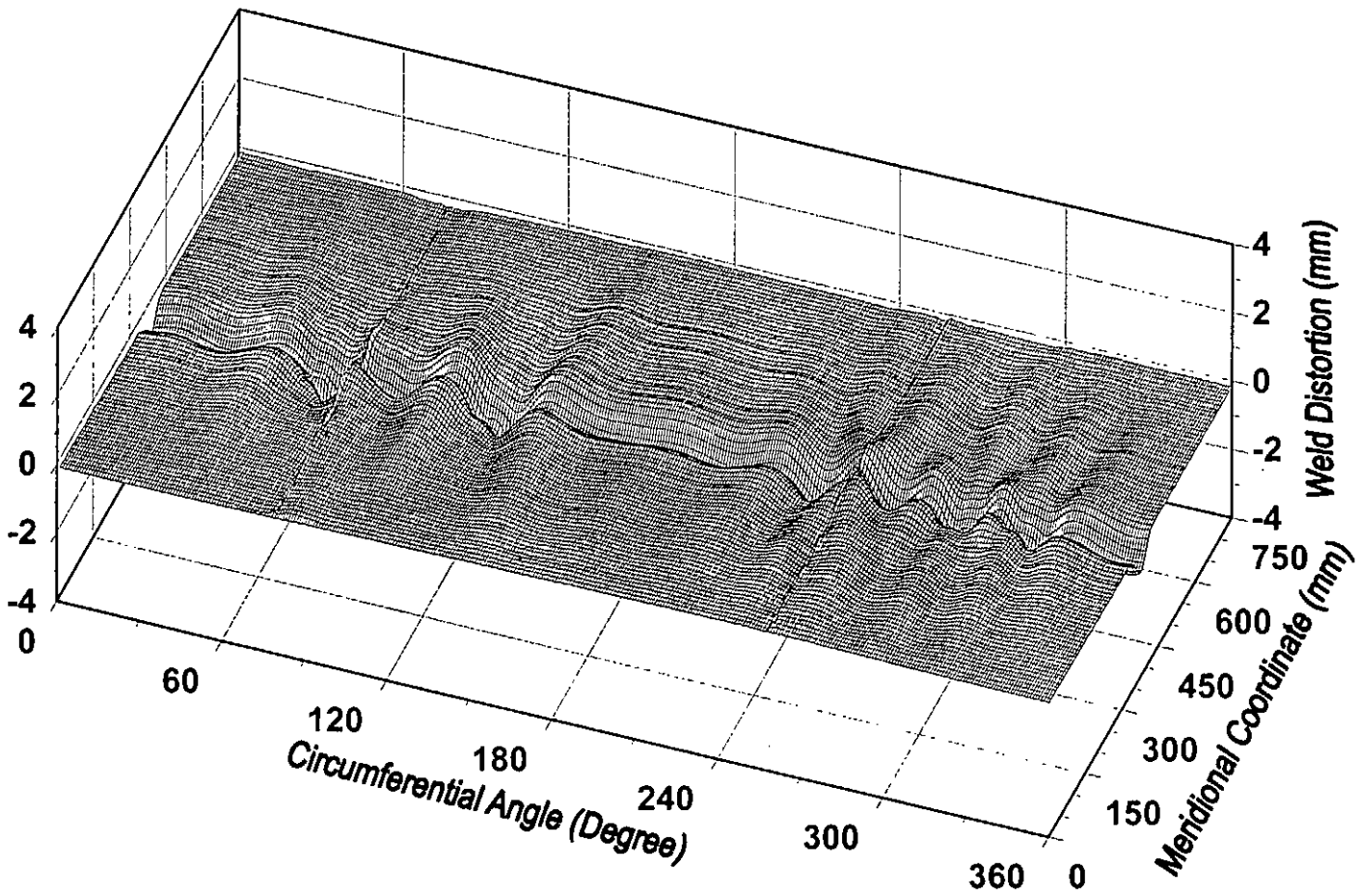

Figure 7.9 Welding distortion in Specimen 09SC due to a single circumferential weld

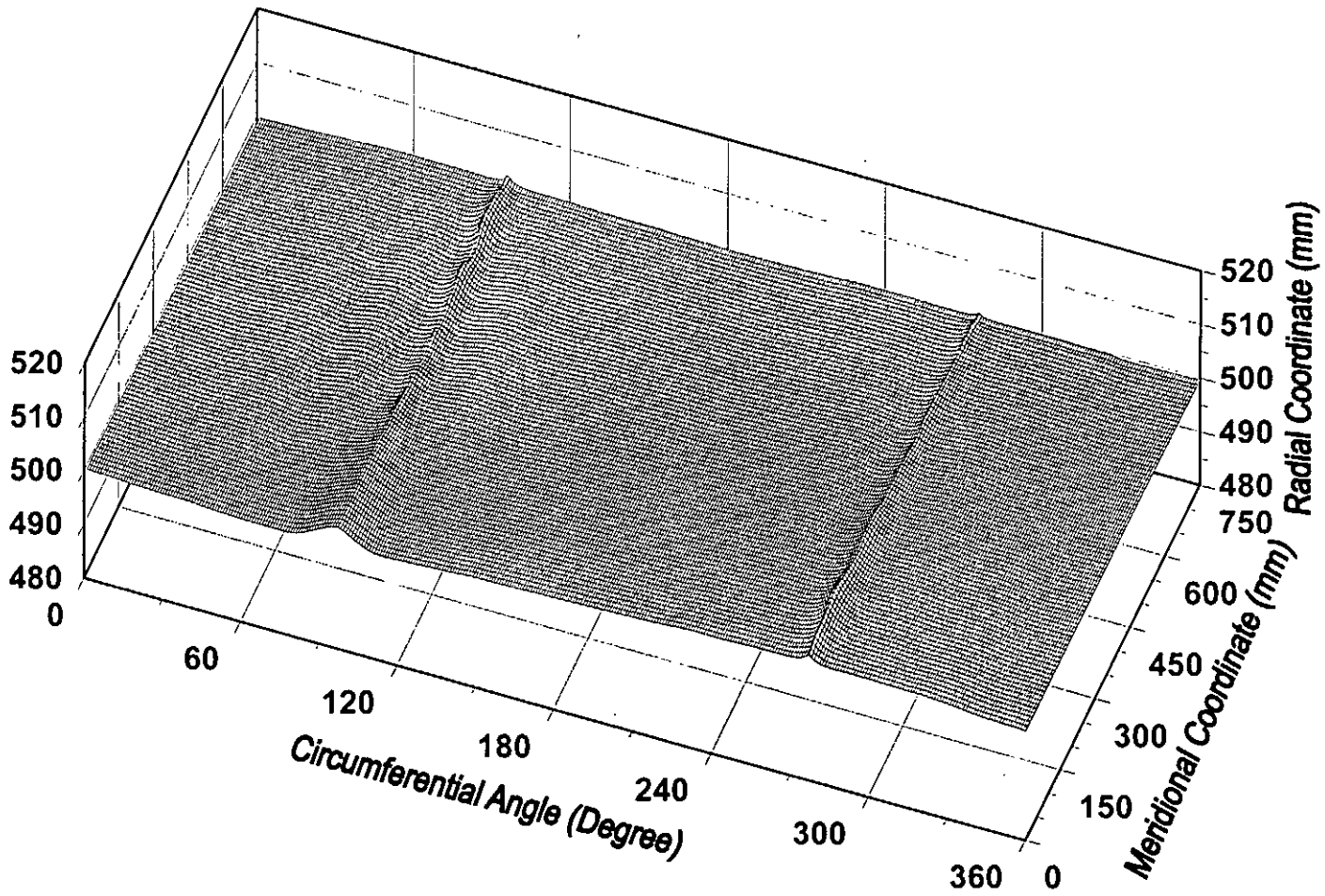

Figure 7.10 Initial surface of Specimen 09QC04 before Stage II welding

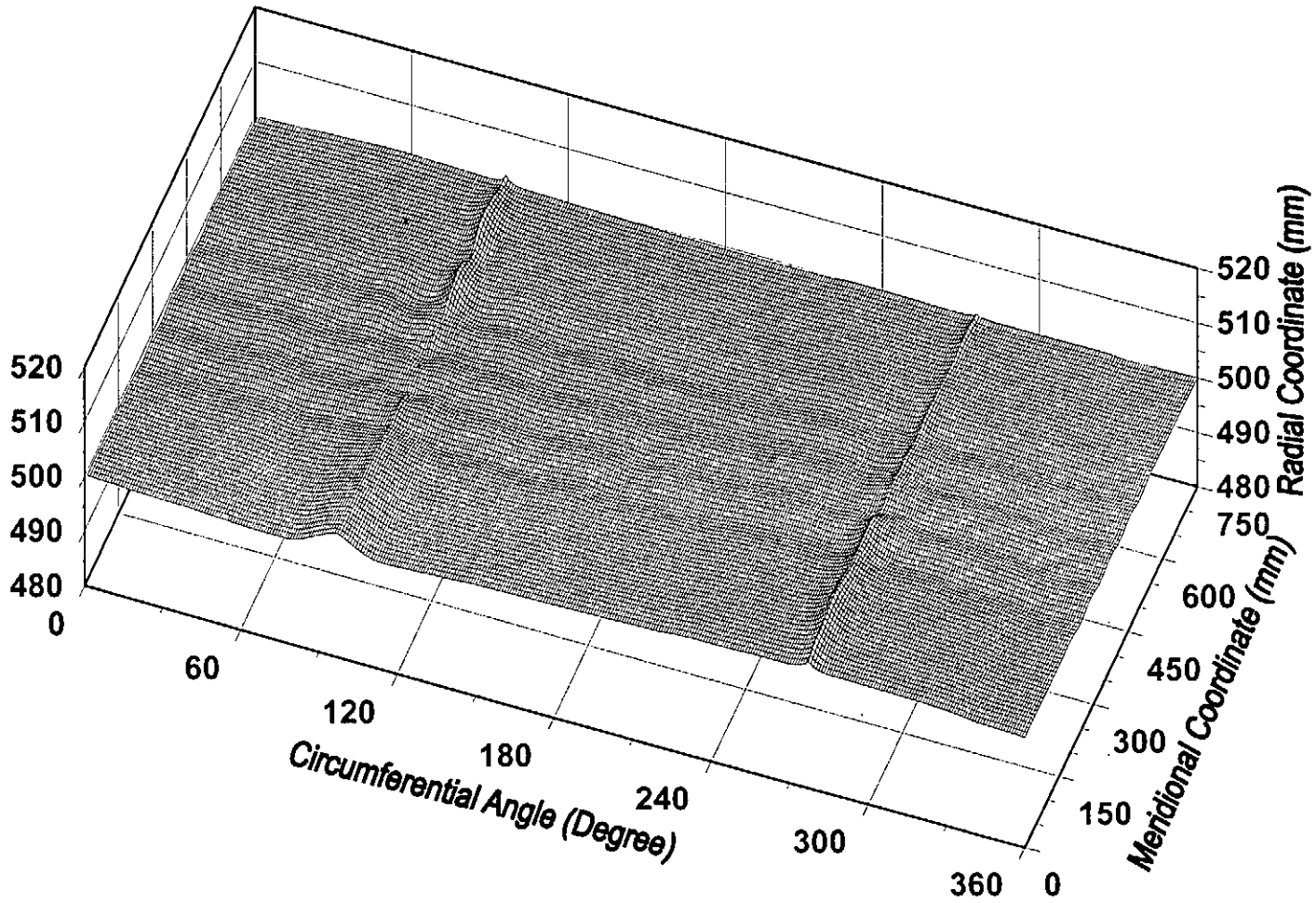

Figure 7.11 Initial surface of Specimen 09QC04 after Stage II welding

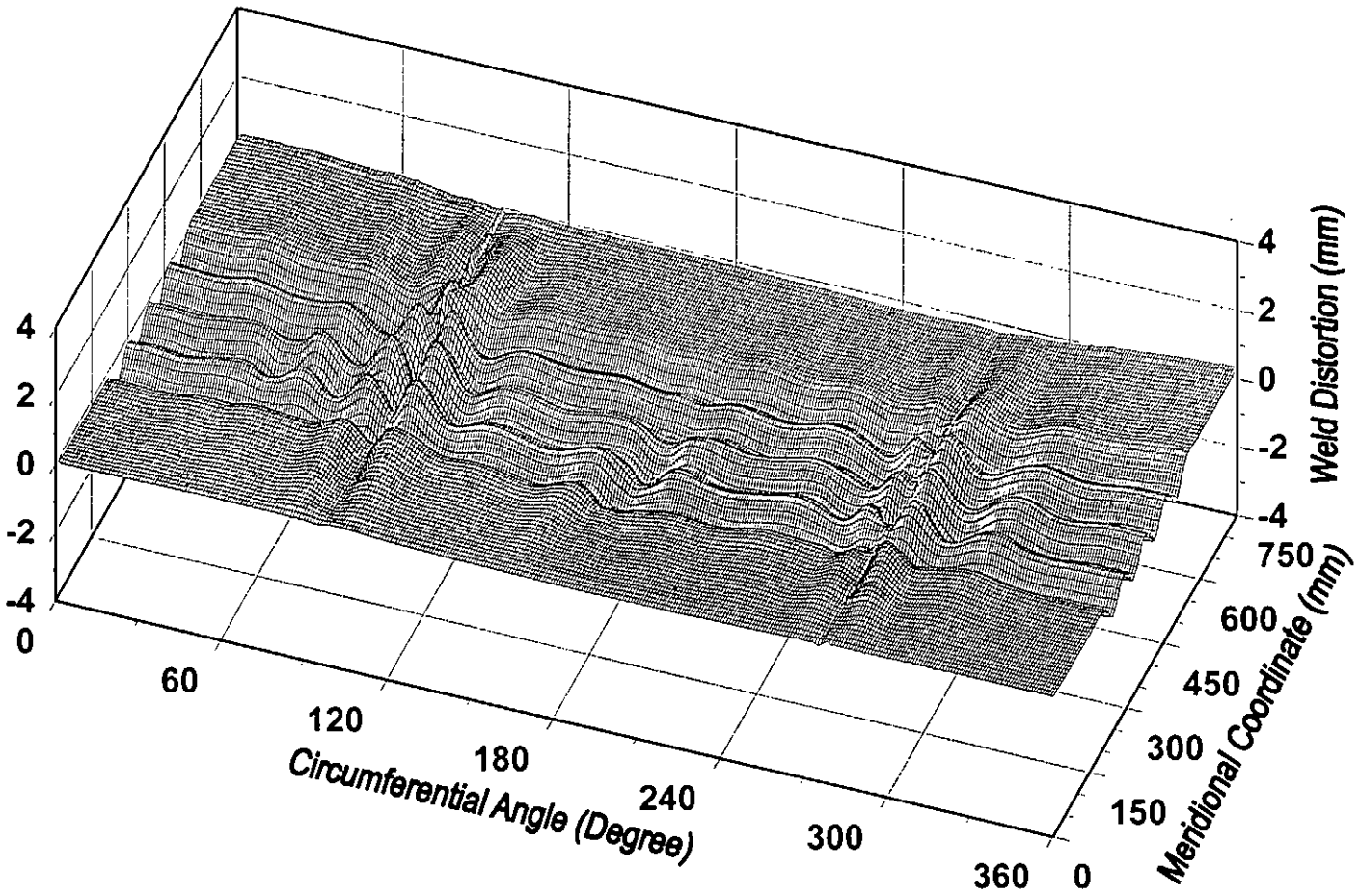

Figure 7.12 Welding distortion in Specimen 09QC04 due to four circumferential welds

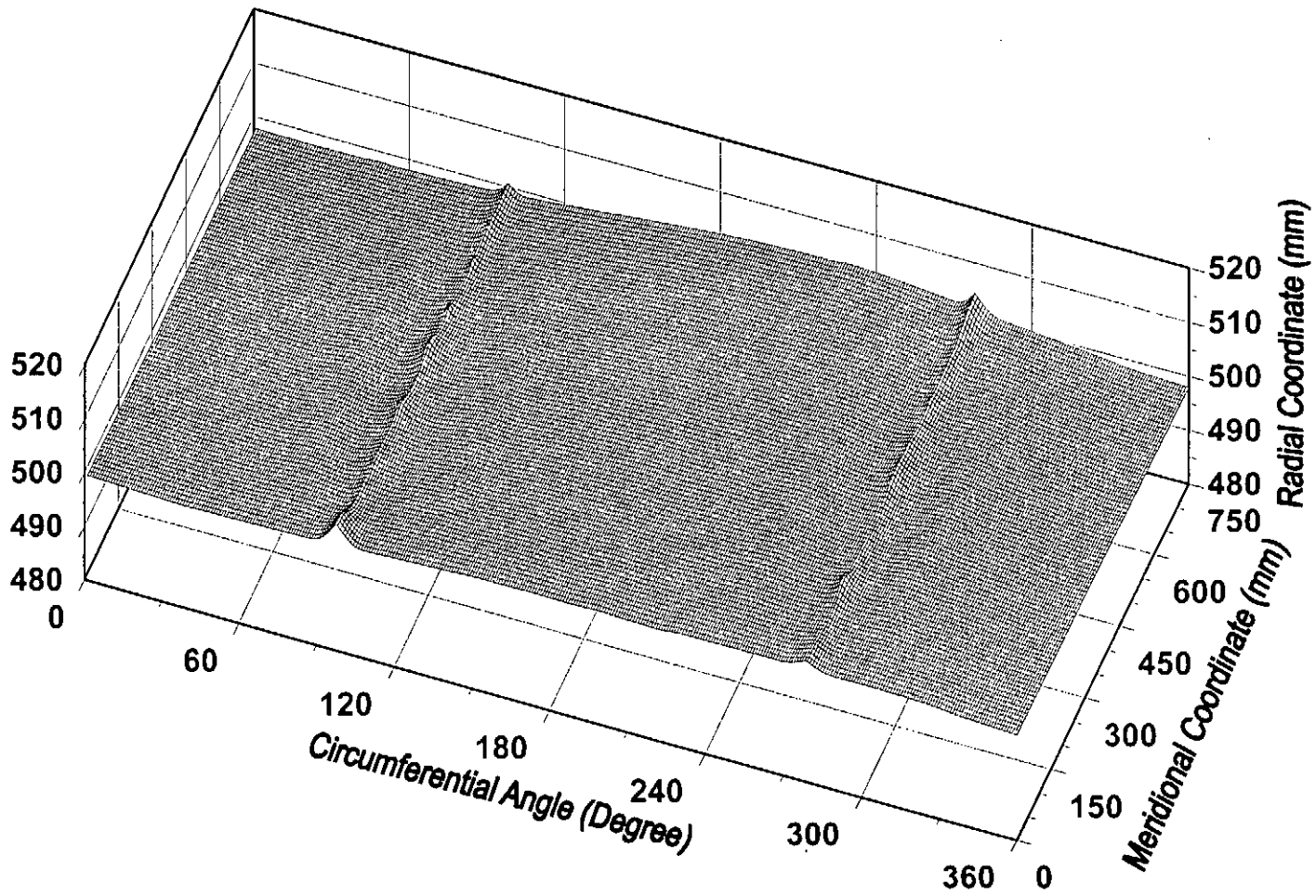

Figure 7.13 Initial Surface of Specimen 09P0408 before Stage II welding

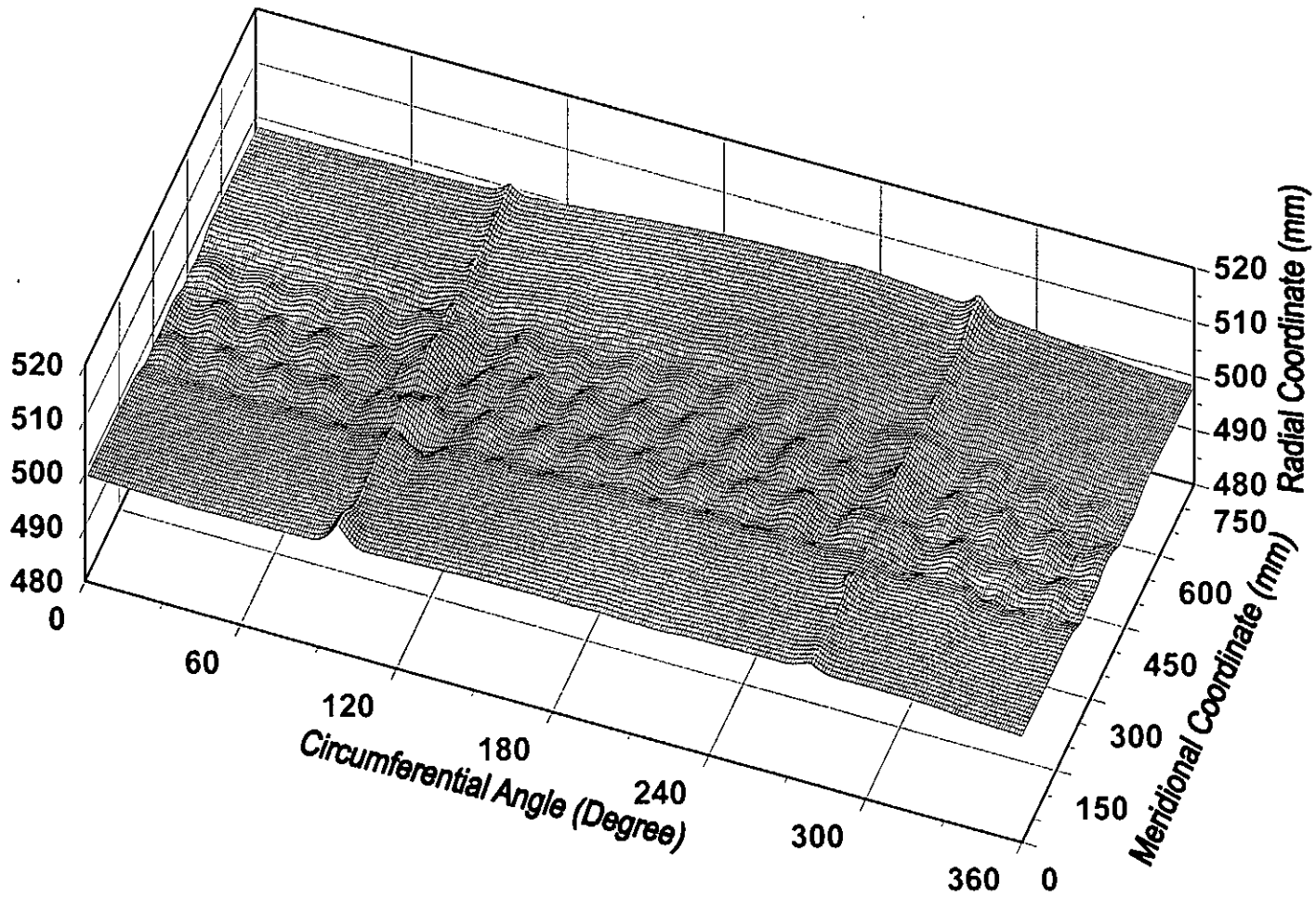

Figure 7.14 Initial surface of Specimen 09P0408 after Stage II welding

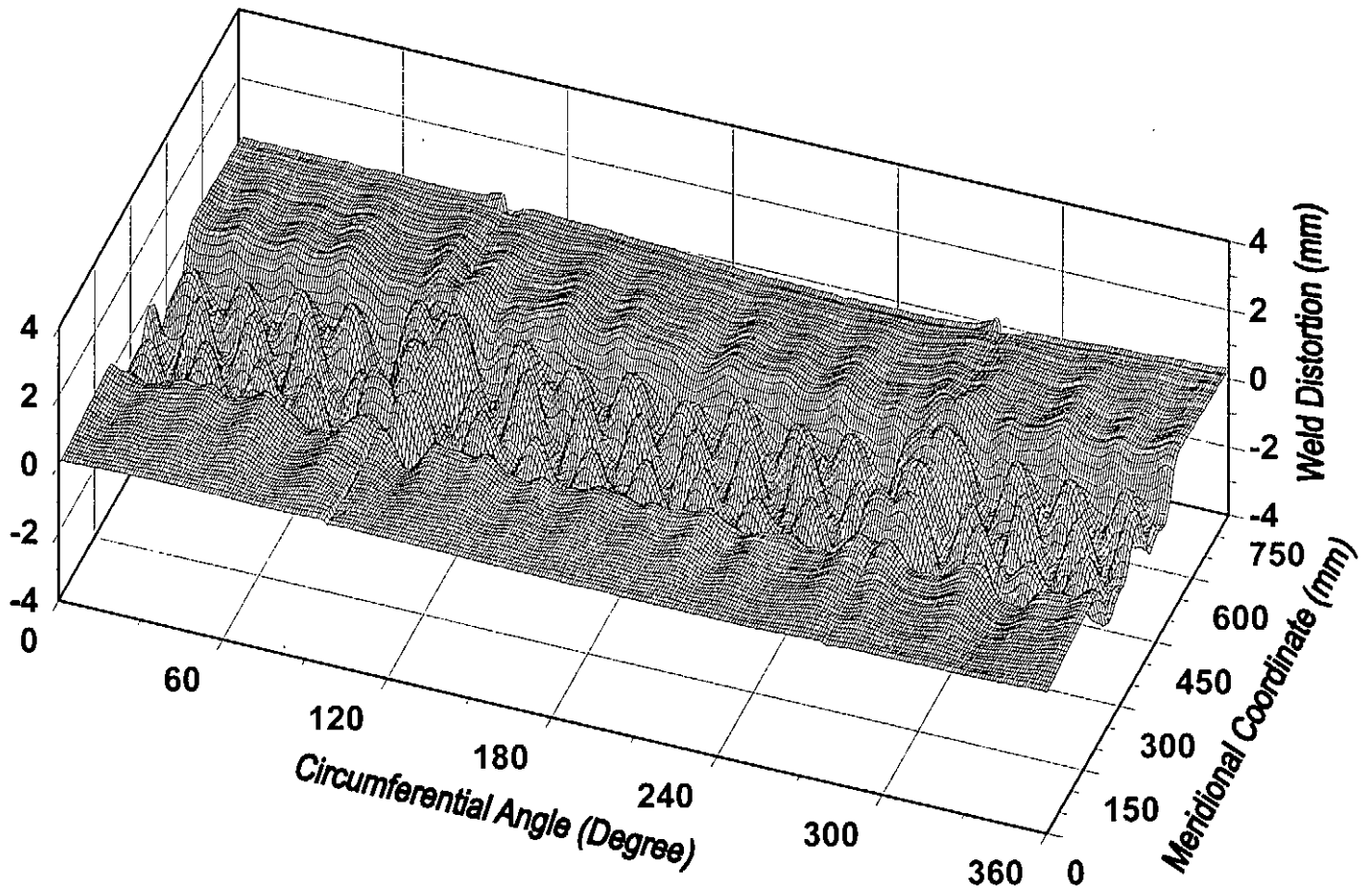

Figure 7.15 Welding distortions in Specimen 09P0408 due to patterned welds

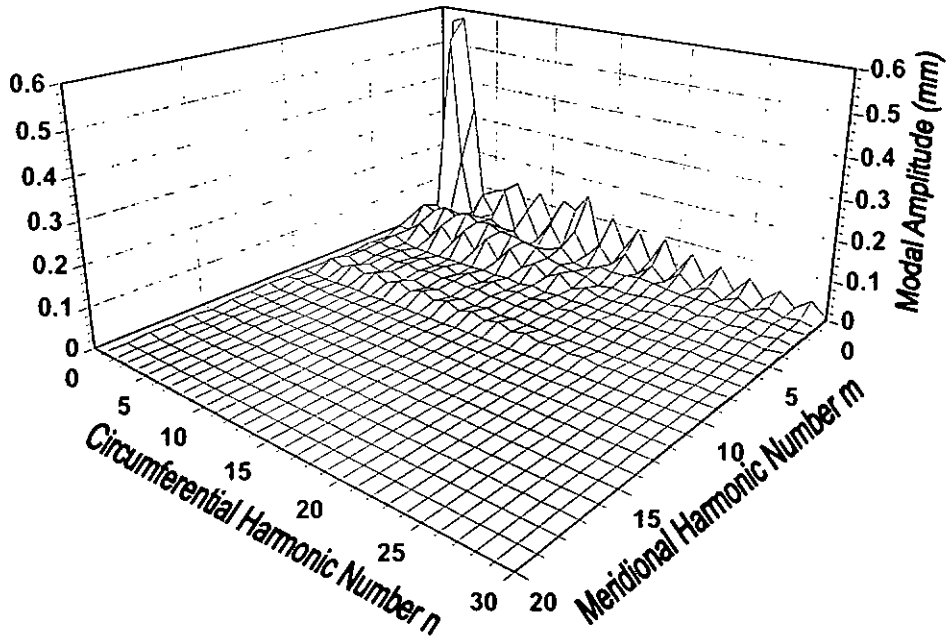

(a) Before Stage II welding

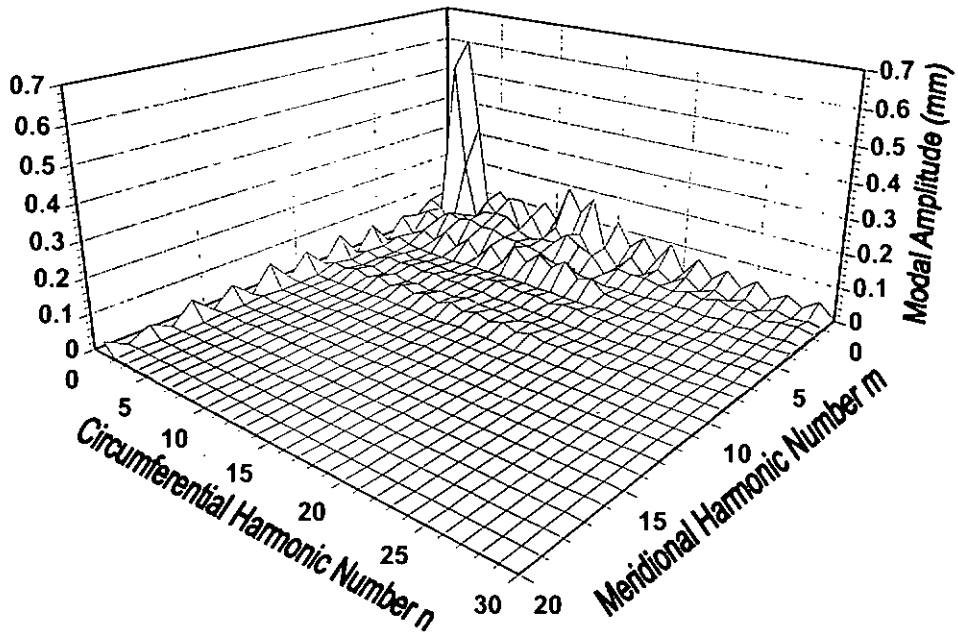

(b) After Stage II welding

Figure 7.16 Spectra of Fourier series deduced for imperfections on in Specimen 09SC: complete surface option

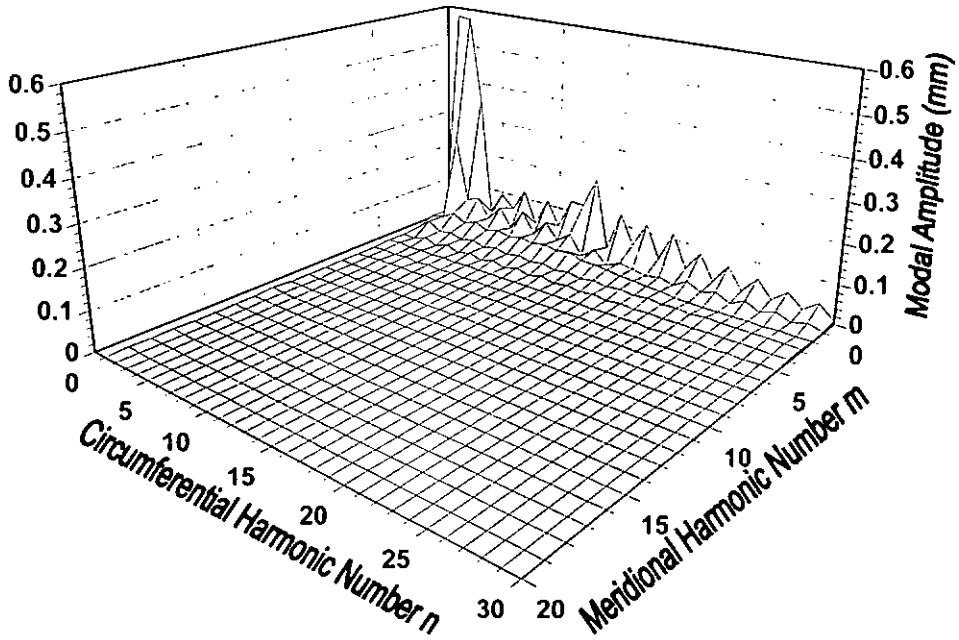

(a) Before Stage II welding

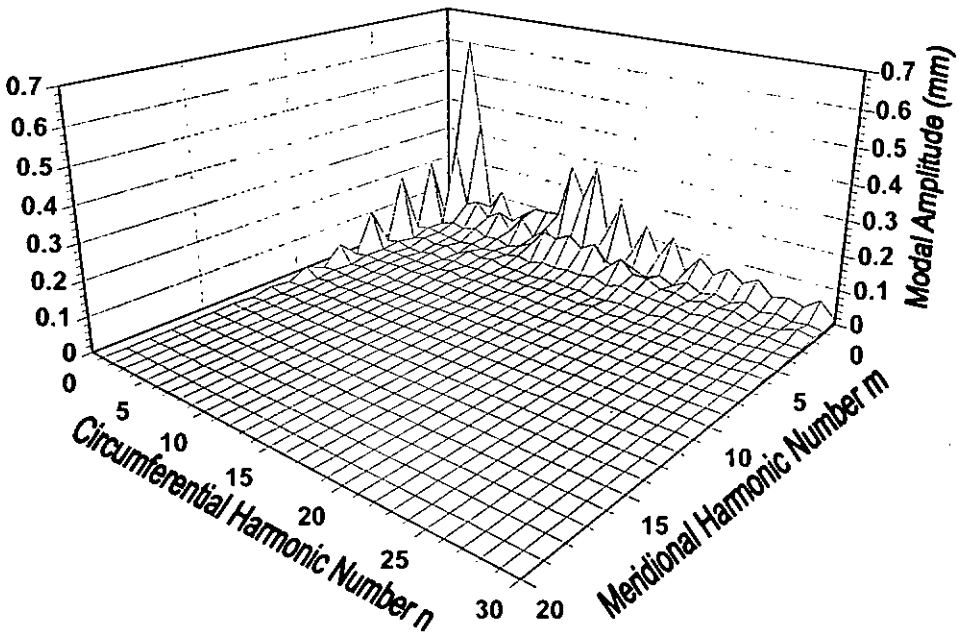

(b) After Stage II welding

Figure 7.17 Spectra of Fourier series deduced from imperfections in Specimen 09SC: middle region option

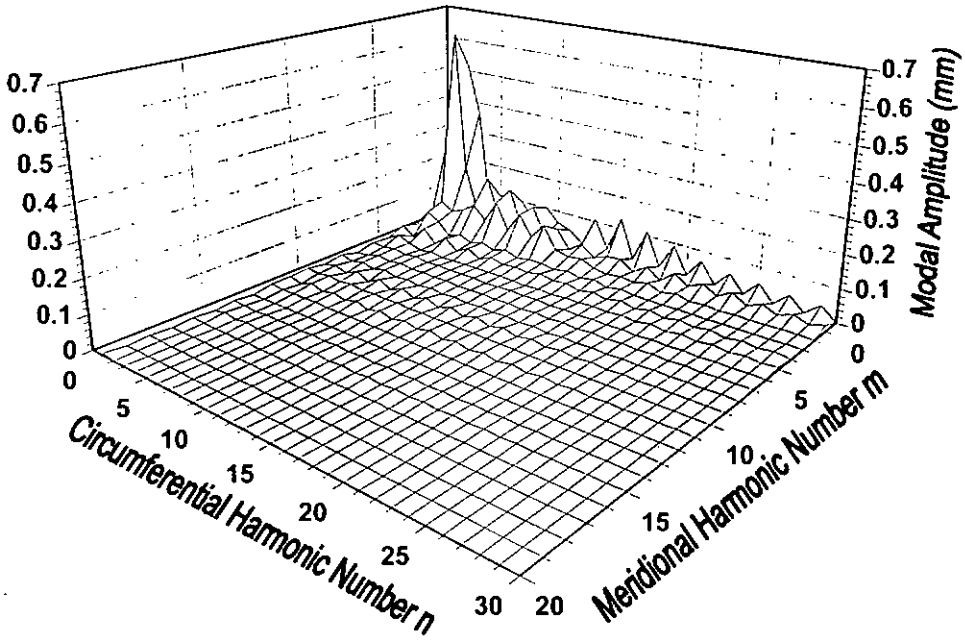

(a) Before Stage II welding

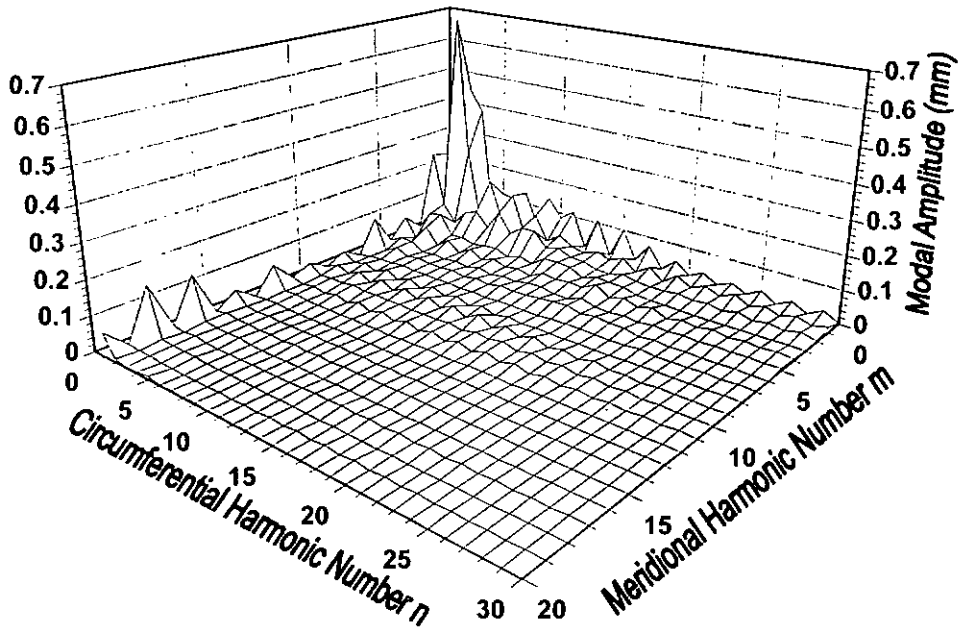

(b) After Stage II welding

Figure 7.18 Spectra of Fourier series deduced from imperfections in Specimen 09QC04: complete surface option

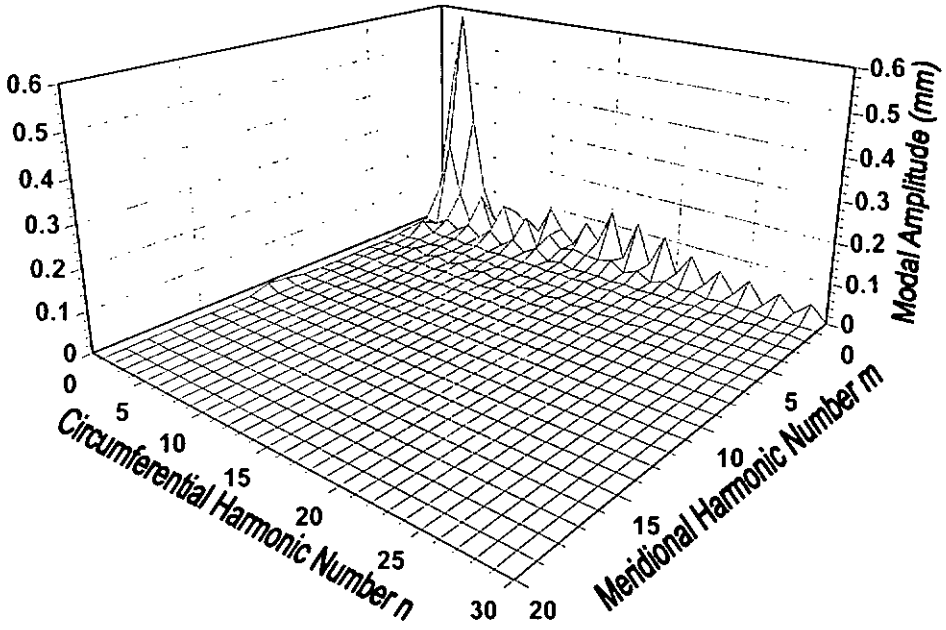

(a) Before Stage II welding

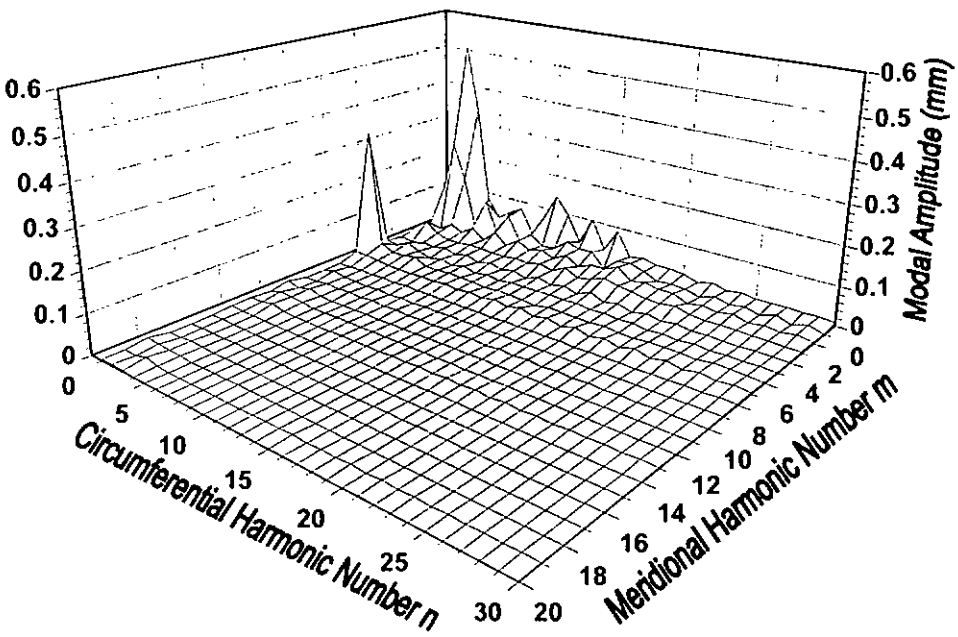

(b) After Stage II welding

Figure 7.19 Spectra of Fourier series deduced from imperfections in Specimen 09QC04: middle region option

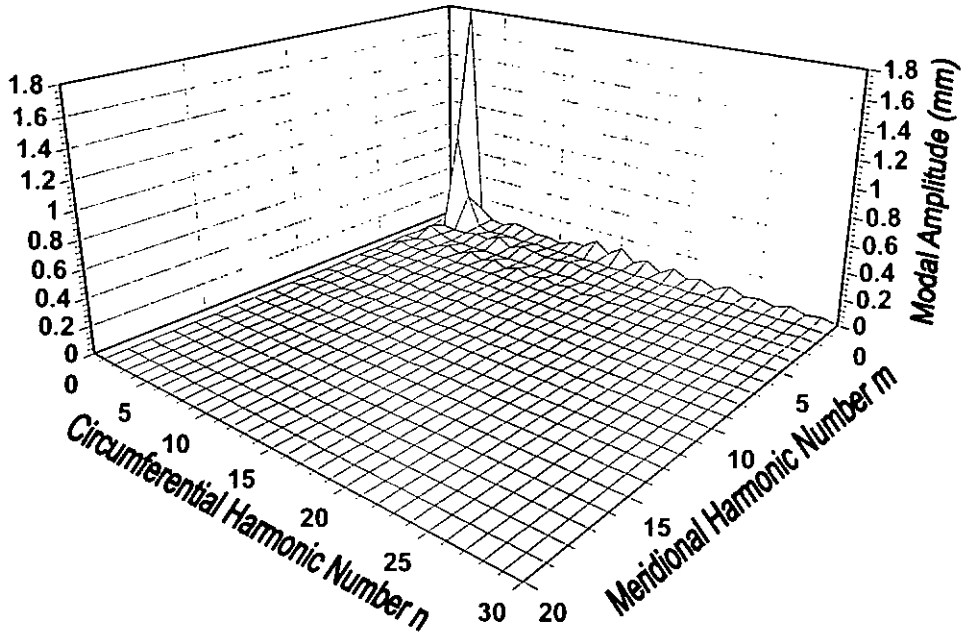

(a) Before Stage II welding

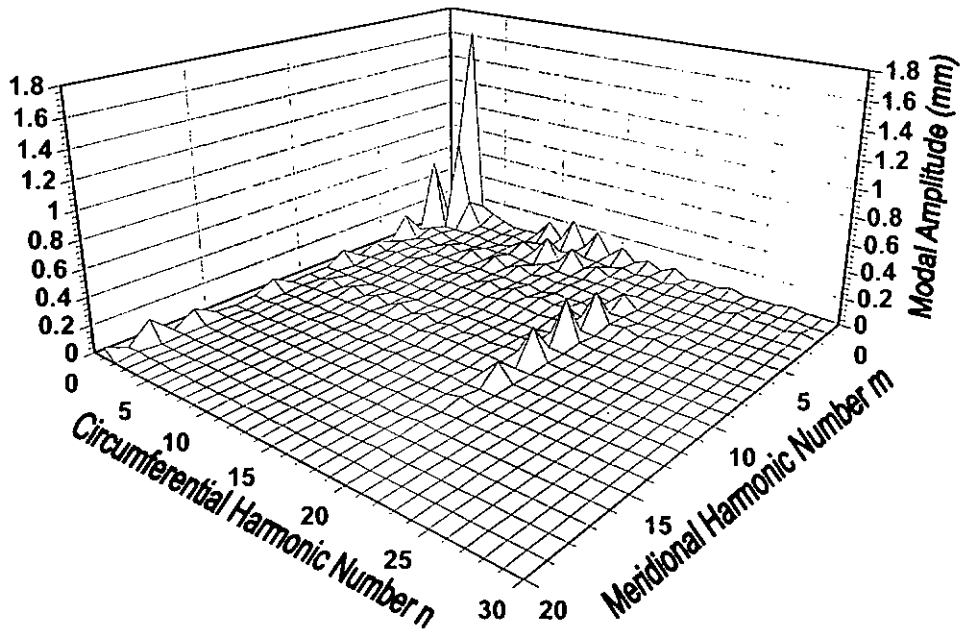

(b) After Stage II welding

Figure 7.20 Spectra of Fourier series deduced from imperfections in Specimen 09P0408: complete surface option

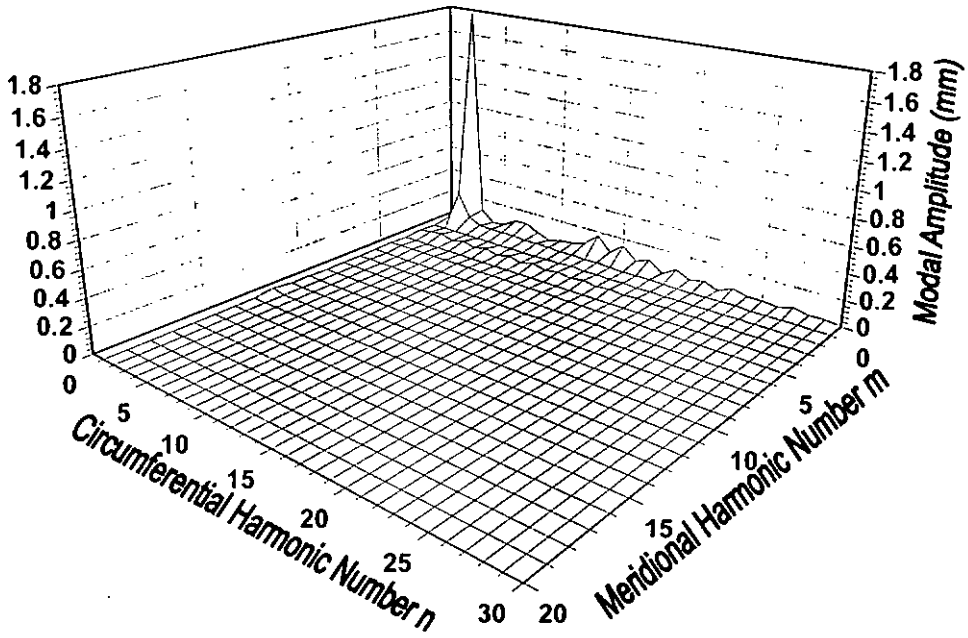

(a) Before Stage II welding

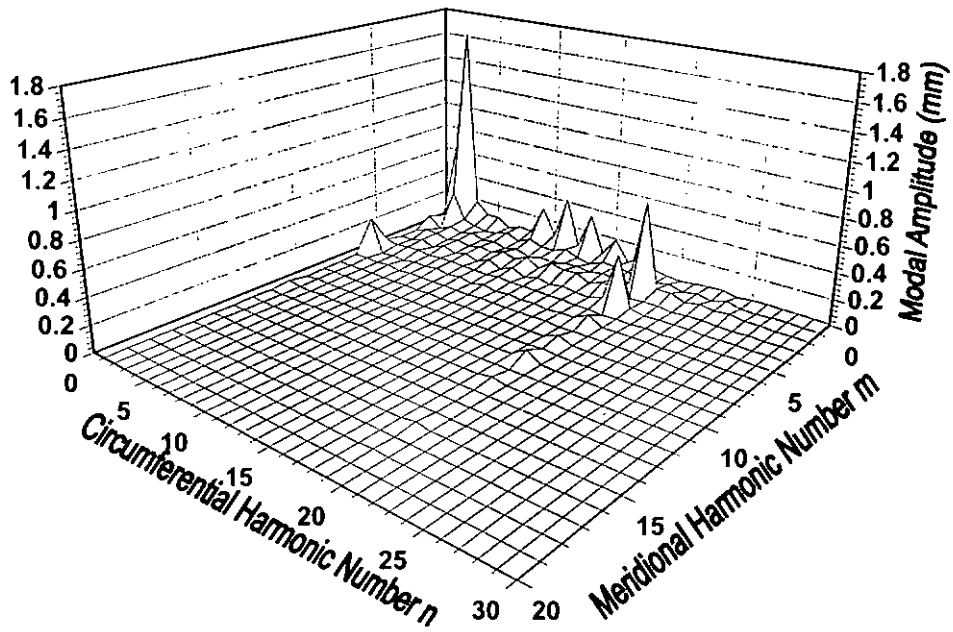

(b) After Stage II welding

Figure 7.21 Spectra of Fourier series deduced from imperfections in Specimen 09P0408: middle region option

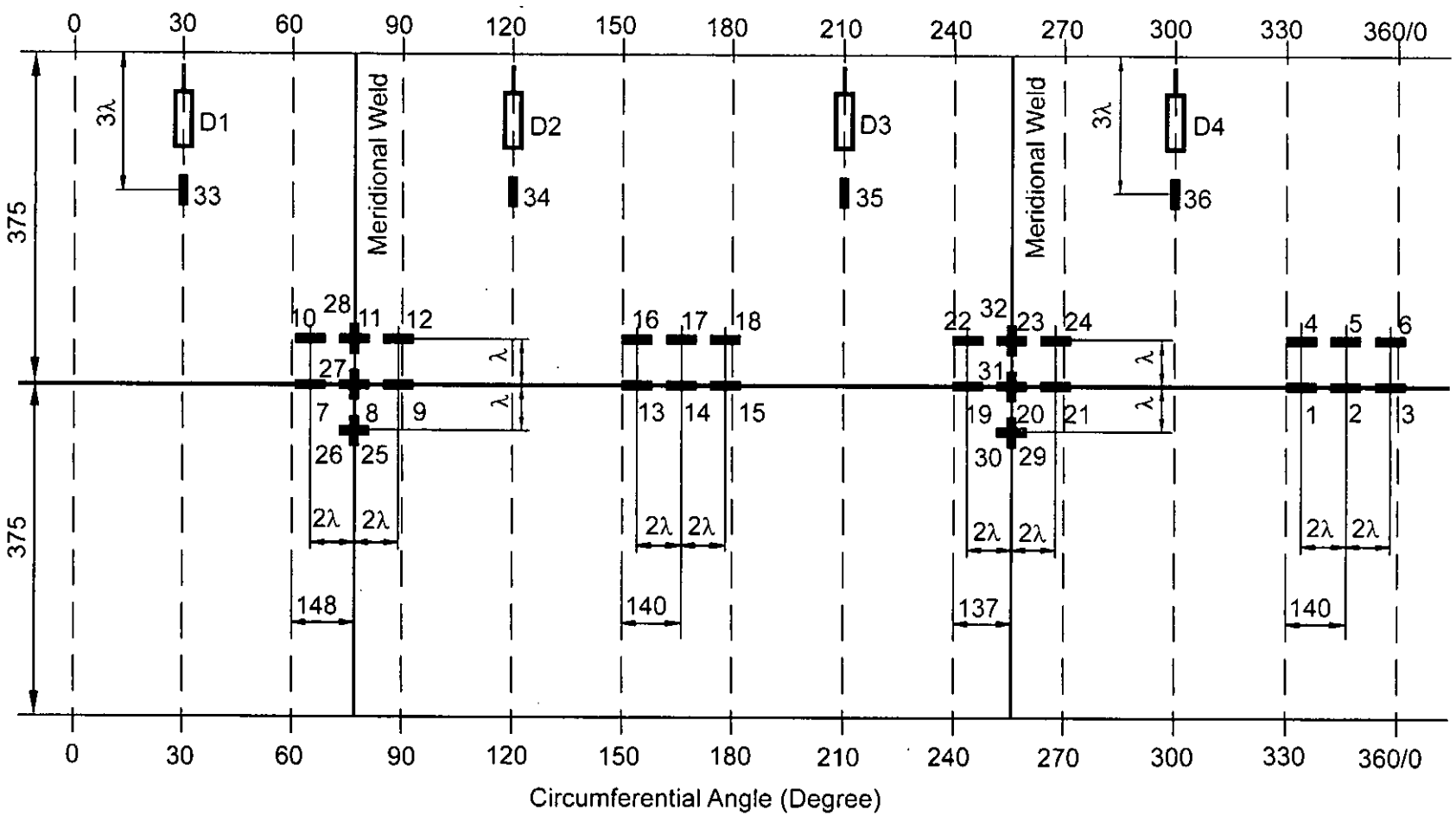

Figure 7.22 Layouts of dial gauges and strain gauges on Specimen 09SC

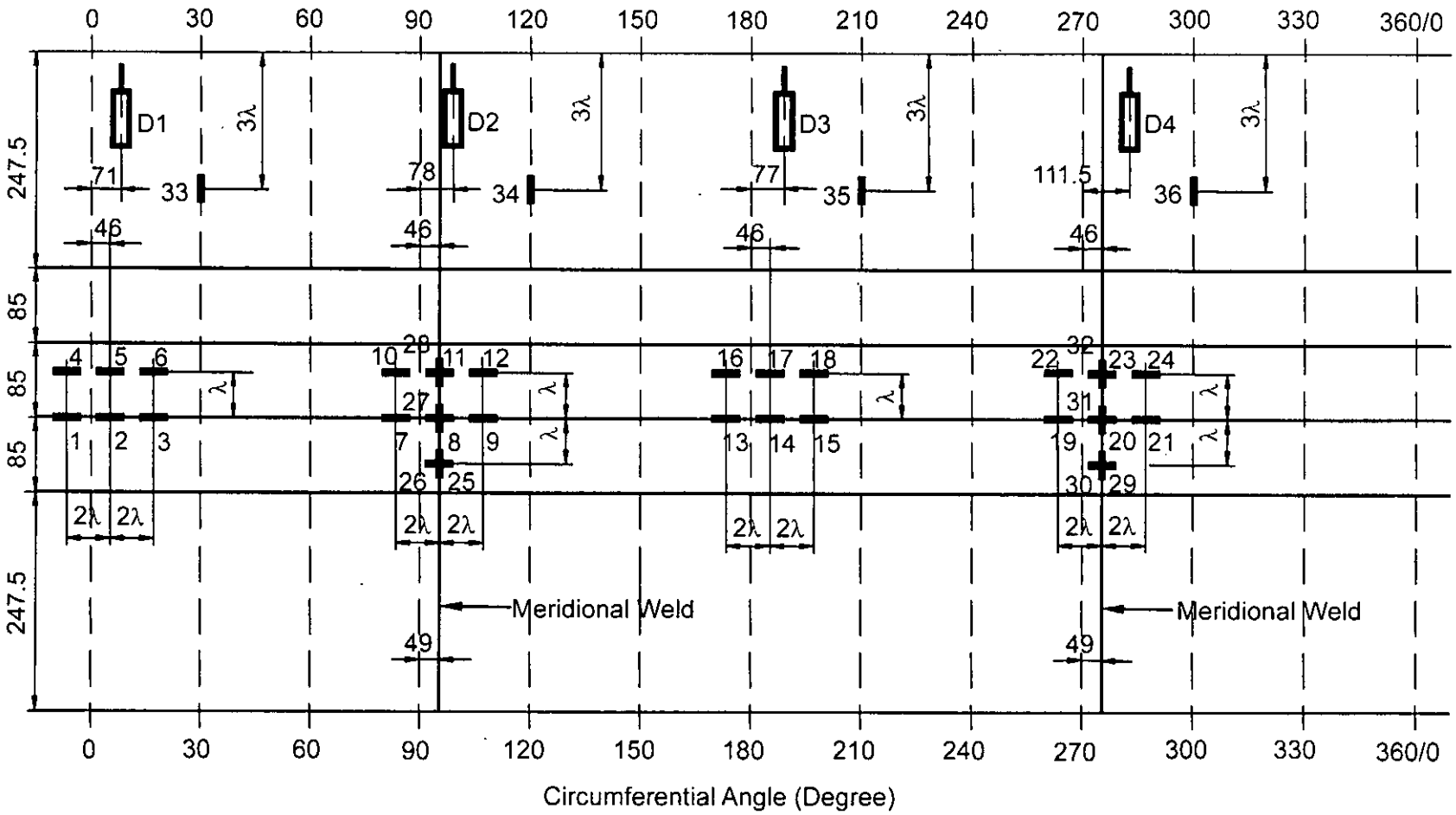

Figure 7.23 Layouts of dial gauges and strain gauges on Specimen 09QC04

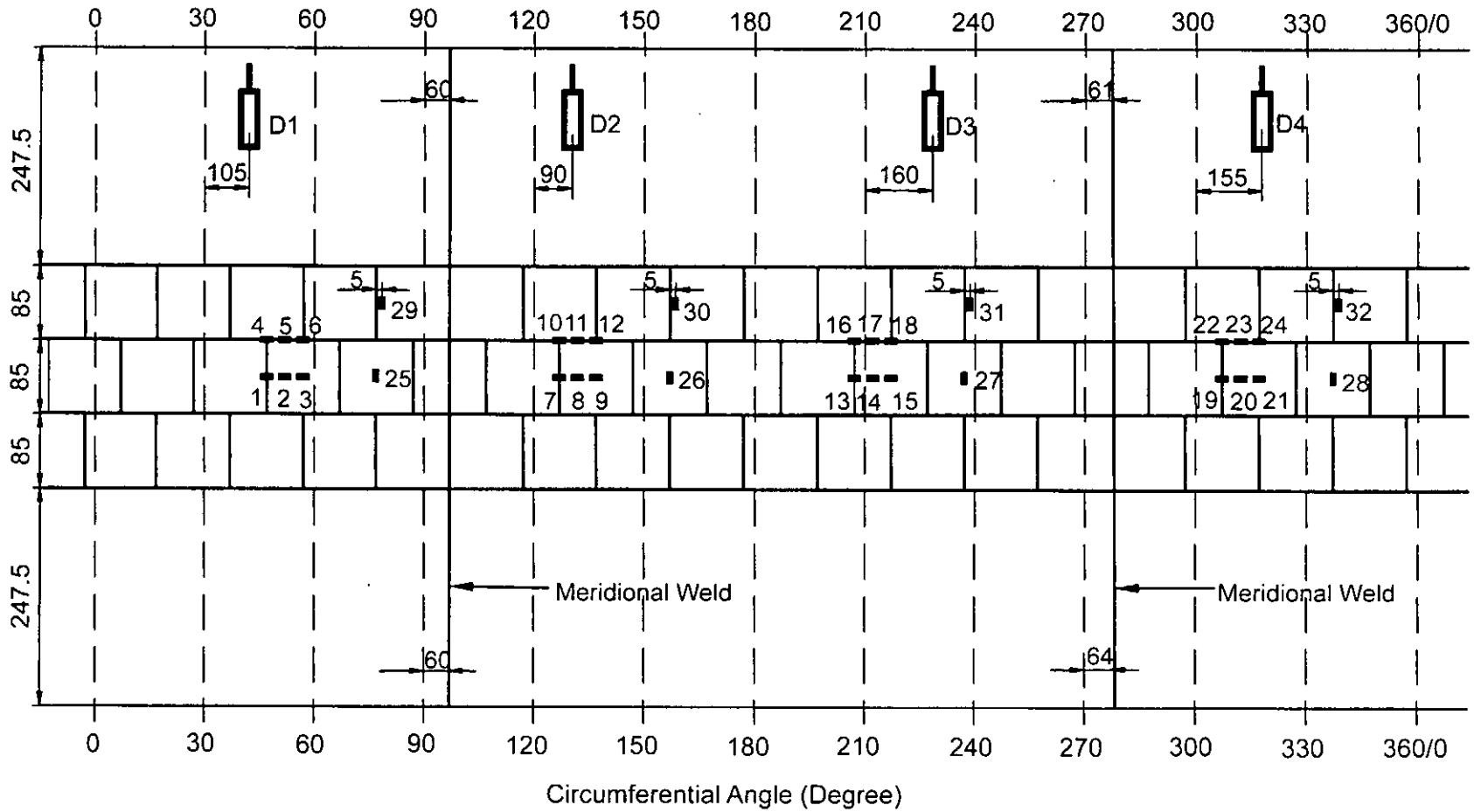

Figure 7.24 Layouts of dial gauges and strain gauges on Specimen 09P0408

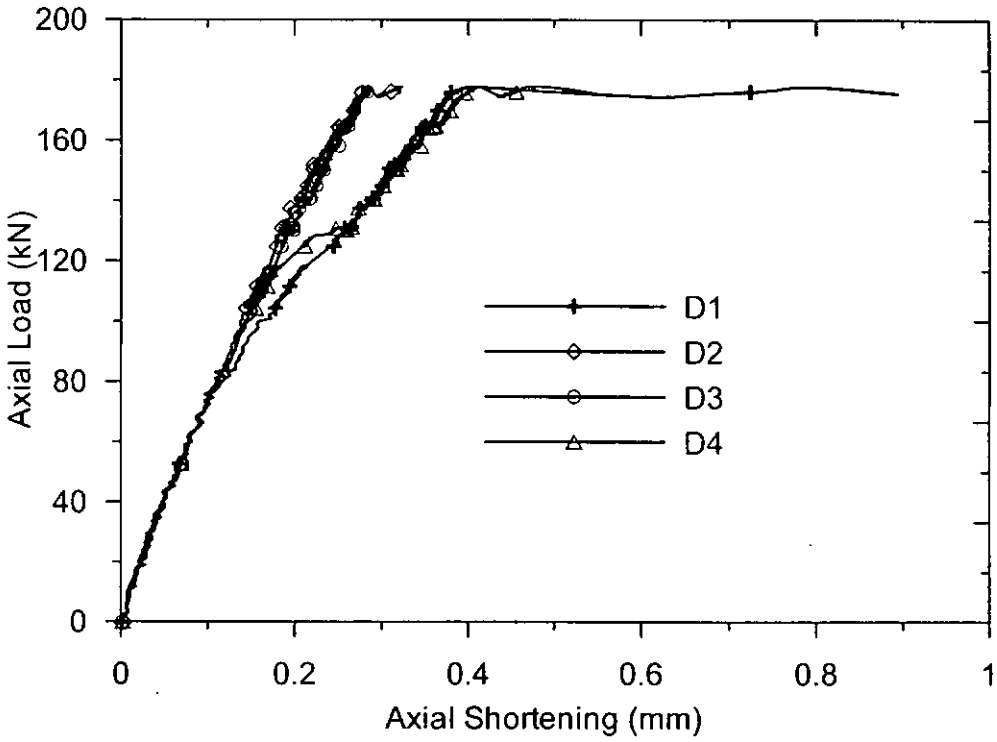

Figure 7.25 Load-axial shortening curves of Specimen 09SC

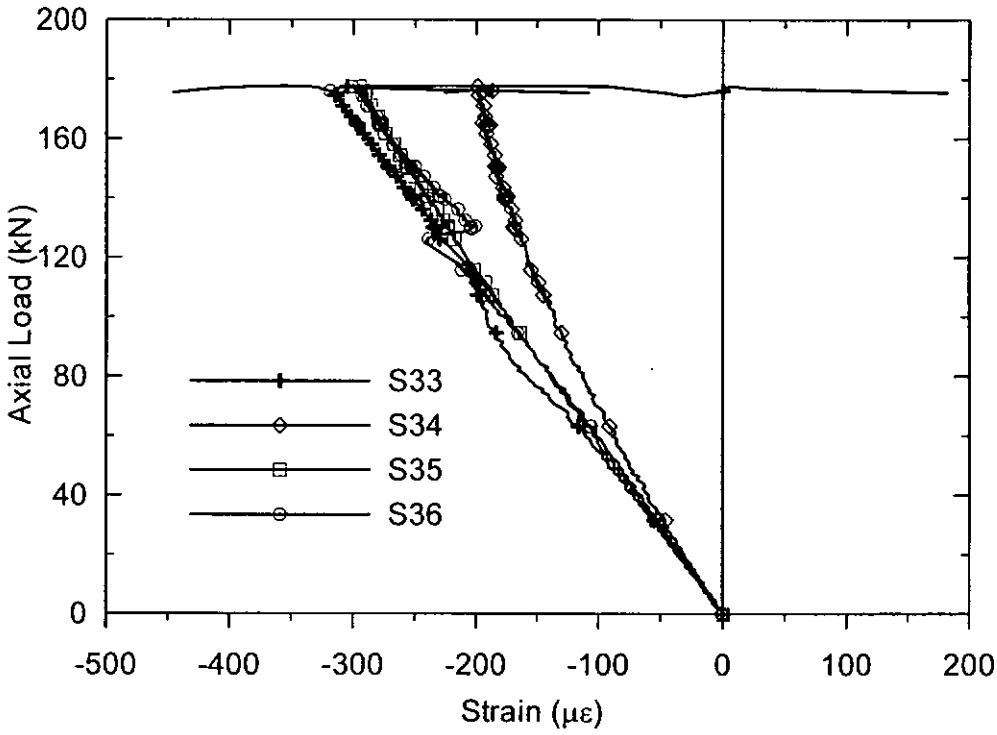

Figure 7.26 Load-axial strain curves of Specimen 09SC: strain gauges S33-S36

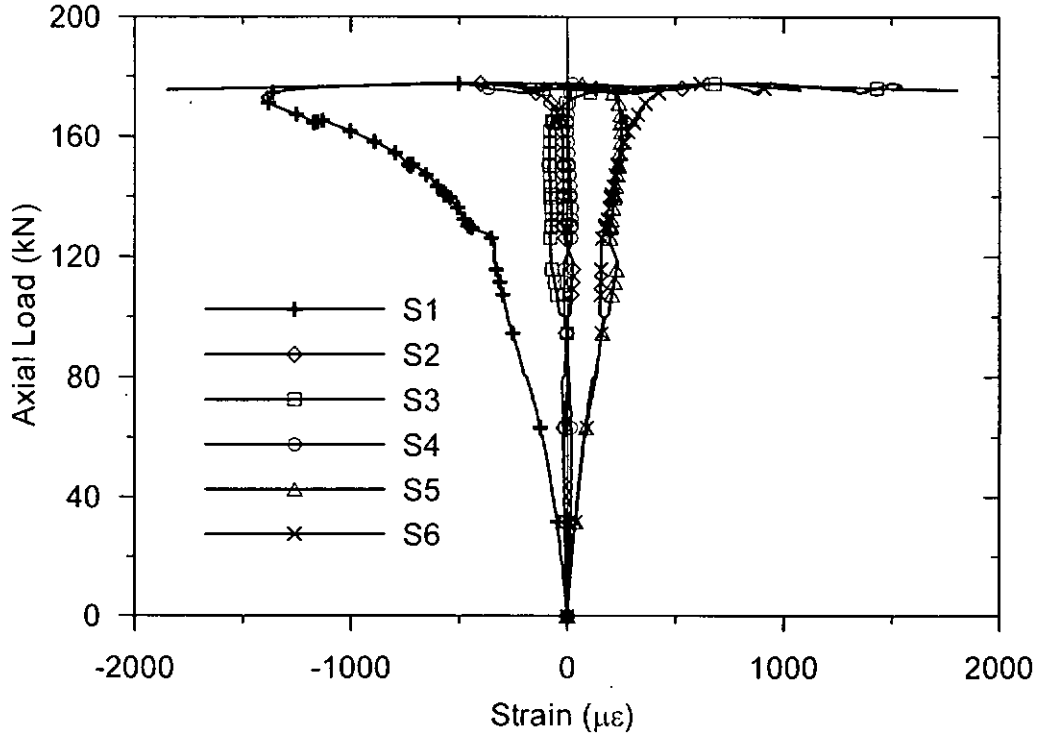

Figure 7.27 Load-circumferential strain curves of Specimen 09SC: strain gauges S1-S6

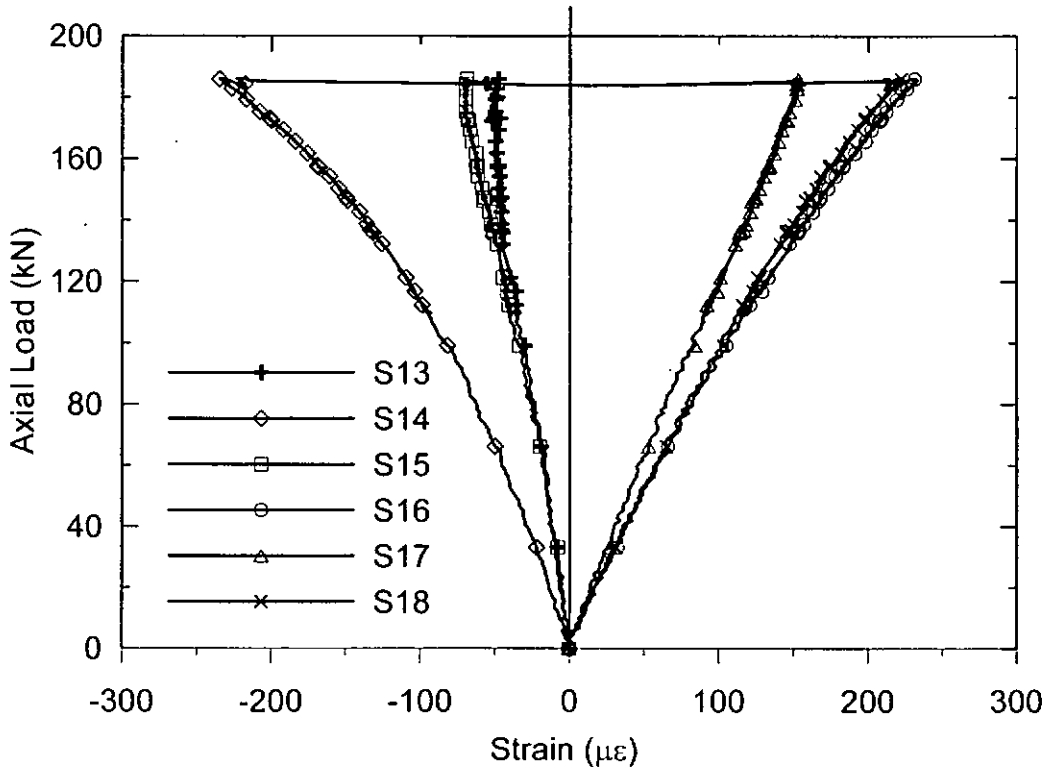

Figure 7.28 Load-circumferential strain curves of Specimen 09SC: strain gauges S13-S18

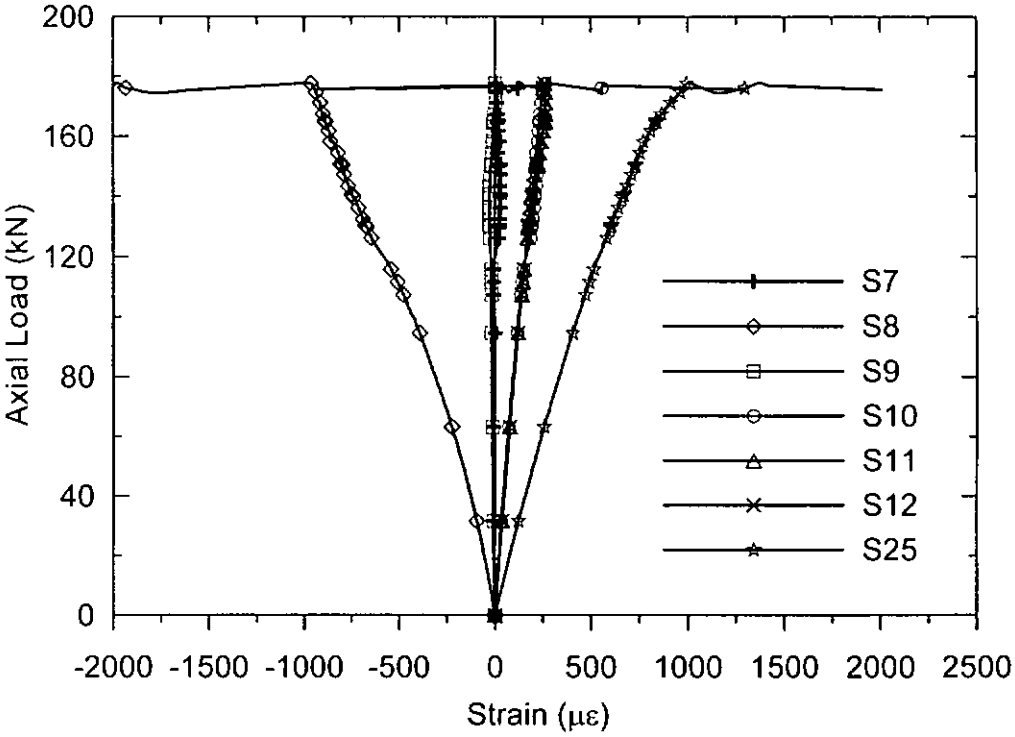

Figure 7.29 Load-circumferential strain curves of Specimen 09SC: strain gauges S7-S12 & S25

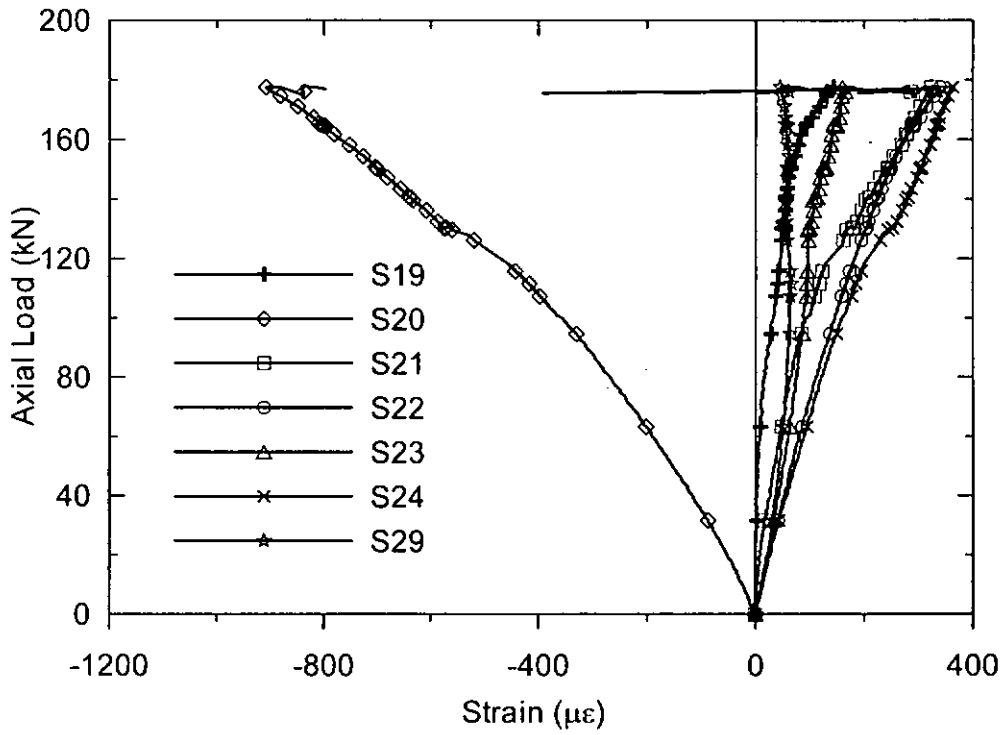

Figure 7.30 Load-axial strain curves of Specimen 09SC: strain gauges S19-S24 & S29

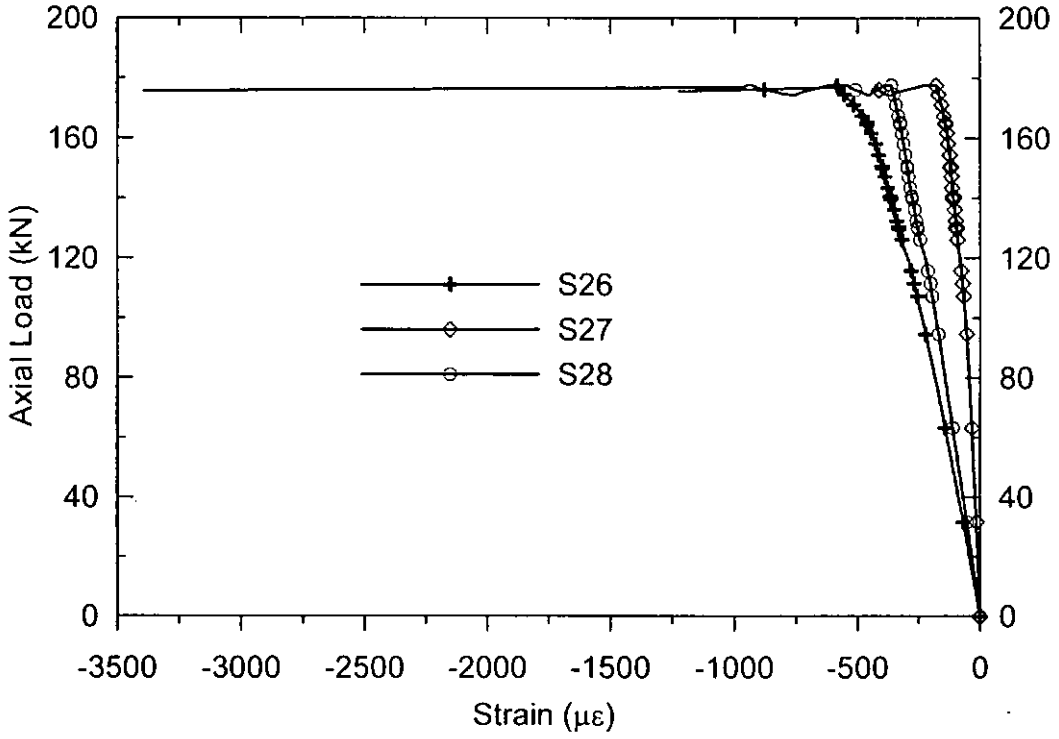

Figure 7.31 Load-axial strain curves of Specimen 09SC: strain gauges S26-S28

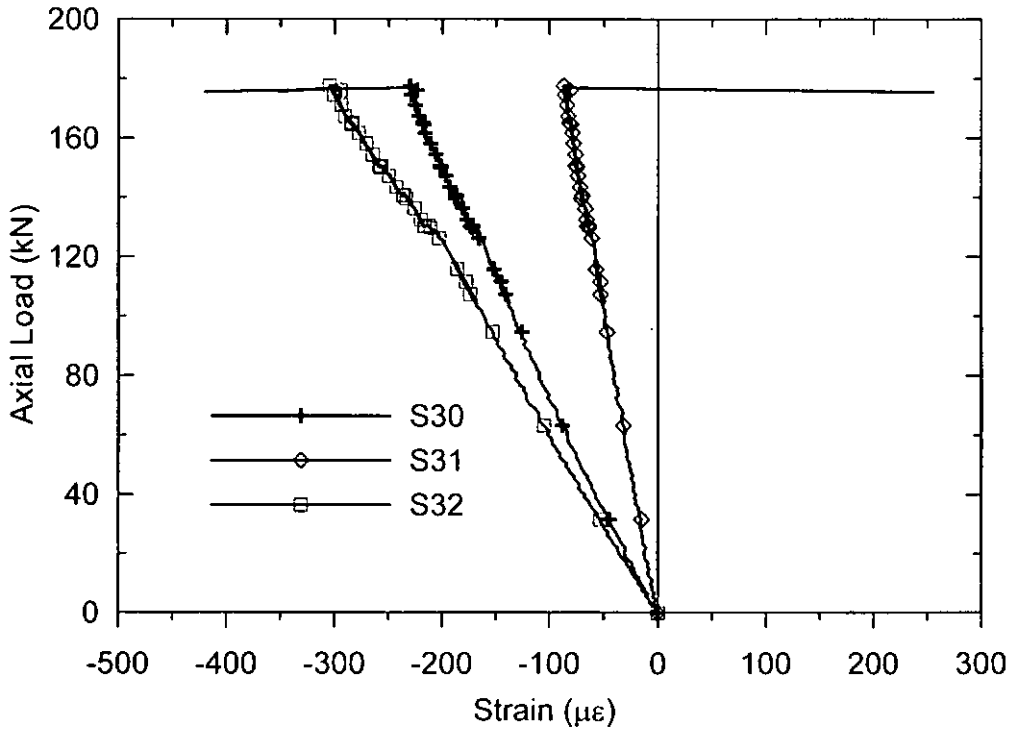

Figure 7.32 Load-axial strain curves of Specimen 09SC: strain gauges S30-S32

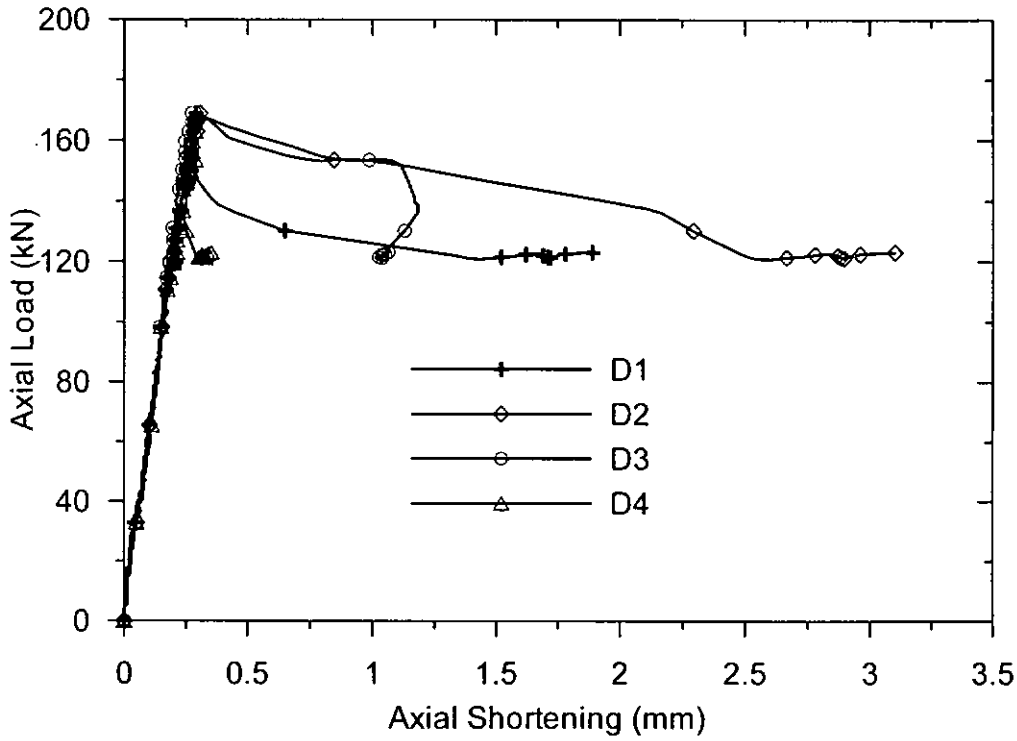

Figure 7.33 Load-axial shortening curves of Specimen 09QC04

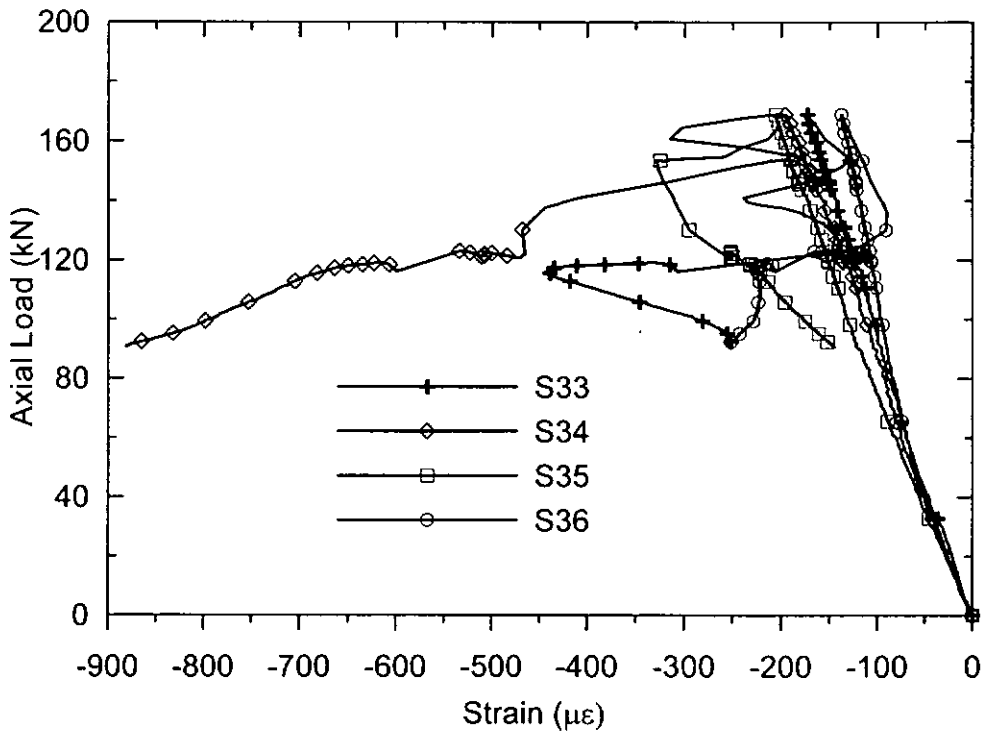

Figure 7.34 Load-axial strain curves of Specimen 09QC04: strain gauges S33-S36

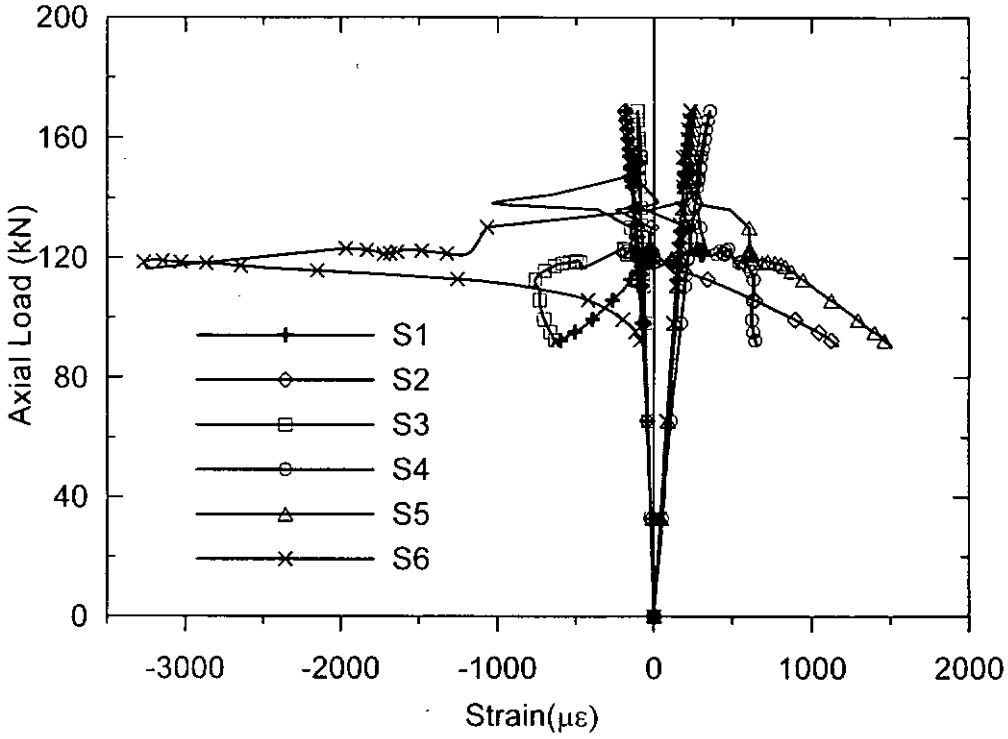

Figure 7.35 Load-circumferential strain curves of Specimen 09QC04: strain gauges S1-S6

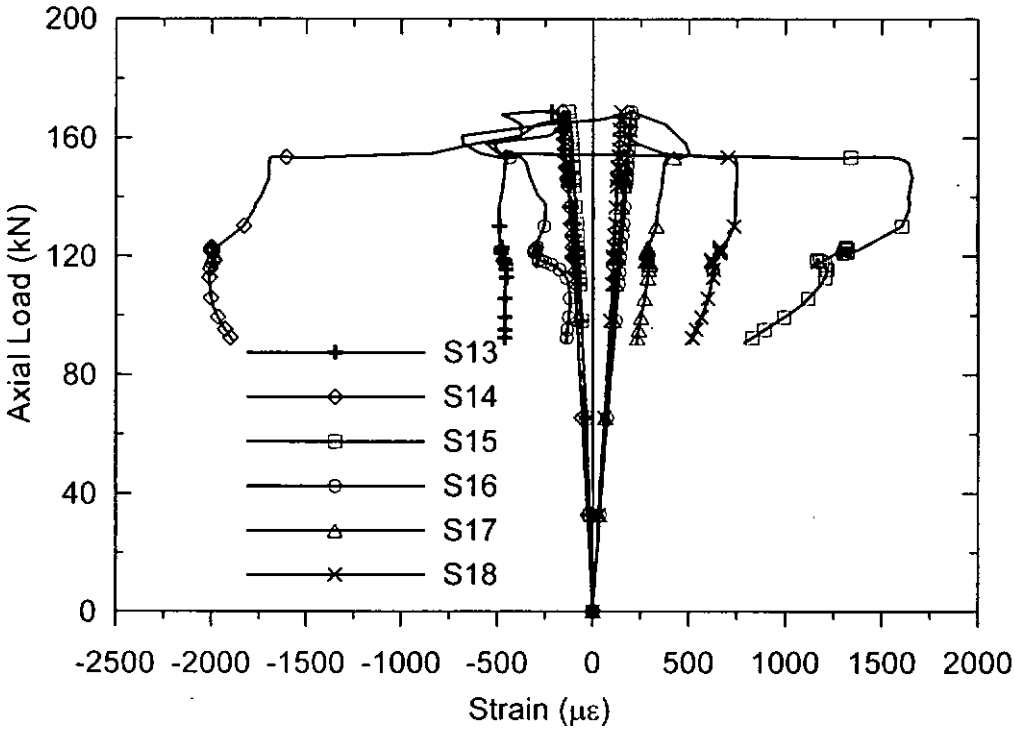

Figure 7.36 Load-circumferential strain curves of Specimen 09QC04: strain gauges S13-S18

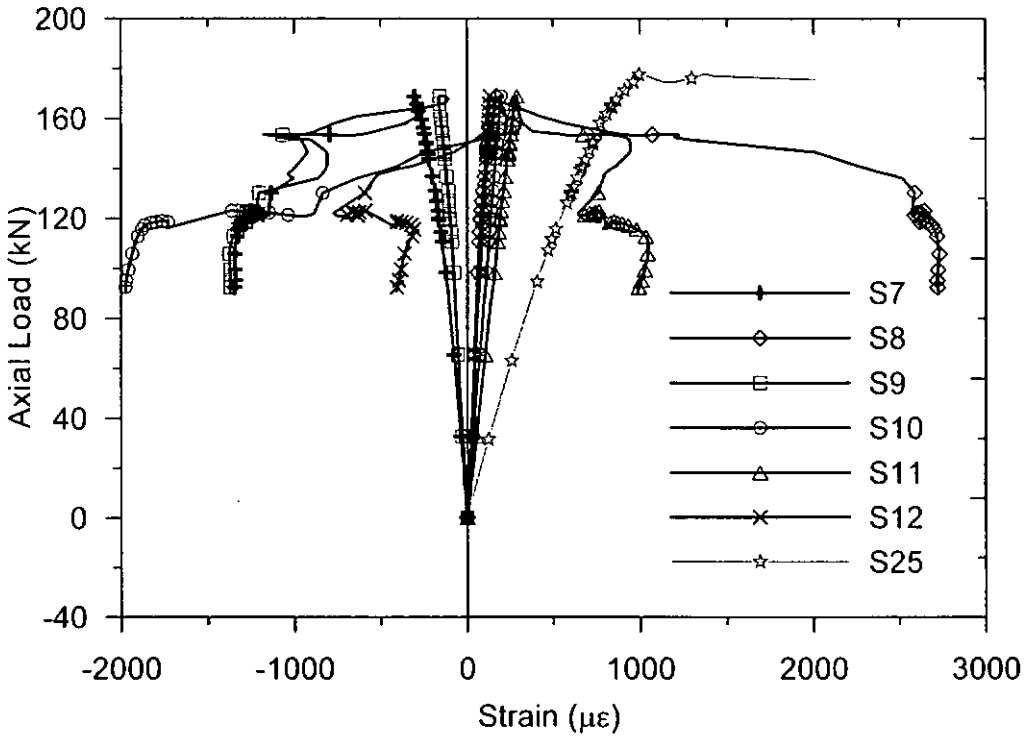

Figure 7.37 Load-circumferential strain curves of Specimen 09QC04: strain gauges S7-S12 & S25

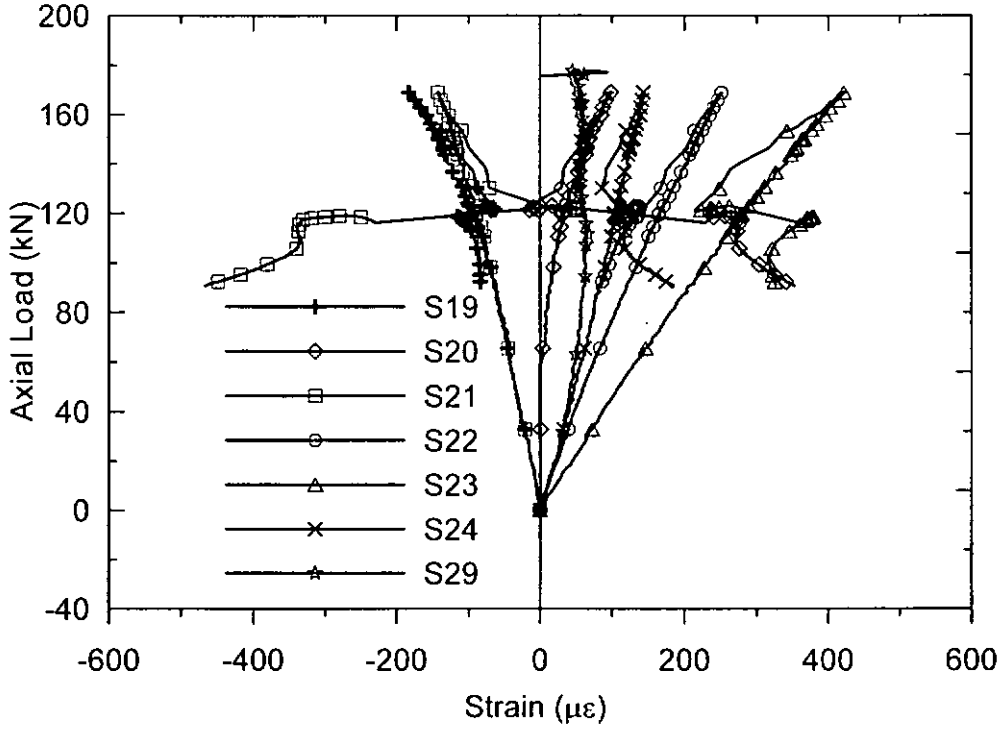

Figure 7.38 Load-circumferential strain curves of Specimen 09QC04: strain gauges S19-S24 & S29

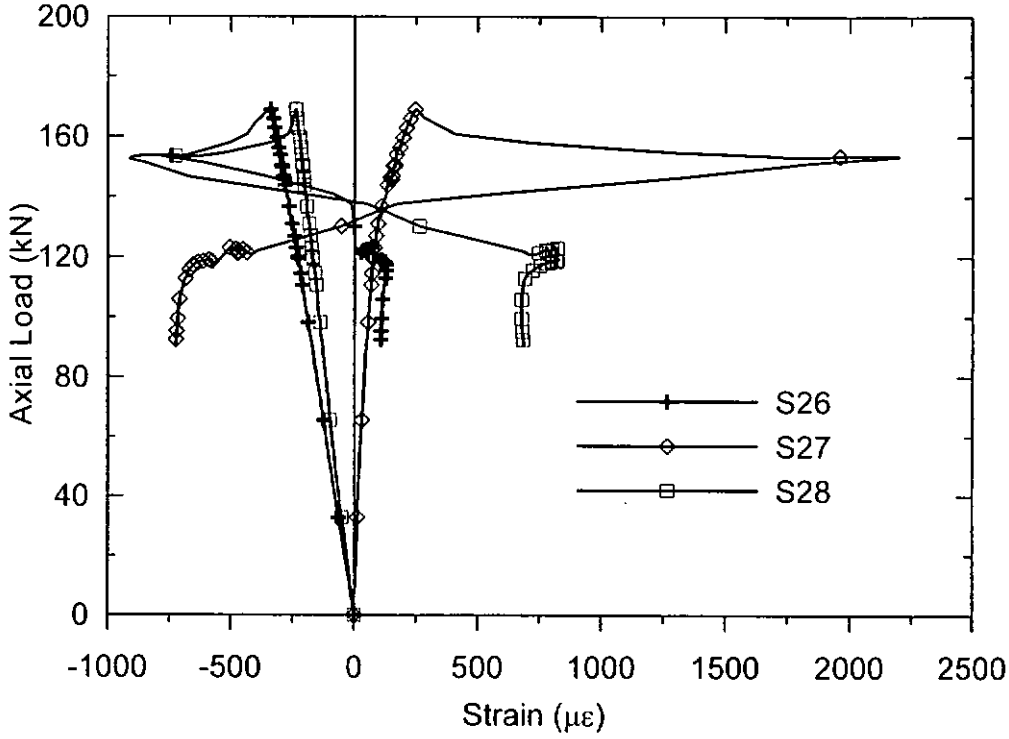

Figure 7.39 Load-axial strain curves of Specimen 09QC04: strain gauges S26-S28

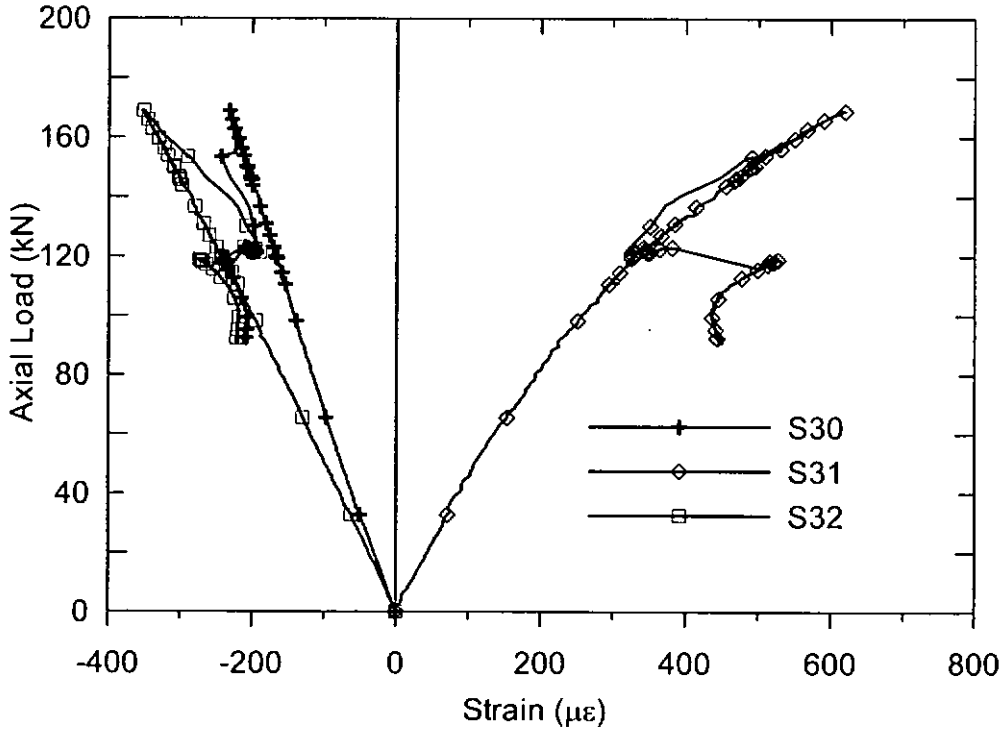

Figure 7.40 Load-axial strain curves of Specimen 09QC04: strain gauges S30-S32

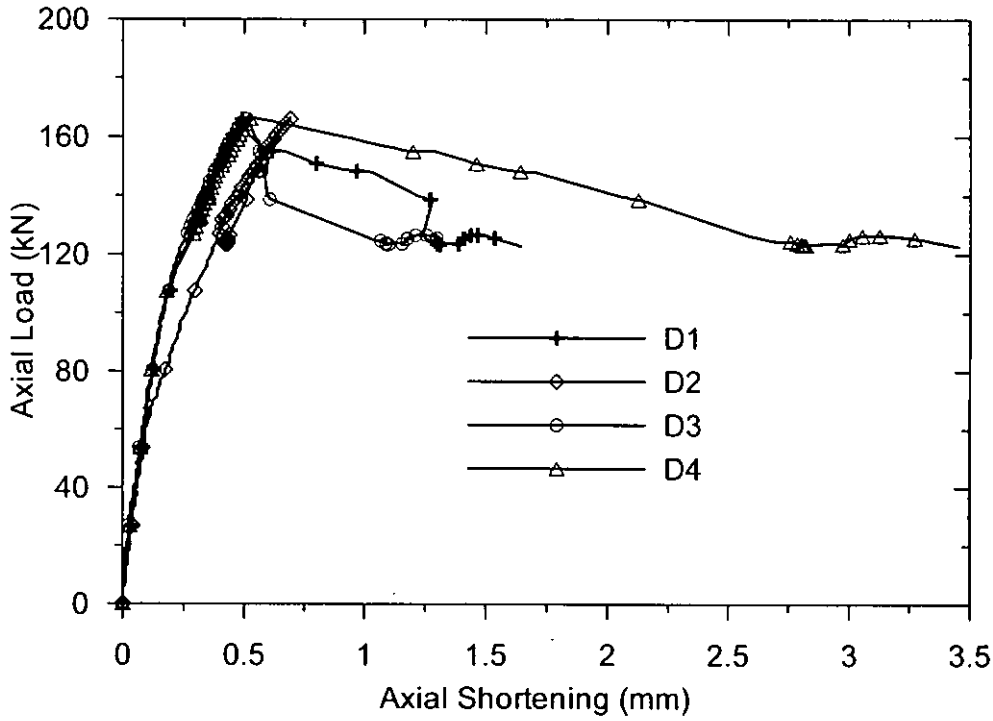

Figure 7.41 Load-axial shortening curves of Specimen 09P0408

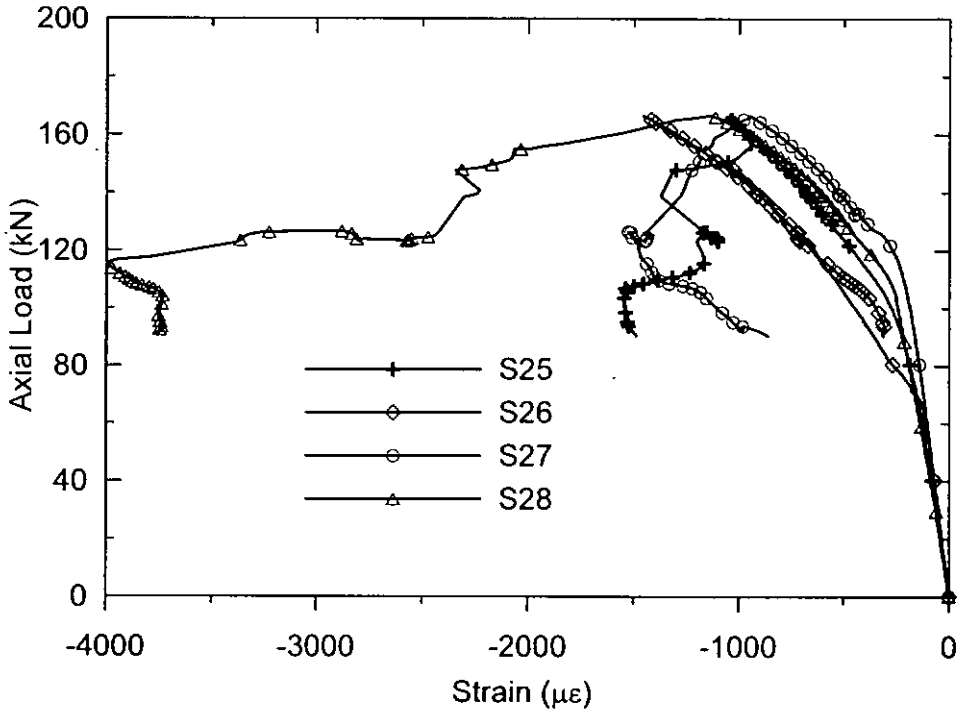

Figure 7.42 Load-axial strain curves of Specimen 09P0408: strain gauges S25-S28

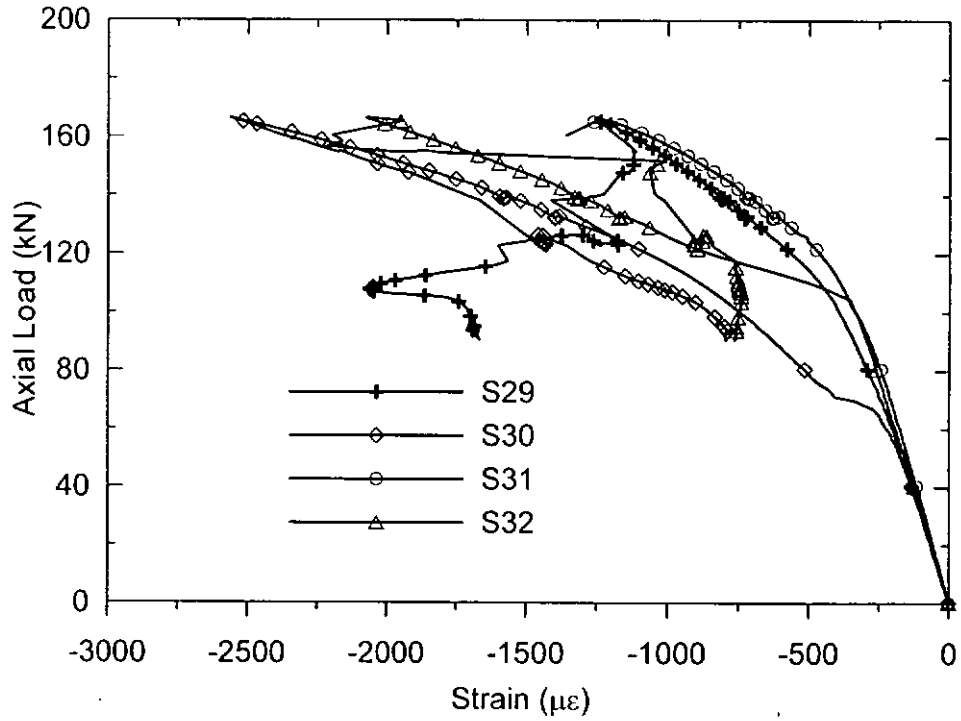

Figure 7.43 Load-axial strain curves of Specimen 09P0408: strain gauges S29-S32

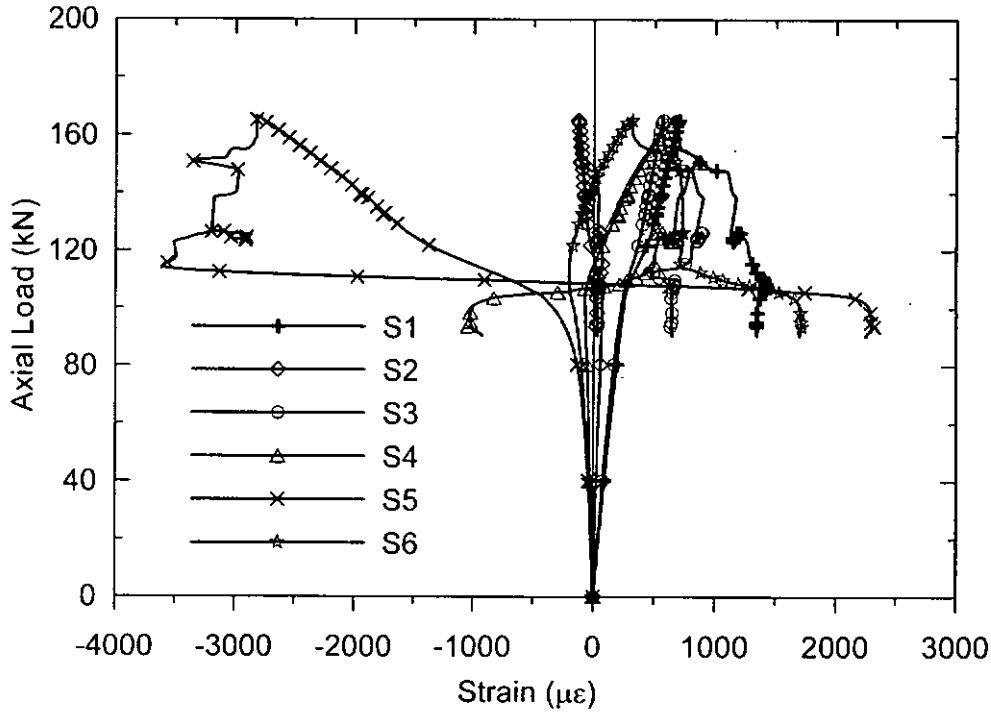

Figure 7.44 Load-circumferential strain curves of Specimen 09P0408: strain gauges S1-S6

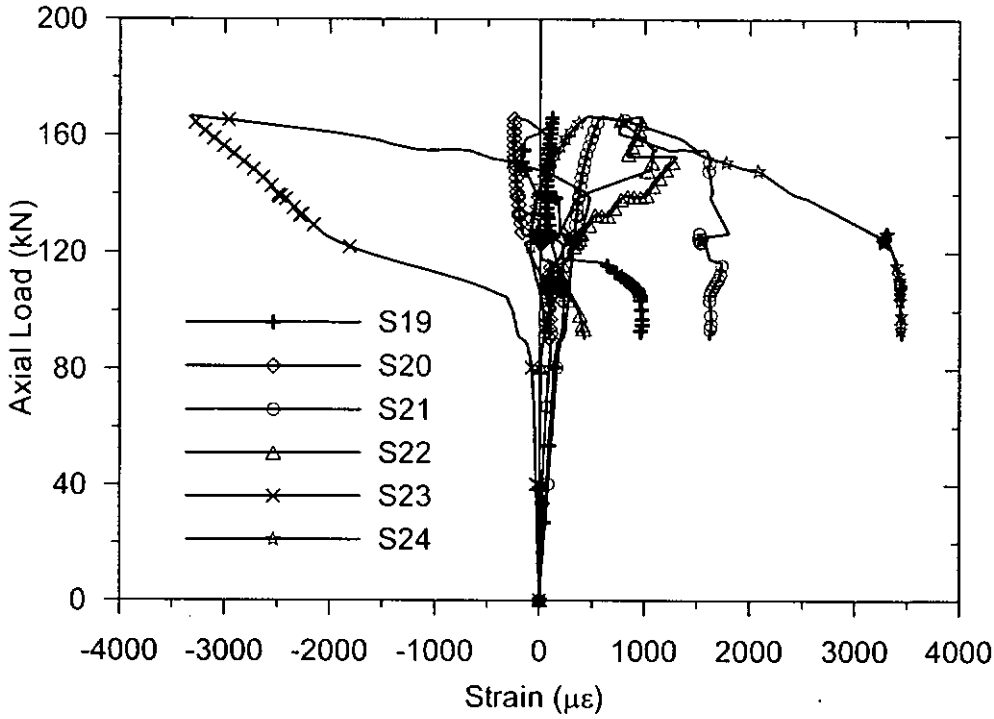

Figure 7.45 Load-circumferential strain curves of Specimen 09P0408: strain gauges S19-S24

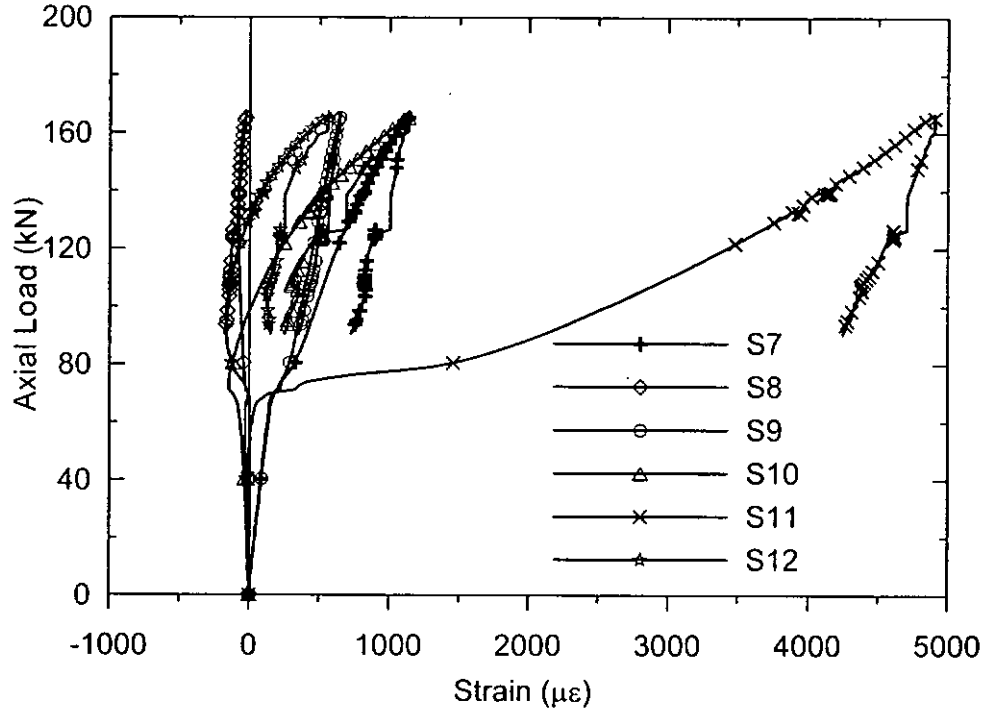

Figure 7.46 Load-circumferential strain curves of Specimen 09P0408: strain gauges S7-S12

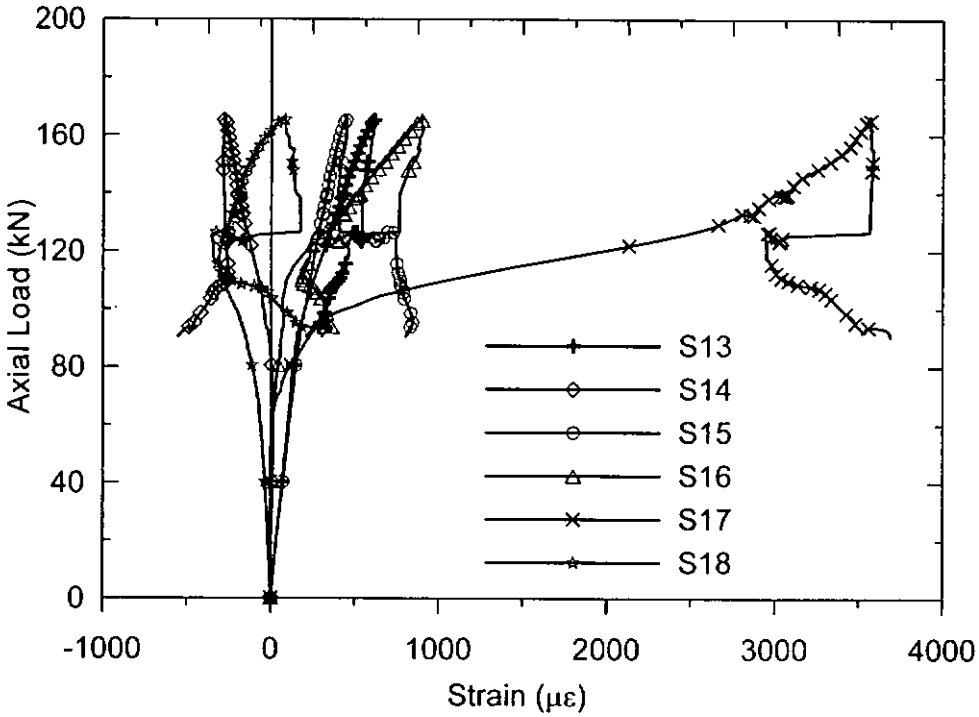

Figure 7.47 Load-circumferential strain curves of Specimen 09P0408: strain gauges S13-S18

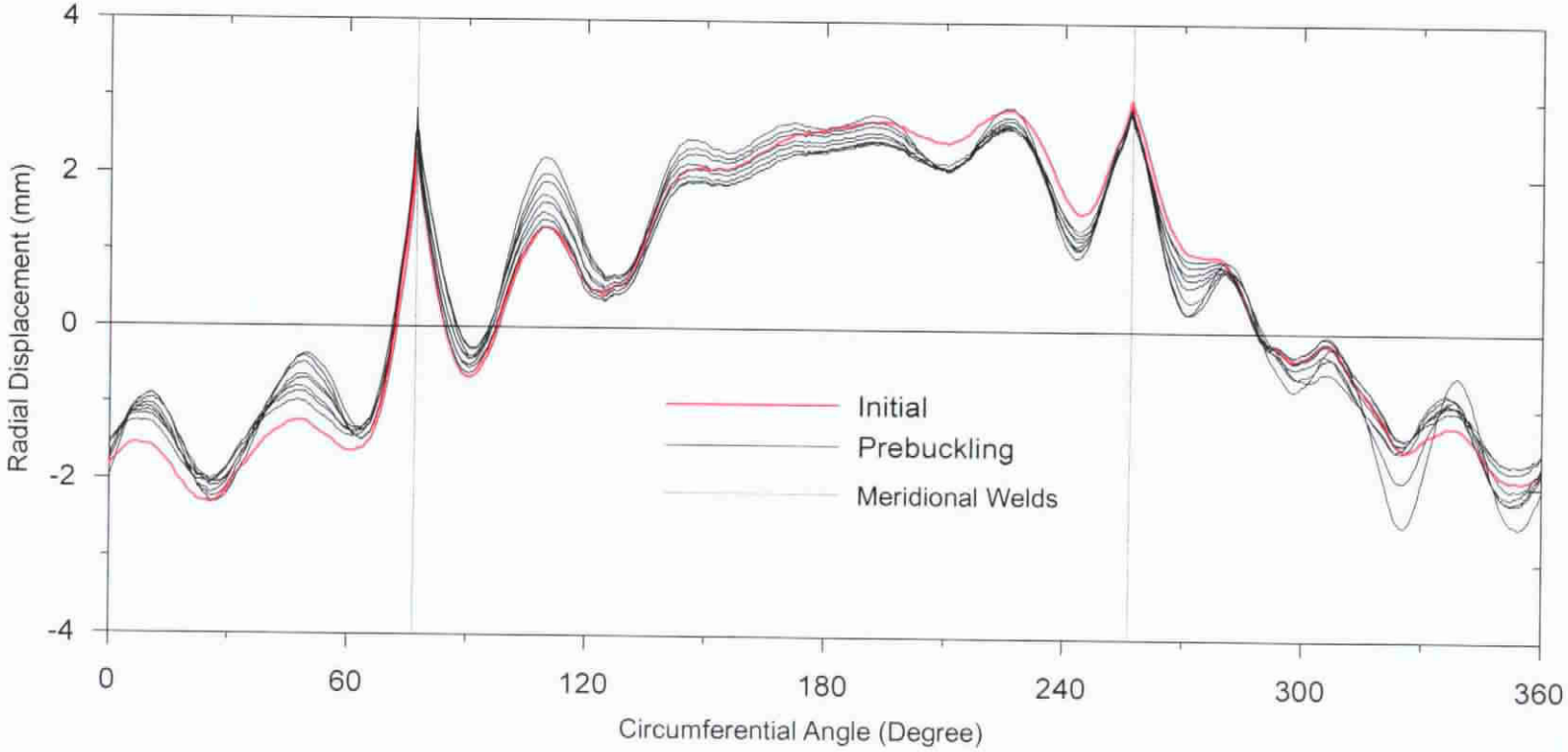

Figure 7.48 Prebuckling shapes of the above-weld circumference of Specimen 09SC

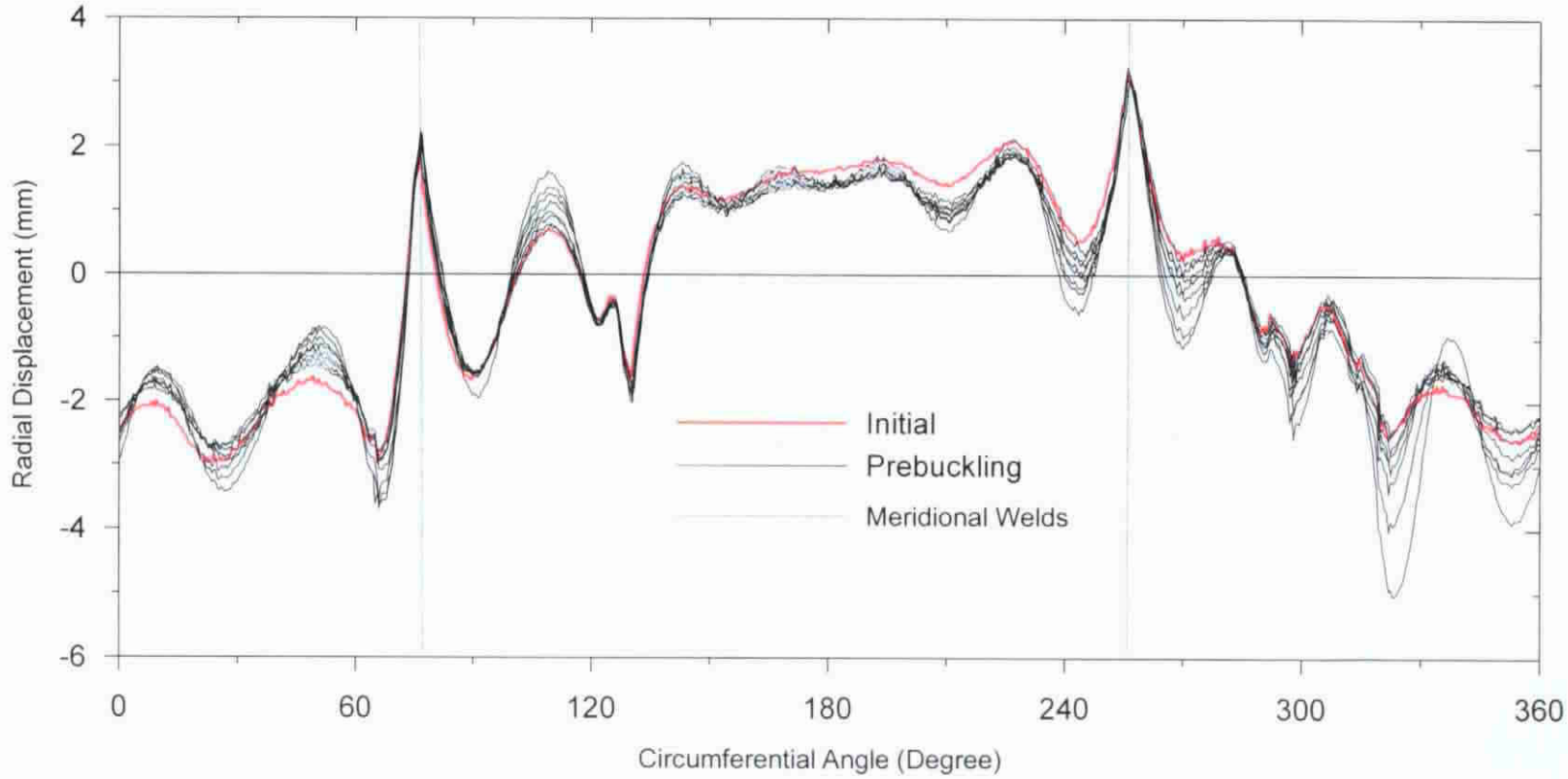

Figure 7.49 Prebuckling shapes of the weld circumference of Specimen 09SC

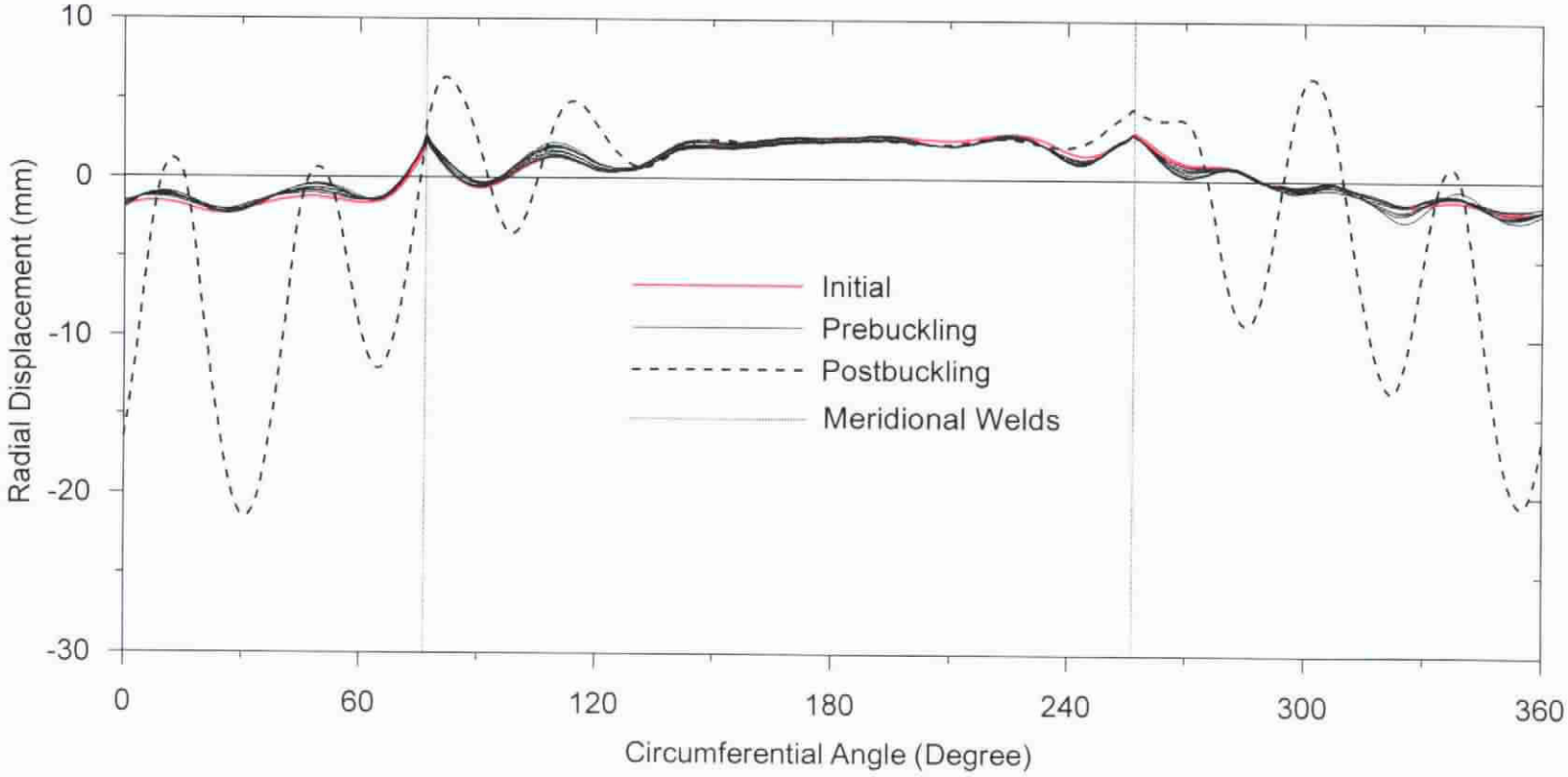

Figure 7.50 Prebuckling shapes versus a postbuckling shape of the above-weld circumference of Specimen 09SC

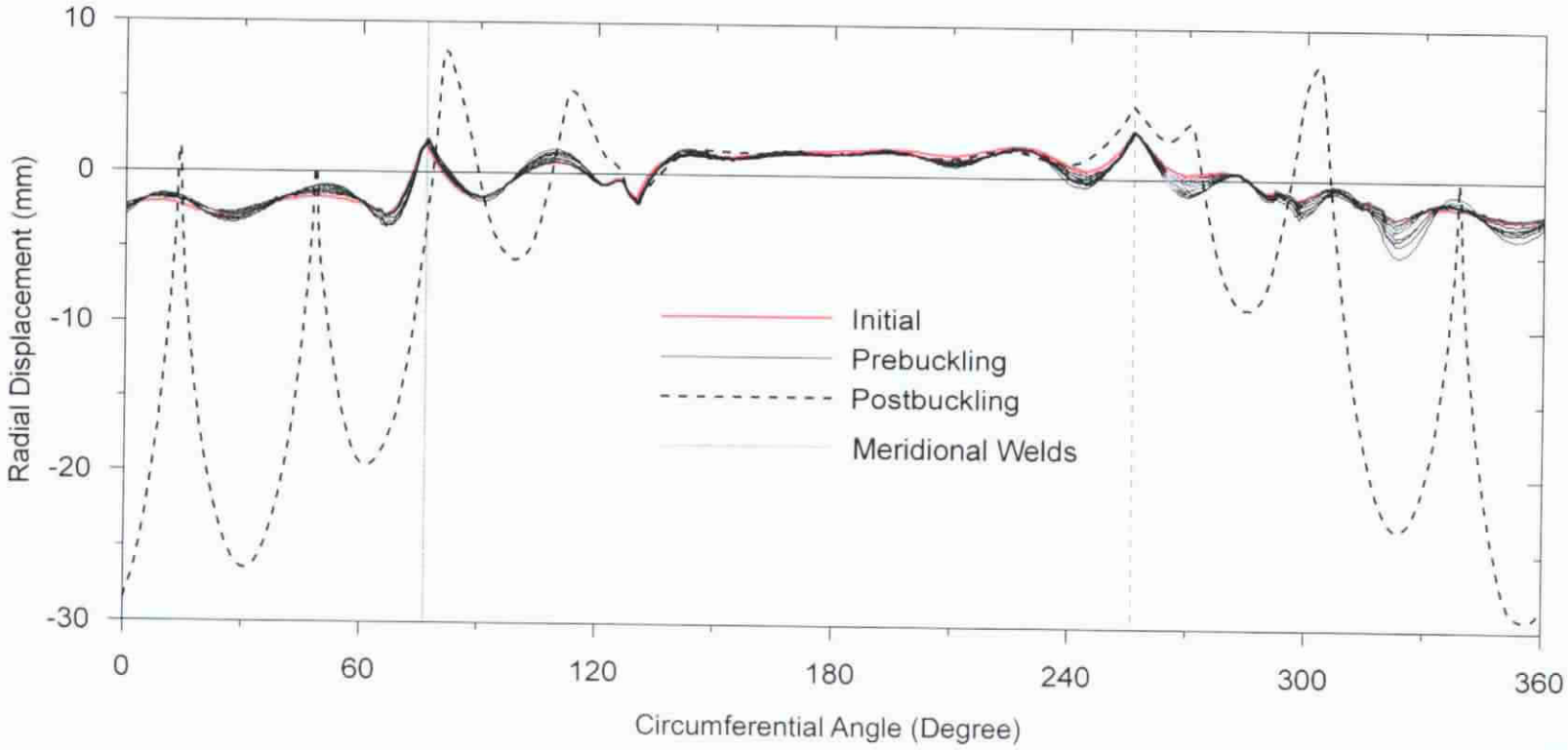

Figure 7.51 Prebuckling shapes versus a postbuckling shape of the weld circumference of Specimen 09SC

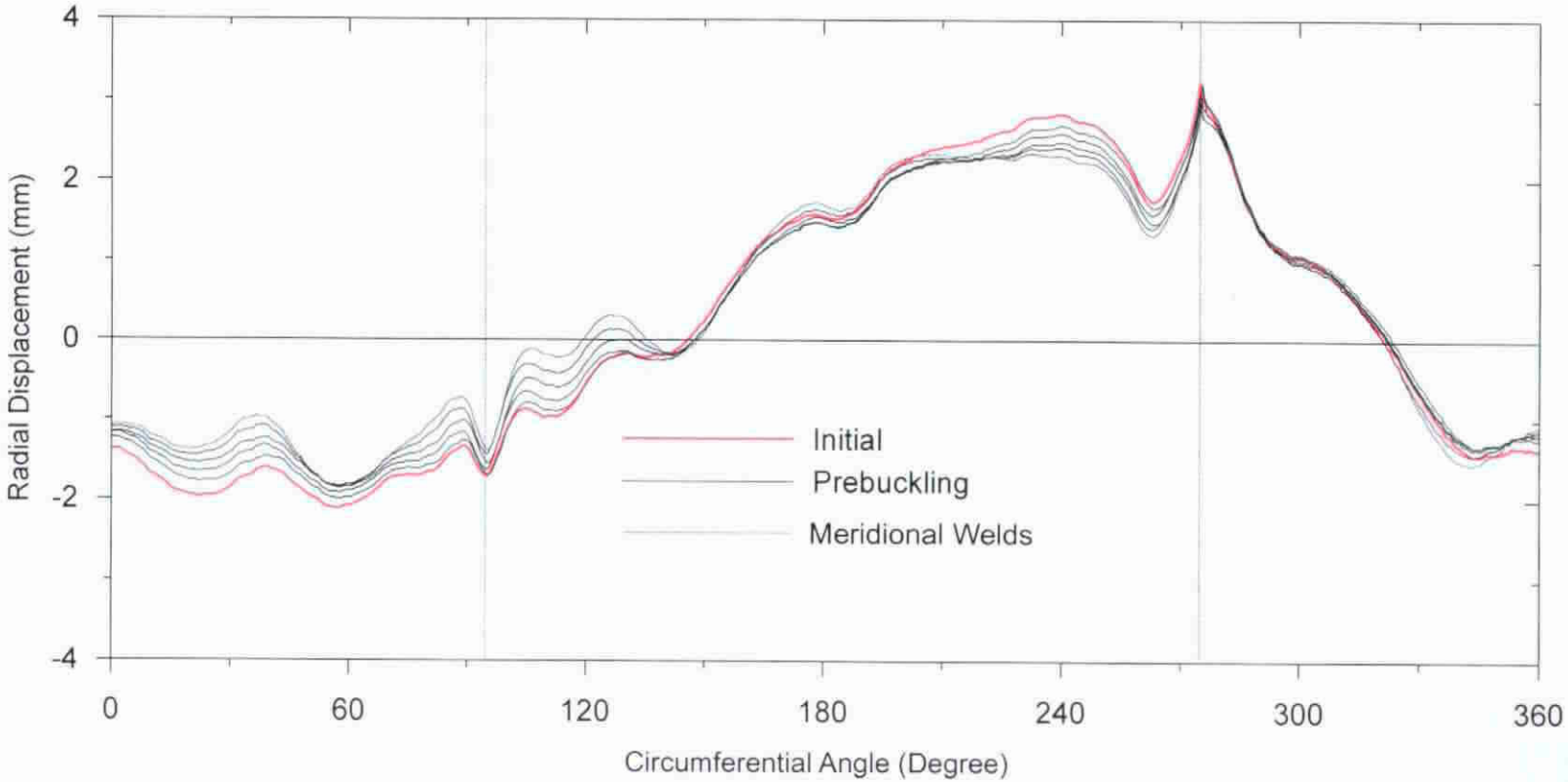

Figure 7.52 Prebuckling shapes of the above-weld circumference of Specimen 09QC04

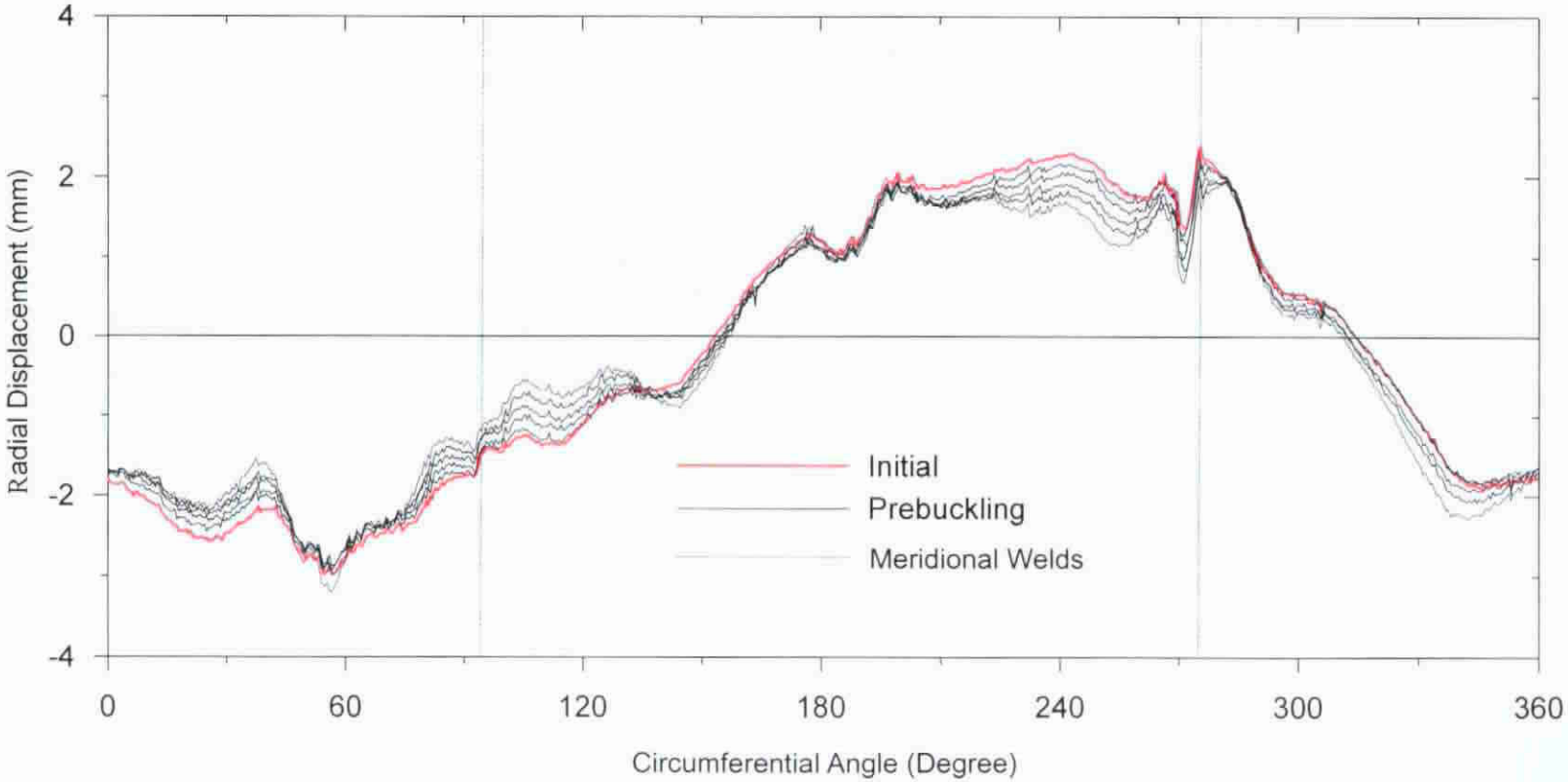

Figure 7.53 Prebuckling shapes of the weld circumference of Specimen 09QC04

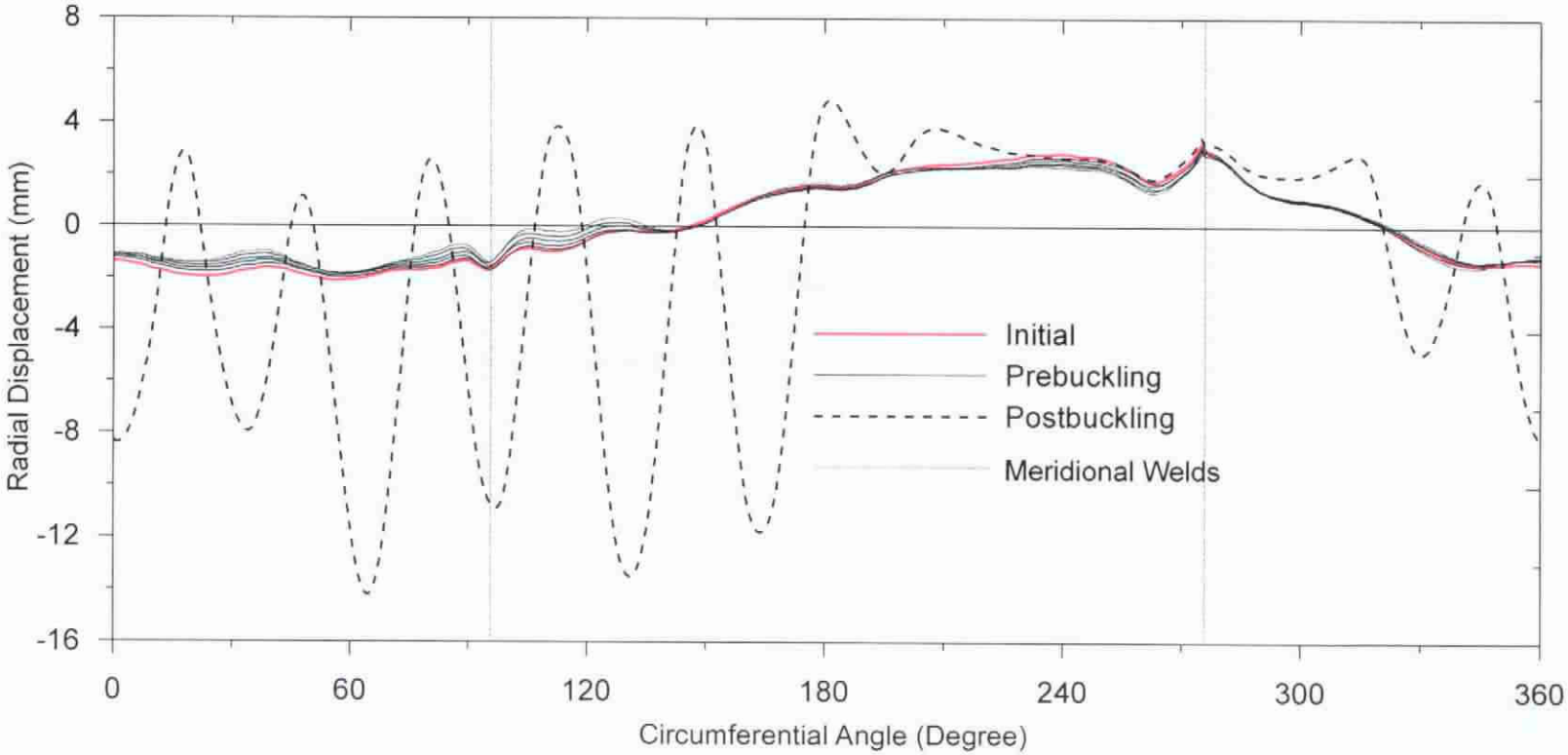

Figure 7.54 Prebuckling shapes versus a postbuckling shape of the above-weld circumference of Specimen 09QC04

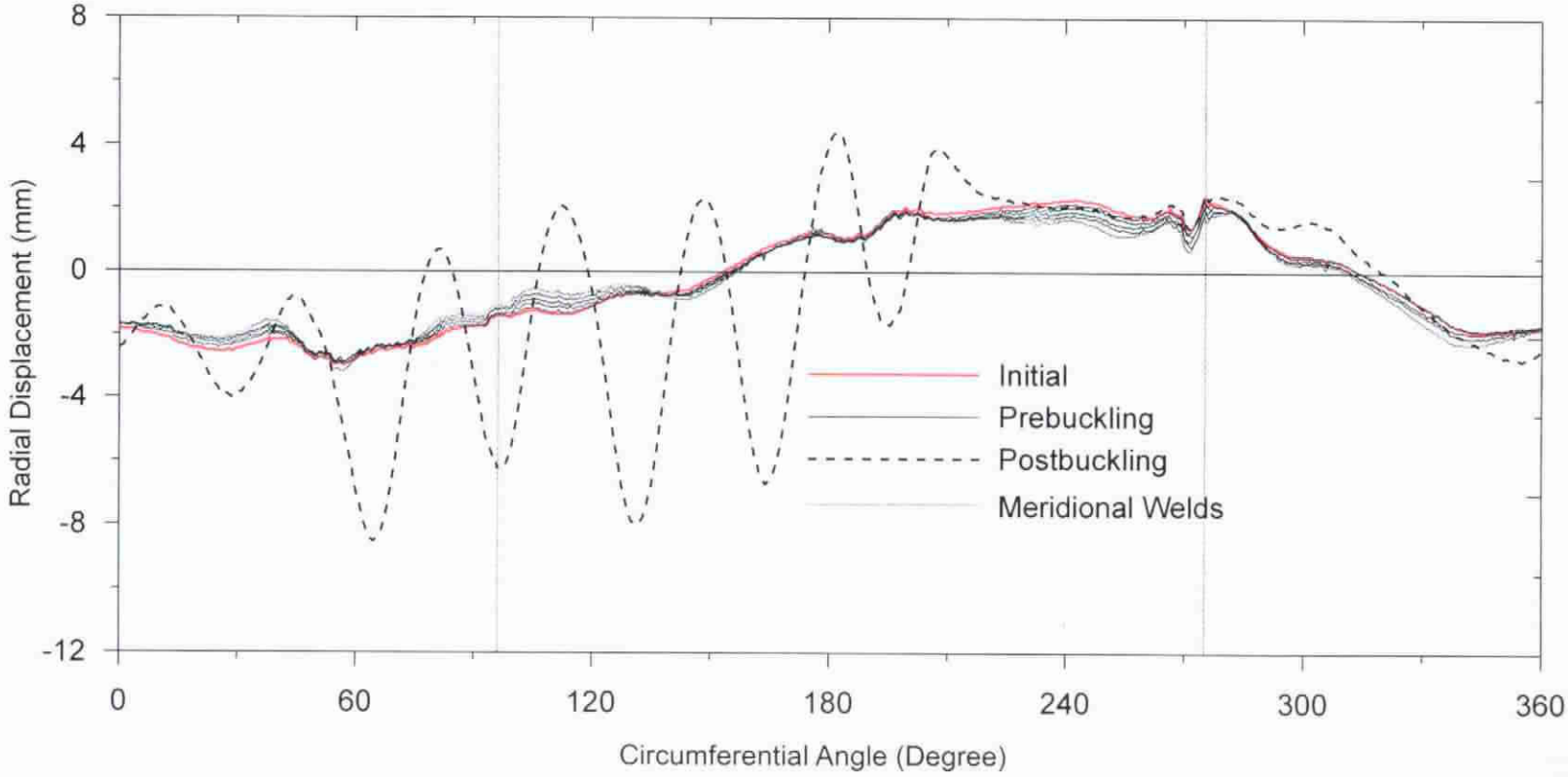

Figure 7.55 Prebuckling shapes versus a postbuckling shape of the weld circumference of Specimen 09QC04

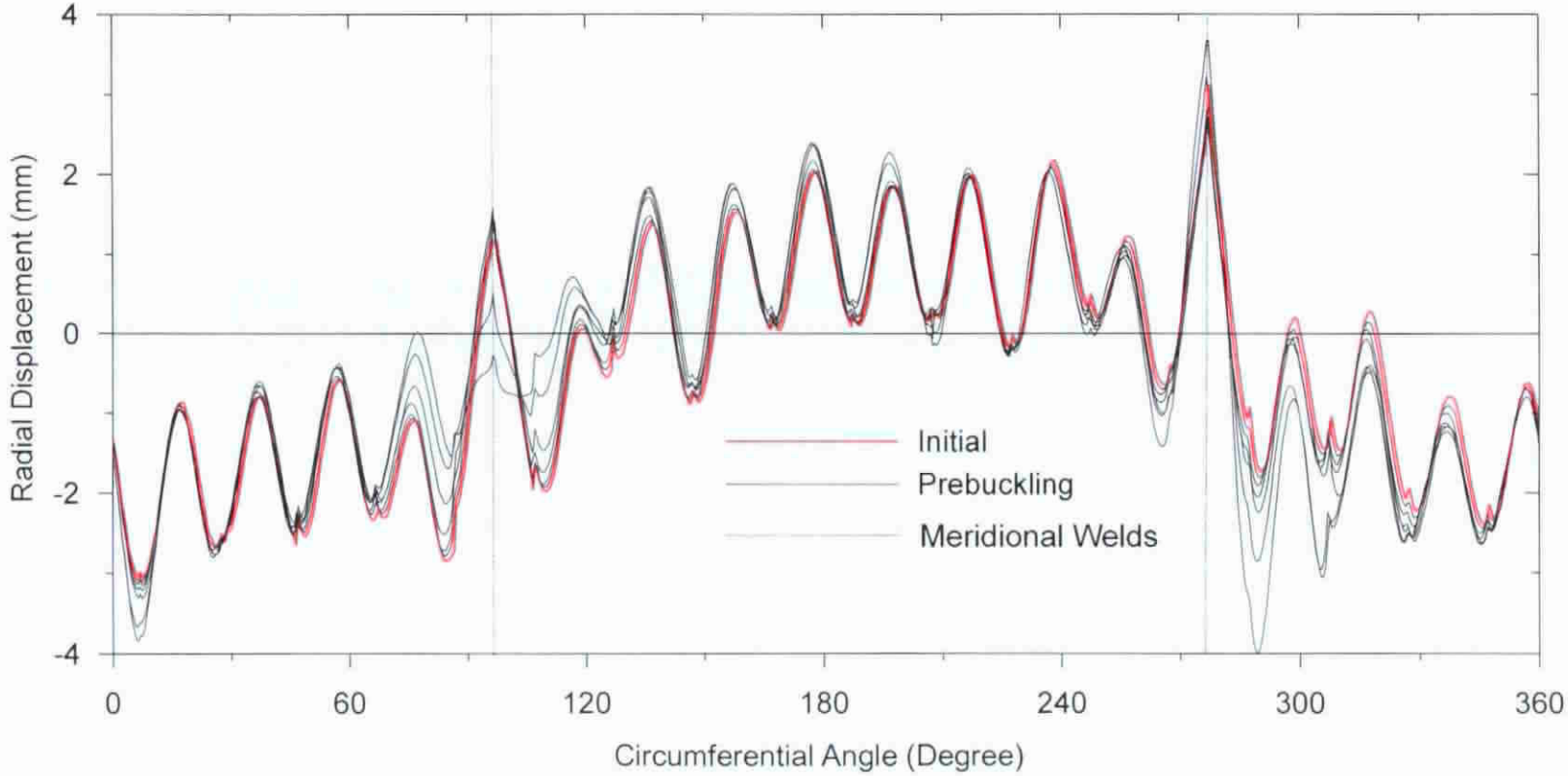

Figure 7.56 Prebuckling shapes of the mid-strake circumference of Specimen 09P0408

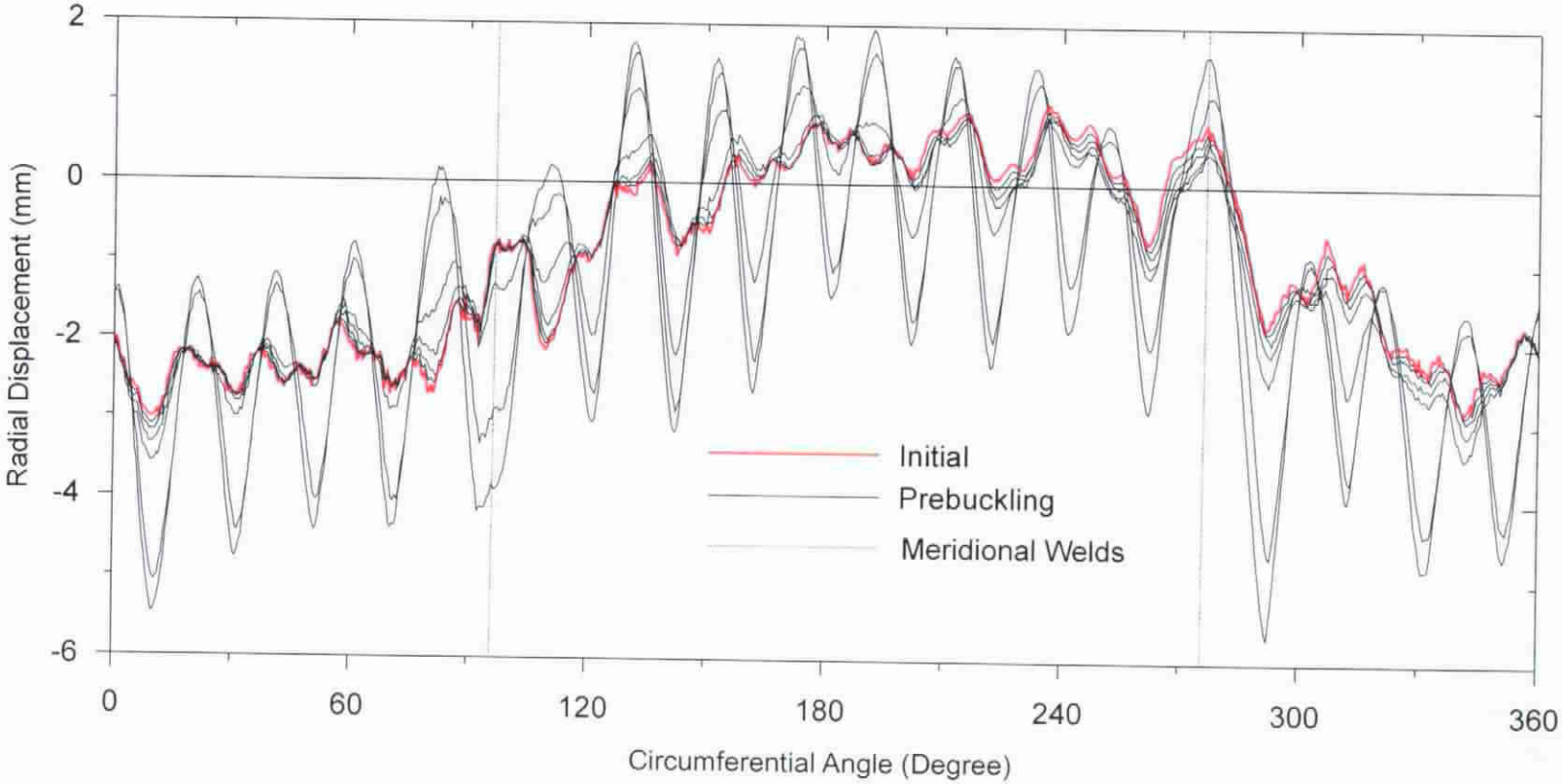

Figure 7.57 Prebuckling shapes of the weld circumference of Specimen 09P0408

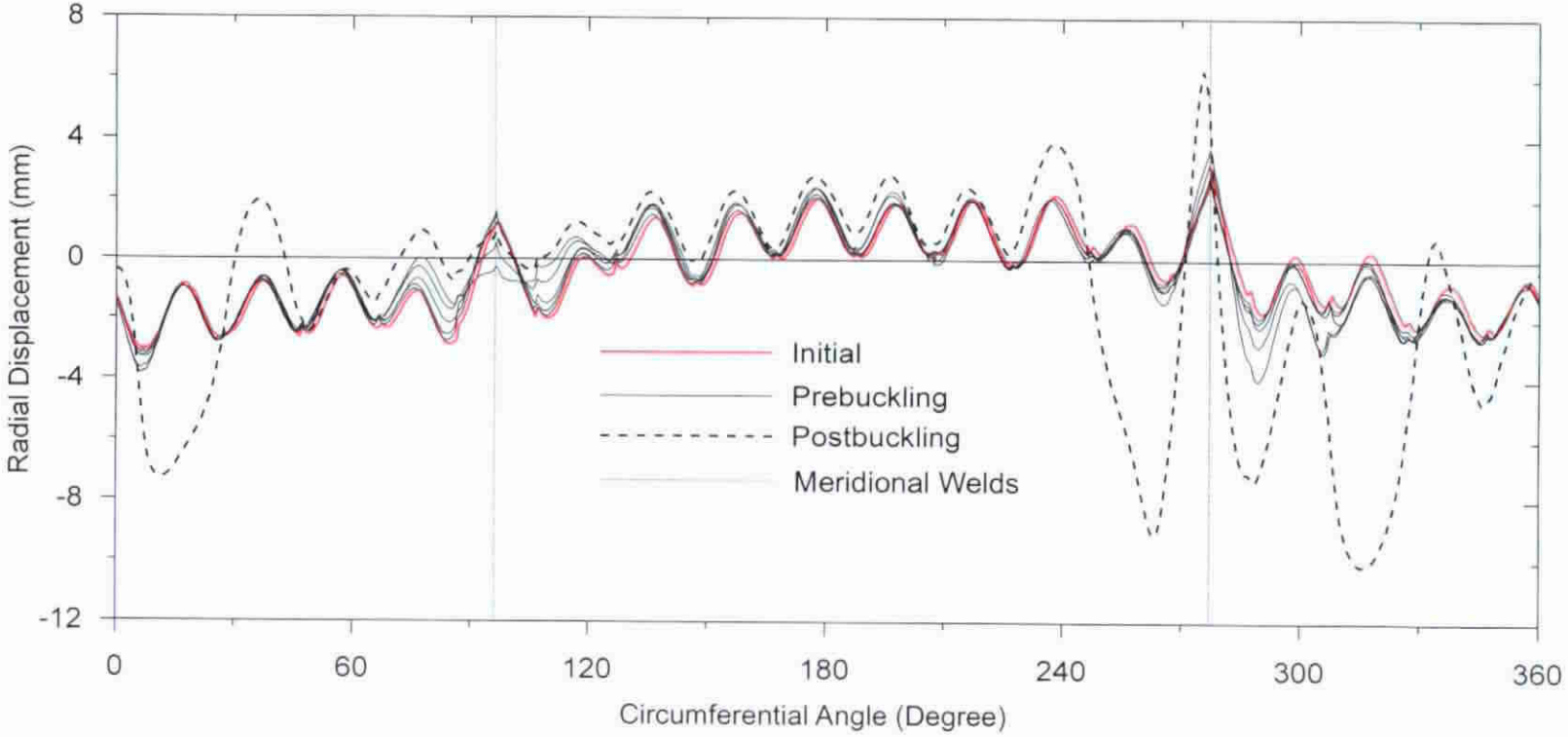

Figure 7.58 Prebuckling shapes versus a postbuckling shape of the mid-strake circumference of Specimen 09P0408

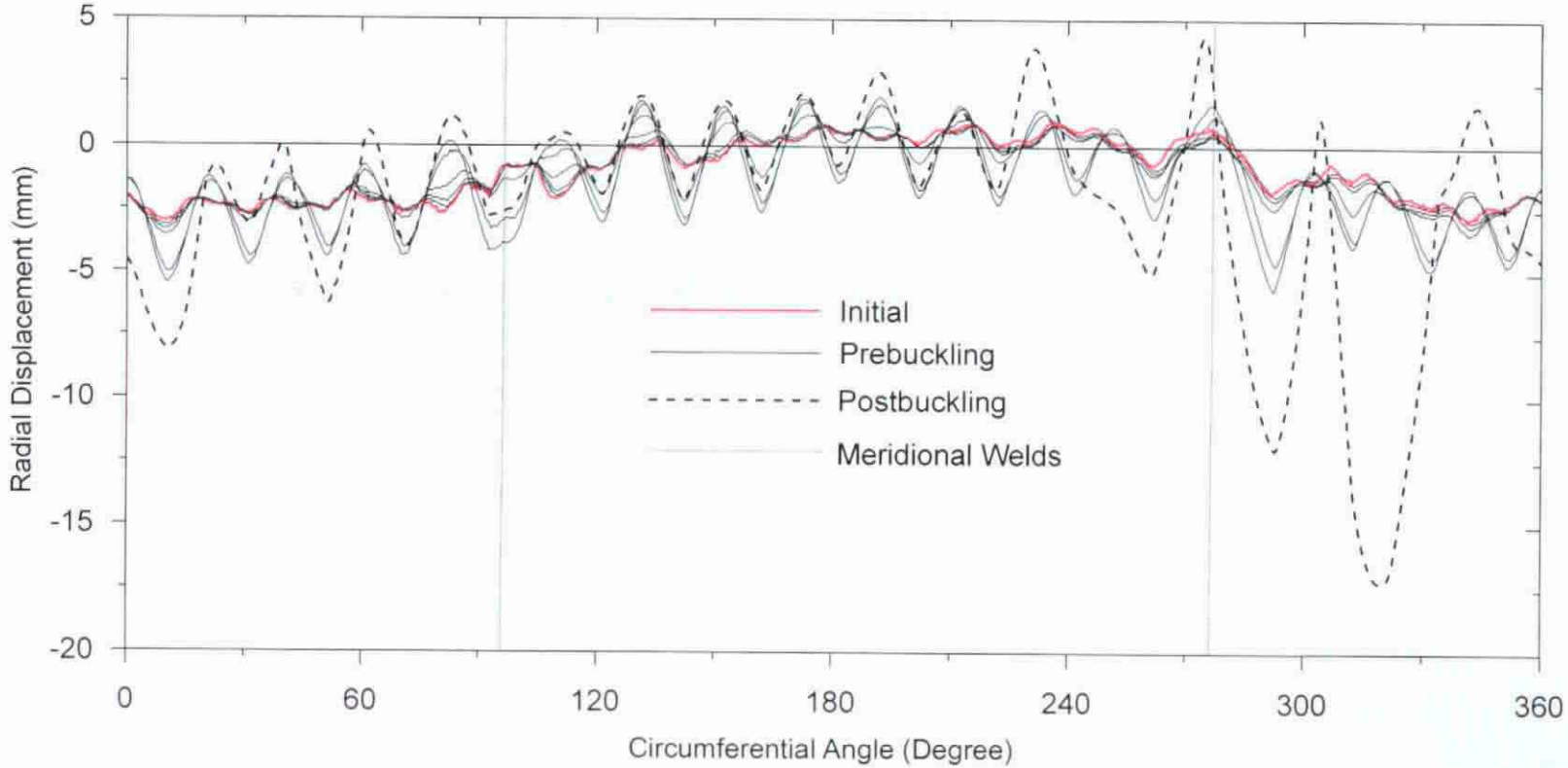

Figure 7.59 Prebuckling shapes versus a postbuckling shape of the weld circumference of Specimen 09P0408

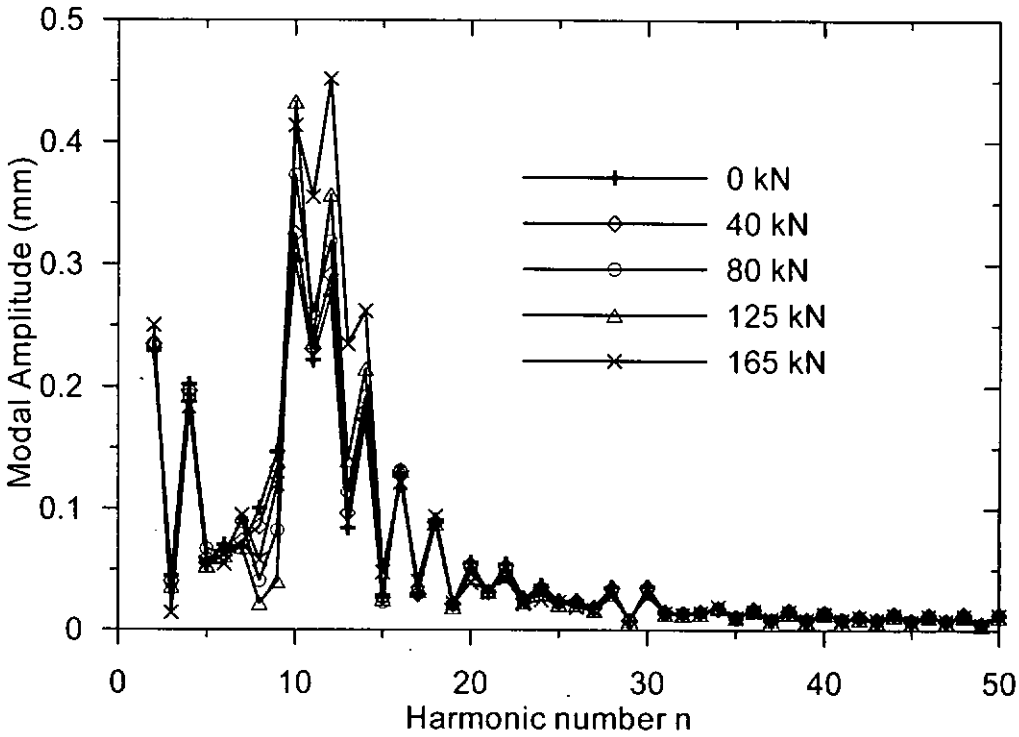

Figure 7.60 Growth of modal amplitude for the above-weld circumference in Specimen 09SC

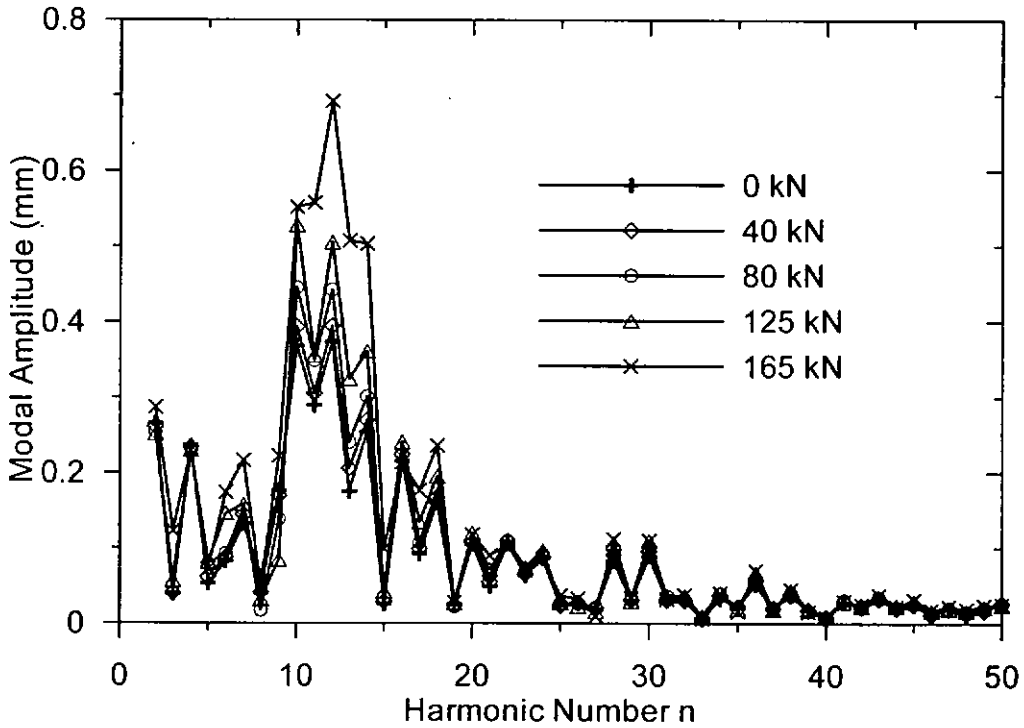

Figure 7.61 Growth of modal amplitude for the weld circumference in Specimen 09SC

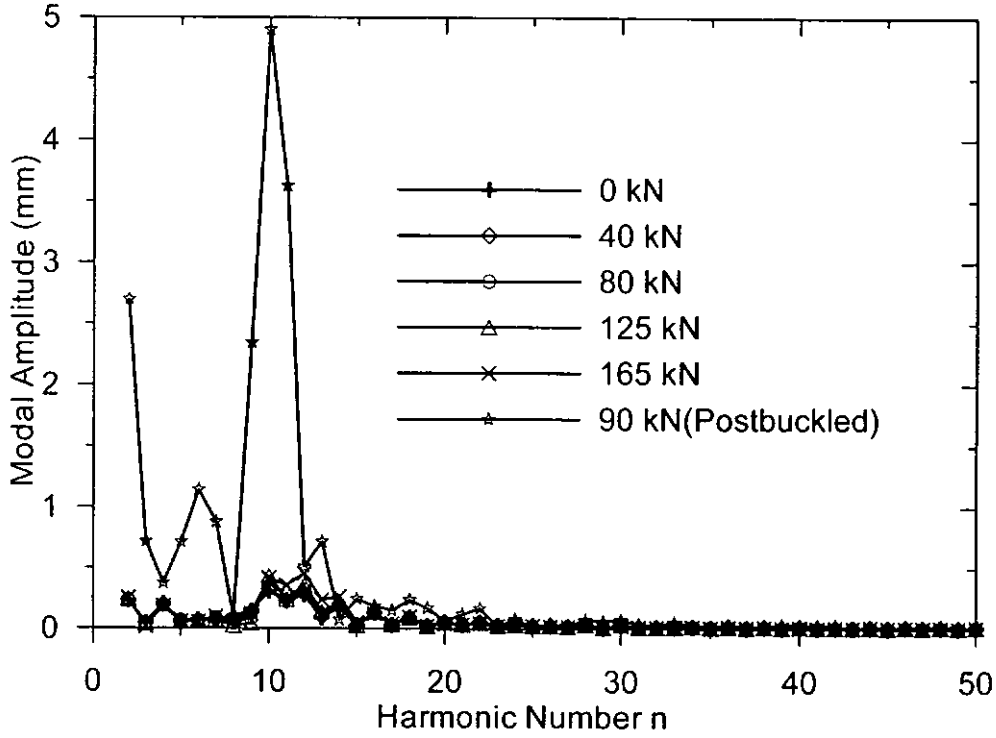

Figure 7.62 Growth of modal amplitude for the above-weld circumference of Specimen 09SC including a postbuckling state

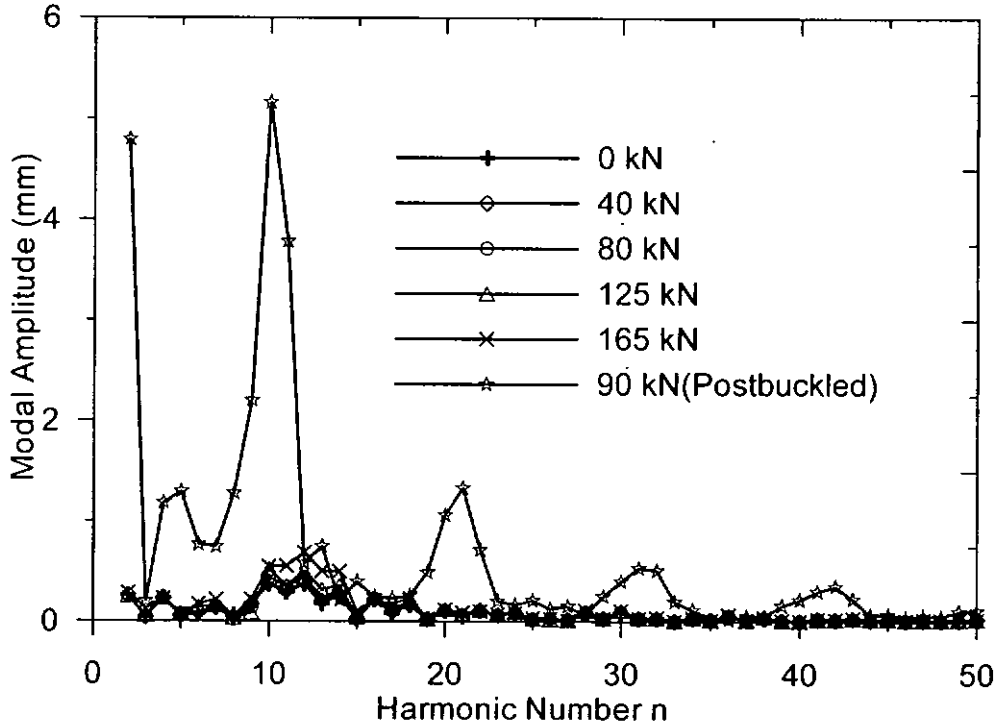

Figure 7.63 Growth of modal amplitude for the weld circumference of Specimen 09SC including a postbuckling state

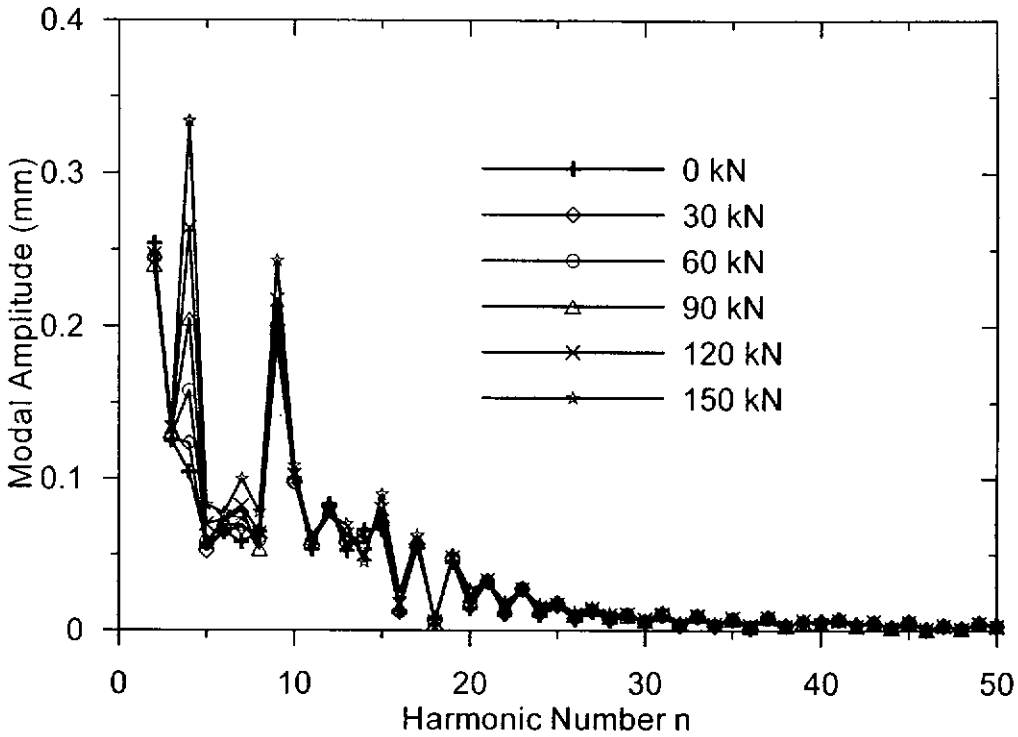

Figure 7.64 Growth of modal amplitude for the above-weld circumference in Specimen 09QC04

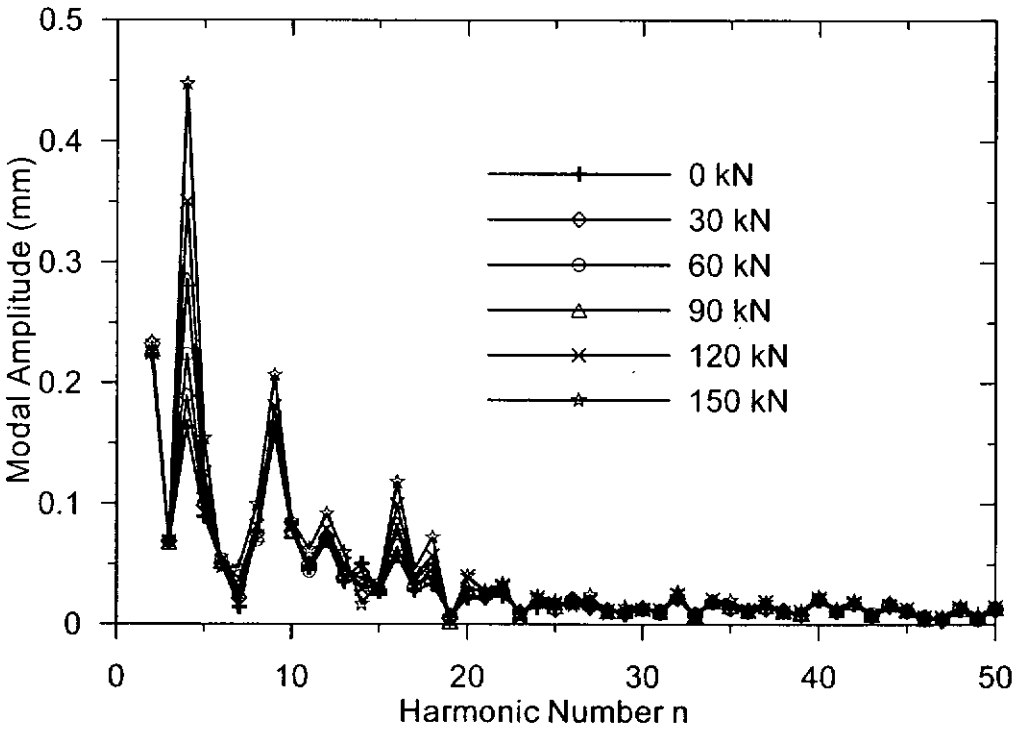

Figure 7.65 Growth of modal amplitude for the weld circumference in Specimen 09QC04

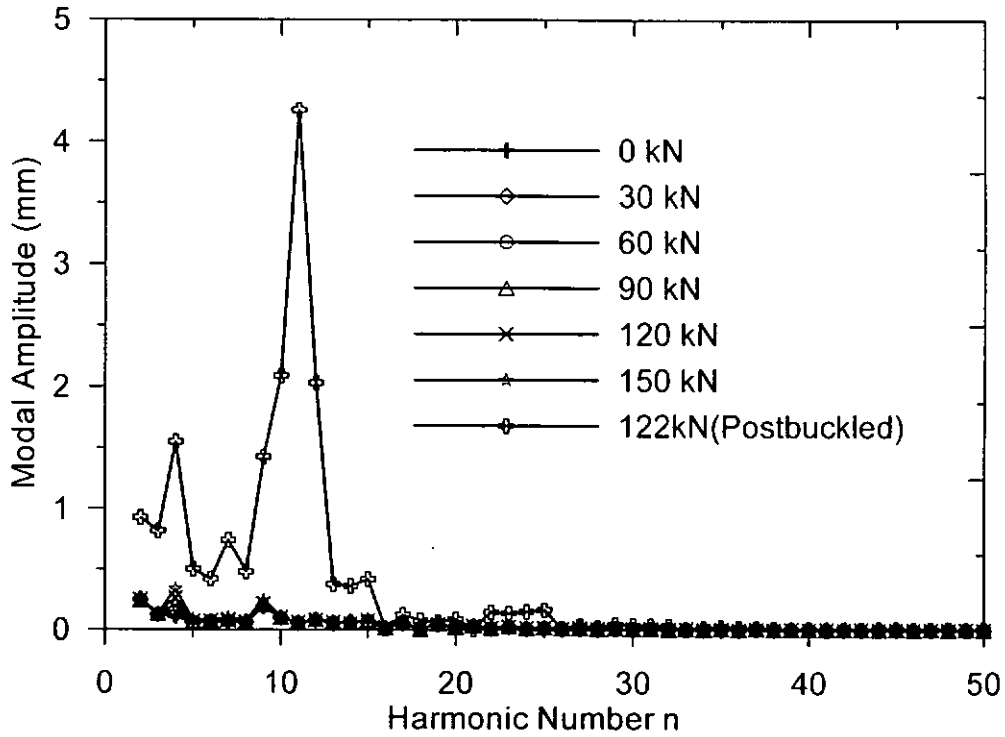

Figure 7.66 Growth of modal amplitude for the above-weld circumference of Specimen 09QC04 including a postbuckling state

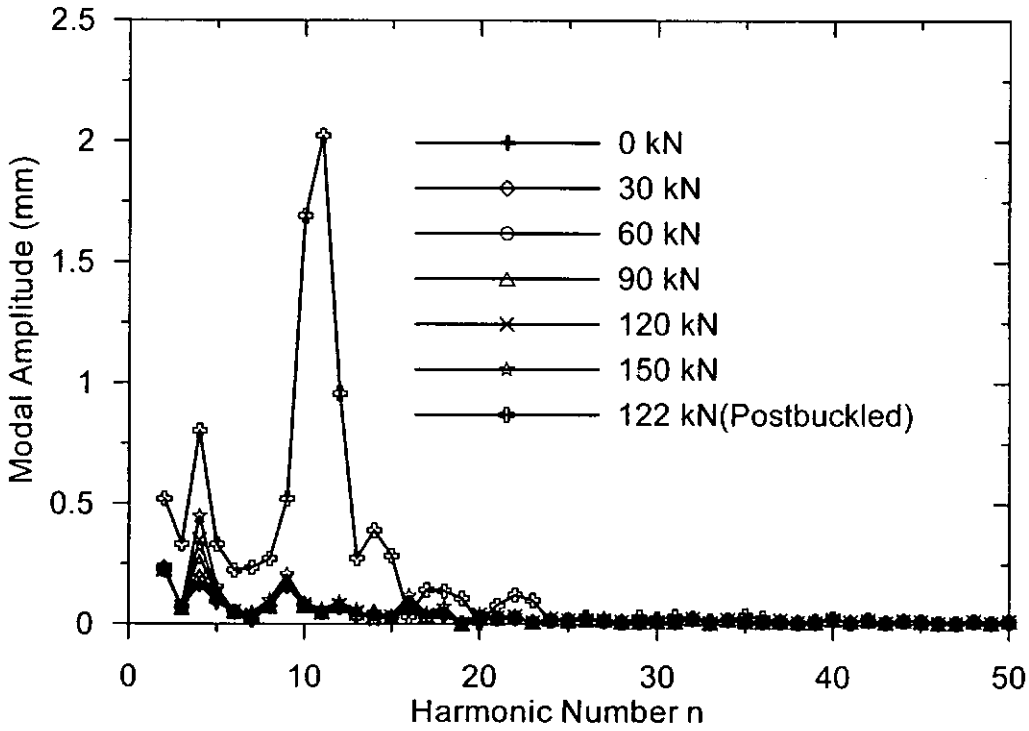

Figure 7.67 Growth of modal amplitude for the weld circumference of Specimen 09QC04 including a postbuckling state

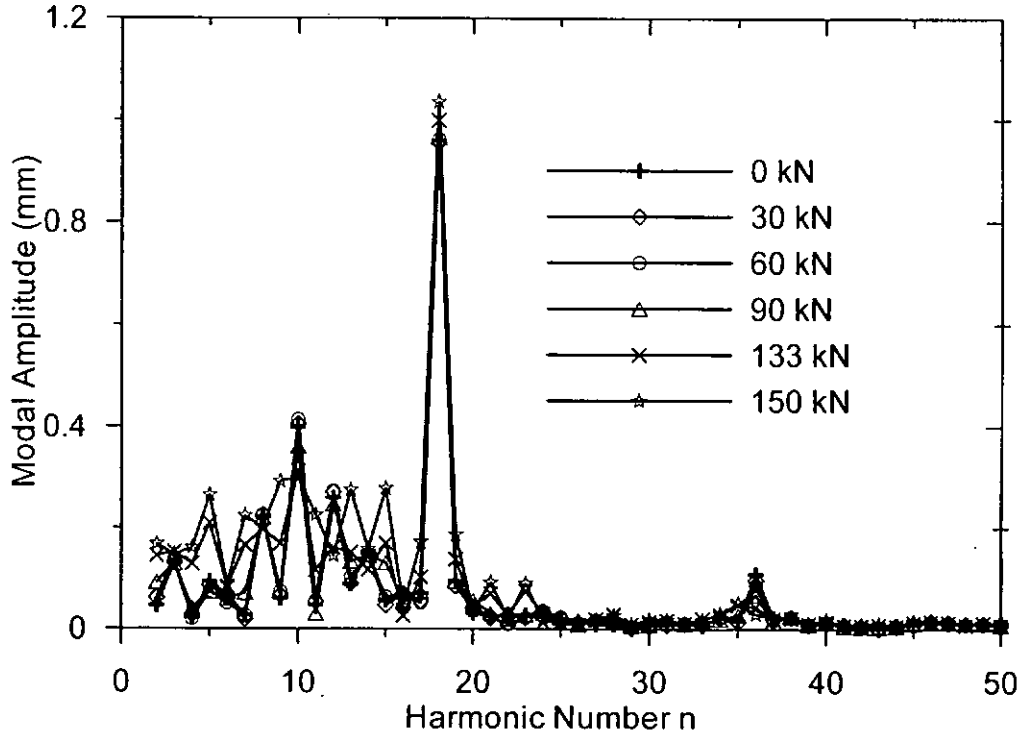

Figure 7.68 Growth of modal amplitude for the mid-panel circumference in Specimen 09P0408

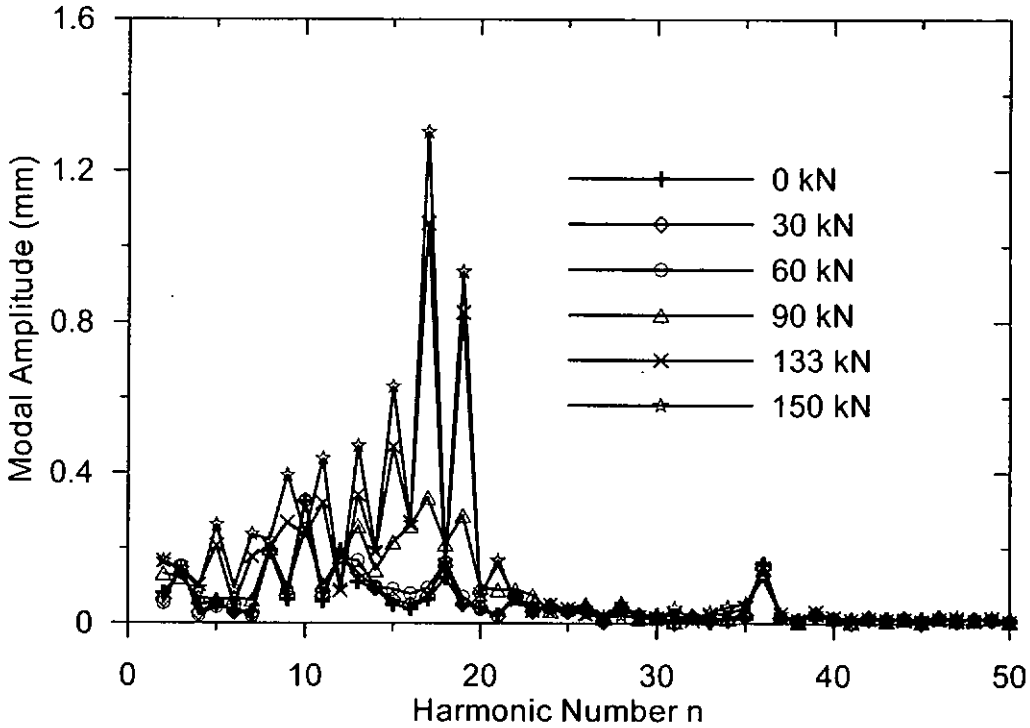

Figure 7.69 Growth of modal amplitude for the weld circumference in Specimen 09P0408

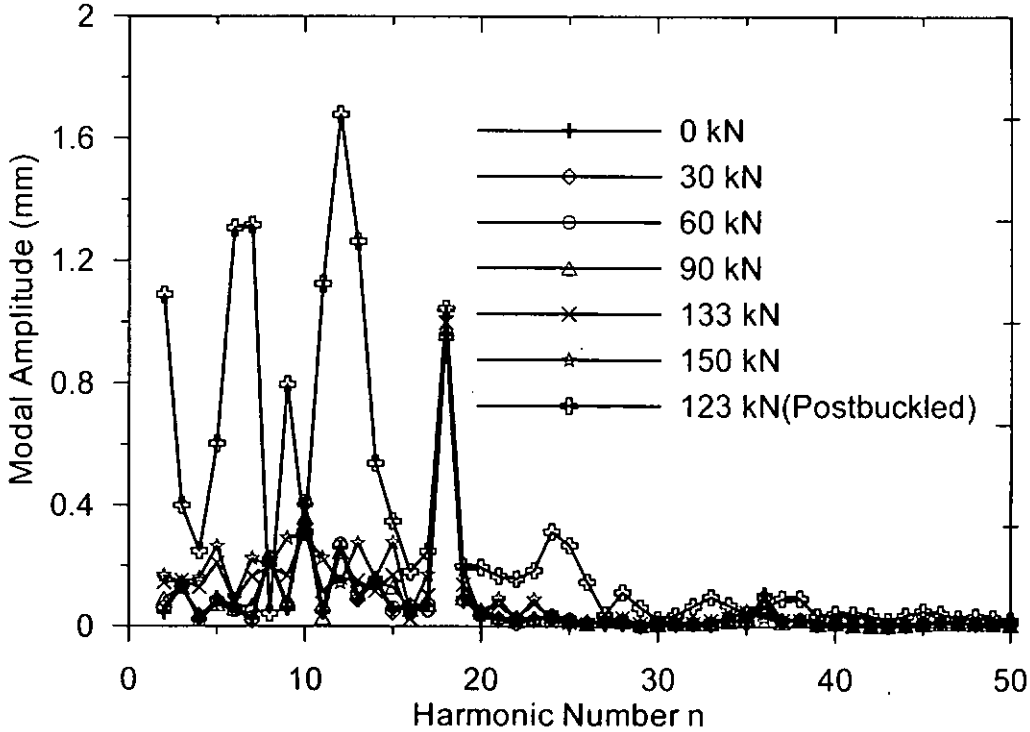

Figure 7.70 Growth of modal amplitude for the mid-panel circumference of Specimen 09P0408 including a postbuckling state

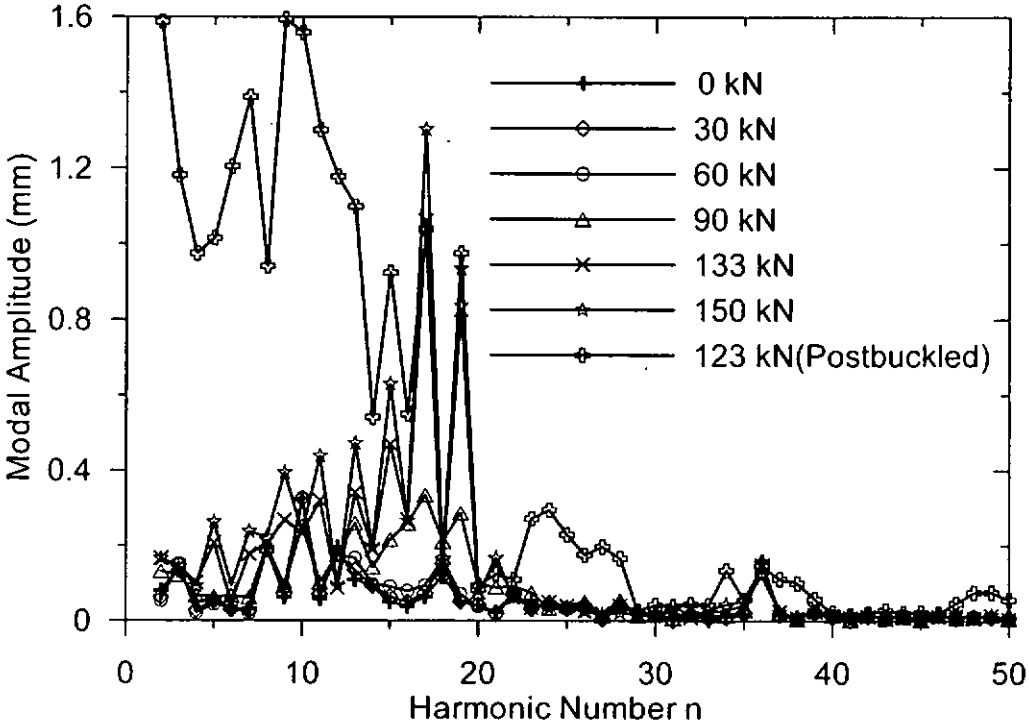

Figure 7.71 Growth of modal amplitude for the weld circumference of Specimen 09P0408 including a postbuckling state

Figure 7.72 Photograph of Specimen 09SC after postbuckling failure

Figure 7.73 Photograph of Specimen 09QC after postbuckling failure

Figure 7.74 Photograph of Specimen 09P0408 after postbuckling failure

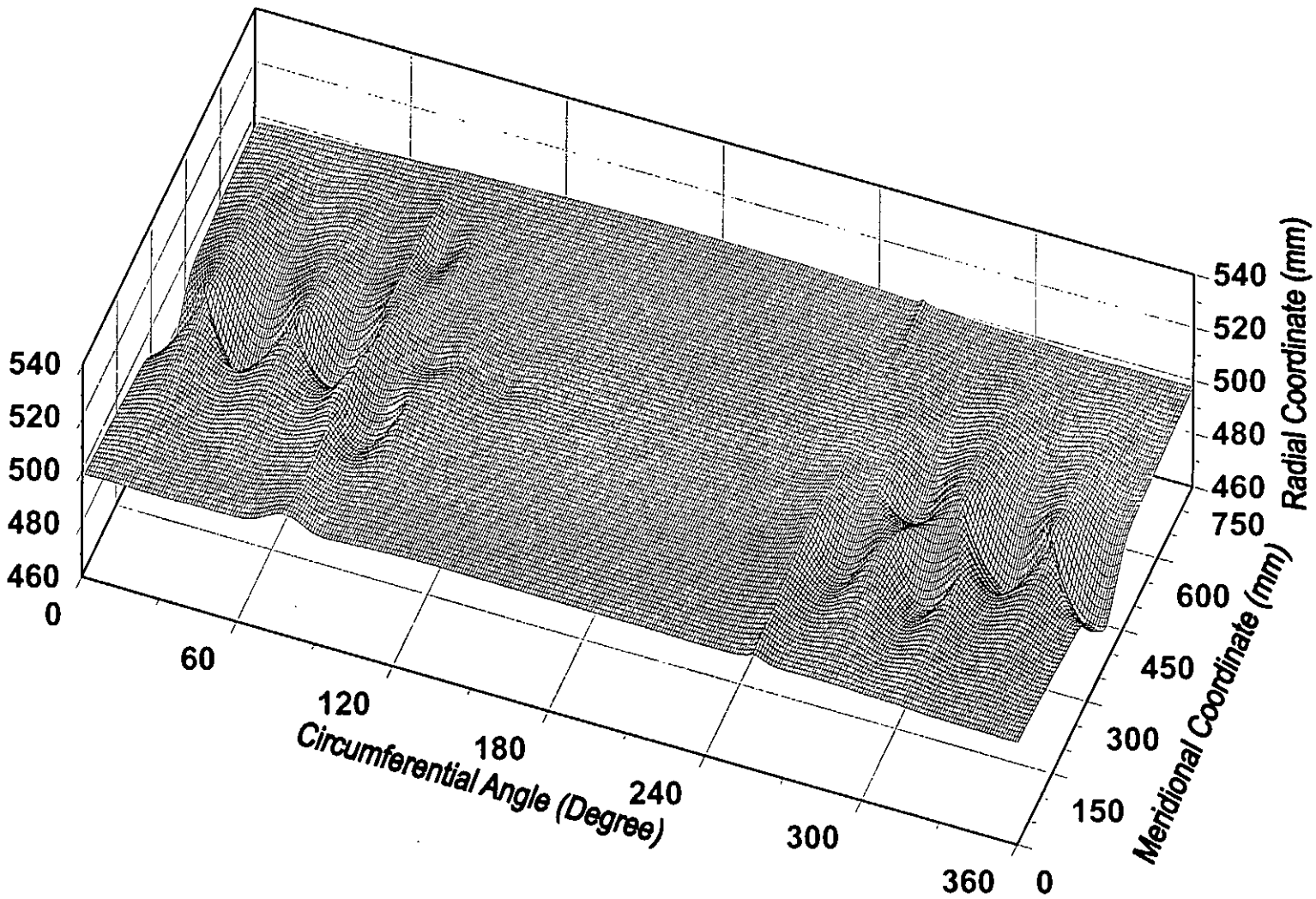

Figure 7.75 Three dimensional plot of the surface of Specimen 09SC after buckling failure

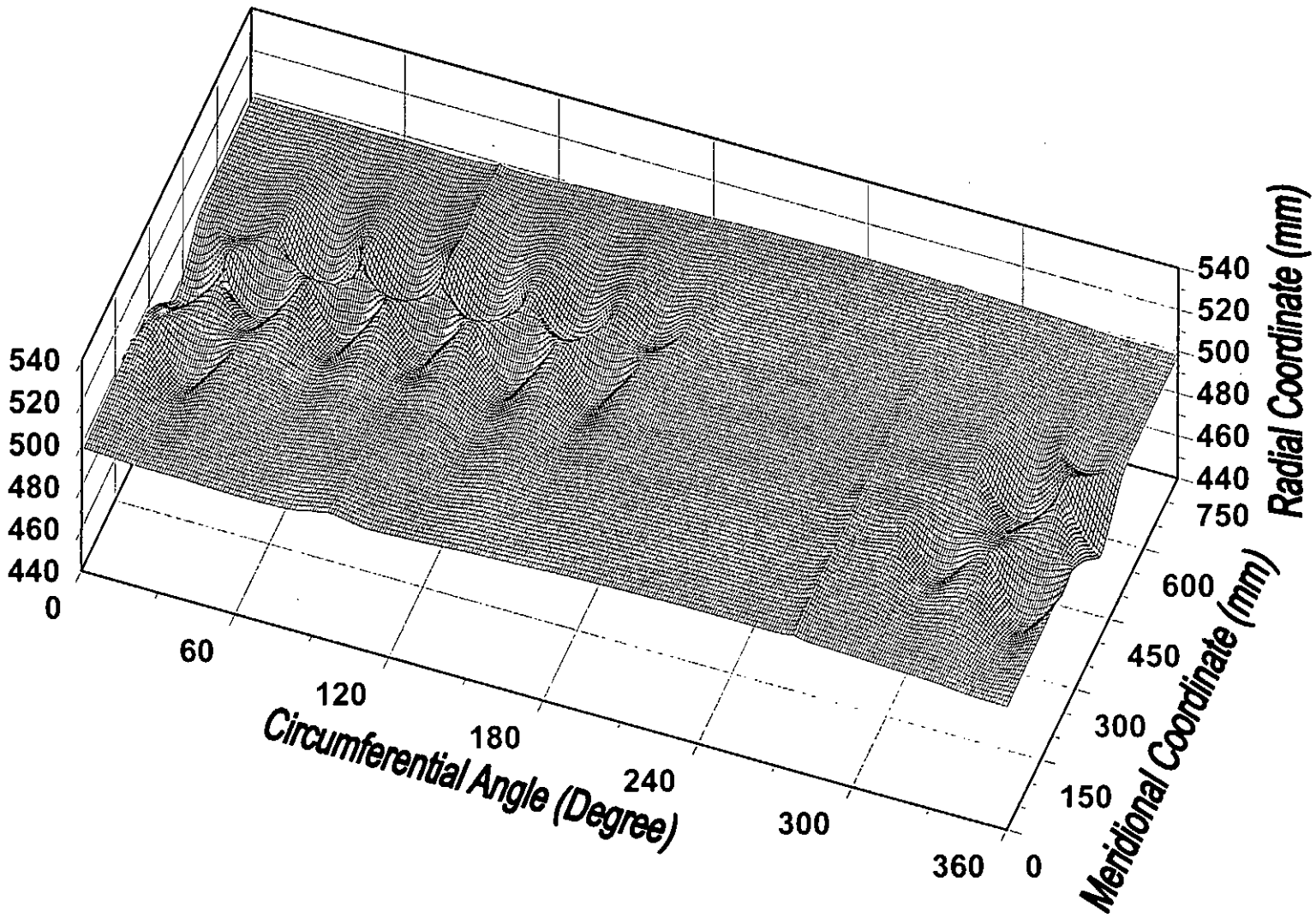

Figure 7.76 Three dimensional plot of the surface of Specimen 09QC04 after buckling failure

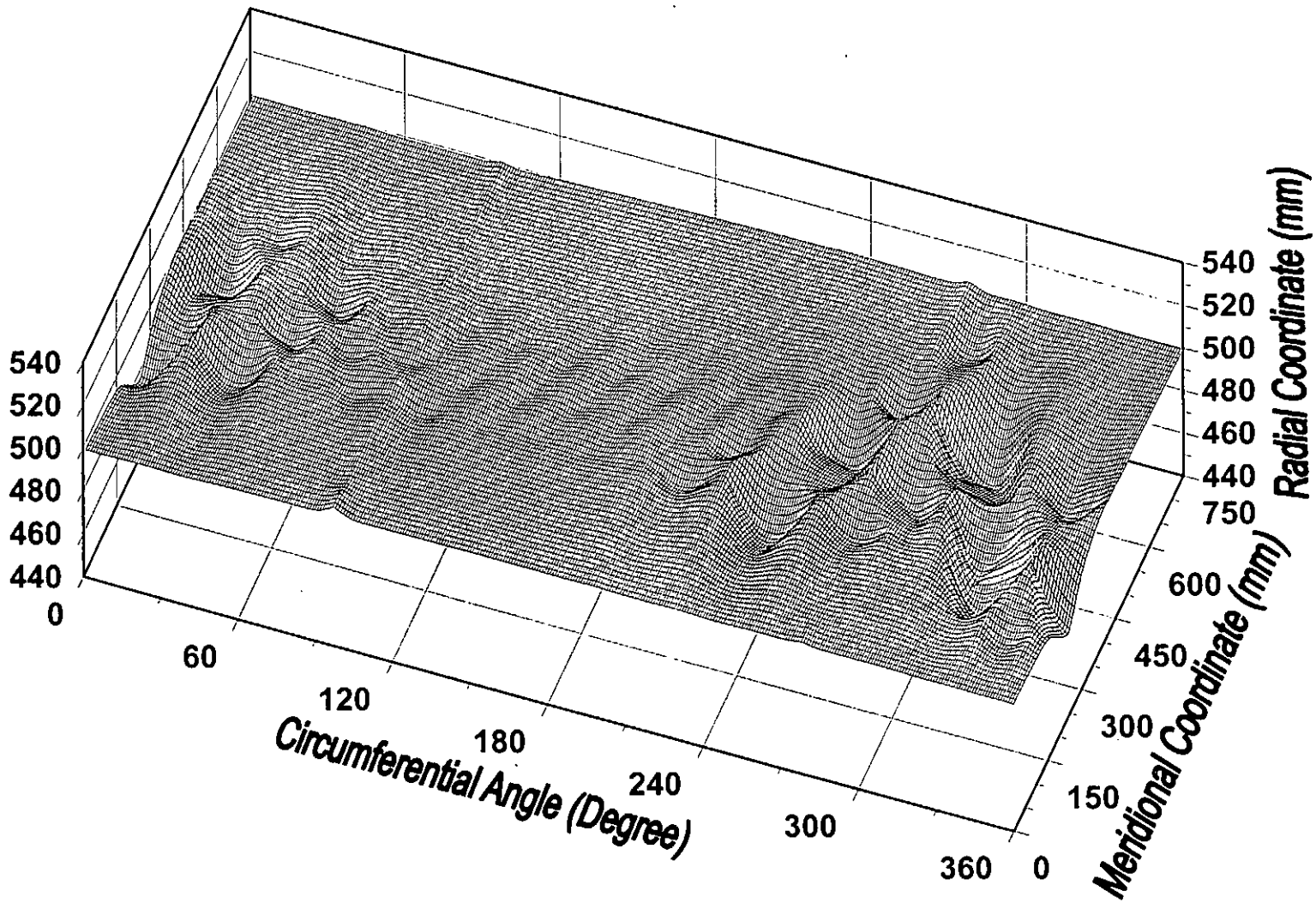

Figure 7.77 Three dimensional plot of the surface of Specimen 09P0408 after buckling failure

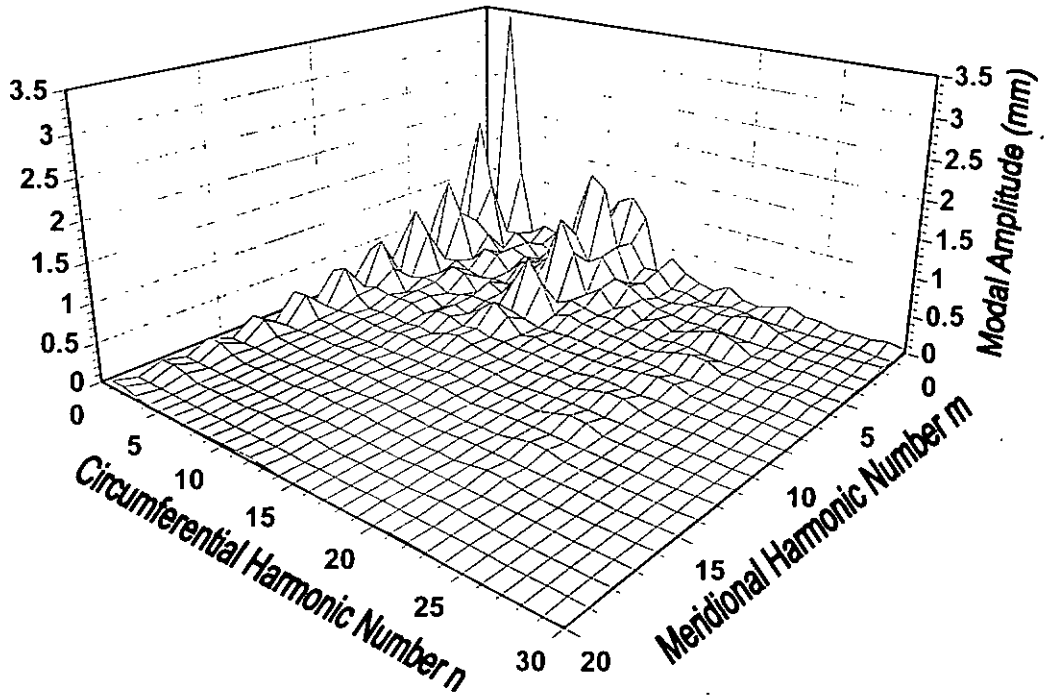

Figure 7.78 Spectrum of Fourier series for the post-buckled surface of Specimen 09SC

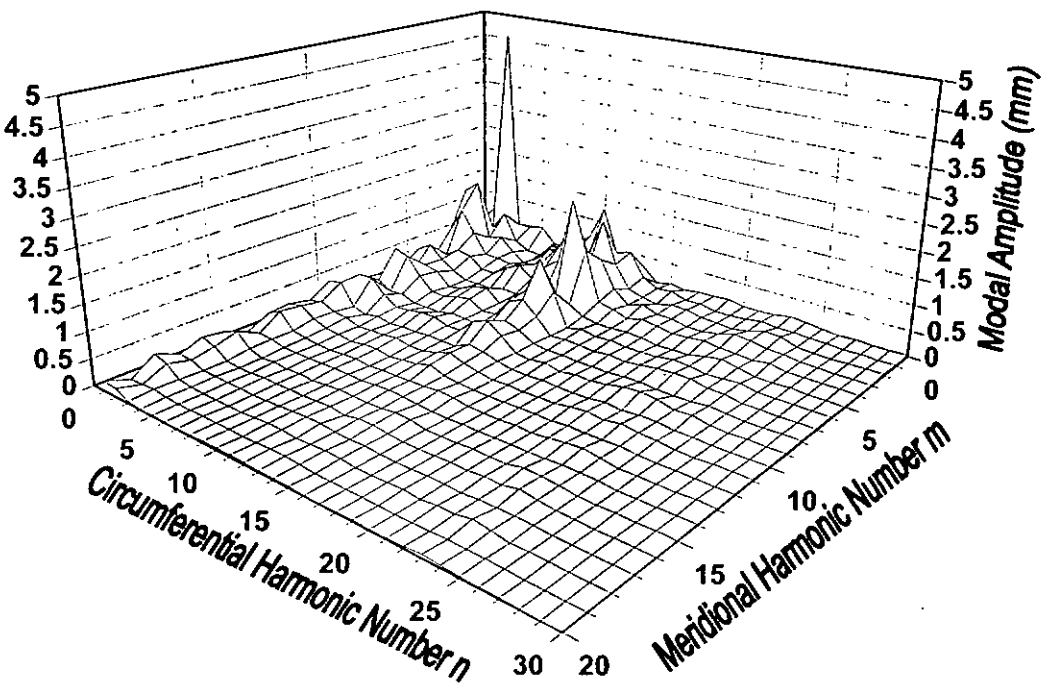

Figure 7.79 Spectrum of Fourier series for the post-buckled surface of Specimen 09QC04

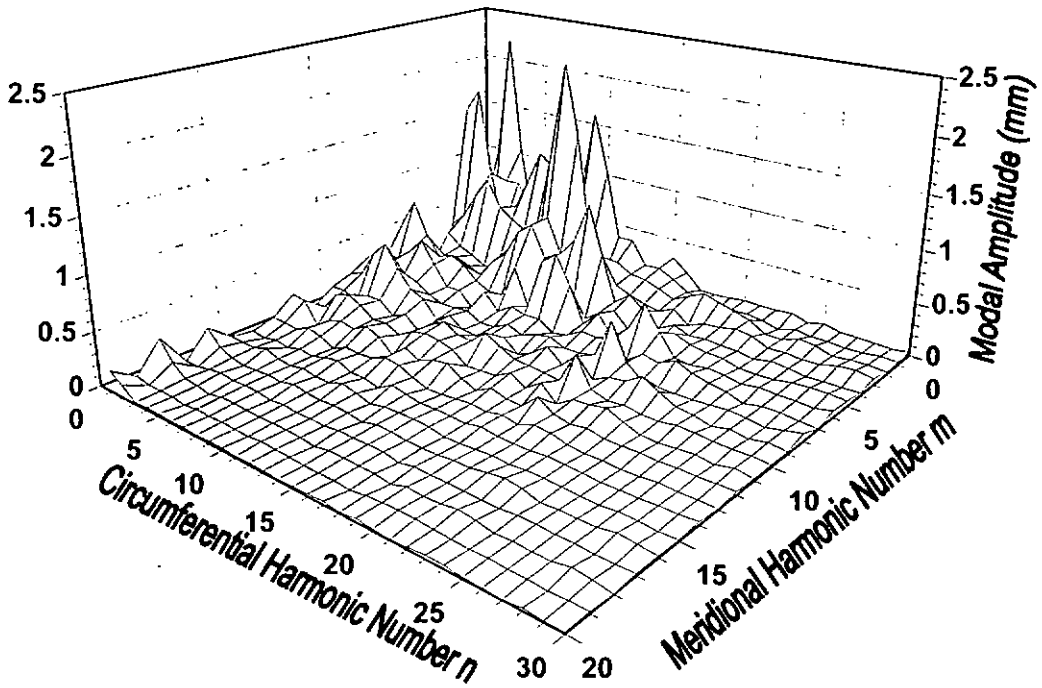

Figure 7.80 Spectrum of Fourier series for the post-buckled surface of Specimen 09P0408

CHAPTER 8

FINITE ELEMENT MODELLING OF BUCKLING EXPERIMENTS ON EXTENSIVELY WELDED STEEL CYLINDERS

8.1 INTRODUCTION

This chapter presents finite element models of the buckling experiments described in Chapter 7, the numerical results obtained from these models, and the comparisons of the numerical results with the experimental results presented in Chapter 7. The effect of the residual stresses in these model shells on their buckling behaviour is a main focus of the present chapter. Existing research suggests that welding induced residual stresses may have a significant effect on the buckling strength of shells (e.g., Ravn-Jensen and Tvergaard, 1990; Guggenberger, 1996; Rotter, 1996; Hübner *et al*, 2003a), but these studies have been theoretical and are inconclusive.

In this chapter, numerical results from finite element models of the model shells with a precise representation of the measured imperfections are presented and compared with test results. Since the numerical models did not include any residual stresses, the discrepancies between the test and numerical results provide an indication of the effect of residual stresses and other possible factors.

8.2 SOME GENERAL ISSUES OF NUMERICAL MODELLING

The dimensions and the measured imperfections of the model shells were presented in Chapter 7. The material properties of the steel were also given in Chapter 7. It was shown in Chapter 7 that rolling of the sheets had almost no effect on the material properties. In

the numerical models, the material properties for the steel after rolling were used. In the laboratory experiments, two rigid end rings were attached to both the bottom and top ends of each shell specimen; the bottom rigid end ring was clamped to a rigid support table, while the top rigid end ring was connected to a stiff loading cone in the shell buckling test facility. The bottom end condition was modelled as fully clamped in the finite element models, and while the top end ring was modelled as a strake of unrestrained shell having a wall thickness of 9mm and a height of 10mm. The Young's modulus of this strake was assigned a value which is 625 times the elastic modulus of other parts of the shell. This factor was chosen according to the ratio of second moment of area of the actual end ring to that of the shell strake used to model the actual ring. The shells were again modelled using the 4-node doubly curved general-purpose finite membrane strain shell element S4 available in the finite element package ABAQUS (Hibbitt, Karlsson & Sorensen, 1998). Numerical integration across the shell thickness was by Simpson's rule with 9 integration points.

8.3 MESH CONVERGENCE STUDY

A mesh convergence study was first conducted on a 60^0 shell segment of full height extracted from specimen 09P0408 to arrive at an appropriate mesh for the subsequent numerical modelling work. Specimen 09P0408 was chosen as the subject of study because this specimen had both circumferential welds and many short meridional welds and thus a more complicated distribution of imperfection. Four meshes were examined: (a) Mesh I with elements of $4.5mm \times 4.36mm$ ($4.5mm$ along the height and $4.36mm$ or 0.5^0 around the circumference); (b) Mesh II with elements of $4.5mm \times 4.36mm$ - $13.5mm \times 4.36mm$ ($4.5mm$ - $13.5mm$ along the height and $4.36mm$ or 0.5^0 over the circumference); (c) Mesh III with elements of $9mm \times 8.73mm$ ($9mm$ along the height and $8.73mm$ or 1^0 around the circumference); (d) Mesh IV with elements of $13.5mm \times 13.09mm$ ($13.5mm$ over the height and $13.09mm$ or 1.5^0 around the circumference). For Mesh II, the smaller elements of $4.5mm \times 4.36mm$ were used in the middle region of $12\sqrt{Rt}$ where the patterned welds were located plus 2λ (λ is the meridional bending half-wavelength and = $2.444\sqrt{Rt}$) at each end of the region. As a

result, the effect of the patterned welds is believed to completely confined to the small element region. In the rest of the shell, larger elements of $13.5mm \times 4.36mm$ with a transition zone at each end of the small elements region were used (Figure 8.1). The boundary conditions adopted for the shell segment are the same as those adopted for the complete shell, but the two meridional edges of the shell segment were imposed with symmetric boundary condition.

For a rigorous study on mesh convergence, both linear and non-linear buckling analyses were performed. Table 8.1 lists the linear buckling stresses of the four meshes and the relative differences from the linear buckling stress of Mesh I. Mesh II gave nearly the same linear buckling stress as that of Mesh I, so Mesh II can be considered to be a sufficiently converged mesh in terms of the linear buckling stress. Mesh I, which is treated as the reference mesh here, had elements with a length as small as $l/11.6\lambda$, which is believed to lead to accurate predictions. Mesh III, which is significantly coarser than Mesh II, delivered a linear buckling stress with a difference of 2.96% compared to that of Mesh I. Mesh IV is seen to be too coarse to give results of acceptable accuracy.

Figure 8.2 shows the load axial-shortening curves from non-linear analyses of the shell segment using the four different meshes, in which the axial shortening shown is that of the middle node M at the top edge of the shell segment. Obviously, the curve obtained with Mesh II is identical to that from Mesh I, but the two curves from Meshes III and IV are a little different from the curve from Mesh I near and after the peak load.

The results shown in Figure 8.2 demonstrate that Mesh II is an accurate mesh for both linear buckling analyses and non-linear analyses, but is more economic than Mesh I without any loss of accuracy in all practical terms. Mesh II was therefore adopted in modelling all three test specimens. In the numerical model of Specimen 09SC, this meshing scheme was slightly modified by using the smaller elements in a zone of 3λ rather than 2λ above and below the circumferential weld, leading to 103 elements over the shell height (including the element covering the rigid shell strake at the top end). The meridional discretizations of specimens 09QC04 and 09P0408 are identical to that of the shell segment in the mesh convergence study, leading to 127 elements over the shell height (including the end ring element). For all three specimens, the circumference was

divided into 720 elements at a spacing of 0.5^0. The total number of elements used is 74160 for Specimen 09SC, and 91440 for specimens 09QC04 and 09P0408, respectively. Consequently, each buckling analysis required a large amount of computational effort.

8.4 RESULTS FROM LINEAR BUCKLING ANALYSES

The buckling stresses from linear analyses of the three specimens and their relative differences with respect to the corresponding test results are shown in Table 8.2. The predictions of the linear buckling analyses differ from the test results by different amounts for the three specimens. For Specimen 09SC, the linear buckling stress is the same as the test buckling stress, but this is a mere coincidence as the linear buckling analysis normally overestimates the buckling stress. For Specimen 09QC04, the difference is 23%, which is in agreement with the upper bound nature of the linear buckling stress. This difference is 6.8% for specimen 09P0408, again indicating that the linear buckling stress is an upper bound solution.

The buckling modes from the linear buckling analyses are displayed in Figure 8.3. the buckling modes all have deformations concentrated around the 90^0 meridian where the geometric imperfections are much larger than those of elsewhere. The numerical buckling modes do not agree well with the deformations observed in the experiments, as in the experiments, the vicinity of 90^0 meridian was not necessary the critical region. Moreover, the shapes of linear buckling modes are also somewhat different from those observed in the experiments.

8.5 RESULTS FROM NON-LINEAR ANALYSES

The finite element ultimate loads of the three specimens from non-linear analyses and their relative differences from the corresponding test results are also presented in Table 8.2. It is clear that the finite element ultimate loads are slightly lower than the experimental loads, with the relative differences being as small as 3.5%-7.7%. Since the residual stresses in the specimens were omitted in the numerical models, the fact that finite element buckling

loads are lower than the experimental values may be interpreted to imply that the omitted residual stresses are of some benefit to the buckling strength. This observation confirms the conclusion reached by previous researchers (e.g. Rotter, 1996; Hübner *et al*, 2003a) that residual stresses in cylindrical shells under axial compression are of some benefit to the buckling strength.

The deformation modes of the specimens at the ultimate loads of the non-linear analyses are shown in Figure 8.4. It is clear that the non-linear deformation modes are significantly different from the buckling modes predicted by linear buckling analyses. Nevertheless, these deformation modes are somewhat similar in shape to buckles observed during the experiments on specimens 09QC04 and 09P0408 in the deep postbuckling stage. A similar relationship can not found for Specimen 09SC. The deformation modes of the test specimens may be very sensitive to random factors not considered in the finite element models, particularly residual stresses, therefore, the differences observed between the numerical and experimental deformation modes are not surprising.

The load-axial shortening curves of selected nodes in the finite element models are shown in Figures 8.5-8.7 respectively, together with those from the experiments. It is seen that the load-axial shortening curves from numerical analyses agree well with the experimental curves in the early stage of loading. When the load reaches a certain level, local buckling developed in the test caused the test curve to deviate from the numerical curve. Examples showing this phenomenon include the curve of the top node at 30^0 of Specimen 09SC and those of all selected nodes of Specimen 09P0408.

In the post-buckling range, the numerical load-axial shortening curves can hardly be compared with the test curves in most cases, either because the experimental curves are not available, or when they are available, they are very different from the numerical curves. There are however a few exceptions, including the node at 30^0 of Specimen 09SC and the nodes at 8.1^0 and 312.8^0 of Specimen 09QC04, for which the numerical and experimental curves show significant similarity. The differences between the numerical predictions and the experimental results in the predicted deformed shapes may be attributed to factors ignored in numerical models, such as residual stresses and the effect of welding on material properties. In these numerical analyses, the axial load was applied to the initially

stress-free geometrically imperfect model, and the steel material had properties as determined from tensile tests of the welding-free steel coupons. In the laboratory experiments, the shell has substantial residual stresses from welding and perhaps also rolling, and the steel material in the vicinity of welding could have been altered by welding. Both factors are mainly related to welding.

At a low load level, the experimental behaviour can be closely predicted by nonlinear finite element analysis because residual stresses and material property alterations are not critical at low loads; the important material parameter for low loads is the elastic modulus which is not significantly affected by welding. Therefore, at low loads, the finite element model could predict the experimental behaviour closely.

When the applied axial load is sufficiently high, residual stresses can have two effects. First, locally high compressive residual stresses combined with the axial compressive stresses from the applied axial load may lead to local buckling. This explains the premature development of small buckles during the experiments and the appearance of such buckles change the deformed shape and the load-axial shortening relationship. Second, the residual stresses combined with stresses from the applied axial load can lead to premature yielding, again altering the deformed shape and the load-axial shortening relationship. The second factor is expected to be of less significance in the present shells until the deep postbuckling stage, as they are very thin. These factors explain why there are significant differences in the deformed shapes between the tests and the finite element analyses. In the stage of post-buckling when yielding becomes important, the welding-induced alternations to material properties may also become significant.

The fact that the ultimate loads from nonlinear analyses are close to the test results are another phenomenon confirming that the differences in the deformed shapes are due to welding effects and in particular residual stresses. These residual stresses are in self-equilibrium so compressive residual stress zones are localised and separated by tensile residual stress zones. The localised nature of these residual compressive stresses means that when a local buckle develops, the axial stresses in that region can no longer increase. The stresses in the shell wall then undergo a process of re-distribution during which more stresses are attracted by other parts of the shell wall until the next local buckle occurs. The overall axial load can continue to increase until no further redistribution is possible.

8.6 CONCLUSIONS

This chapter has been concerned with the finite element modelling of the buckling experiments on welded steel cylinders under axial compression presented in Chapter 7. Results from both linear buckling analyses and non-linear analyses considering both geometric and material nonlinearities have presented and compared with experimental results.

The finite element models, which were built using shell element S4 in the finite element package ABAQUS, included the geometric imperfections precisely measured during the experiments, but omitted the associated residual stresses and any welding effect on steel material properties because they were not measured. Based on a mesh convergence study, an accurate but economic mesh was used to model the test specimens.

The buckling loads from the finite element linear buckling analyses are significantly higher than the corresponding experimental loads for two of the specimens. This is consistent with common expectations that a linear buckling analysis generally gives an upper bound on the actual buckling load. For one of the specimen, however, the linear buckling load coincides with the test buckling load, which is unexpected. In addition, the linear buckling modes are generally very different from those observed during the experiments.

The ultimate loads of the shells from geometrically and materially non-linear analyses are close to but slightly lower than the experimental values, confirming that residual stresses can have a small beneficial effect on the buckling strength, a conclusion that has been reached by previous researchers through theoretical studies. The load-axial shortening curves from the non-linear analyses agree well with the experimental curves at early stages of loading, but near the attainment of the peak load and afterwards, the finite element curves do not generally agree with the experimental curves. The deformed shapes from the nonlinear analyses are also significantly different from those observed during the experiments. These differences are attributed to factors not included in the numerical models, mainly the inevitable residual stresses associated with the welds and to some extent the changes in material properties induced by welding.

In summary, non-linear finite element analyses of axially-compressed welded cylindrical shells of the kind studied here, with geometric imperfections taken into account, can give close predictions of the buckling loads. The residual stresses in the shell wall can cause significant changes in the deformation history and shape, but their effect on the buckling strength is small and beneficial. The residual stresses can be safely ignored in nonlinear finite element analyses aimed at close predictions of the buckling strengths.

Table 8.1 Linear buckling stresses of a shell segment from different meshes, σ_{cl} = 212.78 MPa

Mesh $(mm \times mm)$	I	II	III	IV
$\sigma_{cr}^{(i)}/\sigma_{cl}$	0.3171	0.3171	0.3265	0.3438
$(\sigma_{cr}^{(i)} - \sigma_{cr}^{(I)})/\sigma_{cr}^{(I)}$	0%	0.006%	2.96%	8.43%

Table 8.2 Buckling stresses of the test specimens from linear buckling analyses and non-linear analyses, σ_{cl} = 212.78MPa

Specimen	Test Result	Linear Buckling Analysis		Non-linear Analysis	
		Numerical Result	Relative Difference	Numerical Result	Relative Difference
09SC	$0.298\sigma_{cl}$	$0.298\sigma_{cl}$	0%	$0.275\sigma_{cl}$	-7.7%
09QC04	$0.283\sigma_{cl}$	$0.348\sigma_{cl}$	23%	$0.273\sigma_{cl}$	-3.5%
09P0408	$0.279\sigma_{cl}$	$0.298\sigma_{cl}$	6.8%	$0.26\sigma_{cl}$	-6.8%

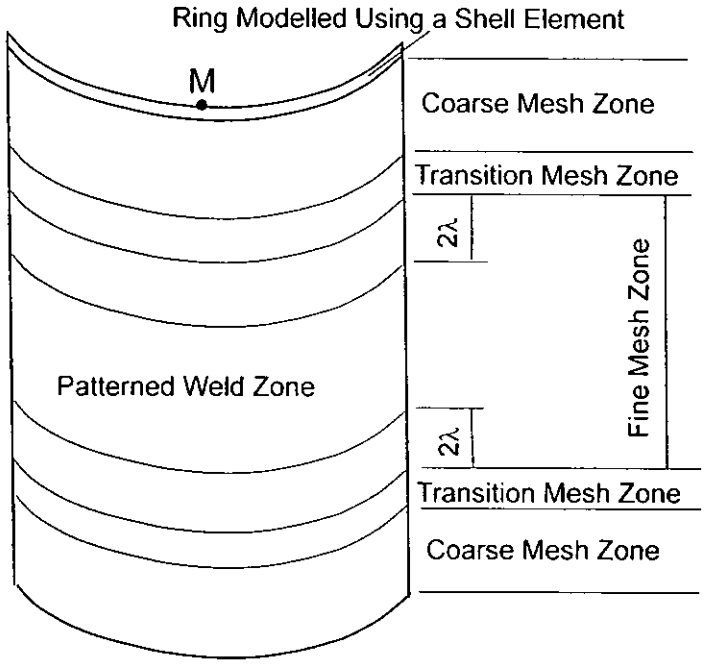

Figure 8.1 The 60^0 shell segment model

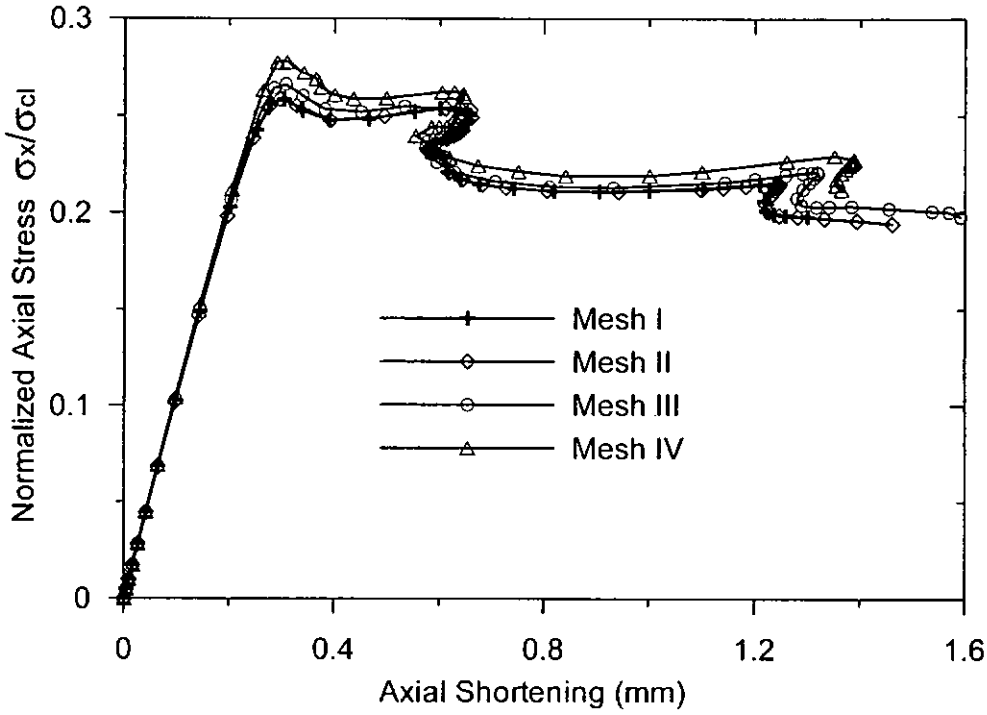

Figure 8.2 Load-axial shortening curves of Node M from various meshes, σ_{cl} = 212.78MPa

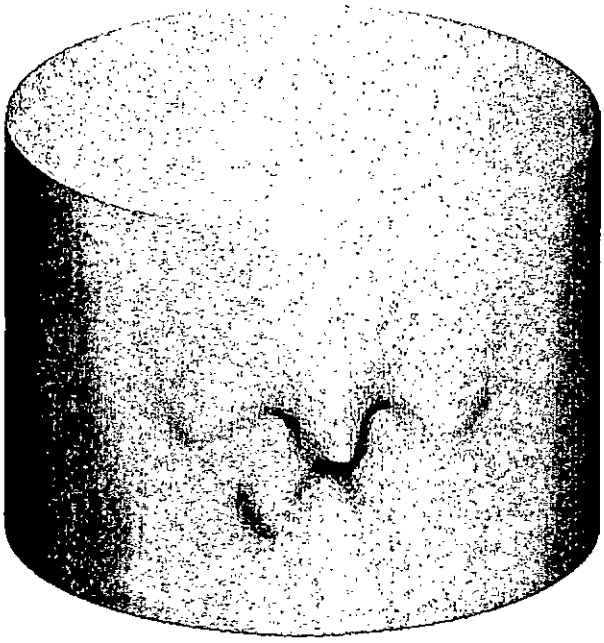

(a) Specimen 09SC

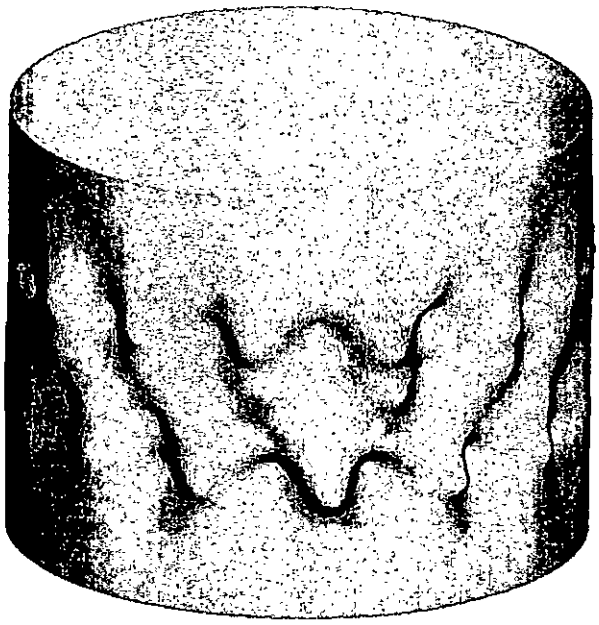

(b) Specimen 09QC04

Figure 8.3 Linear buckling modes

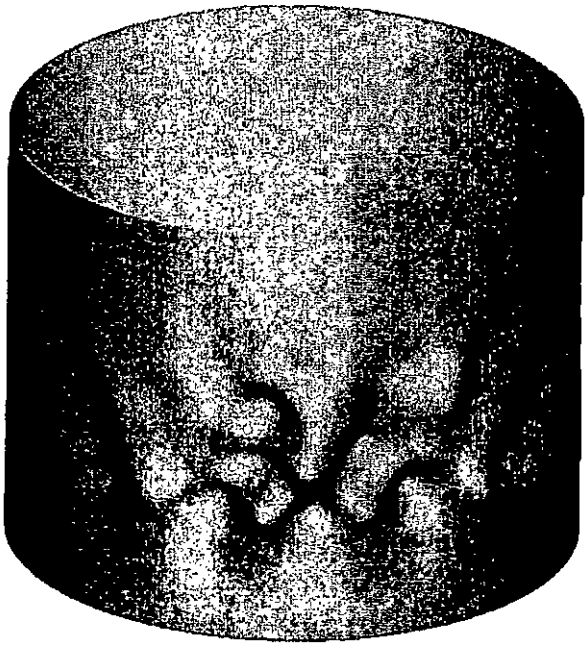

(c) Specimen 09P0408

Figure 8.3 Linear buckling modes

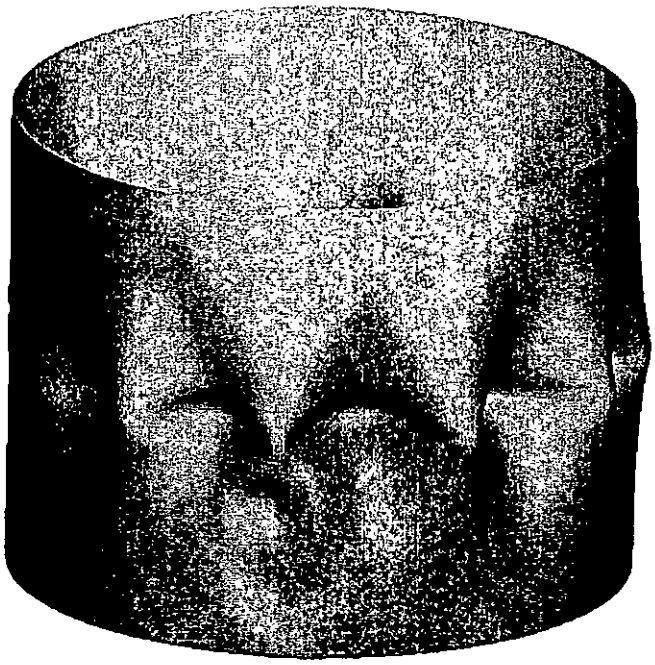

Scale of deformation=20

(a) Specimen 09SC

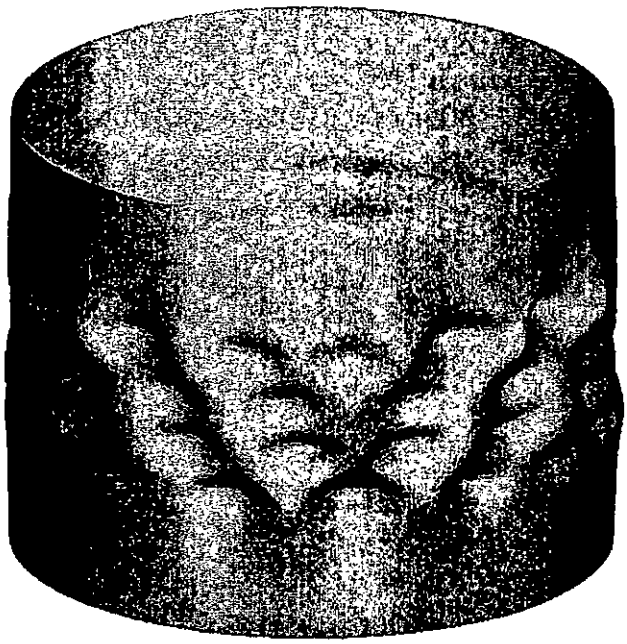

Scale of deformation=20

(b) Specimen 09QC04

Figure 8.4 Deformation shapes at peak load from non-linear analyses

Scale of deformation=20

(c) Specimen 09P0408

Figure 8.4 Deformation shapes at peak load from non-linear analyses

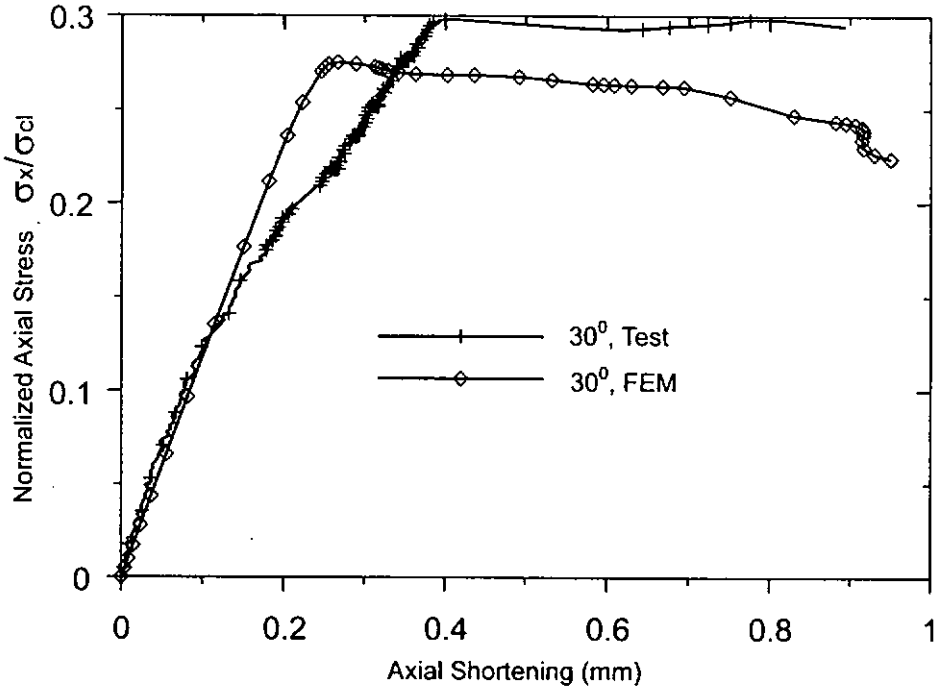

(a) Top point of the 30^0 meridian

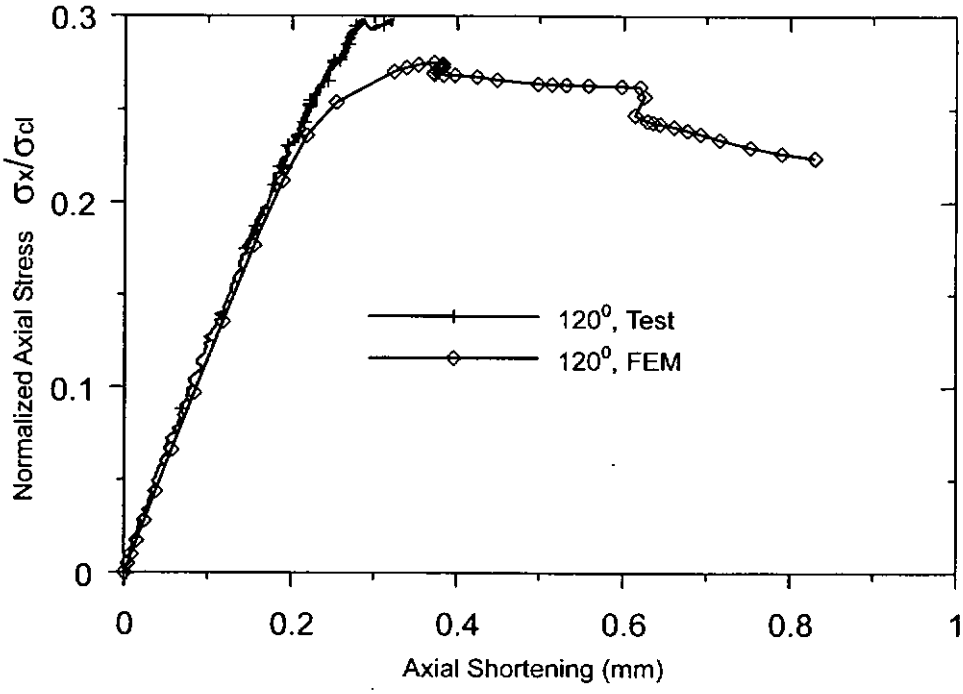

(b) Top point of the 120^0 meridian

Figure 8.5 Load-axial shortening curves of selected locations in Specimen 09SC, σ_{cl} = 212.78 MPa

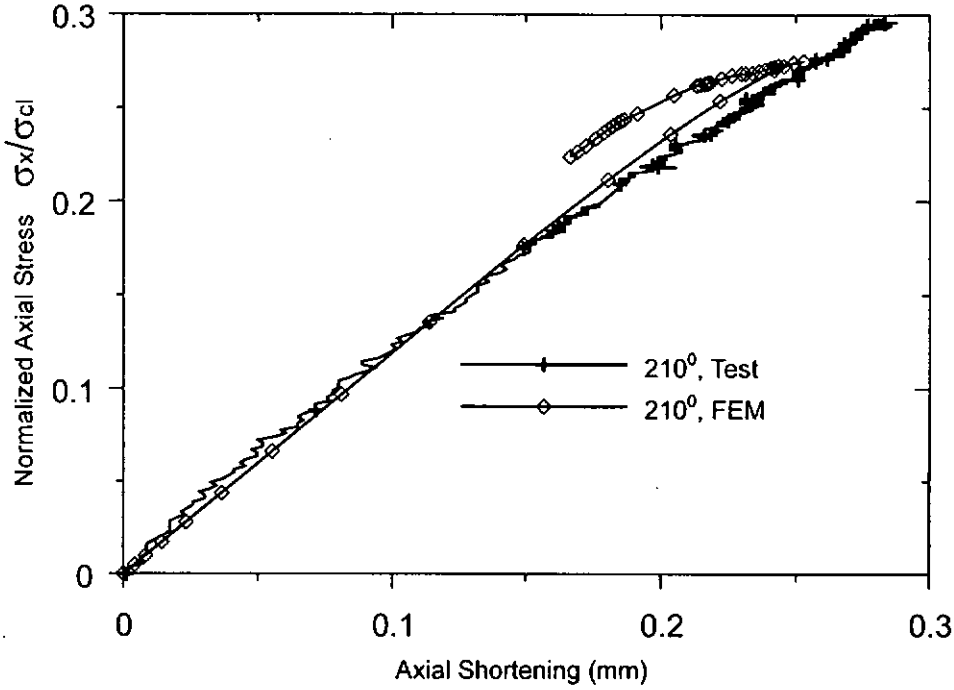

(c) Top point of the 210^0 meridian

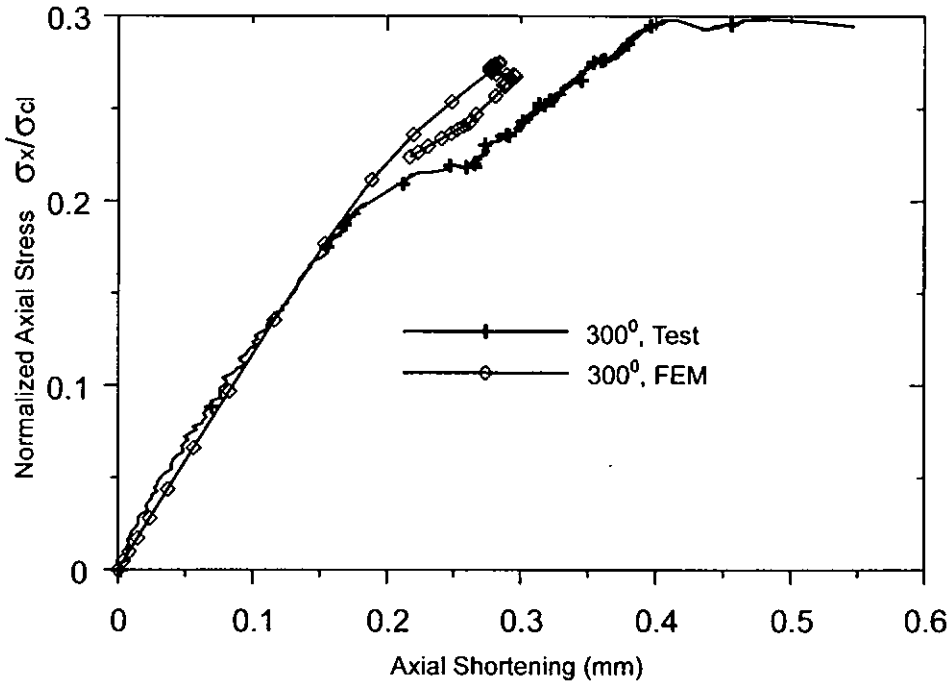

(d) Top point of the 300^0 meridian

Figure 8.5 Load-axial shortening curves of selected locations in Specimen 09SC, σ_{cl} = 212.78 MPa

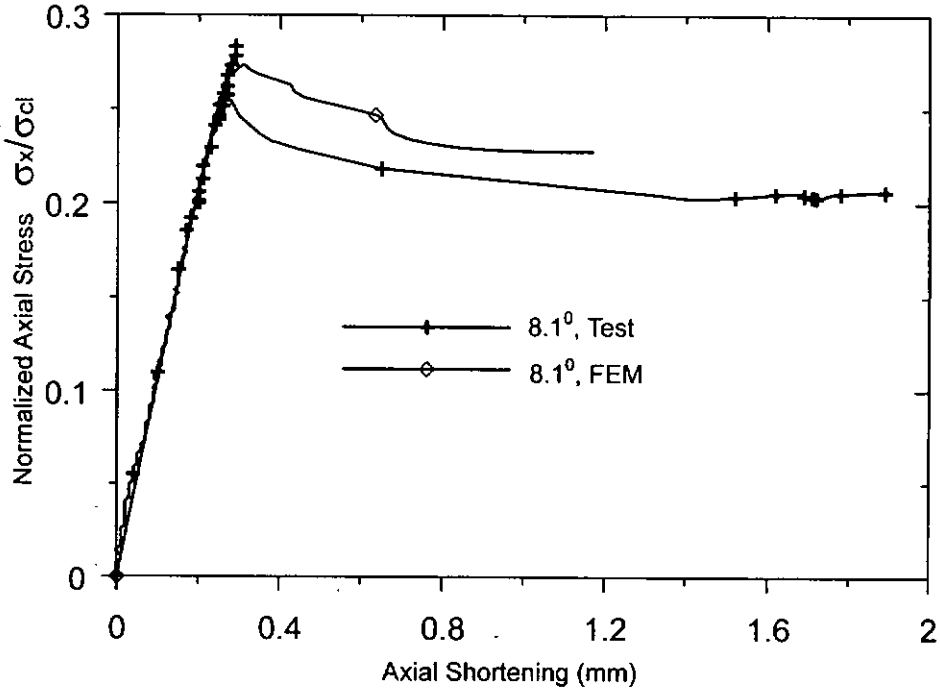

(a) Top point of the 8.1^0 meridian

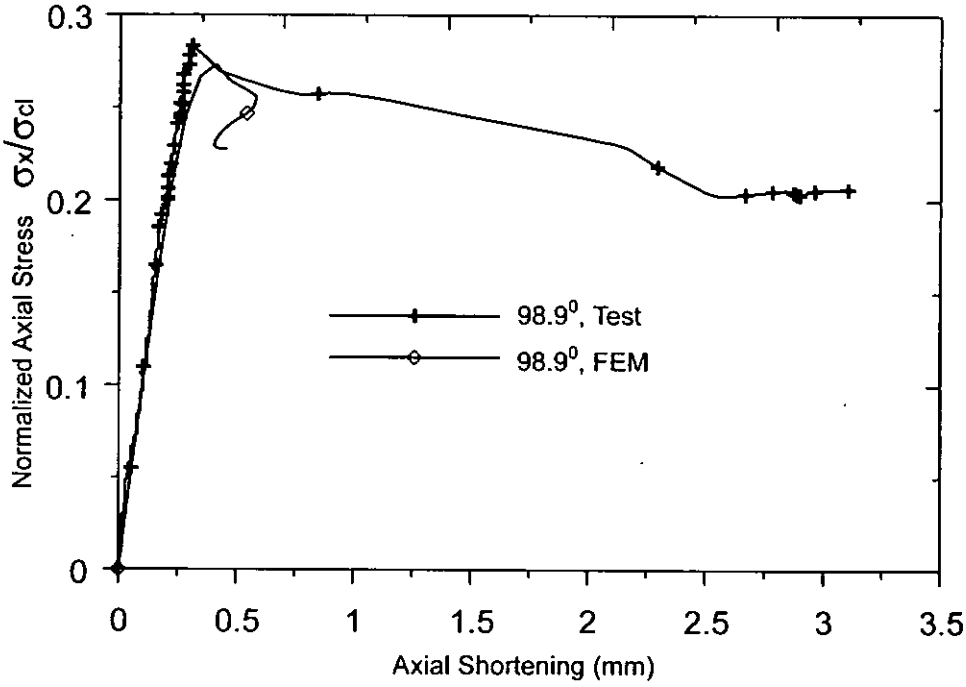

(b) Top point of the 98.9^0 meridian

Figure 8.6 Load Axial Shortening Curves of the Selected Nodes at Specimen 09QC04, σ_{cl} = 212.78 MPa

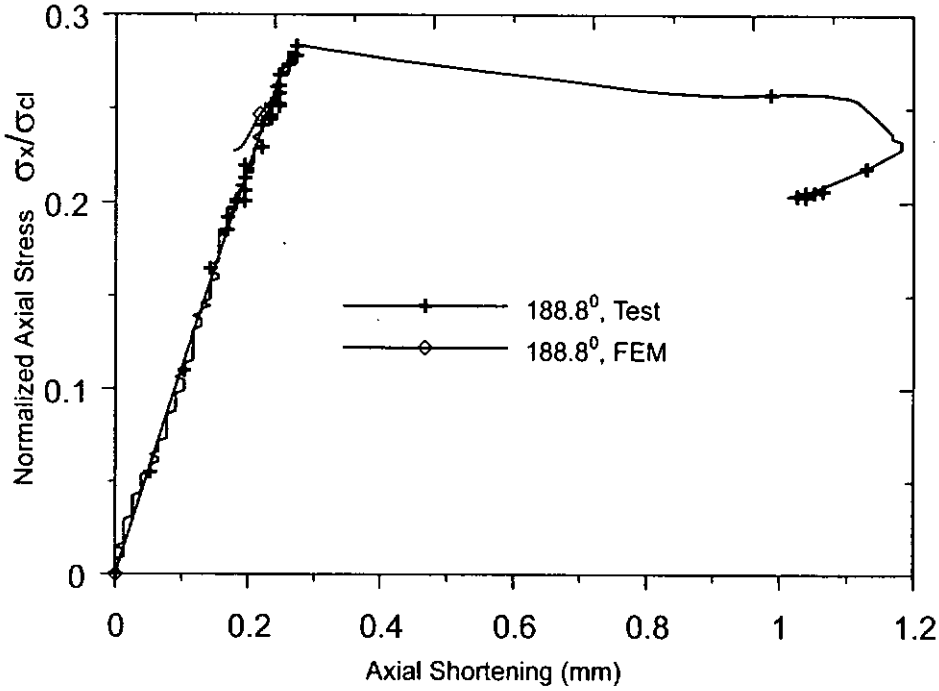

(c) Top point of the 188.8^0 meridian

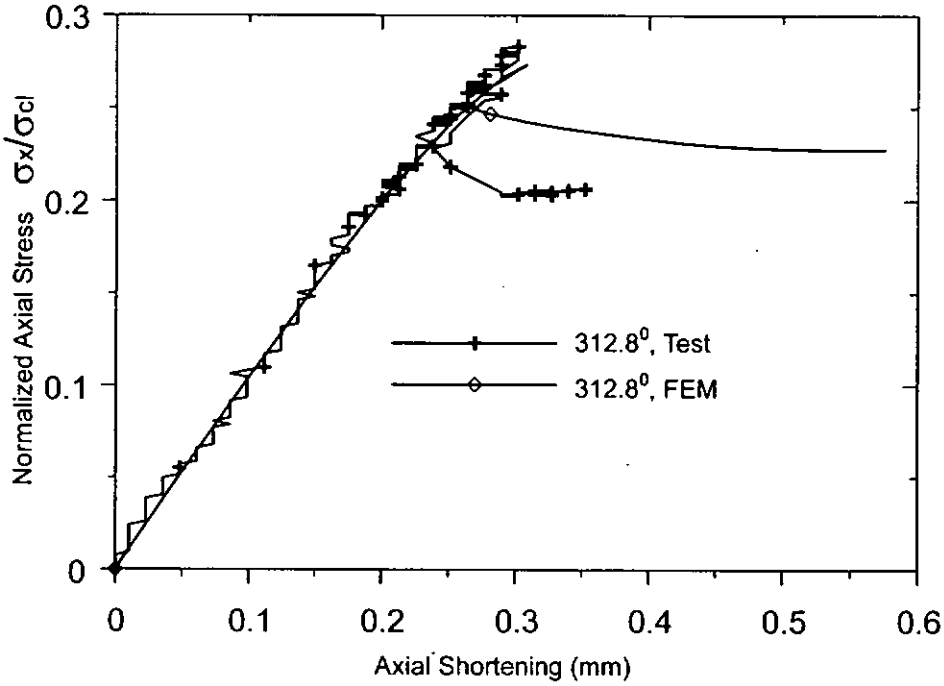

(d) Top point of the 312.8^0 meridian

Figure 8.6 Load Axial Shortening Curves of the Selected Nodes at Specimen 09QC04, σ_{cl} = 212.78 MPa

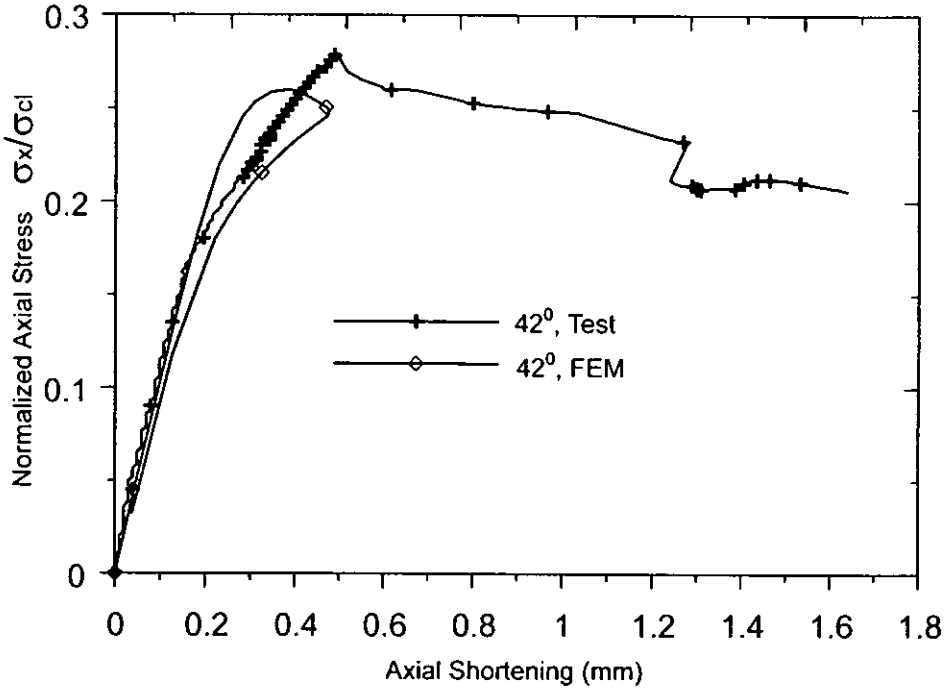

(a) Top point of the 42^0 meridian

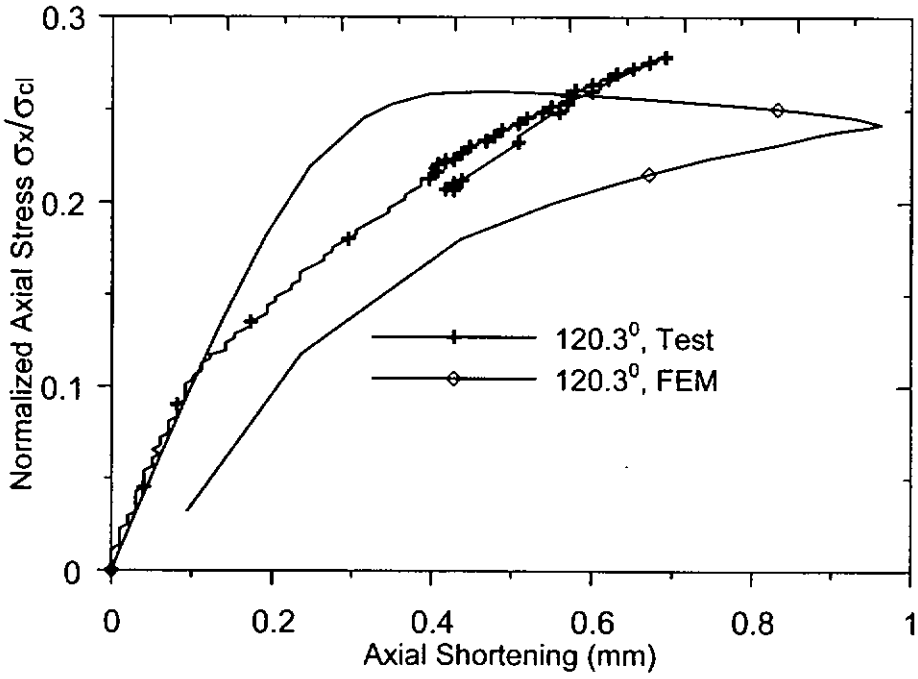

(b) Top point of the 120.3^0 meridian

Figure 8.7 Load-axial shortening curves of selected locations in Specimen 09P0408, σ_{cl} = 212.78 MPa

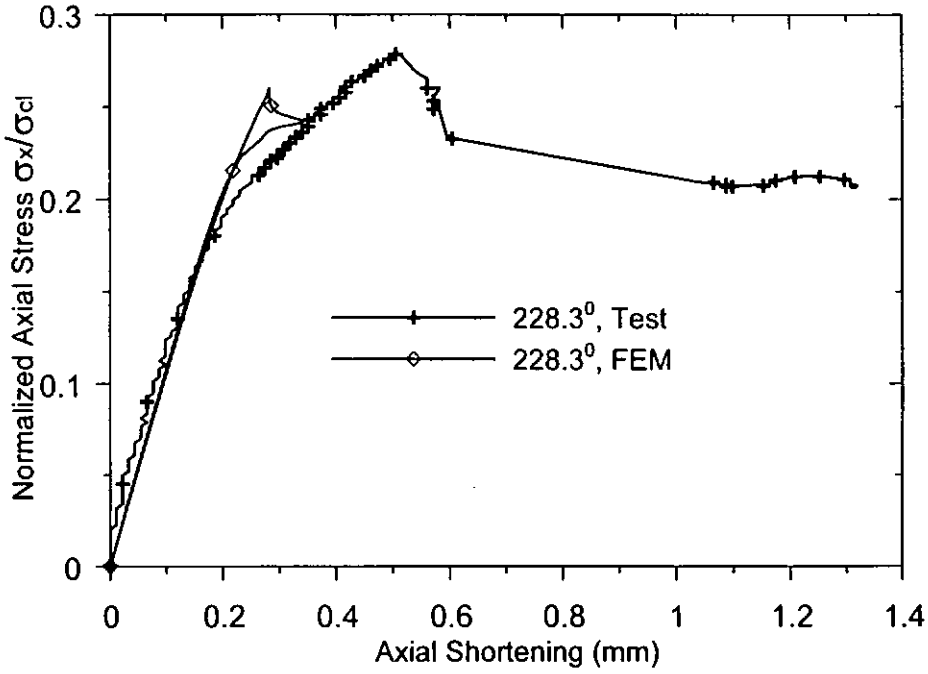

(c) Top point of the 228.3^0 meridian

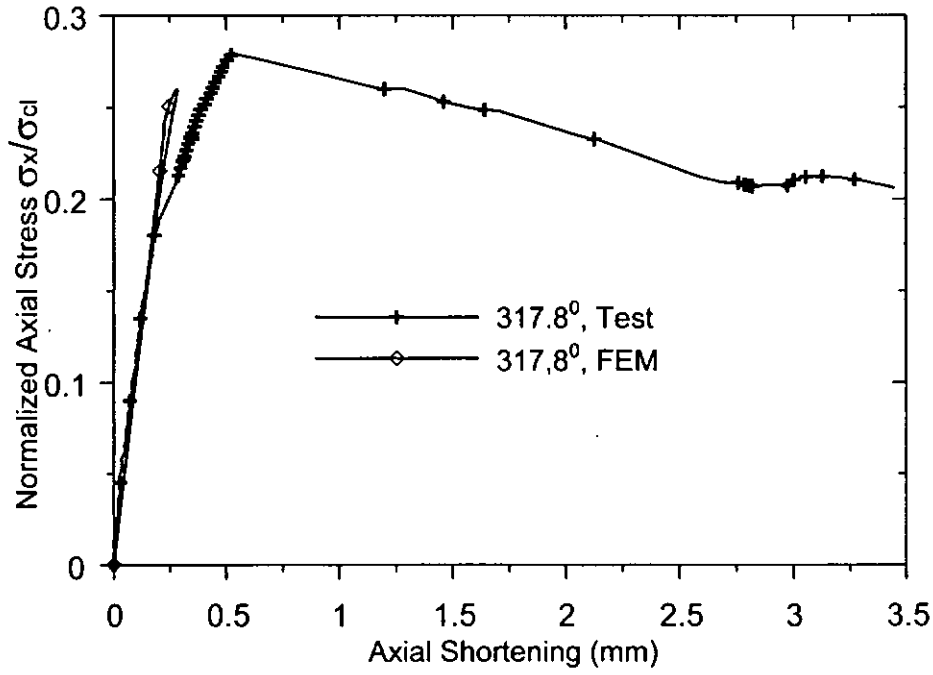

(d) Top point of the 317.8^0 meridian

Figure 8.7 Load-axial shortening curves of selected locations in Specimen 09P0408, σ_{cl} = 212.78 MPa

CHAPTER 9

EXTENSIVELY WEDLED STEEL CYLINDERS UNDER COMBINED AXIAL COMPRESSION AND INTERNAL PRESSURE

9.1 INTRODUCTION

Cylindrical shells in steel silos are subject to both axial compression and internal pressure as a consequence of interactions between the stored bulk solid and the shell wall. The buckling strength under axial compression, which often dominates the design of a cylindrical shell, is acutely sensitive to both the form and the amplitude of the imperfections in the shell (see review by Teng, 1996). When the shell is simultaneously subject to internal pressure, this imperfection sensitivity declines (Rotter, 1990). At low levels of internal pressure, an axially compressed cylindrical shell fails by elastic buckling at a load higher than that of the corresponding un-pressurized cylinder; at intermediate levels of internal pressure, further load increases may be found, but the failure mode may change from elastic buckling to plastic buckling; at high levels of internal pressure, the internal pressure reduces the axial buckling strength, and the shell fails by local plastic collapse (Rotter, 1990). The plastic collapse mode often occurs near a boundary condition ('elephant foot failure') but can also occur at local imperfections in the shell wall. Many failures of silos and tanks in service indicate that buckling or collapse failure under combined axial compression and internal pressure is the strength-controlling mode.

This chapter presents the results of a parametric study into the effect of internal pressurization on the buckling and collapse strengths of axially compressed cylindrical shells in steel silos (Ding, 1992). In this study, the behavior of the three large cylindrical shells in the Port Kembla silos with precisely measured geometric imperfections was analyzed for different levels of internal pressurization using the general purpose finite element package ABAQUS (Hibbitt, Karlsson & Sorensen, 1998). The strength gains

arising from internal pressurization were also compared with the existing design rule Eurocode 3 (ENV1993-1-6, 1999). Modifications to this design rule are also proposed.

9.2 PREVIOUS STUDIES

The elastic buckling behavior of thin cylindrical shells under the combined action of axial compression and internal pressure has been explored in many studies (e.g. Lo *et al*, 1951; Fung and Sechler, 1957; Lu and Nash, 1962; Hutchinson, 1965; Gorman and Evan-Iwanowski, 1970; Esslinger and Geier, 1975; Saal *et al*, 1979; Rotter and Teng, 1989, Teng and Rotter, 1992; Hübner et al, 2003a). The strength gains due to internal pressurization are significantly imperfection dependent in the elastic range. Hutchinson (1965) showed that the strength gains due to internal pressurization depend significantly on whether the imperfections in the shell are predominantly axisymmetric or predominantly non-axisymmetric. For a shell with asymmetric imperfections only, the buckling load can approach the classical value at a relatively small internal pressure, whereas for a shell with axisymmetric imperfections only, the elastic buckling load remains much smaller than the classical value even at a much higher internal pressure. These observations have been verified by tests for the case of asymmetric imperfections (e.g. Weingarten *et al*, 1965), as well as for the case of predominantly axisymmetric imperfections (e.g. Bucklin *et al*, 1983; Rotter, 1985a). Hutchinson's theory (1965) was later re-examined by Rotter and Seide (1987) for pressurized cylinders with axisymmetric imperfections, and the low strengths predicted by Hutchinson's theory were confirmed for a wider range of variables, and a more precise approximation developed.

Even within the realm of axisymmetric imperfections, different shapes or wavelengths of imperfections can lead to considerably different results. Teng and Rotter (1992) carried out a systematic investigation into the strengths of axially compressed internally pressurized cylinders with three different forms of axisymmetric imperfections: an inward local depression of TYPE-A of their previous study (Rotter and Teng, 1989), an outward local bulge of the same form, and the sinusoidal imperfection used by Hutchinson (1965). They found that sinusoidal imperfections lead to the slowest strength gains due to internal pressurization, while the inward local depressions lead to the fastest strength gains, with outward local deviations being between the these two. Based on the imperfections

measured on the Port Kembla silos (Ding, 1992), Rotter (1996) proposed four types of axisymmetric imperfections, included them into his numerical analyses, and produced significantly different results.

Residual stresses are always associated with geometric imperfections in welded shell structures such as silos and tanks. However, this effect is seldom examined in theoretical studies due to the difficulty of postulating a pattern of residual stresses in equilibrium. Only a few studies have been found addressing this respect, including Rotter (1996), Pircher and Bridge (2001a), Host et al (2000), and Hübner (*et al*, 2003a) in which residual stresses satisfying equilibrium requirements were imposed by specifying residual strains. These studies suggested that residual stresses due to circumferential welds are somewhat beneficial to the elastic buckling strength. Hübner *et al* (2003a) also examined the effect of the residual stresses arising from meridional welds and patterned welds and reported a slightly detrimental effect for the former but a beneficial effect for the latter.

The plastic failure behaviour of axially compressed cylindrical shells with a high internal pressure has been relatively less explored. For a thin cylindrical shell (here $R/t > 250$) subjected to axial compression only, failure generally occurs at a stress below the yield stress, so only elastic buckling is of concern. However, when a large internal pressure co-exists, yielding may occur in the zone of local bending near a boundary support, a variation in wall thickness, a stiffener, or other local changes. Yielding in a shell can lead to local loss of stiffness, triggering a local axisymmetric plastic collapse failure. Rotter (1983) proposed a first-yield criterion to provide a lower bound to the strengths of perfect cylinders failing in this mode. Rigorous studies have examined this failure mode near a boundary (Rotter, 1985, 1990), at a local axisymmetric imperfection (Rotter, 1988, 1996), and at a lap joint (Teng, 1994). It has been found that the plastic collapse strength of an internally pressurized shell under axial compression is also sensitive to both the form and amplitude of a local axisymmetric imperfection at internal pressures lower than $0.9tf_y/R$ (Rotter, 1996). Between the low range of pressures responsible for elastic buckling failures and the high range of pressures responsible for plastic axisymmetric collapse failures, plastic non-symmetric buckling occurs in perfect shells or axisymmetrically-imperfect shells for a small intermediate range of pressures.

In a real shell with imperfections containing both axisymmetric and complex non-axisymmetric components, the distinction between non-symmetric buckling and axisymmetric collapse is no longer possible as the deformations are always non-axisymmetric in the strict sense. For ease of description, the term "plastic failure" may be used to cover all failures which occur after yielding of steel. The plastic failure strengths of axially compressed internally compressed cylinders with real or realistic imperfections can only be obtained by carrying out geometrically and materially nonlinear imperfect shell analyses of these shells. No such analyses appear to have previously been carried out for shells with precisely measured imperfections. The closest attempt has been that made by Hübner (*et al*, 2003a) who adopted the shrinkage strain method (Rotter, 1996) to simulate imperfections in welded shells, but imperfections from sources other than welding were omitted in their study.

The relevant design rule in Eurocode 3 (ENV1993-1-6, 1999; ENV1993-4-1, 1999) is based on either studies of cylindrical shells with local axisymmetric imperfections due to circumferential welds in silo structures (e.g. Rotter and Teng, 1989; Teng and Rotter, 1992; Rotter, 1996, 1997) or those of perfect cylinders (e.g. Rotter, 1985, 1990). The accuracy of these rules has not been checked with results obtained for shells with real imperfections. This chapter presents a numerical study aimed to correct this deficiency of current knowledge.

9.3 FINITE ELEMENT ANALYSIS

The three imperfect cylindrical shells in the large Port Kembla silos, whose buckling behaviour has been explored in Chapter 5, were employed as the subject shells in the present study. Geometrically and materially nonlinear analyses of these shells were carried out using the general-purpose finite element package ABAQUS (Hibbit, Karlsson & Sorensen, 1998), which was also used in the work presented in the previous chapters. The geometric and material properties of the three shells and their finite element models employed in this study are identical to those described in Chapter 5, but the applied loading now includes internal pressure in addition to axial compression. The geometric imperfections measured on these shells (Ding, 1992) were accurately included in the numerical models as described in Chapter 5.

Although residual stresses always exist in these welded shells, they are not included in these analyses as they were not measured. The omission of residual stresses is unlikely to have significantly affected the predicted behavior, based on the conclusion reached in Chapter 8 that residual stresses in cylinders with many welds have only a small but beneficial effect on the ultimate strength of welded cylinders under axial compression. For elastic cylinders under combined axial compression and internal pressure, it has been shown theoretically that residual stresses due to both circumferential welds only (Rotter, 1996; Hübner *et al*, 2003a) and patterned welds (Hübner *et al*, 2003a) have a small beneficial effect and those arising from meridional welds only have a small detrimental effect on the shell buckling strength. For corresponding cylinders at higher internal pressures and experiencing plastic failures, residual stresses due to circumferential welds only have been found to have little influence on the shell plastic collapse strength (Rotter, 1996), and a similar situation can be expected for shells with realistic imperfections.

Ten levels of pressurization in terms of $\overline{p}_y = pR/tf_y$ were considered for all three shells (Shells A, B and C). These ten levels are $\overline{p}_y$=0.1, 0.2, 0.3, 0.4, 0.5, 0.6, 0.7, 0.8, 0.9, and 1.0. It should be noted that $\overline{p}_y = \overline{p}\sigma_{xRc}/f_y$ ($\overline{p}$, defined by Eqn. 2.15, is the normalized internal pressure used in ENV1993-1-6 (1999), and σ_{xRc} is the elastic critical meridional buckling stress of the shell). Each analysis consisted of two steps: the internal pressure was applied first, followed by the application of axial compression, for which the solution was found in via an incremental-iterative process by the modified Riks method (Riks, 1979).

9.4 FINITE ELEMENT RESULTS

Figures 9.1-9.10 displays the deformed shapes of Shell A at the ultimate load with different levels of internal pressurization. These figures show that the deformed shapes of Shell A are dominated by several large meridional ridges distributed around shell circumference. These ridges become larger with an increase in internal pressurization. Apart from these ridges, there are significant circumferential local bulges at the shell ends. These bulges are believed to be particularly important at high levels of internal

pressurization, as they are similar in shape to the 'elephant foot' failure mode which often occurs near the ends. For the case of internal pressurization only, the deformed shape involves almost uniform radial expansion except near the two edges as can be expected (Figure 9.10).

The deformed shapes of Shell B at the ultimate load for different levels of internal pressurization (Figures 9.11-9.20) assume many small ridges running around the shell circumference at low levels of internal pressurization. In addition, a few meridional ridges and circumferential bulges at the shell ends are also seen. With increases in internal pressurization, the small circumferential ridges give way to the circumferential bulges at the shell ends and the meridional ridges. The circumferential bulges at the shell ends become predominant at high levels of internal pressurization, suggesting a nearly-axisymmetric plastic collapse failure mode.

The deformed shapes of Shell C at the ultimate load are significantly different from those of Shells A and B, as they take the form of many small buckles at low levels of internal pressurization and gradually evolve into feature larger irregular buckles and circumferential local bulges at the shell ends with increases in internal pressurization (Figures 9.21-9.30). Despite that the deformed shapes of the three shells at the ultimate load are different, they have one feature in common: with a high level of internal pressurization, all of them develop large circumferential bulges at the shells end, suggesting a local collapse failure near the shell ends.

Figure 9.31 shows the ultimate strengths of the three shells from nonlinear finite element analyses. When the internal pressure is low ($\overline{p}_y < 0.2$), the shells fail by elastic buckling; at higher internal pressurization ($\overline{p}_y \geq 0.3$), the failure mode changes into plastic buckling. Yielding generally first occurs at on the inner surface near the ends, which confirms Rotter's (1990) observation. It can be seen that the strengths of Shell A are significantly lower than those of Shells B and C, while the strengths of the later two shells are close to each other. This phenomenon can be explained by considering the different forms of their dominant imperfection components. The dominant imperfection components in Shell A are significantly axisymmetric (Figure 5.30) whereas those of Shells B and C are much more unsymmetric (Figures 5.31-5.32). The present results thus concur with the existing

conclusion that axisymmetric imperfections lead to the lowest strength gains from internal pressurization (Hutchinson, 1965).

9.5 COMPARISON WITH CODE PREDICTIONS

Eurocode 3 (ENV1993-1-6, 1999) adopted Rotter's (1998a) proposal which employs two equations to depict the elastic buckling strength at low levels of internal pressurization (Eqn 2.14) and plastic buckling/collapse strength at high levels of internal pressurization (Eqn 2.16). Eqn 2.14 is based on many recent studies (e.g. Rotter and Teng, 1989; Teng and Rotter, 1992, Rotter, 1996, 1997) which considered a shell with a single axisymmetric weld depression or part of a shell including one axisymmetric weld depression with anti-symmetric boundary conditions imposed at its both ends to simulate the effect of interaction between adjacent weld depressions, Eqn 2.16 was proposed on the basis of Rotter's (1990) study in which a short length of a perfect shell near the base was studied.

The ultimate loads from the present finite element analyses are compared in Figures 9.32-9.34 with the predictions of the design rule in Eurocode 3 (ENV1993-1-6,1999; ENV1993-4-1, 1999) for Shells A, B, and C, respectively. At low levels of internal pressurization when the shells are governed by elastic buckling, Eqn 2.14 overestimates the finite element results of Shell A but underestimate those of Shells B and C. The conservative predictions of Eqn 2.14 for Shells B and C can be easily understood, as Eqn 2.14 was deduced from axisymmetrically imperfect shells which show slower strength gains with internal pressurization, whereas the dominant imperfection components in Shells B and C are unsymmetric. The optimistic predictions of Eqn 2.14 for Shell A with axisymmetric imperfection components being dominant may be attributed to the fact that the interaction between adjacent weld depressions is not well represented by Eqn 2.14. This equation was derived on the basis of studies considering a single circumferential weld depression (e.g., Rotter and Teng, 1989, Teng and Rotter, 1992).

At higher levels of internal pressurization, the shells fail by buckling/collapse after plastic deformation, and Eqn 2.16 gives unconservative predictions for all three shells. The code predictions are only slightly unconservative for Shells B and C, but considerably unsafe for Shell A. This may be attributed to that fact that Eqn 2.16 was derived from the results

of a perfect shell, so the effect of geometric imperfections was ignored. The imperfections do play a significant role in shell plastic buckling/collapse failures, and this can be easily understood by comparing the ultimate loads of the three shells: the ultimate loads of Shell A are considerably lower than those of Shells B and C due to the different forms of the dominant imperfection components in these three shells. It may be concluded that, for a shell subject to the combined action of axial compression and internal pressure, axisymmetric imperfections lead to the lowest strength not only in elastic range but also in the plastic range.

9.6 DESIGN PROPOSAL

From the above discussions, it becomes obvious that the design rule in Eurocode 3 (ENV1993-1-6, 1999) can be rather unsafe for the design of steel silos, so modifications should be made to Eqns 2.14 and 2.16 for a safe design.

Both of these two equations are semi-empirical approximations to numerical results, so modifications to these equations can only follow the same semi-empirical procedure. In addition, it is preferable that the modified equations are in the same form so that they can conveniently replace the existing equations in the code. The finite element ultimate loads of Shell A should be the basis of the modifications, as they are the lowest among the three shells. Based on the above considerations, the following two equations are proposed to represent the imperfection factors based on the elastic buckling and plastic failure loads of Shell A, respectively:

$$\alpha_{xpe} = \alpha_x + (1-\alpha_x)\left(\frac{0.8\bar{p}}{\bar{p} + 0.3/\sqrt{\alpha_x}}\right) \tag{9-1}$$

$$\alpha_{xpp} = \left(1 - \frac{\bar{p}}{\bar{\lambda}_x}\right)\left(1 - \frac{1}{1.12 + s^{3/2}}\right)\left(\frac{s^2 + 1.21\bar{\lambda}_x^2}{1.54s(s+1)}\right) \tag{9-2}$$

$$\bar{p} = \frac{pR}{t\sigma_{xRc}} \tag{9-3}$$

$$s = \frac{1}{400}\frac{R}{t} \tag{9-4}$$

where α_{xpe} is the imperfection reduction factor with the effect of internal pressurization included, α_{xpp} is a factor accounting for pressure-induced plastic destabilization, σ_{xRc} is the elastic axial buckling stress of the perfect shell given by Eqn 2.1 for shells of intermediate lengths, p is the internal pressure, $\bar{\lambda}_x$ is the non-dimensional shell slenderness parameter given by $\bar{\lambda}_x = \sqrt{f_y/\sigma_{xRc}}$, and f_y is the yield stress.

Actually, Eqns 9.1 and 9.2 were obtained from Eqns 2.14 and 2.16 by the multiplication of knock down factors of 0.8 and 0.65, respectively. The use of knock down factors to provide lower predictions is reasonable for empirical expressions, as the relationships between parameters in the original expressions are maintained.

Figure 9.35 shows comparisons of the failure loads of the three shells with the predictions of Eqns 9.1 and 9.2. It is clear that the predictions of Eqns 9.1 and 9.2 agree well with the FE predictions for Shell A, and these two equations lead to safe designs for all three shells.

9.7 CONCLUSIONS

This chapter has presented the first ever rigorous investigation into the failure behaviour and strength of extensively welded steel cylindrical shells with precisely measured geometric imperfections subject to the combined action of axial compression and internal pressure. A series of geometrically and materially nonlinear analyses were carried out for the three cylindrical shells of the large Port Kembla silos using ABAQUS (Hibbit, Karlsson and Sorensen, 1998). These analyses covered ten different levels of internal pressurization. The results were discussed and compared with predictions of the relevant design rule in Eurocode 3 (ENV1993-1-6, 1999).

It has been found that the dominant imperfection components identified for a shell subjected to axial compression alone also govern the failure strength of the shell under the combined action of axial compression and internal pressure. Axisymmetric imperfections have been found to lead to the lowest failure strengths in both the elastic range and the elastic-plastic range.

The predictions of the design rule in Eurocode 3 (ENV1993-1-6, 1999) have been shown to be un-conservative when the dominant imperfection components are axisymmetric. This is believed to be a result of the basis of the design rule in the code: the rule was based on results of numerical models which did not taken into proper account the effect of interaction between adjacent weld depressions. Modifications to the existing rule have been proposed and this new rule leads to safe predictions for all three shells.

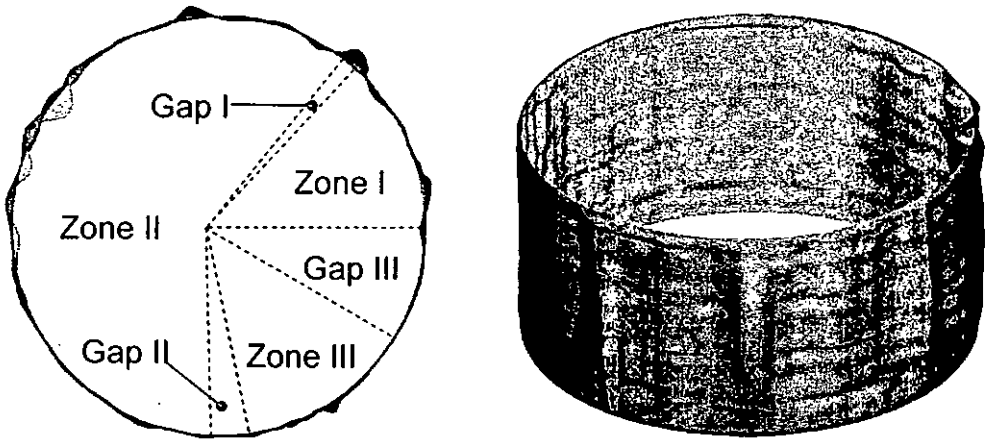

(a) Plan View (b) Perspective View

Deformation scaled by a factor of 50

Figure 9.1 Deformed shape of Shell A at ultimate load ($\bar{p}_y = 0.1$)

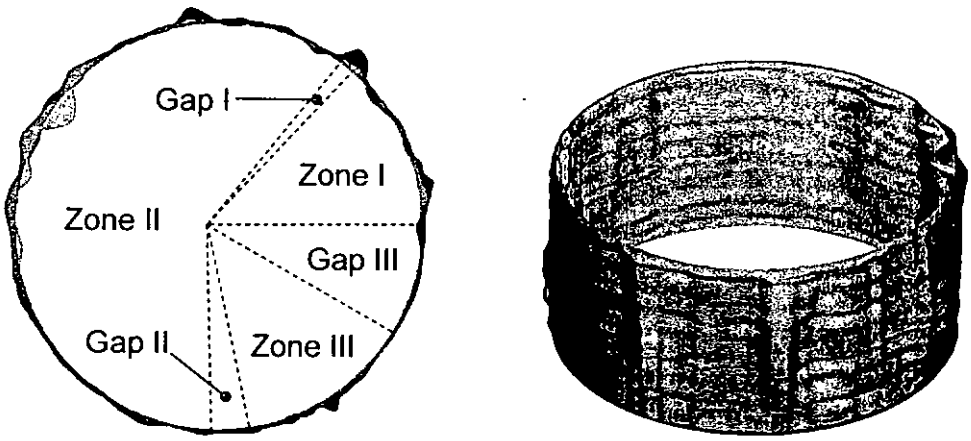

(a) Plan View (b) Perspective View

Deformation scaled by a factor of 50

Figure 9.2 Deformation mode of Shell A at ultimate load ($\bar{p}_y = 0.2$)

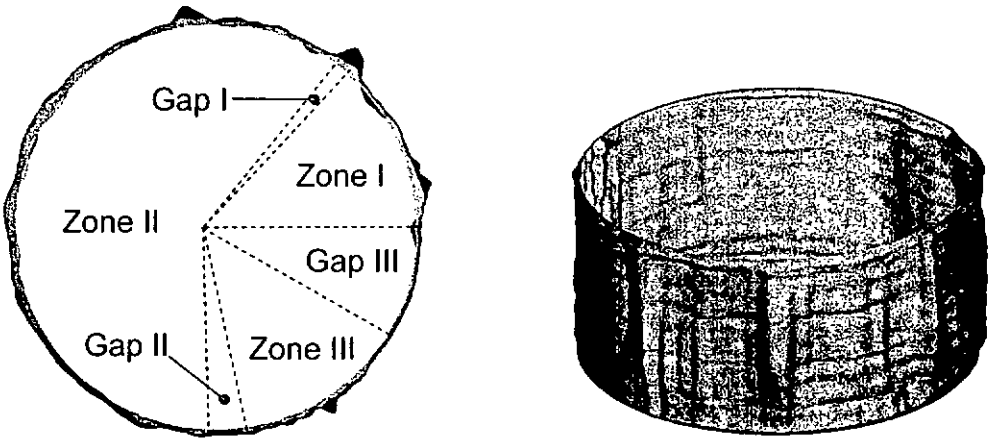

(a) Plan View (b) Perspective View

Deformation scaled by a factor of 50

Figure 9.3 Deformed shape of Shell A at ultimate load ($\bar{p}_y = 0.3$)

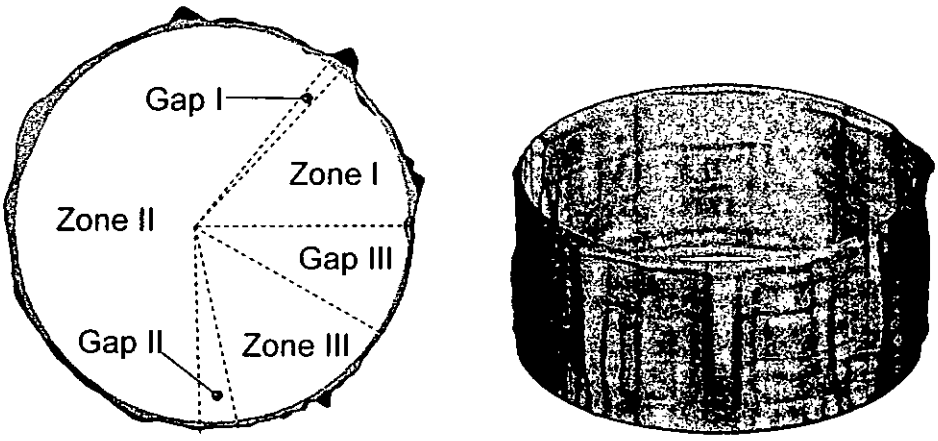

(a) Plan View (b) Perspective View

Deformation scaled by a factor of 50

Figure 9.4 Deformed shape of Shell A at ultimate load ($\bar{p}_y = 0.4$)

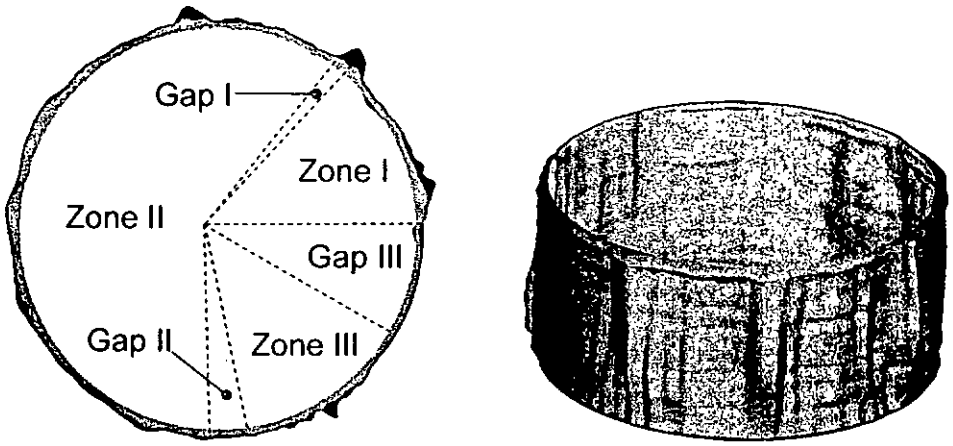

(a) Plan View (b) Perspective View

Deformation scaled by a factor of 50

Figure 9.5 Deformed shape of Shell A at ultimate load ($\bar{p}_y = 0.5$)

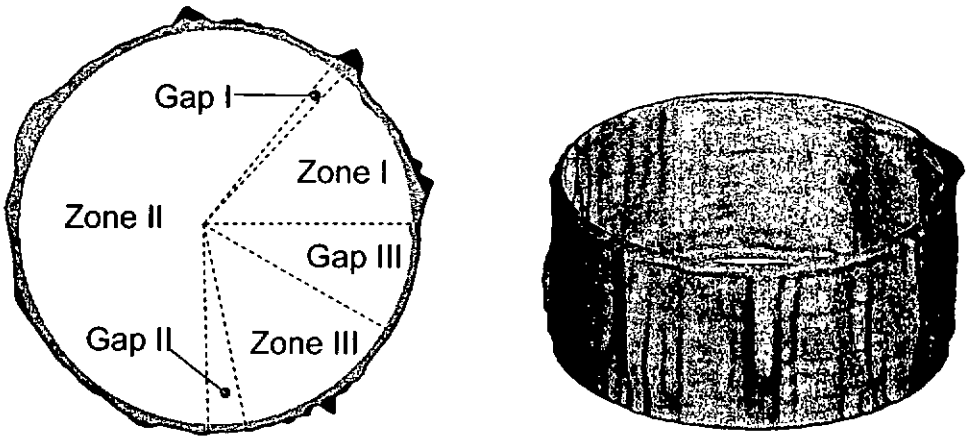

(a) Plan View (b) Perspective View

Deformation scaled by a factor of 50

Figure 9.6 Deformed shape of Shell A at ultimate load ($\bar{p}_y = 0.6$)

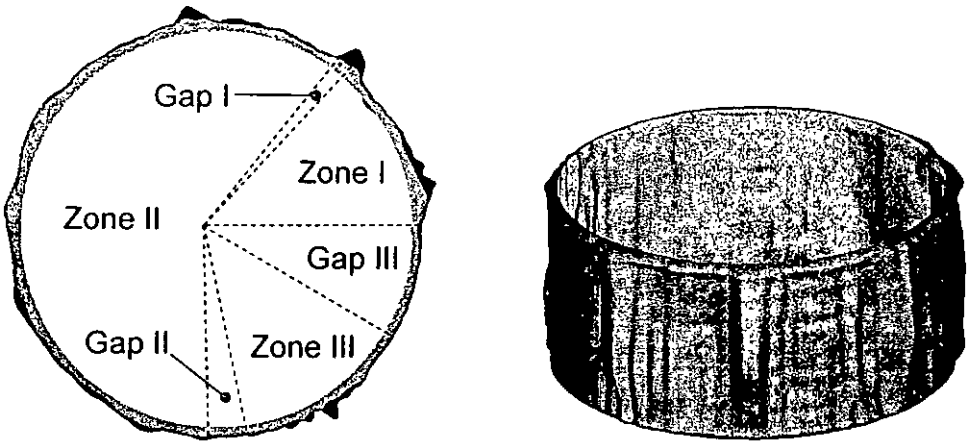

(a) Plan View (b) Perspective View

Deformation scaled by a factor of 50

Figure 9.7 Deformed shape of Shell A at ultimate load ($\bar{p}_y = 0.7$)

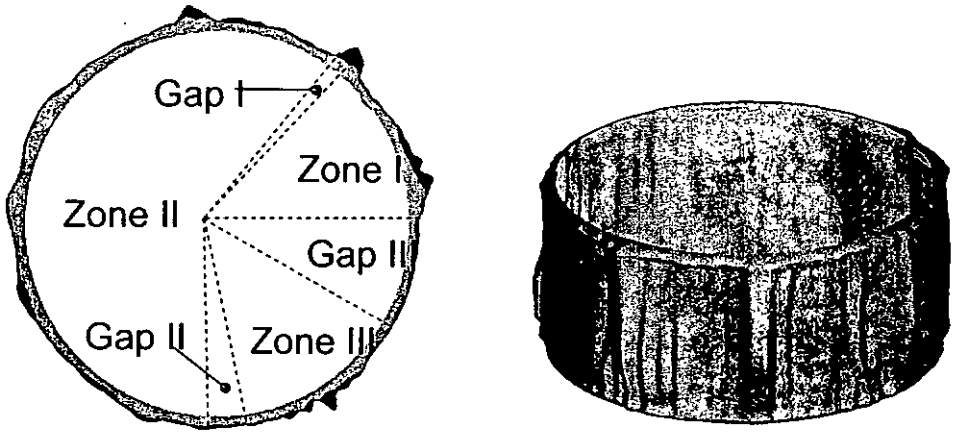

(a) Plan View (b) Perspective View

Deformation scaled by a factor of 50

Figure 9.8 Deformed shape of Shell A at ultimate load ($\bar{p}_y = 0.8$)

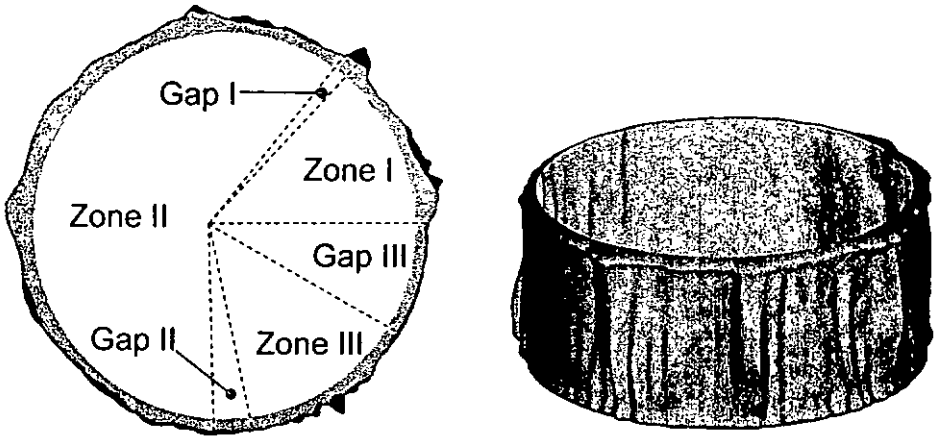

(a) Plan View (b) Perspective View

Deformation scaled by a factor of 50

Figure 9.9 Deformed shape of Shell A at ultimate load ($\bar{p}_y = 0.9$)

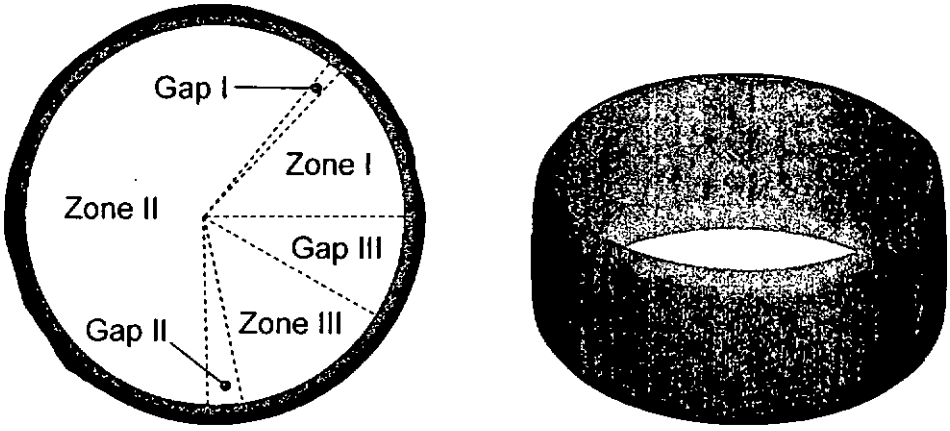

(a) Plan View (b) Perspective View

Deformation scaled by a factor of 50

Figure 9.10 Deformed shape of Shell A at ultimate load ($\bar{p}_y = 1.0$)

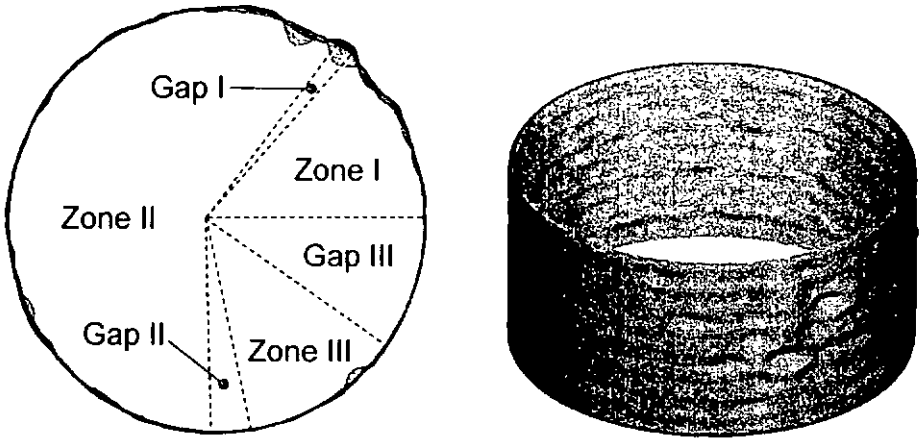

(a) Plan View (b) Perspective View

Deformation scaled by a factor of 50

Figure 9.11 Deformed shape of Shell B at ultimate load ($\bar{p}_y = 0.1$)

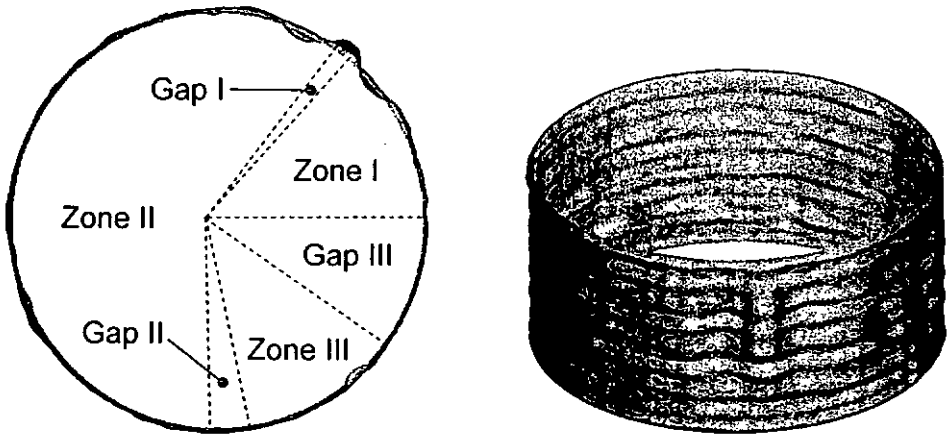

(a) Plan View (b) Perspective View

Deformation scaled by a factor of 50

Figure 9.12 Deformed shape of Shell B at ultimate load ($\bar{p}_y = 0.2$)

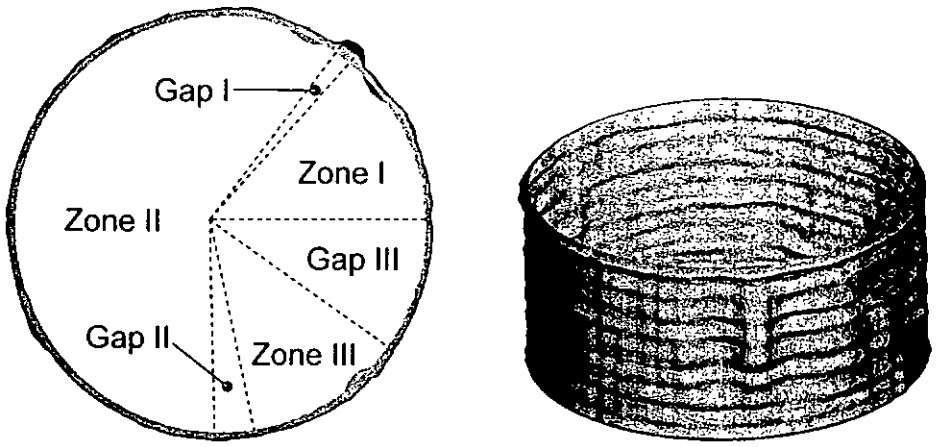

(a) Plan View (b) Perspective View

Deformation scaled by a factor of 50

Figure 9.13 Deformed shape of Shell B at ultimate load ($\bar{p}_y = 0.3$)

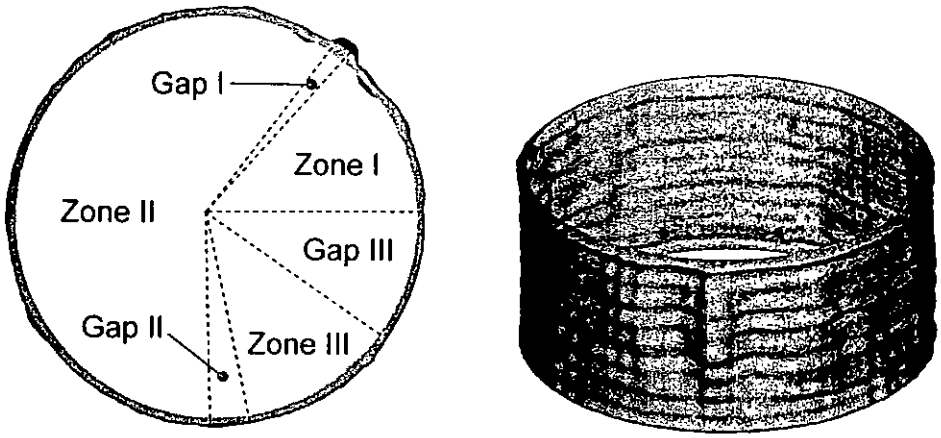

(a) Plan View (b) Perspective View

Deformation scaled by a factor of 50

Figure 9.14 Deformed shape of Shell B at ultimate load ($\bar{p}_y = 0.4$)

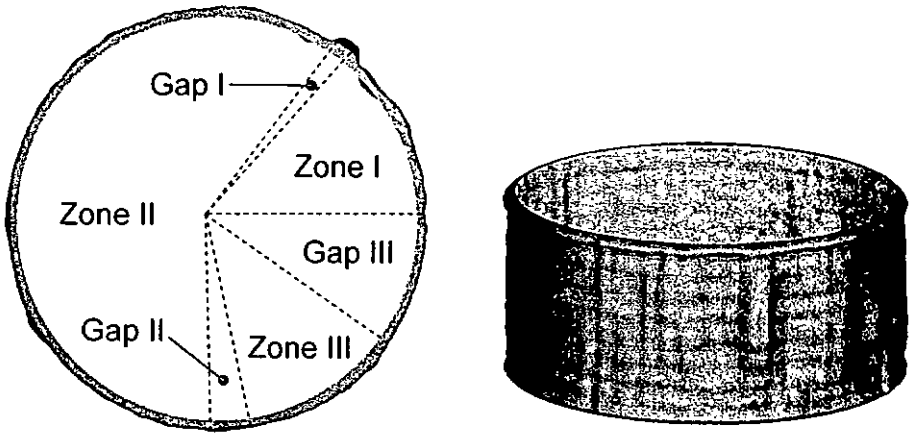

(a) Plan View (b) Perspective View

Deformation scaled by a factor of 50

Figure 9.15 Deformed shape of Shell B at ultimate load ($\bar{p}_y = 0.5$)

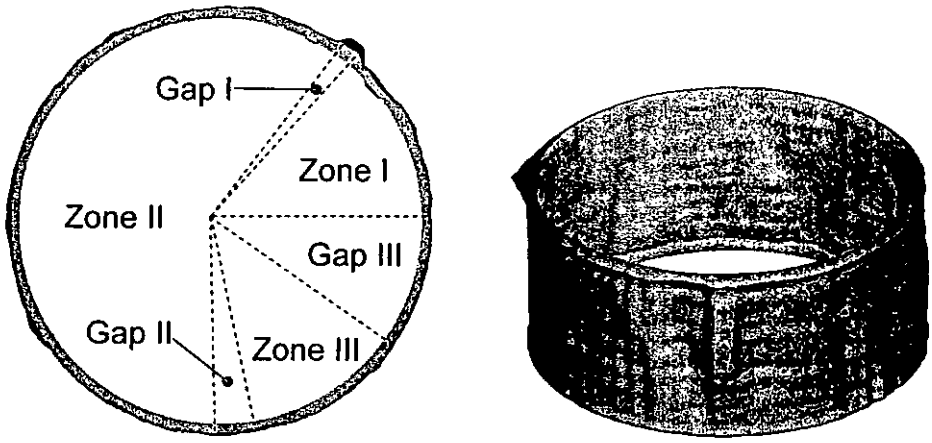

(a) Plan View (b) Perspective View

Deformation scaled by a factor of 50

Figure 9.16 Deformed shape of Shell B at ultimate load ($\bar{p}_y = 0.6$)

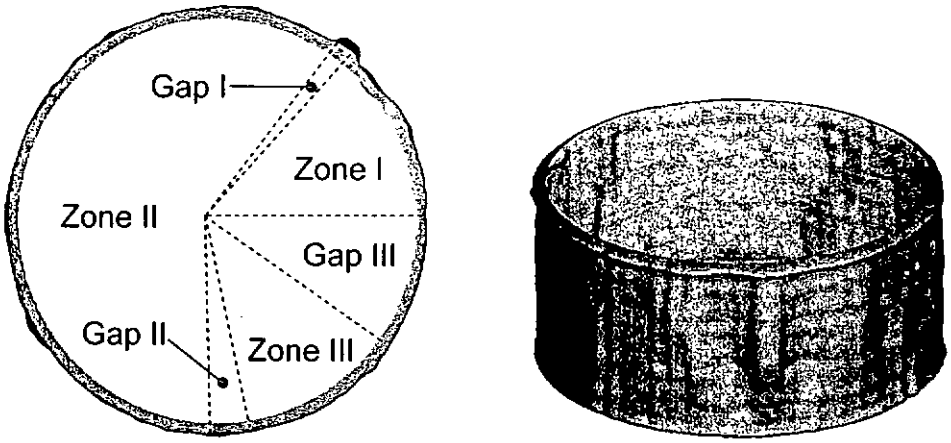

(a) Plan View (b) Perspective View

Deformation scaled by a factor of 50

Figure 9.17 Deformed shape of Shell B at ultimate load ($\bar{p}_y = 0.7$)

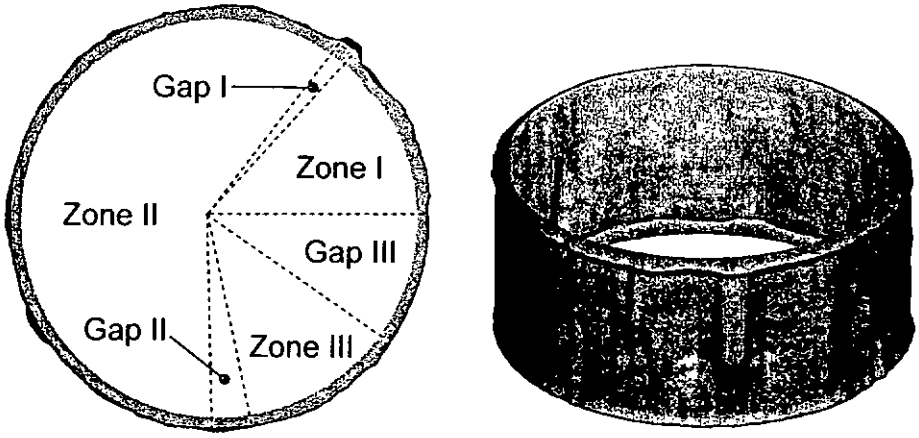

(a) Plan View (b) Perspective View

Deformation scaled by a factor of 50

Figure 9.18 Deformed shape of Shell B at ultimate load ($\bar{p}_y = 0.8$)

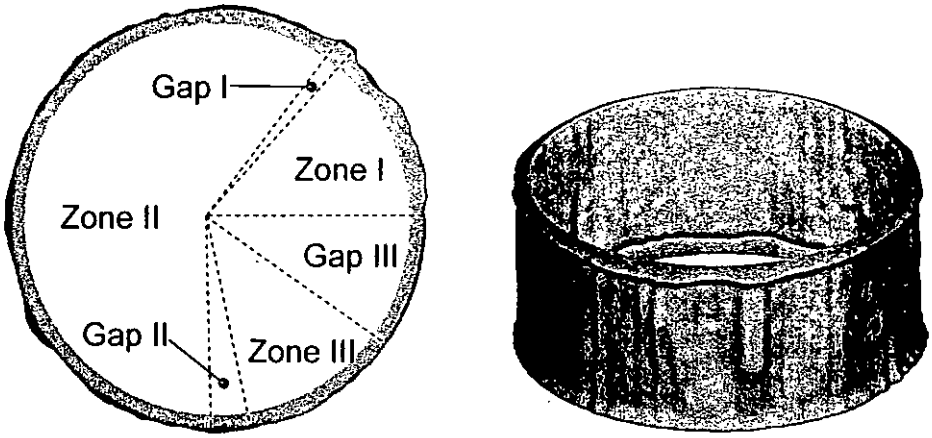

(a) Plan View (b) Perspective View

Deformation scaled by a factor of 50

Figure 9.19 Deformed shape of Shell B at ultimate load ($\bar{p}_y = 0.9$)

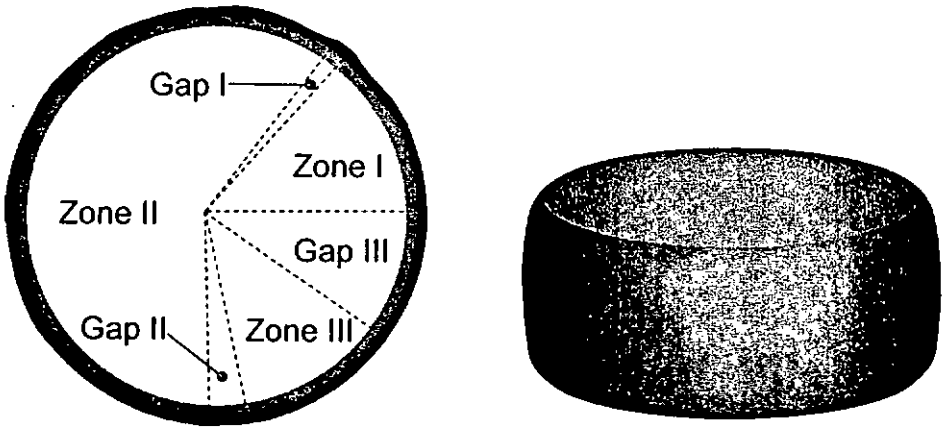

(a) Plan View (b) Perspective View

Deformation scaled by a factor of 50

Figure 9.20 Deformed shape of Shell B at ultimate load ($\bar{p}_y = 1.0$)

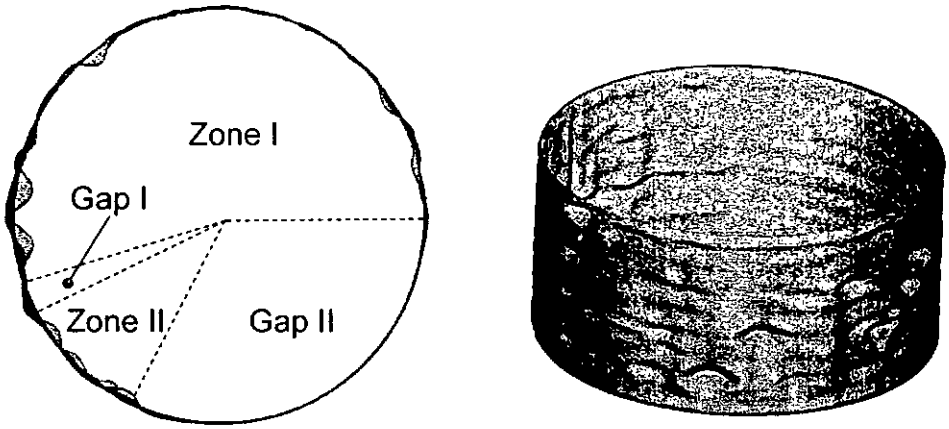

(a) Plan View (b) Perspective View

Deformation scaled by a factor of 50

Figure 9.21 Deformed shape of Shell C at ultimate load ($\bar{p}_y = 0.1$)

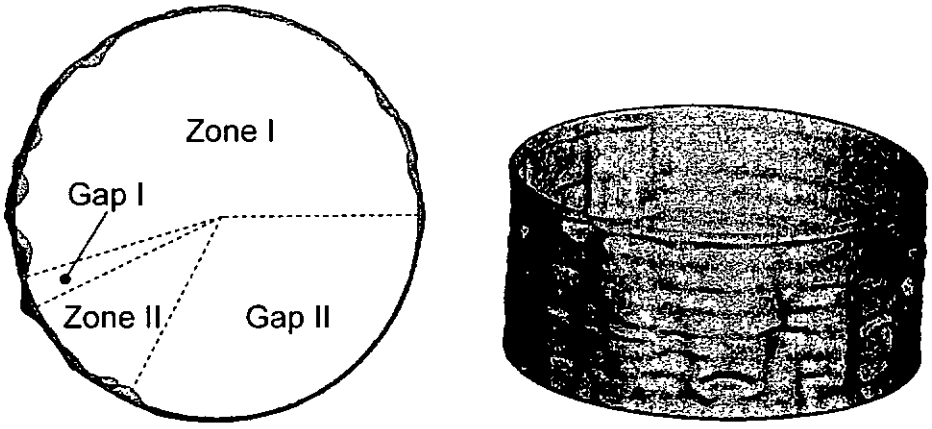

(a) Plan View (b) Perspective View

Deformation scaled by a factor of 50

Figure 9.22 Deformed shape of Shell C at ultimate load ($\bar{p}_y = 0.2$)

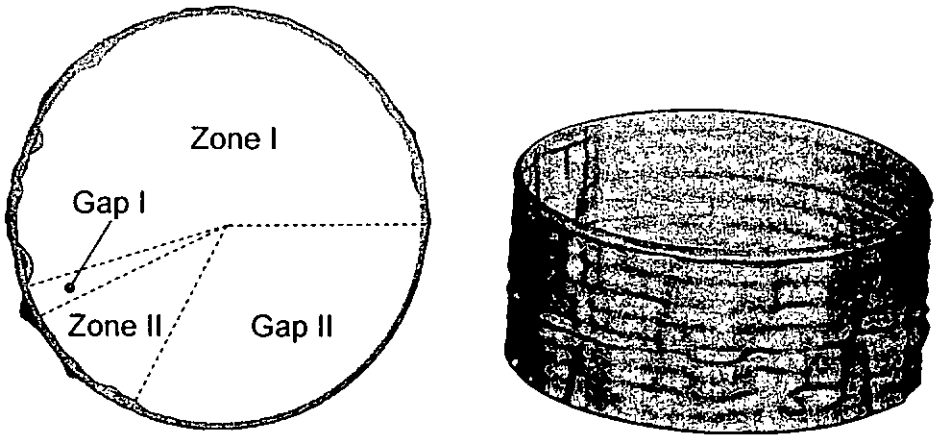

(a) Plan View (b) Perspective View

Deformation scaled by a factor of 50

Figure 9.23 Deformed shape of Shell C at ultimate load ($\bar{p}_y = 0.3$)

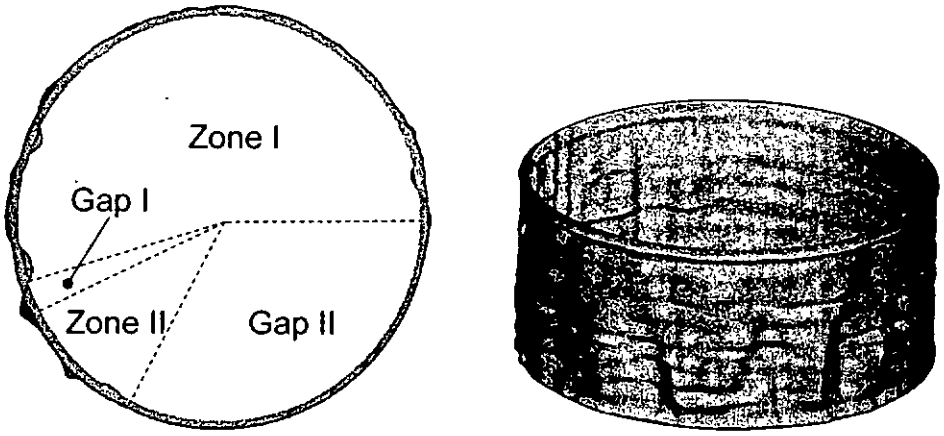

(a) Plan View (b) Perspective View

Deformation scaled by a factor of 50

Figure 9.24 Deformed shape of Shell C at ultimate load ($\bar{p}_y = 0.4$)

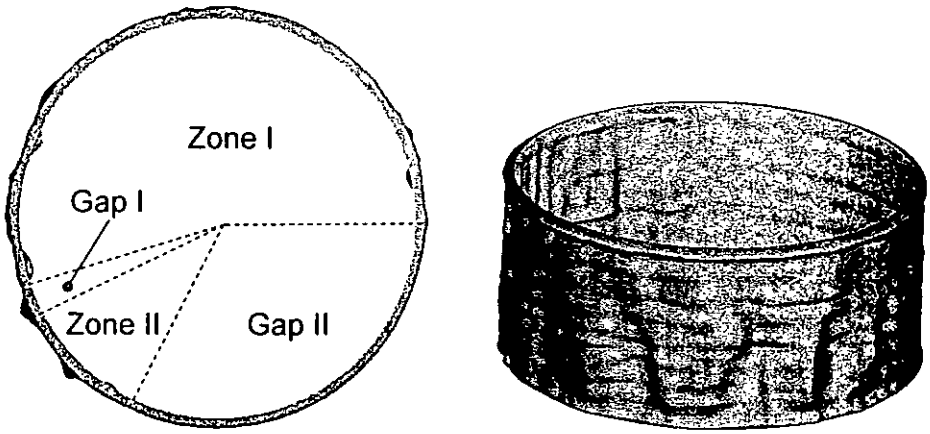

(a) Plan View (b) Perspective View

Deformation scaled by a factor of 50

Figure 9.25 Deformed shape of Shell C at ultimate load ($\bar{p}_y = 0.5$)

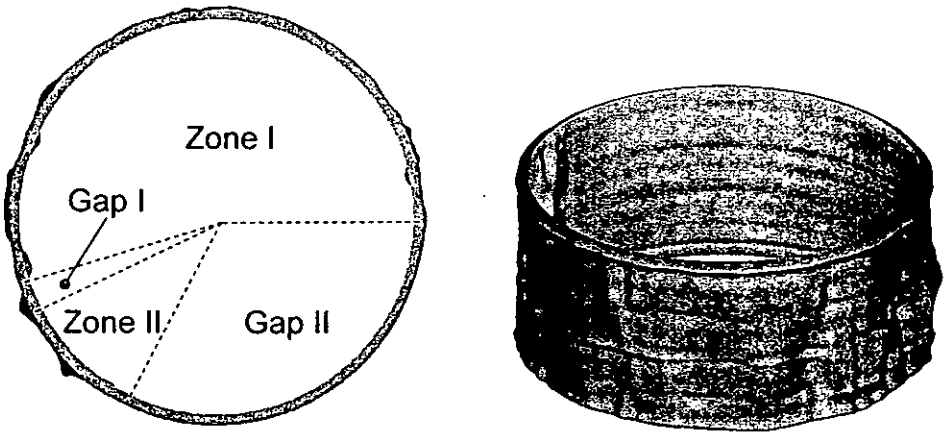

(a) Plan View (b) Perspective View

Deformation scaled by a factor of 50

Figure 9.26 Deformed shape of Shell C at ultimate load ($\bar{p}_y = 0.6$)

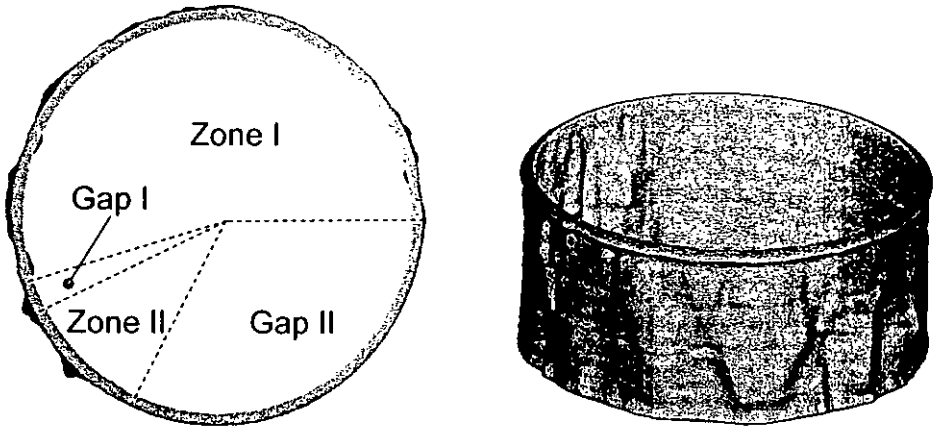

(a) Plan View (b) Perspective View

Deformation scaled by a factor of 50

Figure 9.27 Deformed shape of Shell C at ultimate load ($\bar{p}_y = 0.7$)

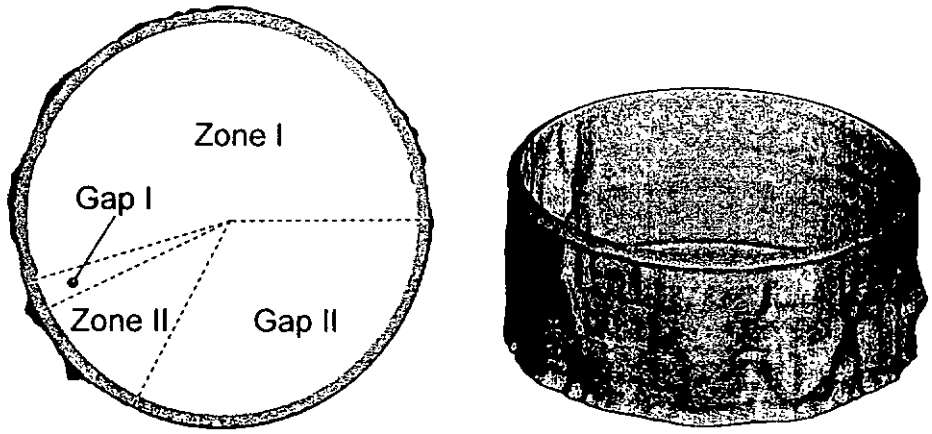

(a) Plan View (b) Perspective View

Deformation scaled by a factor of 50

Figure 9.28 Deformed shape of Shell C at ultimate load ($\bar{p}_y = 0.8$)

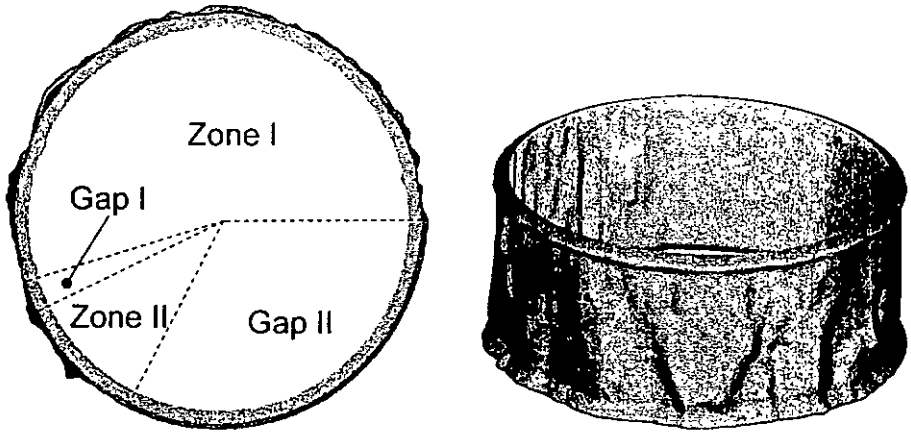

(a) Plan View (b) Perspective View

Deformation scaled by a factor of 50

Figure 9.29 Deformed shape of Shell C at ultimate load ($\bar{p}_y = 0.9$)

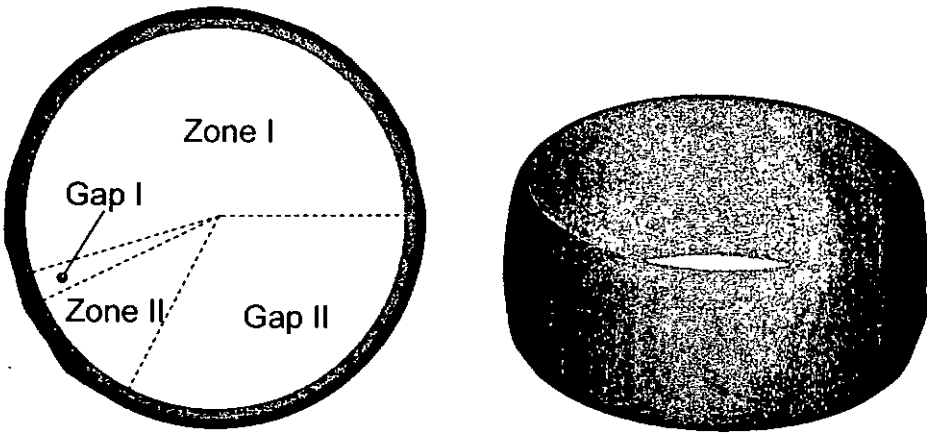

(a) Plan View (b) Perspective View

Deformation scaled by a factor of 50

Figure 9.30 Deformed shape of Shell C at ultimate load ($\bar{p}_y = 1.0$)

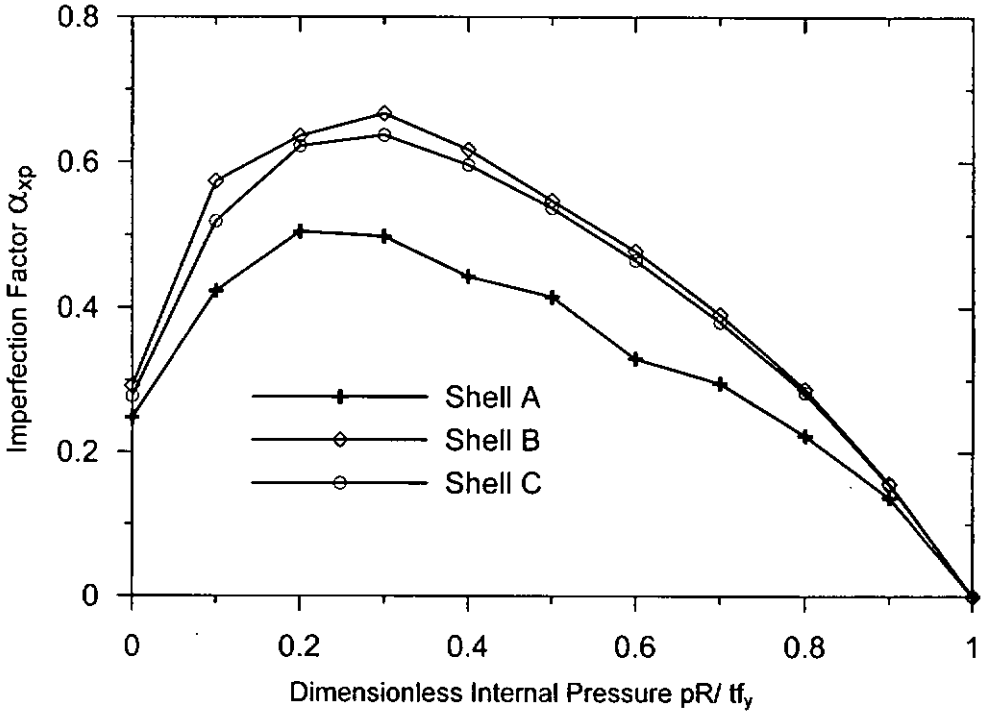

Figure 9.31 Imperfection factors deduced from finite element results

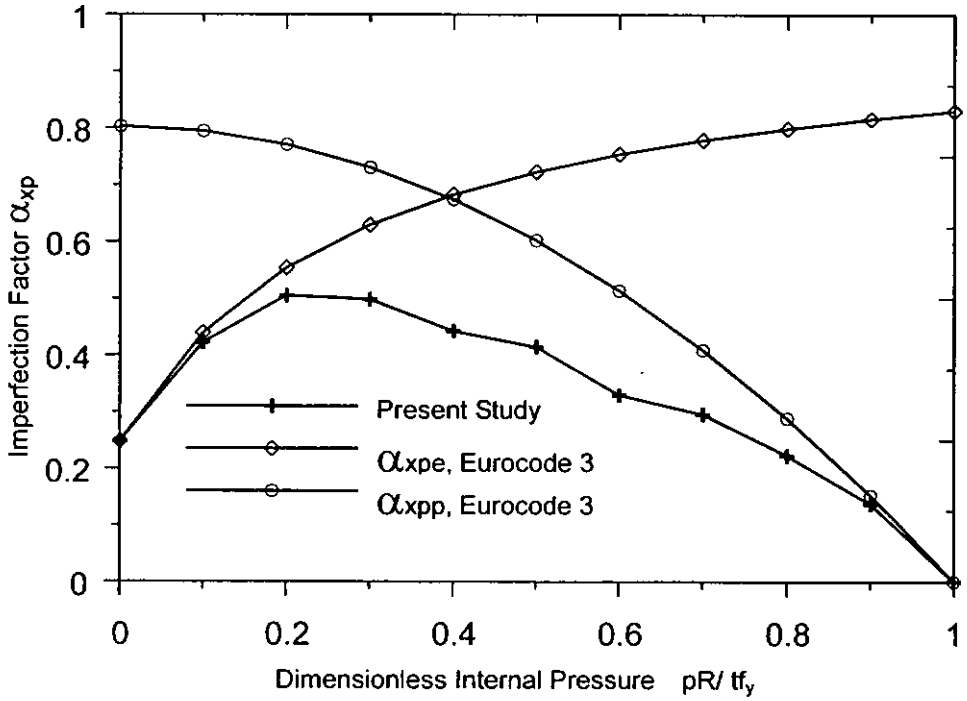

Figure 9.32 Comparison between FE results and predictions of Eurocode 3: Shell A

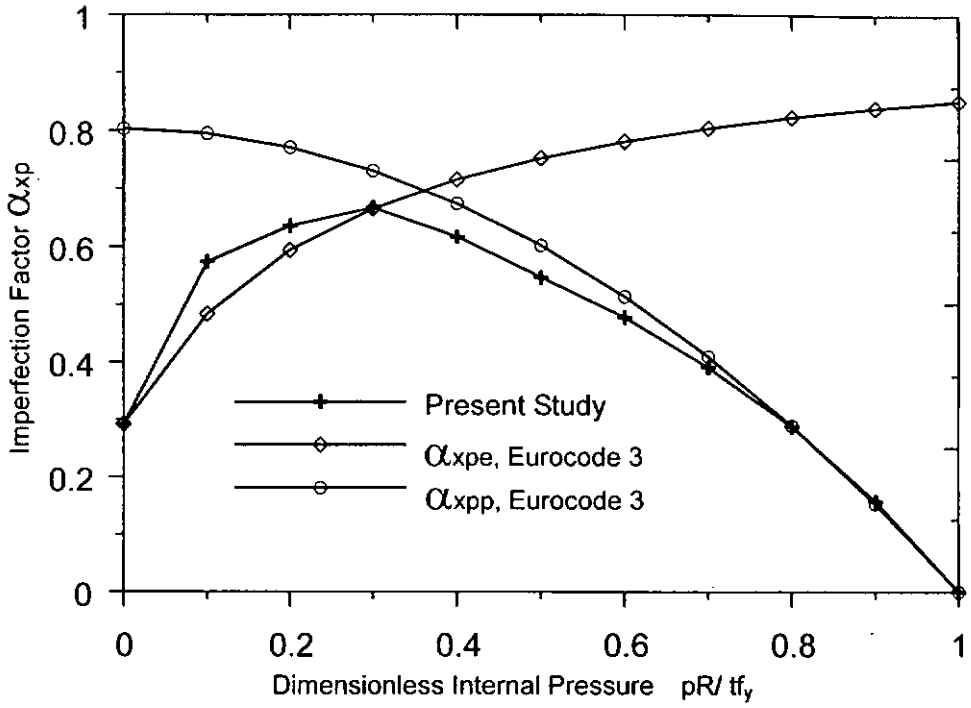

Figure 9.33 Comparison between FE results and predictions of Eurocode 3: Shell B

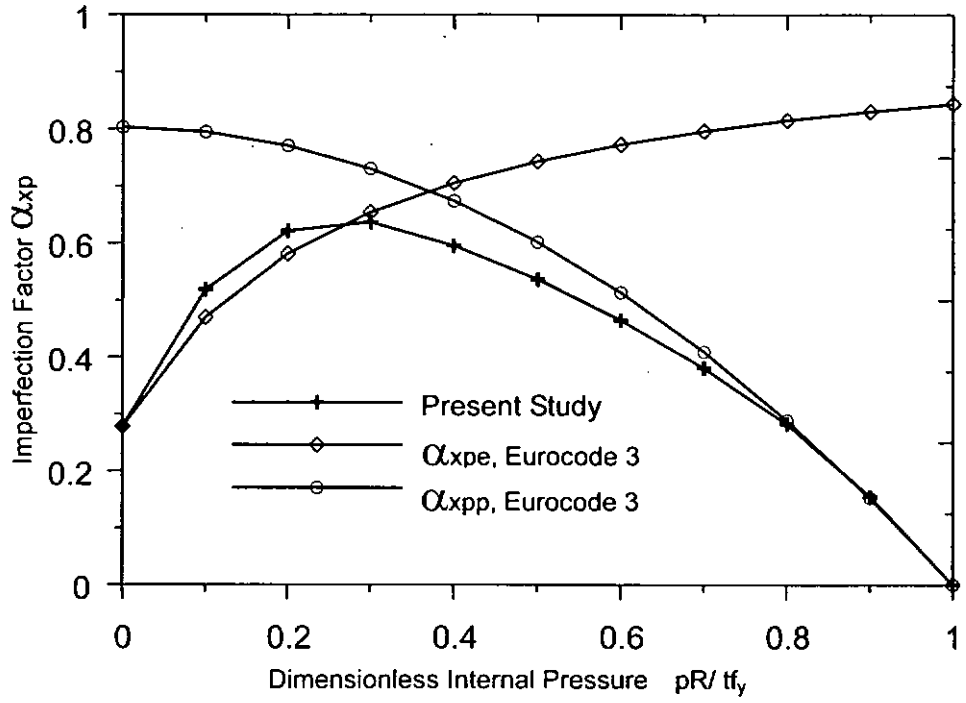

Figure 9.34 Comparison between FE results and predictions of Eurocode 3: Shell C

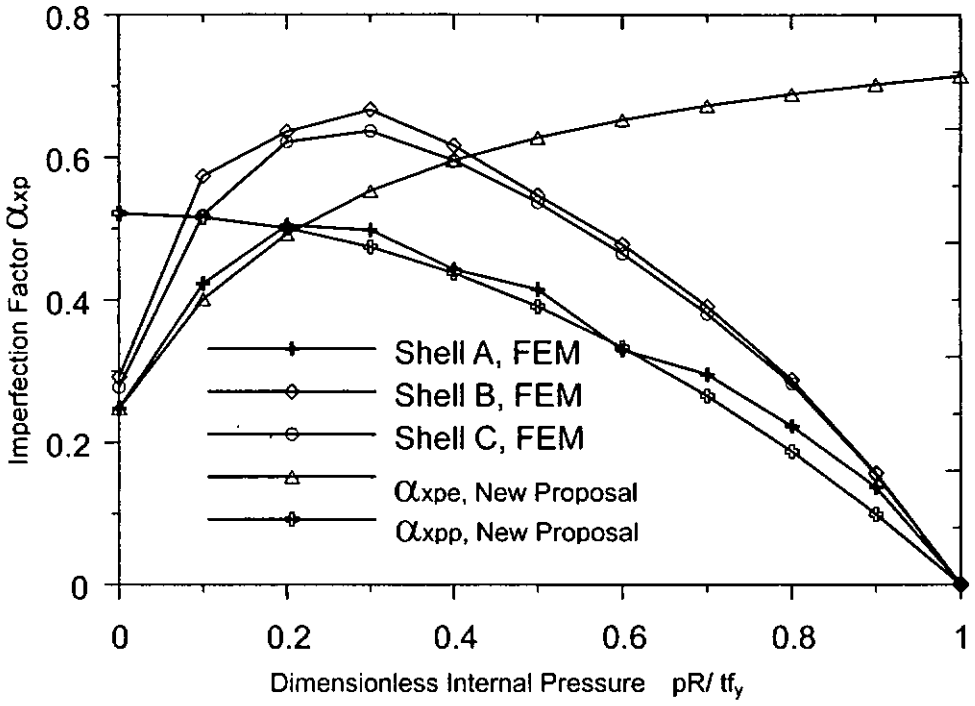

Figure 9.35 Comparison between FE results and predictions of new proposal

CHAPTER 10

CONCLUSIONS

10.1 INTRODUCTION

This thesis has been concerned with the buckling behaviour of extensively welded cylindrical shells under axial compression. This is an issue of great importance to the safe and economic design of large civil engineering steel shell structures such as steel silos and tanks, as evidenced by the many axial buckling failures of these structures that have been recorded.

The buckling strength of axially compressed cylindrical shells is very sensitive to both the form and the amplitude of imperfections in the shell wall and the form of imperfections depends strongly on the fabrication process. Imperfections in large civil engineering shell structures are very complicated as they are constructed by the unique process of welding together a large number of small rolled panels. To achieve a sound understanding of the effect of these imperfections, they need to be accurately modeled in buckling studies. However, previous studies on the buckling behavior of these shells have generally adopted simple substitute imperfections.

In this project, both theoretical analyses and experiments have been carried out to study the characteristics of imperfections in steel shells with many welds and their effect on buckling behaviour under axial compression. To this end, an iterative Fourier decomposition method was first proposed to overcome the difficulty of interpreting imperfections measured at non-uniformly distributed sampling points. This method was then employed to analyze geometric imperfections measured on three large steel silos at Port Kembla, Australia. The characteristic components of these imperfections due to many welds were identified and the Fourier series deduced to allow interpolation of these imperfections over a fine mesh of data points for

subsequent finite element modeling. A systematic study was next performed to examine the effect of these imperfections as well as their different components on the buckling strength of the shells. The numerical results were compared with code predictions.

While detailed measurements of imperfections are available for the three large silos, the residual stresses in these shells due to welding are unknown. As residual stresses may have a significant effect on the buckling strength, an experimental study was conducted to provide an indirect evaluation of this effect. In this experimental study, three small-scale model shells were fabricated by a novel two-stage technique, which was implemented with a sophisticated experimental set-up. Experimental results from axial compression tests of these model shells were compared with finite element predictions, leading to the conclusion that residual stresses have only a small but beneficial effect on the buckling strength.

Finally, a parametric study was conducted to explore the buckling strength of cylindrical shells in large steel silos with measured geometric imperfections subject to the combined action of axial compression and internal pressure. The numerical results were compared with predictions of the design rule of Eurocode 3. Modifications to the design rule were also proposed. The major findings of the present project are summarized below.

10.2 FOURIER REPRSENTATIONS OF IMPERFECTION MEASUREMENTS WITH NON-UNIFORM INTERVALS

Imperfection measurements are generally taken at discrete points (i.e., the sampling points), as a result of the prevailing measurement technology available today. Imperfection measurements on a shell structure are often made with non-uniform intervals, because some parts of the shell surface are normally inaccessible to the measurement system due to various obstructions (e.g. service ladders). The conventional method of Fourier decomposition was found to be inaccurate for such imperfections, so a new iterative Fourier decomposition method was presented in Chapter 3 to provide an accurate Fourier representation of such imperfections. An accurate Fourier series is found by an iterative procedure in which the

residual errors in the Fourier series at the sampling points are further decomposed into a Fourier series. Although the work was conducted in the context of interpreting discrete imperfection measurements made on a shell surface, the method is applicable to the Fourier decomposition of any forms of discrete data taken at sampling points with non-uniform intervals. The following conclusions can be drawn based on the results and discussions presented in this chapter:

1. For a set of uniformly-spaced discrete data, the conventional Fourier decomposition method leads to accurate representation of the discrete data only if the number of data points exceeds $2k+1$ if the discrete data are from source functions $A\cos k\theta$ and $B\sin k\theta$.
2. For a set of non-uniformly spaced discrete data, the conventional Fourier decomposition method does not provide an accurate representation of the discrete data even if the number of data points is sufficiently large.
3. An accurate Fourier series can be found for a set of non-uniformly spaced discrete data by an iterative procedure in which the residual errors in the Fourier series at the sampling points are further decomposed into Fourier series.

10.3 ANALYSIS OF GEOMETRIC IMPERFECTIONS IN LARGE EXTENSIVELY WELDED STEEL SILOS

Chapter 4 presented several analyses of imperfections in some large steel silos. The mathematical basis of a Fourier series representation was discussed, as well as the performance of various forms of Fourier series and their suitability to represent different forms of imperfections. Conclusions were then drawn and an appropriate choice of Fourier series representation was made to represent different forms of imperfections. Comments were made on the choices made by previous researchers, who used Fourier series to represent cylindrical shell imperfections, Furthermore, the inappropriate choices made on some occasions were identified and their consequences highlighted. A typical modal amplitude deduction procedure for a complicated Fourier series was demonstrated and the amplitude expressions for various Fourier series were presented for ease of reference. In addition, the

procedure of deriving the 'best-fit' cylinder to obtain the net "real" imperfections with respect to the "best-fit" reference cylinder was presented.

Systematic Fourier decompositions of the imperfections measured by Ding (1992) in the three large steel silos at Port Kembla, Australia, were carried out. Imperfections on circumferences at selected levels of each silo were decomposed using 1D full-wave general (FWG) series, while the imperfections on selected meridians of each silo were analyzed using 1D half-wave cosine (HWC) series. In addition, the complete 2D imperfection data in a selected height range in each of the silos was decomposed using 2D Fourier series with a HWC representation in the axial direction and a FWG representation in the circumferential direction.

Based on the results and discussions presented in this chapter, the following conclusions can be drawn:

1. FWG series taking the form of full-wave cosine series plus sine series can be used to represent imperfections with the same end values. An example is the case of imperfection variation around the circumference of a cylindrical shell, where the starting and finishing values must necessarily be identical. The HWC series is a versatile Fourier series that can be used to represent every form of imperfection pattern with a high accuracy: this form of Fourier series is often used to represent imperfections with different end values. The half-wave sine (HWS) series may be used to interpret imperfections with zero end values: this Fourier series is often replaced by a FWG series because the latter is more complete with a full set of cosine and sine series. Half-wave general (HWG) series in the form of cosine series added with sine series should never be used. Neither full-wave cosine series nor full-wave sine series are suitable for the representation of imperfections, because the imperfections in cylindrical shells do not necessarily take the form of symmetric or anti-symmetric shapes with respect to the middle point of the region considered.
2. The number of terms used in the Fourier series should be chosen based on the number of data sampling points according to Table 4.1, so that the representation errors (in terms of the sum of the squares of the errors at the sampling points) can be minimized.

3. The Iterative Fourier decomposition method, which was proposed in the context of one-dimensional Fourier decompositions, is also very effective in 2D Fourier decompositions of cylindrical shell imperfections, when the data is obtained at non-uniformly distributed sampling points.
4. The higher harmonic terms of a Fourier series, whose coefficients may seem small, play an important role in reducing the errors in Fourier representations and capturing important local features of the imperfection form.
5. Although there is little visual similarity between the global imperfection patterns on the three silos studied, the spectra of these imperfections in Fourier decompositions show some remarkable common features, such as the dominant wave patterns clustering in lower harmonic terms of the Fourier series and the circumferential wave patterns that are much richer than the meridional ones.
6. There are some very marked global features of the imperfections: the low-harmonic wave patterns display overwhelmingly large amplitudes which may be attributed to the global imperfections such as out-of-roundness and meridional tilt in these silos.
7. In addition to these very large amplitudes in large scale shape errors, there exist some pronounced wave patterns of imperfections that are closely related to the number of panels in each silo shell, indicating the dependence of the geometric imperfection patterns on the fabrication process for the structure.

10.4 BUCKLING BEHAVIOR OF LARGE EXTENSIVELY WELDED STEEL CYLINDERS WITH MEASURED GEOMETRIC IMPERFECTIONS

A finite element study of the buckling and postbuckling behavior of three shells taken from the three Port Kembla silos with measured geometric imperfections was presented in Chapter 5. The measured imperfections were accurately represented and incorporated into linear and nonlinear finite element buckling analyses using ABAQUS. A block imperfection approach was suggested and found to be effective in identifying the critical imperfection components that are responsible for most of the shell buckling strength reduction. In this approach, finite

element analyses are carried out for a series of block imperfections obtained by progressively excluding the lower harmonic terms of the imperfection to determine the effect of the imperfection components represented by the lower harmonic terms. Moreover, automated computer procedures were developed to numerically "measure" dimple depths in both the meridional and the circumferential directions. These dimple depths together with values of the out-of-roundness parameter allowed the determination of the fabrication quality classes of the three shells according to the stipulations in ENV1993-1-6 (1999). Finally, the finite element linear and nonlinear buckling loads were compared with appropriate code predictions.

The results and discussions presented in this chapter allow the following major conclusions to be made about the behavior of the three silo shells (Shells A, B and C for Silos A, B and C respectively):

1. Geometric imperfections arising from the panel method of construction are severely detrimental to the shell buckling strength. Despite that the three shells were constructed by the same method and had the same geometric and material properties, they differ significantly in their buckling and post-buckling behavior as a result of the different geometric imperfections in the three shells.

2. Although the Fourier series representing the imperfections contain a large number of terms, the lower harmonic terms in both the meridional and circumferential directions dominate the buckling strength. There are significant differences between the dominant components of the three shells.

3. Based on the stipulations in ENV1993-1-6 (1999), the fabrication quality classes of the three shells are all controlled by their dimple depths rather the out-of-roundness parameter. According to the maximum dimple depths, the fabrication quality of Shells A, B and C is close to the worst of Classes C, A and B respectively. That is, the same construction procedure led to a spread of quality over all three quality classes defined by the Eurocode (ENV1993-1-6 1999).

4. A comparison of code predictions of buckling strengths with nonlinear finite element results indicated that the current rules of Eurocode 3 are too optimistic about Class A shells but two pessimistic about other shells. It is also significant that strictly speaking, Shell A falls outside of the three quality classes defined in the code although its buckling strength

is much higher than the code prediction for a Class C shell. The relationship between buckling strengths and quality classes requires further research.

10.5 TECHNIQUES FOR BUCKLING EXPERIMENTS ON EXTENSIVELY WELDED STEEL CYLINDERS

The theoretical work presented Chapter 5 led to a good understanding of the buckling and post-buckling behavior of real imperfect cylindrical shells in steel silos when subject to axial compression for the first time. In this theoretical work, residual stresses, which always co-exist with the geometric imperfections in these shells, have been ignored. Since residual stresses in thin shells can hardly be measured, their effect of buckling strengths has been studied only on the basis of assumed residual stresses. Such studies are however inconclusive.

The most reliable approach for assessing the effect of residual stresses is to carry out buckling experiments on shells in which both geometric imperfections and residual stresses are realistically replicated. As the effect of geometric imperfections can be expected to be closely predicted by a finite element model which includes precisely measured geometric imperfections in the test shell, a comparison between the finite element predictions and the test result can reveal the overall effect of residual stresses and other effects (e.g. unintended non-uniformity in loading). If the finite element buckling load is in close agreement with the test buckling load, it can then be concluded that the effect of residual stresses in the shell is unimportant to the buckling strength. Such an experimental study was presented in Chapters 6-8.

In Chapter 6, techniques for buckling experiments on extensively welded steel cylindrical shells were presented. Modifications made to an existing test rig to upgrade the facility for the planned buckling experiments on welded cylinders under axial compression were first described. An MTS actuator was employed to achieve displacement-control loading. A load transfer system, which consisted of a load transfer cylinder, a universal joint, a flat loading cone, and a loading ring with a sharp edge, was designed to transform the point load of the

MTS actuator into a uniform ring load on the shell specimen. Moreover, the problem of gear clearance in the rotational movement of the measurement system was eliminated so that the imperfection survey of the entire surface of a cylindrical shell specimen could be carried out automatically, reducing significantly the measurement effort. The overall experimental set-up for these buckling experiments was also explained. Transducers and strain gauges were installed inside the model shell to avoid any interference with shape surveys on the external surface of the shell surface.

An innovative technique was presented for the fabrication of small models of large steel cylindrical shells constructed from many welded panels as commonly found in large steel silos and tanks. The new technique consists of two stages: (as) production of a high quality model by rolling two sheets (or a single sheet) and welding along the meridional seams; and (b) 'welding' in the form of controlled heat input in a required pattern of circumferential and meridional 'welds' on the central portion of the shell surface. The experimental set-ups and the detailed fabrication procedure were described. The proposed technique for the first time provides a feasible method for the production of realistic small-scale models of large cylindrical shells in steel silos and tanks. It is believed that the technique will greatly facilitate future experimental research on the buckling behavior of cylindrical shells built from many welded panels under many loading conditions, including axial compression with or without internal pressure, external pressure, shear and torsion, non-uniform pressures on silos from various sources and local loads such as column support reaction forces.

10.6 BUCKLING EXPERIMENTS ON EXTENSIVELY WELDED STEEL CYLINDERS

Chapter 7 presented the results from careful buckling experiments on extensively welded steel cylinders under axial compression. Three model shells, referred to as specimens 09SC, 09QC04, and 09P0408, were tested. Apart from the two meridional welds required to form the shell, Specimen 09SC had a single circumferential weld at the mid-height, specimen 09QC04 had four circumferential welds which were symmetrically located at a constant spacing within

the mid-height region of the shell, while specimen 09P0404 had many short meridional welds in addition to the four circumferential welds, forming a typical pattern of welds as is generally present in a typical silo or tank; the welds divided the mid-height region of the shell wall into many rectangular panels.

The material properties of the as-supplied thin steel sheets were determined and the effects of rolling on the material properties were examined and found to be very small. The initial surfaces of the specimens were surveyed before and after Stage II welding as well as after the tests. Two small pieces of the shell wall were cut from specimen 09P0408 after testing for thickness measurements and the thickness variations due to Stage II welding were very small. As a result, the middle surface of a test shell was deduced from the external surface as measured by shrinking it by half the thickness.

The imperfections in the specimens before and after Stage II welding were carefully analyzed to reveal their characteristics. A clear relationship was found to exist between the imperfections and the welds. These imperfection analyses confirmed the success of the model fabrication techniques presented in Chapter 6, as the imperfections had the desired characteristics associated with the welds introduced in the Stage II operation.

The buckles observed in specimens 09SC and 09QC04 were found to have a diamond shape, while the buckles in specimen 09P0408 had a pattern closely associated with the weld pattern. Fourier decompositions of the post-buckling deformations of the specimens showed that the dominant components of deformations are described by the lower harmonic terms.

The initial and deformed shapes of two selected circumferences were monitored during each test, and the results were represented by one-dimensional Fourier series. During loading, the modal amplitudes of the lower harmonic terms were found to grow rapidly, and these represent the controlling components of deformations. The important harmonic terms of the post-buckled circumferences are significant different from those of the pre-buckling circumferences, which confirms the phenomenon of mode changes during post-buckling deformation. In addition, the variations of axial shortenings and strain readings at selected

locations were reported. Most of the strain readings can be easily understood, but some of the readings, from gauges installed at intersections of welds, cannot be easily expected.

The buckling loads of these specimens are much lower than those of shells with imperfections of many other known patterns, demonstrating the severity of these imperfections in reducing the shell buckling load.

10.7 FINITE ELEMENT MODELLING OF BUCKLING EXPERIMENTS ON EXTENSIVELY WELDED STEEL CYLINDERS

For a fuller understanding of the buckling behavior of the three laboratory models, a finite element study of these test specimens was presented in Chapter 8. Results from both linear buckling analyses and non-linear analyses considering both geometric and material nonlinearities were presented and compared with experimental results.

The finite element models, which were built using shell element S4 in the finite element package ABAQUS, included the geometric imperfections precisely measured during the experiments, but omitted the associated residual stresses and any welding effect on steel material properties because they were not measured. Based on a mesh convergence study, an accurate but economic mesh was used to model the test specimens.

The buckling loads from the finite element linear buckling analyses are significantly higher than the corresponding experimental loads for two of the specimens. This is consistent with common expectations that a linear buckling analysis generally gives an upper bound on the actual buckling load of such shells. For one of the specimen, however, the linear buckling load coincides with the test buckling load, which is unexpected. In addition, the linear buckling modes are generally very different from those observed during the experiments.

The ultimate loads of the shells from geometrically and materially non-linear analyses are close to but slightly lower than the experimental values, confirming that residual stresses can

have a small beneficial effect on the buckling strength, a conclusion that has been reached by previous researchers through theoretical studies. The load-axial shortening curves from the non-linear analyses agree well with the experimental curves at early stages of loading, but near the attainment of the peak load and afterwards, the finite element curves do not generally agree with the experimental curves. The deformed shapes from the nonlinear analyses are also significantly different from those observed during the experiments. These differences are attributed to factors not included in the numerical models, mainly the inevitable residual stresses associated with the welds and to some extent the changes in material properties induced by welding.

In summary, non-linear finite element analyses of axially-compressed welded cylindrical shells of the kind studied here, with geometric imperfections taken into account, can give close predictions of the buckling loads. The residual stresses in the shell wall can cause significant changes in the deformation history and shape, but their effect on the buckling strength is small and beneficial. These residual stresses can be safely ignored in nonlinear finite element analyses aimed at close predictions of the buckling strengths.

10.8 EXTENSIVELY WEDLED STEEL CYLINDERS UNDER COMBINED AXIAL COMPRESSION AND INTERNAL PRESSURE

Chapter 9 presented the first ever rigorous investigation into the failure behaviour and strength of extensively welded steel cylindrical shells with precisely measured geometric imperfections subject to the combined action of axial compression and internal pressure. A series of geometrically and materially nonlinear analyses were carried out for the three cylindrical shells of Ding's (1992) Port Kembla silos using ABAQUS (Hibbit, Karlsson and Sorensen, 1998). These analyses covered ten different levels of internal pressurization. The results were discussed and compared with predictions of the relevant design rule in Eurocode 3 (ENV1993-1-6, 1999).

It was found that the dominant imperfection components identified for a shell subjected to axial compression alone also govern the failure strength of the shell under the combined action of axial compression and internal pressure. Axisymmetric imperfections were found to lead to the lowest failure strengths in both the elastic range and the elastic-plastic range.

The predictions of the design rule in Eurocode 3 (ENV1993-1-6, 1999) were shown to be un-conservative when the dominant imperfection components are axisymmetric. This is believed to be a result of the basis of the design rule in the code: the rule was based on results of numerical models which did not taken into proper account the effect of interaction between adjacent weld depressions. Modifications to the existing rule were proposed and this new rule gives safe predictions for all three shells.

10.9 FUTURE RESEARCH

The thesis has dealt with the buckling behaviour of extensively welded cylinders with uniform support and under uniform axial compression, with or without the presence of internal pressure. In the design of these shells, their buckling strengths under many other loading conditions may be important as well. As a foundation to the solution of more complex problems, a series of studies should be carried out on the buckling behavior of extensively welded shells under various fundamental load cases, including external pressure, torsion and shear. Additional work is also required for the case of axial compression, particularly on the definition of axial buckling strengths in conjunction with quality classes, as the relevant rules in Eurocode 3 have been found to be too optimistic about Class A shells but too pessimistic about Class C shells in the present project. Subsequent to these studies, the more complex problems of extensively welded cylinders under non-uniform/local loads should be tackled. Example non-uniform/local loading conditions include steel silos and tanks supported on discrete columns, wind loading, foundation settlement, eccentric discharge of bulk solids from silos, and earthquake loading. Although a limited amount of research has been carried out for some of these loading conditions (e.g. Rotter, 2001, Song, 2002), none of them have considered real measured imperfections or strictly realistic imperfections in these shells.

REFERENCE

Abramovich, H., Singer, J. and Weller, T. (1991) "The influence of initial imperfections on the buckling of stiffened cylindrical shells under combined loading", *Buckling of Shell Structures on Land, in the Sea and in the Air*, J.F. Jullien, ed., Elsevier Applied Science, London and New York, pp.1-10.

Abramovich, H., Yaffe, R. and Singer, J. (1987). "Evaluation of stiffened shell characteristics from imperfection measurements", *Journal of Strain Analysis*, **22(1)**: 17-23.

ACI 313-97 (1998). *Standard Practice for Design and Construction of Concrete Silos and Stacking Tube for Storing Granular Materials (ACI 313-97) and Commentary –ACI 313R-97*, American Concrete Institute, Michigan.

Allen, M.F. (1989). "Testing, evaluation, and repair methods for structural stability of coal silos", *Proceedings, the 51st American Power Conference*, pp.788-797.

Almroth, B.O. (1963). "Postbuckling behaviour of axially compressed circular cylinders", *AIAA Journal*, **1**: 630-633.

Almroth, B.O. (1966). "Influence of edge conditions on the stability of axially compressed cylindrical shells", *AIAA Journal*, **4(1)**: 134-140.

Amazigo, J.C. and Budiansky, B. (1972). "Asymptotic formula for the buckling stresses of axially compresses cylinders with localized or random axisymmetric imperfections", *Journal of Applied Mechanics*, **E-39**: 179-184.

Amiro, Y. and Zarutskii, V.A. (1996). "Experimental Study of the Stability of Stiffened Shells (Review)", *International Applied Mechanics*, **32(9)**: 659-668.

Arbocz, J. (1968). *The Effect of General Imperfections on the Buckling of Cylindrical Shells*, PhD thesis, California Institute of Technology, Pasadena.

Arbocz, J. (1974). "The effect of initial imperfections on shell stability", *Thin-Shell Structures: Theory, Experiment, and Design*, Y.C. Fung and E.E. Sechler, eds., Prentice Hall, Englewood Cliffs, N.J., pp.205-245.

Arbocz, J. (1982). "The imperfection data bank, a means to obtain realistic buckling loads." *Buckling of Shells*, E. Ramm, ed., Springer Verlag, New York, pp.535-567.

Arbocz, J. (1983). "Shell stability analysis: theory and practice", *Collapse, the Buckling of Structures in Theory and Pratice*, J.M.T. Thompson and G.W. Hunt, eds, Cambridge University Press.

Arbocz, J. (1987). "Post-Buckling Behaviour of Structures: Numerical Techniques for More Complicated Structures", *Lecture Notes in Physics*, H. Araki et al. eds., Springer-Verlag, Berlin, pp.84-142.

Arbocz, J. and Abramovich, H. (1979). *The Initial Imperfection Data Bank at the Delft University of Technology – Part I, Report LR-290*, Delft University of Technology, the Netherlands.

Arbocz, J. and Babcock, C.D. (1969). "The effect of general imperfections on the buckling of cylindrical shells", *Journal of Applied Mechanics, ASME*, **36**: 28-38.

Arbocz, J. and Babcock, C.D. (1982) "Stability Analysis of Shells Using the STAGS Computer Code", *Buckling of Shells in Offshore Structures*, J.E. Harding, P.J. Dowling & N. Agelidis, eds., Granada Publishing, New York, pp.549-574.

Arbocz, J. and Starnes Jr, J.H. (2002). "Future directions and challenges in shell stability analysis", *Thin-Walled Structures*, **40**: 729-754.

Arbocz, J. and Hol, J.M.A.M. (1991). "Collapse of axially compressed cylindrical shells with random imperfections", *AIAA Journal*, **29(12)**: 2247-2256.

Arbocz, J. and Williams, J.G. (1977). "Imperfection surveys on a 10ft diameter shell structure", *AIAA Journal*, **15(7)**: 949-956.

AS 3774 (1990). *Loads on Bulk Solid Containers*, Standard Association of Australia, Sydney.

Babcock, C.D. (1974). "Experiments in shell buckling", *Thin-Shell Structures: Theory, Experiment, and Design*, Y.C. Fung and E.E. Sechler, eds., Prentice-Hall, Englewood Cliffs, New Jersey, pp.345-369.

Babcock, C.D. (1983). "Shell stability." *Journal of Applied Mechanics, ASME*, **50**:935-940.

Babcock, C.D. and Sechler, E.E. (1963). "The effect of initial imperfections on the buckling stress of cylindrical shells", *NASA TN D-2005*.

Berry, P.A. (1997). *Buckling under Axial Compression of Cylindrical Shells with Circumferential Weld Shrinkage Depression*, PhD Thesis, Department of Civil Engineering, University of Sydney, March, 1997.

Berry, P.A., Bridge, R.Q. and Rotter, J.M. (1996). "Imperfection measurement of cylinders using automated scanning with a laser displacement meter", *Strain*, **32(1)**: 3-7.

Berry, P.A., Rotter, J.M., and Bridge, R.Q. (2000). "Compression tests on cylinders with circumferential weld depressions", *Journal of Engineering Mechanics*, **126(4)**: 405-413.

Bisagni, C. (1999). "Experimental buckling of thin composite cylinders in compression", *AIAA Journal*, **37(2)**: 276-278.

Bornscheuer, F.W. and Hafner, L (1983). "The influence of an imperfect circumferential weld on the buckling strength of axially loaded circular cylindrical shells", *Proceedings, Third International Colloquium on Stability and Metal Structures*, Paris, pp.407-414.

Bornscheuer, F.W., Hafner, L. and Ramm, E. (1983). "Zur stabilität eines kreiszylindrs mit einer rundschweissnäht unter axialbelastung (On the stability of circular cylinder with a circumferential weld and axial load)", *Der Stahlbau*, **52(10)**: 313-318, (in German).

Brendel, B. and Ramm, E. (1980). "Linear and nonlinear stability analysis of cylindrical shells", *Computers and Structures*, **12**: 549-558.

Brush, D.O. and Almorth, B.O. (1975). *Buckling of Bars, Plates, and Shells*, McGraw-Hill, New York, N.Y.

BS 5061 (1974). *Specifications for Cylindrical Forage Tower Silos and Recommendations for Their Use*, British Standard Institution, London.

BSEN1002-1 (2001). *Metallic Materials-Tensile Testing-Part 1: Method of Test at Ambient Temperature*, European Committee for Standardization, Brussels.

Bucklin, R.A., Ross, I.J. and White, G.M. (1983). "The influence of grain pressure on the buckling loads of thin-walled bins", *ASAE, Paper No. 83-4005*.

Budiansky, B. (1976). *Buckling of Structures. Proc. IUTAM Symp.*, Cambridge, USA, June, 1974, Springer, Berlin, Heidelberg, and New York.

Budiansky, B. and Hutchinson, J.W. (1966). "A survey of some buckling problems", *AIAA Journal*, **4(9)**: 1505-1510.

Bushnell, D. (1981). "Buckling of shells-pitfall for designers." *AIAA Journal*, **19(9)**:1183-1226.

Bushnell, D. (1982). "Plastic buckling of various shells." *Journal of Pressure Vessel Technology, ASME*, **104**:51-72.

Bushnell, D. (1989). *Computerized buckling analysis of shells*, Kluwer Academic Publishers, Dordrecht, The Netherland.

Buzek, J.R. (1989). *Useful Information on the Design of Steel Bins and Silos*, American Iron and Steel Institute, Washington, D.C.; Steel Plate Fabricators Association, Inc., Westchester, IL, USA.

Calladine, C.R. (1972). "Structural consequences of small imperfections in elastic thin shells of revolution", *International Journal of Solids and Structures*, **8**: 679-697.

Calladine, C.R.(1995). "Understanding imperfection-sensitivity in the buckling of thin-walled shells." *Thin-Walled Structures*, **23**:215-235.

Cederbaum, G. and Arbocz, J. (1996) "On the reliability of the imperfection-sensitive long isotropic cylindrical shells", *Structural Safety*, **18(1)**, 1-9.

Chisholm, N.W.T. (1977). "Photogrammetry for cooling tower shape surveys", *Photogrammetric Record*, **9(50)**, 173-191.

Chryssanthopoulos, M.K. and Poggi, C. (1995). "Stochastic imperfection modelling in shell buckling strudies", *Thin-Walled Structures*, **23(1-4)**: 179-200.

Chryssanthopoulos, M.K. and Poggi, C. (2001). "Collapse strength of unstiffened conical shells under axial compression", *Journal of Constructional Steel Research*, **57(2)**: 165-184.

Chryssanthopoulos M.K., Giavotto, V. and Poggi, C. (1991) "Statistical Imperfection Models for Buckling Analysis of Composite Shells", *Buckling of Shell Structures on Land, in the Sea and in the Air*, J.F. Jullien, ed., Elsevier Applied Science London and New York, pp.1-10.

Chryssanthopoulos, M.K., Baker, M.J., and Dowling, P.J. (1991a). "Statistical analysis of imperfections in stiffened cylinders." *Journal of Structural Engineering, ASCE*, **117(7)**: 1979-1997.

Chryssanthopoulos, M.K., Baker, M.J., and Dowling, P.J. (1991b). "Imperfection modeling for buckling analysis of stiffened cylinders", *Journal of Structural Engineering, ASCE*, **117(7)**: 1998-2017.

Chryssanthopoulos M.K., Giavotto, V. and Poggi, C. (1991) "Statistical Imperfection Models for Buckling Analysis of Composite Shells", *Buckling of Shell Structures on Land, in the Sea and in the Air*, J.F. Jullien, ed., Elsevier Applied Science, London and New York, pp.1-10.

Chryssanthopoulos, M.K., Pariatmono, N. and Spagnoli, A. (1997). "Buckling tests of unstiffened and stiffened conical shells in compression", *Proceedings, International Conference on Carrying Capacity of Steel Shell Structures*, V. Krupka and P. Schneider, eds., October 1-3, Brno, Czech Republic, pp.16-23.

Clark, E. (1850). "The Britannia and Conway Tubular Bridges, with general inquiries on beams and on the properties of materials used in construction" Vol.1, Day and Son, Lincolin's Inn Fields, and John Weale, High Holborn, Lodon.

Clarke, M.J. and Rotter, J.M. (1988). *A Technique of the Measurement of Imperfections in Prototype Silos and Tanks*, University of Sydney, Research Report No. R565.

Cohen, A.G. (1966). "Buckling of axially compressed cylindrical shells with ring-stiffened edges", *AIAA Journal*, **4(10)**: 1859-1862.

Coleman, R., Ding, X.L. and Rotter, J.M. (1992). "The measurement of imperfection in full-scale steel silos", *Proceedings of 4th International Conference on Bulk Material Storage, Handling, and Transportation*, Institution of Engineers, Australia, Wollongong, July, pp.467-472.

Combescure, A.(1986). "Static and dynamic buckling of large thin shells", *Nuclear Engineering and Design*, **92**: 339-354.

Coppa, A.P. (1966). "Measurement of initial geometric imperfections of cylindrical shells", *AIAA Journal*, **4(1)**: 172-175.

Crisfield, M.A. (1981). "A fast incremental/iterative solution procedure that handles 'snap-through'". *Computers and Structures*, **13**:55-62.

Croll, J.G.A., Kaleli, F., and Kemp, K.O. (1979a). "Meridionally imperfect cooling towers", *J. Engrg. Mech. Div., ASCE*, **105(5)**: 761-777.

Croll, J.G.A., Kaleli, F., Kemp, K.O., and Munro, J. (1979b). "A simplified approach to the analysis of geometrically imperfect cooling towers", *Engineering Structures*, **1**: 92-98.

Danielson, D.A. (1974). "Theoretical method to investigate the post-buckling behavior by assuming the imperfections in the buckling mode", *Theory of Shell Stability*, Y.C. Fung and E.E Scheler, eds., Prentice Hall, Englewood Cliffs, N.J.

Deml, M. and Wunderlich, W. (1997). "Direct evaluation of the 'worst' imperfection shape in shell buckling", *Comput. Methods Appl. Mech. Engrg.* **149**: 201-222.

DIN 18800 Part 4 (1990). *Stahlbauten:stabilitätsfälle, schalenbeulen,* Deutsches Institut für Normung, Berlin.

Ding, X.L.(1992). *"Precise engineering surveying-application to the measurement of large scale steel silos."* PhD Thesis, University of Sydney, Australia.

Ding, X.L., Coleman, R. and Rotter, J.M. (1991). "A profile measurement system and its application in precise engineering surveying", *Proc. of 58th FIG PC Meeting and Int. Symp.* Beijing, pp.87-101.

Ding, X.L., Coleman, R. and Rotter, J.M. (1996a). "Surface profiling system for measurement of engineering structures", *Journal of Surveying Engineering, ASCE*, **122(1)**: 3-13.

Ding, X.L., Coleman, R. and Rotter, J.M. (1996b). "Technique for precise measurement of large-scale silos and tanks", *Journal of Surveying Engineering, ASCE*, **122(1)**: 14-25.

Donnell, L.H.(1934). "A new theory for the buckling of thin cylinders under axial compression and bending", *Trans. ASME*, **56**: 795-806.

Donnell, L.H. and Wan, C.C. (1950). "Effects of imperfections on buckling of thin cylinders and columns under axial compression". *Journal of Applied Mechanics*, **17(1)**:73-83.

Dowling, P.J. and Harding, J.E. (1982). "Experimental behaviour of ring and stringer stiffened shells", *Buckling of Shells in Offshore Structures*, J.E. Harding, P.J., and N. Agelidis, eds., Granada, London, pp.73-107.

Dowling, P.J., Harding, J.E., Agelidis, N. and Fahy, W. (1982). "Buckling of orthogonally stiffened cylindrical shells used in offshore engineering", *Buckling of Shells*, E. Ramm, ed., Springer-Verlag, Berlin, pp.239-273.

ECCS (1988). *Buckling of steel shells: European recommendations*. 4th Edition. European Convention for Constructional Steelwork, Brussels.

Elishakoff, I. and Arbocz, J. (1982). "Reliability of axially compressed cylindrical shells with random axisymmetric imperfections", *International Journal of Solids and Structures*, **18(7)**: 563-585.

Elishakoff, I. and Arbocz, J. (1985). "Reliability of axially compressed cylindrical shells with general nonsymmetric imperfections", *Journal of Applied Mechanics*, **52**:122-128.

Ellinas, C.P., Croll, J.G.A., and Kemp, K.O. (1980). "Cooling towers with circumferential imperfections", *J. Struct. Div., ASCE*, **106(12)**: 2405-2423.

ENV 1991-4 (1995). *Eurocode 1: Basis of Design and Actions on Structures, Part 4: Actions in Silos and Tanks*. European Committee for Standardization, Brussels.

ENV 1993-1-6 (1999). *Eurocode 3: design of steel structures. Part 1-6: general rules-supplementary rules for shell structures*. European Committee for Standardization, Brussels.

ENV 1993-4-1 (1999). *Eurocode 3: design of steel structures. Part 4-1: Silos*. European Committee for Standardization, Brussels.

Esong, I.E., Elghazouli, A.Y. and Chryssanthopoulos, M.K. (1998). "Measurement techniques for buckling sensitive composite shells", *Strain*, **34(1)**: 11-17.

Esslinger, M. and Geier, B. (1975). *Postbuckling behaviour of structures*. CISM, Springer, New York, N.Y.

Esslinger, M. and Geier, B. (1977). "Buckling loads of thin-walled circular cylinders with axisymmetric irregularities." *Steel Plated Structures: An International Symposium*, P.J., Dowling, J.E. Harding, and P.A. Frieze, eds. Crosby Lockwood Staples, London, U.K., pp.865-888.

Ethrog, U. (1986). "Measuring the deformations of storage tanks", *Photogrammetria*, **40**: 299-310.

Evans, W.T., Russell, R.M. and White, A. (1987). "Application of holographic interferometry to cylinder deformation", *Journal of Strain Analysis*, **22(2)**: 63-74.

Fischer, G. (1965). "Influence of boundary conditions on stability of thin-walled cylindrical shells under axial load and internal pressure", *AIAA Journal*, **3(4)**:736-738.

Flügge, W. (1932). "Die stabilität der kreiszylinderschale", *Ingenieur-Archiv*, **3(5)**:463-506.

Flügge, W. (1934). *Statik und Dynamic der Schalen*, 1st ed. Berlin: Springer, 1934.

Foster, C.G. (1987). "Axial compression buckling of conical and cylindrical shells", *Experimental Mechanics*, **27**: 255-261.

Fujii, F. and Choong, K.K. (1992). "Branch-switching in bifurcation of structures". *Journal of Engineering Mechanics, ASC E*, **118(8)**: 1578-1595.

Fung, Y.C. and Sechler, E.E. (1957). "Buckling of thin-walled circular cylinders under axial compression and internal pressure", *Journal of Aeronautical Science*, **24(5)**: 351-356.

Galletly, G.D. and Bart, R. (1956). "The effect boundary conditions and initial out-of-roundness on the strength of thin-walled cylinders subject to external hydrostatic pressure", *Journal of Applied Mechanics*, **23(3)**: 351-358.

Gaylord, E.H. and Gaylord, C.N. (1984). *Design of Steel Bins for Storage of Bulk Solids*, Prentice-Hall, Englewood Cliffs, N.J.

Godoy, L.A. (1987). "A simplified bending analysis of imperfect spherical pressure vessels", *Int. J. Pressure Vessels and Piping*, **27**: 385-399.

Godoy, L.A. (1993). "On loads equivalent to geometrical imperfections in shells", *Journal of Engineering Mechanics*, **119(1)**: 186-190.

Godoy, L.A., Quinones, D. and Wagner, R. (1988). "Shallow shells with local deviations in shape", *IASS Bulletin*, **No.66:** 55-62.

Gorman, D.J. and Evan-Iwanowski, R.M. (1970). "An analytical and experimental investigation of the effects of large prebuckling deformations on the buckling of clamped thin-walled circular cylindrical shells subject to axial loading and internal pressure". *Dev. in Theor. and Appl. Mech.* **4**:415-426.

Goto, Y. and Zhang, C. H. (1999). "Plastic buckling transition modes in moderately thick cylindrical shells", *Journal of Engineering Mechanics*, **125(4)**: 426-434.

Green, D.R. and Nelson, H.M. (1982). "Compression tests on large-scale stringer-stiffened tubes", *Buckling of Shells in Offshore Structures*, J.E. Harding, P.J. Dowling, and N. Agelidis, eds., Granda, London, pp.25-43.

Greiner, R. and Derler, P. (1995). "Effect of imperfections on wind-loaded cylindrical shells", *Thin-Walled Structures*, **23**: 271-281.

Guggenberger, W. (1995). "Buckling and postbuckling of imperfect cylindrical shells under external pressure", *Thin-Walled Structures*, **23**: 351-366.

Guggenberger, W. (1996). "Effect of geometric imperfections taking into account the fabrication process and consistent residual stress fields of cylinders under local axial loads", *Proc., Int. Workshop on Imperfections in Metal Silos*, INSA, Lyon, April 1996, pp.219-231.

Guggenberger, W. (1997). "Collapse, failure analysis and repair of a high-tensile steel digester tank", *Proceedings, International Conference on Carrying Capacity of Steel Shell Structures*, V. Krupka and P. Schneider, eds., October 1-3, Brno, Czech Republic, pp.324-332.

Guggenberger, W. (1998). "Proposal for design rules of axially loaded steel cylinders on local supports", *Thin-Walled Structures*, **31**: 169-185.

Gupta, A.K. and Al-Dabbagh, A. (1982). "Meridional imperfection in cooling tower design: update", *J. Struct. Div. ASCE*, **108(8)**: 1697-1708.

Hang, K.J. and Tong, G.S. (1985). "Analysis of hyperbolic cooling towers with local imperfections", *Engineering Structures*, **7**: 273-279.

Hansen, J.S. (1977). "General random imperfections in the buckling of axially loaded cylindrical shells", *AIAA Journal*, **15(9)**: 1250-1256.

Hibbitt, Karlsson & Sorensen (1998). *ABAQUS/Standard Theory and User's Manuals*, Pawtucket, R.I.

Hoff, N.J. (1961). "Buckling of thin shells", *Proceedings, Aerospace Symposium of Distinguished Lecturers in Honor of Dr. Theodore von Kármán on his 80th Anniversary.* The Institute of Aerospace Science, New York.

Hoff, N.J. (1965). "Low buckling stresses of axially compressed circular cylindrical shells of finite length", *Journal of Applied Mechanics, ASME*, **32**:533-541.

Hoff, H.J. (1966). "The perplexing behavior of thin cylindrical shells in axial compression", *Israel Journal of Technology*, **4(1)**:1-28.

Hoff, N.J. and Rehfield W. (1965). "Buckling of axially compressed cylindrical shells at stresses smaller than the classical critical value", *Journal of Applied Mechanics, ASME*, **32**:542-546.

Hoff, N.J. and Soong, T.C. (1965). "Buckling of circular cylindrical shells in axial compression", *International Journal of Mechanical Sciences*, **7(7)**:489-520.

Hoff, N.J. and Soong, T.C. (1969). "Buckling of axially compressed circular cylindrical shells with non-uniform boundary conditions", *Thin Walled Steel Structures*, K.C. Rockey and H.V. Hill, eds., Crosby Lockwood and Son, Ltd., London.

Hoff, N.J., Madsen, W.A., and Mayers, J. (1966). "Postbuckling equilibrium of axially compressed circular cylindrical shells", *AIAA Journal*, **4**:126-133.

Holst, J.M.F.G., Rotter, J.M. and Calladine, C.R. (1999). "Imperfections in cylindrical shells resulting from fabrication misfits", *Journal of Engineering Mechanics*, **125(4)**: 410-418.

Holst, J.M.F.G., Rotter, J.M. and Calladine, C.R. (2000). "Imperfections and buckling in cylindrical shells with consistent residual stresses", *Journal of Constructional Steel Research*, **54**: 265-282.

Holt, M. (1952). "A procedure for determining the allowable out-of-roundness for vessels under external pressure", *Transactions of the American Society of Mechanical Engineers*, **74**: 1225-1230.

Hornung, U. and Saal, H. (2002). "Buckling loads of tank shells with imperfections", *International Journal of Non-linear Mechanics*, **37**: 605-621.

Horton, W.H. (1977). *On the Elastic Stability of Shells*, NASA CR-145088.

Hübner, A., Teng, J.G. and Saal, H. (2003a). "Buckling behavior of extensively welded steel cylinders", to be published.

Hübner, A., Teng, J.G. and Saal, H. (2003b). "Large welded steel cylinders: imperfections, residual stresses and buckling behaviour, in preparation.

Hutchinson, J. (1965). "Axial buckling of pressurized imperfect cylindrical shells", *AIAA Journal* **3(8)**: 1461-1466.

Hutchinson, J.W., Tennyson, R.C. and Muggeridge, D.B. (1971). "Effect of a local axisymmetric imperfection on the buckling behavior of a circular cylindrical shell under axial compression", *AIAA Journal*, **9(1)**: 48-52.

Ignatenko, V.M. (1978). "Failures of structural steel bins and critical design consideration", *Proceedings, Metal Structures Conference*, Institution of Engineers, Australia, Perth.

ISO 11697 (1995)...*Bases for Design of Structures-Loads Due to Bulk Materials*, International Organization for Standardization, Switzerland.

Jasper, M.T. and Sullivan, J.W.W. (1931). "The collapsing strength of steel tubes", *Transactions of the American Society of Mechanical Engineers*, **53**: 219-245.

Jenkyn, R.T. and Goodwill, D.J. (1987). "Silo Failures: Lessons to be Learned", *Engineering Digest*, September, pp.17-22.

Jensen, H. and Turnell, C. (1997). "Large steel grain silos." *Structural Engineering International*, **7(1)**: 49-52.

JIS B8511 (1987). *Construction of Welded Aluminum and Aluminum Alloy Cylindrical Silos*, Japanese Industrial Standard, Translated and published by Japanese Standards Association, Tokyo.

Jullien, J.F. (1991). Buckling of Shell Structures, on Land, in the Sea and in the Air. *Proc. Int. Coll.*, Lyon, September 1991. Elsevier Applied Science, London and New York.

Jullien, J.F. (1996). "Alternative methods of measuring geometric imperfections with an assessment of their advantages and disadvantages", *Proceedings, International Workshop on Imperfections in Metal Silos: Measurement, Characterisation, and Strength Analysis*, CA-Silo, Lyon, France, April, pp.191-200.

Kármán T.H. Von and Tsien, H.S. (1941). "Buckling of circular cylindrical shells under axial compression". *Journal of the Aeronautical Sciences*, **8**: 303-312.

Kempner, J. (1954). "Postbuckling behavior of axially compressed circular cylindrical shells", *Journal of Aeronautical Science*, **21**:329-335.

Knoedel, P. and Ummenhofer, T. (1996). "Substitute imperfections for the prediction of buckling loads in shell design", *Proceedings, International Workshop on Imperfections in Metal Silos*, CA-Silo, Lyon, France, 19 April, 1996, pp.87-102.

Knoedel, P., Ummenhofer, T. and Schulz, U. (1995). "On the modeling of different types of imperfections in silo shells", *Thin-Walled Structures*, **23(1-4)**: 283-293.

Koiter, W.T. (1945). *On the Stability of Elastic Equilibrium*, PhD thesis, Technische Hooge School, Delft, 1945 (in Dutch). English translation by E. Riks: Technical Report AFFDL-TR-70-25, Air Force Flight Dynamic Laboratory, Wright-Patterson Air Force Base, Ohio, 1970.

Koiter, W.T. (1963a). "The effect of axisymmetric imperfections on the buckling of cylindrical shells under axial compression", *Proceedings of Koninklijke Nederlandse Akademie van Wetenschappen*, **Series B, 66(5)**: 265-279.

Koiter, W.T. (1963b). "Elastic stability and postbuckling behavior", *Proceedings, Symposium Nonlinear Problems*, University of Wisconsin, Madison, pp.257-275.

Kreyszig E. (1999). *Advanced Engineering Mathematics*. 8th ed. New York: John Wiley & Sons, 1999.

Krishnakumar, S. and Foster, C.G. (1989). "Whole-field optical examination of cylindrical shell deformation", *Experimental Mechanics*, **29**:16-22.

Krishnakumar, S. and Foster, C.G. (1991) "Buckling of Axially Compressed Cylindrical Shells with Local Geometric imperfections", *Buckling of Shell Structures on Land, in the Sea and in the Air*, J.F. Jullien, ed., Elsevier Applied Science, London and New York, pp.33-42.

Lambert, F.W. (1968). *The Theory and Practical Design of Bunkers*, British Constructional Steelwork Association, Publication No.32.

Lancaster, E.R., Calladine, C.R. and Palmer, S.C. (2000). "Paradoxical buckling behavior of thin cylindrical shell under axial compression", *International Journal of Mechanical Sciences*, **42(5)**: 843-865.

Leggett, D.M.A. and Jones, R.P.N. (1942). "The behavior of a cylindrical shell under axial compression when the buckling load has been exceeded", *Aeronautical Research Council*, London, R.& M. 2190.

Lin, X. and Teng, J.G. (2003) "Iterative Fourier decomposition of imperfection measurements at non-uniformly distributed sampling points", *Thin-Walled Structures*, **41(10)**:901-924.

Lo, H., Crate, H. and Schwartz, E.B. (1951). *Buckling of Thin-Walled Cylinder under Axial Compression and Internal Pressure, NACA TR 1027.*

Lock, W.H.(1989). *The Behaviour of Thin-walled Steel Cylinders with Single and Multiple Circumferential Welded Joints under Axial Compression, Part II Project,* Department of Engineering, University of Cambriage.

Lorenz, R. (1908). "Achsensymmetrische verzerrungen in dünnwandigen hohlzylindern", *Zeitschrift des Vereines Deutscher Ingenieure*, **52(43)**:1706-1713.

Lu, S.V. and Nash, W.A. (1962). *Buckling of Initially Imperfect Axially Compressed Cylindrical Shells, NACA TN D-1510.*

Lunchick, M.E. and Short, R.D. (1957). "Behavior of cylinders with initial shell deflections", *Journal of Applied Mechanics*, **24**: 559-564.

Lundquist, E.E.(1933). "Strength tests of thin-walled duraluminium cylinders in compression", *NACA Report No. 473, National Advisory Committee for Aeronautics*, Washington.

Mandal, P. Calladine, C.R. (2000). "Buckling of thin cylindrical shells under axial compression", *International Journal of Solids and Structures*, **37**: 4509-4525.

Mclean, R.F. (1984). "Safer silos." *Developments in thin-walled structures-2*, J. Rhodes and A.C. Walker, eds., Elsevier Applied Science, London, 211-237.

Michielsen, H.F. (1948). "The behaviour of thin cylindrical shells after buckling under axial compression", *Journal of Aeronautical Science*, **15**: 738-744.

Miller, C.D. (1982). "Summary of buckling tests on fabricated cylindrical shells in USA", *Buckling of Shells in Offshore Structures*, J.E. Harding, P.J., and N. Agelidis, eds., Granada, London, pp.429-446.

Miller, C.D. and Grove, R.B. (1986). "Pressure testing of large-scale torispherical heads subject to knuckle buckling", *International Journal of Pressure Vessels and Piping*, **22**: 147-159.

Moss, M. (1990). "Light measurement – for more accurate tank calibration", *Petroleum Review*, April, pp.174-178.

Moy, S.S. and Niku, S.M. (1983). "Finite element techniques for the analysis of cooling tower shells with geometric imperfections", *Thin-Walled Structures*, **1**: 239-263.

Ohira, H. (1961). "Local buckling theory of axially compressed cylinders", *Proceedings of 11th Japanese National Congress on Applied Mechanics*, pp.37-41.

Ohira, H. (1963). "Linear local buckling theory of axially compressed cylinders and various eigenvalues", *Proceedings of 5th International Symposium on Space Technology and Science*, Tokyo, pp.511-526.

Odland, J. "Buckling resistance of unstiffened and stiffened circular cylindrical shell structures", *Norwegian Maritime Research*, **6(3)**: 2-22.

Papo, H. and Shmutter, B. (1978). "Tank calibration by sterophotogrammetry", *Photogrammetria*, **34**: 101-109.

Pavlovic, P. (1997). "The testing and repair of steel silo", *Construction and Building Materials*, **11(5-6)**: 353-363.

Pham, L. and Mansell, D.S. (1985) "Survey of research needs for metal structures." *Proceedings, Metal Stmructures Conference*, Institution of Engineers, Australia, Melbourne, pp.172-177.

Pinkney, R.B., Stephens, M.J., Murray, D.W. and Kulak, G.L. (1983). "Use of measured imperfections to predict the buckling of axially loaded cylindrical shells", *Can. J. Civ. Eng.* **10**: 662-669.

Pircher, M. and Bridge, R. (2001a). "The influence of circumferential weld-induced imperfections on the buckling of silos and tanks", *Journal of Constructional Steel Research*, **57**:569-580.

Pircher, M. and Bridge, R. (2001b). "Buckling of thin-walled silos and tanks under axial load-some new aspects", *Journal of Structural Engineering*, **127(10)**: 1129-1136.

Pircher, M., Berry, P.A., Ding, X.L. and Bridge, R.Q. (2001). "The shape of circumferential weld-induced imperfections in thin-walled steel silos and tanks", *Thin-Walled Structures*, **39**: 999-1014.

Poggi, C. (1996). "Bifurcation and limit points in unstiffened cones under axial compression", *Proceedings, International Workshop on Imperfections in Metal Silos*, CA-Silo, Lyon, France, 19 April, 1996, pp.141-152.

Ramm, E. (1981). "Strategies for tracing nonlinear response near limit points". *Nonlinear Finite Element Analysis in Structural Mechanics*, W. Wunderlich, E. Stein and K.J. Bathe eds., Spring-Verlag, New York, pp.63-89.

Ramm, E. (1982). Buckling of Shells. *Proc. (2 volumes) State-of -the-Art Coll.*, Stuttgart, May, 1982. Stuttgart: Uniersität, Institut für Baustatik., 1982.

Ravenet, J. (1981). "Silo problems", *Bulk Solid Handling*, **1(4)**: 667-679.

Ravenet, J. (1983). "The development of industrial silos throughout the world during the last 100 years", *Bulk Solid Handling*, **3(1)**: 127-140.

Ravn-Jensen, K. and Tvergaard, V. (1990). "Effect of residual stresses on plastic buckling of cylindrical shells", *International Journal of Solids and Structures*, **26(9)**: 993-1004.

Riks, E.(1979). "An incremental approach to the solution of snapping and buckling problems". *International Journal of Solids and Structures*, **15**:529-551.

Robertson, A. (1928). "The strength of tubular struts", Report and Memo No. 1185. *Technical Report Aeronautical Research Committee*, **Vol. III**, 935-975.

Rotter, J.M. (1983). "Stress amplifications in unstiffened steel silos and tanks". *Research Report R437*, School of Civil and Mining Engineering, University of Sydney, Sydney, Australia.

Rotter, J.M. (1985a). Local Inelastic Collapse of Pressurized Thin Cylindrical Steel Shells under Axial Compression, *Research Report R502*, School of Civil and Mining Engineering, University of Sydney, Sydney, Australia.

Rotter, J.M. (ed.) (1985b). *Design of Steel Bins for the Storage of Bulk Solids*, School of Civil and Mining Engineering, University of Sydney, Australia.

Rotter, J.M. (1985c). "Buckling under axial compression", *Design of Steel Bins for the Storage of Bulk Solids*, School of Civil and Mining Engineering, University of Sydney, Australia.

Rotter, J.M. (1985d). "Buckling of ground-supported cylindrical steel bins under vertical compressive wall loads", *Proceedings, Metal Structures Conference, Institution of Engineers*, Australia, Melbourne, May, 1985, pp.112-127.

Rotter, J.M. (1985e) "Stability Problems in Cylindrical Bins under Axial Compression", *Proceedings, Joint US/Australian Workshop on the Loading, Analysis and Stability of Thin Shell Bins, Tanks and Silos*, University of Sydney, March 1985, pp 106-117.

Rotter, J.M. (1988). "Calculated buckling strengths for the cylindrical wall of 10,000 tonne silos at Port Kembla", *Investigation Report S663*, School of Civil and Mining Engineering, University of Sydney, June.

Rotter, J.M. (1990). "Local collapse of axially compressed pressurized thin steel cylinders", *Journal of Structural Engineering, ASCE*, **116(7)**: 1955-1970.

Rotter, J.M. (1995a). "Challenges for the future in designing bulk solids storages", *Containment Structures: Risk, Safety and Reliability, Proceedings of the IABSE Colloquium*, B. Simpson, ed. 11-12 July, 1995, London, UK, pp.11-34.

Rotter, J.M. (1995b). "Proposal for cylinder axial compression buckling strength to be described in terms of amplitude of imperfection", *ECCS TWG8.4, CEN TC250/SC3 PT3 and PT4 Working Paper*, May, 1995.

Rotter, J.M. (1996). "Buckling and collapse in internally pressurized axially compressed silo cylinders with measured axisymmetric imperfections: imperfections, residual stresses and local collapse", *Proceedings, International Workshop on Imperfections in Metal Silos*, INSA, Lyon, April 1996, pp.119-139.

Rotter, J.M. (1997). "Pressurised axially compressed cylinders", *Proceedings, International Conference on Carrying Capacity of Steel Shell Structures*, 1-3 October, 1997, Brno, Czech Republic, pp.354-360.

Rotter, J.M. (1998a). "Development of proposed European design rules for buckling of axially compressed cylinders", *Advances in Structural Engineering*, **1(4)**: 273-286.

Rotter, J.M. (1998b). "Shell structures: the new European standard and current research needs." *Thin-Walled Structures*, **31(1-3)**: 3-23.

Rotter, J.M. (1998c). "Design standards and calculations for imperfect pressurised axially compressed cylinders", *Proceedings, International Conference on Carrying Capacity of Steel Shell Structures*, October, 1997, Brno, pp.354-360.

Rotter, J.M. (2001). *Guide for the Economic Design of Circular Metal Silos*, Spon Press, London and New York, 2001.

Rotter, J.M. (2003) "Buckling of cylindrical shells under axial compression", *Buckling of Thin Metal Shells*, J.G. Teng and J.M. Rotter, eds, Spon Press, London, pp.42-87.

Rotter, J.M. and Seide, P. (1987). "On the design of unstiffened cylindrical shells subject to axial load and internal pressure", *Stability of Plate and Shell Structures, Proceedings, of ECCS Colloquium*, P. Dubas and D. Vandepitte, eds., 6-8 April, 1987, Ghent University, pp.539-548.

Rotter, J.M. and Teng, J.G. (1989). "Elastic Stability of Cylindrical Shells with Weld Depressions", *Journal of Structural Engineering, ASCE*, **115(5)**: 1244-1263.

Rotter, J.M. Coleman, R., Ding, X.L. and Teng, J.G. (1992) "The measurement of imperfections in cylindrical silos for buckling strength assessment", *Proceedings, 4th International Conference on Bulk Materials: Storage, Handling and Transportation.* Institution of Engineers, Australia, Wollongong, July, pp.473-479.

Rotter, J.M., Jumikis, P.T., Fleming, S.P. and Porter, S.J. (1989). "Experiments on the buckling of thin-walled model silo structures". *Journal of Constructional Steel Research*, **13**:271-299.

Saal, H. (1977). "Buckling of circular cylindrical shells under combined axial compression and internal pressure", *Proceedings, Second International Colloquium on Stability of Steel Structures*, April, 1977, Liege.

Saal, H., Kahmer, H. and Reif, A. (1979). "Beullasten axial gedruckter kreiszylinderschalen mit innendruck-neue versuche und vorshriften", *Der Stahlbau*, **48(9)**: 262-269.

Schmidt, H. (2000). "Stability of steel shell structures –General report", Journal of Constructional Steel Research, **55(1-3)**, 159-181.

Schmidt, H. and Swadlo, P. (1996). "Two buckling tests demonstrating the influence of the pattern of geometric and structural imperfections on the axial compressive buckling strength of cylindrical shells", *Proceedings, International Workshop on Imperfections in Metal Silos*, INSA, Lyon, April 1996, pp.181-190.

Schmidt, H. and Swadlo, P. (1997). "Strength and stability design of unstiffended cylinder/cone/cylinder and cone/cone shell assemblies under axial compression", *Proceedings, International Conference on Carrying Capacity of Steel Shell Structures*, V. Krupka and P. Schneider, eds., October 1-3, Brno, Czech Republic, pp.361-367.

Schmidt, H. and Winterstetter, Th. A. (1999). "Buckling interaction strength of cylindrical steel shells under axial compression and torsion", *Advances in Steel Structures, Proceedings, Second International Conference on Advances in Steel Structures*, S.L. Chan and J.G. Teng, eds., Elsevier, pp.597-604.

Schulz, U. (1970). *On the Stability of Cylindrical Shells*, PhD Thesis, University of Karlsruhe, (in German).

Scott, N.D., Harding, J.E. and Dowling, P.J. (1987). "Fabrication of small scale stiffened cylindrical shells", *Journal of Strain Analysis for Engineering Design*, **22(2)**: 97-102.

Shmutter, B. and Ethrog, U. (1971). "Calibration of storage tanks", *Photogrammetric Engineering*, **37(3)**: 261-266.

Shover, D.R. (1968). *On the Problem of Geometrical Imperfections in Thin Circular Cylindrical Shells*, PhD Thesis, California Institute of Technology, Pasadena.

Simmonds, J.G. and Danielson, D.A. (1970). "New results for the buckling load of axially compressed cylindrical shells subject to relaxed boundary conditions", *Journal of Applied Mechanics*, **37**: 93-100.

Singer, J. (1982a). "Buckling experiments on shells – a review of recent developments", *Solid Mechanics Archives*, **7**: 213-313.

Singer, J. (1982b). "The status of experimental buckling investigations of shells", *Buckling of Shells*, E. Ramm, ed., Springer-Verlag, New York, pp.501-534.

Singer, J. (1997). "Experimental studies in shell buckling", *Proceedings, 1997 38th AIAA/ASME/ASCE/AHS/ASC Structures, Structural Dynamics and Materials Conference*, Vol. 3, pp.1922-1932.

Singer, J. and Abramovich, H. (1995). "The development of shell imperfection measurement techniques", *Thin-Walled Structures*, **23**: 379-398.

Singer, J., Abramovich, H. and Yaffe, R. (1978). "Initial imperfection measurements of stringer-stiffened shells", *TAE Report No.330*, Department of Aeronautical Engineering, Technion, December, 1978.

Singer, J., Abramovich, H. and Yaffe, R. (1979). "Initial imperfection measurements of stringer-stiffened shells and buckling predictions", *Proc. 21st. Israel Annual Conference on Aviation and Astronautics, Israel Journal of Technology*, **17**:324-338.

Singer, J., Arbocz, J. and Babcock, C.D. (1971) "Buckling of Imperfect Stiffened Cylindrical Shells under Axial Compression", *AIAA Journal*, **9(1)**: 68-75.

Singer, J., Arbocz, J. and Weller, T. (2002). *Buckling Experiments: Experimental Methods in Buckling of Thin-Walled Structures, Volume 2: Shells, Built-up Structures, Composites, and Additional Topics,* John Wiley & Sons, Inc., New York.

Song, C.Y. (2002). *Buckling of Cylindrical Shells under Non-uniform Stress States*, PhD Thesis, Department of Civil and Structural Engineering, The Hong Kong Polytechnic University.

Southwell, R.V. (1914). "On the general theory of elastic stability", *Philosophical Transactions of the Royal Society of London, Series A*, **213**: 187-244.

Speicher, G. and Saal, H. (1991). "Numerical calculation of limit loads for shells of revolution with particular regard to the applying equivalent initial imperfections", *Buckling of Shell Structures on Land, in the Sea and in the Air,* J.F. Jullien, ed., Elsevier Applied Science, London, pp.466-475.

Stewart, R.T. (1906). "Collapsing pressure of Bessemer steel lap-welded tubes, three to ten inches in diameter", *Transactions of the American Society of Mechanical Engineers*, **27**: 730-822.

Stein, M. (1962). "The effect on the buckling of perfect cylinders of prebuckling deformations and stresses induced by edge support", *Collected Papers on Instability of Shell Structures, NASA Technical note*, D1510, pp.217-226.

Tam, C.K.W. and Croll, J.G.A. (1988). "Elastic stress concentrations in cylindrical shells containing local damage", *Applied Solid Mechanics*, Vol. 2, A.S. Tooth and J. Spence, eds, Elsevier Applied Science, Barking, United Kingdom.

Teng, J.G. (1994). "Plastic collapse at lap-joints in pressurized cylinders under axial load", *Journal of Structural Engineering, ASCE*, **120(1)**: 23-45.

Teng, J.G. (1996). "Buckling of thin shells: recent advances and trends." *Applied Mechanics Reviews, ASME*, **49(4)**: 263-274.

Teng, J.G. and Rotter, J.M. (1992). "Buckling of pressurized axisymmetrically imperfect cylinders under axial loads", *Journal of Engineering Mechanics, ASCE*, **118(2)**: 229-247.

Teng, J.G. and Rotter, J.M. (1996). "Structural design of steel silos: a decade of progress". *Proceedings of Asia-Pacific Conference on Shell and Spatial Structures*, T.T. Lan, ed., May 21-25, Beijing, China, pp.74-81.

Teng, J.G. and Song, C.Y. (1999). "On the nonlinear analysis of shells with eigenmode-affine imperfections", *Advances in Steel Structures, Proceedings, Second International Conference on Advances in Steel Structures*, S.L. Chan and J.G. Teng, eds., Elsevier, pp.687-695.

Teng, J.G. and Song, C.Y. (2001). "Numerical models for nonlinear analysis of elastic shells with eigenmode-affine imperfections", *International Journal of Solids and Structures*, **38(18)**: 3263-3280.

Teng, J.G. and Zhao, Y., and Lam, L. (2001). "Techniques for buckling experiments on steel silo transition junctions", *Thin-Walled Structures*, **39**: 685-707.

Tennyson, R.C. (1964). "An Experimental Investigation of the Buckling of Circular Cylindrical Shells in Axial Compression Using the Photoelastic Technique", *UTIAS Report No. 102*, Institute of Aerospace Science, University of Toronto, Toronto, Canada.

Tennyson, R.C. and Muggeridge, D.B. (1969). "Buckling of axisymmetric imperfect circular cylindrical shells under axial compression", *AIAA Journal*, **7(11)**: 2127-2131.

Timoshenko, S.P. (1910). "Einige stabilitätsprobleme aus der elastizitätstheorie." *Zeitschrift für Mathematik und Physik*, **58(4)**:337-385.

Timoshenko, S.P. (1934). *Theory of Elastic Stability*, 1st ed. New York: McGraw-Hill, 1936.

Trahair, N.S., Abel, A., Ansourian, P., Irvine, H.M., and Rotter, J.M. (1983). *Structural Design of Steel Bins for Bulk Solids*, Australian Institute of Steel Construction, Sydney.

Wagner, W. and Wriggers, W. (1988). "A simple method for the calculation of post-critical branches". *Engineering Computations*, **5**: 103-109.

Walker, A.C. and Sridharan, S. (1977). "Buckling of compressed, longitudinal stiffened cylindrical shells", BOSS'79. *Proceedings, 2nd. International Conference on the Behaviour of Off-shore Structures*, Imperial College, London, pp.341-356.

Walker, A.C., Andronicou, A. and Shridharan, S. (1982). "Experimental investigation of the buckling of stiffened shells using small scale models", *Buckling of Shells in Offshore Structures*, J.E. Harding, P.J., and N. Agelidis, eds., Granada, London, pp.45-71.

Weare, F. (1989). "Silo design and construction." In *Silos: Design, Construction and Repair,* Institution of Civil Engineers, Structural Engineering Group Half Day Meeting, Lodon, 15, November, pp.9-11.

Weingarten, V.I., Morgan, E.J. and Seide, P. (1965). "Elastic stability of thin-walled cylindrical and conical shells under combined internal pressure and axial compression", *AIAA Journal*, **3(6)**: 1118-1125.

Wempner, G.A. (1971). "Discrete approximations related to non-linear theories of solids". *International Journal of Solids and Structures*, **7**:1581-1599.

Wood, J.G.M. (1980). "Thin-walled silo structures, failure, testing and design", *Thin-Walled Structures: Recent Technical Advances and Trends in Design, Research, and Construction*, J. Rhodes and A.C. Walker, eds., Wiley, New York, pp.339-350.

Wood, J.G.M. (1997). "Silos: evolution by failure." *Structural Engineering International*, **7(2)**: 116-117.

Wozniak, R.S. (1979). "Steel tanks", *Structural Engineering Handbook*, 2nd Edition, Section 23, E.H. Gaylord and C.N. Gaylord, eds., McGraw-Hill, New York.

Wriggers, P., Wagger, W. and Miehe, C. (1987). "A quadratically convergent procedure for the calculation of stability points in finite element analysis". *Comput. Methods Appl. Mech. Engrg.*, **70**:329-347.

Wunderlich, W. and Albertin, U. (2000). "Analysis and load carrying behavior of imperfection sensitive shells", *Int. J. Numer. Meth. Engng.* **47**: 255-273.

Yamaki, N. (1984). *Elastic Stability of Circular Shells*, North Holland, Amsterdam.

Yamaki, N. and Kodama, S. (1972). "Buckling of circular cylindrical shells under axial compression-report 3: solutions based on Donnell type equations considering prebuckling edge rotations", *Report of the Inst. of High Speed Mech.*, No. 25, Tohoku, Univ., pp.99-141.

Zhao, Y. (2001) *Stability and Strength of Steel Silo Transition Junction*, PhD Thesis, Department of Civil and Structural Engineering, The Hong Kong Polytechnic University.

Zhao, Y. and Teng, J.G. (2001). "Buckling experiments on cone-cylinder intersections under internal pressure", *Journal of Engineering Mechanics*, **127(12)**: 1231-1239.

Zhu, E., Mandal, P. and Calladine, C.R. (2002). "Buckling of thin cylindrical shells: an attempt to resolve a paradox", *International Journal of Mechanical Sciences*, **44**: 1583-1601.